DRUG DELIVERY TO THE BRAIN USING POLYMER THERAPEUTICS AS AN INTRANASAL PLATFORM FOR PEDIATRIC GLIOBLASTOMA TREATMENT

Doctoral Thesis: Tetiana Melnyk

Supervisors:
Prof. María Jesus Vicent
Dr. Inmaculada Conejos-Sánchez

Valencia, January 2024

UNIVERSITAT POLITÈCNICA DE VALÈNCIA
CENTRO INVESTIGACION PRINCIPE FELIPE

DRUG DELIVERY TO THE BRAIN USING POLYMER THERAPEUTICS AS AN INTRANASAL PLATFORM FOR PEDIATRIC GLIOBLASTOMA TREATMENT

Doctoral Thesis
Tetiana Melnyk

Supervisors:
Prof. María Jesus Vicent
Dr. Inmaculada Conejos-Sánchez

Tutor:
Dr. Ramon Martinez-Mañez

Valencia, January 2024

ABSTRACT

Malignant brain and central nervous system tumors account for ~21% of tumors in children and represent the second leading cause of pediatric cancer deaths after leukemia. Standard chemotherapy allows a ~95% five-year survival rate for patients with low-grade gliomas. Unfortunately, high-grade gliomas remain generally incurable and suffer from high mortality rates – a 4.7% five-year survival for glioblastoma multiform (GBM) patients and less than one year in patients with diffuse intrinsic pontine glioma (DIPG). Low levels of drug delivery through the blood-brain barrier (BBB) and the associated poor survival rate highlight the necessity for novel treatment approaches for an unmet clinical need.

Intranasal administration offers a promising non-invasive approach that circumvents hepato-gastrointestinal metabolism and the BBB, thereby enabling direct nose-to-brain delivery. Polypeptide-based materials, particularly polyglutamates (PGAs), represent excellent candidates for brain delivery due to their biodegradability and multivalency, which supports the covalent introduction of drugs and targeting moieties to facilitate the nose-to-brain transition. Covalent conjugation of therapeutic agents to the polymeric main chain offers prolonged stability in the blood circulation and increased control over the drug release in the tumor microenvironment if adequately designed considering endogenous triggers, including acidic pH, an increased reductive environment, or the overexpression of specific proteases.

This thesis focuses on developing novel, rationally-designed PGA-drug conjugates as a safe and efficient intranasal platform for targeted delivery and drug release in the brain as a pediatric glioma treatment. We developed a family of PGA-drug conjugates incorporating the CDK inhibitor palbociclib that employed different stimuli-responsive linkers and varying drug loading levels. The significance of conformation, geometry, and topology of carriers in drug delivery systems is often overlooked and inadequately investigated, making it an intriguing research area with the potential to uncover crucial aspects of drug delivery systems designed rationally. In this thesis, we studied the effect of the conjugated hydrophobic drug palbociclib on the solution conformation of linear and star-shaped PGAs. We demonstrated system evolution upon increased drug loading with small-angle X-ray scattering and circular dichroism. Moreover, we established a link between conjugate conformation and their biological activity, as evaluated in patient-derived GBM and DIPG cells. Our findings illustrated the necessity of a deep understanding of the physico-chemical properties of studied nanosystems that can aid in predicting their biological outcome.

For the rapid development of an intranasal formulation based on PGA carriers, we successfully established an ex vivo screening platform based on vertical Franz diffusion cells with sheep mucosa. We evaluated several systems based on linear and star-shaped PGA with conjugated moieties (including docosahexaenoic acid, hyaluronic acid, odorranalectin), crosslinked particles (via azide-alkyne cycloaddition or disulfide bonds), and physical mixtures with a hyaluronic acid cross polymer (HA-CP®). After intranasal administration with selected candidates, we performed biodistribution studies, followed by ex vivo quantification with the IVIS spectrum in vivo imaging system and fluorescent assays after organ homogenization and brain histological studies. The obtained data demonstrated nose-to-brain transportation, internalization of conjugates in the olfactory bulb, and, most interestingly, robust diffusion through different brain areas, even reaching the hippocampus. We also scaled up selected systems and preparations for biological evaluation in an in vivo model that is currently ongoing. Overall, we were able to design, develop, and validate different PGA-based platforms capable of arriving at the brain via intranasal, which might be the base for the treatment of multiple brain-related disorders.

RESUMEN

Los tumores malignos del cerebro y del sistema nervioso central representan el 21% de los tumores en niños y son la segunda causa principal de muerte por cáncer pediátrico después de la leucemia. La tasa de supervivencia de gliomas de bajo grado a cinco años con quimioterapia estándar es un 95 %. Desafortunadamente, los gliomas de alto grado siguen siendo incurables y poseen altas tasas de mortalidad: una supervivencia a cinco años del 4,7 % para pacientes con glioblastoma multiforme (GBM) y menos de un año en pacientes con glioma pontino intrínseco difuso (DIPG). Los bajos niveles de penetración del fármaco a través de la barrera hematoencefálica y la baja tasa de supervivencia asociada resaltan en la necesidad de nuevas propuestas de tratamiento para esta necesidad clínica no cubierta.

La administración intranasal ofrece un enfoque no invasivo prometedor que elude el metabolismo hepato-gastrointestinal y la barrera hematoencefálica, constituyendo una ruta directa de la nariz al cerebro. Los materiales basados en polipéptidos y, en particular, los poliglutamatos (PGA) representan excelentes candidatos para la administración de agentes terapéuticos en el cerebro debido a su biodegradabilidad y multivalencia, lo que permite la unión covalente de fármacos y grupos directores que puedan contribuir a cruzar las diferentes barreras biológicas existentes desde la nariz hasta el cerebro. La conjugación covalente del agente terapéutico a la cadena polimérica ofrece una estabilidad prolongada en la circulación sanguínea y un mayor control sobre la liberación del fármaco en el microambiente tumoral si se diseña adecuadamente teniendo en cuenta estímulos endógenos como el pH ácido, el aumento del entorno reductivo o la sobreexpresión de proteasas específicas.

Esta tesis se centra en el diseño racional y desarrollo de nuevos conjugados PGA-fármaco y una plataforma intranasal segura y eficiente para la administración dirigida y la liberación del fármaco en el cerebro como tratamiento del glioma pediátrico. Se desarrolló una familia de conjugados de poliglutamatos que incorporan palbociclib, un inhibidor de CDK, utilizando diferentes espaciadores sensibles a estímulos, así como diferente carga de fármacos. La importancia de la conformación, geometría y topología del transportador en sistemas de administración de fármacos a menudo se pasa por alto y/o se investiga de manera inadecuada, lo que lo convierte en un área de investigación intrigante con el potencial de descubrir aspectos cruciales de dichos sistemas para su diseño racional. En esta tesis, estudiamos el efecto de la conjugación de un fármaco hidrofóbico – palbociclib sobre la conformación en solución de PGAs lineales y en forma de estrella. Con dispersión de rayos X de ángulo pequeño y dicroísmo circular, demostramos la evolución del conjugado polipeptídico al aumentar la carga de fármaco. Además, establecimos el vínculo entre la conformación de los conjugados y su actividad biológica en células GBM y DIPG derivadas de pacientes. Nuestros hallazgos ilustran la necesidad de una comprensión profunda de las propiedades fisicoquímicas de los nanosistemas estudiados que pueden ayudar a predecir su resultado biológico.

Para el cribado rápido y la validación de la formulación intranasal, establecimos con éxito una plataforma de detección ex vivo basada en células de difusión verticales de Franz con mucosa nasal de oveja. Varios sistemas basados en PGA lineal y en forma de estrella modificadas con diferentes ligandos (incluyendo el ácido docosahexaenoico, ácido hialurónico (HA), odorranalectina), así como sistemas entrecruzados del PGA en forma de estrella y la mezcla física con un HA entrecruzado (HA-CP®). A continuación, se realizó estudios de biodistribución mediante administración intranasal de los candidatos seleccionados, seguidos de la cuantificación ex vivo con la técnica IVIS y el ensayo de fluorescencia estándar después de la homogeneización de órganos y los estudios histológicos del cerebro. Los datos obtenidos mostraron claramente la presencia de las diferentes plataformas en el cerebro e, su internalización en células del bulbo olfativo y, lo que es más interesante, una buena difusión en el cerebro a través de diferentes áreas, llegando incluso a detectarse en el hipocampo. Los candidatos seleccionados se han escalado y en la actualidad su evaluación biológica en un modelo in vivo está en curso. En conclusión, se ha diseñado, desarrollado y validado diferentes plataformas basadas en PGA capaces de llegar al cerebro a través de la administración intranasal, constituyendo una base prometedora para el tratamiento de múltiples trastornos relacionados con el cerebro.

RESUM

Els tumors malignes del cervell i del sistema nerviós central representen el 21% dels tumors en nens i són la segona causa principal de mort per càncer pediàtric després de la leucèmia. La quimioteràpia estàndard permet al voltant del 95% de les taxes de supervivència a cinc anys dels pacients amb gliomes de baix grau. A diferència dels gliomes d'alt grau que continuen sent incurables amb taxes de mortalitat altes: una supervivència a cinc anys del 4,7 % per a pacients amb glioblastoma multiforme (GBM) i menys d'un any en pacients amb glioma pontí intrínsec difús (DIPG). Els nivells baixos de penetració del fàrmac a través de la barrera hematoencefàlica i la baixa taxa de supervivència associada ressalten en la necessitat de noves propostes de tractament per a una necessitat clínica no satisfeta.

L'administració intranasal ofereix un enfocament no invasiu prometedor que eludeix el metabolisme hepatogastrointestinal i la barrera hematoencefàlica, cosa que permet l'administració directa del nas al cervell. Els materials basats en polipèptids i, en particular, els poliglutamats (PGA) representen excel·lents candidats per a l'administració al cervell a causa de la seva biodegradabilitat i multivalència, la qual cosa dóna suport a la introducció covalent de fàrmacs i grups objectiu i pot facilitar la transició del nas al cervell. La conjugació covalent de l'agent terapèutic a la cadena polimèrica ofereix una estabilitat prolongada en la circulació sanguínia i un major control sobre l'alliberament del fàrmac al microambient tumoral si es dissenya adequadament tenint en compte disparadors endògens com el pH àcid, l'augment de l'entorn reductiu o la sobreexpressió de proteases específiques.

Aquesta tesi se centra en el desenvolupament de nous conjugats PGA-fàrmac dissenyats racionalment i una plataforma intranasal segura i eficient per a l'administració dirigida i l'alliberament del fàrmac al cervell com a tractament del glioma pediàtric. Es va desenvolupar una família de conjugats de poliglutamat que incorporen l'inhibidor de CDK palbociclib, utilitzant diferents enllaçadors sensibles a estímuls i nivells variables de càrrega de fàrmacs. La importància de la conformació, la geometria i la topologia del transportador en els sistemes d'administració de fàrmacs sovint es passa per alt i s'investiga de manera inadequada, cosa que la converteix en una àrea de recerca intrigant amb el potencial de descobrir aspectes crucials dels sistemes dadministració de fàrmacs dissenyats de manera racional. En aquesta tesi estudiem l'efecte del fàrmac hidrofòbic conjugat – palbociclib sobre la conformació en solució de PGA lineals i en forma d'estrella. Amb dispersió de raigs X d'angle petit i dicroisme circular, demostrem l'evolució del sistema conjugat en augmentar la càrrega de fàrmac. A més, establim el vincle entre la conformació dels conjugats i la seva activitat biològica provada en cèl·lules GBM i DIPG derivades de pacients. Les nostres troballes van il·lustrar la necessitat d'una comprensió profunda de les propietats fisicoquímiques dels nanosistemes estudiats que poden ajudar a predir-ne el resultat biològic.

Per a la detecció ràpida de la formulació intranasal basada en els portadors de PGA, vam establir amb èxit una plataforma de detecció ex vivo basada en cèl·lules de difusió verticals de Franz amb mucosa d'ovella. Diversos sistemes basats en PGA lineal i en forma d'estrella amb fraccions conjugades (inclòs l'àcid docosahexaenoic, àcid hialurònic (HA), odorranalectina), així com partícules reticulades (a través de cicloaddició azida-alquí o enllaços disulfur) i la barreja física amb un HA es van provar els polímers creuats (HA-CP®). Els estudis de biodistribució després de l'administració intranasal es van fer en candidats seleccionats, seguits de la quantificació ex vivo amb la tècnica IVIS i l'assaig de fluorescència estàndard després de l'homogeneïtzació d'òrgans i els estudis histològics del cervell. Les dades obtingudes van mostrar clarament el transport del nas al cervell, la internalització cel·lular dels conjugats al bulb olfactiu i, el que és més interessant, una bona difusió del cervell a través de diferents àrees, arribant fins i tot a l'hipocamp. Els sistemes seleccionats es van ampliar i la preparació per a l'avaluació biològica en un model in vivo està en curs. En general, vam ser capaços de dissenyar, desenvolupar i validar diferents plataformes basades en PGA capaces d'arribar al cervell mitjançant l'administració intranasal, la qual cosa podria ser la base per al tractament de múltiples trastorns relacionats amb el cervell.

ACKNOWLEDGEMENT

I would like to express my deepest gratitude to all those who have contributed to the successful completion of my thesis and provided invaluable guidance and support throughout the process.

First and foremost, I extend my heartfelt appreciation to my supervisor, Dr. María Jesus Vicent and Dr. Inmaculada Conejos-Sánchez for their unwavering dedication, insightful feedback, and constant encouragement. Their expertise, patience, and mentorship have been instrumental in shaping the direction and quality of my work. I am truly grateful for their guidance and the time they devoted to helping me achieve my goals. I would also like to acknowledge the entire team of the Polymer Therapeutics Laboratory and CIPF staff for providing me with the necessary resources, facilities, and opportunities to pursue my degree.

Throughout my scientific journey, there were individuals who played exceptional roles. Among them, I would like to thank Ester Masia, who was probably my unofficial supervisor in the biological part and played a pivotal role in my scientific journey. Thank you, Esther, for sharing comprehensive knowledge about cell cultures and being one of the few who supported my curiosity and crazy ideas to try extra things not written in the protocol. Also, I want to acknowledge Alicia Martinez and Domingo Gil, without whom the flow cytometry experiments would not be possible. I am also thankful to Mario Soriano for his assistance with electron microscopy experiments and his skillful guidance in distinguishing actual objects from artifacts under the microscope. I also want to express my appreciation to Alberto Hernandez for his time and patience during my studies with Confocal Microscopy and for graciously handling the unexpected mishap when the cell culture plate inadvertently melted into the objective. Also, I would like to thank Pilar Fortea Martín, whose smile and cheerful "Buenos días" never fails to brighten my spirits.

Furthermore, I am thankful to my friends and family for their continuous support, understanding, and motivation. Their belief in my abilities and unwavering encouragement have been a constant source of inspiration throughout this journey.

I would like to express my deepest appreciation to the experts who served as members of my examination committee. Their constructive criticism, valuable suggestions, and thought-provoking discussions have significantly enhanced the overall quality of my thesis. Last but not least, I would like to acknowledge the contributions of all the research participants, without whom this study would not have been possible. Their willingness to share their experiences and insights has enriched the findings and added value to my work.

In conclusion, I extend my heartfelt gratitude to everyone who has played a role, big or small, in the successful completion of my thesis work. Your support and guidance have been invaluable, and I am truly appreciative of the knowledge and skills I have gained through this experience.

LIST OF ABBREVIATIONS

AAA	Amino acid analysis
ACN	Acetonitrile
AcOH	Acetic acid
AD	Administered dose
ADRs	Adverse drug reactions
AKT	Serine-threonine protein kinase
AME	Adsorptive-mediated endocytosis
ANOVA	Analysis of variance
APC	Adenomatous polyposis coli
ApoE	Apolipoprotein E
Arg	Arginine
Asp	Aspartic acid
BBB	Blood-brain barrier
BET	Bromodomain and extraterminal domain
BG	Bowman's gland
BL	Basal lamina
Boc	Tert-butyloxycarbonyl
BSA	Bovine serum albumin
BSH	Borocaptate sodium
BT	Brain tumor
BTA	Benzene-tricarboxylic acid
BTB	Blood-tumor barrier
BV	Blood vessel
CA-A4	Combretastatin-A4
CAC	Critical aggregation concentration
CAT	Cationic amino acid transporter
CBT	Congenital brain tumor
CD	Circular dichroism
CD44	Cluster of differentiation 44
CDK4/6	Cyclin-dependent kinase 4 and 6
CED	Convection enhanced delivery
CHCl$_3$	Chloroform
CMC	Critical micelle temperature
CMT	Carrier-mediated transporter
CNS	Central nervous system

CNT2	Nucleoside transporter
CSC	Cancer stem cell
CSF	Cerebrospinal fluid
CT	Computed tomography
CuSO$_4$	Copper(II) sulfate
Cy5.5	Cyanine5.5
Cys	Cysteine
D$_2$O	Deuterium oxide
DAPI	4′,6-diamidino-2-phenylindole
DCM	Dichloromethane
DDS	Drug delivery system
DEPT	Distortionless enhancement by polarization transfer
DHA	Docosahexaenoic acid
DIC	Diisopropylcarbodiimide
DIEA	N,N-diisopropylethylamine
DIPG	Diffuse intrinsic pontine glioma
DLS	Dynamic light scattering
DMAP	4-dimethylaminopyridine
DMF	N,N'-dimethylformamide
DMSO	Dimethylsulfoxide
DMTMM	4-(4,6-dimethoxy-1,3,5-triazin-2-yl)-4-methyl-morpholinium
DNA	Deoxyribonucleic acid
DOSY	Diffusion-ordered spectroscopy
DOX	Doxorubicin
DP	Degree of polymerization
DTT	Dithiothreitol
EC	Endothelial cell
EDC	1-ethyl-3-(3-dimethylaminoporopyl)carbodiimide
EGFR	Epidermal growth factor receptor
EMA	European medicines agency
EO	Ethylene oxide
EPR	Enhanced permeability and retention effect
FATP	Fatty acid transporter
FDA	Food and drug administration
FTIR	Fourier-transform infrared spectroscopy
GBC	Globose basal cell
GBM	Glioblastoma multiforme

———

G-CSF	Granulocyte colony-stimulating factor
GFLG	Glycine-phenylalanine-leucine-glycine
GIT	Gastro-intestinal tract
Glu	Glutamic acid
GLUT1	Hexose transporter
GPC	Gel permeation chromatography
GSH	Glutathione
H$_2$	Hydrogenation
H$_2$SO$_4$	Sulfuric acid
HA	Hyaluronic acid
HA-CP	Hyaluronic acid cross- polymer hydrogel
HBCs	Horizontal basal cells
HBr	Hydrobromic acid
HCl	Hydrochloric acid
HER2	Human epidermal growth factor receptor 2
HGG	High-grade glioma
HLB	Hydrophilic-lipophilic balance
HMBC	Heteronuclear multiple bond correlation
HMQC	Heteronuclear single-quantum coherence
HOBt	Hydroxybenzotriazole
HPLC	High-performance liquid chromatography
HPMA	N-(2-hydroxypropyl)methacrylamide
i.n.	Intranasal administration
i.v.	Intravenous administration
IBT	Infant brain tumor
IC$_{50}$	Half maximal inhibitory concentration
IgM	Immunoglobulin M
IONP	Iron oxide nanoparticle
iPrOH	Isopropyl alcohol
IR	Insulin receptor
K$_2$CO$_3$	Potassium carbonate
LC/MS	Liquid chromatography-mass spectrometry
LEP-R	Leptin receptor
Lf	Lactoferrin receptor
LGG	Low-grade glioma
LinPGA	Linear poly-L-glutamic acid
LMWP	Low molecular weight protamine

LP	Lamina propria
LRP	Lipoprotein receptor-related protein
LVs	Lymphatic vessels
Lys	Lysine
MALS	Multi-angle light scattering
MB	Medulloblastoma
MBC	Metastatic breast cancer
MCT	Monocarboxylic acid transporter
MeOH	Methanol
MMR	Mismatch repair
MOPP	Mechlorethamine, Oncovin, Procarbazine, and Prednisone Chemotherapy
MRI	Magnetic resonance imaging
MSD	Mean square displacement
mTOR	Mammalian Target of Rapamycin
MTS	3-[4,5,dimethylthiazol-2-yl]-5-[3-carboxymethoxy-phenyl]-2-[4-sulfophenyl]-2h-tetrazolium
MWCO	Molecular weight cutoff
NaOH	Sodium hydroxide
NCA	N-carboxyanhydride
NCT	National clinical trial
NF	Neurofibromatosis
NH$_4$OH	Ammonium hydroxide
NHS	N-hydroxysuccinimide
NMP	N-methyl-2-pyrrolidone
NMR	Nuclear magnetic resonance
NP	Nanoparticle
OAT	Organic anion transporter
OB	Olfactory bulb
OCT	Organic cation transporter
OE	Olfactory epithelium
OEC	Olfactory ensheathing cell
OG	Oregon green
OL	Odorranalectin
ONF	Olfactory nerve fibroblast
ORN	Olfactory receptor neuron
OSN	Olfactory sensory neuron

PAMAM	Poly(amidoamine)
PBLG	Poly(γ-benzyl)-L-glutamate
PBS	Phosphate-buffered saline
PBT	Proton beam therapy
Pd/C$_{act}$	Palladium on carbon catalyst
PDC	Polymer-drug conjugate
PDI	Polydispersity index
PEG	Polyethylene glycol
PEI	Polyethylenimine
PES	Phenazine ethyl sulfate
PET	Positron emission tomography
PGA	Poly-L-glutamic acid
Phe	Phenylalanine
PI3K	Phosphoinositide 3-kinase
PLGA	Poly(lactic-co-glycolic acid)
pLys	Polylysine
PMS	Phenazine methosulfate
PO	Propylene oxide
PT	Polymer therapeutics
pTSA	P-toluenesulfonic acid
PTX	Paclitaxel
pTyr	Polytyrosine
RAGE	Receptor of advanced glycation end products
Rb	Retinoblastoma
RGD	Arginine-glycine-aspartic acid motif
RI	Refractive index
rLTL	Relative leukocyte telomere length
RME	Receptor-mediated endocytosis
ROP	Ring-opening polymerization
RT	Room temperature
SANDACH	Subproductos Animales No Destinados Al Consumo Humano (Animal Byproducts Not Destined for Human Consumption)
SAXS	Small-angle X-ray scattering
SCLC	Small cell lung cancer
SEC	Size exclusion chromatography
SEM	Standard error of the mean
Ser	Serine

SFDA	State food and drug administration
SHH	Sonic hedgehog
siRNA	Small interfering RNA
SMO	Smoothened homologue
SPARC	Secreted protein and rich in cysteine
SPIO	Superparamagnetic iron oxide nanoparticle
StPGA	Star-shaped poly-L-glutamic acid
StPGA-CL	Crosslinked star-shaped poly-L-glutamic acid
SUS	Sustentacular
TAT	Transactivator of transcription
TCA	Trichloroacetic acid
TDL	Total drug loading
TEA	Triethylamine
TEM	Transmission electron microscopy
TERT	Telomerase reverse transcriptase
TFA	Trifluoroacetic acid
TfR	Transferrin receptor
THF	Tetrahydrofuran
Thr	Threonine
TKI	Tyrosine kinase inhibitor
TMS	N-trimethylsilyl
TMSI	Trimethylsilyl iodide
TNBC	Triple-negative breast cancer
TNF-alpha	Tumor necrosis factor-alpha
TSC	Tuberous sclerosis complex
Tyr	Tyrosine
UV-Vis	Ultraviolet-visible
Val-Cit	Valine-citrulline
VEGF	Vascular endothelial growth factor
VHL	Von Hippel-Lindau disease
WGA-HRP	Wheat-germ agglutinin horseradish peroxidase
WHO	World health organization
WNT	Wingless

TABLE OF CONTENTS

OBJECTIVES

This Ph.D. project was granted by the AECC- Valencia headquarters (Asociación Española contra el Cáncer) and is included in the global project ERC-Consolidator Grant MyNano with the objective of designing a drug delivery system for pediatric glioblastoma treatment via the intranasal administration route. Accordingly, the **General Objective** is to design, develop, and validate a polypeptide-based drug delivery system based on polyglutamic acid, specific conjugation of active agents to the polymeric backbone through the use of stimuli-responsive linkers for tumor targeting, and enhancement of nose-to-brain transport assisted by the surface decoration of the polymeric particles with mucodiffusive/mucoadhesive moieties.

This global aim frames the following **Specific Objectives**:

1. Development of an intranasal drug delivery platform for drug delivery to the brain

1.1. *Synthesis of polyglutamate polymeric systems* with varying shapes and sizes to investigate the impact of carrier structure on biological outcomes

1.2. *Development and characterization of polyglutamate polymeric systems* capable of enhancing nasal mucosa permeation

1.3. *Establishment of an ex vivo model* for mucosa permeation validation of the developed systems

1.4. Intranasal administration *biodistribution studies* of the selected candidates

2. Rational design, synthesis, and validation of novel polyglutamate-based palbociclib constructs for pediatric brain tumor treatment

2.1. *Synthesis and characterization of a family of polyglutamate-based conjugates* incorporating the CDK inhibitor palbociclib, connected through various stimuli-responsive linkers

2.2. *In vitro characterization of designed systems* in patient-derived cell lines to identify correlations between the physicochemical properties of the conjugates and their biological activity

2.3. *Identification of a combination therapy* and determination of the synergistic ratio with palbociclib and optimization of the formulation for the combination pair for the intranasal platform

Chapter 1

Introduction

1. Pediatric Brain Tumor

Brain tumors (BT) are a group of systemic diseases involving abnormal growth of mass of malignant (cancerous) or benign (non-cancerous) cells in or around the brain.[1,2] Currently, more than 130 different types and variants of brain tumors have been identified based on histogenesis combined with recent advances in molecular pathophysiology and tumor genetics, according to the World Health Organization (WHO) recommendations.[3] Of note, the types and distribution of pediatric brain tumors are different from ones developed by adults[4,5] and require a personalized pediatric disease focus. Moreover, a subgroup of adolescents from 15 to 19 has a higher overall incidence of brain tumors than children 0-14 years old and different disease distribution.[6]

The poor efficacy of brain tumor therapies often relates to the presence of the blood-brain barrier (BBB), which limits drug delivery.[7] The choice of therapeutics represents another reason; for instance, high-grade pediatric brain tumors undergo a treatment schedule used for adults - temozolomide, lomustine alone, or in combination with bevacizumab, which remains highly questionable and ineffective, with only a temporary improvement in quality of life observed.[8] The poor efficiency of current treatments precludes the utility of early diagnosis and thus forms an urgent need for novel research specifically dedicated to pediatric brain tumors.

1.1.   Classification and Staging of Pediatric BT

Brain lesions are classified according to location: either *supratentorial* (upper part of the brain) – comprising the two cerebral hemispheres, lateral and third ventricles, choroid plexus, pineal gland, hypothalamus, pituitary gland, and optic nerve; and *infratentorial* (the lower back part of the brain) - includes the cerebellum, tectum, fourth ventricle, and brain stem (midbrain, pons, and medulla) (**Figure 1.1**).[9] Very young children tend to suffer from supratentorial tumors (70% of cases); in contrast, older children tend to develop infratentorial tumors.[10] The new WHO classification maintained Roman numerals I, II, III, or IV, which represent the brain tumor severity, with the latter being the most lethal grade.[3] Most pediatric brain tumors (approximately 58%) are malignant with poor prognosis;[11] meanwhile, 96% of children with nonmalignant tumors in the USA survived ten years after diagnosis.[4]
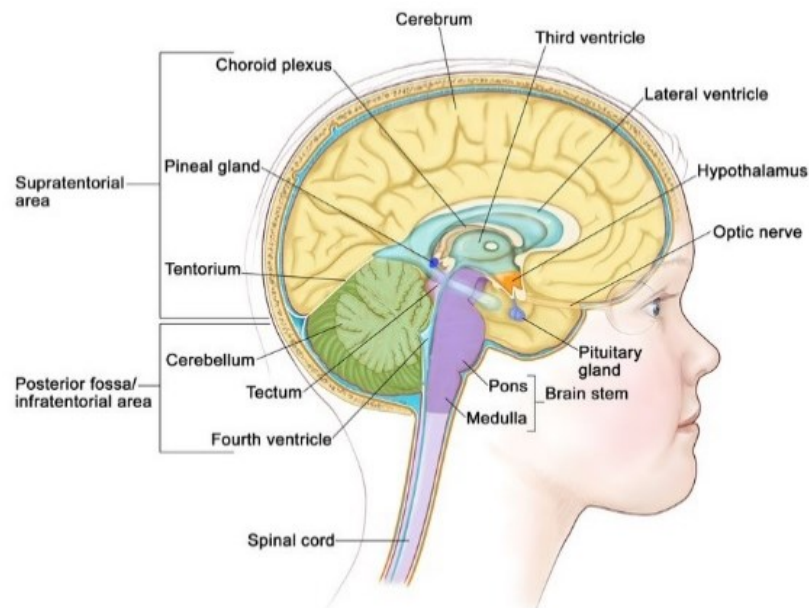
Figure 1.1. Brain anatomy: supratentorial area - cerebrum, lateral and third ventricles, choroid plexus, pineal gland, hypothalamus, pituitary gland, and optic nerve; infratentorial area - cerebellum, tectum, fourth ventricle, brain stem (midbrain, pons, and medulla).[9]

The histopathology-based classification of pediatric brain tumors includes neuronal tumors (predominantly embryonal tumors, most common include medulloblastoma, atypical teratoid/rhabdoid tumors, and CNS tumors) and glial tumors

(most common include astrocytoma, oligodendroglioma, ependymoma, brain stem glioma, optic nerve glioma, and diffuse intrinsic pontine glioma [DIPG]).[12] Medulloblastoma represents a group of different neoplasms that, according to the revised WHO classification, includes four subgroups: wingless (WNT), sonic hedgehog (SHH), group 3 (harbor *MYC* amplification), and group 4 (isochromosome 17q) with age-related prevalence distribution of above-mentioned subgroups (**Figure 1.2**).[3,13]
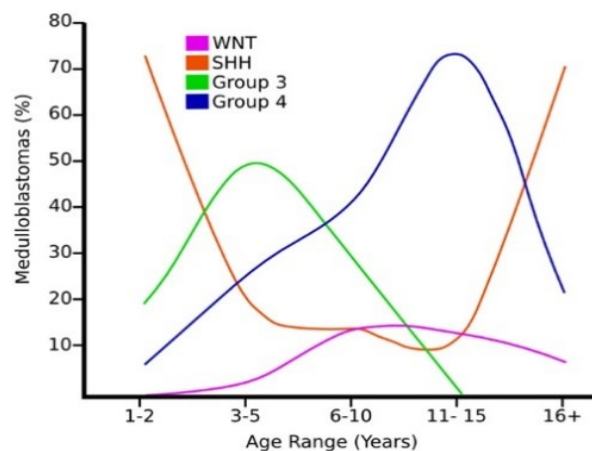
Figure 1.2. Age distribution of medulloblastoma subtypes.[13]

According to the WHO, glioma represents a prevalent CNS tumor type in children classified into low-grade (LGG) and high-grade glioma (HGG).[3] Pediatric LGGs rarely undergo malignant transformation; such slow-growing grade I or II lesions become chronic but rarely life-threatening diseases. Meanwhile, HGGs that include anaplastic astrocytoma (grade III), glioblastoma multiform (GBM), and DIPG remain incurable. The 5-year survival rate for GBM patients is 4.7%,[14] while for DIPG patients, the survival prediction is less than one year.[15]

Pediatric tumors are also classified according to the age of diagnosis, as childhood (0-14 years) and adolescence (15-19 years).[16] Within the childhood group, there are two subgroups distinguished: congenital brain tumors (CBT, diagnosed within sixty days after birth) and infant brain tumors (IBT, children younger than one year). CBT and IBT are sporadic malignancies accounting for only 0.5–1.9 % of pediatric brain tumors and are also defined as fetal intracranial tumors.[17] The CBT incidence rate has increased during the last twenty years, mainly due to improved routine ultrasound diagnosis, with teratoma and neuroblastoma being the most common histological type.[18] For IBTs, the vast majority derived from gliomas (63%), with astrocytomas being the predominant type (36%).[17]

The upper age limit for pediatric cancer remains under debate in Europe but stands at 24 years in the USA and 29 years in Canada; this factor has significant implications for the collection of statistical data and resource requirements in clinical programs dedicated to adolescents and young adults.[6]

1.2.   Statistics: Incidence, Mortality and Survival Rate

Pediatric cancer suffers from a significant disease burden with a constantly increased incidence rate (by 0.8 per year since 1975),[19] mainly contributed to by an increase in leukemia and brain tumor cases [20]. Around 400,000 children are diagnosed with a brain malignancy worldwide each year.[21]

The prognoses for children with brain tumors depend on the tumor's histopathological features and location. Children with brain tumors generally have poor survival and high treatment-associated morbidity.[22] Over the last four decades, advances in early diagnosis, neurosurgical techniques, supportive care, and combination chemotherapy have substantially improved the five-year survival rate of childhood cancer;[23] however, the progress regarding brain tumor treatment has fallen behind. For example, mortality rates have dropped 3.7 times from 1975 for leukemia compared to only 1.5 times in brain and CNS tumors, which now represent the leading cause of pediatric cancer death.[20]

Depending on the tumor type and received therapy, the five-year net survival is approximately 80% in high-income countries; however, it represents only 10 % of pediatric cancers diagnosed worldwide, with the majority of patients residing in low and middle-income countries with scarce data available for diagnosis of pediatric brain tumors and the survival rate underestimated or not reported at all.[24] Of note, those patients surviving to five years remain at high risk of cancer recurrence and progression, chronic diseases, and functional impairments.[25] This contributes to a substantial global burden, where 97.3% of cases represent lost years of healthy life due to premature mortality, and the remaining 2.7% represent lost years due to disease-related disability.[26]

The prognosis and survival of pediatric patients depend on multiple factors, including tumor type and the age of diagnosis (**Figure 1.3**).
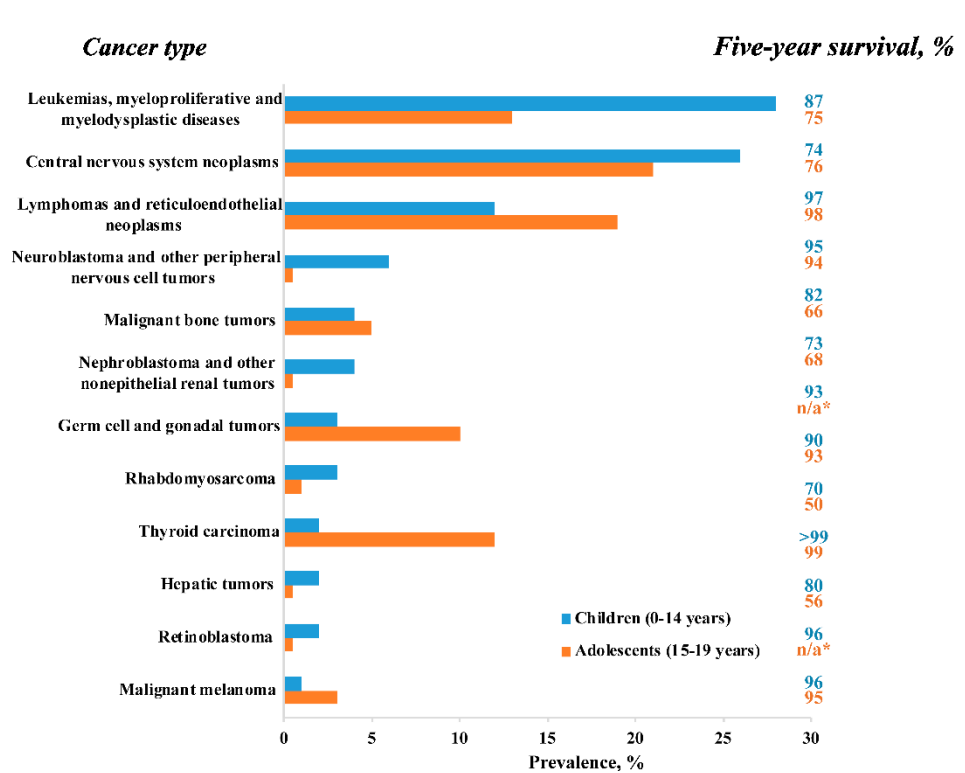
Figure 1.3. Cancer prevalence and 5-year relative survival rate in children (0-14 years) and adolescents (15-19 years). * Statistic could not be calculated due to less than <25 cases (Adapted from Siegel et al.)[19]

Malignant brain and CNS tumors represent the most common solid tumors and the second leading cause of cancer deaths in children after leukemia. In adolescents, CNS tumors overtake leukemia, becoming the most prevalent tumor type, while lymphomas and thyroid carcinomas displayed an increased incidence rate compared to children.[19]

1.3. Genetic and Environmental Risk Factors

Despite increasing research into identifying risk factors, we still lack a clear understanding of the primary reasons for pediatric brain tumor development. Genetic disorders explain around 4% of brain tumors.[27] As a result of emerging new technologies for rapid and inexpensive genotyping of the whole genome, eight studies that encompass genome-wide analysis have been carried out regarding brain tumors in adults. The findings of these studies revealed thirty genetic variations linked to a higher risk of developing malignancy, with around 30% of cases explained by the identified variants.[2]

Unfortunately, no published genotyping data for pediatric brain tumors exist; therefore, the contribution of genetic factors remains primarily unknown. Even though most brain tumors cannot be explained by family history, the studies of familial cases have revealed several genetic syndromes associated with an increased risk of malignancy.

Neurofibromatosis type 1 (NF1) and type 2 (NF2) (incidence 1:3000)[28] represent the most common genetic syndrome with demonstrated brain tumor predisposition to LGGs.[29] Mutations in tuberous sclerosis complex (TSC1 or TSC2, tumor suppressor genes of the mammalian target of rapamycin (mTOR) pathway) (incidence 1:6000) associated with benign/rarely malignant neoplasms, with a predominant appearance of subependymal giant cell astrocytoma brain lesions.[30] Von Hippel-Lindau disease (VHL), an autosomal dominant neoplasia caused by germline VHL gene mutation (incidence 1: 39000), is associated with hemangioblastoma and endolymphatic sac tumors.[31] Li-Fraumeni syndrome, caused by germline mutations in the TP53 gene, also leads to an increased risk of brain tumor development, including osteosarcoma, rhabdomyosarcoma, and brain tumors.[32] Cowden syndrome (incidence 1:1,000,000), which is associated with PTEN germline mutations, leads to meningiomas and gangliocytomas.[33] The family history of colorectal cancers with adenomatous polyposis coli and DNA mismatch repair gene alterations and associated brain lesions known as Turcot syndrome, linked to medulloblastoma development.[34,35] Gorlin's syndrome (*PTCH1 gene mutation)*, a familial tumor characterized by autosomal-dominant inheritance, strongly correlates with medulloblastoma development.[36] Rhabdoid Tumor Predisposition Syndrome is caused by germline and somatic mutations in SMARCB1 or SMARCA4 genes and is associated with atypical teratoid/rhabdoid tumors in patients younger than three years of age.[37]

Gene studies conducted in pooled datasets have identified genomic risk variants (**Table 1.1**); however, most results are based on small sample sizes without validation and would require additional studies to establish reliable conclusions. Most genes altered in pediatric brain tumors (**Table 1.1**) are also altered in brain tumors in adults; however, while the IDH1 and IDH2 mutations (genes coding isocitrate dehydrogenase) represent common molecular markers of LGGs in adults,[38] these mutations are rare for LGGs in pediatric patients.[39] Notably, while specific genetic mutations and syndromes increase pediatric cancer risk, not all individuals with these mutations or syndromes will develop cancer. Epidemiologic studies consistently associate ionizing radiation with an increased risk of brain tumor development, as independently documented for atomic bomb survivors, occupational studies,[2] and diagnostic irradiation with computerized and positron emission tomography during pregnancy.[40] As they display more significant levels of radiosensitivity, children suffer more from irradiation and a higher risk of brain tumor development (predominantly meningiomas and gliomas) later in life.[41] A study of over 10,000 children treated with low-dose irradiation for tinea capitis (ringworm of the scalp) in Israel demonstrated an increase in head and neck tumor incidence (up to thirty-fold), meningiomas (nine-fold), and gliomas (two-fold).[42]

Table 1.1. *Genetic variants with increased risk of pediatric brain tumor development*

Gene	Enzyme coded, functional role	Patient numbers	Associated brain tumors	Ref.
CYP1A1	Cytochrome P450, xenobiotic detoxification phase I	172	Meningioma Brain stem tumors	[43]
NOS1	Nitric oxide (NO) synthase, NO production in neuronal tissues			
GSTT1 and GSTM1	Glutathione S-transferases, involved in the xenobiotic detoxication phase II	172, 284	Glioma, Glioblastoma, Meningioma	[43], [44]
AICDA	Activation-induced cytidine deaminase, mechanism of mutagenesis, antibody diversity	70	n/a	[45]
CASP1	Cysteine-aspartic acid protease, execution phase of apoptosis			
H3F3A	Histone protein H3.3, epigenetic regulation	48, 86	DIPG, HGG, LGG	[46], [47]
CREBBP MLL2 ZMYM3 SMARCA4	Histone acetyltransferase, Histone methyltransferase, Histone deacetylase, Chromatin remodeler, epigenetic regulation	274	MB MB, HGG MB, HGG	[48]
BRAF	Signal transduction kinases, cell proliferation	66	LGG	[49]
CCND2, PTCH1, GLI2	Cyclin D2, Patched-1 protein, Zinc finger protein of Gli family, mediators of sonic hedgehog signaling pathway	243	MB	[50]
IRS2	Insulin receptor substrate 2	48	MB	[51]
CDKN2BAS	Long non-coding RNA	160	MB	[52]
RTEL1	Regulator of telomere length, DNA helicase	245	Astrocytoma non-astrocytoma subtypes	[53]
CCDC26	Long non-Coding RNA			

MB – medulloblastoma, HGG – high-grade glioma, LGG – low-grade glioma, DIPG – diffuse intrinsic pontine glioma

Allergies and atopic diseases also associate with an altered risk of glioma;[54] however, studies with contradicting results exist.[55] The primary hypothesis to support an inverse correlation between allergies and brain tumor risk is the activation of immune surveillance, which would more effectively remove "defective" cells.[54] Studies of patients with allergies and asthma demonstrated the relevance of leukocyte telomere

length (rLTL), which is shorter than in glioma patients.[56] These results correlate with reported increased activity of telomerase reverse transcriptase (TERT) in glioma patients, which enables immortality for cancer cells via telomere extension.[57]

In conclusion, genetics play a significant role in pediatric cancer risk, with several common genetic mutations and syndromes associated with increased cancer risk. Over the last decades, extensive endeavors have been undertaken to comprehend the correlation between external and environmental factors, genetic disorders, and pediatric cancer; however, these efforts have had limited success. Poor availability of statistical data, difficulties in establishing collaborations with the hospitals, a significantly smaller number of studies dedicated to brain tumors in children than in adults, a lack of established *in vivo* models, and a lack of research groups working specifically with pediatric tumors represent the main reasons for the insufficient amount of research for these malignancies. Identifying specific mutations, underlying molecular mechanisms, and environmental factors that provoke brain tumor development will open new approaches to minimizing incidence rates, identifying new therapeutic targets, and establishing better classification and patient stratification to efficiently apply personalized therapeutic regimes.

1.4 Clinical Management of Pediatric Brain Tumor

Despite numerous investigations, there is still a lack of established recommendations for disease management and clear directions for therapy selection.[17] The traditional treatment for pediatric brain tumors includes surgery, chemotherapy, and radiation therapy, which have several limitations and side effects that can affect a patient's quality of life.

Surgery often represents the first line of treatment for brain tumors, which continues to be a complex and intricate medical procedure. Since 1879, when Sir William MacEwen reported the first successful operation of a pediatric brain tumor,[58] advancements in medical technology have significantly improved the ability of neurosurgeons to safely and effectively remove pediatric brain tumors. Nevertheless, significant challenges exist with removing an entire tumor without damaging healthy brain tissue; furthermore, some types of brain tumors (such as DIPG) located in critical brain areas cannot be surgically removed. New emerging technologies, such as neuronavigational, intraoperative magnetic resonance imaging, computed tomography, and ultrasound, have enabled neurosurgeons to perform maximal tumor resection with greater precision and safety.[59]

Radiation therapy is commonly used to control the growth of certain types of brain tumors (often combined with surgery or chemotherapy) and alleviate tumor-associated symptoms. Unfortunately, radiotherapy in pediatric patients suffers from associated long-term cognitive and neurological effects, including learning difficulties and memory problems, and side effects such as fatigue, headaches, hair loss, and skin

irritation.[60] Proton beam therapy represents an innovative radiation therapy that targets the tumor site and delivers a higher radiation dose to critical subregions of the targeted volume. As a result, proton beam therapy increases the likelihood of administering a therapeutically relevant dose of radiation, decreases the impact of side effects, and is expected to form part of the future of pediatric radiotherapy.[61]

Over the last 30 years, *chemotherapy* has been extensively evaluated in different schedules, doses, and combinations for pediatric brain tumor treatment, resulting in noteworthy advancements for specific children (particularly those with medulloblastoma).[62] These outcomes come at a high cost to quality of life; chemotherapy can have long-term adverse effects on cognitive and neurological development; furthermore, intravenous administration may require prolonged hospital stays and increase the risk of infections. Furthermore, while there has been considerable progress with low-grade brain tumors such as medulloblastoma, the same cannot be said for HGG. In this case, no single chemotherapeutic regimen has shown significant outcomes.

The optimal treatment approach for pediatric brain tumors depends on the specific subtype, with various strategies available to maximize treatment efficacy while minimizing potential side effects. Before the 1980s, irradiation following surgery represented the standard protocol for CBT and IBT, even given a lack of evidence of increased survival and significant neurotoxicity, which led to the consideration of withdrawing treatment entirely for these patients.[10] The successful use of intensive postoperative chemotherapy: mechlorethamine, oncovin, procarbazine, and prednisone (or "MOPP") in seventeen medulloblastoma or ependymoma patients of less than 36 months of age represented the first demonstrated beneficial strategy of delaying irradiation.[22] MOPP improved survival and decreased long-term morbidity by preserving normal neurological and intellectual development.

This approach highlighted a shift in the treatment paradigm for CBT and IBT, which was confirmed by several clinical studies (HIT SKK87 and HIT SKK92) that employed procarbazine, ifosfamide, methotrexate, cisplatin, cytarabine, and vincristine chemotherapy.[63] Other studies with carboplatin, vincristine, cyclophosphamide, methotrexate, and cis-platinum[64,65] also demonstrated survival benefits upon delayed or no radiotherapy.

Over the last four decades, advances in neurosurgical techniques, early diagnosis, supportive care, and combination chemotherapy have substantially improved the five-year survival rate of pediatric cancer.[23] Pediatric LGGs are usually cured after total surgical excision and vinblastine monotherapy[66] or vincristine plus carboplatin,[67] leading to an overall five-year survival rate reaching 95 %.[68] An alternative multimodal chemotherapy regimen includes thioguanine, procarbazine, lomustine, and vincristine; differences in toxicity may guide the physician's choice of therapy.[67] In the case of LGG recurrence, a combination therapy of Bevacizumab (monoclonal antibody inhibiting angiogenesis) and irinotecan demonstrated a high responsiveness rate.[69] Contrary to this, the current treatment strategies for HGGs, which include temozolomide or lomustine

with or without bevacizumab,70 beyond radiotherapy, remain highly questionable and ineffective.[8]

Maximal tumor resection upon surgery remains the first-line treatment for medulloblastoma, with additional radiotherapy for children over three years.[71] The postsurgical multimodal chemotherapy for medulloblastoma patients depends on risk stratification: cisplatin, vincristine, lomustine or cisplatin, vincristine, and cyclophosphamide regime for average-risk medulloblastoma [72] and topotecan during radiation [73] followed by cyclophosphamide, cisplatin, and vincristine for high-risk medulloblastoma [74]. Another protocol for high-risk medulloblastoma includes carboplatin and vincristine during radiation, ifosfamide, and etoposide [75], or cisplatin, cyclophosphamide, and vincristine [76]

An exciting and novel strategy using oncolytic virus mutants may represent an alternative to current standard chemotherapy for HGGx; this approach displays a good toxicity profile and extremely high and tunable specificity for malignant glioma cells.[77] There are two primary approaches in anti-glioma treatment: i) the use of replication-defective viruses to deliver suicide genes or ii) replication-competent viruses, where the therapeutic effect is achieved by lysis of tumor cells by viruses.[78] ONYX-015, an adenovirus mutant with E1B-55k deletion, demonstrated *in vivo* therapeutic efficacy in glioblastoma xenograft models and is currently in clinical trials for head and neck tumors with promising preliminary data.[79] Another reported adenovirus mutant, Ad5-Delta24, demonstrated efficacy in experimental intracranial (U-87 MG, U-251 MG) and subcutaneous (D54 MG) murine models.[80] Oncolytic virus technology may also be applied to engineer a viral vector with additional genetic information. Komata et al. applied this strategy to obtain a viral vector constitutively expressing caspase-6 under the hTERT gene promoter (upregulated in malignant cells and not active in normal brain tissue) with demonstrated promising *in vivo* results in subcutaneous U373-MG and U87-MG xenograft model.[81] Adding the peptide enriched with arginine-glycine-aspartic acid motifs (RGD) to Ad5-Delta-24 improved this virus mutant's infectivity, with increased survival when evaluated in a DIPG immunocompetent murine model and exciting data from the rechallenge experiment indicating the formation of immune memory in long-term survivors.[82] Successful virotherapy studies are also reported for medulloblastoma patients, demonstrating the potential of this novel therapy.[83,84] The Forsyth group demonstrated the oncolytic potential of a myxoma virus in a medulloblastoma orthotopic murine model, with a prolonged median survival of 21 days versus 12.5 days for the control group, which can be increased further up to 25 days when combined with rapamycin treatment (mTOR inhibitor).[84] In 2015, the based on live oncolytic herpes virus T-VEC (Imlygic™) was approved by the FDA for recurrent unresectable melanoma with demonstrated high efficiency combined with a PD-1 inhibitor and well-tolerable side-effects [85]. After injection at the lesion site, the virus invades the cells unselectively but cannot replicate in healthy cells and only affects cancerous cells. Twenty-three clinical trials are ongoing to evaluate Imlygic™ alone or combined with checkpoint inhibitors, chemotherapy, or radiation therapy for different cancers [86].

Unfortunately, the high cost of oncolytic virus therapy represents one of the main limitations for clinical translation;[85] however, this therapeutic approach's high specificity and tolerability raise hopes for applications in combating pediatric cancers.

The discovery of the leading genetic and biochemical alteration that underlies a medulloblastoma subtype boosted studies dedicated to developing targeted therapies. The predominant dysregulated pathways associated with medulloblastoma subtypes are as follows: wingless (WNT) – group 1, sonic hedgehog (SHH) – group 2, *MYC* amplification – group 3, abnormal chromosome structure involving duplication of the long arm of chromosome (isochromosome 17q) - group 4.[3,13]

The dysregulated hedgehog (SHH) signaling pathway is common to many cancer types. Several compounds specifically targeting smoothened homolog (SMO), a transmembrane protein, have been developed, with three already on the market for basal cell carcinoma, acute myeloid leukemia, and many others in clinical trials.[87] For the SHH medulloblastoma group, therapy with an SMO inhibitor (CDC-0449) prompted a rapid response in a metastatic medulloblastoma patient who received all possible combinations of treatments but displayed disease relapse and progression; however, this patient also developed resistance.[88] Interestingly, studies of arsenic trioxide, approved as a second-line therapy for acute promyelocytic leukemia, revealed the mechanism of action: targeting the GLI protein - a downstream component of the hedgehog pathway, which proves helpful to overcome resistance to SMO inhibitors.[89] The recently discovered drug, Saridegib (IPI-926), prompted clinical remission and extended survival with decreased drug resistance in an aggressive $Ptc^{C/C}$ murine medulloblastoma model.[90] Identifying the mechanisms to overcome resistance development and using selective inhibitors for medulloblastoma patients with altered hedgehog pathways represents a desirable therapeutic strategy.

Regarding medulloblastoma cases displaying altered Wnt pathways, only a few inhibitors with limited efficacy and reported cross-talks between the Wnt/β-catenin and PI3K)/Akt signaling pathways have been developed.[91] Initially isolated from beetles, cantharidin has been traditionally used as an anticancer agent in Chinese medicine.[92] Cantharidin and its analog norcantharidin suppressed the Wnt/β-catenin signaling pathway and displayed antitumor efficacy in a DAOY medulloblastoma cell line-based orthotopic xenograft animal model.[93]

Due to a lack of information regarding medulloblastoma groups 3 and 4, no specific treatment has been reported for these subgroups. The reported higher expression of histone deacetylase genes HDAC5 and HDAC9 in these medulloblastoma subgroups with poor prognosis may highlight possible therapeutic targets.[94] A recent high-throughput screen identified dacinostat and quisinostat as effective histone deacetylase inhibitors resulting in elevated apoptosis and tumor suppression in subcutaneous DAOY xenograft model.[95] Robinson et al. identified the *EZH2, KDM6A*, and ZMYM3 genes - involved in epigenetic dysregulation - specifically in medulloblastoma groups 3 and 4 and may represent promising targets for these subgroups.[96] Recently discovered and

approved for clinical trials, the EZH2 inhibitor EPZ-6438 (Tazemetostat) has demonstrated *in vivo* efficacy with prolonged survival in orthotopic xenograft models.[97] Furthermore, several EZH2 inhibitors, including Tazemetostat, have already demonstrated meaningful responses in clinical trials.[98,99]

Identifying molecular pathways involved in the pathogenesis of pediatric brain tumors remains essential for determining new therapeutic targets, as this can lead to the development of new drugs with increased specificity and, thus, reduced side effects, potentially leading to the substitution of the current standard treatment protocol of maximal surgical tumor resection, irradiation, and high doses of common non-specific chemotherapy. The main problem with the chemotherapeutic approach remains rapid removal and unspecified distribution of typically small cytotoxic/cytostatic drugs in the body.[100] This created an urgent need to identify better treatment options with enhanced activity and reduced side effects compared to traditional chemotherapy, particularly for high-grade gliomas, and therefore, nanomedicine emerged as a promising strategy.

2. Nanomedicine – a promising Tool to Improve the Efficacy of Standard Chemotherapy

Nanomedicines are a broad group of medically active, chemically unrelated entities with sizes in nanometer range. The unique and versatile properties of various nanostructures have been successfully applied in diagnosing, monitoring, and curing numerous diseases.[107] **Figure 1.4** illustrates the timeline of approved nanomedicines with significant milestones, applications, and types of drug delivery systems achieved.
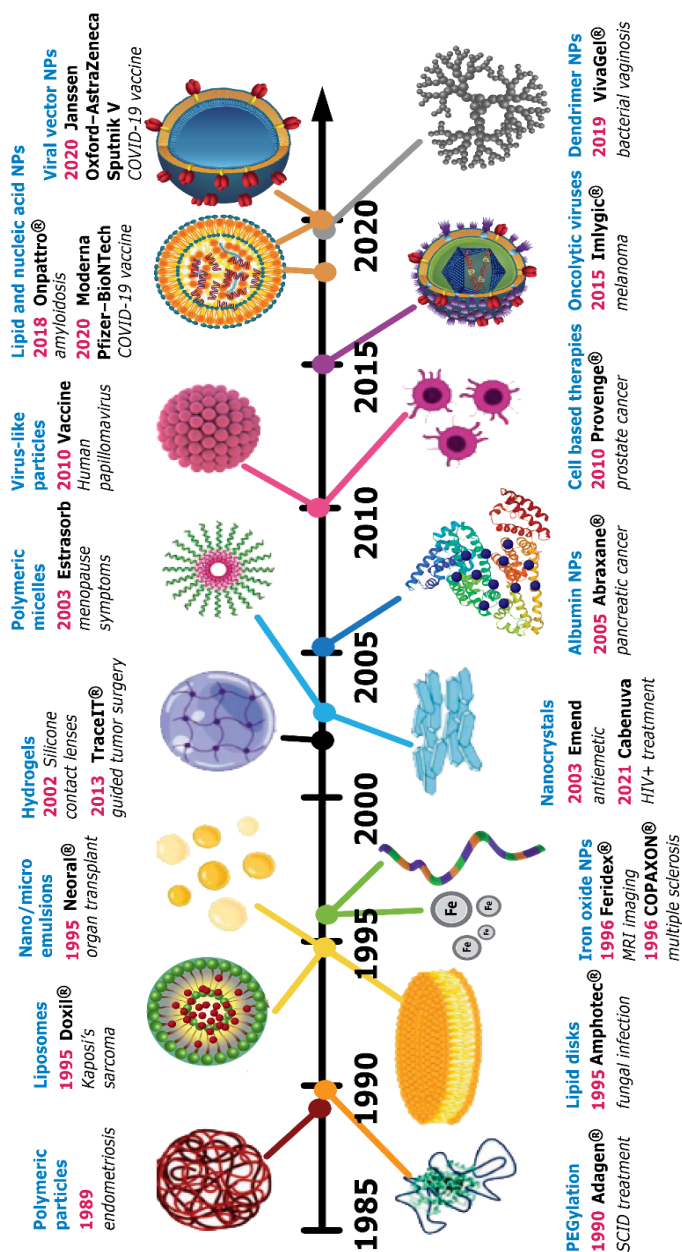
Figure 1.4. Historical timeline of the approved nanomedicine formulation with the significant milestones. Adapted from Abdel-Mageed et al. and Melnyk et al. [101,102]

Nanomedicine has already achieved clinical benefits, with 100 formulations approved for routine clinical use and 563 undergoing clinical trials.[103] Possible applications of nanomedicines cover a broad range of diseases of different natures, varying from benign Acne Vulgaris (e.g., Sebacia Microparticle®) to vaccines (e.g., mRNA-1273®) and advanced metastatic malignancies (e.g., Trodelvy®). Nanoformulation can drastically improve therapeutic agents' safety and efficacy profile and, therefore, has a leading position in cancer treatment and diagnosis, providing innovative strategies with minimized side effects.[104] While the initial development of nanomedicine for oncology was relatively slow, the recent decade showed a drastic increase in clinically approved formulations, with 14 nanomedicines approved after 2016 **(Table 1.2).**

Table 1.2 Anticancer nanomedicines approved on the market after 2016

Tradename	Year of approval	Type	Base	Active element	Application
Vyxeos® (CPX-351)	2017	Loaded liposome	Liposome	Cytarabine: Daunorubicin	Acute myeloid leukemia
Doxophos®	2017	Micelle	XR-17	Doxorubicin	Various cancers
Besponsa®	2017	Antibody-drug conjugate	Inotuzumab	Ozogamicin (calicheamicin)	Acute lymphoblastic leukemia
Mylotarg®	2017	Antibody-drug conjugate	Gemtuzumab	Ozogamicin (calicheamicin)	Acute lymphoblastic leukemia
Asparlas®	2018	Polymer-Protein conjugates	PEG-L-asparaginase	-	Acute lymphoblastic leukemia
Hensify®	2019	Nanoparticles	HfO2	HfO_2+radiotherapy	Various cancers
Polivy®	2019	Antibody-drug conjugate	anti-CD79b	MMAE	Various blood cancers
Padcev®	2019	Antibody-drug conjugate	enfortumab	MMAE	Various cancers
Enhertu®	2020	Antibody-drug conjugate	trastuzumab	Deruxtecan	Various solid cancers
Blenrep®	2020	Antibody-drug conjugate	J6M0 mAb	MMAF	Breast cancer, Multiple myeloma
Trodelvy®	2020	Antibody-drug conjugate	hRS7 mAb	SN-38	Various cancers
Zynlonta®	2021	Antibody-drug conjugate	Loncastuximab	SG3199 (PBD dimer)	Lymphoma
Delytact®	2021	Oncolytic virus	Teserpaturev/*G47Δ*	-	Brain cancers
Elahere®	2022	Antibody-drug conjugate	Mirvetuximab	Soravtansine	ovarian, fallopian tube, or primary peritoneal cancer

One of the possible classifications of nanomedicines is shown in **Figure 1.5** and is based on the nature of the carrier composition, i.e., organic or inorganic.[112]

Applications may differ on a case-by-case basis, and every group offers specific advantages and suffers from various disadvantages.
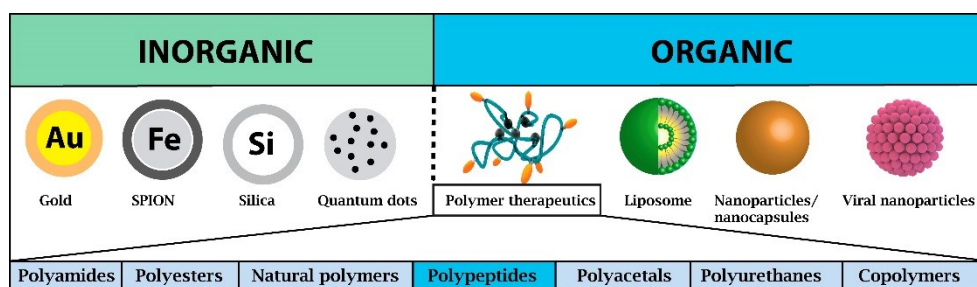

Figure 1.5 Classifications of nanomedicine used for drug delivery with a focus on Polymer Therapeutics, one of the most successful nanomedicines.[102]

Inorganic nanoparticles have been explored for drug delivery, gene delivery, and imaging applications.[116] Initially, four iron oxide (IO) nanoparticles coated with different polymeric agents successfully passed clinical trials and achieved approval as imaging agents: Feridex (1996), Resovist (2001), Gastromark (1996), and Ferumoxtran (2005);[117,118] however, most were withdrawn from the market due to the approval of more efficient Gadolinium (Gd)-based contrast agents.[117] Side-by-side comparison of Gd-based and Fe-based formulations for contrast enhancement of intracranial tumor demonstrated more clear and homogeneous lesion morphology in the case of Gd; however, the comparison found equivalent lesion volumes for both formulations.[119] Finally, NanoTherm, another IO nanoparticle, was approved in 2011 as a thermal ablation agent for tumor treatment, while AuroShell (gold [Au] nanoparticles) is undergoing Phase I clinical trials (NCT02680535).[120]

Within the organic nanomedicines with demonstrated clinical benefits, one could include liposomes, lipid nanoparticles, polymeric micelles, polymer therapeutics, nanogels, nanoparticles, and nanocrystals.[105] Organic nanotherapeutics have rapidly expanded as a promising field in cancer therapy since the clinical approval of a liposomal formulation of DOX - Doxil/Caelyx® - in 1995.[106] Since then, liposomes have been widely used nanocarrier for many chemotherapeutic medications and continue to hold the top spot in the field of drug delivery.[107] After Doxil, eight liposomal formulations[107,108] have been approved by the FDA and EMA for cancer treatment: DaunoXome® (daunorubicin, 1996, Kaposi's sarcoma), Myocet® (DOX, 2000, breast cancer), Mepact® (mifamurtide, 2009, osteogenic sarcoma), Marqibo (vincristine, 2012, leukemia), Onivyde® (irinotecan, 2015, pancreatic cancer),[104] Lipusu® (paclitaxel [PTX], 2006, solid tumors)[109], and Depocyt® (Cytarabine, 2000, lymphomatous meningitis)[110] as monotherapies and recently Vyxeos (cytarabine and daunorubicin, 2017, leukemia) as a combination therapy.[108]

Overall, simple formulation, ease of large-scale production, high biocompatibility, and the capacity to accommodate lipophilic and hydrophilic medicines represent the critical benefits of liposomal formulations.[111] PEGylation has been commonly used to overcome the rapid clearance of liposomes by the mononuclear phagocyte system; however, studies have shown that PEGylated liposomes trigger anti-PEG IgM production from spleen B cells, resulting in accelerated clearance and enhanced hepatic uptake upon their second injection.[112]

Nanoparticles for applications in oncology reached the market almost a decade later than liposomes. The first approved nanoparticle (licensed in 2005) was Abraxane (albumin nanoparticles with encapsulated PTX), a first-line treatment of metastatic breast cancer.[146] Yuan et al. have demonstrated that the free form of PTX increased the frequency of breast cancer stem cells (CSCs); however, treatment with Abraxane demonstrated a lower frequency of CSCs in metastatic diseases, revealing that a polymeric formulation can affect the drug presentation to the cell-bio interface, thereby overcoming the adaptive resistance mechanisms in cancer cells.[147]

Among polymer therapeutics, the first anticancer formulation entering the market was polymeric micelle Genexol-PM, approved in 2007 (South Korea). It comprises (PEG-poly-(D,L-lactide) diblock copolymer encapsulated with PTX), which allows higher PTX dose administration without increasing toxicity (NCT03013491).[120] Polymeric micelles combine the advantages of high drug loading of liposomes with the versatile synthetic plasticity of polymers.

Clinical translation of nanomedicine remains highly challenging despite the significant advances in the area. Among the main factors complicating the aforementioned transition reproducibility of manufacturing short- and long-term safety issues, requirements for new regulatory procedures and clinical trial designs, among others[113–115]. The limitations of *in vitro* and *in vivo* models that do not fully recapitulate human diseases, the shortage of reliable analytical protocols and methods to measure uptake and nanotoxicology, and the lack of established regulations regarding nanomedicine formulations are other challenges to overcome.[116] A serious shift towards facilitating nanomedicine translation to clinic appeared evident after the successful approval of a family of COVID-19 vaccines. Acceleration of bureaucratic procedures, clarification of regulatory requirements, and clinical trial organization will firmly push the entire field of nanomedicine[117]. Especially promising signs for the future development of nanomedicines is a rapidly expanding field of pandemic-related products, including immunotherapy and gene delivery employing, among others, liposomes[103].

This thesis focuses on developing polymer therapeutics[118,119] and polypeptide-drug conjugates, in particular,[102] which is covered in the following sections (see *Chapter 2.3.1 Polypeptide-based Nanomedicine: An Alternative to PEGylation and 2.3.2 Rational Design of Polypeptide-drug conjugates for Cancer Treatment*).

2.1. Polymer Therapeutics

Polymer therapeutics represent one of the most successful types of polymer-based nanomedicines. The term itself was coined by Prof Ruth Duncan[119] and refers to a family of polymer-based nano-sized pharmaceuticals considered as new chemical entities encompassing polymeric drugs (polymers with inherent activity), polymer-drug and polymer-protein conjugates, polymeric micelles where the drug is covalently linked to the polymer carrier, and polyplexes (polyelectrolyte complexes use as non-viral vectors).[105,120–122] All described polymer therapeutic subtypes use specific water-soluble polymers, either as the biological component or as a non-reactive functional component within a multifaceted system to enhance the delivery of drugs, proteins, or genes. As the field progresses, PT has incorporated additional self-assembling polymeric systems and an expanding array of hybrid nanosystems that incorporate inorganic elements or lipid components (**Figure 1.6**).[102,118]
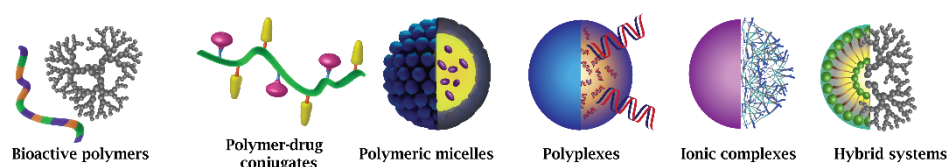

Bioactive polymers   Polymer-drug conjugates   Polymeric micelles   Polyplexes   Ionic complexes   Hybrid systems

Figure 1.6. Classifications of Polymer Therapeutics used for drug delivery.[102]

Polymeric drugs include polymer therapeutics in which no specific active agents are conjugated to the polymer, but rather, the polymer itself shows specific activity. Copaxone® (Teva Pharmaceuticals), commonly known as glatiramer acetate, was the most successful representative of this class and appeared among the top ten best-selling medications in the USA.[120,123] Copaxone® is a random copolymer of L-glutamic acid, L-alanine, L-lysine, and L-tyrosine with a molecular weight range of 2.5 to 20 kDa.[124] Despite a lack of complete understanding regarding the mechanism of action, Copaxone® may mimic the myelin basic protein, the insulating covers of neurons whose lack or damage causes multiple sclerosis. In 2015, the first generic version (Glatopa®) was approved as a fully substitutable biosimilar.[125] Despite initial success, progress in the field of polymeric drugs remains somewhat sporadic and serendipitous.

Polymer-protein conjugates are a class of Polymer therapeutics in which protein (active moiety) is conjugated with several polymeric chains. Polymers used in such constructs are usually biologically inert (e.g., polyethylene glycol, polysarcosine) and aim to increase protein stability. The first licensed Polymer-protein conjugate was Adagen® (PEGylated bovine adenosine deaminase). This protein-polymer conjugate acted as an enzyme replacement therapy for adenosine deaminase insufficiency.[126] Following regulatory approval, the significance of biologically inert polymers in increasing the half-life of small therapeutic molecules and proteins was established, and

currently, thirty products have been commercialized as next-generation or advanced polymer-based treatments.[127,128]

To note, over the past few decades, PEG has been widely accepted as a safe food additive and is frequently used in pharmaceutical formulations; however, pre-existing antibodies against PEG were found in 25% of healthy blood donors[129] and 42% of people who had never received PEGylated pharmaceuticals.[130] Immune responses to PEGylated prodrugs pose a risk for inflammation and accelerated blood clearance of the second dose of subsequently administered PEGylated products that may impact clearance and therapeutic effectiveness.[131] There is evidence that PEG alters the P-glycoprotein transporter's function regardless of its molecular weight.[132] Undergoing biological changes in the body, PEG may produce harmful carboxylic metabolites linked to acidosis and hypercalcemia.[133] Moreover, long-term PEGylated drug administration can also cause an accumulation of non-biodegradable PEG fragments in lysosomes and the liver.[134] These issues have compelled researchers to explore other safer polymer alternatives.

Polyplexes are complexes of usually two polymers with opposite charges. Commonly, polyplexes are aimed as non-viral vectors and are composed of negatively charged RNA/DNA with polycations. Polyethyleneimines and polypeptides (poly-L-lysine, poly-L-ornithine, and poly-L-arginine) are commonly used as polycations in such complexes.[135] While no polyplex gene therapies are currently clinically approved, with the recent increase in clinical trials involving RNA delivery, one can expect approval of the first formulation of this class within the next decade.

Polymer-drug conjugates are a class of polymer therapeutics in which an active substance (low molecular weight drug) is covalently conjugated to functional groups presented on polymer chains. Drugs used in such formulations are typically hydrophobic, and conjugation with polymers substantially increases their solubility without using aggressive excipients commonly applied in clinical practice. While no class members were approved when writing this thesis, more than ten formulations are currently undergoing clinical trials.[136]

2.2. Polymer-drug Conjugates: Promising Concepts to Increase Therapeutic Effectiveness

In particular, for low-molecular-weight therapeutics, rationally designed nanomedicines could enhance their lifetime in the bloodstream, improve non-specific targeting, and diminish the possible overall toxicity in the body associated with adverse side effects. This refers to the concept of the "magic bullet," coined by Nobel laureate Paul Ehrlich.[103] The main limitations of small molecule drugs for oncology include a lack of specificity and capability to cross various biological barriers and relatively quick removal of most of the drug from the body.[137] The discovery of the enhanced permeability and retention (EPR) effect raised the idea that incorporating a small drug

into nanosize structures will enhance its half-life in circulation and increase its concentration in cancer tissues. The EPR effect is a passive accumulation of nanoscopic objects with a diameter of 10-200 nm in cancer tissues due to the leaky vasculature and the defectiveness of the lymphatic drainage system.[138] To benefit from the EPR effect, most nanosystems are designed with sizes falling in the 10-200 nm range. Many nanoparticles that take advantage of the EPR effect have appeared and found applications as drug delivery systems.[107] The use of active targeting strategies and combination strategies using multivalent nanoplatforms could further improve the efficiency of polymer-drug conjugates (PDCs) aimed at oncology.[139]

While passive targeting by simple size modulation can be applied for virtually any nanomedicine, the critical advantage of PDCs is the ability to covalently link therapeutic agents to the polymeric backbone and achieve precise control over drug release kinetics. Polymer therapeutics enable customized drug loading and the incorporation of drug combinations and biologically responsive linkers designed to release drugs in response to specific biological conditions, such as those present at tumor sites [140,141]. PDCs benefit from the intrinsic characteristics of polymers and have been successfully employed to enhance the solubility, permeability, and bioavailability of hydrophobic and hydrophilic drug moieties [102]. Their optimal size (~10-100 nm) can be modulated, leading to longer blood circulation times and greater efficacy than unmodified "free" drugs [142].

Another specific benefit of PDCs is the potential to bypass multidrug resistance by benefitting from lysosomotropic drug delivery.[143] Free and loaded drugs in liposomes, upon entering the cell, remain close to the inner lipid membrane and can be efficiently pumped out by non-specific ABC proteins.[144] On the contrary, PDCs internalize via endocytosis, and the cleaved drug is then released from lysosomes in the cytoplasm far from the inner cell membrane, thus minimizing its removal from the cell.[143]

The pioneered concept of drug conjugation was described in 1954 by Jatzkewitz,[145], who worked with N-vinylpyrrolidone-mescaline; however, this novel concept did not receive wide acceptance. The first polymer-drug conjugate model was proposed by Ringsdorf[146] and was based on the polymeric backbone that includes three different units: the drug (therapeutic agent) with a cleavable spacer, a solubilizing group, and a targeting moiety towards a specific receptor or one that affects body distribution. Kopecek and Duncan[147] further explored these ideas and evaluated N-(2-Hydroxypropyl)methacrylamide (HPMA)-Dox conjugates as the first polymer-anticancer drug conjugate in 1994.[148]

There are several pharmaceutically relevant polymer classes – poly(amino acid)s, polyethers, polyesters, polycarbonates, poly(2-oxazoline)s, poly(N-acrylamide)s, polyphosphoesters, poly(N-vinyl amide)s, polysiloxanes, poly(allylamine)s, poly(vinyl ester/alcohol/ether)s, poly-R-acrylates, polyurethanes, polystyrenes, polyanhydrides, polyolefins - that are widely used as a drug delivery systems.[149] While any water-soluble polymer with a sufficient amount of active functional groups can be used for drug conjugation, increasing experimental data demonstrated that body response will depend strongly on the nature of the polymer. It has generally become accepted that

biocompatibility, biodegradability, low immunogenicity, and synthetic flexibility are among the crucial requirements for base polymers suitable for PDC development. Among polymers matching all the above-mentioned criteria, polyamino acids or synthetic polypeptides most closely resemble proteins, natural macromolecules ubiquitously found in the body.

2.3. Polypeptide-based Nanomedicine: an Alternative to PEGylation and Liposomes

Proteins and peptides are compounds involved in various biological processes; they play a vital role in catalysis, transport, gene expression, immune response, and crucial tools in biotechnological applications for both medicinal and diagnostic objectives.[150] For various pharmacological applications, naturally occurring proteins (e.g., albumin, soy and whey protein, collagen, gelatin, the ferritin/apoferritin cages, plant-derived viral capsids, and heat shock proteins) accessible to chemical and genetic modifications have all been used and characterized as drug delivery systems.[150] Time-consuming manufacturing and purification processes and serious concerns about the immunogenicity of the final products of the formulations based on naturally occurring proteins, along with a shortage of natural resources, can explain their relatively slow translation into the clinics. For manufacturing of macromolecular drugs, the natural resources are scarce on the protein of interest; therefore, recombinant biotechnology, which involves strain engineering and protein purification, is commonly used for recombinant hormones, interferons, interleukins, growth factors, tumor necrosis factors, blood clotting factors, thrombolytic medicines, and enzymes production.[151]

Synthetic polypeptides with various precursor materials and limitless opportunities for post-modification adjustments have generated significant interest and research efforts in drug delivery as an alternative to PEG and natural proteins.[102] In the polymer therapeutics subfamilies, polypeptides (based on amino acids) are present as polymeric drugs, and polymeric micelles, polyplexes, polymer-drug, and polymer-protein conjugates.[152] Among more than 500 amino acids (AAs) that have been discovered or synthesized in the last 30 years as stable or intermediate compounds,[153] only seven found in the human genetic code possess characteristics that allow their use as building blocks for polypeptide-drug conjugates. The main criteria are the feasibility of further polymer chain modification and conjugation of a therapeutic agent, targeting moiety and/or fluorescent probe, that reduces the total number of AAs to seven options: glutamic (Glu) and aspartic acids (Asp), positively charged arginine (Arg) and lysine (Lys), uncharged polar (Ser), and uncharged hydrophobic tyrosine (Tyr).[102]

Synthetic polypeptides present numerous benefits when compared to other nanomedicines, including (i) enhanced water solubility, making them suitable for highly hydrophobic drugs; (ii) prolonged plasma half-life due to their increased hydrodynamic

volume, reducing kidney clearance; (iii) protection against proteolytic enzymes and non-specific cellular uptake; (iv) minimization aggregation, immunogenicity, and antigenicity, (v) enhanced pharmacokinetics (PK) at the levels of the entire body, individual cells, and subcellular structures.

The safety profile of polypeptides was recognized early in 1959 when poly-L-glutamate (PGA) was studied as a plasma expander[154] and is currently proven to be an effective drug delivery system[102,155]. Additionally, these materials can have an unexpectedly large loading capacity and surpass even liposomes' loading efficiency, as reported recently for block polytyrosine micelles (PEG-PTyr) with exceptional DOX encapsulation reaching 63 % wt.[156] Other than improved plasma half-life and stealth effect of a cargo, polypeptidic formulations can interact with cell bio-nano interface and can be beneficial to improve the drug efficacy. Toshiyama et al. compared the efficiency of ubenimex – a protease inhibitor of arginyl aminopeptidase, conjugated to PEG polymer and PEG-pLys block copolymer and demonstrated that the polypeptide-based block copolymer was more effective in vitro than PEG conjugate.[157] Subsequent *in vivo* studies in the HuH7 hepatocarcinoma xenograft model confirmed the superiority of polypeptidic formulation by the higher suppression of tumor growth; additionally, the presence of the PEG block reduced the toxicity of pLys by shielding the polypeptide's cationic nature.[157] The recent overview of polypeptide-based nanomedicine applications is described elsewhere.[102,158]

2.3.1. Synthetic Strategies for Functionalized Polypeptide Synthesis

Solid-phase synthesis, recombinant technology, and ring-opening polymerization (ROP) of α-amino acid N-carboxy anhydrides (NCA) are the main strategies for creating synthetic polypeptide materials. NCA-ROP is a scalable, economical, rapid, and straightforward means of creating high-molecular-weight polymers and block copolymers with polydispersity below 1.2.[159] Two main routes exist to prepare functional polypeptides via NCA-ROP: prepare the functional monomer and conduct the polymerization (**Figure 1.7A**) or conduct postpolymerization modification (**Figure 1.7B**).[160]
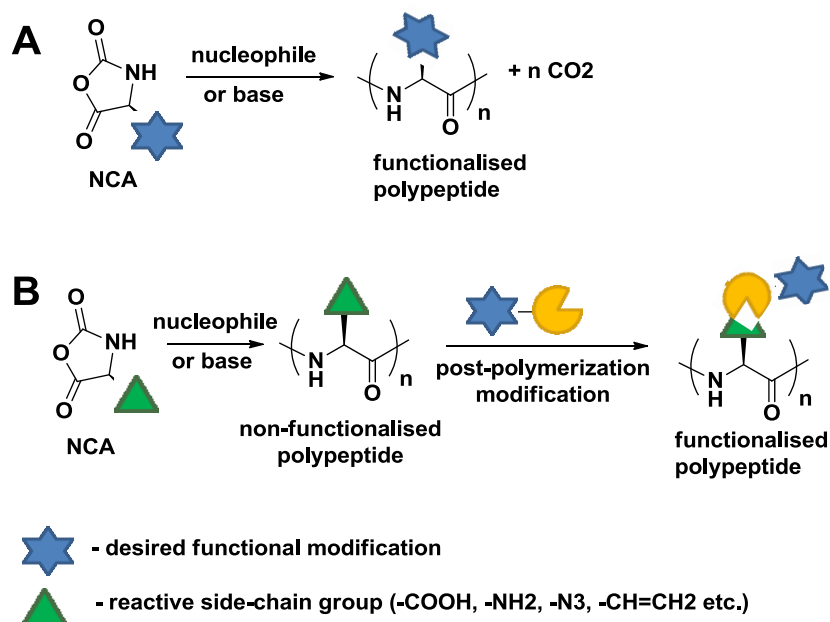
Figure 1.7. Schematic representation of the synthesis of functionalized polypeptides: **(A)** polymerization of sidechain-modified functional monomers, **(B)** conjugating a desired functional group to a reactive polypeptide sidechain. Adapted from Deming et al.[160]

The post-polymerization modification, widely used in the drug delivery field, focuses on the covalent modification of the carrier rather than encapsulation; this supports the incorporation of several modalities (e.g., fluorescent probes, targeting moiety, or therapeutic agents) within the same polymeric backbone, the preservation of functional polypeptide groups, and the maintenance of carrier solubility properties [161].

2.3.1.1 NCA-ROP - The Mechanism and Recent Advances

The initiator's nucleophilicity and basicity determine the initiation of NCA-ROP. In the case of using primary amines as an initiator, two competing processes are possible: the normal amine mechanism or the activated monomer mechanism (**Figure 1.8 A and B**).[162]
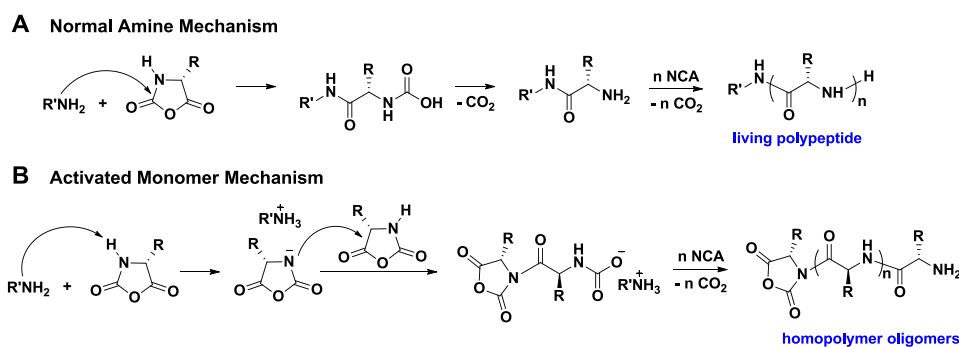
A Normal Amine Mechanism

B Activated Monomer Mechanism

Figure 1.8. NCA-ROP: (A) normal amine mechanism, (B) activated monomer mechanism. Adapted from Cheng et al.[162]

Chain propagation occurs via the normal amine mechanism if the initiator has sufficient nucleophilicity; however, the side reactions and homopolymer formation occur via the activated monomer mechanism if the initiator is significantly basic.[163] Because of the activated monomer side reaction, block copolypeptides prepared from NCA-ROP using amine initiators have structure differences from the theoretical prediction by monomer feed compositions and have high homopolymer contamination.[162]

Several approaches have been proposed to control NCA-ROP with precise monomer consumption and preserve polymerization's living nature. A lack of suitable analytical tools for polymer characterization, especially to analyze polymer end functionality to improve the protocol, represents the main reason why NCA-ROP, known for over 100 years, has been delayed in terms of application. Vayaboury et al. reported using non-aqueous capillary electrophoresis coupled to mass spectrometry to study Lys NCA-ROP in dimethylformamide at different temperatures.[164] The authors demonstrated that decreasing the temperature to 0^0C preserves 99% of the living polymer during polymerization, while at 50^0C and room temperature, 80% were attributed to dead non-reactive polymer; however, reaction completion required four to seven days at $0\ ^0C$.[164] The Vicent group demonstrated that using tetrafluoroborate initiators and conducting polymerization under an inert atmosphere and highly anhydrous conditions allowed control over NCA-ROP, which obtained, in addition to classical linear polypeptides, star-shaped analogs with low polydispersity.[165] Using *N*-trimethylsilyl amine initiators generates polypeptides with controlled functional groups at the C-termini and decreases the reaction time from several days to 24 h at room temperature.[166]

Another approach to obtaining controlled, living NCA-ROP was proposed by the Deming group, which developed novel transition-metal analogs of strong-base initiators that allow the reaction to be completed in 30-60 min at room temperature.[167] Of note, using these organometallic complexes (extremely air- and moisture-sensitive) requires special equipment and experimental conditions that are more challenging to

implement than traditional polymerizations and involves safety concerns regarding residual metals concerning the polypeptides when used in drug delivery.

In recent publications, the Hadjichristidis group demonstrated that purification and NCA-ROP with high-vacuum techniques could control polymerization with predictable molecular weights and a high degree of polymerization.[168] This approach maintains conditions necessary for the living NCA polymerization initiated by primary amines, leading to a simple and easily controlled protocol suitable for polypeptides with various architectures and amino acids.

Unfortunately, the long polymerization times, requirements of highly pure and anhydrous reagents, side reactions, and the obtained high molecular weight polymers (DP>400) remain concerns for applying NCA-ROP. Recently, Cheng et al. reported using crown ethers to accelerate the ROP of γ-benzyl-L-glutamate NCAs initiated by conventional primary amines, reaching 95% of monomer conversion with an 18-crown-6 ether in 18 min.[169] In this case, rapid polymerization kinetics outpace several side reactions, and polymerization can be carried out even in the presence of moisture or aqueous solvents. The recently reported addition of a small amine scavenger allowed the synthesis of various polypeptides directly from unpurified NCAs.[170]

2.3.1.2 The Protecting Groups for Direct Fabrication of Polypeptides via NCA-ROP

Protected NCA monomers should be used to fabricate polypeptides with a pendant functional group, followed by the deprotection steps. In particular, PGA, polyaspartic acid, and polylysine, due to their facile synthesis, purification, and straightforward functionalization strategies, are the most synthesized polypeptides used for drug delivery.[102] The examples of protected NCA monomers and deprotection protocols are summarized in **Table 1.3**.

Table 1.3. Protected monomers and deprotection protocols of common NCA-ROP

Structure	Name/Deprotection conditions	Ref.
	γ-benzyl-L-glutamic acid NCA	
	HBr/TFA, room temperature, 5-16 h	171
	HBr/Acetic acid, 30 ^{0}C, 1 h	172
	NaOH/THF, 4 ^{0}C, 16 h	171
	NaOH/dioxane, room temperature, 12 h	172
	H_2/Pd on C_{act}, acetic acid, 24 h	173
	TMSI, DCM, 40 ^{0}C,12-24 h	172,174
	ROH, DCM, pTSA$_{cat}$,55 ^{0}C, 24 h	175
	β-benzyl-L-aspartic acid NCA	
	HBr/TFA, CHCl$_3$, 25 ^{0}C, 2-3 h	176
	0.8M NaOH aq., 25 ^{0}C, 50 h	176
	2-Aminoethyldiisopropylamine, 35 ^{0}C, NMP/DMF/CHCl$_3$/CH$_2$Cl$_2$, 1-120 h	177
	N-Z-L-lysine NCA (Benzyl Carbamate)	
	HBr/TFA, 1 h	178
	N-Boc-L-lysine NCA	
	TFA, 60 min, room temperature	178
	N-Trifluoroacetamide-L-lysine NCA	
	K$_2$CO$_3$/MeOH aq. Reflux 4 h	178
	N-Fmoc-L-lysine NCA (9-Fluorenylmethyl Carbamate)	
	20% (v/v) piperidine in DMF, 1 h, room temperature	178
	N-Nvoc-L-lysine NCA (6-Nitroveratryl Carbamate)	
	Irradiation λ=360 nm, DMF, H$_2$SO$_{4cat}$, 1 h	178

NCA - N-carboxyanhydrides, ROP – ring-opening polymerization, HBR - hydrobromic acid, TFA - trifluoroacetic acid, NaOH - sodium hydroxide, NMP - N-methyl-2-pyrrolidone, THF - tetrahydrofuran, H_2/Pd on C$_{act}$ - hydrogenation with palladium on carbon catalyst, TMSI - trimethylsilyl iodide, CHCl$_3$ - chloroform, DCM - dichloromethane, ROH - alcohol, PTSA$_{cat}$ - p-toluenesulfonic acid, K$_2$CO$_3$ - potassium carbonate, MeOH - methanol, DMF - n,n'-dimethylformamide, H$_2$SO$_{4cat}$ - sulfuric acid, Boc-tert-butyloxycarbonyl, Fmoc – 9-Fluorenylmethyloxycarbonyl, Nvoc – nitroveratryloycarbonyl.

Several deprotection strategies were developed for poly-γ-benzyl-L-glutamic acid due to the abundance of potential side reactions. Deprotection with strong acids, usually hydrobromic acid (HBr), can lead to chain cleavage caused by a reaction between the amide backbone and protonated side-chain ester groups.[179] Deprotection in basic conditions avoids molecular weight loss but leads to significant racemization.[173] An alternative method is hydrogenation with a palladium charcoal catalyst; however, this strategy is only effective for a molecular weight less than 10 kDa since protected polypeptides with higher molecular weight adopt stable helical conformation, which impedes the access of the catalyst to the ester group.[173] Subramanian et al. demonstrated clean conversion without racemization and chain cleavage with trimethylsilyl iodide (TMSI);[174] however, this reagent can react with ether linkages, and so cannot be used with PEGylated polypeptides.[180] Han et al. confirmed that TMSI could avoid chain cleavage, while deprotection with HBr or NaOH decreases the molecular weight of the PGA acid chain by three or four times, respectively.[172] Deprotection strategies include ester exchange with different functional alcohols under mild conditions and p-toluenesulfonic acid (pTSA) as a catalyst.[175]

Acid hydrolysis represents the primary deprotection strategy for poly-benzyl-L-aspartic acid,[176] supporting fewer side reactions compared to poly-γ-benzyl-L-glutamic acid; however, this strategy can also prompt the formation of a β-aspartyl linkage through cyclic imide intermediate product formation, especially under basic hydrolysis conditions [181]. Amines can also assist deprotection of the benzyl group through an aminolysis reaction when preparing polyaspartamide.[177]

Deprotection of the polylysine amino group is conducted under mild conditions with no evidence of racemization or chain cleavage; different orthogonal protective groups can be simultaneously introduced during polymerization.[178]

Recently, the Lu group reported using epoxy compounds as ultra-fast scavengers of HCl.[182] This strategy allows ring-closure reactions for NCA to occur under moist conditions, enabling access to many NCA monomers with unprotected functional groups that can be polymerized without needing time and resource-consuming deprotection steps.[182] Alternatively, the Liu group reported the possibility of NCA-ROP initiated by tetraalkylammonium carboxylates, which trigger fast polymerization without catalysts, which can be operated in an aqueous environment and allows multiblock copolymer synthesis (demonstrated for 15 blocks).[183]

Due to facile synthesis, easy purification of NCA monomers, good solubility of resulting polypeptides, and straightforward chemistry for postpolymerization modification secured PGA, polyaspartate, and polylysine in the leading positions as carriers in drug delivery.[102,184]

2.3.1.3 Covalent Drug Linkage – the Strategic Advantage of Polypeptide-drug Conjugates

Covalent stimuli-responsive linkers can provide site-specific drug release to reduce the off-target effects of nanomedicines. Differences in microenvironmental factors, such as acidic pH, hypoxic core, redox environment, or presence of specific enzymes, and external stimuli such as photo-irradiation, magnetic, electric field, ultrasound, and temperature can be used to design an intelligent, responsive linker tailored to the targeted tissue or organ.[185] The primary types of drug linkers used for the polypeptide-drug formulation are shown in **Figure 1.9**.
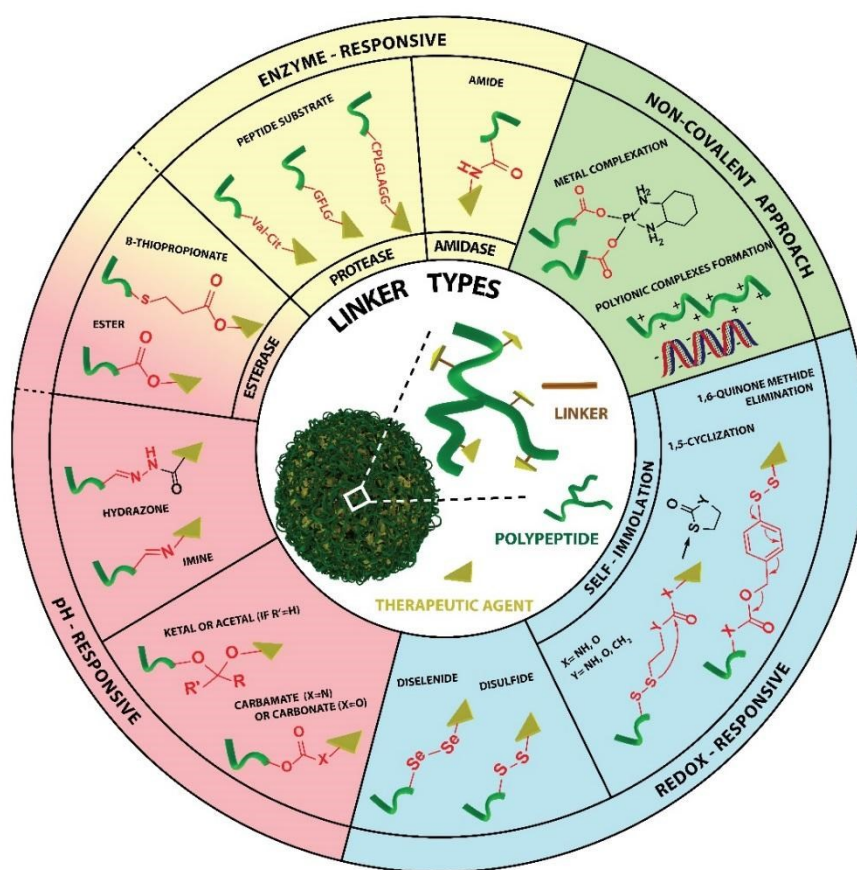

Figure 1.9. The different types of responsive linkers reported for polypeptide-drug conjugates. Adapted from Melnyk et al.[102]

In the case of combination therapy, where the simultaneous delivery of selected drugs in a synergistic ratio remains crucial, the covalent linkage of drugs into the same polymeric chain provides a tremendous advantage and increases efficacy [186,187]. Another

possibility for stimuli responsiveness is to employ intrinsic polyelectrolyte polypeptides that undergo conformational changes and helix-coil transitions depending on pH when shielding/exposure of side-chain charges occurs [188]. The responsive linkage introduced between blocks in copolymers or as crosslinking agents can create stimuli responsiveness of polymeric nanoconstruct.[189–191]

Due to the focus of this thesis on PGA, the following sections will summarize the recent advances and linking strategies related exclusively to this polypeptide.

2.3.1.4 Direct Conjugation via Side-chain Available Group

The side-chain carboxylic group of PGAs allows a direct conjugation of drugs, targeting moieties and fluorescent probes via esterification or amidation reactions [192]. The most advanced clinical trial involved Xyotax (Opaxio, CT-2103), which is currently undergoing clinical trials Ph (III) for non-small cell lung cancer and ovarian cancer.[193] The highly effective chemotherapeutic agent PTX, widely used for various cancer treatments, is not well tolerated and presents with severe adverse drug reactions and poor solubility; however, upon conjugation via ester bonds, PGA provides valuable advantages over free drug administration, including improved water-solubility, and rapid 10-20 min infusions compared to 3-24 h for free drugs, which also require premedication with corticosteroids and antihistamines.[194] Polymeric formulations present less frequent adverse drug reactions and enhanced radiotherapy effects and, when used with chemotherapy as a radiosensitizer, demonstrated comparable efficacy to free drugs, favorable progression-free, and increased overall survival.[195] In addition to ovarian cancer, Opaxio has been evaluated in several other clinical studies for non-small cell lung cancer (phase 3) and breast cancer (phase 2), with comparable efficacy to the free drug and favorable progression-free and overall survival.[193] Despite promising results, the Opaxio formulation can be improved by embedding a targeting moiety or enhancing drug release by improving linker responsiveness. The modification of PGA with carbocysteine represents an exciting proposal to improve the inadequate solubility of free PTX, which requires> 10 h to get 50 mg/ml saline solution, while the conjugate is freely soluble.[196] Adding an extra carboxylic group to the polymeric chain improved conjugate solubility and allowed PTX conjugation via β-thiopropionate esters that undergo more rapid hydrolysis and more efficiently release the drug than when using a non-activated ester bond. *In vivo* studies in the NCI-H460 tumor animal model showed improved tumor suppression compared to the saline group; however, the comparison with the free drug was missing.[196] The NK012 formulation of SN-38 (the active metabolite of irinotecan with 1000-fold higher activity) covalently bound to PEG-PGA via an ester bond[197,198] represents another example of PDCs in clinical trials for refractory solid tumors (phase I), metastatic or recurrent colorectal cancer (phase II), relapsed small cell lung cancer (phase II), advanced metastatic triple negative breast cancer (phase II). Evaluations of combination therapies comprising NK012 with carboplatin in triple negative breast cancer (phase 1) and with 5-fluorouracil and leucovorin in colorectal cancer (phase I)

are ongoing.[193] CT-2106 (camptothecin conjugated using an ester bond and glycine spacer) is in clinical trials (phase I/II) for colon and ovarian cancer.[193,198]

Using high molecular weight polymers as carriers for tumor drug delivery is reported to improve the therapeutic efficacy of the drugs[102,199,200]. Even so, such drug delivery systems are usually associated with poor tissue penetration compared to low molecular weight carriers. An exciting example of PEG-PGA conjugated via an ester bond with combretastatin-A4 (CA4 nanoparticles) demonstrated a significant advantage for tumor suppression compared to the free drug.[199] *In vivo* studies using a murine colon C26 tumor model demonstrated the preferential distribution of conjugates around tumor vessels, where combretastatin-A4 (a vascular disrupting agent) caused tumor damage 72 h after a single injection of CA4 nanoparticles with 74% tumor suppression compared to quick relapse when treated with a free drug and tumor suppression only 24%. A subsequent study sought to improve the efficacy of CA4 nanoparticles and inhibit metastasis through a combination-based therapeutic approach using the CXCR4 antagonist Plerixafor.[200] Treatment with CA4 nanoparticles in an orthotopic 4T1 mammary adenocarcinoma mouse model revealed CXCR4 overexpression and severe hypoxia that can promote metastasis; the addition of Plerixafor significantly improved the tumor inhibition rate from 67.6% (single agent) up to 91.3% (combination therapy), with lung metastasis significantly reduced compared to the control group.

In most studies, PDCs display lower levels of toxicity in vitro compared to free drugs but a higher level of activity in a broad range of tumors *in vivo*,[192] which can be explained by the lower clearance rate of high molecular weight conjugates from the body compared to fast renal clearance of low molecular drugs. Therefore, even simple covalent linkage benefits the targeted delivery via passive accumulation.[192] The next generation of stimuli-responsive linkers, including hydrazone and disulfide linkers, exploit the full potential of targeted delivery, and controlled drug release is highly interesting.

2.3.1.5 Acid-labile linkers in Polyglutamate (PGA) Conjugates

Acid-sensitive linkers take advantage of acidic pH-triggered linker cleavage within the tumor microenvironment or endolysosomes [201] and include orthoester, acetal/ketal, imine, hydrazone, and cis-aconityl moieties.[202,203]

The most commonly used pH-responsive linkers are imine and hydrazone due to the relatively straightforward reaction between the aldehyde or ketone group and the amine or hydrazide group in mild acidic conditions. The stability of the hydrazone linker can be altered by incorporating electron-donating or electron-withdrawing groups through resonance or steric influences, modulating the drug release kinetics.[204] Hydrazone bonds due to the delocalization of electron density by forming resonance structures, which decreases the carbon's electrophilicity, possess higher stability than

imine linkage and are thus preferred for polymer conjugate preparation (**Figure 1.10A**). The introduction of a positive charge on the nitrogen (trimethylhydrazonium ion) and impedance to protonation increase stability towards hydrolysis even at low pH 5,0. Another strategy to increase linker stability involves incorporating an aromatic element (Ar) into a carbonyl compound group.[204] The strategy to stabilize the hydrazone bond can be summarized in the following relation: **Ar**–CH=N–N–CO–**Ar** ∼ **Ar**–CH=N–N–CO–**Aliph** ∼ **Aliph**–CH=N–**N**+R₃ >> **Aliph**–CH=N–N–CO–**Ar** > **Aliph**–CH=N–N–CO–**Aliph**, and explained by overlapping p-orbitals of a double bond and aromatic ring stabilizing the structure disfavor the protonation (**Figure 1.10B**). pH-dependent release represents the main characteristic of hydrazone linkers depicted in **Figure 1.10 A and B**.
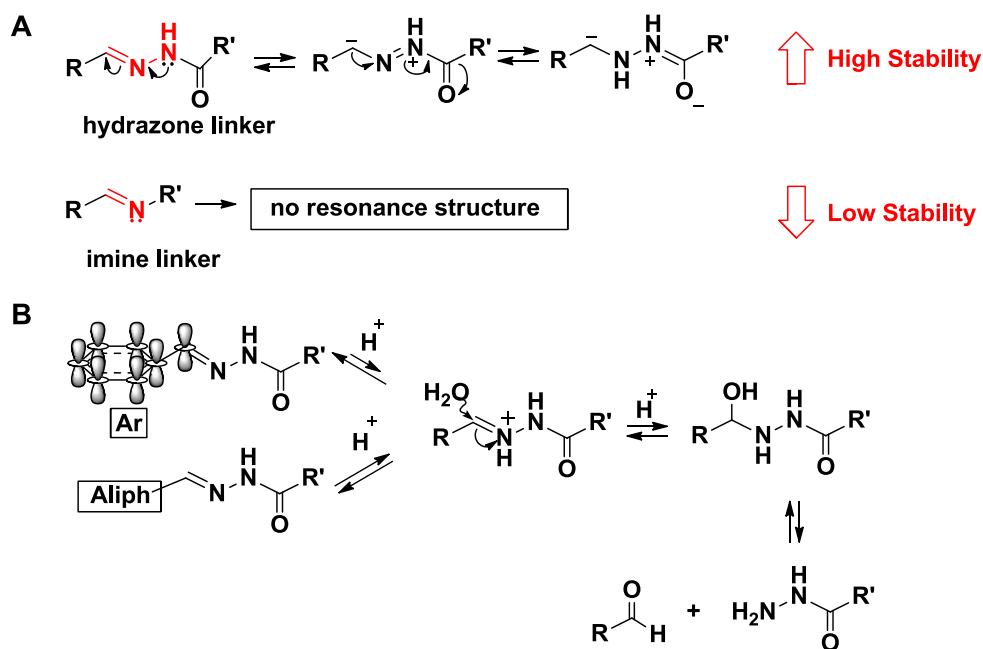

Figure 1.10. (A) Resonance structures and electron delocalization in hydrazone linkage and imine linkage, adapted from Seidi et al. [204] **(B)** Mechanism of the hydrazone linker hydrolysis, stabilized by aromatic ring (Ar) in comparison with alkyl chain (Aliph), adapted from Kalia et al.[205]

As a highly effective cytotoxic agent with a reactive carbonyl group, doxorubicin has been widely used in polymeric systems via hydrazone linkage.[206–210] As demonstrated in various studies, conjugated DOX via hydrazine linker proved to

be relatively stable in blood circulation[209,210] with slow kinetics at pH 7.4 and accelerated release at pH 5.0-6.6 characteristic of the tumor microenvironment.[206–208] Arroyo-Crespo et al. reported that a shorter hydrazone linker between PGA and DOX improved efficacy in a preclinical metastatic triple-negative breast cancer model in combination with aminoglutethimide attached via glycine spacer.[207]

Acetals or ketals are another example of pH-sensitive bonds that are stable in basic conditions and hydrolyzed rapidly in acidic conditions. Therefore, they have been extensively used to protect the carbonyl groups during synthesis.[211] Instability in aqueous acidic conditions has been limited to their use as a linker; however, cyclic acetals possess higher stability due to the detained hydrolysis, as depicted in **Figure 1.11**. Therefore, cyclic acetals are more preferred for drug delivery systems, as an example of gemcitabine conjugated to polyaspartic acid chain[212] showed stability at physiological pH 7.4 with drug release 5.3% at 72 h and increased release to 14.7 % at pH 5.5 and 33.3 % at pH 4.2.
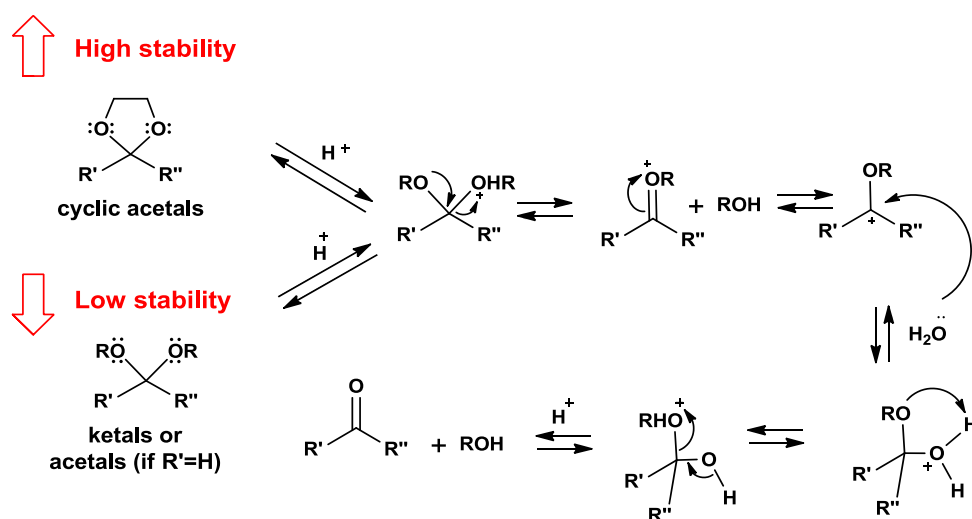

Figure 1.11. Mechanism of the acetals/ketals hydrolysis, adapted from Carey et al.[211]

Extensive use of pH labile linkers does not prove the absolute advantage of such systems with limitations. Usually, pH differences between normal and tumor tissue are insufficient to trigger the response of nanoparticles, and the acidic pH is located far from the blood vessels, limiting the responsiveness in perivascular regions.[201] Therefore, other stimuli-responsive linkers should be evaluated and compared for selected targeted tissue if possible.

2.3.1.6 Redox Responsive Linkers in PGA Conjugates

The increased redox potential controlled by intracellular glutathione triggers the disulfide linkage degradation that is 1000-fold lower compared to the cytosol environment, which guarantees high stability in plasma.[213] Combining specific redox-triggered release with a self-immolative spacer designed to degrade spontaneously and release the intact unmodified drug is an interesting strategy that has vastly grown over the past decade.[214] Similarly to the hydrazone linker, the stability of disulfide self-immolative linkers can be enhanced by introducing electron-donating groups (e.g., methyl groups) next to the disulfide bond; however, aromatic groups favor bond dissociation and so aryl disulfides display less stability.[215]

A simple strategy of disulfide linkage can be applied if the therapeutic agent possesses a thiol group. As an example, borocaptate sodium (BSH), a common therapeutic agent for boron neutron capture therapy, was attached to pegylated polyglutamates (PEG-PGA)[216] and polylysine (PEG-pLys)[217] via a small spacer to guarantee stability under physiological conditions and rapid release in the presence of the reductive environment. Unfortunately, most therapeutic agents lack the thiol groups required to create a simple disulfide linkage, requiring an additional synthetic step to take advantage of this linking strategy. In the self-immolative approach, disulfide-containing linkers release a free drug after a triggered cleavage (**Figure 1.12 A and B**).
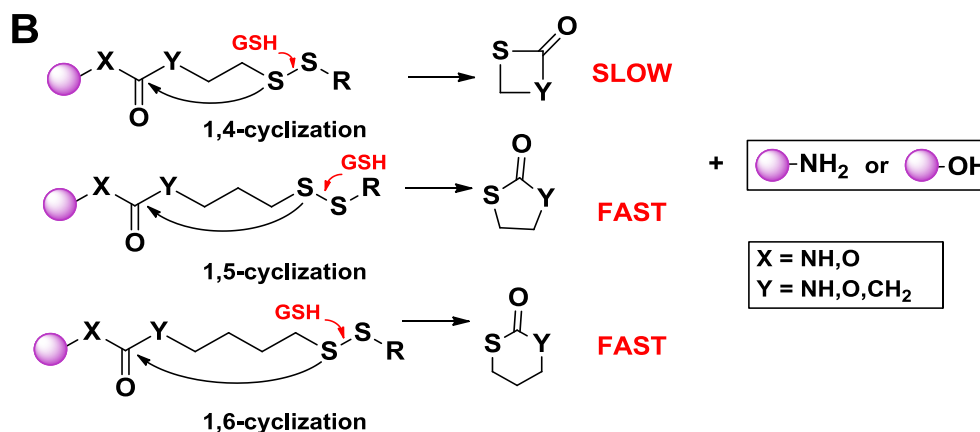

A

1,4-quinone methide elimination

X = NH,O

1,6-quinone methide elimination
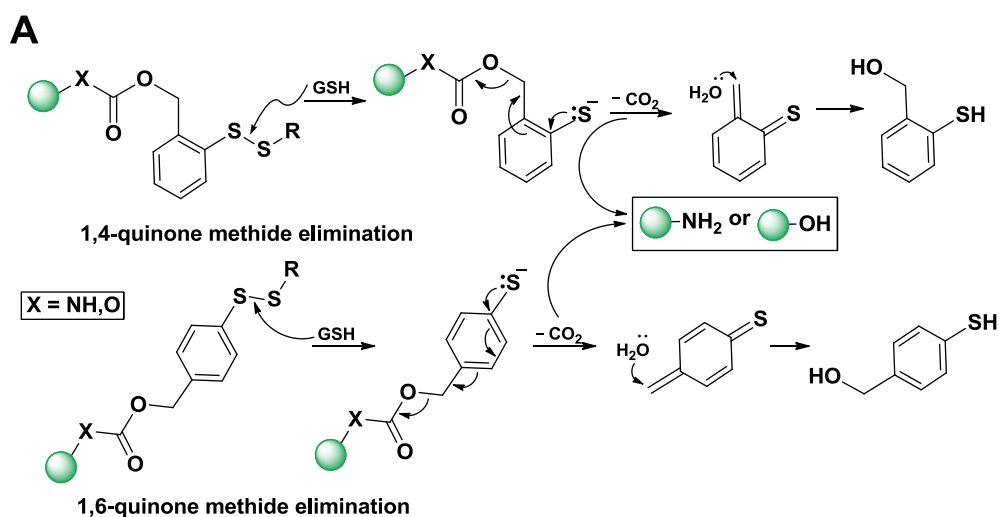
Figure 1.12 Mechanism of disulfide-based self-immolation linker degradation via (**A**) 1,4- and 1,6-quinone methide elimination or (**B**) intramolecular 1,4-, 1,5-, 1,6-cyclization adapted from Deng Z. et al. [218] and Meng X. et al.[219]

The degradation process of disulfide bonds under redox conditions sequentially triggers chemical rearrangements, such as the quinone methide elimination (**Figure 1.12A**) or intramolecular cyclization reactions (**Figure 1.12B**).

Adding an electron-donating group, which enhances the electron density within the aromatic ring, accelerates electron transfer, leading to quinone methide elimination; meanwhile, electron-withdrawing groups produce the opposite effect.[204] The rate of cyclization for the second type of self-immolative linkers is governed by the electrophilic nature of the carbonyl group, resulting in carbonates degrading more rapidly than carbamates. The cycle type is crucial, with lower ring strain being energetically favored. A study of polymer conjugates with curcumin revealed that the 1,5-membered cycle exhibited faster drug release kinetics than 1,4-cyclization.[220] Other studies of camptothecin nanoparticles[221] and monomethyl auristatin E nanoparticles[222] verified enhanced drug release when exposed to a reducing agent (DTT or GSH) and a significantly lower release rate in a reductive-free environment. Taking into account the described properties of various disulfide linkers, in this thesis, a rapid 1,5-cyclization motif was selected to construct a family of conjugates; more detailed synthetic steps and physicochemical characterizations are discussed in *Chapter 3, Section 3.2.2 Synthesis of Redox-responsive PGA-palbociclib Conjugates using a Disulfide Linker.*

2.3.1.7 Amino Acid or Peptide Spacer as a Linker Strategy for PGA

The use of peptide linkers cleaved in response to specific carboxypeptidases overexpressed in tumor cells[223,224] represents a well-established strategy for antibody-drug conjugates with various examples for Val-Cit linker[225,226] and Val-Ala linker.[227] There is an interesting study by Wei et al.[228] that designed an improved version of the peptidic linker, cyclobutane-1,1-dicarboxamide-Cit, that is hydrolyzed predominantly by cathepsin B with limited cleavage by other cathepsin enzyme family.

Regarding polypeptide materials, the application of peptidic linkers for drug delivery systems is scarcely presented. Li et al. reported the application of the GPLGLAG peptide, a substrate for the MMP-2 metalloprotease for the oligo-glutamate-porphyrin-oligoarginine prodrug for targeted photodynamic therapy active in tumor tissue.[229] Additionally, Arroyo-Crespo et al. evaluated the biological impact of a single amino acid, dipeptide, or GFLG spacer for PGA-aminoglutethimide conjugates in combination with conjugated DOX via an amide linker.[187] The authors demonstrated the importance of a small Gly linker to induce a favorable shift in drug release, size, secondary structure, and biological activity.

As the highly promising and relatively not explored linker for polypeptidic carriers, in this thesis, we have selected Val-Cit, which is discussed in more detail in *Chapter 3, Section 3.2.3 Synthesis of an Alternative Self-immolative Peptidic Linker for PGA-palbociclib Conjugates.*

2.3.2. Rational Design of Polypeptide-drug Conjugates for Cancer Treatment

Polypeptides are a versatile platform in which parameters can be easily modulated. The numerous chemical and biological aspects must be taken into account during the design and synthesis of successful conjugates, namely:

- Physico-chemical characteristics: size, polydispersity, shape, topology, solubility, hydrophilic/lipophilic balance, stability, biodegradability, drug loading, remaining free drug; type of the linker and mechanism of drug release, surface decoration with targeted moieties
- *In vivo* behavior: biodistribution, route of the administration, pharmacokinetics, protein corona and cell interactions, intracellular trafficking, and specific targets.

The following section will discuss the crucial parameters of polymer-drug conjugates.

2.3.2.1 Molecular Weight/size

Conjugate size determines the fate of PDC in the bloodstream, its targeting capacity, and cell uptake mechanism. **Figure 1.13** summarizes the effect of nanoparticle size on their *in vivo* fate.[270]
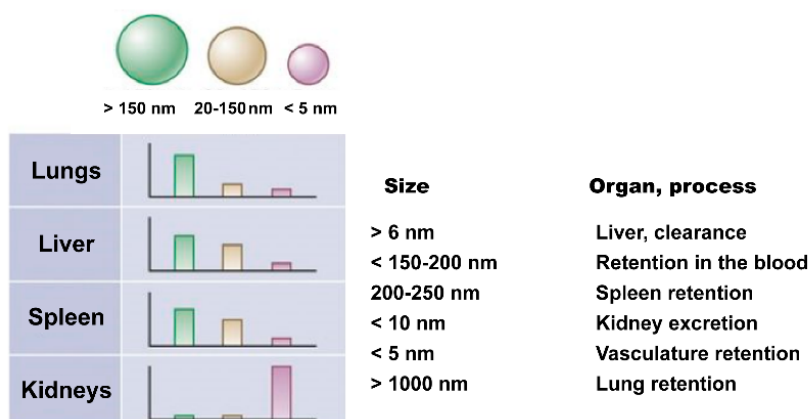

Figure 1.13. Organ clearance and retention depend on nanoparticle size. Adapted from Wei et al. and Blanco et al.[230,231]

After systemic administration with a molecular weight near the renal threshold of 30-60 kDa, polymers with a hydrodynamic radius of 4.5 nm undergo rapid elimination by renal glomerular capillaries and are excreted through the kidneys.[232,233] Thus, PDCs should be larger than 50 kDa to profit from the EPR effect [234]. For example, crosslinked PEG-pLys nanoparticles demonstrated significantly longer blood circulation time and, thus, higher antitumor efficacy than the non-crosslinked formulation and control group.[235]

The distribution of nanoparticles at the tumor site is limited by elevated interstitial fluid pressure, which limits convection; meanwhile, increased extracellular matrix viscosity restricts diffusion, and smaller-sized nanoparticles tend to have better tumor penetration. Cabral et al. examined various size PEG-PGA polymeric micelles of between 30 and 100 nm in size and demonstrated that only 30 nm particles could penetrate effectively inside the tumor.[236] Most antineoplastic drug PDCs used in clinical studies range from 25 to 50 kDa, and their molecular weight directly affects their in vivo behavior.[237] There is an example from Liu et al. that successfully used poor tissue penetration of high molecular weight polymers to specifically target the tumor vessels, the targeted site for a vascular disrupting agent combretastatin-A4, covalently linked to PEG-PGA nanoparticles.[199] However, the molecular weight, polymer structure, and solution conformation are essential for drug delivery systems.

2.3.2.2 Polymer Architecture

The shape and conformation of the polymeric carrier are essential modulators of the in vivo fate of nanoparticles. Most formulated nanoparticles have a spherical form since they are easy to produce and control; however, viruses and bacteria display filament and cylinder shapes in nature. Several studies intended to compare and explain the in-vivo fate of the various nanoparticle architectures depicted in **Figure 1.14**.[231]
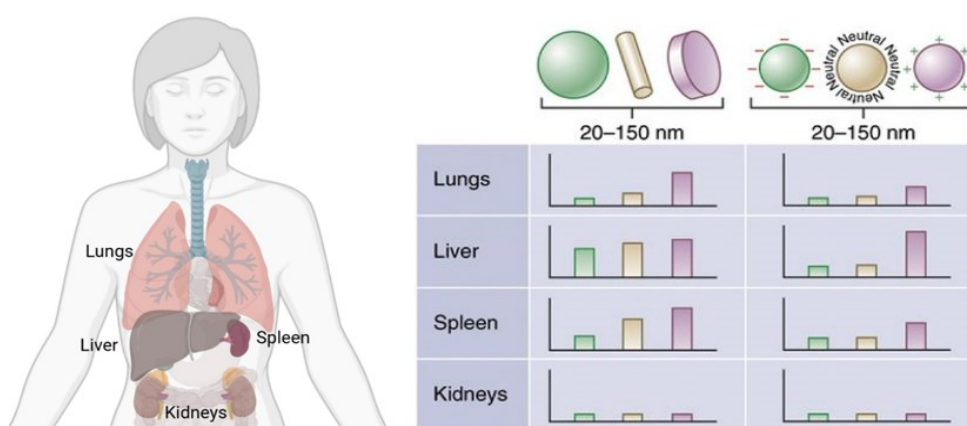

Figure 1.14. Differences in organ accumulation and retention regarding nanoparticle size, shape, and charge. Adapted from Blanco et al.[231]

Several studies demonstrated that circular and branched structures exhibit longer plasma half-life and thus greater efficacy when compared to the linear analog, illustrated for PEG-caprolactone[238], HPMA[239], and PGA[171]. An exciting study aimed to evaluate the effect of polymer architecture on brain delivery for PEG-pLys, which demonstrated that non-PEGylated formulation displayed poor diffusion, conventional linear block PEG-PLL copolymer had a three-fold increase of MSD (Mean square displacement), and branched PEG shell of PLL leads to an 18-fold increase of MSD and almost unhindered diffusion.[240] Regarding cellular uptake, rod-like and worm-like polymeric nanoparticles with conjugated DOX via pH-labile linker demonstrated enhanced toxicity in MCF-7 cells, which might relate to higher cellular uptake.[241] Usually, cylindrical or worm-like nanoparticles demonstrate longer blood circulation time than spherical nanoparticles, which could be explained by the fluid-polymer interactions in the bloodstream.[242] Geng et al.[243] designed an in vitro model of blood vessels and demonstrated that worm-like nanoparticles minimize their interaction with the phagocytes and, in this way, reduce the chances of uptake and elimination from the bloodstream. When nanoparticles flow through the bloodstream, they experience different types of hydrodynamic forces, such as shear and turbulence. Worm-like

micelles resist hydrodynamic forces, making them less likely to stick to the cell surface and, due to the higher surface, the interactions can be easily disrupted by the strong bloodstream flow;[243] however, according to other studies, elongated nanoparticles demonstrated less cellular uptake compared to spherical counterparts.[244] The existing contradictions regarding how nanoparticle shape affects cell uptake can be associated with the type of nanoparticle material, charge, and size parameters that all have impact on the *in vivo* fate. Regardless, most researchers accept that cellular uptake closely relates to nanoparticle shape.

2.3.2.3 Surface Charge of Nanoparticles

The positively charged carriers can benefit from adsorptive mediated transcytosis relying on the electrostatic binding to the negatively charged BBB[221]; however, positively charged nanoparticles usually exhibit high toxicity, which requires extra modification (e.g., PEG) to hide/shield the positive charge. High-density PEG chains prevent opsonization and reduce macrophage uptake via steric hindrance; however, they compromise cellular uptake.[245] Similarly, hydrophobic nanoparticles display good adsorptive properties due to their affinity towards the lipid bilayer but utilize PEGylation to avoid protein binding and rapid clearance from the bloodstream.[246] Nonspecific uptake into the liver and spleen can be reduced by developing nanoparticles with a slightly negative surface charge due to the electrostatic repulsion from the cellular surface.[247]

2.3.2.4 Ligand Density

The display of numerous ligands on a nanoparticle surface, which enhances cell targeting and targeted cell receptor density, represents two critical parameters to consider when improving nanoparticle selectivity.[248,249] Nevertheless, little research has been conducted to evaluate an ideal ligand density. Elias et al.[250] evaluated superparamagnetic iron oxide (SPIO) nanoparticles with different densities of HER2/neu targeting antibodies and concluded that there is an optimum for ligand concentration. The authors suggested that high ligand density on the nanoparticle surface creates a steric hindrance for cell binding or that nanoparticles consume the available receptors and decrease their availability for other nanoparticles.[250]

Reuter et al.[251] observed similar behavior, demonstrating that the fraction of internalized nanoparticles increased only up to the point when ligand density increased. After this point, they observed a decrease in cell uptake, with most of the nanoparticles adsorbed onto the surface instead of undergoing internalization. The authors explained these results by the large contact area of nanoparticles with high ligand density, wrapping nanoparticles by the cell membrane, and, therefore, depletion of available receptors.[251] Ghaghada et al. built a mathematical model to evaluate the saturation of ligand-receptor

interaction and predicted that the liposomal uptake with folate receptors should decrease after reaching approximately 500 ligands per liposome.[252] These theoretical results were independently confirmed by another research group that demonstrated in vitro and in vivo that 0.01-0.03% of folate receptor is the optimal amount for liposomal surface decoration, while a higher amount progressively decreased cellular binding of the liposomes.[253]

Interestingly, ligand density can also affect cell trafficking. Dalal et al.[254] demonstrated the shift from caveolae-mediated endocytosis and perinuclear trafficking for low folate ligand density quantum dots to clathrin-mediated endocytosis and lysosomal trafficking for nanoparticles with high ligand density. In another study, Khalil et al.[255] reported that nanoparticles modified with octaarginine peptide liposomes at low ligand density become internalized mainly through clathrin-mediated endocytosis followed by lysosomal degradation, while those with high ligand density enter the cell via macropinocytosis with lower lysosomal degradation observed.

Understanding the mechanisms and possibilities to modulate intracellular trafficking represents an exciting approach to drug delivery that, combined with specific responsive linkers, can significantly improve the efficiency of the designed formulation.

3. Strategies for Brain Drug Delivery

The poor efficacy of brain tumor therapies relates to the presence of the BBB, which possesses unique characteristics and limits delivery to the brain.[7,256] The BBB structure is depicted in **Figure 1.15**.
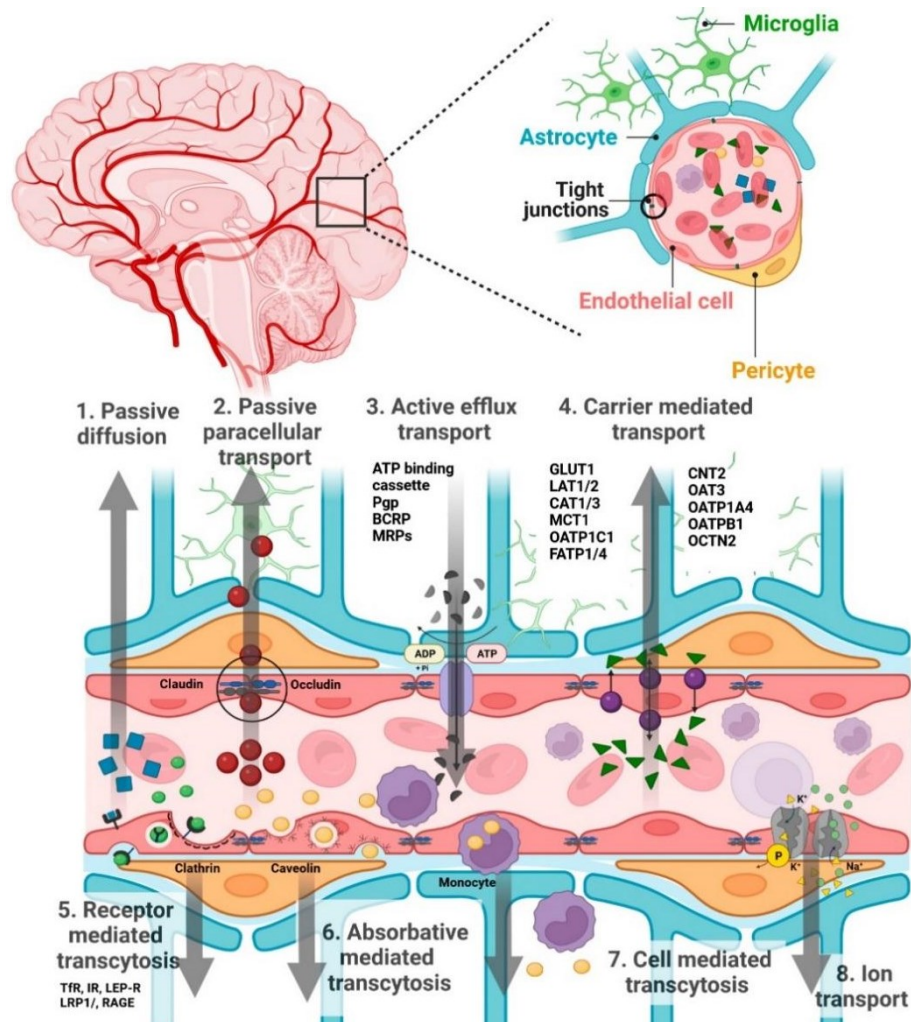
Figure 1.15. Schematic representation of the BBB structure and transport mechanisms across BBB that includes: passive diffusion across endothelial cells (1) or through tight junctions (2) – only limited number of small molecules <400 Da can pass; active efflux transport (3) – directed to eliminate substances from the brain, via ATP binding cassette, P-glycoproteins (Pgp), multidrug resistance proteins (MRPs), breast cancer resistance protein (BCRP); Carrier-mediated transport (4) - can work in both directions to and from the brain; Receptor-mediated transport (5) – require ligand interaction with the receptor and responsible for large molecule transport; Absorptive-mediated transport (6) – caveolin-mediated endocytosis, depends on the ligand interaction with the glycocalyx of brain endothelial cells; cell-mediated transport (7) – relies on the migration of macrophages, neutrophils, and monocytes across BBB; ion transport (8) – regulate the sodium, calcium, and potassium transport, not reported to use for drug delivery systems. Adapted from Daneman and Prat, 2015 and Knox et al.[256,257]

       The structural components of BBB are brain pericytes, astrocytes, neurons, basal membrane, and capillary endothelial cells (ECs) that lack fenestrations and are

linked by tight junctions forming a continuous barrier and impeding paracellular diffusion.[258] Lipinski et al. analyzed the properties of molecules that crossed the BBB and formulated rules describing the characteristics of molecules highly likely to pass through the BBB.[245] Lipinski's rule of five proposes a therapeutic molecule with less than five hydrogen bonds, fewer than ten hydrogen acceptors, a calculated octanol/water partition coefficient Log P of less than five, and a molecular weight of no more than 500 Da is more likely to exhibit increased adsorption or penetration through BBB.[245] Lipinski's rules have been developed and implemented into computational methods to predict structural-functional properties, identify compounds likely to cross the BBB, accelerate the lengthy and expensive process of new molecule development, and conduct evaluations.[259]

As an alternative to Lipinski's rule, suitable for low molecular weight drugs, polymer therapeutics can provide an orthogonal approach to cross BBB via targeted delivery. This represents a promising strategy that can increase the treatment efficiency of drugs in the brain and decrease off-targeting; however, it requires additional synthetic steps and raises the complexity level of the drug delivery system. Overall, there are two main strategies to deliver the drug to the brain: invasive methods, such as intratumoral injections, and non-invasive methods, which involve crossing the BBB (intravenous administration) or bypassing the BBB (intranasal administration). **Figure 1.16** illustrates the main strategies for brain drug delivery with listed advantages and drawbacks. In the following sections, we will discuss the recent advances in brain drug delivery, focusing on polymer therapeutics.
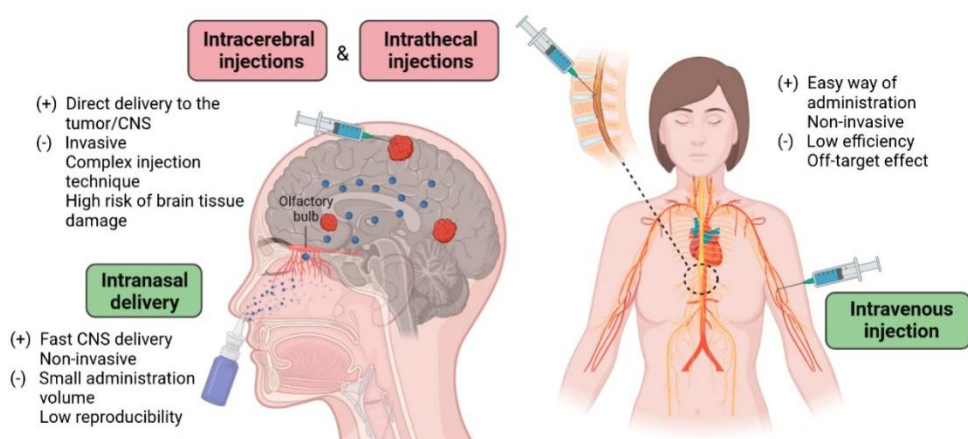

Figure 1.16. Strategies for brain drug delivery: invasive (intracerebral, intrathecal), non-invasive (intravenous, intranasal). Adapted from Mitusova et al.[260]

3.1. Intravenous Administration: Crossing the BBB

There are several strategies to transport medications through the blood-brain barrier followed by intravenous administration: carrier-mediated transport, receptor-mediated endocytosis (RME), and adsorptive-mediated endocytosis (AME).[261]

Carrier-mediated transporter (CMT) proteins are highly expressed on brain endothelial cells and allow the selective passage of small molecules and essential nutrients such as glucose and amino acids to the brain. There are over twenty different CMT proteins identified, with some possessing demonstrated or potential use for targeted brain delivery, including GLUT1 – hexose transporter,[262,263] MCT1/8 - monocarboxylic acid transporter, involved in lactate and pyruvate, transport,[264,265] LAT1/2 – L-type neutral amino-acid transporter,[266–268] CAT1/3 - cationic amino acid transporter, OATP1C1 - thyroid hormone transporter, FATP1/4 – fatty acid transporter, CNT2 - nucleoside transporter, OAT3, OATP1A4, OATP2B1 - organic anion transporter, OCTN2 – organic cation transporter,[257] glutathione transporters.[264,269,270] Interestingly, the LAT1 transporter displays overexpression in HGGs compared to LGGs and may represent an attractive target [271].

Receptor-mediated endocytosis (RME) relies on ligand binding to a corresponding receptor on the cell surface and endocytosis, which allows the transport of large molecules such as hormones and growth factors.[272] Targeted RME nanoparticles have shown promising results in improving drug delivery and reducing off-target effects. Said nanoparticles have used the following receptors: TfR – transferrin receptor,[273–275] Lf – lactoferrin receptor,[276,277] IR – insulin receptor [278,279], LEP-R – leptin receptor, LRP1/2 – lipoprotein receptor, e.g., Angiopep-2,[280,281] RAGE – receptor of advanced glycation end products, e.g., RGD motif to target integrin receptors[282,283], and the folate receptor.[284] The beneficial effect of nanoparticle surface modification with lactoferrin was demonstrated for PEG-PLGA nanoparticles loaded with shikonin.[276] In another study, the Angiopep-2 decoration (LRP receptor target) was used to address the challenges for brain suicide gene delivery with PEI-pLys-PEG block copolymer.[285] Peptide-functionalized nanoparticles demonstrated enhanced BBB crossing in an invasive orthotopic human glioblastoma model and significant tumor reduction compared to non-functionalized nanoparticles and the control group.[285] Another target against the LRP receptor, which displays overexpression in the brain endothelial, is apolipoprotein E (ApoE). Wang et al. demonstrated that decorating PEGylated polycarbonate-based polymer with the COG133 ApoE-mimetic peptide increased nanoparticle tumor accumulation by 4.5 and 10 times after 6 and 24 h of post-systemic administration in an orthotopic medulloblastoma mouse model;[286] furthermore, they observed encouraging therapeutic effects. In another study, Cui et al. designed dual-targeted PLGA nanoparticles that encapsulated PTX and curcumin and employed magnetic guidance and transferrin receptor T7-binding peptide, which resulted in a five-fold enhancement in brain delivery and improved glioma therapy efficacy.[287] All mice that received the nanoparticle survived, as opposed to a 62.5% survival rate for the group

that received free drugs.[287] RME is the most studied and widely used method for targeted brain delivery following intravenous administration.

Adsorptive-mediated endocytosis (AME) is a non-specific strategy that relies on the interaction between positively charged molecules, such as polymers or nanoparticles, and the negatively charged membrane of the BBB. Several carriers can exploit this strategy due to their cationic nature, such as chitosan,[288,289] cationized albumin,[290–292] dendrimers,[293] and polyimines (polyethyleneimine (PEI)[294] and polypropylenimine (PPI)[295]). The adsorption of the nanoparticles on the cell surface is followed by the formation of small vesicles that are taken up by cells; however, strong electrostatic binding to an anionic site does not guarantee passage through the BBB. For example, Monsalve et al. demonstrated that unmodified PEG-chitosan carriers have poor permeation ability across the BBB, which can be significantly improved by adding the mAb OX26 (TrR ligand) to the nanoparticle surface.[288]

Cell-mediated transcytosis uses immunocytes, monocytes, macrophages, dendritic cells, lymphocytes, neutrophils, and stem cells to transport macromolecules across cellular barriers such as the BBB.[296] In most cases, a "Trojan horses" strategy using monocytes is desirable for nanoparticle delivery, with demonstrated high efficiency in bypassing the BBB and targeting inflamed brain areas;[297] however, cell-mediated transport suffers from serious drawbacks associated with poor drug loading, disintegration, and early cargo release.[296]

Although the concept of targeted delivery was postulated more than 100 years ago, no targeted nanomedicine formulations have been clinically approved. The first targeted nanomedicine that entered clinical trials was MCC-465 - a PEGylated immunoliposome encapsulating DOX with F(ab')2 fragment of human Ab attached.[298] MCC-465 demonstrated excellent specificity for cancerous tissues over healthy cells in stomach cancer; however, further clinical trials were discontinued due to the loss of findings. Currently, two liposomal formulations that target the BBB are undergoing clinical trials: 2B3-101 (PEGylated liposome with encapsulated DOX and attached glutathione ligand, Ph1/Ph2); SGT 53 (Cationic liposome, with complexated plasmid DNA and modified with anti-transferrin scFv ligand, Ph2).[299]

Coating nanoparticles with cancer cell-recognizing ligands is an appealing strategy for solid tumor treatment since only a small portion of the injected dose reaches the tumor cells. Dai et al. studied Au and silica nanoparticles with trastuzumab and folate ligands in multiple mouse tumor models: ovarian SKOV-3, glioblastoma U87-MG, lung adenocarcinoma Calu-3, and breast 4T1 xenograft models.[300] They demonstrated no significant differences in targeting tumor tissue between modified and untargeted nanoparticles, with only 0.0014% of the injected dose delivered to the tumor cells and most (0.7%) of nanoparticles trapped in the extracellular matrix or taken up by tumor-associated macrophages.[300] Biancacci et al. demonstrated a similar distribution pattern in the 4T1 triple negative breast cancer mouse model.[301] For PEG-HPMA crosslinked 20–30 nm micelles, two-thirds of tumor accumulated nanoparticles localized to the

extracellular space, and the remaining nanoparticles were predominantly uptaken by F4/80[+] phagocytes.[301] Thus, targeting moieties for nanoparticle surface decoration remains highly questionable. The demonstrated clinical benefits of marketed polymer therapeutics so far can be attributed to establishing a local depot and slow drug release within the tumor microenvironment rather than reaching the tumor cells. Overall, ligand-mediated drug delivery is a promising approach for delivering drugs to brain tumors and selective targeting of cancer cells; however, adverse interactions with tumor-associated macrophages and poor penetration inside the tumor should be considered for the next generation of nanoparticles. Lin et al. developed a double-targeted system based on bovine serum albumin (targets SPARC- and gp60 albumin-binding proteins overexpressed in glioma and endothelial cells of tumor vessels) with conjugated cell-penetrating peptide LMWP, which demonstrated enhanced brain penetration, tumor infiltration, and cellular uptake.[302] Recently, more sophisticated triple-targeted systems were designed to deliver a protein cargo into midbrain organoids after crossing a co-culture model of the BBB, demonstrating a three-fold increase in cargo delivery compared to untargeted nanoparticles.[303]

In the field of pediatric brain tumors, Kumar et al. developed polymeric nanoparticles based on PEGylated polycarbonates with conjugated targeted peptide COG-133 and incorporated a combination of MDB5 (SMO inhibitor) and SF2523 (dual inhibitor of BET and PI3K).[304]The authors demonstrated a higher accumulation of targeted nanoparticles in the tumor site than free drugs and non-targeted nanoparticles and the significant inhibition of medulloblastoma progression in orthotopic medulloblastoma-bearing NSG mice**.

An ideal drug delivery platform should be multimodal, including targeting moiety and covalently attached drugs via specific

stimuli-responsive linkers to direct the drug release in the tumor cells or tumor microenvironment while possessing a good safety profile and being biodegradable. Due to the economic aspects and extended time for development, most reported systems have failed to match all the above-mentioned characteristics that, consequently, obscure the possible benefits of the developed formulation. Only a few studies tried to cover all aspects.

3.2. Local Drug Delivery to the Brain: Intratumoral, Intrathecal, Intracavitary, and Convection-enhanced Therapies

Unfortunately, the clinical translation of targeted nanoparticles has been hindered by the additional step of incorporating a targeting moiety, which can be costly and poorly scalable. This challenge can be addressed by optimizing the process of incorporating targeting moieties or exploring the alternative routes of drug delivery bypassing BBB.

The most direct method for brain delivery bypassing the BBB is the intracerebral injection, which is commonly used for primary brain tumor treatment.[305] The recent preclinical studies with oncolytic Zika virus demonstrated the ability to elicit antiviral immunity and stimulate the apoptosis of glioma stem cells.[306] Direct drug injections into the tumor site have demonstrated promising results in treating brain tumors;[307] however, this method is highly invasive and traumatic for the patient, especially in the pediatric field, where the least harmful strategy is preferable and is highly needed.

One alternative to circumvent BBB is applying local treatment during tumor resection - intracavitary therapy.[308] Utilizing polymers as a drug depo for local delivery presents promising advantages, as it can mitigate significant drawbacks linked to systemic administration, such as suboptimal drug concentration in the brain and unintended off-target effects. The biodegradable copolymer, poly(carboxy phenoxy-propane/sebacic acid) anhydride, impregnated with the alkylating chemical carmustine (also known as Gliadel® wafers) are currently the only approved drug delivery implant for local therapy of HGG.[309] Despite the apparent improvement in overall survival from 23 to 31 weeks in patients with malignant gliomas, the moderate effect might be attributed to rising resistance and insufficient diffusion into the brain parenchyma.[310]

Over the last few years, various biomaterials and anticancer drugs have been evaluated for local delivery. Interesting results were obtained for wafers of PTX-loaded polyphosphoester particles (Paclimer), which enabled sustained drug release for more than thirty days and demonstrated the increase of median survival rate in rat 9L gliosarcoma brain model.[311] The same animal model demonstrated the efficacy of thermosensitive gel based on PEG-polycaprolactone diblock copolymer with embedded PTX (OncoGel), significantly increasing animal survival.[312] The therapeutic benefits of these local polymer-drug methods remain limited and inadequate diffusion from the polymer site into the brain parenchyma poses a severe challenge.

Another strategy for drug delivery to the brain is convection-enhanced delivery, developed in the 1990s by Bobo et al.[313] Convection-enhanced delivery involves the placement of a small catheter into the brain tissue and applying a positive pressure gradient to drive the drug through the catheter into the surrounding tumor tissue. Recently, liposomal DOX with convection-enhanced delivery administration received clinical approval for the intracranial treatment of resectable glioblastoma.[260]

Intrathecal delivery involves direct drug administration into the epidural or subarachnoid space. The injected drug molecules diffuse through the meningeal layers to easily reach the cerebrospinal fluid (CSF) that surrounds the brain and spinal cord and, in this manner, allow the drugs to bypass the BBB.[314] Several nanoparticles were tested regarding intrathecal administration: alginate/chitosan,[315] maltose-beta-cyclodextrin,[316] PAMAM,[317] PEI,[318] liposomes,[319,320] poly(aspartamide),[321] and polystyrene.[322] Interestingly, Shyam et al. studied differently-shaped PEG-PEI nanoparticles, demonstrating that rod-like nanoparticles displayed greater efficiency siRNA delivery to the brain;[323] however, associated safety concerns related to this invasive drug

administration, risk of brain tissue damage, low diffusion to distant brain areas, and rapid clearance within the CSF represent the main challenges for this technique.

3.3. Intranasal Administration

Intranasal administration has gained interest in recent decades due to its non-invasive character and the potential for a more rapid onset of action than traditional systemic delivery systems. Intranasal delivery has several advantages over standard intravenous administration, including a non-burdensome and painless approach, appropriate for children, and improved bioavailability by avoiding the first-pass metabolism in the liver.[324] Frey et al. developed the first intranasal method in 1989 to target CNS neurotrophic factors.[325] Historically, the intranasal approach has been successfully applied for the systemic delivery of small molecules that are unstable or ineffective via oral administration;[326] however, targeted brain delivery via intranasal administration is less studied than intravenous or oral administration. Difficulties in establishing an appropriate ex vivo and in vivo model for nanoparticle screening, a lack of understanding of the transport mechanism across the nasal membrane, unstandardized protocols, and requirements for preclinical studies make intranasal administration a challenging test to establish.

To design an effective formulation for drug delivery to the brain via the intranasal route, it is crucial to understand the transport mechanism involved, the anatomy of the nasal cavity and nervous system, and the pathophysiology of the disease to design and guide nanoparticles to the correct brain location and make nanoparticles more selective for tumor cells[327]. Therefore, the crucial factors will be discussed and linked to treating brain tumor pathology in the following sections.

3.3.1. Mechanisms of Intranasal Drug Delivery to the Brain

Permeation through nasal mucosa depends on drug solubility, residence time, metabolic stability, and mucociliary clearance rate, which should be considered when designing a carrier for intranasal delivery.[328] **Figure 1.17** shows the possible routes of the therapeutics after intranasal administration.
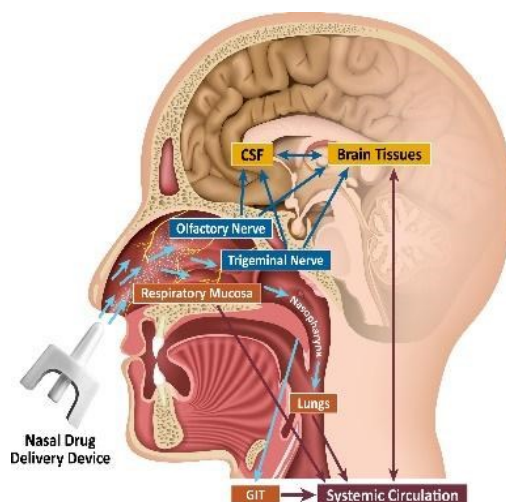
Figure 1.17. Schematic representation of the different drug pathways after intranasal administration: to the brain (blue arrows) or into the systemic circulation (red arrows).[329]

Figure 1.18 demonstrates the structure of olfactory mucosa – the targeted route for intranasal brain delivery.
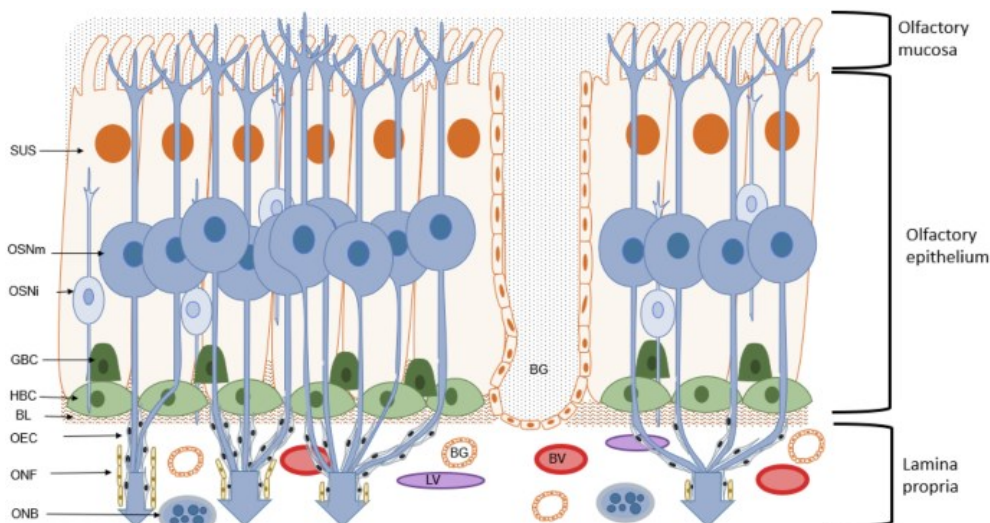

Figure 1.18. Structure of the olfactory mucosa: OE – olfactory epithelium, LP – lamina propria, OSNm – mature olfactory sensory neurons, OSNi - immature olfactory sensory neurons, OB – olfactory bulb, OECs – olfactory ensheating cells, ONFs – olfactory nerve fibroblasts, SUS – sustentacular, BGs – Bowman's glands, ORN – olfactory receptor neurons, GBC – globose basal cells, HBCs – horizontal basal cells, LP – lamina propria, BL – basal lamina, BVs – blood vessels, LVs – lymphatic vessels.[330]

After intranasal administration, the drug can enter the lungs via the nasopharynx or end up in the gastrointestinal tract due to mucociliary clearance. The mucin layer is the first gel-forming barrier that nanoparticles encounter using intranasal administration, which consists of glycoproteins, lipids, salts, enzymes, and cellular debris.[331] The mucin layer is approximately 0.2–0.6 µm deep and is linked via disulfide bonds to other mucin fibers.[332] The mesh space of mucin is 20-200 nm, suitable for small molecule and nanoparticle passage, while larger carriers are efficiently trapped.[333] Hydrophilic negatively-charged nanoparticles will have more chances to pass the mucin layer than lipophilic drugs[331] or positively charged ions, which bind to negatively charged mucins.[334]

After passing the mucin barrier, the remaining drug diffuses in the nasal cavity to the posterior region and reaches the olfactory region. The mechanism of nose-to-brain delivery was initially attributed only to the olfactory pathway;[335] more recently, the contribution of the trigeminal pathway has been confirmed with predominantly delivery to caudal brain regions and the spinal cord.[336,337] Through adsorption in the respiratory mucosa, drugs in the lungs or gastrointestinal tract enter the systemic circulation and must pass BBB to reach the brain.

The neuronal nose-to-brain pathway includes intraneuronal and extraneuronal transport.[328] The intraneuronal olfactory and trigeminal transport require drug internalization by axons and transport inside the nerve until the drug reaches a synaptic cleft of the olfactory bulb or the brain stem. The axonal transport is prolonged; it takes 1.5-6 h for the olfactory nerve and 17-56 h for the longer trigeminal nerve to reach the target destination.[334] Several studies demonstrated that olfactory sensory neurons could endocytose or pinocytose polymeric carriers (insulin,[338] albumin,[339] wheat-germ agglutinin horseradish peroxidase (WGA-HRP)[340]) and even large 50 nm Au nanoparticles.[341] Viruses can utilize axonal endosomal transport for infection, reported for influenza virus via olfactory nerve[342] and for WGA-HRP[343] and Herpes virus[344,345] via the trigeminal nerve.

The extraneuronal pathway occurs along the olfactory or trigeminal nerves by bulk flow processes[346] due to the high turnover rate for the olfactory sensory neurons (OSN). Every 30-60 days, mature OSNs undergo cell death and leave a gap that is replaced by new OSNs[347] (**Figure 1.18**). During the replacement and maturation process, there is a delay in the formation of tight junctions, thus increasing permeability.[346] This delivery route is rapid, taking just a few min for the drug to reach the olfactory bulb and CNS.[328] There is a transcellular drug transport via supporting cells, where the drug passes through the lamina propria.[346] Therefore, the drug transport to the brain following intranasal administration combines the different pathways. Modifying the surface of nanoparticles with mucoadhesive/mucodiffusive agents may facilitate the mucosa passage, which will be discussed in the following section.

3.3.2. Strategies to Increase Mucus Penetration/diffusion of Drug Delivery Systems

Musumeci et al. reported that surfactants such as polysorbate 80 (Tween 80) and PEGylated PLGA formulations increase the uptake by olfactory ensheathing cells compared to chitosan and PLGA nanoparticles.[348] Mistry et al. evaluated polystyrene nanoparticles of different sizes (20, 100, 200 nm) with chitosan or polysorbate 80 coatings and demonstrated that nanoparticles could not cross excised porcine mucosa after 90 min; however, the formulation with polysorbate 80 provided deeper tissue penetration.[349] Further evaluation of these nanoparticles *in vivo*[350] demonstrated no difference when adding polysorbate 80 to the formulation. The lack of conjugation may have induced formulation separation during the intranasal passage, thus highlighting the necessity of a stable covalently linked system. Chitosan nanoparticles were transported to the brain in a significantly lower amount than those without chitosan coating.[350] In contrast, Bonaccorso et al. tested nanoparticles with positive (chitosan/PLGA) and negative (PLGA) charge with added polysorbate 80 and reported brain accumulation for both.[351] Interestingly, the accumulation area in the brain was different (caudal versus rostral) depending on the nanoparticle type.[351]

In another study, Clementino et al. designed nanoparticles with different kinetic profiles that could deliver simvastatin to the brain.[352] Hybrid nanoparticles with lecithin and chitosan demonstrated rapid mucosal permeation, while polycaprolactone nanoparticles stabilized with sodium caproyl hyaluronate or Tween 80 coating displayed slower mucosa passage but higher drug accumulation at later time points.[352]

Kanazawa et al. studied the mechanism of intranasal drug delivery for hydrophilic (PEG-polycaprolactone) and hydrophobic (stearic acid) polymers linked to arginine-rich oligopeptide as an adhesive moiety.[353] The results demonstrated that hydrophobic carriers displayed higher accumulation in the nasal epithelium but lower in the trigeminal nerve, with rapid and high accumulation in the forebrain after 15 min to 1 h and no transport to the hindbrain. A PEGylated-polycaprolactone carrier was found in both forebrain and hindbrain areas associated with olfactory and trigeminal pathways.[353]

To evaluate the impact of a nanoparticle's surface charge, Gabal et al. prepared nanoparticles with similar size and opposite zeta potential and introduced them intranasally in albino mice within a thermosensitive gel.[354] The results demonstrated the improved bioavailability for both systems due to the gel formulation and increased residence time. Toxicity and histopathological studies revealed no alterations for gel formulations, with the highest toxicity observed for cationic nanoparticles, followed by anionic nanoparticles.[354]

The drug permeation through the nasal mucosa depends on several factors, such as the size of the carriers, surface charge, hydrophobicity, and interactions with proteins and cellular receptors during the intranasal administration. We have identified several compounds that are amply reported in the literature for intranasal delivery, such as lectin

peptides, hyaluronic acids, and thermosensitive gels based on poloxamer that will be described in more detail in *"Chapter 2 – Rational Design of a PGA-based Intranasal Platform for Brain Delivery"*.

4. Nanomedicine for Brain Tumor Therapy

Despite the many known types of brain cancers, developments in this field are so scarce that many classes of nanomedicines were never introduced, and nanotherapies for many types of brain cancers were never developed, even on the level of basic cell toxicity tests. Therefore, in the following sections, only the general overview of known nanomedicines for brain tumor therapy will be given.

4.1. Inorganic Nanomedicines for Brain Tumor Therapy

In preclinical studies, several Au-, Fe-, silver (Ag)-, and zinc (Zn)-based nanoparticles have shown promise in glioma models. Au nanoparticles with easily tunable size and shape, large surface area-to-volume ratio, high degree of biocompatibility, and versatile surface modification possibilities represent the most studied carriers for drug delivery.[355] Ruan et al. demonstrated that multi-structured PEGylated 40 nm Au nanoparticles with conjugated doxorubicin (DOX) and Angiopep-2 (a peptide that targets lipoprotein receptor-related protein (LRP) to facilitate crossing the BBB) increased the median survival of C6 glioma bearing mice 1.9-fold compared to control and 1.5-fold compared to non-targeted nanoparticles.[356] Y. Cheng et al. studied the same carrier but modified with a TAT (transactivator of transcription) peptide in the U87 mouse model.[357] TAT-Au nanoparticles demonstrated a striking enhancement of BBB permeation, with 2.9% of the injected dose accumulating in the brain compared to 0.6% of non-targeted Au nanoparticles. Au nanoparticles with incorporated spherical nucleic acid have been evaluated for gene delivery in U87 xenograft orthotopic mice model [358] Au nanoparticles crossed the BBB and brain tumor barrier (BTB) and infiltrated the tumor parenchyma to promote persistent *Bcl2L12* gene silencing and therefore, significant tumor reduction. Another group reported Au nanoparticles coated with PEG, chitosan, and polyethyleneimine to protect small interfering (si)RNA that knocked down over 75% of Ape1-expression in pediatric patients with ependymoma and medulloblastoma cells as a beneficial means to circumvent radiotherapy resistance of pediatric brain tumor.[359] Biocompatible IO nanoparticles can also be used without polymer coating. Norouzi et al. used IO nanoparticles loaded with DOX[360] and demonstrated a 2.8-fold increase in DOX uptake in human U251 glioblastoma cells compared to the administration of the free drug and significant inhibition of cell proliferation. In other studies, Duong et al.[361] identified the *MXD3* gene as a new therapeutic target for high-risk neuroblastoma patients. The formulated IO nanoparticles with complexated siRNAs effectively knocked down *MXD3* expression in neuroblastoma cells and significantly increased cell apoptosis. Moreover, the authors demonstrated the synergistic effect of their IO nanoparticles with MXD3 siRNA and

DOX, vincristine, cisplatin, or maphosphamide – common drugs used in neuroblastoma treatment.[361]

Most of the described metal-based particles use polymer coatings to improve biocompatibility and reduce cytotoxicity. Therefore, classifying such materials as inorganic nanoparticles can be ambiguous compared to initially developed IO and Au nanoparticles. This fact illustrates the paradigm shift in drug delivery towards hybrid materials incorporating advantages from combined materials.

4.2. Organic Nanomedicine for Brain Tumor Therapy

Recent preclinical studies have shown that Glabrescione B, a selective GLI1 inhibitor encapsulated in self-assembling mPEG5kDa-cholane micelles, can efficiently inhibit tumor growth in allograft and orthotopic models of Hedgehog-dependent medulloblastoma.[362] In another study, the authors engineered high-density lipoprotein-mimetic nanoparticles incorporating an SHH inhibitor (LDE225), apolipoprotein A1, and an anti-CD15 antibody to achieve dual-targeted delivery.[363] The in vivo studies in two mouse models of SHH medulloblastoma (the SmoA1-GFP model and the Patched (PTC) knockout model) demonstrated that animals treated with liposomal formulation exhibited a well-maintained cerebellar structure and minimal tumor growth. In contrast, the vehicle-treated control group presented with a disrupted cerebellar structure, a blunted edge of lobes, and significant tumor growth.[363] Another study using dual-targeted liposomes with Angiopep-2 ligand, anti-CD133 antibody, and temozolomide exhibited the capacity to drastically reduce tumor size in orthotopic glioblastoma mice model.[364]

Numerous preclinical examples reveal the potential of polymer therapeutics in pediatric tumor treatment and highlight the necessity to support such studies and facilitate their transition into clinics. For example, promising results for hedgehog inhibitors of particular interest for the medulloblastoma SHH group have been reported; [87,88] however, the tolerable side effects in adults can be a significant issue for treatment in young children, demonstrating the negative effect of HhAntag (SMO inhibitor) on skeletal growth and permanent defects in joint structures in young mice.[365] To tackle this issue, Hwang et al.[366] demonstrated that the use of poly(2-oxazoline) nanoparticles with encapsulated vismodegib (an SMO inhibitor) increased the survival of transgenic mice, with 30% of animals surviving for extended periods (more than 35 days) compared to control groups and vismodegib-treated animals, where the average survival was twenty days. Another study with a similar carrier and loaded palbociclib (CDK4/6 inhibitor) demonstrated that encapsulation reduced drug toxicity, improved pharmacokinetics with enhanced CNS accumulation, and extended the overall survival of animals from twenty-one days (free drug) and nineteen days (control group) to twenty-seven days.[286] Several polymeric nanoparticles have been designed to deliver miRNA to the brain over the last few years. For example, Lopez-Bertoni et al. designed poly(β-amino ester) nanoparticles

and demonstrated their minimal cytotoxicity, with high intracellular transport efficacy and cytosol-targeted environmentally driven cargo release in a glioblastoma xenograft mice model.[367]

Despite promising preclinical results for polymer therapeutics, only a few liposomal formulations and Au nanoparticles are currently in ongoing clinical trials in pediatric brain tumors as drug delivery systems and IO nanoparticles as MRI contrast agents (summarized in **Table 1.4**).

The development of nanotherapies for brain cancer therapy, despite the urgent clinical need and absence of alternative approaches, remains very limited, mainly because of the formidable task of crossing the blood-brain barrier. So far, no successful nanoplatform for crossing BBB reached clinical trials, and no new approaches, even moderately successful, appeared in this field. The intranasal approach seems more appealing for nanoparticle delivery to the brain, and many ex vivo models for intranasal delivery research are already available. While no clinically approved platforms exist for intranasal delivery, they provide more space for manipulation, as evidenced by the development of novel devices and slow, steady expansion of potentially suitable small molecules, nanomedicines, and formulations. Polypeptide therapeutics are especially promising for intranasal delivery due to proven biocompatibility, potential biodegradation in CNS tissues without toxic side products, and virtually limitless synthetic versatility.

Considering the above description, this Ph.D. thesis is focused on developing new polypeptide therapeutics based on poly-L-glutamic acid, looking for potential therapies in treating pediatric glioma via intranasal drug delivery.

Table 1.4. Ongoing clinical trials using nanoparticles for pediatric brain tumors. . [193]

Formulation	Drug	Clinical Trials	Status	Last update	Age, years	Type of Cancer/Application
Liposomes	Irinotecan	NCT02013336	Ph 1, recruiting	31-Mar-22	1-20	Recurrent or Refractory Solid Tumors, Ewing Sarcoma, Rhabdomyosarcoma, Neuroblastoma, Osteosarcoma
Liposomes	Doxorubicin	NCT02536183	Ph 1, recruiting	13-Dec-21	A <21 B <30	Solid Tumors, Rhabdomyosarcoma, Ewing Sarcoma, Soft Tissue Sarcomas, Osteosarcoma, Neuroblastoma, Wilms Tumor, Hepatic Tumor, Germ Cell Tumors
Liposomes	Doxorubicin	NCT00019630	Ph 1, completed	28-Apr-15	<21	Soft Tissue Sarcoma Childhood Liver Cancer Bone Cancer Brain Tumor Kidney Tumor
Liposomes	Doxorubicin	NCT02557854	Ph 1, Withdrawn	19-Mar-19	1-40	Rhabdomyosarcoma, Neuroblastoma, Sarcoma, Sarcoma, Ewing Osteosarcoma, Desmoid
Liposomes	Cytarabine	NCT00003073	Ph 1, unknown	23-Mar-10	1-21	Brain and CNS Tumors, Leukemia Lymphoma, Unspecified Childhood Solid Tumor
Au NPs	Panobinostat	NCT03566199	Ph 1, completed	25-Feb-22	2-21	DIPG
Au NPs	Panobinostat	NCT04264143	Ph 1, recruiting	10-Mar-22	1-17	DIPG, Diffuse Pontine and Thalamic Gliomas, Diffuse Midline Glioma
SPION NPs	n/a	NCT00978562	n/a, completed	03-Aug-22	1-17	MRI contrast, Brain Neoplasms
Dextran-coated iron oxide NPs	n/a	NCT00659334	Ph 2, terminated	21-Dec-22	1-17	MRI contrast, Brain Neoplasms

5. References

1. Pichaivel, M., Anbumani, G., Theivendren, P. & Gopal, M. An Overview of Brain Tumor. in (ed. Agrawal, A.) Ch. 1 (IntechOpen, 2022). doi:10.5772/intechopen.100806.
2. Ostrom, Q. T. *et al.* Risk factors for childhood and adult primary brain tumors. *Neuro. Oncol.* **21**, 1357–1375 (2019).
3. Louis, D. N. *et al.* The 2016 World Health Organization Classification of Tumors of the Central Nervous System: a summary. *Acta Neuropathol.* **131**, 803–820 (2016).
4. Ostrom, Q. T. *et al.* CBTRUS Statistical Report: Primary Brain and Other Central Nervous System Tumors Diagnosed in the United States in 2012-2016. *Neuro. Oncol.* **21**, v1–v100 (2019).
5. Bauchet, L. *et al.* Clinical epidemiology for childhood primary central nervous system tumors. *J. Neurooncol.* **92**, 87–98 (2009).
6. Barr, R. D. Adolescents, young adults, and cancer-the international challenge. *Cancer* **117**, 2245–2249 (2011).
7. Pinheiro, R. G. R., Coutinho, A. J., Pinheiro, M. & Neves, A. R. Nanoparticles for targeted brain drug delivery: What do we know? *Int. J. Mol. Sci.* **22**, (2021).
8. Hauser, P. Classification and Treatment of Pediatric Gliomas in the Molecular Era. *Child. (Basel, Switzerland)* **8**, (2021).
9. PDQ, P. T. E. B. Childhood Central Nervous System Atypical Teratoid/Rhabdoid Tumor Treatment (PDQ®). in (2002).
10. Duffner, P. K. *et al.* The treatment of malignant brain tumors in infants and very young children: an update of the Pediatric Oncology Group experience. *Neuro. Oncol.* **1**, 152–161 (1999).
11. Schmidt, L. S. *et al.* Incidence of childhood central nervous system tumors in the Nordic countries. *Pediatr. Blood Cancer* **56**, 65–69 (2011).
12. Pollack, I. F. & Jakacki, R. I. Childhood brain tumors: epidemiology, current management and future directions. *Nat. Rev. Neurol.* **7**, 495–506 (2011).
13. Northcott, P. A. *et al.* Medulloblastoma Comprises Four Distinct Molecular Variants. *J. Clin. Oncol.* **29**, 1408–1414 (2011).
14. Omuro, A. & DeAngelis, L. M. Glioblastoma and Other Malignant Gliomas: A Clinical Review. *JAMA* **310**, 1842–1850 (2013).
15. Warren, K. E. Diffuse intrinsic pontine glioma: poised for progress. *Front. Oncol.* **2**, 205 (2012).
16. Steliarova-Foucher, E., Stiller, C., Lacour, B. & Kaatsch, P. International classification of childhood cancer, third edition. *Cancer* **103**, 1457–1467 (2005).
17. Sugimoto, M., Kurishima, C., Masutani, S., Tamura, M. & Senzaki, H. Congenital Brain Tumor within the First 2 Months of Life. *Pediatr. Neonatol.* **56**, 369–375 (2015).
18. Orbach, D. *et al.* Neonatal cancer. *Lancet Oncol.* **14**, e609–e620 (2013).
19. Siegel, R. L., Miller, K. D., Fuchs, H. E. & Jemal, A. Cancer statistics, 2022. *CA. Cancer J. Clin.* **72**, 7–33 (2022).
20. Ward, E., DeSantis, C., Robbins, A., Kohler, B. & Jemal, A. Childhood and adolescent cancer statistics. *CA. Cancer J. Clin.* **64**, 83–103 (2014).
21. Steliarova-Foucher, E. *et al.* International incidence of childhood cancer, 2001-10: a population-based registry study. *Lancet. Oncol.* **18**, 719–731 (2017).
22. Ater, J. L. *et al.* MOPP chemotherapy without irradiation as primary postsurgical therapy for brain tumors in infants and young children. *J. Neurooncol.* **32**, 243–252 (1997).
23. Armstrong, G. T. Long-term survivors of childhood central nervous system malignancies: the experience of the Childhood Cancer Survivor Study. *Eur. J. Paediatr. Neurol. EJPN Off. J.*

Eur. Paediatr. Neurol. Soc. **14**, 298–303 (2010).

24. Bhakta, N. *et al.* Childhood cancer burden: a review of global estimates. *Lancet. Oncol.* **20**, e42–e53 (2019).

25. Armstrong, G. T. *et al.* Late mortality among 5-year survivors of childhood cancer: a summary from the Childhood Cancer Survivor Study. *J. Clin. Oncol. Off. J. Am. Soc. Clin. Oncol.* **27**, 2328–2338 (2009).

26. Force, L. M. *et al.* The global burden of childhood and adolescent cancer in 2017: an analysis of the Global Burden of Disease Study 2017. *Lancet. Oncol.* **20**, 1211–1225 (2019).

27. Johnson, K. J. *et al.* Childhood brain tumor epidemiology: a brain tumor epidemiology consortium review. *Cancer Epidemiol. biomarkers Prev. a Publ. Am. Assoc. Cancer Res. cosponsored by Am. Soc. Prev. Oncol.* **23**, 2716–2736 (2014).

28. Stefanaki, K., Alexiou, G. A., Stefanaki, C. & Prodromou, N. Tumors of Central and Peripheral Nervous System Associated with Inherited Genetic Syndromes. *Pediatr. Neurosurg.* **48**, 271–285 (2012).

29. Gajjar, A. *et al.* Pediatric Brain Tumors: Innovative Genomic Information Is Transforming the Diagnostic and Clinical Landscape. *J. Clin. Oncol.* **33**, 2986–2998 (2015).

30. Grajkowska, W., Kotulska, K., Jurkiewicz, E. & Matyja, E. Brain lesions in tuberous sclerosis complex. Review. *Folia Neuropathol.* **48**, 139–149 (2010).

31. Butman, J. A., Linehan, W. M. & Lonser, R. R. Neurologic manifestations of von Hippel-Lindau disease. *JAMA* **300**, 1334–1342 (2008).

32. Orr, B. A., Clay, M. R., Pinto, E. M. & Kesserwan, C. An update on the central nervous system manifestations of Li-Fraumeni syndrome. *Acta Neuropathol.* **139**, 669–687 (2020).

33. Yakubov, E. *et al.* Hidden association of Cowden syndrome, PTEN mutation and meningioma frequency. *Oncoscience* **3**, 149–155 (2016).

34. Khattab A, M. D. Turcot syndrome. *Turcot Syndrome* https://www.ncbi.nlm.nih.gov/books/NBK534782/ (2022).

35. Hamilton, S. R. *et al.* The molecular basis of turcot's syndrome s. *N. Engl. J. Med.* **332**, 839–847 (1995).

36. Albrecht, S. *et al.* Malignant meningioma in Gorlin's syndrome: cytogenetic and p53 gene analysis. Case report. *J. Neurosurg.* **81**, 466–471 (1994).

37. Del Baldo, G. *et al.* Rhabdoid Tumor Predisposition Syndrome: From Clinical Suspicion to General Management. *Front. Oncol.* **11**, (2021).

38. Kayabolen, A., Yilmaz, E. & Bagci-Onder, T. IDH Mutations in Glioma: Double-Edged Sword in Clinical Applications? *Biomedicines* **9**, (2021).

39. Buccoliero, A. M. *et al.* IDH1 mutation in pediatric gliomas: has it a diagnostic and prognostic value? *Fetal Pediatr. Pathol.* **31**, 278–282 (2012).

40. Linet, M. S., Kim, K. P. & Rajaraman, P. Children's exposure to diagnostic medical radiation and cancer risk: epidemiologic and dosimetric considerations. *Pediatr. Radiol.* **39 Suppl 1**, S4-26 (2009).

41. Braganza, M. Z. *et al.* Ionizing radiation and the risk of brain and central nervous system tumors: a systematic review. *Neuro. Oncol.* **14**, 1316–1324 (2012).

42. Ron, E., Modan, B., Boice, J. D., Alfandary, E., Stovall, M., Chetrit, A., & Katz, L. Tumors of the Brain and Nervous System after Radiotherapy in Childhood. *N. Engl. J. Med.* **319**, 1033–1039 (1988).

43. Salnikova, L. E., Zelinskaya, N. I., Belopolskaya, O. B., Aslanyan, M. M. & Rubanovich, A. V. Association study of xenobiotic detoxication and repair genes with malignant brain tumors in children. *Acta Naturae* **2**, 58–65 (2010).

44. Salnikova, L. E., Belopolskaya, O. B., Zelinskaya, N. I. & Rubanovich, A. V. The potential effect of gender in CYP1A1 and GSTM1 genotype-specific associations with pediatric brain tumor. *Tumour Biol. J. Int. Soc. Oncodevelopmental Biol. Med.* **34**, 2709–2719 (2013).

45. Jeon, S. *et al.* Genetic variants of AICDA/CASP14 associated with childhood brain tumor. *Genet. Mol. Res.* **12**, 2024–2031 (2013).

46. Schwartzentruber, J. *et al.* Driver mutations in histone H3.3 and chromatin remodelling genes in paediatric glioblastoma. *Nature* **482**, 226–231 (2012).

47. Wu, G. *et al.* Somatic histone H3 alterations in pediatric diffuse intrinsic pontine gliomas and non-brainstem glioblastomas. *Nat. Genet.* **44**, 251–253 (2012).

48. Huether, R. *et al.* The landscape of somatic mutations in epigenetic regulators across 1,000 paediatric cancer genomes. *Nat. Commun.* **5**, 3630 (2014).

49. Pfister, S. *et al.* BRAF gene duplication constitutes a mechanism of MAPK pathway activation in low-grade astrocytomas. *J. Clin. Invest.* **118**, 1739–1749 (2008).

50. Dahlin, A. M. *et al.* CCND2, CTNNB1, DDX3X, GLI2, SMARCA4, MYC, MYCN, PTCH1, TP53, and MLL2 gene variants and risk of childhood medulloblastoma. *J. Neurooncol.* **125**, 75–78 (2015).

51. Baocheng, W. *et al.* Polymorphisms of insulin receptor substrate 2 are putative biomarkers for pediatric medulloblastoma: considering the genetic susceptibility and pathological diagnoses. *Nagoya J. Med. Sci.* **79**, 47–54 (2017).

52. Chen, Y.-D., Zhang, N., Qiu, X.-G., Yuan, J. & Yang, M. LncRNA CDKN2BAS rs2157719 genetic variant contributes to medulloblastoma predisposition. *J. Gene Med.* **20**, (2018).

53. Adel Fahmideh, M. *et al.* CCDC26, CDKN2BAS, RTEL1 and TERT Polymorphisms in pediatric brain tumor susceptibility. *Carcinogenesis* **36**, 876–882 (2015).

54. Amirian, E. S. *et al.* Approaching a Scientific Consensus on the Association between Allergies and Glioma Risk: A Report from the Glioma International Case-Control Study. *Cancer Epidemiol. biomarkers Prev. a Publ. Am. Assoc. Cancer Res. cosponsored by Am. Soc. Prev. Oncol.* **25**, 282–290 (2016).

55. Lupatsch, J. E. *et al.* Childhood brain tumours, early infections and immune stimulation: A pooled analysis of the ESCALE and ESTELLE case-control studies (SFCE, France). *Cancer Epidemiol.* **52**, 1–9 (2018).

56. Andersson, U. *et al.* The association between longer relative leukocyte telomere length and risk of glioma is independent of the potentially confounding factors allergy, BMI, and smoking. *Cancer Causes Control* **30**, 177–185 (2019).

57. Guterres, A. N. & Villanueva, J. Targeting telomerase for cancer therapy. *Oncogene* **39**, 5811–5824 (2020).

58. Macewen, W. An Address on the Surgery of the Brain and Spinal Cord. *Br. Med. J.* **2**, 302–309 (1888).

59. Zebian, B. *et al.* Recent technological advances in pediatric brain tumor surgery. *CNS Oncol.* **6**, 71–82 (2016).

60. Donahue, B. Short- and Long-Term Complications of Radiation Therapy for Pediatric Brain Tumors. *Pediatr. Neurosurg.* **18**, 207–217 (1992).

61. Merchant, T. E. Proton Beam Therapy in Pediatric Oncology. *Cancer J.* **15**, (2009).

62. Gottardo, N. G. & Gajjar, A. Chemotherapy for Malignant Brain Tumors of Childhood. *J. Child Neurol.* **23**, 1149–1159 (2008).

63. Timmermann, B. *et al.* Role of radiotherapy in anaplastic ependymoma in children under age of 3 years: Results of the prospective German brain tumor trials HIT-SKK 87 and 92. *Radiother. Oncol.* **77**, 278–285 (2005).

64. Duffner, P. K. *et al.* Postoperative chemotherapy and delayed radiation in children less than three years of age with malignant brain tumors. *N. Engl. J. Med.* **328**, 1725–1731 (1993).

65. Lashford, L. S. *et al.* An intensive multiagent chemotherapy regimen for brain tumours occurring in very young children. *Arch. Dis. Child.* **74**, 219–223 (1996).

66. Bouffet, E. *et al.* Phase II study of weekly vinblastine in recurrent or refractory pediatric low-grade glioma. *J. Clin. Oncol. Off. J. Am. Soc. Clin. Oncol.* **30**, 1358–1363 (2012).

67.   Ater, J. L. *et al.* Randomized study of two chemotherapy regimens for treatment of low-grade glioma in young children: a report from the Children's Oncology Group. *J. Clin. Oncol. Off. J. Am. Soc. Clin. Oncol.* **30**, 2641–2647 (2012).

68.   Sturm, D., Pfister, S. M. & Jones, D. T. W. Pediatric Gliomas: Current Concepts on Diagnosis, Biology, and Clinical Management. *J. Clin. Oncol.* **35**, 2370–2377 (2017).

69.   Packer, R. J. *et al.* Objective response of multiply recurrent low-grade gliomas to bevacizumab and irinotecan. *Pediatr. Blood Cancer* **52**, 791–795 (2009).

70.   Liu, A. K., Macy, M. E. & Foreman, N. K. Bevacizumab as therapy for radiation necrosis in four children with pontine gliomas. *Int. J. Radiat. Oncol. Biol. Phys.* **75**, 1148–1154 (2009).

71.   DeSouza, R.-M., Jones, B. R. T., Lowis, S. P. & Kurian, K. M. Pediatric Medulloblastoma – Update on Molecular Classification Driving Targeted Therapies. *Frontiers in Oncology* vol. 4 https://www.frontiersin.org/articles/10.3389/fonc.2014.00176 (2014).

72.   Packer, R. J. *et al.* Phase III study of craniospinal radiation therapy followed by adjuvant chemotherapy for newly diagnosed average-risk medulloblastoma. *J. Clin. Oncol. Off. J. Am. Soc. Clin. Oncol.* **24**, 4202–4208 (2006).

73.   Stewart, C. F. *et al.* Results of a phase II upfront window of pharmacokinetically guided topotecan in high-risk medulloblastoma and supratentorial primitive neuroectodermal tumor. *J. Clin. Oncol. Off. J. Am. Soc. Clin. Oncol.* **22**, 3357–3365 (2004).

74.   Strother, D. *et al.* Feasibility of four consecutive high-dose chemotherapy cycles with stem-cell rescue for patients with newly diagnosed medulloblastoma or supratentorial primitive neuroectodermal tumor after craniospinal radiotherapy: results of a collaborative study. *J. Clin. Oncol. Off. J. Am. Soc. Clin. Oncol.* **19**, 2696–2704 (2001).

75.   Needle, M. N. *et al.* Adjuvant chemotherapy for the treatment of intracranial ependymoma of childhood. *Cancer* **80**, 341–347 (1997).

76.   https://www.ispn.guide/tumors-of-the-nervous-system-in-children/chemotherapy-for-tumors-in-the-nervous-system-of-children-homepage/management-with-chemotherapy-of-tumors-in-the-nervous-system-of-children/chemotherapy-for-medulloblastomas-in-children/chemo. The ISPN Guide to Pediatric Neurosurgery.

77.   Jiang, H., McCormick, F., Lang, F. F., Gomez-Manzano, C. & Fueyo, J. Oncolytic adenoviruses as antiglioma agents. *Expert Rev. Anticancer Ther.* **6**, 697–708 (2006).

78.   Auffinger, B., Ahmed, A. U. & Lesniak, M. S. Oncolytic virotherapy for malignant glioma: translating laboratory insights into clinical practice. *Front. Oncol.* **3**, 32 (2013).

79.   Geoerger, B. *et al.* Oncolytic activity of the E1B-55 kDa-deleted adenovirus ONYX-015 is independent of cellular p53 status in human malignant glioma xenografts. *Cancer Res.* **62**, 764–772 (2002).

80.   Jiang, H. *et al.* Comparative effect of oncolytic adenoviruses with E1A-55 kDa or E1B-55 kDa deletions in malignant gliomas. *Neoplasia* **7**, 48–56 (2005).

81.   Komata, T. *et al.* Treatment of malignant glioma cells with the transfer of constitutively active caspase-6 using the human telomerase catalytic subunit (human telomerase reverse transcriptase) gene promoter. *Cancer Res.* **61**, 5796–5802 (2001).

82.   Martínez-Vélez, N. *et al.* The oncolytic virus Delta-24-RGD elicits an antitumor effect in pediatric glioma and DIPG mouse models. *Nat. Commun.* **10**, 2235 (2019).

83.   Hutzen, B. *et al.* Treatment of medulloblastoma using an oncolytic measles virus encoding the thyroidal sodium iodide symporter shows enhanced efficacy with radioiodine. *BMC Cancer* **12**, 508 (2012).

84.   Lun, X. Q. *et al.* Targeting human medulloblastoma: oncolytic virotherapy with myxoma virus is enhanced by rapamycin. *Cancer Res.* **67**, 8818–8827 (2007).

85.   FDA Approves First Oncolytic Virus Therapy: Imlygic for Melanoma. *Oncol. Times* **37**, (2015).

86.   Russell, L. & Peng, K.-W. The emerging role of oncolytic virus therapy against cancer.

Chinese Clin. Oncol. Vol 7, No 2 (April 29, 2018) Chinese Clin. Oncol. (Cancer Immunother. (2018).

87. Niyaz, M., Khan, M. S. & Mudassar, S. Hedgehog Signaling: An Achilles' Heel in Cancer. *Transl. Oncol.* **12**, 1334–1344 (2019).

88. Rudin, C. M. *et al.* Treatment of medulloblastoma with hedgehog pathway inhibitor GDC-0449. *N. Engl. J. Med.* **361**, 1173–1178 (2009).

89. Beauchamp, E. M. *et al.* Arsenic trioxide inhibits human cancer cell growth and tumor development in mice by blocking Hedgehog/GLI pathway. *J. Clin. Invest.* **121**, 148–160 (2011).

90. Lee, M. J. *et al.* Hedgehog pathway inhibitor saridegib (IPI-926) increases lifespan in a mouse medulloblastoma model. *Proc. Natl. Acad. Sci. U. S. A.* **109**, 7859–7864 (2012).

91. Baryawno, N. *et al.* Small-molecule inhibitors of phosphatidylinositol 3-kinase/Akt signaling inhibit Wnt/beta-catenin pathway cross-talk and suppress medulloblastoma growth. *Cancer Res.* **70**, 266–276 (2010).

92. Efferth, T. *et al.* Molecular modes of action of cantharidin in tumor cells. *Biochem. Pharmacol.* **69**, 811–818 (2005).

93. Cimmino, F. *et al.* Norcantharidin impairs medulloblastoma growth by inhibition of Wnt/β-catenin signaling. *J. Neurooncol.* **106**, 59–70 (2012).

94. Milde, T. *et al.* HDAC5 and HDAC9 in medulloblastoma: novel markers for risk stratification and role in tumor cell growth. *Clin. cancer Res. an Off. J. Am. Assoc. Cancer Res.* **16**, 3240–3252 (2010).

95. Zhang, S. *et al.* A high-throughput screening identifies histone deacetylase inhibitors as therapeutic agents against medulloblastoma. *Exp. Hematol. Oncol.* **8**, 30 (2019).

96. Robinson, G. *et al.* Novel mutations target distinct subgroups of medulloblastoma. *Nature* **488**, 43–48 (2012).

97. Zhang, H. *et al.* EZH2 targeting reduces medulloblastoma growth through epigenetic reactivation of the BAI1/p53 tumor suppressor pathway. *Oncogene* **39**, 1041–1048 (2020).

98. Morschhauser, F. *et al.* Tazemetostat for patients with relapsed or refractory follicular lymphoma: an open-label, single-arm, multicentre, phase 2 trial. *Lancet. Oncol.* **21**, 1433–1442 (2020).

99. Li, C. *et al.* Finding an easy way to harmonize: a review of advances in clinical research and combination strategies of EZH2 inhibitors. *Clin. Epigenetics* **13**, 62 (2021).

100. Corrie, P. G. Cytotoxic chemotherapy: clinical aspects. *Medicine (Baltimore).* **36**, 24–28 (2008).

101. Abdel-Mageed, H. M., AbuelEzz, N. Z., Radwan, R. A. & Mohamed, S. A. Nanoparticles in nanomedicine: a comprehensive updated review on current status, challenges and emerging opportunities. *J. Microencapsul.* **38**, 414–436 (2021).

102. Melnyk, T., Đorđević, S., Conejos-Sánchez, I. & Vicent, M. J. Therapeutic potential of polypeptide-based conjugates: Rational design and analytical tools that can boost clinical translation. *Adv. Drug Deliv. Rev.* **160**, 136–169 (2020).

103. Shan, X. *et al.* Current approaches of nanomedicines in the market and various stage of clinical translation. *Acta Pharm. Sin. B* **12**, 3028–3048 (2022).

104. Bulbake, U., Doppalapudi, S., Kommineni, N. & Khan, W. Liposomal Formulations in Clinical Use : An Updated Review development. 1–33 (2017) doi:10.3390/pharmaceutics9020012.

105. Duncan, R. & Vicent, M. J. Polymer therapeutics-prospects for 21st century: The end of the beginning. *Advanced Drug Delivery Reviews* vol. 65 60–70 (2013).

106. Barenholz, Y. C. Doxil ® — The fi rst FDA-approved nano-drug : Lessons learned. *J. Control. Release* **160**, 117–134 (2012).

107. Mojarad-Jabali, S. *et al.* An update on actively targeted liposomes in advanced drug delivery

to glioma. *Int. J. Pharm.* **602**, 120645 (2021).

108. Krauss, A. A. C. *et al.* FDA Approval Summary: (Daunorubicin and Cytarabine) Liposome for Injection for the Treatment of Adults with High-Risk Acute Myeloid Leukemia. (2018) doi:10.1158/1078-0432.CCR-18-2990.

109. Koudelka, Š. & Turánek, J. Liposomal paclitaxel formulations. *J. Control. Release* **163**, 322–334 (2012).

110. Salehi, B. *et al.* Liposomal Cytarabine as Cancer Therapy: From Chemistry to Medicine. *Biomolecules* **9**, (2019).

111. Mukhtar, M. *et al.* Nanomaterials for Diagnosis and Treatment of Brain Cancer: Recent Updates. *Chemosensors* vol. 8 (2020).

112. Ishida, T. *et al.* Injection of PEGylated liposomes in rats elicits PEG-specific IgM, which is responsible for rapid elimination of a second dose of PEGylated liposomes. *J. Control. Release* **112**, 15–25 (2006).

113. Younis, M. A., Tawfeek, H. M., Abdellatif, A. A. H., Abdel-Aleem, J. A. & Harashima, H. Clinical translation of nanomedicines: Challenges, opportunities, and keys. *Adv. Drug Deliv. Rev.* **181**, 114083 (2022).

114. Hare, J. I. *et al.* Challenges and strategies in anti-cancer nanomedicine development: an industry perspective. *Adv. Drug Deliv. Rev.* **108**, 25–38 (2017).

115. Metselaar, J. M. & Lammers, T. Challenges in nanomedicine clinical translation. *Drug Deliv. Transl. Res.* **10**, 721–725 (2020).

116. Lundy, D. J., Nguyễn, H. & Hsieh, P. C. H. Emerging Nano-Carrier Strategies for Brain Tumor Drug Delivery and Considerations for Clinical Translation. *Pharmaceutics* vol. 13 (2021).

117. Đorđević, S. *et al.* Current hurdles to the translation of nanomedicines from bench to the clinic. *Drug Deliv. Transl. Res.* **12**, 500–525 (2022).

118. Ashford, M. B., England, R. M. & Akhtar, N. Highway to Success—Developing Advanced Polymer Therapeutics. *Adv. Ther.* **4**, 2000285 (2021).

119. Duncan, R. THE DAWNING ERA OF POLYMER THERAPEUTICS. *Nat. Rev.* **2**, 347–360 (2003).

120. Duncan, R. Polymer therapeutics: Top 10 selling pharmaceuticals — What next? *J. Control. Release* **190**, 371–380 (2014).

121. Canal, F., Sanchis, J. & Vicent Maria, J. Polymer – drug conjugates as nano-sized medicines. *Curr. Opin. Biotechnol.* **22**, 894–900 (2011).

122. Rodriguez-Otormin, F., Duro-Castano, A., Conejos-Sánchez, I. & Vicent, M. J. Envisioning the future of polymer therapeutics for brain disorders. *WIREs Nanomed Nanobiotechnol* **11**, e1532 (2019).

123. Weinstock-Guttman, B., Nair, K. V., Glajch, J. L., Ganguly, T. C. & Kantor, D. Two decades of glatiramer acetate: From initial discovery to the current development of generics. *J. Neurol. Sci.* **376**, 255–259 (2017).

124. Song, J. Y. *et al.* Glatiramer acetate persists at the injection site and draining lymph nodes via electrostatically-induced aggregation. *J. Control. Release* **293**, 36–47 (2019).

125. Bell, C. *et al.* Development of Glatopa® (Glatiramer Acetate): The First FDA-Approved Generic Disease-Modifying Therapy for Relapsing Forms of Multiple Sclerosis. *J. Pharm. Pract.* **31**, 481–488 (2018).

126. Javia, A. *et al.* Polymer-drug conjugates: Design principles, emerging synthetic strategies and clinical overview. *Int. J. Pharm.* **623**, 121863 (2022).

127. Yadav, D. & Dewangan, H. K. PEGYLATION: an important approach for novel drug delivery system. *J. Biomater. Sci. Polym. Ed.* **32**, 266–280 (2021).

128. Ibrahim, M. *et al.* Polyethylene glycol (PEG): The nature, immunogenicity, and role in the hypersensitivity of PEGylated products. *J. Control. Release* **351**, 215–230 (2022).

129. Garay, R. P., El-Gewely, R., Armstrong, J. K., Garratty, G. & Richette, P. Antibodies against

polyethylene glycol in healthy subjects and in patients treated with PEG-conjugated agents. *Expert Opin. Drug Deliv.* **9**, 1319–1323 (2012).

130. Yang, Q. & Lai, S. K. Anti-PEG immunity: emergence, characteristics, and unaddressed questions. *WIREs Nanomedicine and Nanobiotechnology* **7**, 655–677 (2015).

131. Elsadek, N. E. *et al.* Pegfilgrastim (PEG-G-CSF) induces anti-PEG IgM in a dose dependent manner and causes the accelerated blood clearance (ABC) phenomenon upon repeated administration in mice. *Eur. J. Pharm. Biopharm.* **152**, 56–62 (2020).

132. Shen, Q. *et al.* Modulation of intestinal P-glycoprotein function by polyethylene glycols and their derivatives by in vitro transport and in situ absorption studies. *Int. J. Pharm.* **313**, 49–56 (2006).

133. Webster, R. *et al.* PEGylated proteins: Evaluation of their safety in the absence of definitive metabolism studies. *Drug Metab. Dispos.* **35**, 9–16 (2007).

134. Thi, T. T. H. *et al.* The importance of Poly(ethylene glycol) alternatives for overcoming PEG immunogenicity in drug delivery and bioconjugation. *Polymers (Basel).* **12**, 298 (2020).

135. Ita, K. Polyplexes for gene and nucleic acid delivery: Progress and bottlenecks. *Eur. J. Pharm. Sci.* **150**, 105358 (2020).

136. Thakor, P. *et al.* Polymer–drug conjugates: recent advances and future perspectives. *Drug Discov. Today* **Articles i**, (2020).

137. Ehrlich, P. Address in Pathology, ON CHEMIOTHERAPY: Delivered Before the Seventeenth International Congress of Medicine. *Br. Med. J.* **2**, 353–359 (1913).

138. Matsumura, Y. & Maeda, H. A New Concept for Macromolecular Therapeutics in Cancer Chemotherapy : Mechanism of Tumoritropic Accumulation of Proteins and the Antitumor Agent Smancs. *Cancer Res.* **46**, 6387–6392 (1986).

139. Wong, C. H., Siah, K. W. & Lo, A. W. Estimation of clinical trial success rates and related parameters. *Biostatistics* **20**, 273–286 (2019).

140. Duncan, R. Polymer therapeutics as nanomedicines : new perspectives. *Curr. Opin. Biotechnol.* **22**, 492–501 (2011).

141. Canal, F., Sanchis, J. & Vicent, M. J. Polymer–drug conjugates as nano-sized medicines. *Curr. Opin. Biotechnol.* **22**, 894–900 (2011).

142. Zagorodko, O., Arroyo-crespo, J. J., Nebot, V. J. & Vicent, M. J. Polypeptide-Based Conjugates as Therapeutics: Opportunities and Challenges. *Macromol. Biosci.* **17**, 1–22 (2017).

143. Duncan, R. Designing polymer conjugates as lysosomotropic nanomedicines. *Biochem. Soc. Trans.* **35**, 56–60 (2007).

144. Choi, C. H. ABC transporters as multidrug resistance mechanisms and the development of chemosensitizers for their reversal. *Cancer Cell Int.* **5**, 1–13 (2005).

145. H., J. Jatzkewitz 1954. *Hoppe Seylers Z Physiol Chem* **297**, 149–156 (1954).

146. Ringsdorf, H. Structure and properties of pharmacologically active polymers. *J. Polym. Sci.* **51**, 135–153 (1975).

147. Duncan, R. Soluble Synthetic Polymers as Potential Drug Carriers. *Adv. Polym. Sci.* **57**, 51–101 (1984).

148. Seymour, L. W. *et al.* Tumour tropism and anti-cancer efficacy of polymer-based doxorubicin prodrugs in the treatment of subcutaneous murine B16F10 melanoma. *Br. J. Cancer* **70**, 636–641 (1994).

149. Wakaskar, R. R. General overview of lipid – polymer hybrid spongosomes and cubosomes. *J. Drug Target.* **26**, 311–318 (2018).

150. Aljabali, A. A. A. *et al.* Protein-Based Drug Delivery Nanomedicine Platforms: Recent Developments. *Pharm. Nanotechnol.* **10**, 257–267 (2022).

151. Ferrer-Miralles, N., Saccardo, P., Corchero, J. L., Xu, Z. & García-Fruitós, E. General introduction: recombinant protein production and purification of insoluble proteins. *Methods*

Mol. Biol. **1258**, 1–24 (2015).

152. Duncan, R., Edward, K. & Avenue, V. I. I. The dawning era of polymer therapeutics. **2**, 347–360 (2003).

153. Wagner, I. & Musso, H. New Naturally Occurring Amino Acids. *Angew. Chemie Int. Ed. English* **22**, 816–828 (1983).

154. Kenny, A. D. Evaluation of Sodium Poly-α, L-glutamate as a Plasma Expander. *Proc. Soc. Exptl. Biol. Med.* **100**, 778–780 (1959).

155. Sun, H. *et al.* Cancer Nanomedicines Based on Synthetic Polypeptides Cancer. *Biomacromolecules* **20**, 4299–4311 (2019).

156. Gu, X. *et al.* Polytyrosine nanoparticles enable ultra-high loading of doxorubicin and rapid enzyme-responsive drug release. *Biomater. Sci.* **6**, 1526–1534 (2018).

157. Toshiyama, R. *et al.* Poly(ethylene glycol)–poly(lysine) block copolymer–ubenimex conjugate targets aminopeptidase N and exerts an antitumor effect in hepatocellular carcinoma stem cells. *Oncogene* **38**, 244–260 (2019).

158. Wang, X. *et al.* Polypeptide-based drug delivery systems for programmed release. *Biomaterials* **275**, 120913 (2021).

159. Kricheldorf, H. R. Polypeptides and 100 Years of Chemistry of α-Amino Acid N-Carboxyanhydrides. *Angew. Chemie Int. Ed.* **45**, 5752–5784 (2006).

160. Deming, T. J. Synthesis of Side-Chain Modified Polypeptides. *Chem. Rev.* **116**, 786–808 (2016).

161. González-Henríquez, C. M., Sarabia-Vallejos, M. A. & Rodríguez-Hernández, J. Strategies to Fabricate Polypeptide-Based Structures via Ring-Opening Polymerization of N-Carboxyanhydrides. *Polymers (Basel).* **9**, 551 (2017).

162. Cheng, J. & Deming, T. J. Synthesis of Polypeptides by Ring-Opening Polymerization of α-Amino Acid N-Carboxyanhydrides BT - Peptide-Based Materials. in (ed. Deming, T.) 1–26 (Springer Berlin Heidelberg, 2012). doi:10.1007/128_2011_173.

163. Pickel, D. L., Politakos, N., Avgeropoulos, A. & Messman, J. M. A Mechanistic Study of α-(Amino acid)-N-carboxyanhydride Polymerization: Comparing Initiation and Termination Events in High-Vacuum and Traditional Polymerization Techniques. *Macromolecules* **42**, 7781–7788 (2009).

164. Vayaboury, W., Giani, O., Cottet, H., Deratani, A. & Schué, F. Living Polymerization of α-Amino Acid N-Carboxyanhydrides (NCA) upon Decreasing the Reaction Temperature. *Macromol. Rapid Commun.* **25**, 1221–1224 (2004).

165. Conejos-Sánchez, I., Duro-Castano, A., Birke, A., Barz, M. & Vicent, M. J. A controlled and versatile NCA polymerization method for the synthesis of polypeptides. *Polym. Chem.* **4**, 3182–3186 (2013).

166. Lu, H. & Cheng, J. N-Trimethylsilyl Amines for Controlled Ring-Opening Polymerization of Amino Acid N-Carboxyanhydrides and Facile End Group Functionalization of Polypeptides. *J. Am. Chem. Soc.* **130**, 12562–12563 (2008).

167. Deming, T. J. Living polymerization of α-amino acid-N-carboxyanhydrides. *J. Polym. Sci. Part A Polym. Chem.* **38**, 3011–3018 (2000).

168. Aliferis, T., Iatrou, H. & Hadjichristidis, N. Living polypeptides. *Biomacromolecules* **5**, 1653–1656 (2004).

169. Xia, Y. *et al.* Accelerated polymerization of N-carboxyanhydrides catalyzed by crown ether. *Nat. Commun.* **12**, 732 (2021).

170. Xue, T. *et al.* Streamlined Synthesis of PEG-Polypeptides Directly from Amino Acids. *Macromolecules* **53**, (2020).

171. Duro-Castano, A. *et al.* Well-Defined Star-Shaped Polyglutamates with Improved Pharmacokinetic Profiles As Excellent Candidates for Biomedical Applications. *Mol. Pharm.* **12**, 3639–3649 (2015).

172. Han, J. *et al.* The synthesis, deprotection and properties of poly(γ-benzyl-l-glutamate). *Sci. China Chem.* **56**, 729–738 (2013).

173. Hanby, W. E., Waley, S. G. & Watson, J. 632. Synthetic polypeptides. Part II. Polyglutamic acid. *J. Chem. Soc.* 3239–3249 (1950) doi:10.1039/JR9500003239.

174. Subramanian, G. *et al.* Structure of Complexes of Cationic Lipids and Poly(Glutamic Acid) Polypeptides: A Pinched Lamellar Phase. *J. Am. Chem. Soc.* **122**, 26–34 (2000).

175. Guo, J., Huang, Y., Jing, X. & Chen, X. Synthesis and characterization of functional poly(γ-benzyl-l-glutamate) (PBLG) as a hydrophobic precursor. *Polymer (Guildf).* **50**, 2847–2855 (2009).

176. Saudek, V., Pivcová, H. & Drobník, J. Nmr study of poly(aspartic acid). II. α- and β-Peptide bonds in poly(aspartic acid) prepared by common methods. *Biopolymers* **20**, 1615–1623 (1981).

177. Nakanishi, M., Park, J.-S., Jang, W.-D., Oba, M. & Kataoka, K. Study of the quantitative aminolysis reaction of poly(β-benzyl l-aspartate) (PBLA) as a platform polymer for functionality materials. *React. Funct. Polym.* **67**, 1361–1372 (2007).

178. Hernández, J. R. & Klok, H.-A. Synthesis and ring-opening (co)polymerization of L-lysine N-carboxyanhydrides containing labile side-chain protective groups. *J. Polym. Sci. Part A Polym. Chem.* **41**, 1167–1187 (2003).

179. Blout, E. R. & Idelson, M. POLYPEPTIDES. VI. POLY-α-L-GLUTAMIC ACID: PREPARATION AND HELIX-COIL CONVERSIONS. *J. Am. Chem. Soc.* **78**, 497–498 (1956).

180. Cheng, J. & Deming, T. J. Synthesis of polypeptides by ring-opening polymerization of α-amino acid N-carboxyanhydrides. *Top. Curr. Chem.* **310**, 1–26 (2012).

181. Roweton, S., Huang, S. J. & Swift, G. Poly(aspartic acid): Synthesis, biodegradation, and current applications. *J. Environ. Polym. Degrad.* **5**, 175–181 (1997).

182. Tian, Z.-Y., Zhang, Z., Wang, S. & Lu, H. A moisture-tolerant route to unprotected α/β-amino acid N-carboxyanhydrides and facile synthesis of hyperbranched polypeptides. *Nat. Commun.* **12**, 5810 (2021).

183. Wu, Y. *et al.* Superfast and Water-Insensitive Polymerization on α-Amino Acid N-Carboxyanhydrides to Prepare Polypeptides Using Tetraalkylammonium Carboxylate as the Initiator. *Angew. Chemie Int. Ed.* **60**, 26063–26071 (2021).

184. Deng, C., Wu, J., Cheng, R., Meng, F. & Klok, H. Functional polypeptide and hybrid materials : Precision synthesis via ҫ a-amino acid N-carboxyanhydride polymerization and emerging biomedical applications. *Prog. Polym. Sci.* **39**, 330–364 (2014).

185. El-sawy, H. S., Al-abd, A., Ahmed, T., El-say, K. M. & Torchilin, V. P. Stimuli-Responsive Nano-Architectures Drug Delivery Systems to Solid Tumor Micromilieu : Past, Present and Future Perspectives Stimuli-Responsive Nano-Architectures Drug Delivery Systems to Solid Tumor Department of Pharmaceutics and Pharmaceutical Techn. *ACS Nano* **12**, 10636–10664 (2018).

186. Pisarevsky, E. *et al.* Rational Design of Polyglutamic Acid Delivering an Optimized Combination of Drugs Targeting Mutated BRAF and MEK in Melanoma. *Adv. Ther.* **2000028**, 1–17 (2020).

187. Arroyo-crespo, J. J. *et al.* Anticancer Activity Driven by Drug Linker Modification in a Polyglutamic Acid-Based Combination-Drug Conjugate. *Adv. Funct. Mater.* **1800931**, 1–13 (2018).

188. Song, Z. *et al.* Secondary structures in synthetic polypeptides from N-carboxyanhydrides: design, modulation, association, and material applications. *Chem. Soc. Rev.* **47**, 7401–7425 (2018).

189. Gaoa, Y. & Dong, C.-M. Reduction- and thermo-sensitive core-cross-linked polypeptide hybrid micelles for triggered and intracellular drug release. *Polym. Chem.* **8**, 1223–1232

(2017).

190. Qu, J. *et al.* Reduction / temperature / pH multi-stimuli responsive core cross-linked polypeptide hybrid micelles for triggered and intracellular drug release. *Colloids Surfaces B Biointerfaces* **170**, 373–381 (2018).

191. Li, L. *et al.* Redox-sensitive core cross-linked polyethylene glycol-polypeptide hybrid micelles for anticancer drug delivery. *J. Nanosci. Nanotechnol.* **17**, 4532–4541 (2017).

192. Li, C. Poly(l-glutamic acid)–anticancer drug conjugates. *Adv. Drug Deliv. Rev.* **54**, 695–713 (2002).

193. https://clinicaltrials.gov. clinicaltrials (Acessed June 2023).

194. Singer, J. W. Paclitaxel poliglumex (XYOTAX™, CT-2103): A macromolecular taxane. *J. Control. Release* **109**, 120–126 (2005).

195. Chou, P., Huang, Y., Cheng, M., Rau, K. & Fang, Y. Improvement of Paclitaxel-Associated Adverse Reactions (ADRs) via the Use of Nano-Based Drug Delivery Systems : A Systematic Review and Network Meta-Analysis. *Int J Nanomedicine* **15**, 1731–1743 (2020).

196. Han, L. *et al.* Synthesis and biological evaluation of an anticancer drug delivery system: Poly(L-γ-glutamyl-L-carbocisteine)-paclitaxel nanoconjugate. *Mater. Sci. Eng. C* **81**, 113–119 (2017).

197. Hamaguchi, T. *et al.* A phase II study of NK012, a polymeric micelle formulation of SN-38, in unresectable, metastatic or recurrent colorectal cancer patients. *Cancer Chemother. Pharmacol.* **82**, 1021–1029 (2018).

198. Wen, Y. *et al.* Camptothecin-based nanodrug delivery systems. *Cancer Biol. Med.* **14**, 363–370 (2017).

199. Liu, T. *et al.* A poly (L-glutamic acid)-combretastatin A4 conjugate for solid tumor therapy : Markedly improved therapeutic efficiency through its low tissue penetration in solid tumor. *Acta Biomater.* **53**, 179–189 (2017).

200. Jiang, J. *et al.* Combretastatin A4 nanodrug combined plerixafor for inhibiting tumor growth and metastasis simultaneously. *Biomater. Sci.* **7**, 5283–5291 (2019).

201. Chen, B. *et al.* Current Multistage Drug Delivery Systems Based on the Tumor Microenvironment. *Theranostics* **7**, 538–558 (2017).

202. Praveen, K. *et al.* pH-Responsive "Supra-Amphiphilic" Nanoparticles Based on Homoarginine Polypeptides. *ACS Appl. Bio Mater.* **2**, 4162–4172 (2019).

203. Deirram, N., Zhang, C., Kermaniyan, S. S., Johnston, A. P. R. & Such, G. K. pH-Responsive Polymer Nanoparticles for Drug Delivery. *Macromol. Rapid Commun.* **40**, 1800917 (2019).

204. Seidi, F., Jenjob, R. & Crespy, D. Designing Smart Polymer Conjugates for Controlled Release of Payloads. *Chem. Rev.* **118**, 3965–4036 (2018).

205. Kalia, J. & Raines, R. T. Hydrolytic stability of hydrazones and oximes. *Angew. Chemie - Int. Ed.* **47**, 7523–7526 (2008).

206. Prabaharan, M., Grailer, J. J., Pilla, S., Steeber, D. A. & Gong, S. Amphiphilic multi-arm-block copolymer conjugated with doxorubicin via pH-sensitive hydrazone bond for tumor-targeted drug delivery. *Biomaterials* **30**, 5757–5766 (2009).

207. Arroyo-Crespo, J. J. *et al.* Tumor microenvironment-targeted poly-L-glutamic acid-based combination conjugate for enhanced triple negative breast cancer treatment. *Biomaterials* **186**, 8–21 (2018).

208. Sui, B. *et al.* Self-Assembled Micelles Composed of Doxorubicin Conjugated Y-Shaped PEG-Poly(glutamic acid)2 Copolymers via Hydrazone Linkers. *Molecules* **19**, 11915–11932 (2014).

209. Li, B. *et al.* A dual pH- and reduction-responsive anticancer drug delivery system based on PEG–SS–poly(amino acid) block copolymer. *RSC Adv.* **7**, 30242–30249 (2017).

210. Kaminskas, L. M. *et al.* Pulmonary administration of a doxorubicin-conjugated dendrimer enhances drug exposure to lung metastases and improves cancer therapy. *J. Control. Release*

183, 18–26 (2014).

211. Carey, F. A. & Sundberg, R. J. *Advanced Organic Chemistry Part A: Structure and Mechanisms. Advanced Organic Chemistry* (2007). doi:10.1021/ed065pA139.2.

212. Takemoto, H. *et al.* Polymeric modification of gemcitabine via cyclic acetal linkage for enhanced anticancer potency with negligible side effects. *Biomaterials* **235**, 119804 (2020).

213. Tsuchikama, K. & An, Z. Antibody-drug conjugates: recent advances in conjugation and linker chemistries. *Protein Cell* **9**, 33–46 (2018).

214. Gavriel, A. G., Sambrook, M. R., Russell, A. T. & Hayes, W. Recent advances in self-immolative linkers and their applications in polymeric reporting systems. *Polym. Chem.* **13**, 3188–3269 (2022).

215. Klahan, B., Seidi, F. & Crespy, D. Oligo(thioether-ester)s Blocks in Polyurethanes for Slowly Releasing Active Payloads. *Macromol. Chem. Phys.* **219**, 1–9 (2018).

216. Mi, P. *et al.* Block copolymer-boron cluster conjugate for effective boron neutron capture therapy of solid tumors. *J. Control. Release* **254**, 1–9 (2017).

217. Liu, J., Ai, X., Zhang, H., Zhuo, W. & Mi, P. Polymeric micelles with endosome escape and redox-responsive functions for enhanced intracellular drug delivery. *J. Biomed. Nanotechnol.* **15**, 373–381 (2019).

218. Deng, Z., Hu, J. & Liu, S. Disulfide-Based Self-Immolative Linkers and Functional Bioconjugates for Biological Applications. *Macromol. Rapid Commun.* **41**, 1–14 (2020).

219. Gao, M. *et al.* All-active antitumor micelles via triggered lipid peroxidation. *J. Control. Release* **286**, 381–393 (2018).

220. Meng, X. *et al.* Self-immolative micellar drug delivery: The linker matters. *Nano Res.* **11**, 6177–6189 (2018).

221. Li, Y., Lu, H., Liang, S. & Xu, S. Dual Stable Nanomedicines Prepared by Cisplatin-Crosslinked Camptothecin Prodrug Micelles for Effective Drug Delivery. *ACS Appl. Mater. Interfaces* **11**, 20649–20659 (2019).

222. Qi, R. *et al.* Nanoparticle conjugates of a highly potent toxin enhance safety and circumvent platinum resistance in ovarian cancer. *Nat. Commun.* **8**, (2017).

223. Turk, B. Targeting proteases: successes, failures and future prospects. *Nat. Rev. Drug Discov.* **5**, 785–799 (2006).

224. Kessenbrock, K., Plaks, V. & Werb, Z. Matrix Metalloproteinases: Regulators of the Tumor Microenvironment. *Cell* **141**, 52–67 (2010).

225. Caculitan, N. G. *et al.* Cathepsin B Is Dispensable for Cellular Processing of Cathepsin B-Cleavable Antibody-Drug Conjugates. *Cancer Res.* **77**, 7027–7037 (2017).

226. Kern, J. C. *et al.* Novel Phosphate Modified Cathepsin B Linkers: Improving Aqueous Solubility and Enhancing Payload Scope of ADCs. *Bioconjug. Chem.* **27**, 2081–2088 (2016).

227. Wang, Y., Fan, S., Zhong, W., Zhou, X. & Li, S. Development and Properties of Valine-Alanine based Antibody-Drug Conjugates with Monomethyl Auristatin E as the Potent Payload. *Int. J. Mol. Sci.* **18**, (2017).

228. Wei, B. *et al.* Discovery of Peptidomimetic Antibody–Drug Conjugate Linkers with Enhanced Protease Specificity. *J. Med. Chem.* **61**, 989–1000 (2018).

229. Li, S.-Y. *et al.* Protease-Activable Cell-Penetrating Peptide–Protoporphyrin Conjugate for Targeted Photodynamic Therapy in Vivo. *ACS Appl. Mater. Interfaces* **7**, 28319–28329 (2015).

230. Wei, Y., Quan, L., Zhou, C. & Zhan, Q. Factors relating to the biodistribution & clearance of nanoparticles & their effects on in vivo application. *Nanomedicine* **13**, 1495–1512 (2018).

231. Blanco, E., Shen, H. & Ferrari, M. Principles of nanoparticle design for overcoming biological barriers to drug delivery. *Nat. Biotechnol.* **33**, 941–951 (2015).

232. Haag, R. & Kratz, F. Polymer Therapeutics: Concepts and Applications. *Angew. Chemie Int. Ed.* **45**, 1198–1215 (2006).

233. Pasut, G. & Veronese, F. M. Polymer–drug conjugation, recent achievements and general strategies. *Prog. Polym. Sci.* **32**, 933–961 (2007).

234. Noguchi, Y. *et al.* Early Phase Tumor Accumulation of Macromolecules: A Great Difference in Clearance Rate between Tumor and Normal Tissues. *Japanese J. Cancer Res.* **89**, 307–314 (1998).

235. Takeda, K. M. *et al.* Effect of shear stress on structure and function of polyplex micelles from poly(ethylene glycol)-poly(L-lysine) block copolymers as systemic gene delivery carrier. *Biomaterials* **126**, 31–38 (2017).

236. Cabral, H. *et al.* Accumulation of sub-100 nm polymeric micells in poorly permeable tumours depends on size. *Nat. Nanotechnol.* **6**, 815–823 (2011).

237. Feng, Q. & Tong, R. Anticancer nanoparticulate polymer-drug conjugate. *Bioeng. Transl. Med.* **1**, 277–296 (2016).

238. Nasongkla, N. *et al.* Dependence of pharmacokinetics and biodistribution on polymer architecture: effect of cyclic versus linear polymers. *J. Am. Chem. Soc.* **131**, 3842–3843 (2009).

239. Etrych, T. *et al.* HPMA copolymer-doxorubicin conjugates: The effects of molecular weight and architecture on biodistribution and in vivo activity. *J. Control. release Off. J. Control. Release Soc.* **164**, 346–354 (2012).

240. Berry, S. *et al.* Enhancing intracranial delivery of clinically relevant non-viral gene vectors. *RSC Adv.* **6**, 41665–41674 (2016).

241. Karagoz, B. *et al.* Polymerization-Induced Self-Assembly (PISA) – control over the morphology of nanoparticles for drug delivery applications. *Polym. Chem.* **5**, 350–355 (2014).

242. Truong, N. P., Whittaker, M. R., Mak, C. W. & Davis, T. P. The importance of nanoparticle shape in cancer drug delivery. *Expert Opin. Drug Deliv.* **12**, 129–142 (2015).

243. Geng, Y. *et al.* Shape effects of filaments versus spherical particles in flow and drug delivery. *Nat. Nanotechnol.* **2**, 249–255 (2007).

244. Florez, L. *et al.* How shape influences uptake: interactions of anisotropic polymer nanoparticles and human mesenchymal stem cells. *Small* **8**, 2222–2230 (2012).

245. Lipinski, C. A., Lombardo, F., Dominy, B. W. & Feeney, P. J. Experimental and computational approaches to estimate solubility and permeability in drug discovery and development settings. *Adv. Drug Deliv. Rev.* **23**, 3–25 (1997).

246. van Vlerken, L. E., Vyas, T. K. & Amiji, M. M. Poly(ethylene glycol)-modified nanocarriers for tumor-targeted and intracellular delivery. *Pharm. Res.* **24**, 1405–1414 (2007).

247. Yamamoto, Y., Nagasaki, Y., Kato, Y., Sugiyama, Y. & Kataoka, K. Long-circulating poly(ethylene glycol)-poly(D,L-lactide) block copolymer micelles with modulated surface charge. *J. Control. release Off. J. Control. Release Soc.* **77**, 27–38 (2001).

248. Woythe, L., Tito, N. B. & Albertazzi, L. A quantitative view on multivalent nanomedicine targeting. *Adv. Drug Deliv. Rev.* **169**, 1–21 (2021).

249. Alkilany, A. M. *et al.* Ligand density on nanoparticles: A parameter with critical impact on nanomedicine. *Adv. Drug Deliv. Rev.* **143**, 22–36 (2019).

250. Elias, D. R., Poloukhtine, A., Popik, V. & Tsourkas, A. Effect of ligand density, receptor density, and nanoparticle size on cell targeting. *Nanomedicine* **9**, 194–201 (2013).

251. Reuter, K. G. *et al.* Targeted PRINT Hydrogels: The Role of Nanoparticle Size and Ligand Density on Cell Association, Biodistribution, and Tumor Accumulation. *Nano Lett.* **15**, 6371–6378 (2015).

252. Ghaghada, K. B., Saul, J., Natarajan, J. V, Bellamkonda, R. V & Annapragada, A. V. Folate targeting of drug carriers: A mathematical model. *J. Control. Release* **104**, 113–128 (2005).

253. Reddy, J. A. *et al.* Folate-targeted, cationic liposome-mediated gene transfer into disseminated peritoneal tumors. *Gene Ther.* **9**, 1542–1550 (2002).

254. Dalal, C., Saha, A. & Jana, N. R. Nanoparticle Multivalency Directed Shifting of Cellular

Uptake Mechanism. *J. Phys. Chem. C* **120**, 6778–6786 (2016).

255. Khalil, I. A., Kogure, K., Futaki, S. & Harashima, H. High Density of Octaarginine Stimulates Macropinocytosis Leading to Efficient Intracellular Trafficking for Gene Expression*. *J. Biol. Chem.* **281**, 3544–3551 (2006).

256. Daneman, R. & Prat, A. The blood-brain barrier. *Cold Spring Harb. Perspect. Biol.* **7**, a020412 (2015).

257. Knox, E. G., Aburto, M. R., Clarke, G., Cryan, J. F. & O'Driscoll, C. M. The blood-brain barrier in aging and neurodegeneration. *Mol. Psychiatry* **27**, 2659–2673 (2022).

258. Dong, X. Current strategies for brain drug delivery. *Theranostics* **8**, 1481–1493 (2018).

259. Walters, W. P. Going further than Lipinski's rule in drug design. *Expert Opin. Drug Discov.* **7**, 99–107 (2012).

260. Mitusova, K. *et al.* Overcoming the blood–brain barrier for the therapy of malignant brain tumor: current status and prospects of drug delivery approaches. *J. Nanobiotechnology* **20**, 412 (2022).

261. Béduneau, A., Saulnier, P. & Benoit, J.-P. Active targeting of brain tumors using nanocarriers. *Biomaterials* **28**, 4947–4967 (2007).

262. Dhanikula, R. S., Argaw, A., Bouchard, J.-F. & Hildgen, P. Methotrexate loaded polyether-copolyester dendrimers for the treatment of gliomas: enhanced efficacy and intratumoral transport capability. *Mol. Pharm.* **5**, 105–116 (2008).

263. Hao, Z. *et al.* Liposomes modified with P-aminophenyl-α-d-mannopyranoside: A carrier for targeting cerebral functional regions in mice. *Eur. J. Pharm. Biopharm.* **84**, 505–516 (2013).

264. Grover, A., Hirani, A., Pathak, Y. & Sutariya, V. Brain-targeted delivery of docetaxel by glutathione-coated nanoparticles for brain cancer. *AAPS PharmSciTech* **15**, 1562–1568 (2014).

265. Devi, R., Jain, A., Hurkat, P. & Jain, S. K. Dual Drug Delivery Using Lactic Acid Conjugated SLN for Effective Management of Neurocysticercosis. *Pharm. Res.* **32**, 3137–3148 (2015).

266. Killian, D. M., Hermeling, S. & Chikhale, P. J. Targeting the Cerebrovascular Large Neutral Amino Acid Transporter (LAT1) Isoform Using a Novel Disulfide-Based Brain Drug Delivery System. *Drug Deliv.* **14**, 25–31 (2007).

267. Vyas, A., Jain, A., Hurkat, P., Jain, A. & Jain, S. K. Targeting of AIDS related encephalopathy using phenylalanine anchored lipidic nanocarrier. *Colloids Surfaces B Biointerfaces* **131**, 155–161 (2015).

268. Liu, J. *et al.* Functionalized nanocarrier combined seizure-specific vector with P-glycoprotein modulation property for antiepileptic drug delivery. *Biomaterials* **74**, 64–76 (2016).

269. Geldenhuys, W., Mbimba, T., Bui, T., Harrison, K. & Sutariya, V. Brain-targeted delivery of paclitaxel using glutathione-coated nanoparticles for brain cancers. *J. Drug Target.* **19**, 837–845 (2011).

270. Geldenhuys, W., Wehrung, D., Groshev, A., Hirani, A. & Sutariya, V. Brain-targeted delivery of doxorubicin using glutathione-coated nanoparticles for brain cancers. *Pharm. Dev. Technol.* **20**, 497–506 (2015).

271. Kobayashi, K. *et al.* ENHANCED TUMOR GROWTH ELICITED BY L-TYPE AMINO ACID TRANSPORTER 1 IN HUMAN MALIGNANT GLIOMA CELLS. *Neurosurgery* **62**, (2008).

272. Xiao, G. & Gan, L.-S. Receptor-Mediated Endocytosis and Brain Delivery of Therapeutic Biologics. *Int. J. Cell Biol.* **2013**, 703545 (2013).

273. Ulbrich, K., Hekmatara, T., Herbert, E. & Kreuter, J. Transferrin- and transferrin-receptor-antibody-modified nanoparticles enable drug delivery across the blood–brain barrier (BBB). *Eur. J. Pharm. Biopharm.* **71**, 251–256 (2009).

274. Visser, C. C. *et al.* Targeting liposomes with protein drugs to the blood–brain barrier in vitro. *Eur. J. Pharm. Sci.* **25**, 299–305 (2005).

275. Fornaguera, C. *et al.* PLGA nanoparticles prepared by nano-emulsion templating using low-energy methods as efficient nanocarriers for drug delivery across the blood-brain barrier. *J. Control. release Off. J. Control. Release Soc.* **211**, 134–143 (2015).

276. Li, H. *et al.* Lactoferrin functionalized PEG-PLGA nanoparticles of shikonin for brain targeting therapy of glioma. *Int. J. Biol. Macromol.* **107**, 204–211 (2018).

277. Qiao, R. *et al.* Receptor-Mediated Delivery of Magnetic Nanoparticles across the Blood–Brain Barrier. *ACS Nano* **6**, 3304–3310 (2012).

278. Boado, R. J., Zhang, Y., Zhang, Y., Wang, Y. & Pardridge, W. M. GDNF fusion protein for targeted-drug delivery across the human blood–brain barrier. *Biotechnol. Bioeng.* **100**, 387–396 (2008).

279. Ulbrich, K., Knobloch, T. & Kreuter, J. Targeting the insulin receptor: nanoparticles for drug delivery across the blood–brain barrier (BBB). *J. Drug Target.* **19**, 125–132 (2011).

280. Habib, S. & Singh, M. Angiopep-2-Modified Nanoparticles for Brain-Directed Delivery of Therapeutics: A Review. *Polymers (Basel).* **14**, (2022).

281. Re, F. *et al.* Functionalization of liposomes with ApoE-derived peptides at different density affects cellular uptake and drug transport across a blood-brain barrier model. *Nanomedicine Nanotechnology, Biol. Med.* **7**, 551–559 (2011).

282. You, Y., Yang, L., He, L. & Chen, T. Tailored mesoporous silica nanosystem with enhanced permeability of the blood-brain barrier to antagonize glioblastoma. *J. Mater. Chem. B* **4**, 5980–5990 (2016).

283. Miura, Y. *et al.* Cyclic RGD-linked polymeric micelles for targeted delivery of platinum anticancer drugs to glioblastoma through the blood-brain tumor barrier. *ACS Nano* **7**, 8583–8592 (2013).

284. McCord, E. *et al.* Folate Receptors' Expression in Gliomas May Possess Potential Nanoparticle-Based Drug Delivery Opportunities. *ACS Omega* **6**, 4111–4118 (2021).

285. Gao, S. *et al.* A non-viral suicide gene delivery system traversing the blood brain barrier for non-invasive glioma targeting treatment. *J. Control. Release* **243**, 357–369 (2016).

286. Lim, C. *et al.* Enhancing CDK4/6 inhibitor therapy for medulloblastoma using nanoparticle delivery and scRNA-seq-guided combination with sapanisertib. *Sci. Adv.* **8**, eabl5838 (2022).

287. Cui, Y. *et al.* Dual-Targeting Magnetic PLGA Nanoparticles for Codelivery of Paclitaxel and Curcumin for Brain Tumor Therapy. *ACS Appl. Mater. Interfaces* **8**, 32159–32169 (2016).

288. Monsalve, Y. *et al.* PEG-g-chitosan nanoparticles functionalized with the monoclonal antibody OX26 for brain drug targeting. *Nanomedicine (Lond).* **10**, 1735–1750 (2015).

289. Kim, J.-Y., Choi, W. Il, Kim, Y. H. & Tae, G. Brain-targeted delivery of protein using chitosan- and RVG peptide-conjugated, pluronic-based nano-carrier. *Biomaterials* **34**, 1170–1178 (2013).

290. Agarwal, A., Agrawal, H., Tiwari, S., Jain, S. & Agrawal, G. P. Cationic ligand appended nanoconstructs: A prospective strategy for brain targeting. *Int. J. Pharm.* **421**, 189–201 (2011).

291. Kamalinia, G. *et al.* Cationic albumin-conjugated chelating agent as a novel brain drug delivery system in neurodegeneration. *Chem. Biol. Drug Des.* **86**, 1203–1214 (2015).

292. Lu, W., Wan, J., Zhang, Q., She, Z. & Jiang, X. Aclarubicin-loaded cationic albumin-conjugated pegylated nanoparticle for glioma chemotherapy in rats. *Int. J. cancer* **120**, 420–431 (2007).

293. Muniswamy, V. J. *et al.* 'Dendrimer-Cationized-Albumin' encrusted polymeric nanoparticle improves BBB penetration and anticancer activity of doxorubicin. *Int. J. Pharm.* **555**, 77–99 (2019).

294. Park, T.-E. *et al.* Enhanced BBB permeability of osmotically active poly(mannitol-co-PEI) modified with rabies virus glycoprotein via selective stimulation of caveolar endocytosis for RNAi therapeutics in Alzheimer's disease. *Biomaterials* **38**, 61–71 (2015).

295. Janaszewska, A. *et al.* The biodistribution of maltotriose modified poly(propylene imine) (PPI)

dendrimers conjugated with fluorescein—proofs of crossing blood–brain–barrier. *New J. Chem.* **36**, 350–353 (2012).

296. Batrakova, E. V, Gendelman, H. E. & Kabanov, A. V. Cell-mediated drug delivery. *Expert Opin. Drug Deliv.* **8**, 415–433 (2011).

297. Tong, H.-I. *et al.* Monocyte Trafficking, Engraftment, and Delivery of Nanoparticles and an Exogenous Gene into the Acutely Inflamed Brain Tissue - Evaluations on Monocyte-Based Delivery System for the Central Nervous System. *PLoS One* **11**, e0154022 (2016).

298. Matsumura, Y. *et al.* Phase I and pharmacokinetic study of MCC-465, a doxorubicin (DXR) encapsulated in PEG immunoliposome, in patients with metastatic stomach cancer. *Ann. Oncol. Off. J. Eur. Soc. Med. Oncol.* **15**, 517–525 (2004).

299. Reilly, R. K. O. & Pearce, A. K. Insights into active targeting of nanoparticles in drug delivery : advances in clinical studies and design considerations for cancer nanomedicine Insights into active targeting of nanoparticles in drug delivery : advances in clinical studies and design co. *Bioconjug. Chem.* **30**, 2300–2311 (2019).

300. Dai, Q. *et al.* Quantifying the Ligand-Coated Nanoparticle Delivery to Cancer Cells in Solid Tumors. *ACS Nano* **12**, 8423–8435 (2018).

301. Biancacci, I. *et al.* Optical imaging of the whole-body to cellular biodistribution of clinical-stage PEG-b-pHPMA-based core-crosslinked polymeric micelles. *J. Control. Release* **328**, 805–816 (2020).

302. Lin, T. *et al.* Blood–Brain-Barrier-Penetrating Albumin Nanoparticles for Biomimetic Drug Delivery via Albumin-Binding Protein Pathways for Antiglioma Therapy. *ACS Nano* **10**, 9999–10012 (2016).

303. Veszelka, S. *et al.* A Triple Combination of Targeting Ligands Increases the Penetration of Nanoparticles across a Blood-Brain Barrier Culture Model. *Pharmaceutics* **14**, (2021).

304. Kumar, V. *et al.* Polymeric nanomedicine for overcoming resistance mechanisms in hedgehog and Myc-amplified medulloblastoma. *Biomaterials* **278**, 121138 (2021).

305. Lu, C.-T. *et al.* Current approaches to enhance CNS delivery of drugs across the brain barriers. *Int. J. Nanomedicine* **9**, 2241–2257 (2014).

306. Chen, Q. *et al.* Treatment of Human Glioblastoma with a Live Attenuated Zika Virus Vaccine Candidate. *MBio* **9**, (2018).

307. Le Reste, P. J. *et al.* Local intracerebral inhibition of IRE1 by MKC8866 sensitizes glioblastoma to irradiation/chemotherapy in vivo. *Cancer Lett.* **494**, 73–83 (2020).

308. Triarico, S. *et al.* Improving the Brain Delivery of Chemotherapeutic Drugs in Childhood Brain Tumors. *Cancers* vol. 11 (2019).

309. Brem, H. *et al.* Placebo-controlled trial of safety and efficacy of intraoperative controlled delivery by biodegradable polymers of chemotherapy for recurrent gliomas. The Polymer-brain Tumor Treatment Group. *Lancet (London, England)* **345**, 1008–1012 (1995).

310. Rahman, R. *et al.* Childhood Brain Tumors: A Review of Strategies to Translate CNS Drug Delivery to Clinical Trials. *Cancers* vol. 15 (2023).

311. Li, K. W. *et al.* Polilactofate microspheres for Paclitaxel delivery to central nervous system malignancies. *Clin. cancer Res. an Off. J. Am. Assoc. Cancer Res.* **9**, 3441–3447 (2003).

312. Tyler, B. *et al.* A thermal gel depot for local delivery of paclitaxel to treat experimental brain tumors in rats: Laboratory investigation. *J. Neurosurg. JNS* **113**, 210–217 (2010).

313. Bobo, R. H. *et al.* Convection-enhanced delivery of macromolecules in the brain. *Proc. Natl. Acad. Sci. U. S. A.* **91**, 2076–2080 (1994).

314. Fowler, M. J. *et al.* Intrathecal drug delivery in the era of nanomedicine. *Adv. Drug Deliv. Rev.* **165–166**, 77–95 (2020).

315. Cereda, C. M. S. *et al.* Bupivacaine in alginate and chitosan nanoparticles: an in vivo evaluation of efficacy, pharmacokinetics, and local toxicity. *J. Pain Res.* **11**, 683–691 (2018).

316. Karashima, K. *et al.* Prolongation of intrathecal and sciatic nerve blocks using a complex of

levobupivacaine with maltosyl-beta-cyclodextrin in rats. *Anesth. Analg.* **104**, 1121–8, tables of contents (2007).

317.   Dai, H. *et al.* Intrinsic targeting of inflammatory cells in the brain by polyamidoamine dendrimers upon subarachnoid administration. *Nanomedicine (Lond).* **5**, 1317–1329 (2010).

318.   Helmschrodt, C. *et al.* Polyethylenimine Nanoparticle-Mediated siRNA Delivery to Reduce α-Synuclein Expression in a Model of Parkinson's Disease. *Mol. Ther. Nucleic Acids* **9**, 57–68 (2017).

319.   Kitamura, I. *et al.* Intrathecal chemotherapy with 1,3-bis(2-chloroethyl)-1-nitrosourea encapsulated into hybrid liposomes for meningeal gliomatosis: an experimental study. *Cancer Res.* **56**, 3986–3992 (1996).

320.   Kim, S., Kim, D. J., Geyer, M. A. & Howell, S. B. Multivesicular liposomes containing 1-beta-D-arabinofuranosylcytosine for slow-release intrathecal therapy. *Cancer Res.* **47**, 3935–3937 (1987).

321.   Uchida, S. *et al.* In vivo messenger RNA introduction into the central nervous system using polyplex nanomicelle. *PLoS One* **8**, e56220 (2013).

322.   Householder, K. T., Dharmaraj, S., Sandberg, D. I., Wechsler-Reya, R. J. & Sirianni, R. W. Fate of nanoparticles in the central nervous system after intrathecal injection in healthy mice. *Sci. Rep.* **9**, 12587 (2019).

323.   Shyam, R. *et al.* Intraventricular Delivery of siRNA Nanoparticles to the Central Nervous System. *Mol. Ther. Nucleic Acids* **4**, e242 (2015).

324.   Agrawal, M. *et al.* Nose-to-brain drug delivery: An update on clinical challenges and progress towards approval of anti-Alzheimer drugs. *J. Control. Release* **281**, 139–177 (2018).

325.   Frey WH., 2nd. (WO/1991/007947) Neurologic Agents for Nasal Administration to the Brain (priority date 51289) Geneva, Switzerland: World Intellectual Property Organization; 1991.

326.   Hussain, A. A. Intranasal drug delivery. *Adv. Drug Deliv. Rev.* **29**, 39–49 (1998).

327.   Dhuria, S. V, Hanson, L. R. & Frey, W. H. 2nd. Intranasal delivery to the central nervous system: mechanisms and experimental considerations. *J. Pharm. Sci.* **99**, 1654–1673 (2010).

328.   Costa, C. P., Moreira, J. N., Sousa Lobo, J. M. & Silva, A. C. Intranasal delivery of nanostructured lipid carriers, solid lipid nanoparticles and nanoemulsions: A current overview of in vivo studies. *Acta Pharm. Sin. B* **11**, 925–940 (2021).

329.   Cloyd, J., Haut, S., Carrazana, E. & Rabinowicz, A. L. Overcoming the challenges of developing an intranasal diazepam rescue therapy for the treatment of seizure clusters. *Epilepsia* **62**, 846–856 (2021).

330.   Keller, L.-A., Merkel, O. & Popp, A. Intranasal drug delivery: opportunities and toxicologic challenges during drug development. *Drug Deliv. Transl. Res.* **12**, 735–757 (2022).

331.   Sigurdsson, H. H., Kirch, J. & Lehr, C.-M. Mucus as a barrier to lipophilic drugs. *Int. J. Pharm.* **453**, 56–64 (2013).

332.   Verdugo, P. Goblet cells secretion and mucogenesis. *Annu. Rev. Physiol.* **52**, 157–176 (1990).

333.   Lai, S. K. *et al.* Rapid transport of large polymeric nanoparticles in fresh undiluted human mucus. *Proc. Natl. Acad. Sci. U. S. A.* **104**, 1482–1487 (2007).

334.   Gänger, S. & Schindowski, K. Tailoring Formulations for Intranasal Nose-to-Brain Delivery: A Review on Architecture, Physico-Chemical Characteristics and Mucociliary Clearance of the Nasal Olfactory Mucosa. *Pharmaceutics* vol. 10 (2018).

335.   Thorne, R. G., Emory, C. R., Ala, T. A. & Frey, W. H. Quantitative analysis of the olfactory pathway for drug delivery to the brain. *Brain Res.* **692**, 278–282 (1995).

336.   Thorne, R. G., Pronk, G. J., Padmanabhan, V. & Frey, W. H. 2nd. Delivery of insulin-like growth factor-I to the rat brain and spinal cord along olfactory and trigeminal pathways following intranasal administration. *Neuroscience* **127**, 481–496 (2004).

337.   Ross, T. M. *et al.* Intranasal administration of interferon beta bypasses the blood-brain barrier to target the central nervous system and cervical lymph nodes: a non-invasive treatment

strategy for multiple sclerosis. *J. Neuroimmunol.* **151**, 66–77 (2004).

338. Renner, D. B., Frey, W. H. & Hanson, L. R. Intranasal delivery of siRNA to the olfactory bulbs of mice via the olfactory nerve pathway. *Neurosci. Lett.* **513**, 193–197 (2012).

339. Kristensson, K. & Olsson, Y. Uptake of exogenous proteins in mouse olfactory cells. *Acta Neuropathol.* **19**, 145–154 (1971).

340. Broadwell, R. D. & Balin, B. J. Endocytic and exocytic pathways of the neuronal secretory process and trans synaptic transfer of wheat germ agglutinin-horseradish peroxidase in vivo. *J. Comp. Neurol.* **242**, 632–650 (1985).

341. De Lorenzo, A. J. D. The Olfactory Neuron and the Blood-Brain Barrier. in *Ciba Foundation Symposium - Internal Secretions of the Pancreas (Colloquia on Endocrinology)* 151–176 (1970). doi:https://doi.org/10.1002/9780470715369.ch9.

342. van Riel, D. *et al.* Evidence for Influenza Virus CNS Invasion Along the Olfactory Route in an Immunocompromised Infant. *J. Infect. Dis.* **210**, 419–423 (2014).

343. Anton, F. & Peppel, P. Central projections of trigeminal primary afferents innervating the nasal mucosa: A horseradish peroxidase study in the rat. *Neuroscience* **41**, 617–628 (1991).

344. DEATLY, A. M., HAASE, A. T., FEWSTER, P. H., LEWIS, E. & BALL, M. J. Human herpes virus infections and Alzheimer's disease. *Neuropathol. Appl. Neurobiol.* **16**, 213–223 (1990).

345. Ball, M. J., Lukiw, W. J., Kammerman, E. M. & Hill, J. M. Intracerebral propagation of Alzheimer's disease: Strengthening evidence of a herpes simplex virus etiology. *Alzheimer's Dement.* **9**, 169–175 (2013).

346. Crowe, T. P., Greenlee, M. H. W., Kanthasamy, A. G. & Hsu, W. H. Mechanism of intranasal drug delivery directly to the brain. *Life Sci.* **195**, 44–52 (2018).

347. Li, Y., Field, P. M. & Raisman, G. Olfactory ensheathing cells and olfactory nerve fibroblasts maintain continuous open channels for regrowth of olfactory nerve fibres. *Glia* **52**, 245–251 (2005).

348. Musumeci, T., Pellitteri, R., Spatuzza, M. & Puglisi, G. Nose-to-brain delivery: evaluation of polymeric nanoparticles on olfactory ensheathing cells uptake. *J. Pharm. Sci.* **103**, 628–635 (2014).

349. Mistry, A., Stolnik, S. & Illum, L. Nose-to-Brain Delivery: Investigation of the Transport of Nanoparticles with Different Surface Characteristics and Sizes in Excised Porcine Olfactory Epithelium. *Mol. Pharm.* **12**, 2755–2766 (2015).

350. Mistry, A. *et al.* Effect of physicochemical properties on intranasal nanoparticle transit into murine olfactory epithelium. *J. Drug Target.* **17**, 543–552 (2009).

351. Bonaccorso, A. *et al.* Nose to brain delivery in rats: Effect of surface charge of rhodamine B labeled nanocarriers on brain subregion localization. *Colloids Surfaces B Biointerfaces* **154**, 297–306 (2017).

352. Clementino, A. R. *et al.* Structure and Fate of Nanoparticles Designed for the Nasal Delivery of Poorly Soluble Drugs. *Mol. Pharm.* **18**, 3132–3146 (2021).

353. Kanazawa, T. *et al.* Enhancement of nose-to-brain delivery of hydrophilic macromolecules with stearate- or polyethylene glycol-modified arginine-rich peptide. *Int. J. Pharm.* **530**, 195–200 (2017).

354. Gabal, Y. M., Kamel, A. O., Sammour, O. A. & Elshafeey, A. H. Effect of surface charge on the brain delivery of nanostructured lipid carriers in situ gels via the nasal route. *Int. J. Pharm.* **473**, 442–457 (2014).

355. Weintraub, K. Biomedicine: The new gold standard. *Nature* **495**, S14–S16 (2013).

356. Ruan, S. *et al.* Tumor microenvironment sensitive doxorubicin delivery and release to glioma using angiopep-2 decorated gold nanoparticles. *Biomaterials* **37**, 425–435 (2015).

357. Cheng, Y. *et al.* Blood-brain barrier permeable gold nanoparticles: an efficient delivery platform for enhanced malignant glioma therapy and imaging. *Small* **10**, 5137–5150 (2014).

358. Jensen, S. A. *et al.* Spherical nucleic acid nanoparticle conjugates as an RNAi-based therapy

for glioblastoma. *Sci. Transl. Med.* **5**, 209ra152 (2013).

359. Liu, Z., Yan, H. & Li, H. Silencing of DNA repair sensitizes pediatric brain tumor cells to γ-irradiation using gold nanoparticles. *Environ. Toxicol. Pharmacol.* **53**, 40–45 (2017).

360. Norouzi, M. *et al.* Doxorubicin-loaded iron oxide nanoparticles for glioblastoma therapy: a combinational approach for enhanced delivery of nanoparticles. *Sci. Rep.* **10**, 11292 (2020).

361. Duong, C. *et al.* Novel targeted therapy for neuroblastoma: silencing the MXD3 gene using siRNA. *Pediatr. Res.* **82**, 527–535 (2017).

362. Infante, P. *et al.* Glabrescione B delivery by self-assembling micelles efficiently inhibits tumor growth in preclinical models of Hedgehog-dependent medulloblastoma. *Cancer Lett.* **499**, 220–231 (2021).

363. Kim, J. *et al.* Engineered biomimetic nanoparticle for dual targeting of the cancer stem-like cell population in sonic hedgehog medulloblastoma. *Proc. Natl. Acad. Sci. U. S. A.* **117**, 24205–24212 (2020).

364. Kim, J. S., Shin, D. H. & Kim, J.-S. Dual-targeting immunoliposomes using angiopep-2 and CD133 antibody for glioblastoma stem cells. *J. Control. Release* **269**, 245–257 (2018).

365. Kimura, H., Ng, J. M. Y. & Curran, T. Transient inhibition of the Hedgehog pathway in young mice causes permanent defects in bone structure. *Cancer Cell* **13**, 249–260 (2008).

366. Hwang, D. *et al.* Poly(2-oxazoline) nanoparticle delivery enhances the therapeutic potential of vismodegib for medulloblastoma by improving CNS pharmacokinetics and reducing systemic toxicity. *Nanomedicine Nanotechnology, Biol. Med.* **32**, 102345 (2021).

367. Lopez-Bertoni, H. *et al.* Bioreducible Polymeric Nanoparticles Containing Multiplexed Cancer Stem Cell Regulating miRNAs Inhibit Glioblastoma Growth and Prolong Survival. *Nano Lett.* **18**, 4086–4094 (2018).

Chapter 2

Rational Design of a Polyglutamate-based Intranasal Platform for Brain Delivery

2.1 Introduction

Despite significant advances in recent years, the treatment of brain tumors has fallen behind compared to other tumor types. The poor efficacy of brain tumor therapies may relate to the presence of the blood-brain barrier, which possesses unique characteristics and limits the delivery of therapeutic agents to the brain [1]. The blood-brain barrier protects the brain from foreign substances and organisms and blocks 98% of small and 100% water-soluble drugs or large-molecule biotherapeutics (i.e., genetic material, antibodies, and proteins) [2,3]. Despite the low percentage (0.2 - 1%) of the injected dose of a formulation that will reach the brain following intravenous administration [3–6], this route remains the standard and clinically preferable route for rapid, single/repeated administration for cancer treatment. The need to perform drug administration over several h with a high required dosage (due to low drug bioavailability) brings high overall toxicity and severe side effects; therefore, improvements to intravenous administration strategies are required. Nanomedicine-based formulations have the potential to overcome these problems by incorporating moieties that facilitate the crossing of drugs through the blood-brain barrier via adsorptive-mediated, carrier-mediated, or receptor-mediated transcytosis [7]. Unfortunately, we still lack appropriate strategies to transport large-molecule biological agents into the central nervous system (i.e., the brain). This problem has impacted the pharma industry [8–10], as the lack of penetration into the brain remains a significant bottleneck that impedes taking many therapeutics to market [2,9,11].

Intranasal administration has emerged as an alternative treatment route that takes advantage of direct nose-to-brain delivery through the trigeminal and olfactory nerves and skips the blood-brain barrier [12]. The main advantages of intranasal administration

include easy self-medication, appropriateness for children (the target population in our case), improved drug bioavailability, bypass of liver metabolism, the need for a lower dosage to achieve therapeutic outcomes, and the associated reduction in off-target effects [13]. Notably, three significant limitations still prevent effective intranasal delivery and brain diffusion of biological therapeutics: i) drug degradation and toxic/immunogenic side effects, ii) unoptimized carrier formulation (low nasal drug absorption, particularly important for hydrophilic drugs, peptides, and proteins), and iii) complex physiological events (e.g., rapid mucociliary clearance, brain diffusion, and controlled and sustained drug release). Nose-to-brain transport can be facilitated by polymeric formulations, which enhance solubility, stability, and permeation through the mucosa; additionally, nose-to-brain transport can decrease nasal irritation and systemic exposure compared to free drug administration. Recent nanotechnological advancements have made substantial contributions towards solving these problems [14], and newly developed polymer- or lipid-based nanoparticles have improved nose-to-brain delivery of a variety of therapeutics (up to a 14-fold increase in brain bioavailability compared to intravenous administration [15–18]); however, intranasally-administered nanosystems have yet to reach the clinical development phase [13,15]. Polymer therapeutics based on amino acids [19], particularly polyglutamates (PGAs), represent excellent candidates for brain delivery given their biodegradability and robust safety profile, as recognized in 1959 following the evaluation of PGA as a plasma expander [20]. PGAs possess low immunogenicity, high biocompatibility, and biodegradability and undergo intracellular protease degradation by cathepsin B, which is highly upregulated in most malignant cells [21], making PGA a focus of interest in cancer research [19,22]. PGA provides versatile hierarchical and structural possibilities for incorporating several agents: drugs, targeting moieties, specific markers, and fluorescent probes that have generated interest in such materials and their application to drug delivery [19].

The attractive nature of synthetic PGA-based materials derives from the highly economical polymerization techniques involved compared to solid-phase peptide synthesis or the resource-dependent and time-consuming manufacturing processes associated with natural polymers accompanied by higher immunogenicity. Traditionally, synthetic polypeptide production proceeds via inexpensive α-amino acid N-carboxy anhydride ring-opening polymerization (NCA-ROP) techniques, which provide the potential for large-scale production. Most of the 200 monomers described in the literature are commercially available and widely used for biomedical applications [23]. In addition to classical linear polypeptides, NCA-ROP supports the straightforward generation of non-linear polypeptide architectures (i.e., star-shaped brushes and hyperbranched polypeptides) [24]. Additionally, unnatural amino acids and D-enantiomers can be easily added during polymerization, which supports the structural diversity of block copolymers to benefit targeted tissue accumulation [25].

As pointed out in Chapter 1 (Section 2.3.1), NCA-ROP ongoing developments from countless research groups have evolved the field to a point where polypeptides can be formulated on demand with precise weight, architectural control, narrow polydispersity

index (PDI), and tailored end group fidelity [23,26]. Traditionally, a primary amine or its salt derivatives (hydrochloride [27] and tetrafluoroborate [28]) initiates the polymerization process in anhydrous solvents under an inert atmosphere. The process is controlled by cooling down the reaction mixture [29] or using a high vacuum technique [30] to accelerate the process and monomer consumption, thus reducing reaction time. The use of transition metal catalysts (Co [31,32], Fe [31], Pd [33], Pt [33], Ru [34], Ir [34], Al [35], Ni [32,36]) provides an alternative strategy for the synthesis of well-defined homopolymers and block-copolymers by accelerating polymer chain propagation and significantly reducing side-reactions present in a conventional NCA-ROP [37].

Recent advances in NCA-ROP have enabled the rapid, controlled, and reproducible synthesis of long polypeptide chains with narrow size distribution in scalable processes with good yields and no detectable racemization of amino acids [23,28,38–40]. Multivalence and straightforward surface modification of synthetic polypeptides are widely used for drug/imaging modality conjugation [19]. PGA side-chain modification is usually accomplished via esterification or amidation reactions by carbodiimide coupling with high modification efficiencies (up to 90 mol%) [23], highlighting the high loading capacity of such materials. The use of PGA nanoparticles has been successfully reported for peptide-based vaccines [41,42] or as the vaccine adjuvant [43] via intranasal administration, with no studies found that report the targeted brain delivery so far.

In this chapter, we tackled the challenges related to mucosa permeation by rationally designing mucoadhesive/mucodiffusive PGA-based polymeric materials. For this aim, we employed different strategies. First is the introduction of targeting ligands by covalent linkage such as (i) lectins (Section 2.2.4.), which have evidenced their strong and rapid binding to sugar moieties in the glycosylated lipids cell membranes in the nasal mucosa [44]. Thus, their covalent binding to the PGA systems will improve nose-to-brain passage due to the enhancement of transepithelial transport. Also, (ii) Omega-3 fatty acids have been shown to facilitate mucosal transport through natural diffusion across the BBB through their natural receptors CD36 and fatty acid-binding protein (FABP) [45,46] (Section 2.2.6.). Secondly, hyaluronic acid (HA) (Section 2.2.5.), a widely exploited natural anionic polysaccharide with an excellent mucoadhesive capacity, can prolong retention time, increasing drug absorption via mucosal tissues [47–50], among other advantages. Finally, crosslinked polyglutamate constructs, which negatively charged glutamic acid, might allow hydrogen bonding with the mucosa and repulsion-induced diffusion interlocking of the polymer arms. We have explored disulfide crosslinking of PGA architectures for the adjustment of wettability (contact angle with the mucosa), flexibility of polymer arms for interpenetration into the mucosa, and facilitate chemical adsorption to the mucosa via disulfide interchange with cysteine-rich glycoproteins.

The successful development of an intranasal platform involves several critical stages, including understanding the drug transport mechanism, disease pathophysiology, and brain anatomy, selecting appropriate ex vivo/in vivo models and experimental parameters for therapeutic evaluation, and rationally designing materials with all these

aspects in mind [51]. The lack of appropriate models for rapid screening and evaluating promising formulations, thus hindering their clinical progress, represents a primary obstacle in developing successful intranasal formulations. Developing in vitro models that reflect the in vivo reality to screen candidates for intranasal delivery remains of significant interest and has been dictated by economic and ecological aspects to accelerate drug development and reduce the number of animals employed. Ex vivo models based on diffusion apparatuses are a recurring choice. The most common diffusion cells include the µFLUX™ diffusion cell (Pion Inc.) [52], Navicyte Vertical System (Harvard Apparatus Inc.) [53], Navicyte Horizontal System (Harvard Apparatus Inc.) [54], In-Line Cell (PermeGear Inc.) [55], and Franz vertical diffusion cell (Hanson Research Inc., PermeGear Inc.) [56,57]. These diffusion cells are classified as horizontal or vertical depending on membrane position.

Diverse permeation models are classified based on the membrane type used (in vitro, in vitro cell lines, and ex vivo) [58]. In vitro models employ artificial membranes such as polyamide membranes (Sartorius™, pore size: 0.45 µm) [56] and have advantages such as robustness; however, they do not represent all in vivo scenarios. A modified horizontal cell called "Side-By-Side™" (PermeGear Inc.) has been used for inline spectrophotometrical real-time measurements to evaluate nasal powder formulations of drugs with different lipophilicities [59]. The authors evaluated three membranes: a mixed cellulose-ester membrane (Metricel®, pore size: 0.45 µm), a polycarbonate membrane (Isopore™, pore size: 0.40 µm), and a regenerated cellulose membrane (Whatman™, pore size: 0.45 µm), which demonstrated a high correlation between offline and inline results. The application of this methodology to excised nasal mucosa (which better represents in vivo scenarios) may be of particular interest.

In vitro, cultured primary cells represent an established tool for various biological assays and recently saw use in the study of drug transport across the nasal epithelium [60]. Limitations to using such cells as part of an intranasal model include the required repeated sampling of cells in the same subject and area and the short supply of human nasal tissue [61]. To overcome these limitations, several groups reported protocols to extend the lifespan of primary epithelial cells [62–66] or prepare immortalized cells [67] to avoid the need for resampling while maintaining the characteristics of nasal cells; however, the modified cell lines are not commercially available, and require a sophisticated cell maintenance medium. Of those cells available, the immortalized human nasal cell line RPMI2650, originating from anaplastic squamous cells, may represent a reasonable compromise as, under appropriate culture conditions, the cells can form polarized epithelium with differences between superficial and basal layers, which resembles the nasal mucosa [56,68].

Ex vivo models based on excised nasal mucosa may represent the optimal model of intact mucosa tissue in vivo. Said models allow the study of permeability, transport across the nasal tissue, metabolic barrier capacity [61], and the effect of therapeutics on mucosal integrity and morphology [69,70]. Considering the difficulties in obtaining human tissue [71], most studies employ freshly excised rabbit [72,73], sheep [74,75], goat [76], cow [77,78], or

pig [79] nasal tissue with minimal time elapsed between animal sacrifice to preserve tissue viability [57,72]. The viability of these tissues depends on the animal species and is estimated at approx. 3-12 h [72,78]; however, freezing mucosal tissue does not compromise barrier integrity and can be used for permeation studies [80]. Despite many advantages, the described ex vivo model cannot be employed to study how formulation residence time or deposition site affects absorption within the nasal cavity and permeation ability of drug formulation [69]. Therefore, the in vivo confirmation to validate the ex vivo model represents a desirable step.

Therefore, in this chapter, we focus on the synthesis of PGA-based carriers with modified surfaces to improve mucosa permeation as well as establishing appropriate models and rationally designing a final platform for intranasal brain delivery in the joint pursuit of *decreased* nasal mucociliary clearance and *increased* permeability across the nasal epithelium.

2.2. Results and Discussion

2.2.1. Synthesis and Characterization of Linear and Star PGA-based Carriers

PGA-based carriers are versatile materials that can be rationally designed depending on required characteristics. Previous studies have demonstrated the differential behavior of PGAs depending on the size and topology regarding cell uptake, blood circulation time, and organ biodistribution after intravenous administration [81]. To study how carrier conformation affects overall physicochemical and biological properties, we synthesized two polymeric platforms based on PGAs: linear (LinPGA) and star-shaped (StPGA).

We employed non-catalytic NCA-ROP [39] of L-glutamic acid monomers with benzyl ester protecting group (NCA-BLG) for the synthesis of PGA-based carriers to avoid the complicated purification steps associated with transition metal complexes, whose toxicity can contribute to the biological activity of final systems and compromise the safety profile of the carriers. As initiators, we employed butane-1-amine for LinPGA and N,N,N-tris(2-aminoethyl)benzene-1,3,5-tricarboxamide synthesized from benzene-tricarboxylic acid (BTA) for StPGA. We conducted the polymerization in anhydrous N,N'-dimethylformamide (DMF$_{anh}$) for three days at 10 °C under an inert atmosphere to obtain poly(γ-benzyl-l-glutamate) (PBLG) protected polymers. We then employed a deprotection step to generate LinPGA and StPGA carriers (**Figure 2.1**)
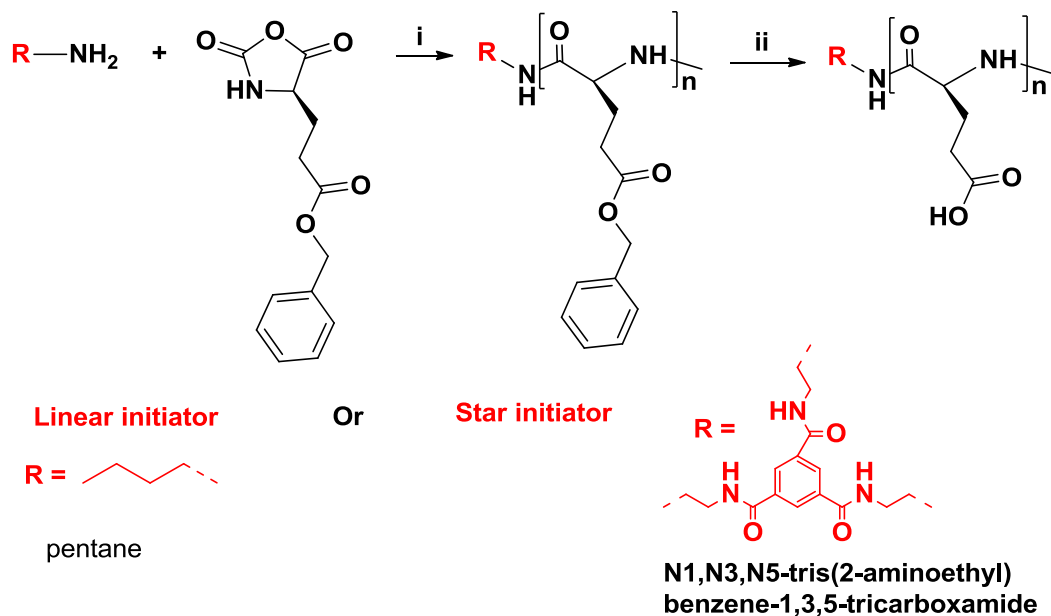
Figure 2.1. Synthesis of LinPGA and StPGA carriers: i) DMF$_{anh}$, 10°C, 72 h; ii) TFA$_{conc}$/HBr, room temperature, overnight (**SI-2.3**)

We monitored polymerization completion and product purity by gel permeation chromatography (GPC) and nuclear magnetic resonance (NMR). We determined the polymerization (DP) degree from GPC (**Figure 2.2A**).
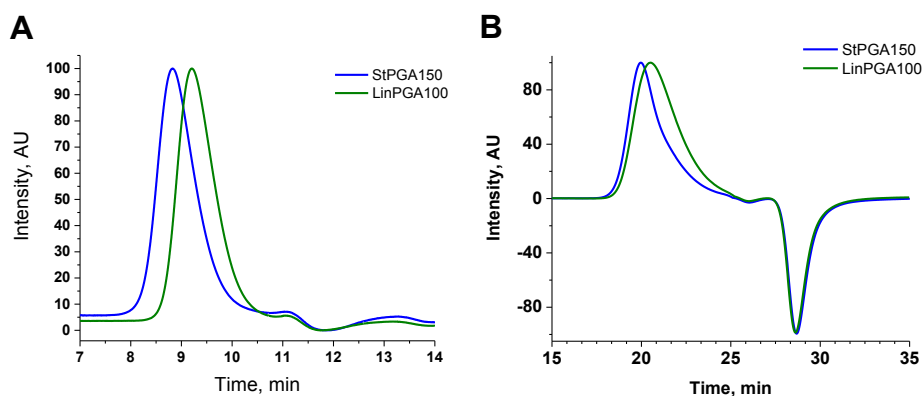
Figure 2.2. Overlaid chromatograms from a series of synthesized PGA carriers with different molecular weights. (**A**) Protected PBLG analyzed by GPC, and (**B**) deprotected PGA analyzed by SEC.
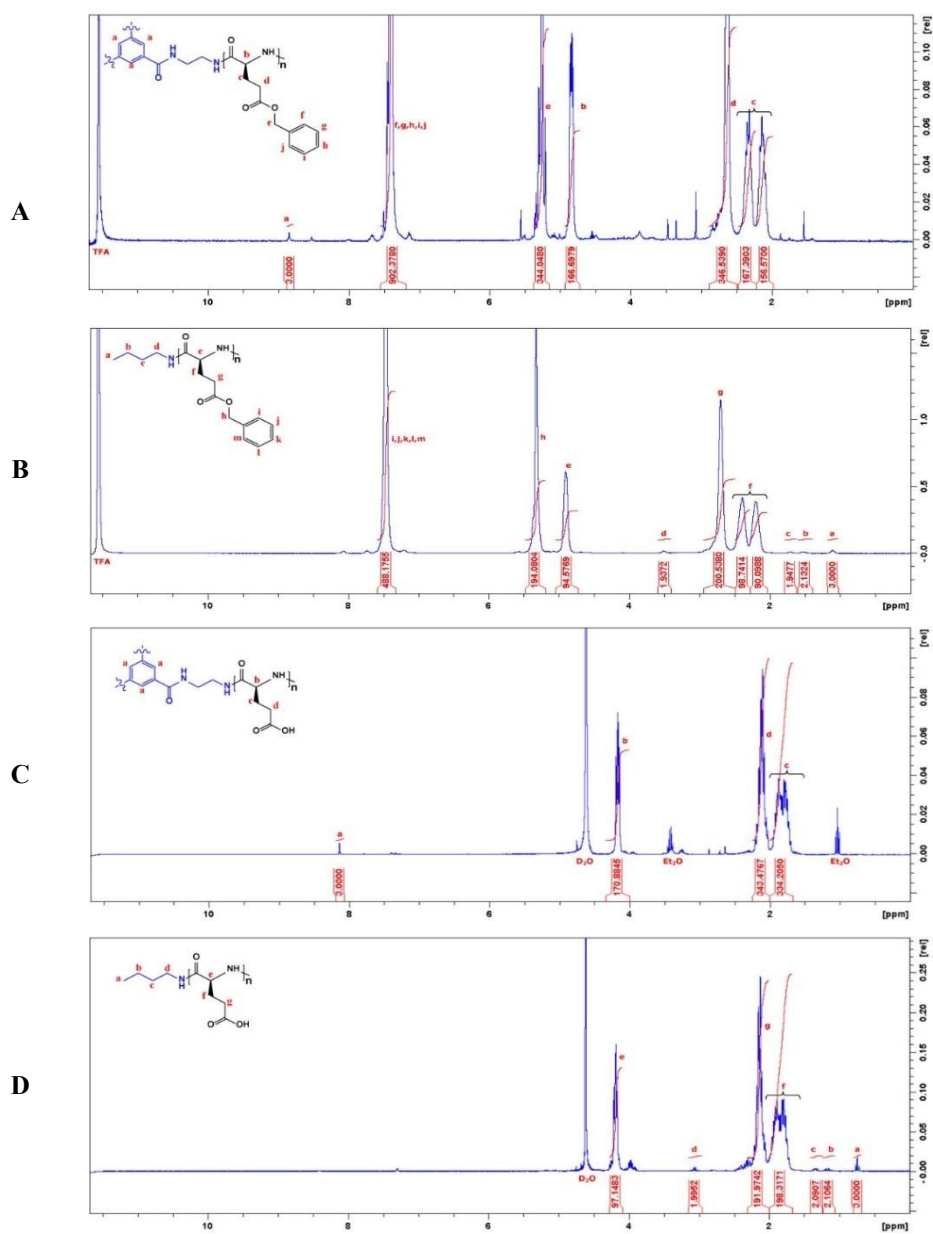
Figure 2.3. ^{1}H-NMR representative spectra of protected polymers: (**A**) StPGA-Bz and (**B**) PGA100-Bz, and deprotected polymers: (**C**) StPGA and LinPGA100 (**D**). Spectra for all synthesized carriers are shown in **Figure S2.4-2.9**.

We verified DP using NMR, where we correlated the peak integral at 8.9 ppm, which corresponds to three aromatic protons (3H) in the case of a star initiator (**Figure 2.3A**) or several peaks that correspond to aliphatic protons at 2.7ppm (2H), 1.7ppm (2H), 1.5ppm (2H), and 1.1ppm (3H) in the case of a linear initiator (Figure 3.3. B) to aliphatic protons at 4.9 ppm (1H), 2.7 ppm (2H), 2.35 ppm, and 2.15 ppm (2H, enantiotopic protons) of glutamic (**Figure 2.3 A and B**).

Table 2.1 summarizes the characteristics of synthesized polymers selected for further studies. We selected LinPGA100 and StPGA150, which maintain similar spatial carrier sizes and allow the study of the effect of conformation on physico-chemical and biological properties (. The DP of polymers agreed well with theoretical values, demonstrating the robustness and versatility of NCA-ROP in obtaining both LinPGA and StPGA with different chain lengths. GPC analysis demonstrated the monodisperse distribution of synthesized polymers (PDI 1.07).

Table 2.1. *Properties of PGA Carriers*

Polymer	Theoretical DP	Obtained DP[1]	Obtained DP[2a]	Obtained DP[2b]	Mn, kDa	PDI
LinPGA100	100	85	96	97	18.8	1.073
StPGA150	150	179	167	170	39.6	1.071

[1]Calculated from GPC, [2]Calculated from NMR ([a]protected, [b]deprotected form), DP – degree of polymerization, represented as glutamic units per chain, PDI – polydispersity index, defined as the ratio between weight (Mw) and number (Mn) average molecular weight, Mw/Mn.

We deprotected PGA carriers with a trifluoroacetic acid (TFA)/hydrobromic acid (HBr) mixture. SEC chromatograms demonstrated comparable results (**Figure 2.2B**) to the GPC analysis (**Figure 2.2A**) - monodisperse distribution with the anticipated elution order of peaks - thereby validating the deprotection protocol suitable for this type of material. We confirmed the complete deprotection of the benzyl group with NMR through the disappearance of protons at 7.5 ppm (5H) and 5.3 ppm (2H) (**Figure 2.3C and D**). The absence of unidentified peaks and the correct integral values provide robust evidence of polymer purity and integrity.

CD spectra obtained for LinPGA and StPGA carriers provided evidence of a random coil conformation in phosphate-buffered saline (PBS), as expected for these materials (**Figure 2.4**).
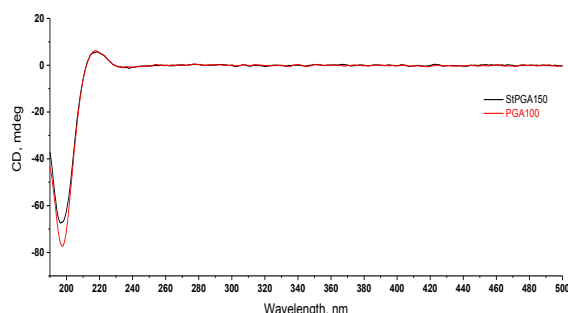
Figure 2.4. CD spectra of selected linear carriers - LinPGA100 (red) and StPGA (black) for further conjugation step and studies (0.2 mg/ml in PBS).

2.2.2. Establishing an Ex Vivo Model for the Study of Mucosal Permeation

Considering the aspects discussed in the introduction, we employed a vertical diffusion apparatus in which a membrane exposed to an air interface represents the in vivo environment to study intranasal delivery. The minimum sample volume for the vertical diffusion cell is 300 µl; horizontal diffusion cells require a minimum of a few mililiters[59].

We selected the Franz diffusion cell as it represents the only standardized and described pharmacopeia method and is commonly used for studies of intranasal formulations [56,57].

We selected excised ovine nasal mucosa as a membrane, as previously described permeability studies using molecules of comparable molecular weights demonstrated that sheep mucosa resembles human tissue better than nasal tissues from other animals [72,80]. Transepithelial electrical resistance – the lower the value, the more permeable or leaky the membrane – is often used to monitor the formation of confluent cell layers [82]; however, this measurement can also be used to compare mucosal tissues. Such studies demonstrated that values for ovine mucosa (100-120 Ω/cm) compared well to human mucosa (88 Ω/cm) but not to rabbit (40-70 Ω/cm) or bovine (42 Ω/cm) mucosa [61], with the latter two values indicating the higher tissue permeability and the risk of overestimation of permeation results. Gerber et al. reported that sheep nasal mucosa possessed a metabolism and transporter expression profile similar to human nasal mucosa [83]. We obtained nasal respiratory mucosal tissue samples from the veterinary school at CEU Cardenal Herrera University (Valencia, Spain) under the SANDACH normative and the biosecurity regulations of the University. **Figure 2.5 A-E** describes the steps to excise nasal tissue (**SI-2.2**) [83].
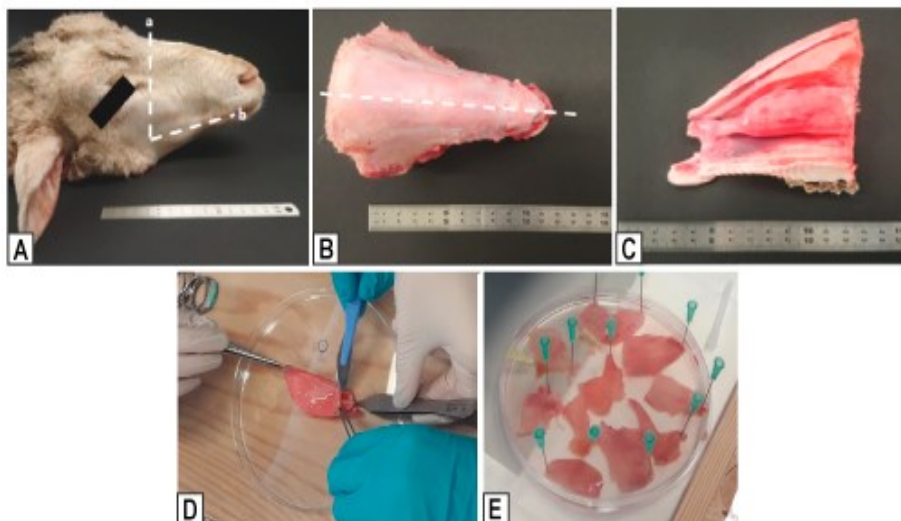
Figure 2.5. Images illustrating the excision of nasal mucosa samples from sheep. (**A**) Decapitation of the animal; (**B**) Longitudinal incision anterior to the eyes of the upper jaw and snout, followed by skin removal; (**C**) Bisection of the snout via vertical incision and removal of the septum, which is rinsed and submerged in ice-cold Dulbecco's (d)PBS buffer for transport; (**D**) Mucosal tissue removal from the septum with forceps and scalpel; and (**E**) Washing excised tissue in dPBS buffer for immediate use or storage at -80°C. Images A-C were adapted from Gerber et al. [83]. Images **D** and **E** represent the tissue samples used for our studies.

We started permeation studies immediately after mucosal excision; in the case of using samples previously stored at -80°C, we quickly thawed tissues at room temperature, washed tissues with PBS buffer (pH 6.4), and mounted tissues onto one half-cell of the Franz diffusion apparatus **(Figure 2.6)**. Of note, the orientation of the tissue so the mucosal side faces the donor chamber represents a crucial step. We fixed the temperature of the Franz cell at 37°C to mimic in vivo conditions as reported in similar studies [71–79].
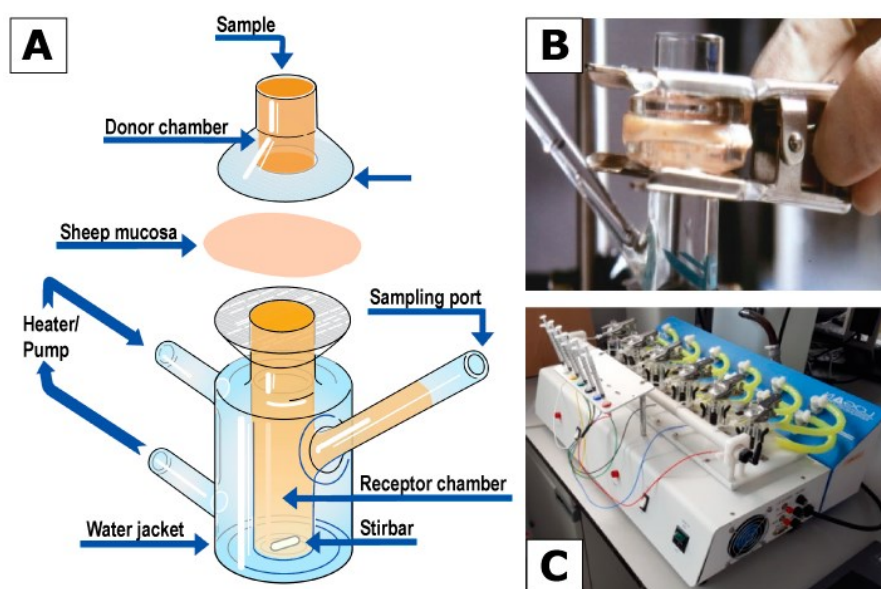
Figure 2.6. **Franz vertical diffusion cell**. (**A**) Image of the mounted sheep mucosa tissue between donor and receptor chambers. (**B**) Image of the vertical Franz diffusion cell. (**C**) This study used the Franz cell permeation system (Logan Instruments Corp., USA.).

We added Oregon Green (OG)-labeled polymeric formulations to the donor chamber of the Franz cell (adding isopropyl alcohol (iPrOH) as a negative control), then covered the cell with Parafilm™ and aluminum foil to protect it from the light. We then isolated samples from the receptor compartment at predetermined intervals up to 24 h and replaced them with an equal volume of PBS buffer (pH 6.4). We then filtered samples and spectrophotometrically measured absorbance at OG maximum λ=492 nm **(Figure 2.7A)**. The detector response displayed linearity in a wide concentration range (from 0.1 µg/ml to 10 µg/ml). For OG quantification, we used two segments of the calibration curve: low concentration range (0.1-0.9 µg/ml) and high concentration range (0.1-10 µg/ml) **(Figure 2.7B)**. The permeation results represent the mean cumulative values for diffused polymeric formulations at the sampling time.
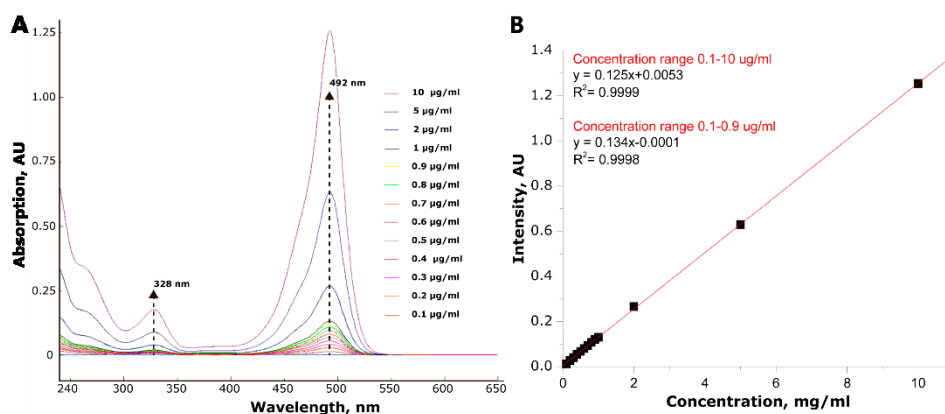
Figure 2.7 (A) UV-Vis spectra of Oregon green (OG) with two absorption maxima at λ=492 nm and λ=328 nm. (**B**) A calibration curve with linear fitting and R^2 value for a high concentration range (0.1-10 µg/ml) and low concentration range (0.1-0.9 µg/ml).

2.2.3. Ex vivo Permeation Studies of Linear and Star Polyglutamates

We initially evaluated two differing PGA architectures – LinPGA and StPGA. We labeled polymers with OG via amide coupling with an N,N′-diisopropylcarbodiimide (DIC) activator and hydroxybenzotriazole (HOBt) to suppress racemization (**SI-2.4**). **Table 2.2** describes the physicochemical characteristics of OG-modified LinPGA and StPGA (LinPGA-OG and StPGA-OG). NMR determined the DP, which agreed with the targeted value. The size of LinPGA and StPGA lay between 10-13 nm, indicating the absence of aggregates in the solution.

Polymer	Parameters	DP*	OG loading (% wt)	Size[a], (D_h, nm)	Size[b], (D_h, nm)
Table 2.2 Physico-chemical characteristics of LinPGA-OG and StPGA-OG					
	Technique	NMR	Fluor	DLS	DLS
LinPGA-OG		97	2.1	9.5±3.7	10.9±2.3
StPGA-OG		170	2.4	10.65±3.5	13.0±0.9

*DP – degree of polymerization, represented as glutamic units per chain, DLS measurements in 1 mg/ml PBS, [b] DLS measurements in 0.1 mg/ml PBS

We next evaluated possible changes in the spatial conformation of LinPGA-OG and StPGA-OG, which may interfere with interactions with biological interfaces [81,84] via circular dichroism (CD) spectroscopy. The ability of peptide bonds to absorb light at 220 nm (n → π transition) and 190 nm (π→ π* transition) allowed us to evaluate the secondary structure of polypeptide [85]. **Figure 2.8** shows the CD spectra of OG labeled LinPGA and StPGA; CD profiles of LinPGA-OG and StPGA-OG are similar to unlabeled polymers, indicating random coil conformation and a lack of structural alterations after dye modification.
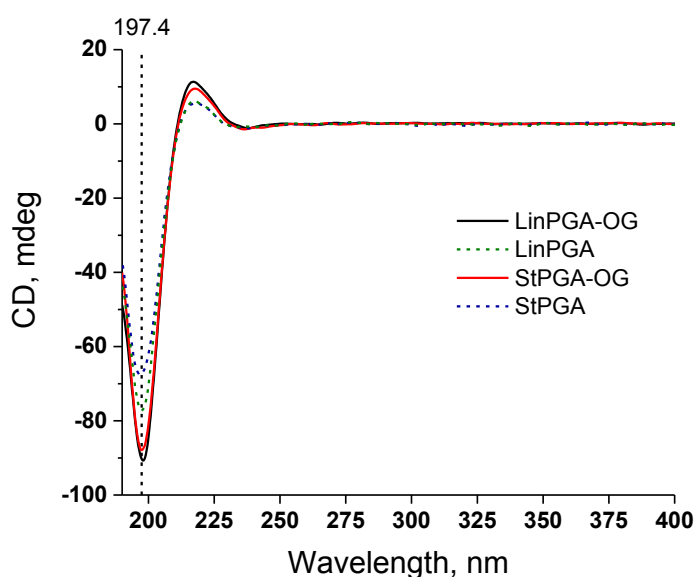
Figure 2.8. CD spectra of LinPGA-OG and StPGA-OG at 0.1 mg/ml in MilliQ water. The average results of three accumulated measurements are displayed.

Figure 2.9. reports the permeation profile of StPGA-OG, LinPGA100-OG, and iPrOH as a negative control. The results suggest that StPGA permeates faster through mucosal tissue than linear analogs; however, both reach the same accumulation value after 24 h. These findings may derive from the more compact globular conformation for the StPGA compared to the linear counterpart demonstrated in **Chapter 3** and agree with data reporting that branched and dendrimeric carriers can rapidly bypass biological barriers [86,87]. The low signal of iPrOH (<1.5%) provides evidence for the absence of interference from compounds extracted from mucosa tissue. We found the spectrophotometric method suitable for permeation kinetic studies in Franz diffusion cells using sheep nasal mucosa.
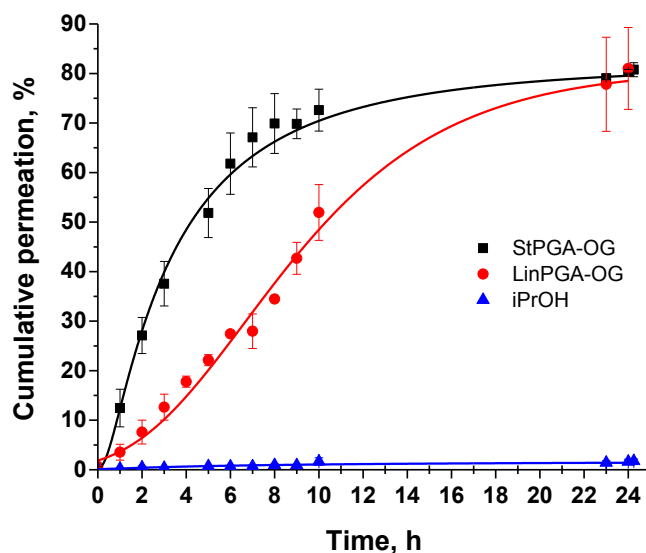
Figure 2.9. Ex vivo permeation study of StPGA-OG, LinPGA-OG, and iPrOH (negative control) in Franz diffusion cells using sheep nasal mucosa. The average results of three experiments are displayed, and the error bars are reported as the standard error of the mean.

We next analyzed LinPGA-OG and StPGA-OG by NMR to confirm stability and ensure that we do not detect OG cleaved by the enzymatic activities of mucosa tissue. We freeze-dried 2 ml aliquots collected at 6 h (the maximum permeation point) and dissolved them in D_2O for NMR analysis **(Figure 2.10.)**. We observed peaks at 4.2, 2.1, and 1.8 ppm that correspond to the aliphatic protons of PGA in the NMR spectra for both StPGA-OG and LinPGA-OG; however, we observed a lower signal intensity for the linear carrier, which agrees with the results of the ex vivo permeation study **(Figure 2.9.)**. We also noted the presence of small intensity peaks at 7.4.-6.7 ppm that can be assigned to the aromatic protons of OG.
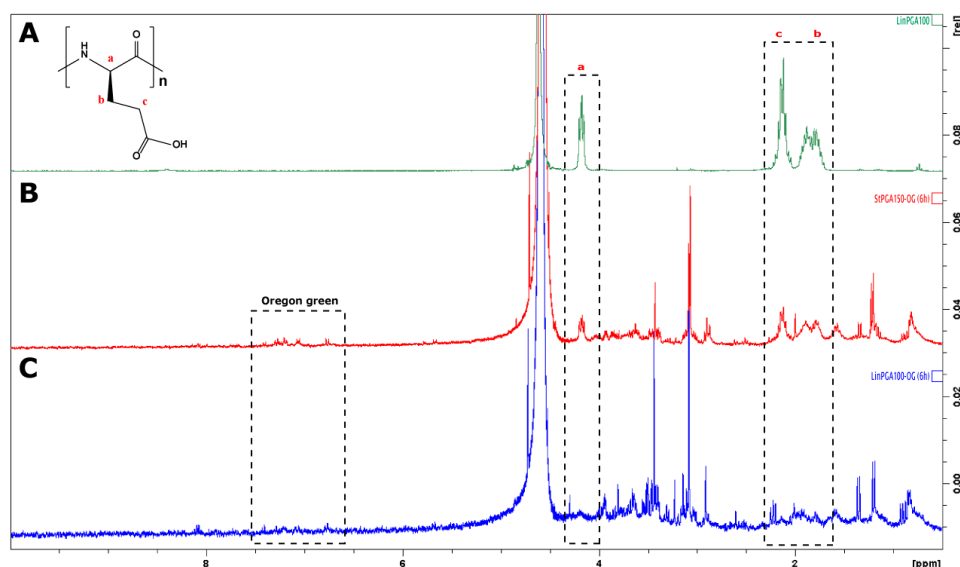
Figure 2.10. Overlaid ^1H *NMR (300 MHz, DO)* spectra for (**A**) LinPGA100, (**B**) StPGA-OG, and (**C**) LinPGA-OG at the 6 h timepoint from the permeation study.

Overall, we established an ex-vivo model based on Franz diffusion cell and sheep mucosa and demonstrated that both StPGA and LinPGA could cross mucosal tissue, although StPGA possesses a more rapid permeation profile; therefore, we developed our intranasal platform based on StPGA.

2.2.4. Functionalization of StPGA with Lectin Binding Peptide

Lectins or agglutinins are a family of specific and reversible carbohydrate-binding proteins that bind to glycosyl ligands and can agglutinate erythrocytes or other cells [88]. Wheat-germ agglutinin conjugated to horseradish peroxidase (WGA-HRP) represented the first lectin employed for targeted intranasal brain delivery [89]. The beneficial 700-fold increase of lectin-modified HRP compared to an unmodified analog after intranasal administration into Sprague-Dawley rats (providing a final concentration in the brain of 140 nM, sufficient for a therapeutic effect [90]) raised interest in lectins/agglutinins as possible targeting moieties for brain delivery.

As natural lectins' high molecular weight (Mw) can result in immunogenicity and diminish mucosal penetration abilities, many groups have attempted to find smaller peptide analogs that mimic lectin. Lü et al. reported a lectin-like peptide with 32 amino acid residues and three disulfide bridges (*Selenocosmia huwena* lectin-I) from the venom of the Chinese bird spider [91]. Meanwhile, Wei Wang et al. purified θ-defensin, another

lectin-like peptide comprising 18 residues with three disulfide bridges, from the leukocytes and bone marrow of the rhesus macaque (*Macaca mulatta*) [92]. Unfortunately, the complex network of disulfide bridges required for structure integrity for these peptides hampered their application as targeting moieties for drug delivery involving conjugation and harsh chemical conditions. Li et al. reported a smaller 17 amino acid peptide with one disulfide bridge - odorranalectin – isolated from skin secretions from the *Odorrana graham* frog, which possessed low toxicity and immunogenicity in mice [44]. Two related studies reported that odorranalectin-conjugated poly (ethylene glycol)-poly (lactic-co-glycolic acid) (PEG-PGLA) nanoparticles improved brain delivery two-fold when compared to non-targeted nanoparticles followed by intranasal administration [93,94]. Similarly, Wu et al. demonstrated an increased relative uptake of Odorranalectin-modified cubosomes (from 1.7 to 3.5-fold) into brain tissues compared to an unmodified carrier [95]. Yang et al. reported the conjugation of a 33 kDa lectin peptide from *Aleuria aurantia* (which specifically binds to the L-fucose located in the olfactory epithelium) and a KLVFF peptide (for β-amyloid targeting) to PEGylated dendrigraft poly-l-lysines as an intranasal brain delivery strategy [96]. The authors employed this conjugate to encapsulate rapamycin and complexated small interfering (si)RNA (against Beta-secretase 1, BACE1); moreover, they verified that this strategy improved cognitive function in a mouse model of Alzheimer's disease. PEG-PGLA nanoparticles loaded with coumarin-6 (a dye) [97] or haloperidol [98] also displayed improved brain delivery upon intranasal administration (2.5 fold and 3.0 fold increase, respectively) following the conjugation of the nanoparticles with a *Solanum tuberosum* lectin (50 kDa) peptide. Gao et al. used *Ulex europeus* agglutinin I (63 kDa) to modify PEG-PLGA nanoparticles, which had a 1.7-fold increased ability to accumulate in brain tissues compared to unmodified nanoparticles [99].

We selected odorranalectin to improve the intranasal delivery of our therapeutic platform due to its smaller size (17 amino acids) and the presence of only one disulfide bridge, which supports various chemical steps without degradation. Moreover, odorranalectin specifically binds to the L-fucose [44] broadly present on the olfactory epithelium of nasal mucosa [100], which will decrease systemic absorption from the respiratory mucosa [44,94,95]. As the N-terminal amino acid is an aromatic tyrosine (Tyr) moiety, we added an extra amino acid - glycine (Gly) - to facilitate the conjugation of odorranalectin to StPGA (**Figure 2.11**). Both the disulfide bridge and the carbohydrate-binding site for L-fucose [44] (composed of the [5]lysine (Lys), [6]cysteine (Cys), [7]phenylalanine (Phe), [16]Cys, and [17]threonine (Thr) residues) must be preserved.

H₂N-Gly-Tyr-Ala-Ser-Pro-Lys-Cys-Phe-Arg-Tyr-Pro-Asn-Gly-Val-Leu-Ala-Cys-Thr-COOH

binding site to L-fucose
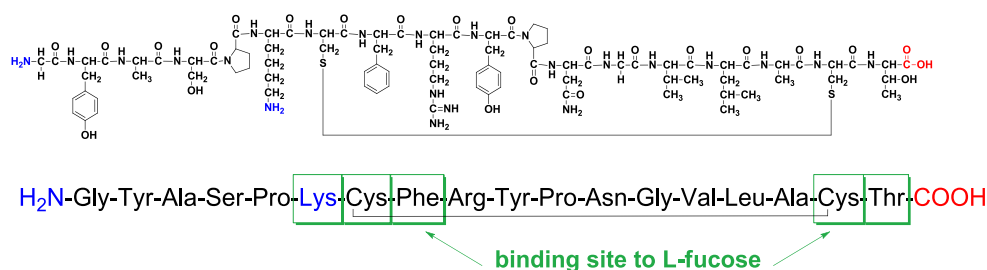
Figure 2.11. The structure of odorranalectin with reactive amino groups (-NH$_2$) is highlighted in blue, the carboxylic group (-COOH) is highlighted in red, and amino acids comprising the binding site for L-fucose are highlighted in green.

We developed two synthetic routes to conjugate odorranalectin to StPGA. The first strategy involved direct conjugation via the amide bond through the peptide N-terminal site to StPGA using a 4-(4,6-dimethoxy-1,3,5-triazin-2-yl) activator (DMTMM) **(Figure 2.12).** The odorranalectin sequence includes an extra amine group in the internal ^{5}Lys, which might lead to side reactions; however, byproduct formation should be partially hindered by the proximity of the disulfide bridge. Odorranalectin conjugation using this strategy supported a 3.8 %mol loading (StPGA-Odorranalectin), as determined by amino acid analysis (**SI-2.5.1**).
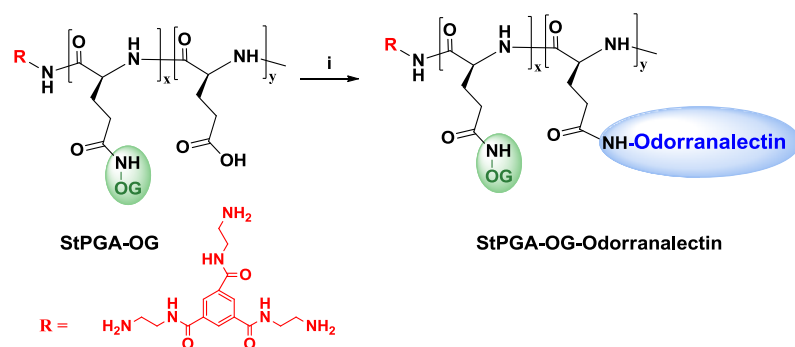
Figure 2.12. Synthesis of StPGA-Odorranalectin via direct coupling: i) DMTMM Cl, MilliQ water, room temperature, 48 h **(SI-2.5.1)**.

The second strategy represents a more controlled conjugation involving protecting groups. Wen et al. previously described the selective conjugation of Odorranalectin to PEG-PLGA nanoparticles [94] by first breaking the disulfide bridge, protecting Cys residues with acetamidomethyl (Acm) groups, and then adding an unprotected Cys amino acid to the N-terminal chain of a peptide for polymer conjugation via a thiol-

maleimide reaction. Unfortunately, the Acm group deprotection conditions (iodine oxidation in acetic acid solution (pH 4.0)) prompt StPGA precipitation. Recently, Kobayashi et al. reported a one-pot/stepwise procedure for aqueous Acm group deprotection using $CuSO_4$ and 1,2-aminothiol at pH 7.0 under aerobic conditions to offer better control during the formation of intramolecular disulfide bridges [101], which could prove suitable for StPGA. We applied a similar approach without breaking the disulfide bridge and using the C-terminal carboxylic acid group. First, we protected two reactive amines of Odorranalectin (N-terminal and [5]Lys) with tert-butyloxycarbonyl (Boc) groups [102] and then conjugated the modified peptide to StPGA previously modified with a monoprotected-diamine (diaminoethane) via C-terminal carboxylic acid (deprotected in concentrated trifluoroacetic acid) (**Figure 2.13**).
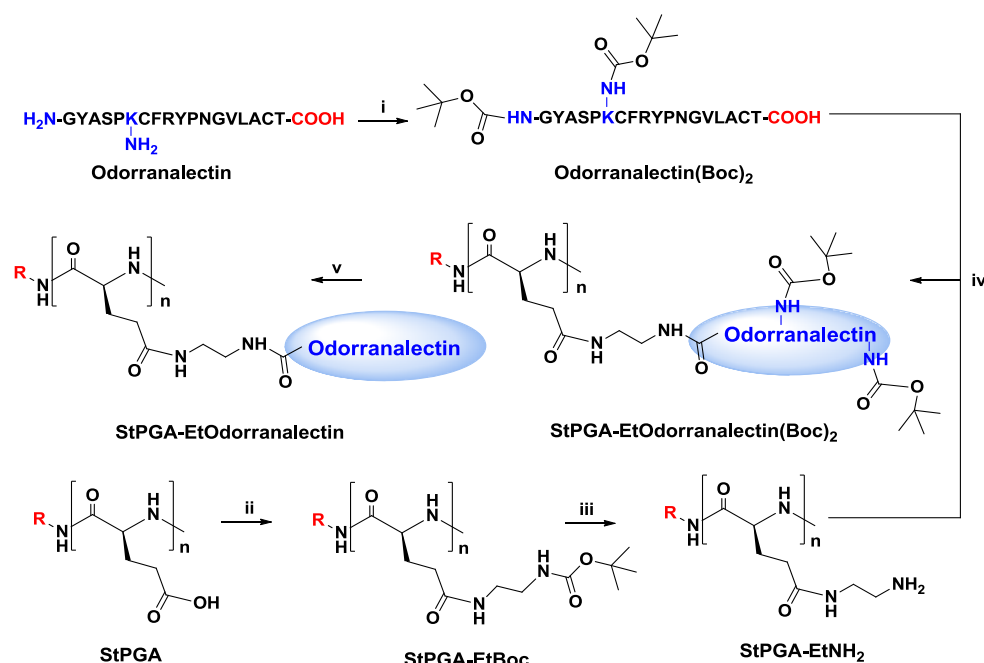
Figure 2.13. Synthesis of StPGA-EtOdorranalectin via C-terminal site: i) Boc$_2$O, THF: H$_2$O (1:1), room temperature, 24 h; ii) N-Boc-1.2-diaminoethane, DMF$_{anh}$, DMTMM BF$_4$, room temperature, 72 h iii) TFA$_{conc}$, room temperature, 2 h; iv) MeOH:H$_2$O (1:1), DMTMM Cl; 72 h; v) TFA$_{conc}$, room temperature, 2 h (**SI-2.5.2**).

To prove the proper protection of amino groups with Boc, we compared ^{1}H NMR spectra of Odorranalectin and Odorranalectin (Boc)$_2$ (**Figure 2.14, Figure S2.21-2.22**). The appearance of a new peak at 1.36 ppm corresponds to the Boc group. In that aliphatic

region, the Boc group overlies with 10 H (from Odorranalectin); therefore, by simple subtraction of these protons from 28 H (obtained at 1.36 ppm for Odorranalectin (Boc)$_2$), we obtained the 18 H corresponding to two Boc groups. Overall, this indicates the robust nature of the protection protocol. The protons in the aromatic region from [2]Tyr, [8]Phe, and [10]Tyr give 13H in total for Odorranalectin (Boc)$_2$, which has a similar chemical shift (7.2-6.7 ppm) as for unprotected Odorranalectin. Well-separated protons from the hydroxyl group of [2]Tyr and [10]Tyr give 2 H in total and have a similar chemical shift (5.6 ppm). The integrals for 6 H from [14]Val and 6 H from [15]Leu are also correct, and the position at 0.9 ppm and 0.8 ppm is similar for unprotected Odorranalectin. The position of the peaks varies slightly due to the different solvents used to record NMR spectra given the different solubility of the compounds: MeOH for Odorranalectin and MeOH:D$_2$O (1:9) for Odorranalectin (Boc)$_2$. Therefore, integrating protons in the crowded aliphatic region remains challenging; however, a well-separated peak at 5.6 ppm corresponding to 2 H characterizes protected and unprotected Odorranalectin. Due to the solvent, we did not detect the exchangeable amide protons (9.1 ppm – 8.3 ppm) for Odorranalectin (Boc)$_2$.

Overall, the NMR results confirmed the successful protection of two amines (terminal and [6]Lys) of Odorranalectin with Boc groups.
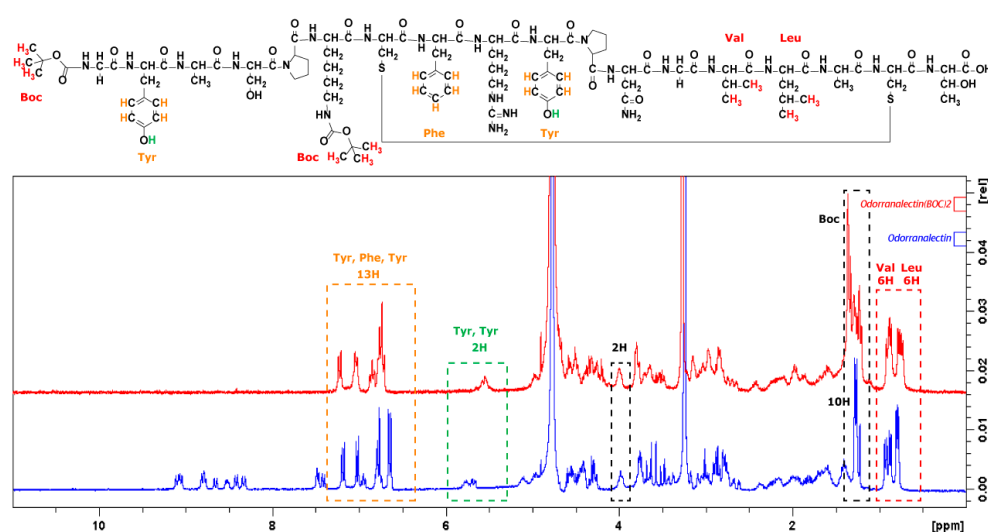
Figure 2.14. Overlaid spectra *^{1}H NMR (300 MHz)* of Odorranalectin (blue) in MeOD and Odorranalectin (Boc)$_2$ (red) in MeOD: D$_2$O (1:9).

SI-2.5.2 describes the intermediate steps for the generation of StPGA-Odorranalectin. **Figure 2.15**. shows the NMR spectra of the final compound. The presence of characteristic protons from [2]Tyr, [8]Phe, and [10]Tyr in the aromatic region and

[14]Val and [15]Leu in the aliphatic region and their broadening indicates the successful conjugation of odorranalectin to StPGA with characteristic peaks at 4.2 ppm, 2.1 ppm, 1.8ppm. The peak at 1.3 ppm from the Boc group disappears for the final compound, confirming the full deprotection. Moreover, the average integral of protons from the Boc group of 18 indicates the stability of the Boc group during conjugation **(SI-2.2.25).** Moreover, we found a similar ratio between the protons from monomeric glutamic units to the protons from the initiator as the starting material, around 150, indicating polymer chain stability during modification. The integrals for 6 H from [14]Val and 6 H from [15]Leu are also correct, and the positions at 0.9 ppm and 0.8 ppm are similar to unconjugated peptides. The correct value of the proton integrals suggests that the modification procedure does not induce the degradation of Odorranalectin. We observed a calculated Odorranalectin modification level of StPGA of 0.9 %mol as determined by amino acid analysis **(SI-2.5.2.4).**
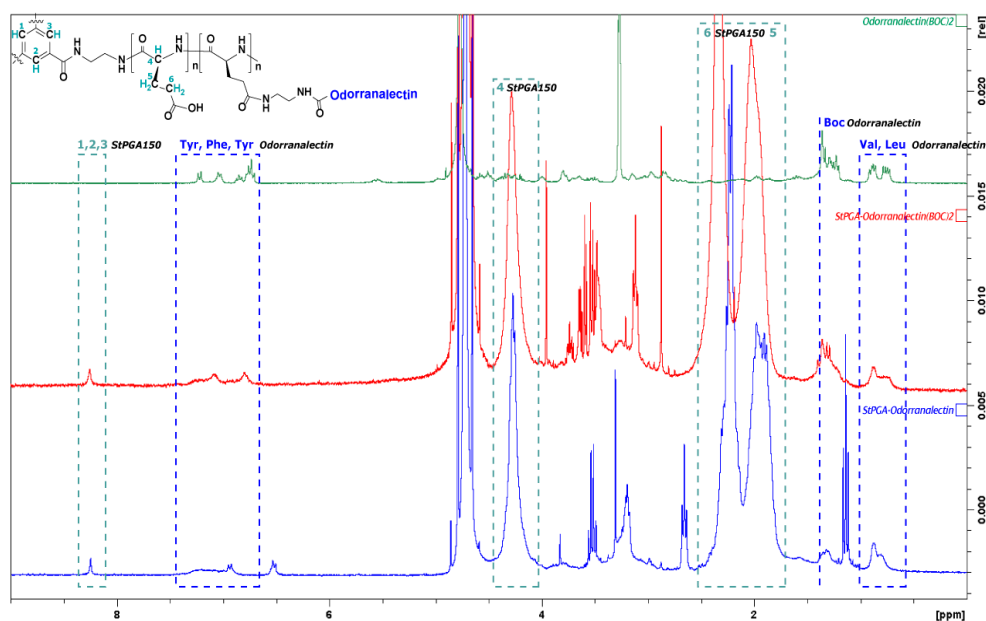
Figure 2.15. Overlaid *^{1}H NMR (300 MHz)* spectra of Odorranalectin (Boc)$_2$ (green), StPGA-Odorranalectin (Boc)$_2$ (red), and StPGA-Odorranalectin (blue).

We next prepared an OG-labeled version of StPGA-Odorranalectin (StPGA-OG-OL) following the standard procedure described in **SI-2.4. Table 2.3** reports the physicochemical characteristics of StPGA-OG-OL prepared via C-terminal and N-terminal peptide modification.

Table 2.3 Physico-chemical characteristics of StPGA-OG-OL (N- or C-terminal modification)						
Polymer	Parameters	DP	OG loading (% wt)	OL loading (% mol)	Size[b], (D_h, nm)	Size[c], (D_h, nm)
	Technique	NMR	Fluor	AA[a] / NMR	DLS	DLS
StPGA-OG-OL (N-terminal)		170	6.2	3.8 / 3.4	9.1±1.4	9.3±1.2
StPGA-OG-OL (C-terminal)		170	1.2	n/a / 0.9	12.4±1.5	9.7±0.8

DP – degree of polymerization, represented as glutamic units per chain, [a] Amino acid analysis, [b] DLS measurements in 1 mg/ml PBS, [c] DLS measurements in 0.1 mg/ml PBS.

Figure 2.16 shows the CD spectra of the two forms of StPGA-OG-OL, which display overall similarity to StPGA **(Figure 3.4.)** - predominant random coil conformation and a lack of structural differences after OL conjugation and OG modification.
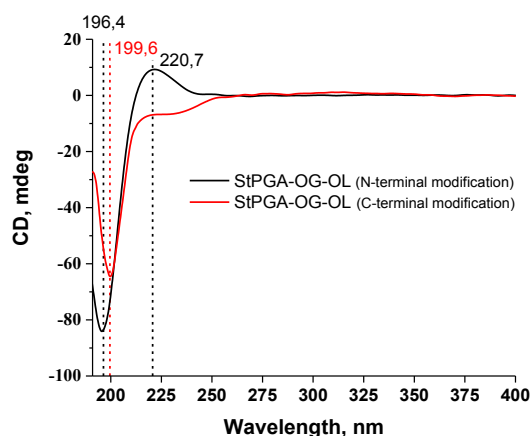
Figure 2.16. CD spectra of StPGA-OG-OL N-terminal modification (black) and C-terminal modification (red) at 0.1 mg/ml in MilliQ water. Average results with three accumulated measurements are displayed.

Of note, we observed a small fraction of an organized structure for StPGA-OG-OL (C-terminal modification) (**Figure 2.16**) – a shift of the minimum of the main peak and disappearance of the peak at 220.7 nm, which may derive from the cumulative effect of the random coil from StPGA and the secondary structure of OL[44]. OL attaches via one covalent bond and may maintain a natural conformation.

In the case of N-terminal modification, a side reaction with internal [5]Lys may distort the organized peptide structure to leave only random coils.

Figure 2.17. shows the permeation profile of StPGA-OG-OL with the N- and C-terminal modification compared to StPGA-OG. The more rapid permeation of C-terminal-derivatized StPGA-OG-OL compared to StPGA-OG agrees well with the reported results in the literature [93–95] and can be explained by reversible binding to the L-fucose site, which is broadly present on nasal epithelium [100]. The lower permeation rate of N-terminal-derivatized StPGA-OG-OL may relate to random peptide modification and the following deterioration of conformation and activity. Furthermore, random OL modifications could lead to a partially crosslinked structure, thus restricting mucosal passage; however, we did not observe any significant differences in hydrodynamic size **(Table 2.3)**. Moreover, the linear permeation profile OL via N-terminal modification **(Figure 2.17)** is more characteristic of gel permeation, as reported [76].
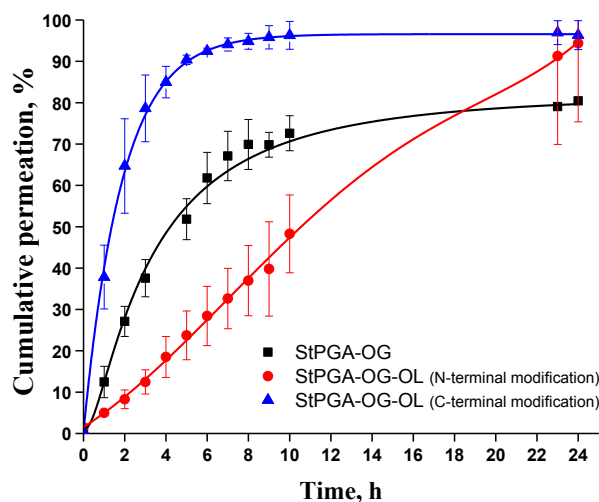
Figure 2.17. Ex vivo permeation profiles of StPGA-OG with N-terminal (red) and C-terminal (blue) modification compared to StPGA-OG (black). The average results of triplicates are displayed, and the error bars are reported as the standard error of the mean.

Overall, C-terminal-derivatized StPGA-OG-OL displayed more rapid permeation than unmodified StPGA-OG or N-terminal-derivatized StPGA-OG-OL; therefore, this modified polymer represents an optimal candidate for further development of the intranasal platform.

2.2.5. Functionalization of StPGA with Hyaluronic acid

Hyaluronic acid (HA) is a naturally occurring biocompatible, biodegradable, and non-immunogenic linear glycosaminoglycan widely used in drug delivery [103]. HA provides a hydrophilic "corona" to nanoparticles [104] and aids endocytosis by targeting the CD44 receptor, which is overexpressed in various tumor cells [105,106]. All these characteristics make HA an interesting tool for cancer-targeted drug delivery.

Nasal mucosa comprises 95% water and around 3% mucins, with electrolytes, proteins, lipids, enzymes, and antibodies making up the last 2% [107]. Mucins are negatively charged glycoproteins; therefore, excipients with positive charges, such as chitosan, represent a common choice for intranasal delivery approaches displaying high mucoadhesion [80]. Interestingly, while possessing a negative charge due to the abundance of carboxylic groups, HA possesses robust adhesion properties thanks to forming hydrogen bonds with biological substrates [47]. Comparisons of mucoadhesion properties using tensile-stress testing of HAs of three different molecular weights (202 kDa, 693 kDa, and 1.9 MDa) in porcine buccal mucosa and bovine submaxillary mucin dispersion demonstrated that mucoadhesive potential increased upon a decrease in molecular weight (202 kDa HA compared well with chitosan hydrochloride – the reference polymer) [48]. Interestingly, a similar evaluation performed in the vaginal environment (porcine vaginal mucosa and gastric mucin dispersion) demonstrated that 202 kDa HA displayed significantly greater mucoadhesion than those observed for chitosan hydrochloride, which authors linked to the slightly acid or close to neutral pH of the evaluated biological tissues [48]. The nasal cavity is also slightly acidic, with an average pH of 6.4 (in the anterior region) and 6.3 (in the posterior region) [108], which can benefit from increased HA mucoadhesion. Moreover, two additional studies have demonstrated enhanced drug adsorption after intranasal administration of formulations using HA [49,50].

To study the ability of HA to increase permeation of StPGA-based formulations, we attempted to link two HA moieties of different molecular weights (10 or 80 kDA) via ester bond formation using two coupling agents - N-hydroxysuccinimide (NHS)/ 1-ethyl-3-(3-dimethyl aminopropyl)carbodiimide (EDC) to form StPGA-HAs (**Figure 2.18**).
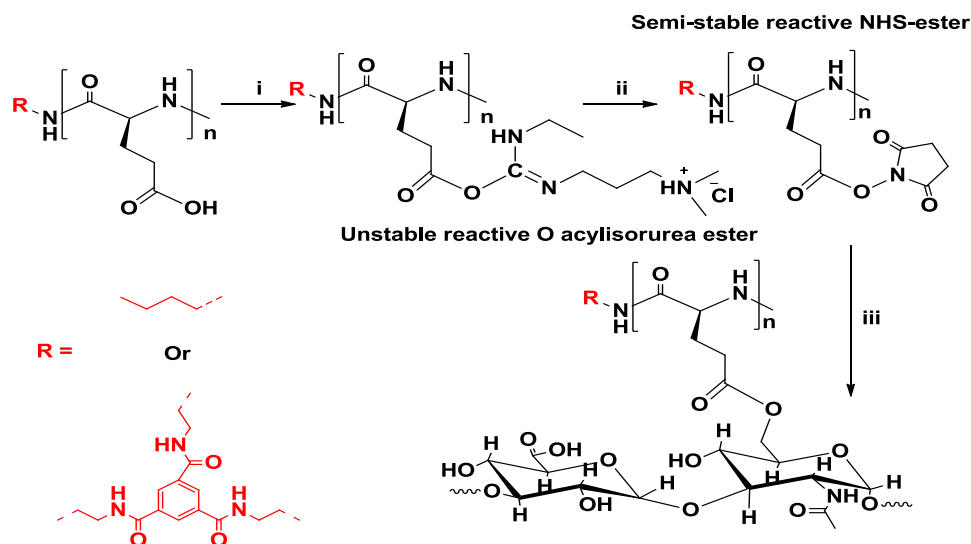
Figure 2.18. Synthesis of StPGA-HAs: i) NHS, EDC, ddH$_2$O pH 6.0, room temperature, 2 h; ii) HA 10 kDa or 80 kDA, room temperature, 48 h (**SI-2.6.1**).

To optimize the purification of the StPGA-HA derivatives, we evaluated Vivaspin® systems with differing molecular weight cut-off values (MWCO): 10 KDa, 30 kDa, 50 kDa, and 100 kDa. First, we weighed 10 kDa or 80 kDa HA and StPGA, dissolved them in MilliQ water and purified them with 30 ml MilliQ water through VivaSpin®. We collected, freeze-dried, and weighed the fractions; Table 2.4 shows the results.

Table 2.4 *Verification of Vivaspin® purification with different MWCO for HA*

VivaSpin MWCO	Sample	m, mg	VivaSpin® residue (Upper chamber), mg/%	VivaSpin® residue (Bottom chamber), mg/%	VivaSpin® residue (absorbed on the membrane), mg/%
10 kDa	HA 10 kDa	30.3	15 /49.5	12/39.6	3.3/10.9
30 kDa	HA 10 kDa	30.0	1/3	28/93.3	1/3.3
50 kDa	HA 10 kDa	30.3	< 0.1 /<0.3	30,5/100	0/0
100 kDa	HA 80 kDa	31.0	< 0.1 /<0.3	32/100	0/0
30 kDa	StPGA*	20.7	7 /17.5	33/82.5	0/0
100 kDa	StPGA*	21.0	0 /0	41/100	0/0

- H-form, molecular weight ~ 20kDa. Solubilizing the StPGA H-form in water required a minimum amount of 2.5 M NaOH; the recalculated solid is around 41 mg of StPGA sodium salt.

As shown in **Table 2.4**, a VivaSpin® with 30 kDa MWCO, which filters out 83% of StPGA and 93% of HA10kDa, allows for the optimal purification of StPGA-HA10kDa. A VivaSpin® with 100 kDa MWCO, which filters out all StPGA and HA80kDa, is optimal for StPGA-HA80kDa (the product should stay in the upper chamber of the VivaSpin® system if at least one molecule of StPGA is attached to HA80kDa). After optimizing purification, we weighed and purified the obtained products using a VivaSpin® MWCO 30kDa (for systems with HA10kDa) and 100 kDa (for systems with HA80kDa). **Table 2.5** shows the obtained results. The bottom chamber of the VivaSpin® system (after sample purification and freeze-drying for all reactions) yielded a jelly product, which can be explained by the filtering of the low fraction of HA and its crosslinking with residual ECD/NHS reagents.

Table 2.5 *Purification of HA-PGA systems with Vivaspin®*

Sample	Targeted mod., %mol	Obtained[a] mod., %mol	VivaSpin® residue (Upper chamber), mg	VivaSpin® residue (Bottom chamber), mg	Yield, %	Reaction efficiency, %
LinPGA100-HA80kDa	5	2.5	14	83 (gelation)	25	49
StPGA-HA10 kDa	5	3.8	30	48 (gelation)	45	76
StPGA-HA10 kDa	10	6.3	39	43 (gelation)	59	63
StPGA-HA80kDa	5	3.0	17	94 (gelation)	23	60
StPGA-HA80kDa	10	5.5	23	95 (gelation)	31	55

[a] calculated by NMR

The NMR spectra of the synthesized PGA-HA derivatives created via direct ester bonding (**Figure 2.19, Figure S2.28- Figure SI 2.32**) demonstrated the presence of EDC residue, which was removed by VivaSpin® purification due to the strong ionic interactions with the carboxylic groups of PGA and HA.
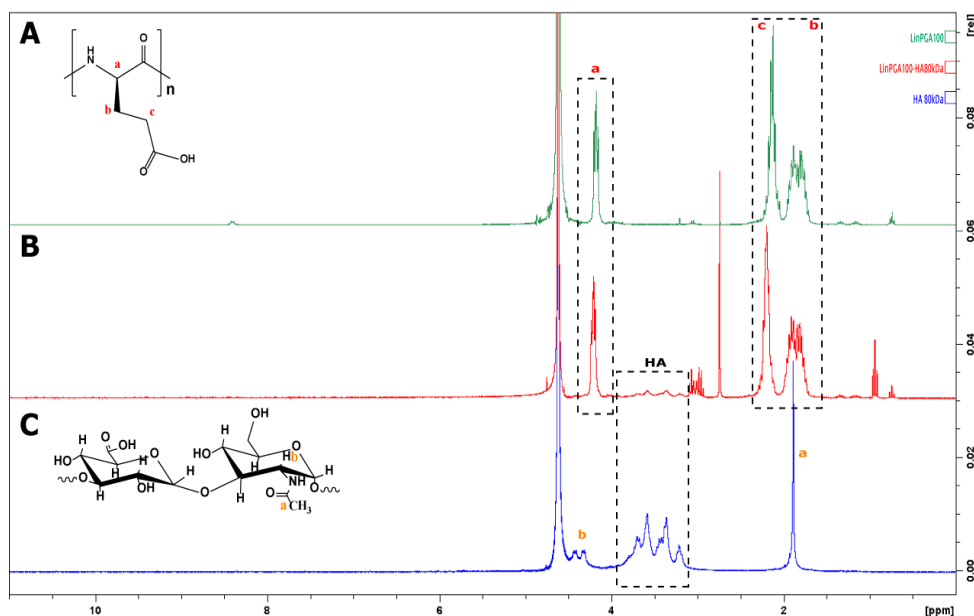
Figure 2.19. Representative ¹H-NMR spectra of (**A**) LinPGA100 (**B**), LinPGA100-HA80kDa, and (**C**) HA 80kDa. Spectra for all synthesized HA carriers are shown in **Figure S2.28**- **Figure SI 2.32**.

Significantly, the induced toxicity from residual EDC can compromise safety profiles. Acid/base precipitation of the systems may help further purification; however, this approach can induce HA degradation given its known sensitivity to pH values less than 4 and greater than 11. Moreover, due to the observed low reaction yield and low reaction efficiency **(Table 2.5),** we considered an alternative modification strategy, such as amide coupling with the DMTMM activator (**Figure 2.20**).
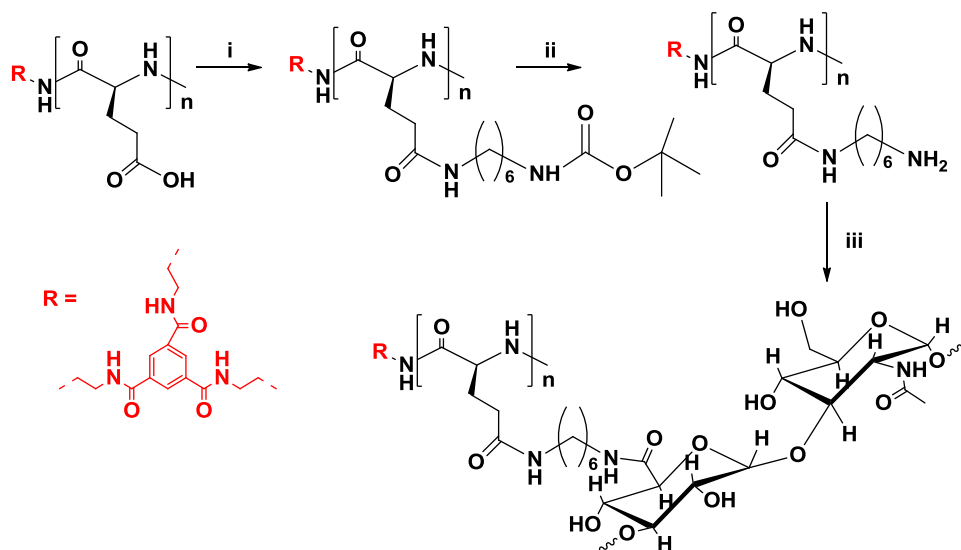
Figure 2.20. Synthesis of StPGA-HA80kDa. i) N-Boc-1.6-hexanediamine HCl, DMF$_{anh}$, DMTMM BF$_4$, DIEA; ii) TFA$_{conc,}$ room temperature, 2 h; iii) HA80kDa, HEPES 10mM, DMTMM Cl, room temperature, 24 h. **(SI-2.5.2)**

SI-2.6.2 describes the intermediate steps of StPGA-HA80kDa synthesis while **SI-2.6.2.2** describes the calculations used for the obtained StPGA:HA80kDa ratio of 2:1. **Figure 2.21.** shows NMR spectra of the final compound, with peaks from StPGA (8.2, 4.2, 2.2, 1.8 ppm) and HA (4.4, 3.9-3.1, 1.8 ppm), the absence of unidentified peaks, and the correct integral values provide robust evidence of polymer purity and integrity.
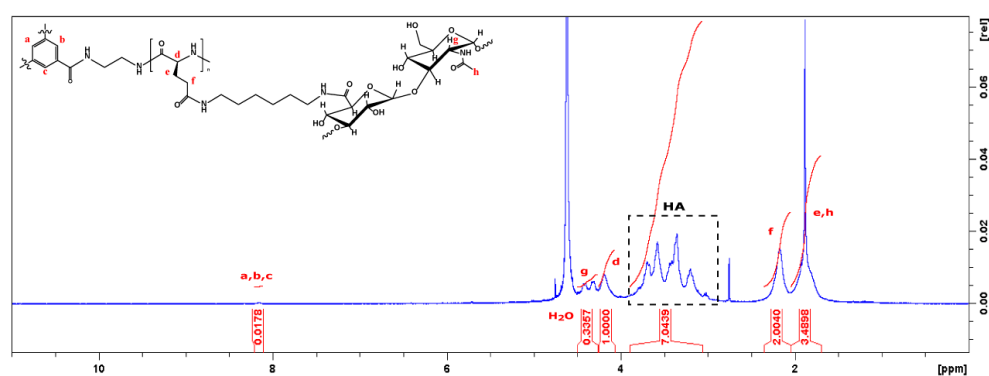
Figure 2.21. ^{1}H-NMR spectra (300 MHz, D$_2$O) of StPGA-HA80kDa (amide coupling)

To ensure covalent linkage between StPGA and HA in StPGA-HA80kDa (amide coupling), we performed 2D NMR diffusion-ordered spectroscopy (DOSY) with NMR data processed with Mestrenova using the Bayesian method **(Figure 2.22)**. The spots from HA and StPGA protons have the same diffusion coefficient and are horizontally aligned, indicating the presence of a single molecule and not a physical mixture.
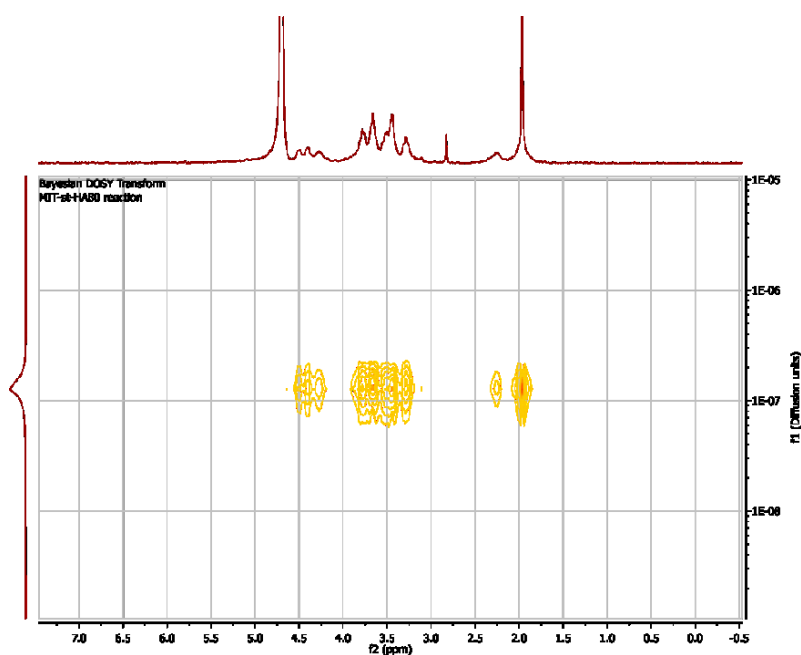
Figure 2.22. DOSY experiment (300 MHz, D$_2$O) of StPGA-HA80kDa (amide coupling)

Size exclusion chromatography (SEC) studies displayed a single homogeneous molecular weight distribution for StPGA-HA80kDa **(Figure 2.23 A and B)**.
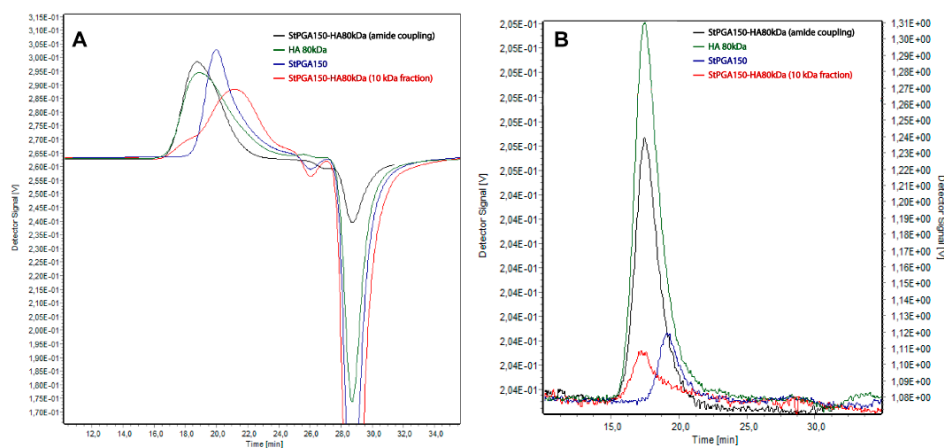
Figure 2.23. SEC chromatograms: overlayed (**A**) RI detector and (**B**) MALS detector for StPGA-HA80kDa (black), HA80kDa (green), StPGA (blue), and StPGA-HA80kDa after Vivaspin® purification (bottom fraction).

We observed the expected elution peak order, with StPGA-HA80kDa displaying a slightly shifted peak toward higher molecular weight (**Figure 2.23 A and B**). The absence of separation with unmodified HA80kDa may be explained by slight differences in molecular weight, where the expected molecular weight of StPGA-HA80kDa is 120 kDa when considering the conjugation ratio (2:1) calculated from NMR spectra **SI-2.6.2.2**. The analysis of the StPGA-HA80kDa sample fraction after Vivaspin® purification (StPGA-HA80kDa [10 kDa fraction]) contains low molecular weight compounds, which indicates a more extended retention time **Figure 2.23 (A)** and low MALS signal **Figure 2.23 (B)** suggest the possibly degraded HA fractions.

We next labeled StPGA-HA80kDa with OG for permeation studies (creating StPGA-HA80kDa-OG) **(SI-2.4)**. **Table 2.6** describes the physicochemical characteristics evaluated; the conjugated ratio of StPGA to HA in StPGA-HA80kDa was 2:1. We found a hydrodynamic radius of 8-9 nm for StPGA-HA80kDa-OG, corresponding to free unimer size in solution. OG modification slightly increases the size of StPGA-HA80kDa, most probably due to the increased hydrophobic interactions and decreased electrostatic repulsion by occupying the hydrophilic carboxylic groups.

__Table 2.6__ Physico-chemical characteristics of StPGA-HA80kDa

Polymer	Parameters	StPGA:HA ratio	OG loading (% wt)	Size[a], (D_h, nm)	Size[b], (D_h, nm)
	Technique	NMR	Fluorescence	DLS	DLS
StPGA-HA80kDa-OG		2:1	3.8	7.8±0.4	9.3±1.3
StPGA-OG		-	2.4	10.65±3.5	13.0±0.9
StPGA		-	-	6.9±1.5	8.7±2.5

[a] DLS measurements in 1 mg/ml PBS, [b] DLS measurements in 0.1 mg/ml PBS

Figure 2.24 shows the CD spectra of StPGA-HA80kDa-OG, StPGA, and HA80kDa. The CD profile of HA80kDa has a much lower intensity value than StPGA-OG; meanwhile, the spectra of StPGA-HA80kDa-OG represent the accumulation of signals from both polymers, as expected. Moreover, the CD profile of StPGA-HA80kDa-OG remains similar to unlabeled polymers (**Figure 2.4**) and StPGA-OG (**Figure 2.8**), indicating predominating random coil conformation and no structural differences after OG and HA modification.
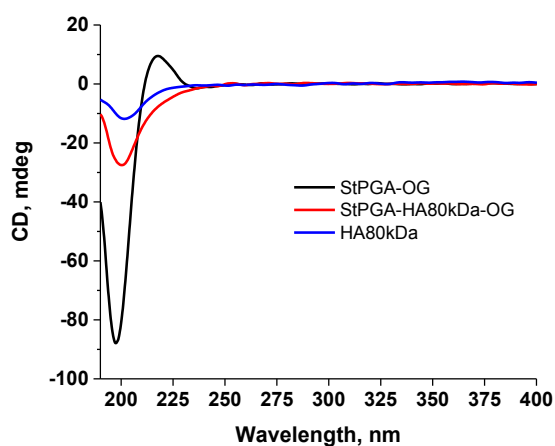
Figure 2.24 CD spectra of StPGA-HA80kDa at 0.1 mg/ml in MilliQ water. Average results with three accumulated measurements are displayed.

Figure 2.25 shows the permeation profile of covalently linked StPGA-HA80kDa-OG, which displays more rapid permeation than StPGA-OG. Interestingly, the physical mixture of StPGA-OG and HA80kDa provides slower and more sustainable permeation, which can be beneficial if prolonged and sustainable release is needed.
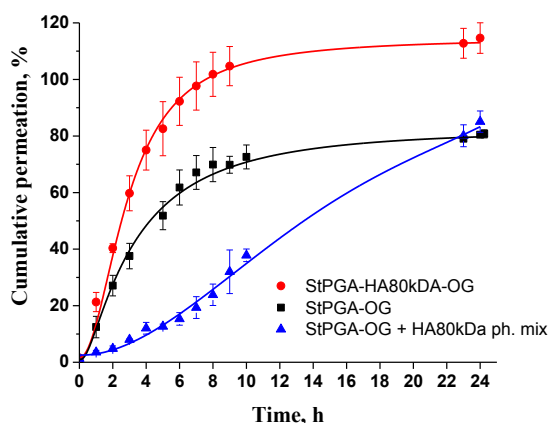
Figure 2.25 Ex vivo permeation of covalently linked StPGA-HA80kDa-OG (red), StPGA-OG (black), and physical mixture (ph. mix) of StPGA-OG and HA80kDa. The average results of triplicates are displayed, and the error bars are reported as the standard error of the mean.

Overall, an N-terminal derivatized StPGA-HA80kDa displays superior permeation features compared to unmodified StPGA and represents an optimal candidate for further development of the intranasal platform.

2.2.6. LinPGA and StPGA Functionalization with Docosahexaenoic Acid

The polyunsaturated fatty acid docosahexaenoic acid (DHA) represents the most abundant component of brain cell membranes and closely associates with optimal neuronal function [109]. DHA microemulsions displayed high and rapid permeation through sheep nasal mucosa, prompting a 10.7-fold increase in brain concentration after intranasal compared to intravenous administration [110]. Madane et al. demonstrated that lipid nanocarriers enhanced the brain uptake of curcumin and increased cytotoxicity in an astrocytoma-glioblastoma cell line (U-373MG) [111]. Inspired by these successful examples of DHA regarding penetration and uptake, we evaluated the DHA modification of PGA to improve mucosal permeation. DHA also acts as a brain nutrient [112], modulates inflammatory responses, and promotes skin wound healing [113,114], providing additional advantages. This research included a collaboration with Dr. Irene Dolz-Pérez, who studied the effect of DHA-based materials as treatment in ischemia-reperfusion and wound healing models during her PhD thesis [115].

We developed a synthetic procedure to conjugate DHA to LinPGA and StPGA via esterification with DMTMM as an activator (**Figure 2.26**).
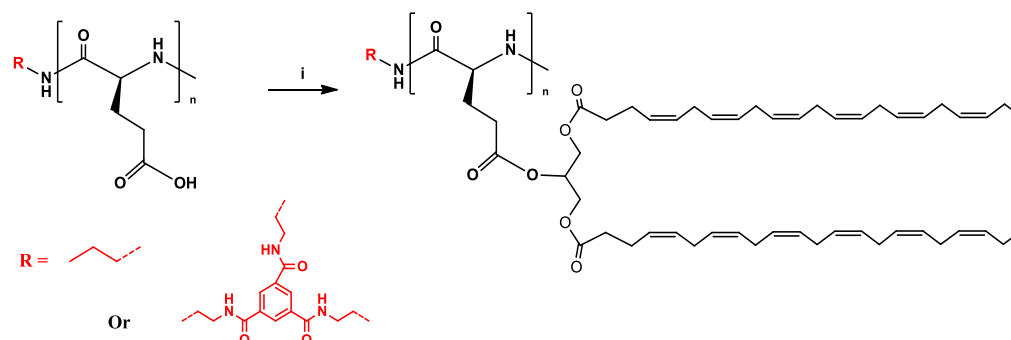
Figure 2.26. Synthesis of DHA conjugates with LinPGA[115] and StPGA carriers: i) DMF_{anh}, DMTMM BF_4, DMAP, DIEA, under N_2 atmosphere, 72 h **(SI-2.7.)**

We determined the amount of DHA conjugated to PGA by NMR via the characteristic peaks of 12 H from the vinyl groups of DHA at 5.17-5.33 ppm and aliphatic terminal $-CH_3$ group at 0.75 ppm (**Figure 2.27**).
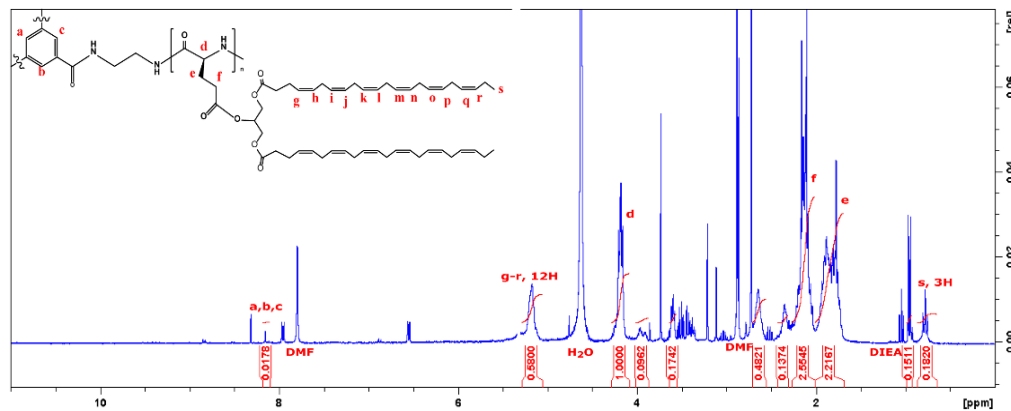
Figure 2.27. Representative ^{1}H-NMR spectra (300 MHz, D_2O) of StPGA-DHA$_6$. The spectra of all DHA conjugates are shown in **SI-2.6**.

We prepared OG-labeled conjugates following the standard procedures described in **SI-2.4**. **Table 2.7** reports the physicochemical characteristics of OG-labeled StPGA-DHA and LinPGA-DHA conjugates.

***Table 2.7** Physico-chemical characteristics of DHA conjugates*

Polymer	Parameters	DHA loading (% mol)	OG loading (% wt)	Size^a, (D_h, nm)	Size^b, (D_h, nm)
	Technique	NMR	Fluoresc.	DLS	DLS
StPGA-DHA$_6$-OG		6.0	0.9	35.1±5.2	42.8±4.5
StPGA-DHA$_2$-OG		1.5	1.9	30.3±2.2	34.5±8.3
PGA-DHA$_6$-OG		6.4	1.5	36.4±5.0	n/a
PGA- DHA$_2$-OG		2.2	2.1	66.9±8.2	n/a

^{a} DLS measurements in 1 mg/ml PBS, ^{b} DLS measurements in 0.1 mg/ml PBS

The values of the hydrodynamic radius of all DHA-modified PGAs are 3-7 times higher than PGAs modified with HA and OL (around 10-13 nm). This agrees well with previously reported PGA-DHA conjugates, where the sizes obtained were confirmed by transmission electron microscopy (TEM) and demonstrated the existence of nanosized, spherical aggregates [115]. Furthermore, this study revealed an inverse relationship between diDHA loading and conjugate size by number (conjugate size decreases as diDHA loading increases)– a phenomenon that may be intimately related to the hydrophilic–lipophilic ratio of conjugates. Higher compaction also occurs as the lipophilic component (diDHA) increases, thereby causing a size reduction; this effect is less marked for StPGA due to the more restricted flexibility that minimizes such conformational changes [115].

Figure 2.28 shows the CD spectra of the four OG-labeled PGA-DHA conjugates; overall, the CD profiles remain similar to unlabeled polymers (**Figure 2.24)**, indicating a predominating random coil conformation and a lack of structural differences after OG modification.

Figure 2.29, which shows the permeation profile of DHA conjugates, provides evidence for the enhanced permeation of StPGA-DHAs compared to linear analogs, although this does not surpass the unmodified labeled carries (StPGA-OG and LinPGA-OG). This result could relate to a larger molecular size of the PGA-DHA conjugates due to aggregation, as mentioned above. Modifying StPGA or LinPGA with DHA did not significantly benefit mucosa permeation, so we discarded this strategy from further studies.
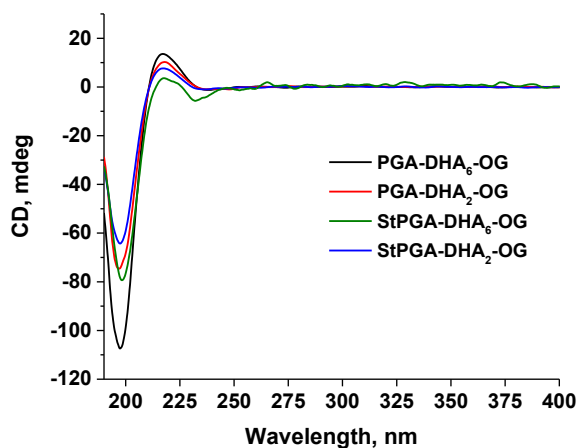
Figure 2.28. The CD spectra of linear (black, red) and star (green, blue) PGA-DHA conjugates with different drug loadings at 0.1 mg/ml in MilliQ water. Average results with three accumulated measurements are displayed.
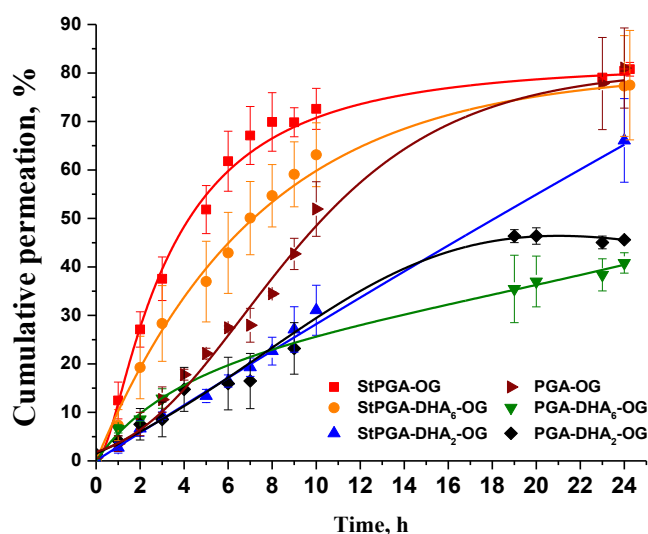
Figure 2.29 Ex vivo permeation study of DHA conjugates with low (PGA- DHA_2-OG, PGA- DHA_2-OG) and high (StPGA- DHA_2-OG, StPGA- DHA_2-OG) degree of modification in comparison with parent carriers StPGA-OG and PGA-OG. Average triplicate results are displayed, and the error bars are reported as the standard error of the mean.

2.2.7. Exploring the Impact of Crosslinking on Mucosal Permeation

StPGA can self-assemble into larger 30–100 nm nanostructures in non-salty aqueous solutions [84]. In physiological media, these nanostructured complexes rapidly disintegrate; therefore, stabilization by covalent bonding provides a stable drug delivery system. Our group previously reported a method to capture such labile structures based on copper-catalyzed azide-alkyne cycloaddition (StPGA-CL) of modified StPGA [84] **(SI-2.8)**. LinPGA cannot form stable ionic interactions with self-assembly properties at the concentration evaluated. StPGA-CL possesses differential properties due to a more negative Z-potential and larger size, such as a marked lymphotropic character [84]. StPGA-CL may also represent an ideal basis for designing polypeptide-based combination conjugates, given the broader capabilities of the modulation of the drug ratio in a quick manner. In the case of intranasal delivery, examples of charged, hydrophilic, and high molecular weight molecules are described as poorly permeable across the nasal membrane [116]; however, surface modification of such nanosystems with absorption enhancers and modification of the chemical structure of the carriers with mucodiffusive, mucoadhesive and/or targeting moieties can help to overcome these issues and improve the passage of nanosystems through mucosal layers [117].

Apart from applying the already mentioned click chemistry as the crosslinking method [84], other strategies can offer specific physico-chemical and/or biological properties to the final construct [118]. For example, disulfide crosslinkers can provide redox sensitivity derived from the 1000-fold increased glutathione level in cytosol compared to the extracellular environment [119,120]. Thiol functionalities may also confer mucoadhesive/mucodiffusive properties due to their interaction with cysteine-rich domain moieties in the mucosa. [121–123]The disulfide crosslinked systems described herein (StPGA-SS-CL) were originally prepared by Dr. Inmaculada Conejos Sánchez (thesis co-supervisor) using modified StPGA with cysteamine pyridyl disulfide followed by a nanoprecipitation strategy with a dithiol agent **(SI-2.9)**.

In close collaboration with the company Polypeptide Therapeutic Solutions S.L. (Valencia, Spain; now Curapath S.L.), we evaluated a hydrogel cross-polymer based on HA and LinPGA crosslinked via L-lysine residues (HA-CP®) [124] HA-CP displays excellent safety and biocompatibility properties and can efficiently incorporate polypeptide-drug conjugates within its structure [125]. We previously evaluated an HA-CP incorporated PGA-corticosteroid conjugate in topical application to treat psoriasis [125]. The results demonstrated HA-CP® as a skin penetration enhancer for delivery of polypeptide conjugates [124,125]. Inspired by these encouraging results, we evaluated the ability of HA-CP® as a vehicle within which we would embed PGA-based nanomedicines to cross the mucosal barrier.

We studied three systems to evaluate the effect of size on mucosal permeation: unimeric StPGA and crosslinked StPGAs created via a click reaction (StPGA-CL) or disulfide bond (StPGA-SS-CL). **Figure 2.30** shows their permeation profile in our ex vivo model.
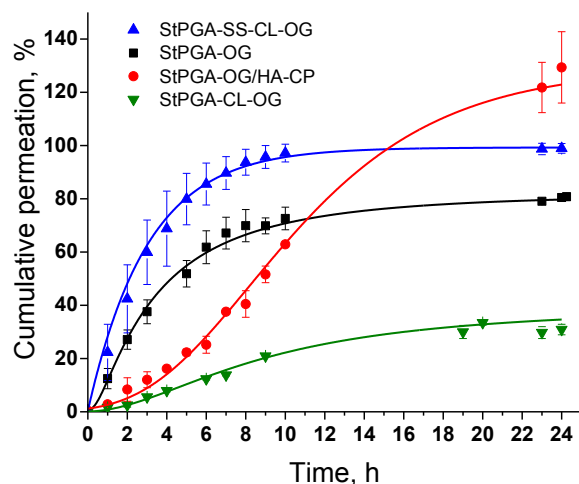
Figure 2.30 Ex vivo permeation study of crosslinked systems prepared via azide-alkyne cycloaddition (StPGA-CL-OG) or using a disulfide crosslinker (StPGA-SS-CL-OG) and StPGA-OG embedded in hydrogel cross-polymers (HA-CP®)[124,125]. The average results of triplicates are displayed, and the error bars are reported as the standard error of the mean.

We observed low permeation for StPGA-CL due to its relatively large size (Rh ~90 nm) compared with the StPGA unimer, which is around 10nm. However, when comparing large systems, StPGA-CL vs. StPGA-SS-CL (Rh~200 nm) size is not the only parameter that matters, and the presence of mucoadhesive/mucodiffusive moieties, such as SH, could be a determinant in enhancing nose-to-brain delivery. The results can be explained by the thiol/disulfide exchange reaction between the polymer and cysteine-rich subdomains of mucus glycoproteins in the mucus layer [121], a strategy already validated with different thiolated polymers (thiomers) based on chitosan, poly(acrylic acid), carboxy-methylcellulose or alginates that demonstrated an enhancement up to 140-fold in their mucoadhesive properties [123]. These findings highlight the importance of mucodiffusive components for a successful intranasal platform.

In parallel, the effect of HA-CP®124 when used as a vehicle/permeation enhancer was also remarkable. Indeed, it could act as a depot for a short time; the permeation is lower than the analogs when PBS is used as vehicles, but at long-term cumulative permeation is significantly different as demonstrated with StPGA without and with HA-CP® (at 24h. Cumulative permeation of 79% vs. 100%, respectively).

The summarized results obtained in the ex vivo permeation study (**Figure 2.31**) emphasized the relevance of (i) mucodiffusive ligand exposure (lower exposure

promotes aggregation/inhibits permeation), (ii) shape (StPGAs displayed more rapid permeation than LinPGAs), and (iii) size (large particles displayed poor diffusion; however, disulfide bond crosslinked carriers demonstrated enhanced permeation and highlighted the importance of the mucodiffusive component).

Using this ex vivo platform, we also identified critical features for the rational surface modification of the final polymeric construct that facilitates nose-to-brain transport. Several systems were selected for further in vivo studies: the star-shaped polyglutamates with covalently linked odorranalectin peptide via C-terminal and crosslinked systems via disulfide bonds that demonstrated the fastest kinetic rate and the hydrogel system HA-CP® with the slower kinetic rate but highest accumulation efficiency at 24 h, that reported to incorporate different components within its structure 32 efficiently and also can be beneficially used as a depot for continuous drug release.
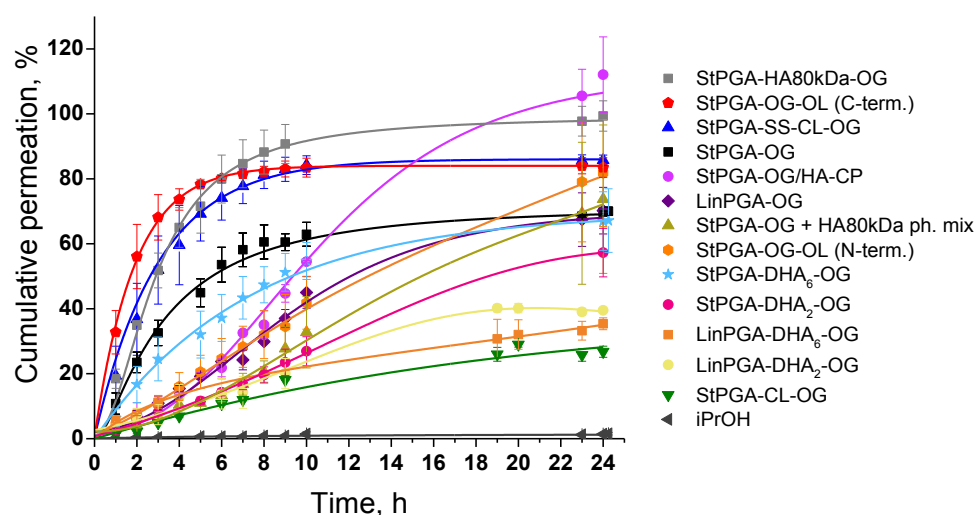
Figure 2.31 Summarized graph of ex vivo permeation study of all tested compounds: linear (LinPGA-OG) and star-shaped (StPGA-OG) polyglutamates, covalently-linked StPGA and HA80kDa (StPGA-HA80kDa-OG) and physical mixture (StPGA-OG + HA80kDa ph. mix); crosslinked systems prepared via azide-alkyne cycloaddition (StPGA-CL-OG) or using a disulfide crosslinker (StPGA-SS-CL-OG), and StPGA-OG embedded in hydrogel cross-polymers (HA-CP®); star-shaped polyglutamates modified with odorranalectin via C-terminal side (StPGA-OG-OL (C-term.)) or N-terminal (StPGA-OG-OL (N-term.); DHA conjugates with low (LinPGA- DHA_2-OG, StPGA- DHA_2-OG) and high (LinPGA- DHA_6-OG, StPGA- DHA_6-OG) degree of modification; iPrOH (negative control). The average results of triplicates are displayed, and the error bars are reported as the standard error of the mean.

2.2.8. In vivo Preliminary Biodistribution Data of Selected Intranasal Platforms

To validate and confirm the ability to reach the brain, we performed biodistribution studies **(SI 2.10)** on healthy mice with the most promising candidates as selected from the ex vivo screening (StPGA, StPGA-OL, and StPGA-SS-CL with and without HA-CP). We labeled each carrier with Cy5.5 **(SI-2.2)** to allow the ex vivo quantification of fluorescence to understand in vivo biodistribution. We performed biodistribution studies in male BALB/c mice after intranasal administration **(SI-2.10).**

We first compared StPGA unimer with and without HA-CP® [124]; at 30 min, 2 h, and 4 h intranasal post-administration, we sacrificed animals, harvested the main organs (brain, liver, heart, spleen, kidney, lungs, and intestine), and analyzed them ex vivo with an IVIS® Spectrum (Perkin Elmer). Additionally, we quantified Cy5.5 fluorescence output on a CLARIOstar Plus plate reader ($\lambda_{excitation}$=640 nm, $\lambda_{emission}$=720 nm) after organ homogenization **(SI-2.2)**. From the results (**Figure 2.32A**), we concluded that our polymers could reach the brain, and the in vivo biodistribution nicely correlates with the ex-vivo kinetic studies, where the HA-CP® vehicle demonstrated being a permeation enhancer as well as acting as a depot that triggers a slower permeation rate at the beginning but with a long-lasting effect. After 4 h, we did not detect any signal from the compounds in the brain indicating a possible scavenging activity, most probably from immune components.
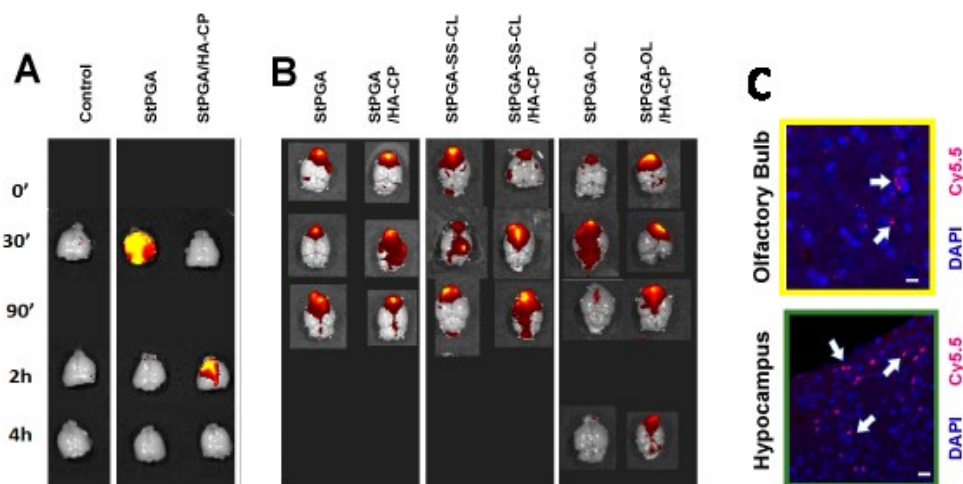
Fig. 2.32. **In vivo biodistribution of intranasally administered Cy5.5-labelled polymeric systems. A)** StPGA alone and incorporated into HA-CP® (StPGA/HA-CP®) after 30 min, 2 h, and 4 h of treatment. **B)** StPGA alone and incorporated into HA-CP® (StPGA/HA-CP®); crosslinked system via disulfide bonds (StPGA-SS-CL) alone and incorporated into HA-CP®, StPGA modified with lectin peptide (StPGA-OL) alone and incorporated into HA-CP® after 0 min, 30 min and 90 min of treatment for all compounds and additional time points 4 h for OL modified systems **C)** Conjugates (white arrows)

localized in cytoplasm in olfactory bulb and hippocampus proving distribution in different brain areas (unpublished Polymers labeled with Cy5.5 (red color) and Nucleus labeled with DAPI (blue color)

In the second stage, we explored the behavior of the selected nanocarriers at shorter times (0 min, 30 min, 90 min) using or not HA-CP® as a permeation enhancer (**Figure 2.32B**) trying, on the one hand, to validate the ability of the polypeptidic carriers to reach the brain and on the other side, to better understand how these nanocarriers can diffuse throughout the brain.

In collaboration with Prof. J.M. García-Verdugo and Dr. V. Herranz-Pérez from the University of Valencia, we performed a histological analysis of the obtained brain slices from the distinct groups by fluorescence confocal microscopy (**Figure 2.32C**). This study indicated a preferential localization of the conjugates (white arrows) in the cytoplasm of cells in the olfactory bulb and the hippocampus, proving good distribution in different brain areas.

The ex vivo quantification of Cy5.5 was used to quantify the % of the administered dose (% AD) of the nanosystems that reached the brain. **Table 2.8** demonstrates the obtained results, with the amount of the polymers physically mixed with HA-CP® delivered to the brain at 2.2% and 2.4% AD for both peptide modification and crosslinked via disulfide bond systems. Such results demonstrated higher efficiency of our polymers for brain delivery compared with intravenous administration, where even re-engineered systems with targeted blood-brain barrier moieties allow around 1% AD of drug delivery [6].

Table 2.8 *Ex vivo Cy5.5 Quantification from biodistribution studies*

Compound	Time	Organ accumulation, %AD[a]					
		Kidney	Heart	Spleen	Lungs	Intestine	Brain
StPGA-OL	30min	0.30			26.1	72.8	0.6
StPGA-OL/HA-CP	30min	0.20				97.4	2.4
StPGA-SS-CL/HA-CP	30min	0.07	<0.05	<0.05	<0.05	99.6	0.4
StPGA-SS-CL/HA-CP	90min	0.10				97.6	2.2

[a] %AD considered as a percentage of the total administered dose, being 100% the sum of all the organs (but having into account the %AD/g tissue)

The performed in vivo studies not only validated our ex vivo screening platform but also confirmed the capability of our systems to achieve brain transport and demonstrated their ability to diffuse within the brain (olfactory bulb, hippocampus,

cerebral cortex). To endorse the potential of our system, pharmacological assays are required and ongoing in our research group in different models and using different bioactive agents.

2.3. Conclusions

We successfully synthesized polymeric platforms based on PGA with different topologies (linear and star-shaped) bearing different functionalities that may provide desired mucoadhesive/mucodiffusive properties (DHA, HA, and OL). We successfully established synthetic protocols to conjugate these compounds with different loadings to PGA carriers. Besides small unimeric systems, we evaluated larger systems crosslinked via azide-alkyne cycloaddition or disulfide bonds. In addition, we used an HA-based crosslinked hydrogel-bearing PGA as a vehicle (HA-CP®)[124], which has been reported as a permeation enhancer in skin delivery [125].

We successfully established an ex vivo model based on vertical Franz diffusion cells with sheep mucosa to mimic human mucosa tissue. We evaluated fluorescently labeled nanocarriers in an ex vivo model and selected the three best formulations of StPGA for further in vivo studies: modified with odorranalectin peptide, crosslinked via disulfide bonds, and incorporated into hydrogel vehicle HA-CP.

We can correlate physicochemical parameters with the ability to enhance mucosa passage based on the kinetic profile of a tested compound. The shape of the carrier represents crucial parameters, where StPGAs demonstrated better permeation than LinPGA. Increasing the size of the delivery system negatively correlated with mucosal permeation; however, particles crosslinked with disulfide bonds can overcome the size limitation by the mechanism of interchanging the thiol bonds and highlights the importance of mucodiffusive components for a successful intranasal drug delivery system. Modification with HA was widely reported to have mucoadhesive properties and slightly improved permeation when covalently conjugated to StPGA (but not when physically mixed with StPGA). PGAs modified with DHA demonstrated poor permeation ability, perhaps due to oxidation and partial aggregation, which leads to an increase in size. HA-CP®, which displays slow kinetics and a high accumulation rate, represents an interesting formulation that can be used for delayed and sustainable drug release. We observed the fastest permeation rate for StPGA modified with odorranalectin peptide (StPGA-OL).

To corroborate our findings, we performed in vivo brain biodistribution studies using vehicle PBS or HA-CP® at different time points, which demonstrated the ability of PGA-based systems to reach the brain and diffuse within different brain areas (olfactory bulb, hippocampus, and cerebral cortex) in an architectural-dependent manner. The StPGA-OL peptide and StPGA-SS-CL incorporated into HA-CP® demonstrated the highest brain accumulation among the tested compounds with 2.4 and 2.2 %AD, respectively.

2.4. Supplementary information

SI-2.1. Materials

SI-2.2. Experimental Methods

SI-2.3. General procedure for the synthesis of poly-L-glutamic acid carriers

SI-2.3.1. General Procedure for the Purification of Initiator for Linear PGA

SI-2.3.2. General Procedure for the Synthesis of Initiator for StPGA

SI-2.3.3. General Procedure for Polymerization

SI-2.3.4. General Procedure for Deprotection of poly-L-glutamic Acid

SI-2.4. General Procedure for the OG Labeling

SI-2.5. General Procedure for the OL Conjugation

SI-2.5.1 Direct OL conjugation to StPGA via N-terminal site

SI-2.5.2. Indirect OL conjugation to StPGA via C-terminal site

SI-2.6. General Procedure for the HA and StPGA Conjugation

SI-2.6.1 Direct HA conjugation via an ester bond

SI-2.6.2. Direct HA conjugation via an amide bond

SI-2.7. General Procedure for DHA Conjugation

SI-2.8. General Procedure for Preparation of Cu-catalyzed Crosslinked StPGA Systems

SI-2.8.1. Preparation of StPGA-propargyl

SI-2.8.2. Preparation of StPGA-azide

SI-2.8.3. Copper-catalyzed azide-alkyne cycloaddition

SI-2.9. General Procedure for Preparation of disulfide crosslinked StPGA Systems

SI-2.9.1. Preparation of StPGA-pyridyl

SI-2.9.1. Nanoprecipitation procedure for obtaining StPGA-SS-CL

SI-2.10. In Vivo Biodistribution Studies

SI-2.1. Materials

All chemicals were reagent grade, obtained from Sigma or Fisher Scientific. All solvents were of analytical grade from Sharlau Chemicals, Sigma, Fisher Scientific, or

freshly distilled in the case of THF anh. Deuterated solvents were obtained from Deutero GmbH. Preparative SEC was performed using Sephadex LH-20 medium from GE. Palbociclib free base was purchased from MedcoChem Co. Ltd (Zhejiang, China). Anhydrous N,N-dimethylformamide (DMF, ≥99.8% anhydrous), methanol (HPLC grade), and tetrahydrofuran anhydrous (99.8%) were purchased from Scharlab SL (Sentmenat, Spain). NCA-Glu (OBz) was provided by PMC Isochem.

SI-2.2. Experimental Methods and Protocols

Nuclear Magnetic Resonance Spectroscopy

NMR measurements were performed on Bruker 300 Ultrashield^{TM} (Bruker, Billerica, United States) with a Bruker B-ACS 60 automation system. 2D experiments were performed with a Bruker 500 Ultrashield plus (Bruker, Billerica, United States) with a Bruker sample case cooled automation system. All the measurements were performed at room temperature. The spectra were processed and analyzed using TopSpin and MestreNova software.

Circular Dichroism Spectroscopy

To measure the absorption of polarized light, the prepared solution was transferred to a quartz cuvette with a light path length of 1cm and measured at room temperature with a J-1500 spectrometer (JASCO corporation, Easton, United States). The resulting spectra were obtained by averaging five consecutive scans. A nitrogen flow of 2.7 L/min was led through the spectrometer.

Size Exclusion Chromatography

The SEC experiment was performed on a Postnova Analytics Modular SEC system (Postnova Analytics GmbH, Landsberg am Lech, Germany) coupled to an RI detector (PN3150 from Postnova Analytics GmbH), a UV-Vis detector (SPD-20A from Shimadzu Scientific Instruments, Kyoto, Japan), a fluorescence detector (RF-20A XS from Shimadzu Scientific Instruments, Kyoto, Japan), and a MALS detector (PN3621 from Postnova Analytics GmbH). Experiment conditions: Column TSKgel G3000PWXL (5 μm, 7.8 mm i.d. x 30 cm, Tosoh Corporation, Tokyo, Japan), Flow: 0.4 ml/min, Solvent: 0.005M PBS, 0.069 M NaCl, Injection volume: 10μL. Samples were prepared in water at a concentration of 2 mg/ml.

Fluorescent Spectroscopy

Fluorescence spectroscopy measurements for OG quantification were performed on an FP-6500 spectrofluorimeter (JASCO, Easton, United States) with an excitation wavelength λ_{ex}= 495 nm and measured emission wavelength λ_{em}= 519 nm. Polymer samples were prepared in water, and the calibration curve of OG was done.

Dynamic Light Scattering

The DLS size and z-potential measurements were performed on a Malvern Zetasizer nanoseries, nano ZS, ZEN3500 (Malvern Instruments, Malvern, UK). Samples of polymers were prepared in PBS at concentrations of 1 mg/ml and 0.1 mg/ml.

Ex-vivo permeation studies

The nasal respiratory mucosal tissue samples were obtained[74] by cutting out the frontal part of the nasal conch of the animal and following separation from the lateral cartilage and connective tissue with forceps and scissors without damaging or scratching the nasal mucosa [52,65], washing with dPBS. The excised tissue was stored directly on the ice during transportation to the laboratory, where a longitudinal incision fully exposed turbinates through the nose, and the mucosa was carefully removed from the underlying bone [123]. Permeation studies were started immediately after the mucosa samples were excised or stored at - 80°C. If frozen, the ovine mucosa was quickly thawed at room temperature, washed with PBS buffer pH 6.4, and mounted onto one half-cell of the Franz diffusion apparatus with a diameter of 10 mm. The recipient compartment contained 8 ml of PBS buffer pH 6.4 stirred with a Teflon-coated magnetic stirrer (1000 rpm) and was equilibrated at 37 °C. 100 μl of the labeled with Oregon Green (OG) dye polymeric formulations were added to the donor chamber, covered with Parafilm™ and aluminum foil to protect from light. 2 ml of samples from the receptor compartment were withdrawn at predetermined time intervals and replaced with an equal volume of PBS buffer pH 6.4. The sample was filtered through a Nylon filter 0.22 μm, and absorbance was measured directly without any additional sample preparation spectrophotometrically at $\lambda=492$ nm, the maximum of OG absorption using Jasco V‑550 UV/Vis Spectro-photometer (Tokyo, Japan) taking PBS buffer pH 6.4 as the blank. Each study was carried out for 24 h and in triplicate. As a negative control, isopropyl alcohol (iPrOH) was used. The results were presented as the mean cumulative values for diffused polymeric formulations at the sampling time point.

Ex-vivo quantification of Cy5.5 of the harvested organs

The harvested and stored organs at -80 0C were quickly thawed at room temperature and placed on ice. Organs were homogenized in dPBS pH=7.4 with Ultraturrax device using optimized buffer volume, ml/homogenization time, sec /rotation speed, rpm depending on the organ: heart (1/60/10000), lungs (1/30/10000), spleen (1/30/10000), liver (2/60/10000), kidney (1.5/60/10000), brain (2/60/7500), intestine (3/60/10000). The Ultraturrax device was washed with M illiQ water and dried after each organ homogenization cycle. The homogenized organ suspension was centrifuged at 4000 rpm for 1 h at 4^0C, and 100 μl of supernatant was transferred in triplicates to a black P96 plate for fluorescence measurement with a CLARIOstar Plus plate reader. The corresponding calibration curve with Cy5.5 in dPBS was prepared in the 0.125-70 ng/ml range, and the fluorescence signal was measured at $\lambda_{excitation}= 640$ nm, $\lambda_{emission}= 700$ nm.

SI-2.3. General Procedure for the Synthesis of poly-L-glutamic Acid

SI-2.3.1. General Procedure for the Purification of Initiator for Linear PGA

Butan-1-amine was freshly distilled in a Dean-Stark apparatus at 85⁰C with LiAlH₄.

SI-2.3.2. General Procedure for the Synthesis of Initiator for StPGA
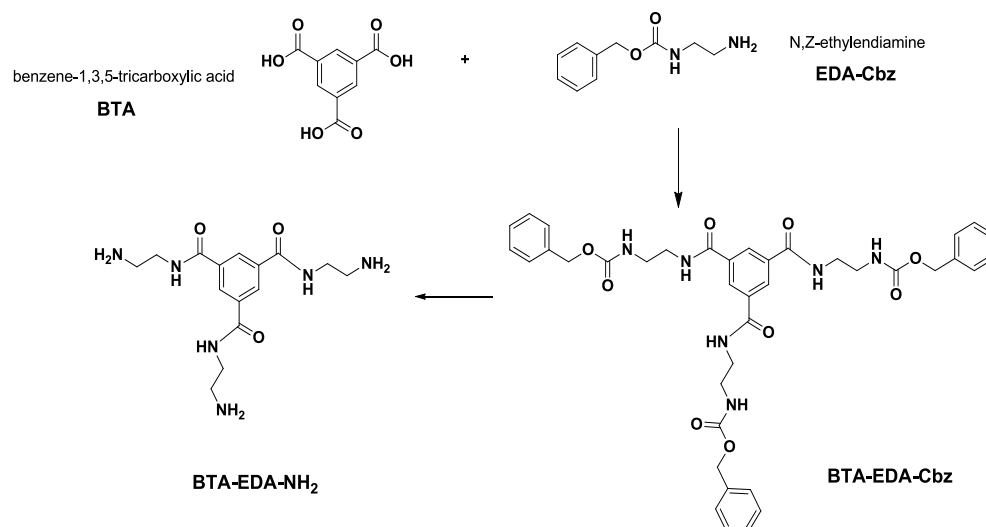
Figure S2.1. Synthesis of star initiator. i) CDI, DMF$_{anh}$, 0°C ii) H₂, MeOH

In a round bottom flask with a stirrer, 1,3,5-benzene tricarboxylic acid (200 mg, 0.95 mmoles, Mw=210.1 g/mol, 1eq.) was dissolved in 5 ml DMF anhydrous, 1,1'-carbonyldiimidazole (540 mg, 3.3 mmole, Mw=162.2 g/mol, 3.5 eq.) was added and allowed to stir for 1 h on ice. Then, N-Z-ethylenediamine hydrochloride (988 mg, 4.3 mmoles, Mw=230.7 g/mol, 4.5 eq.) dissolved in 5 ml DMF anhydrous was added to the mixture, and the reaction was left to proceed for 48 h. The obtained solution was filtered to remove precipitates and precipitated into cold Et₂O. The solid was purified with a silica column (d=2.5 cm, 85 g), using DCM:MeOH (92:8) as the mobile phase. The separation of the compounds was checked with a UV chamber, and the solvent of combined fractions was evaporated under vacuum to obtain a white solid.
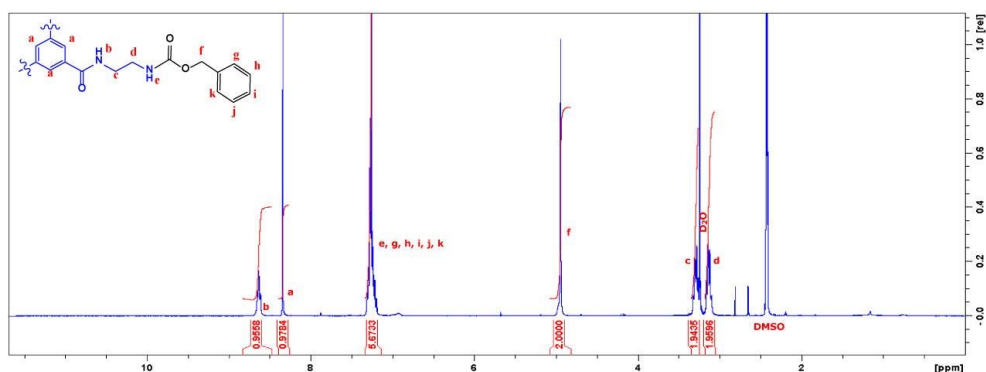
Figure S2.2. **BTA-EDA-Cbz:** Product – white powder. Global yield: 366 mg (52 %). *^{1}H NMR (300 MHz, DMSO-d6)*: 8.63 (t, 1H). 8.34 (s, 1H), 7.32-7.19 (m, 6H), 4.94 (s, 2H), 3.29 (q, 2H), 3.13 (q, 2H).

In a round bottom flask, BTA-EDA-Bz and PdO/C$_{act}$ (37mg, 10%$_{weight}$) were dispersed in 40 ml of MeOH, the system was purged three times vacuum/N$_2$ cycles, and finally, the reaction was allowed to proceed under an H$_2$ atmosphere during 5 h. The reaction was checked with ninhydrin 2% aq. solution staining. The mixture was filtrated through a glass filter with zeolite crust, and the solvent was evaporated under vacuum to obtain a white solid product.
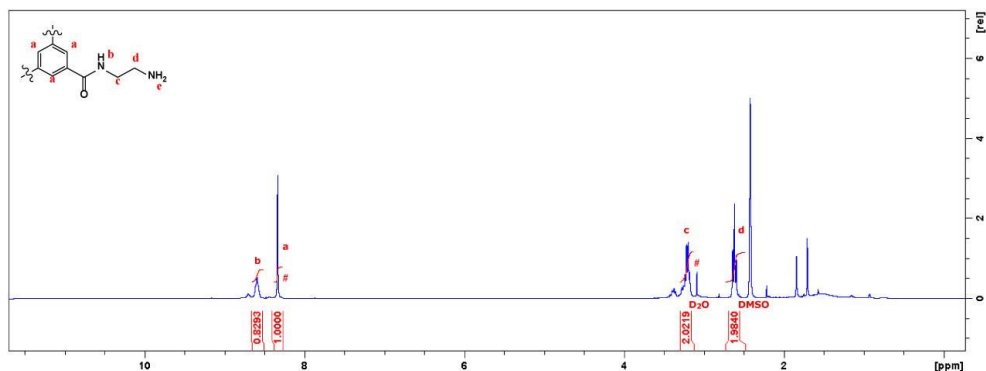
Figure S2.3. **BTA-EDA-NH$_2$:** Product – white powder. Global yield: 140 mg (84 %). *^{1}H NMR (300 MHz, DMSO-d6)*: 8.59 (t, 1H). 8.34 (s, 1H), 3.20 (q, 2H), 2.62 (t, 2H).

SI-2.3.3. General Procedure for Polymerization

NCA-Glu-OBz (3g, 11.4 mmol) was transferred into a Schlenk tube fitted with a stirrer and a stopper. The tube was purged with three vacuum/N$_2$ cycles, and 6 ml of anhydrous DMF was added. Initiator (11.27µl, 0.114 mmol for LinPGA100; 106.5 mg, 0.38 mmol for StPGA30; 53.3 mg, 0.19 mmol for StPGA60; 35.6 mg, 0.127 for StPGA90; 26.6 mg, 0.095 mmol for StPGA120; 21.3 mg, 0.076 mmol for StPGA) was added, and the mixture was left stirring for three days under an inert atmosphere at 10ºC. 6 ml of THF was added, and the mixture was precipitated in cold diethyl ether (100 ml), filtered, and washed with the same solvent (2x100 ml).

Figure S2.4. **LinPGA100-OBn:** Product – white powder. Global yield: 2.5-2.9 g (85-95 %). *¹H NMR (300 MHz, TFA-d)*: 7.48 (br. s, 500H). 5.32 (br. s, 200H), 4.91 (br. s, 100H), 3.51 (m, 2H), 2.71 (br. s, 200H), 2.40 (br. s, 100H), 2.21 (br. s, 100H), 1.72 (m, 2H), 1.52 (m, 2H), 1.11 (m, 3H)

Figure S2.5. **StPGA30-OBn:** Product – white powder. Global yield: 2.5g (85 %). *¹H NMR (300 MHz, TFA-d)*: 8.86 (s, 3H). 7.41 (m, 150H), 5.28 (m, 60H), 4.85 (q, 30H), 2.65 (m, 60H), 2.35 (m, 30H), 2.15 (m, 30H).

Figure S2.6. **StPGA60-OBn:** Product – white powder. Global yield: 2.7g (90 %). *¹H NMR (300 MHz, TFA-d)*: 8.86 (s, 3H). 7.41 (m, 300H), 5.28 (m, 120H), 4.85 (q, 60H), 2.65 (m, 120H), 2.35 (m, 60H), 2.15 (m, 60H).

Figure S2.7. **StPGA90-OBn:** Product – white powder. Global yield: 2.9g (95 %). *¹H NMR (300 MHz, TFA-d)*: 8.86 (s, 3H). 7.41 (m, 450H), 5.28 (m, 180H), 4.85 (q, 90H), 2.65 (m, 180H), 2.35 (m, 90H), 2.15 (m, 90H).
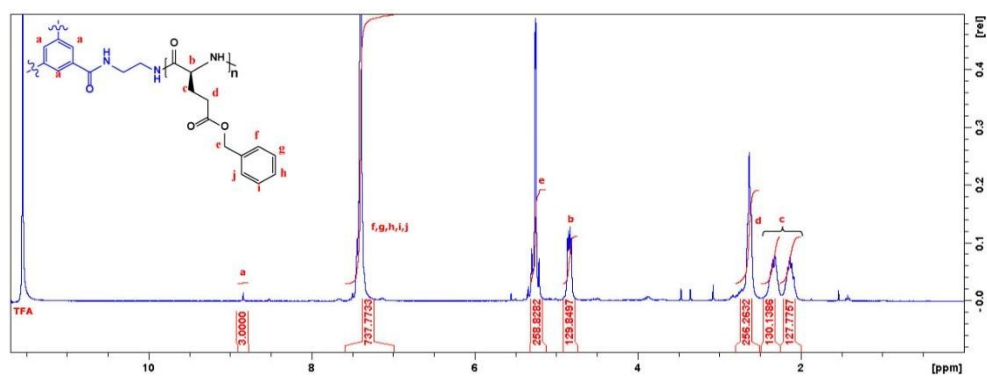
Figure S2.8. **StPGA120-OBn:** Product – white powder. Global yield: 2.6 g (87 %). *¹H NMR (300 MHz, TFA-d)*: 8.86 (s, 3H). 7.41 (m, 600H), 5.28 (m, 240H), 4.85 (q, 120H), 2.65 (m, 240H), 2.35 (m, 120H), 2.15 (m, 120H).
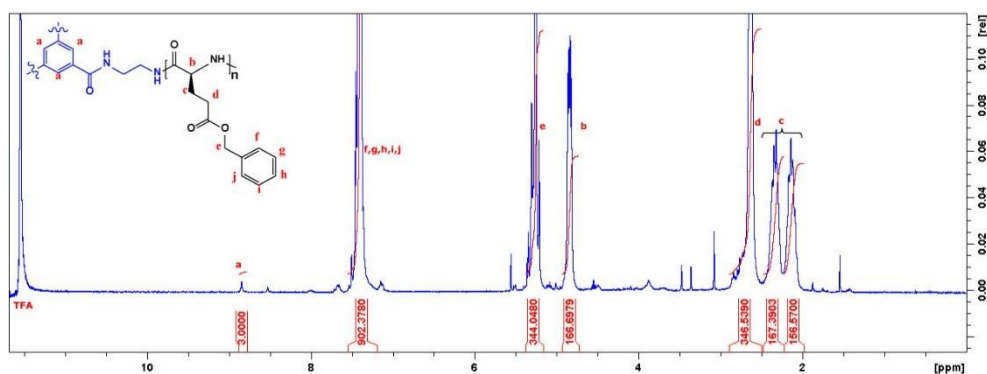
Figure S2.9. **StPGA-OBn:** Product – white powder. Global yield: 2.6-2.9 g (87-95 %). *¹H NMR (300 MHz, TFA-d)*: 8.86 (s, 3H). 7.41 (m, 750H), 5.28 (m, 300H), 4.85 (q, 150H), 2.65 (m, 300H), 2.35 (m, 150H), 2.15 (m, 150H)

117

<u>*SI-2.3.4. General Procedure for Deprotection of Poly-L-glutamic Acid*</u>

The corresponding protected poly-L-glutamic acid was transferred to a round-bottom flask and dissolved in 25 ml of TFA. 48% HBr (2.5 ml) was added, and the mixture reacted overnight. The mixture was precipitated in diethyl ether (200 ml), filtered, and washed with the same solvent (2x200 ml). The polymers in acidic form were used for further reactions without additional purification steps. The PGA Na salt was obtained by redissolving the polymers in 0.5 M NaHCO$_3$ and purified with a Float-A-Lyzer G2 dialysis device (Spectrum Laboratories, Compton, United States) against water for three days and further lyophilized.
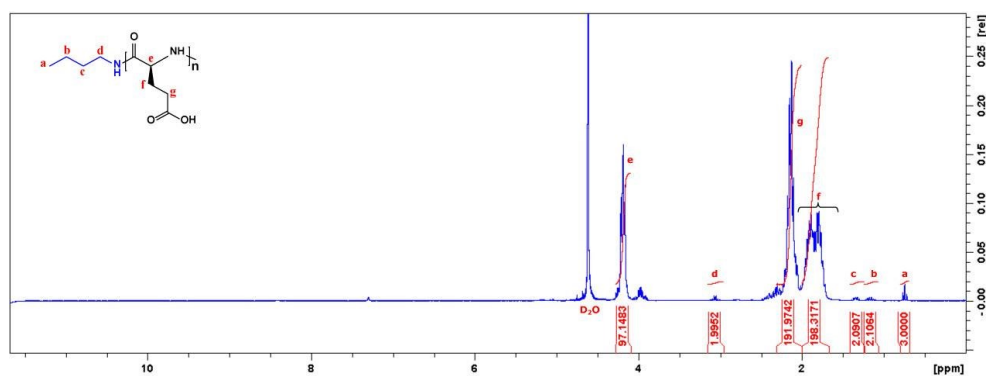
Figure S2.10. **LinPGA100:** Product – white powder. Global yield: 1.3-1.6 g (90-95 %). *^{1}H NMR (300 MHz, TFA-d)*: 4.18 (q, 100H). 3.06 (m, 2H), 2.12 (m, 200H), 1.83 (m, 200H), 1.33 (m, 2H), 1.17 (m, 2H), 0.74 (m, 3H)
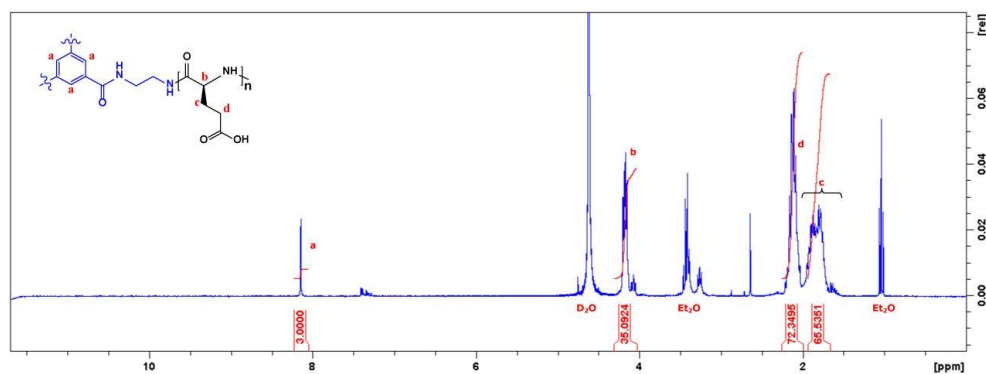
Figure S2.11. **StPGA30:** Product – white powder. Global yield: 1.35 g (92 %). *^{1}H NMR (300 MHz, TFA-d)*: 8.15 (s, 3H), 4.18 (q, 30H), 2.12 (m, 60H), 1.83 (m, 60H)

118
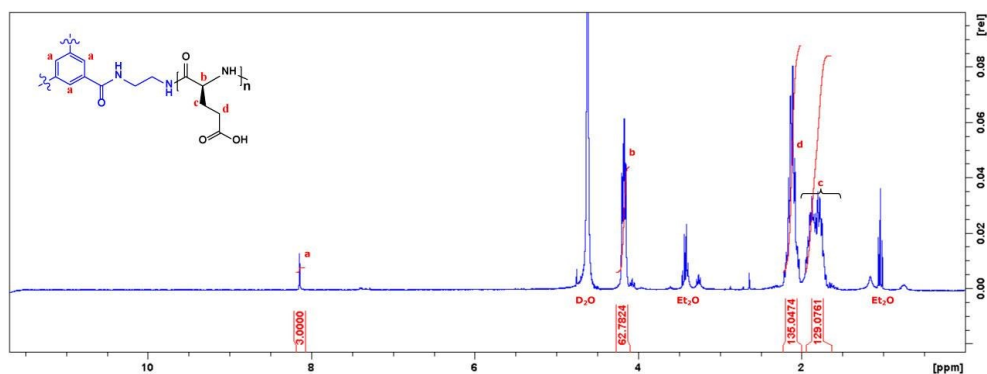
Figure S2.12. **StPGA60:** Product – white powder. Global yield: 1.43 g (90 %). *¹H NMR (300 MHz, TFA-d)*: 8.15 (s, 3H), 4.18 (q, 60H), 2.12 (m, 120H), 1.83 (m, 120H)
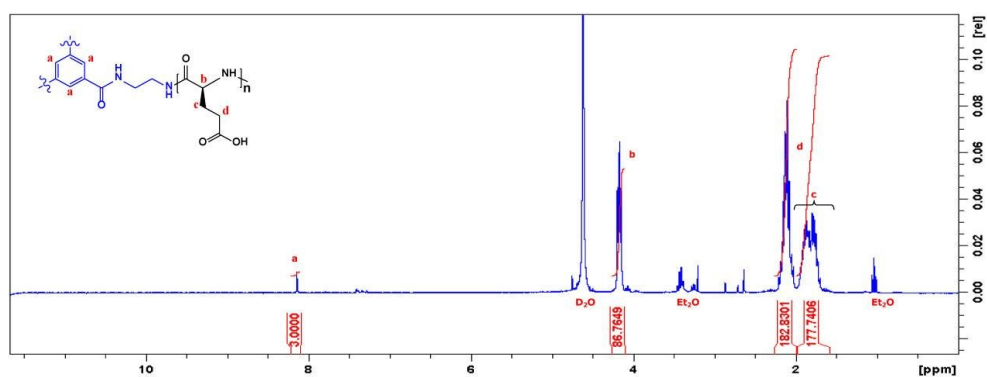
Figure S2.13. **StPGA90:** Product – white powder. Global yield: 1.57 g (92 %). *¹H NMR (300 MHz, TFA-d)*: 8.15 (s, 3H), 4.18 (q, 90H), 2.12 (m, 180H), 1.83 (m, 180H)
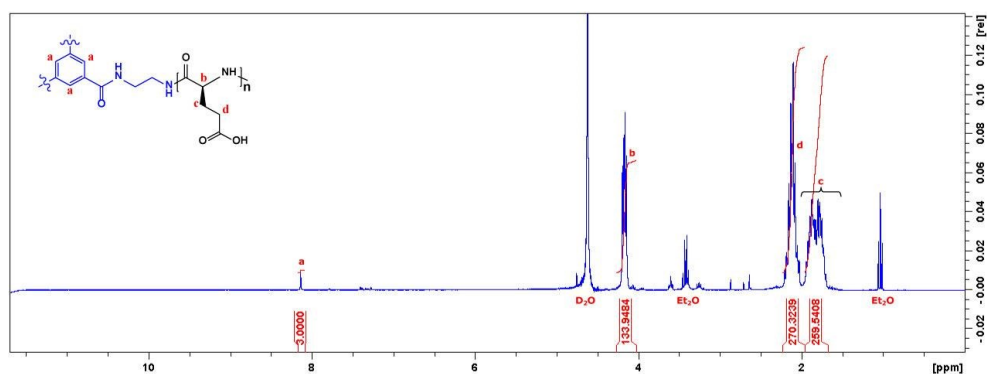
Figure S2.14. **StPGA120:** Product – white powder. Global yield: 1.45 g (95 %). *¹H NMR (300 MHz, TFA-d)*: 8.15 (s, 3H), 4.18 (q, 120H), 2.12 (m, 240H), 1.83 (m, 240H)
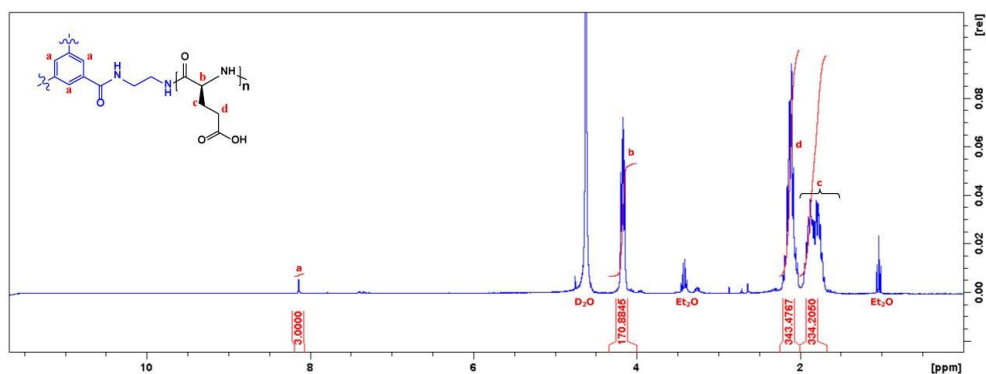
Figure S2.15. **StPGA:** Product – white powder. Global yield: 1.4-1.6 g (90-95%). *¹H NMR (300 MHz, TFA-d)*: 8.15 (s, 3H), 4.18 (q, 150H), 2.12 (m, 300H), 1.83 (m, 300H)

The product purity of the synthesized polymer was assessed by gel permeation chromatography (**Figure S2.16**). **Table 2.1** summarizes the characteristics of synthesized polymers.
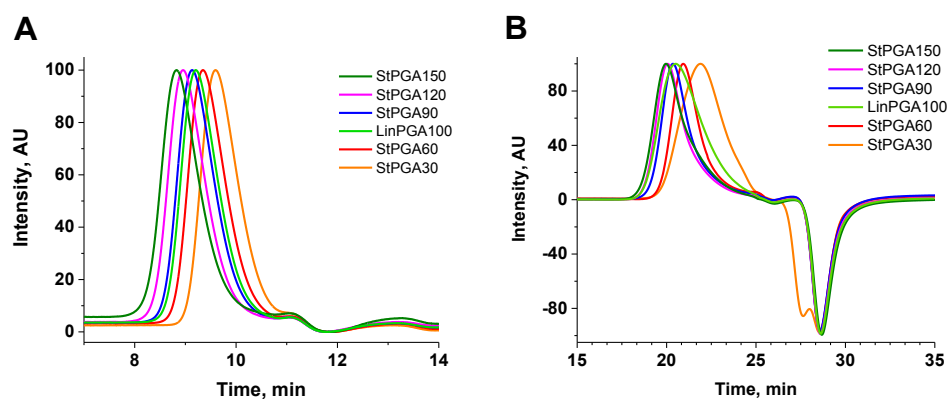
Figure S2.16. Overlaid chromatograms from a series of synthesized PGA carriers with different Mw. (**A**) Protected PBLG analyzed by GPC and (**B**) deprotected PGA analyzed by SEC

Table 2.1. *Properties of Generated PGA carriers*

Polymer	Theoretical DP	Obtained DP[1]	Obtained DP[2a]	Obtained DP[2b]	Mn, kDa	PDI
LinPGA100	100	85	96	97	18.8	1.073
StPGA30	30	36	35	35	8.5	1.068
StPGA60	60	72	64	65	16.2	1.067

StPGA90	90	102	90	89	22.7	1.069
StPGA120	120	131	129	133	29.1	1.082
StPGA150	150	179	167	170	39.6	1.071

[1]Calculated from GPC, [2]Calculated from NMR ([a]protected, [b]deprotected form), DP – degree of polymerization, represented as glutamic units per chain, PDI – polydispersity index, defined as the ratio between weight (Mw) and number (Mn) average molecular weight, Mw/Mn.

SI-2.4. General Procedure for the OG Labeling

In a round bottom flask with a stirrer, St-PGA (100 mg, 0.77 mmol, Mw=129.1 g/mol (Glu unit), 1eq.) was placed in 5 ml of DMF_{anh} under N_2 flow, added DIC (3.8 μl, 0.024 mmol, Mw=126.2 g/mol, ρ=0.806 g/ml, 0.03 eq.), the mixture allowed to stir 5 min at room temperature. Then, HOBt (3.4 mg, 0.025 mmol, Mw=135.1 g/mol, 0.03 eq.) was added directly, and the reaction was left to proceed for 10 min before Oregon Green Cadaverine (3.4 mg, 0.0068 mmol, Mw=496.5 g/mol, ρ=0.806 g/ml, 0.009 eq.) was added, the pH of the solution was adjusted to 8.0 with DIEA, and the solution allowed to stir for 48 h at room temperature protected from light. An equal volume of THF was added to the obtained solution, and the product was precipitated out in cold Et_2O and dried under a vacuum. The crude product was dissolved in 1 ml of 1M $NaHCO_3$ and dialyzed against water (Cellulose ester membrane, cut off 0.5-1 kDa, Spectrum®) for 48h; then the solution was freeze-dried. The conjugates were dissolved in water and purified with Sephadex® G25 column and ddH_2O as a mobile phase. The combined fractions were lyophilized to give an orange powder. The OG loading was calculated by fluorescence spectroscopy measurements performed on an FP-6500 spectrofluorimeter (JASCO, Easton, United States), λ_{ex}= 495 nm, λ_{em}= 519 nm, and a calibration curve with OG **(Figure S2.16)**. Global yield: 85- 95 %. OG loadings: 1.5-2.4 %wt.
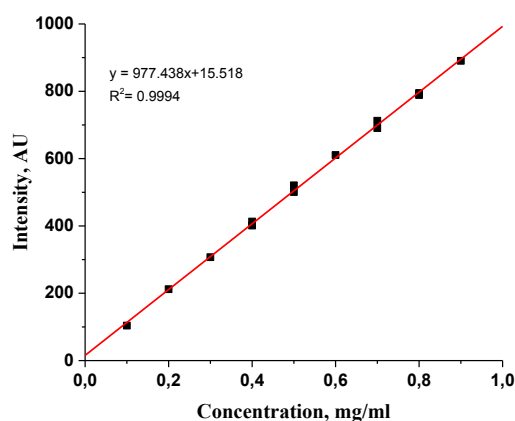
Figure S2.17. Calibration curve used for quantification of OG.
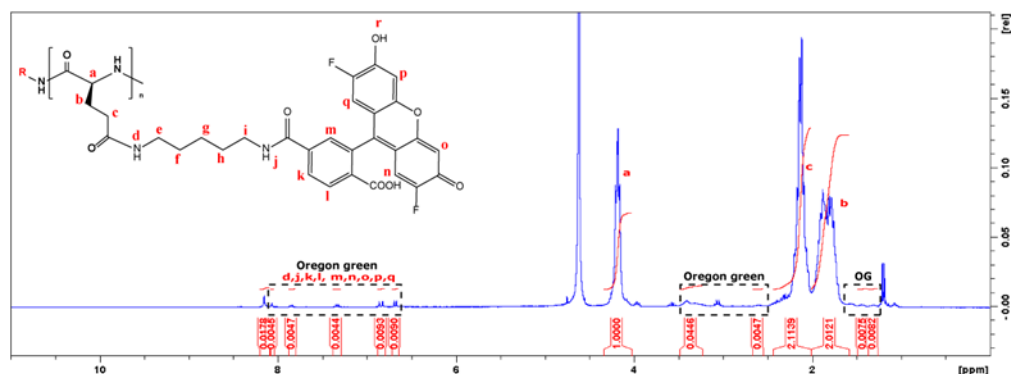
Figure S2.18. **StPGA-OG:** *^{1}H NMR (300 MHz, D$_2$O)*: 8.15 (s, 3H), 8.07 (s, 1H), 7.85 (d, 1H), 7.34 (d, 1H), 6.86 (s, 1H), 6.83 (s, 1H), 6.69 (s, 1H), 6.67 (s, 1H), 4.18 (m, 150H), 3.48-3.23, 2.60, 1.57, 1.45, 1.30 (m, 10H), 2.12 (m, 300H), 1.83 (m, 300H)

SI-2.5. General Procedure for the OL Conjugation

SI-2.5.1 Direct OL conjugation to StPGA via N-terminal site

In a round bottom flask with a stirrer, StPGA-OG (30 mg, 0.20 mmol, Mw=151.1 g/mol (Glu unit), 1eq.) was placed in 3 ml of MilliQ water, added DMTMM Cl (3.1 mg, 0.011 mmol, Mw=276.6 g/mol, 0.055 eq.), the mixture allowed to stir 30 min to activate carboxylic groups. Then, odorranalectin (20 mg, 0.01 mmol, Mw=1945.2 g/mol, 0.05 eq.) was added, the pH of the solution was adjusted to 8.0 with TEA, and the solution was allowed to stir for 48 h at room temperature, protected from light. The crude product was dialyzed against water (Cellulose ester membrane, cut off 3.5-5 kDa, Spectrum®) for 48h, and the solution was freeze-dried. The conjugates were dissolved in water and purified with Sephadex® G25 column and water as a mobile phase. The combined fractions were lyophilized to give a white powder. Global yield 42.9 mg (86 %).

The amount of modification was calculated via amino acid analysis performed by the Scientific and Technological Center at Universitat de Barcelona. First, the lyophilized sample was dissolved in 2 ml of HPLC water. Aliquots of the sample (500 µl), α-aminobutyric acid (2.5 mM solution), and phenol (6M, 1.0 % w/v solution) were mixed and homogenized. Then, 12 M HCl was added to a 6 M HCl (0.3 % w/v phenol) final concentration. Hydrolysis was performed at 110 ^{0}C for 24 h. Finally, the sample was evaporated, resuspended in 1 ml of HPLC water, and filtered. Then, the aliquot of this solution was derivatized with 6-aminoquinolyl-N-hydroxysuccinimidyl carbamate according to the Waters AccQ-Tag method. The derivatized sample was analyzed by HPLC equipped with a UV detector (λ = 254 nm). The peptide concentration was 126.58 nmol/mg sample, and the glutamic acid sample was 3293.68 nmol/mg. The peptide modification was 3.8 %mol (126.58/3293.68=3.84).

Figures S2.19 and S2.20 show the chromatograms of an amino acid standard (0.1 mM) and the hydrolysate sample solution, respectively.
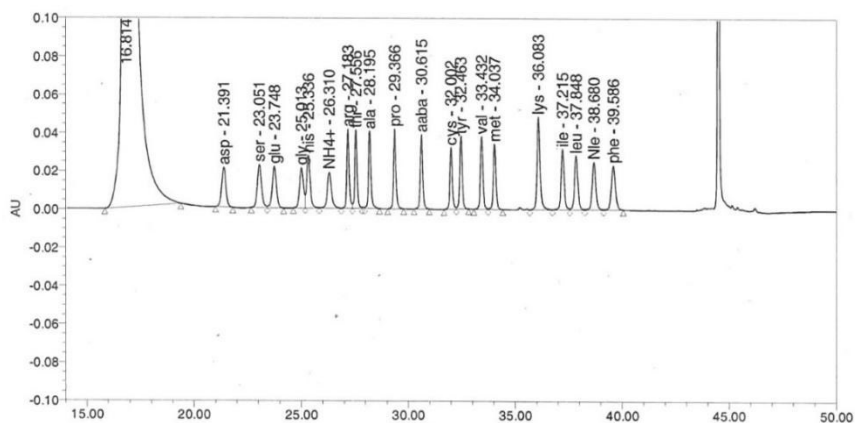
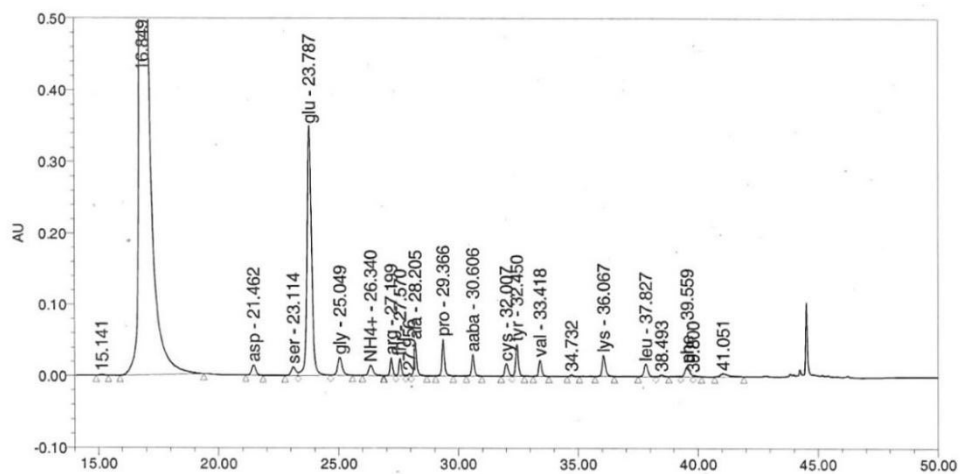**Figure S2.19**. HPLC chromatogram of the standard amino acid solution (0.1 mM)

Figure S2.20. HPLC chromatogram of the hydrolyzed StPGA-odorranalectin sample

SI-2.5.2. Indirect OL conjugation to StPGA via C-terminal site

Figure S2.21 shows the proposed synthetic route for OL conjugation via the C-terminal site.
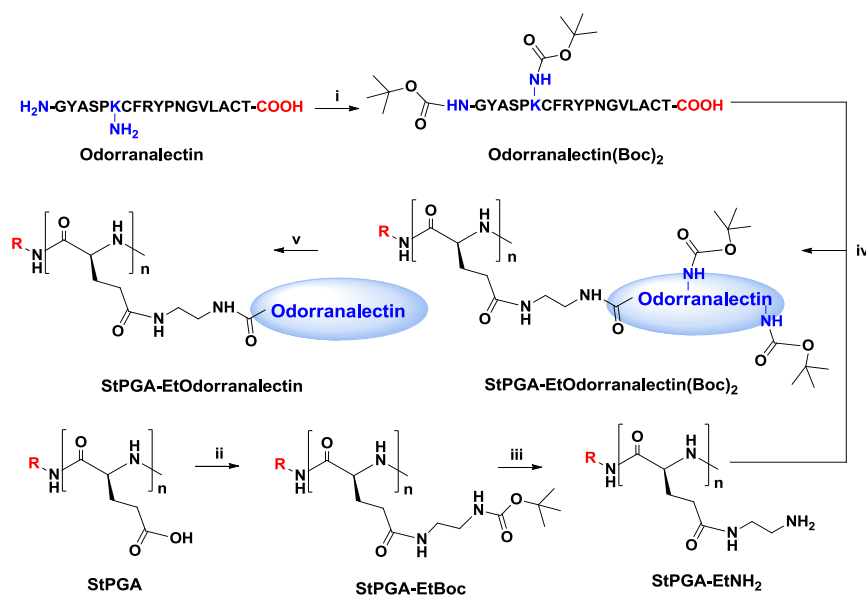
Figure S2.21. Synthesis of StPGA-EtOdorranalectin via C-terminal site: i) Boc$_2$O, THF: H$_2$O (1:1), room temperature, 24 h; ii) N-Boc-1.2-diaminoethane, DMF$_{anh}$, DMTMM BF$_4$; 72 h iii) TFA$_{conc}$, room temperature, 2 h; iv) MeOH: H$_2$O (1:1), DMTMM Cl; 72 h; v) TFA$_{conc}$, room temperature, 2h.

SI-2.5.2.1. Preparation of Odorranalectin (Boc)$_2$

In a round bottom flask with a stirrer, odorranalectin (15 mg, 0.0077 mmol, Mw=1945.2 g/mol, 1 eq.) was placed in 4 ml of water and stirred for 30 min on ice. Then, Boc$_2$O (4 mg, 0.018 mmol, Mw=218.3 g/mol, 2.4 eq.) in 5 ml of THF and NaHCO$_3$ (1.95 mg, 0.023 mmol, Mw=84.0 g/mol, 3.0 eq.) in 1 ml of was added to the mixture, and the reaction was left to proceed for 24 h. The obtained precipitate was centrifuged and washed with water, and the residual THF was evaporated under a vacuum and freeze-dried. The product was dialyzed against water:EtOH (9:1) (Cellulose ester membrane, cut off 3.5-5 kDa, Spectrum®) for 48h, and the solution was freeze-dried.
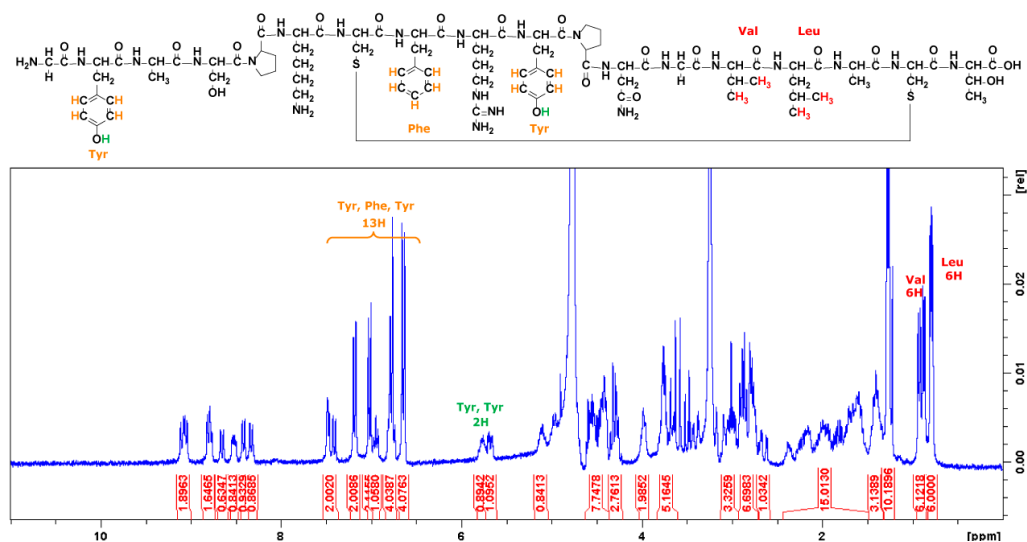
Figure S2.22. **Odorranalectin:** *¹H NMR (300 MHz, MeOD)*: 9.07 (dd, 2H), 8.79 (t, 2H), 8.65 (d, 2H), 8.52 (m, 1H), 8.41 (d, 1H), 8.33 (d, 1H), 7.45 (m, 2H), 7.19 (d, 2H), 7.02 (d, 2H), 6.95 (t, 1H), 6.78 (m, 4H), 6.65 (dd, 4H), 5.77 (m, 1H), 5.68 (dd, 1H), 5.11 (m, 1H), 4.50 (m, 8H), 4.29 (m, 3H), 3.98 (m, 3H), 3.84-3.63 (m, 5H), 3.11-2.95 (m, 3H), 2.91-2.74 (m, 7H), 2.65 (dd, 1H), 2.41-1.53 (m, 15H), 1.41 (m, 3H), 1.27 (m, 10H), 0.90 (dd, 6H), 0.79 (dd, 6H)
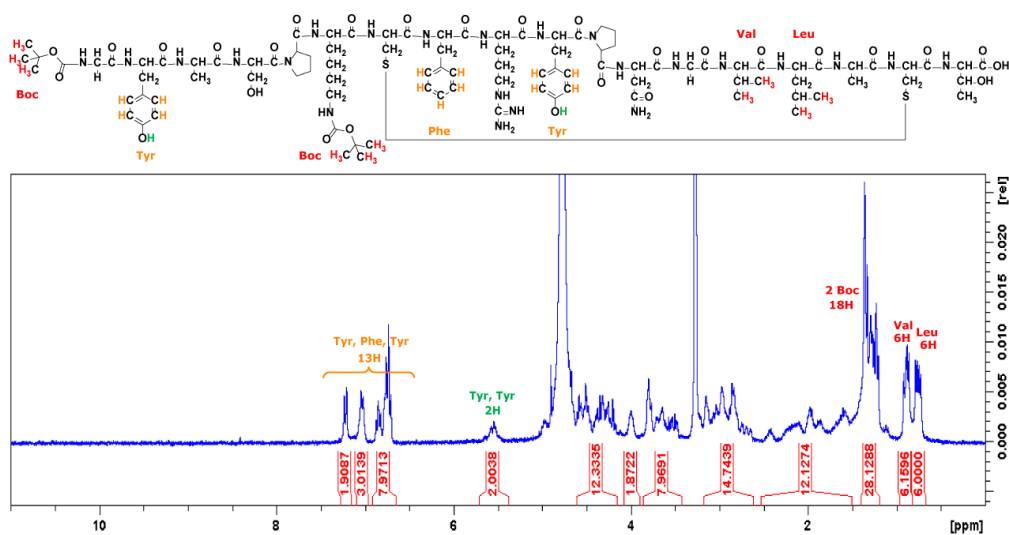
Figure S2.23. **Odorranalectin (Boc)₂:** Product – white powder. Global yield: 17 mg (93 %). *¹H NMR (300 MHz, MeOD: D₂O = 1:9)*: 7.22 (d, 2H), 7.04 (m, 3H), 7.02 (d, 2H), 6.88-6.71 (m, 8H), 5.56 (m, 2H), 4.60-4.19 (m, 12H), 4.29 (m, 3H), 3.82-3.47 (m, 8H), 3.15-2.65 (m, 15H), 2.49-1.51 (m, 12H), 1.40-1.21 (m, 28H), 1.27 (m, 10H), 0.89 (dd, 6H), 0.77 (dd, 6H).

From the peak at 1.40-1.21 ppm, we need to subtract ten protons that overlie from Odorranalectin (Figure S2.21), resulting in eighteen protons corresponding to 2 Boc groups, indicating the complete protection of available amino groups of Odorranalectin.

SI-2.5.2.2. Preparation of StPGA-EtBoc

In a round bottom flask with a stirrer, StPGA H-form (200 mg, 1.55 mmol, Mw=129.1 g/mol (Glu unit), 1eq.) and DMTMM BF$_4$ (71.2 mg, 0.22 mmol, Mw=328.1 g/mol, 0.14 eq.) were dissolved in 15 ml DMF$_{anh}$ under N$_2$, allowed to activate during 30 min, added tert-butyl carbazate (29.8 mg, Mw=160.2 g/mol, 0.12 eq.) in 5 ml of DMF$_{anh}$, adjusted pH to 8 with DIEA, and the reaction was left to proceed for 24 h. An equal volume of THF was added to the obtained solution, and the product was precipitated out in cold Et$_2$O and dried under a vacuum to obtain a white solid. The targeted modification was 12 %mol; the obtained modification was 11 %mol (calculated from *^{1}H NMR* 0.9971/9=11.1) with a reaction efficiency of 93%.
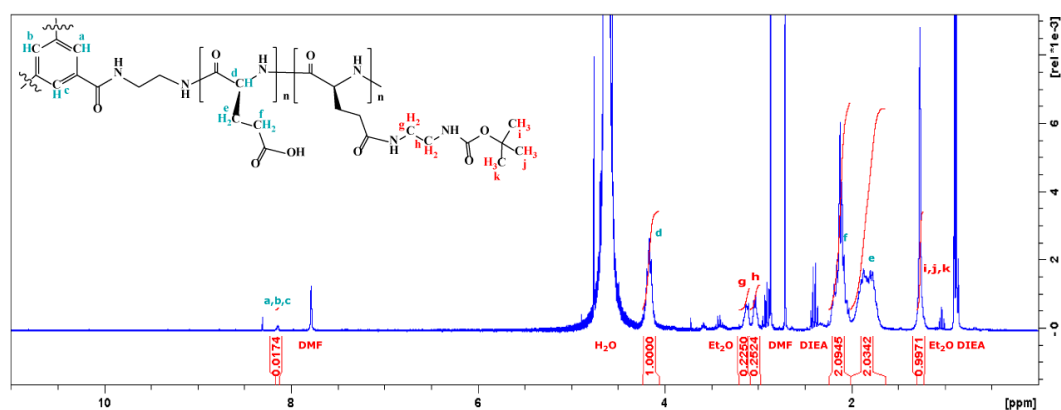
Figure S2.24. **StPGA-EtBoc:** Product – white powder. Global yield: 255 mg (88 %). *^{1}H NMR (300 MHz, D$_2$O)*: 8.15 (s, 1H), 4.16 (m, 150H), 3.12 (m, 2H), 3.03 (m, 2H), 2.11 (m, 300H), 1.82 (m, 300H), 1.27 (s, 9H)

SI-2.5.2.3. Preparation of StPGA-EtNH$_2$

In a round bottom flask with a stirrer, StPGA-EtBoc 250 mg was suspended in 2.5 ml TFA$_{conc}$ and allowed to react for 60 min; check with ninhydrin 2% aq. solution staining was precipitated in cold Et2O, filtered through a glass filter, and dried under a vacuum to obtain a white solid. The completion of the reaction was confirmed with ^{1}H NMR by the disappearance of the signal of the BOC group at 1.27 ppm.

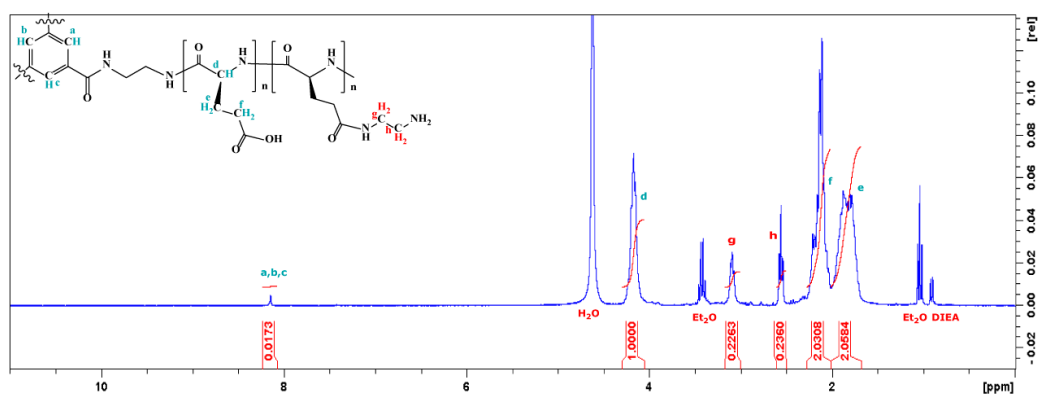**Figure S2.25**. **StPGA-EtNH₂:** Product – white powder. Global yield: 195 mg (85 %). *¹H NMR (300 MHz, D₂O)*: 8.15 (s, 1H), 4.16 (m, 150H), 3.09 (t, 2H), 2.56 (t, 2H), 2.11 (m, 300H), 1.82 (m, 300H).

The obtained white solid was dissolved in 0.5 M aqueous sodium hydrocarbonate solution and dialyzed against water (Cellulose ester membrane, cut off 500-1000Da, Spectrum®) for 48h, and then the solution was freeze-dried.

SI-2.5.2.4. Preparation of StPGA-Odorranalectin (Boc)₂

In a round bottom flask with a stirrer, Odorranalectin(Boc)₂ (14 mg, 0.0065 mmol, Mw=2145.5, 0.02 eq.) and DMTMM Cl (2.2 mg, 0.008 mmol, Mw=276.6 g/mol, 0.025 eq.) were dissolved in 3 ml of MeOH: H₂O (1:1) mixture, allowed to activate during 60 min, added StPGA-EtNH₂ Na-form (40 mg, 0.26 mmol, Mw=151.1 g/mol (Glu unit), 1eq.) adjusted pH to 8 with TEA, and the reaction was left to proceed for 48h at room temperature. The crude product was dialyzed against water:EtOH (9:1) (Cellulose ester membrane, cut off 3.5-5 kDa, Spectrum®) for 48h, and then the solution was freeze-dried. The targeted modification was 2 %mol; the obtained modification was 0.9 %mol (calculated from *¹H NMR* 0.1026/12=0.86) with a reaction efficiency of 43%.
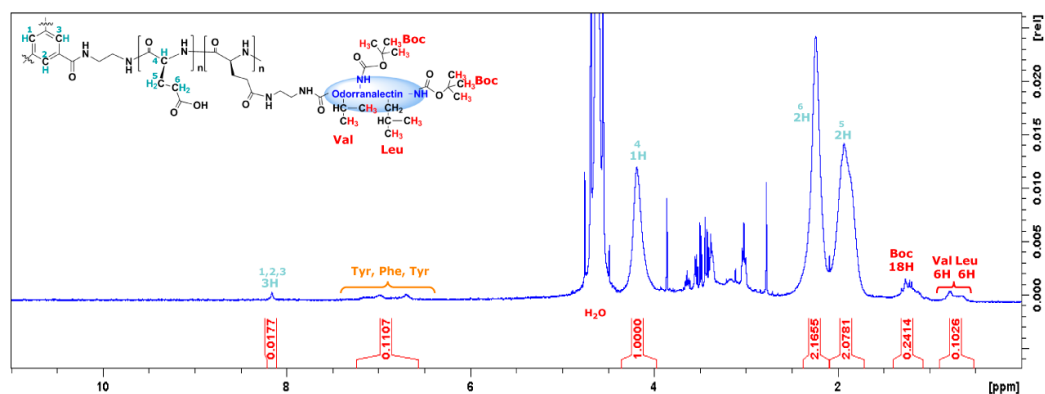
Figure S2.26. **StPGA-Odorranalectin (Boc)₂:** Product – white powder. Global yield: 12 mg (82 %). *¹H NMR (300 MHz, D₂O)*: 8.15 (s, 3H), 7.20-6.65 (m, 13H), 4.18 (m, 150H), 2.26 (m, 300H), 1.94 (m, 300H), 1.23 (m, 28H), 0.80-0.63 (m, 12H).

If we assign a peak at 0.7 ppm to 12 protons from [14]Val and [15]Leu, the aromatic region will be integrated as 13 protons (12x0.111/0.103=12.9), which corresponds to aromatic protons of [2]Tyr, [8]Phe, [10]Tyr. Also, the peak at 1.23 ppm will correspond to 28 protons (12x0.241/0.103=28.1). From this value, we need to subtract ten protons that overlie from Odorranalectin (Figure S2.21), resulting in eighteen protons corresponding to 2 Boc groups, indicating that during the conjugation procedure, there is no Boc group deprotection.

SI-2.5.2.5. Preparation of StPGA-Odorranalectin

In a round bottom flask with a stirrer, StPGA-Odorranalectin (Boc)₂ 12 mg was suspended in 1 ml TFA$_{conc}$ and allowed to react for 60 min; check with ninhydrin 2% aq. The solution staining was precipitated in cold Et₂O, washed three times with 2 ml cold Et₂O, and dried under vacuum to obtain a white solid. The completion of the reaction was confirmed with ¹H NMR by the disappearance of the signal of the BOC group at 1.27 ppm.
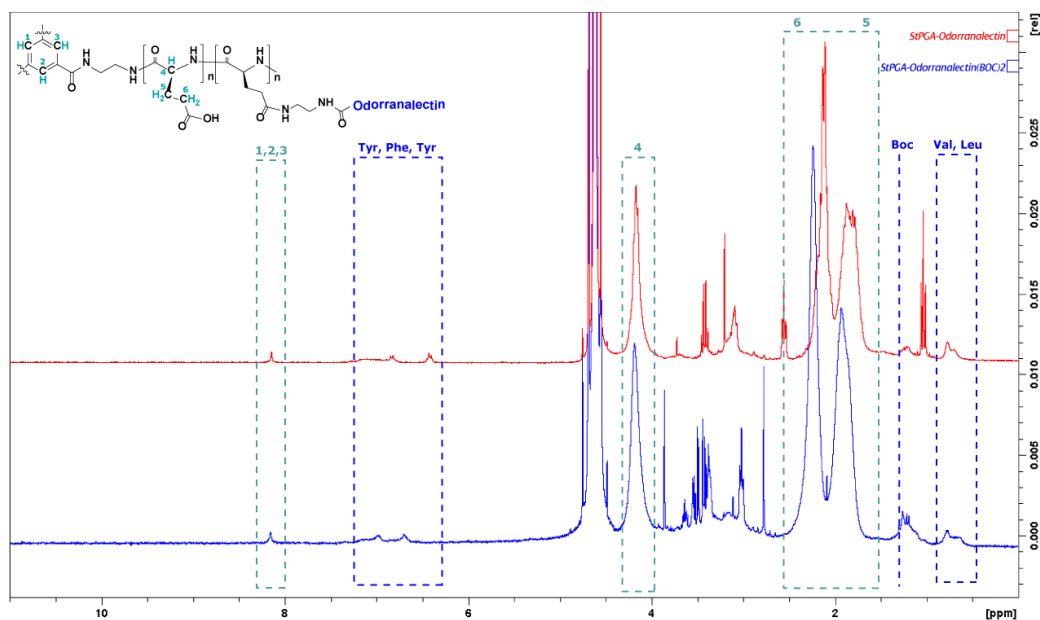
Figure S2.27. **StPGA-Odorranalectin:** Product – white powder. Global yield: 10 mg (84 %). *^{1}H NMR (300 MHz, D$_2$O)*: 8.15 (s, 1H), 4.16 (m, 150H), 3.09 (t, 2H), 2.56 (t, 2H), 2.11 (m, 300H), 1.82 (m, 300H).

The obtained white solid was dissolved in 0.5 M aqueous sodium hydrocarbonate solution and dialyzed against water (Cellulose ester membrane, cut off 500-1000Da, Spectrum®) for 48h, and then the solution was freeze-dried.

SI-2.6. General Procedure for the HA and StPGA Conjugation

SI-2.6.1 Direct HA conjugation via an ester bond

In a round bottom flask with a stirrer, StPGA or PGA100 (50 mg, 0.39 mmol, Mw=129.1 g/mol (Glu unit), 1eq.) was placed in 5 ml of MilliQ water, added NHS (2.2/4.5 mg, 0.019/0.039 mmol, Mw=115.09 g/mol, 0.05/0.10 eq.) and EDC (3.7/7.4 mg, 0.024/0.048 mmol, Mw=155.25 g/mol, 0.05/0.10 eq.), depending on the targeted modification, pH was adjusted till 6.0 with 0.25 M HCl (~100 µl), the mixture allowed to stir for 2 h to activate carboxylic groups. Then, HA 10 kDa or HA80 kDa (7.34/14.68 mg, 0.019/0.039 mmol, Mw=379 g/mol (HA unit), 0.05/0.10 eq.) was added, and the solution was allowed to stir for 48 h at room temperature. The crude product was purified with Vivaspin® (MWCO10KDa, 30kDa, 50 kDa, 100 kDa).
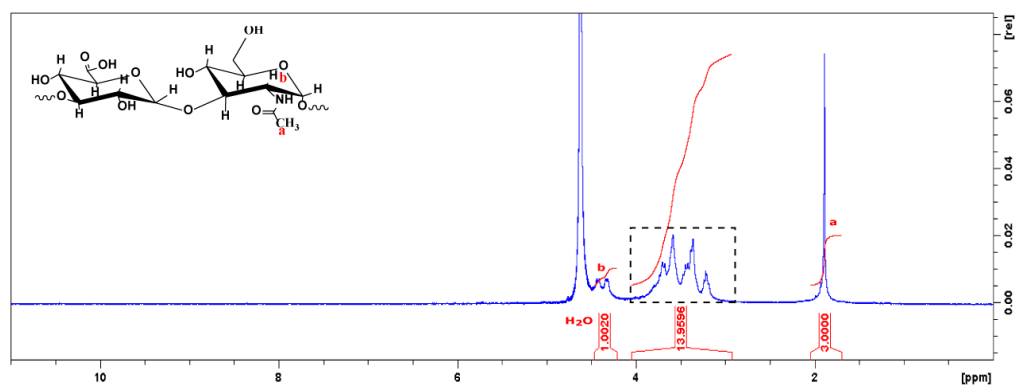
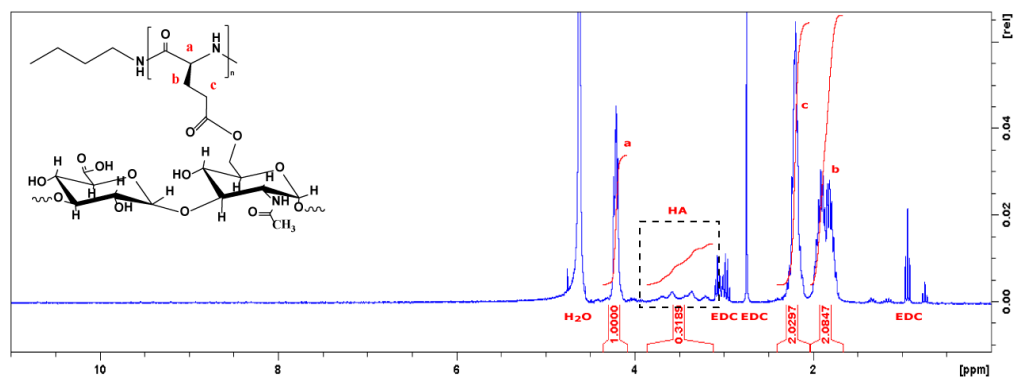**Figure S2.28**. HA80kDa: *¹H NMR (300 MHz, D₂O)*: 4.37 (m, 1H), 3.84-3.14 (m, 14H), 1.89 (m, 3H).

Figure S2.29. LinPGA100-HA80kDa (5 %mol modification ₜₐᵣ𝗀ₑₜₑ𝒹): Product – white powder. Global yield: 14 mg (25%). *¹H NMR (300 MHz, D₂O)*: 4.21 (m, 100H), 3.84-3.16 (m, 13H), 2.20 (m, 200H), 1.85 (m, 200H).
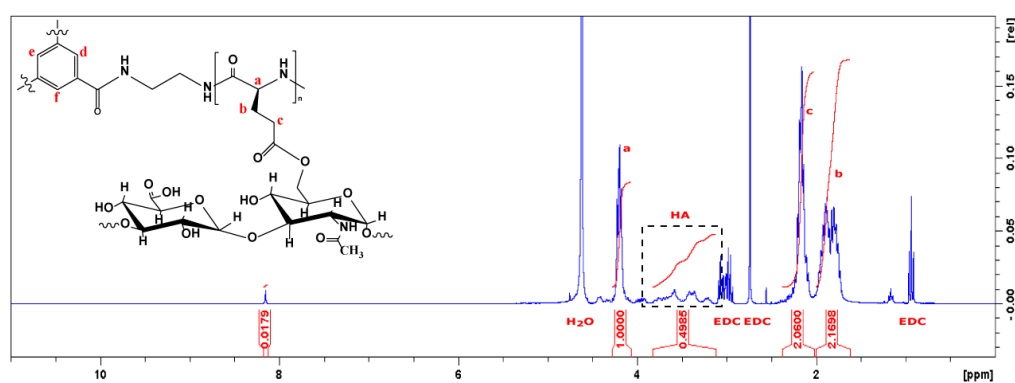

Figure S2.30. StPGA-HA10kDa (5 %mol modification ₜₐᵣ𝗀ₑₜₑ𝒹): Product – white powder. Global yield: 30 mg (45%). *¹H NMR (300 MHz, D₂O)*: 8.15 (s, 3H), 4.21 (m, 150H), 3.84-3.16 (m, 13H), 2.20 (m, 300H), 1.85 (m, 300H).
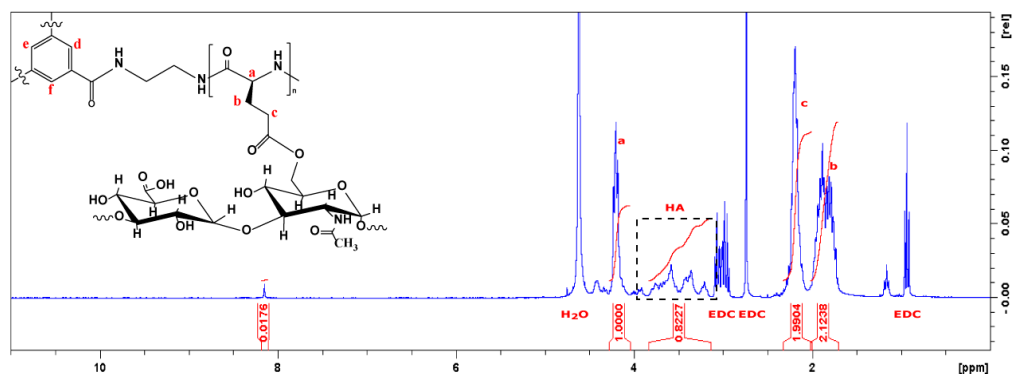
Figure S2.31. StPGA-HA10kDa (10 %mol modification $_{targeted}$): Product – white powder. Global yield: 39 mg (59%). *^{1}H NMR (300 MHz, D$_2$O)*: 8.15 (s, 3H), 4.21 (m, 150H), 3.84-3.16 (m, 13H), 2.20 (m, 300H), 1.85 (m, 300H).
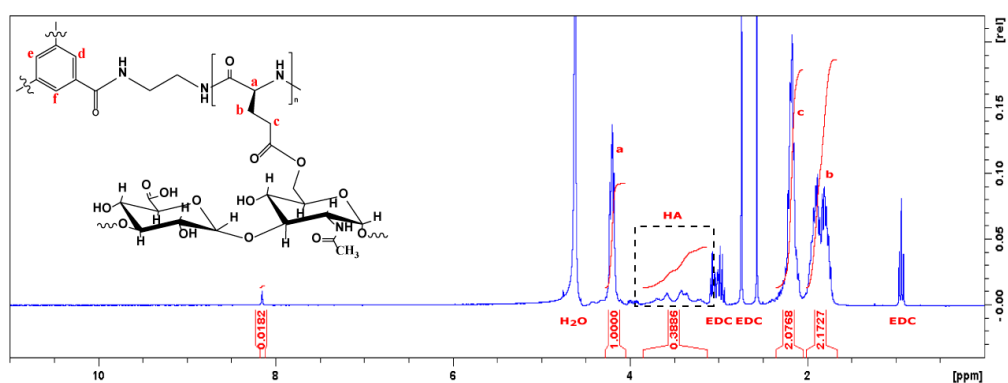

Figure S2.32. StPGA-HA80kDa (5 %mol modification $_{targeted}$): Product – white powder. Global yield: 17 mg (23%). *^{1}H NMR (300 MHz, D$_2$O)*: 8.15 (s, 3H), 4.21 (m, 150H), 3.84-3.16 (m, 13H), 2.20 (m, 300H), 1.85 (m, 300H).
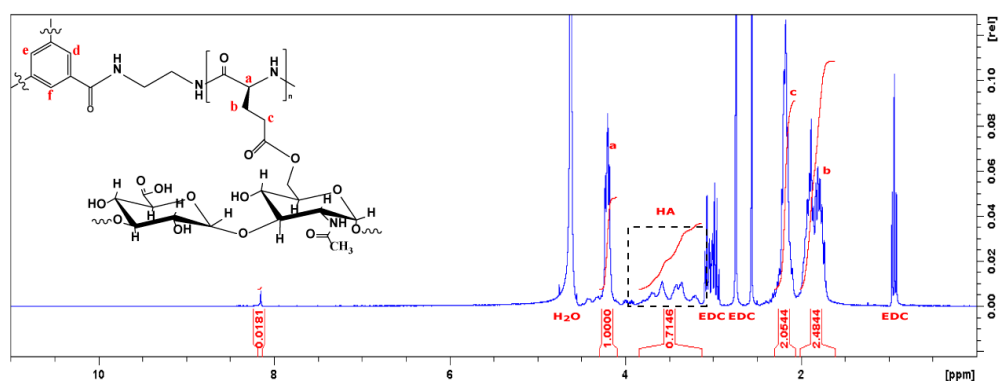

Figure S2.33 StPGA-HA80kDa (10%mol modification $_{targeted}$): Product – white powder. Global yield: 23 mg (31%). *^{1}H NMR (300 MHz, D$_2$O)*: 8.15 (s, 3H), 4.21 (m, 150H), 3.84-3.16 (m, 13H), 2.20 (m, 300H), 1.85 (m, 300H).

Figure S2.34 shows the proposed synthetic route for synthesizing StPGA-HA80kDa polymer via amide coupling.
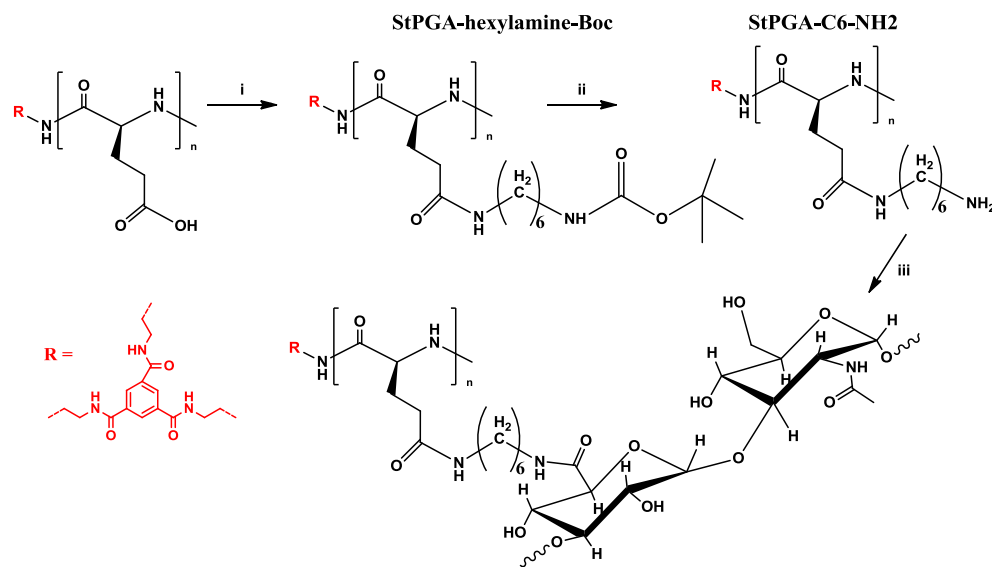

Figure S2.34. Synthesis of StPGA-HA80kDa. i) N-Boc-1.6-hexanediamine HCl, DMF$_{anh}$, DMTMM BF$_4$, DIEA; ii) TFA$_{conc,}$ room temperature, 2 h; iii) HA80kDa, HEPES 10mM, DMTMM Cl, room temperature, 24 h.

SI-2.6.2.1. Preparation of StPGA- hexylamine-Boc

In a round bottom flask with a stirrer, StPGA H-form (200 mg, Mw=129.1 g/mol (Glu unit), 1eq.) and DMTMM BF$_4$ (71.2 mg, Mw=328.1 g/mol, 0.14 eq.) were dissolved in 15 ml DMF$_{anh}$ under N$_2$, allowed to activate during 30 min, added N-Boc-1.6-hexanediamine HCl, (47 mg, Mw=252.8 g/mol, 0.12 eq.) in 5 ml of DMF$_{anh}$, adjusted pH to 8 with DIEA, and the reaction was left to proceed for 48 h. An equal volume of THF was added to the obtained solution, and the StPGA-hexylamine-Boc intermediate was precipitated out in cold Et$_2$O and dried under a vacuum to obtain a white solid. The targeted modification was 12 %mol; the obtained modification was 11.7 %mol (calculated from *^{1}H NMR* 0.4680/4=11.7) with a reaction efficiency of 97%.
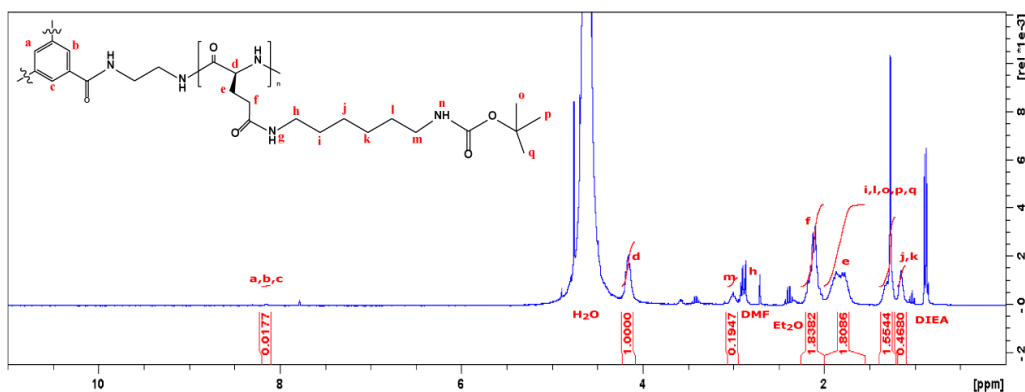
Figure S2.35. St**PGA-hexylamine-Boc:** Product – white powder. Global yield: 212 mg (90 %). *^{1}H NMR (300 MHz, D$_2$O)*: 8.15 (s, 3H), 4.19 (m, 150H), 3.00 (m, 2H), 2.11 (m, 300H), 1.82 (m, 300H), 1.28 (m, 13H), 1.15 (m, 4H)

SI-2.6.2.2. Preparation of StPGA-hexylamine (StPGA-C6-NH$_2$)

In a round bottom flask with a stirrer, StPGA-hexylamine-Boc 212 mg was suspended in 2.5 ml TFA$_{conc}$ and allowed to react for 2 h; the reaction was checked with ninhydrin 2% aq. solution staining was precipitated in cold Et2O, filtered through a glass filter, and dried under a vacuum to obtain a white solid. The completion of the reaction was confirmed with ^{1}H NMR by the disappearance of the signal of the BOC group at 1.27 ppm.
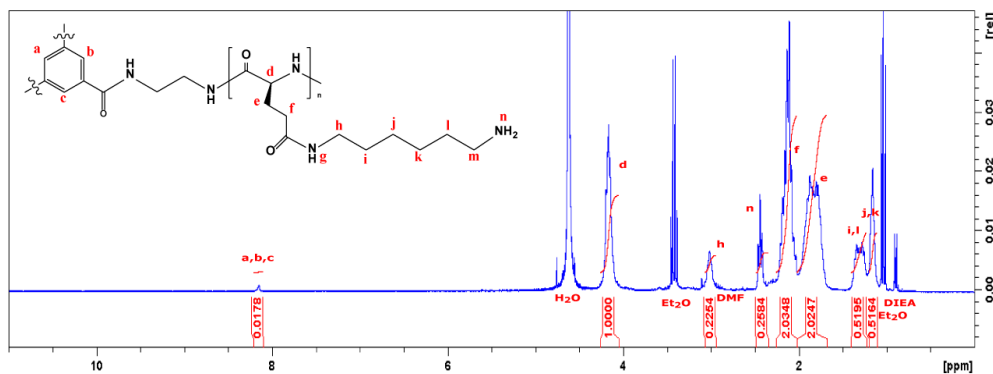

Figure S2.36. St**PGA-C6-NH$_2$:** Product – white powder. Global yield: 186 mg (95 %). *^{1}H NMR (300 MHz, D$_2$O)*: 8.15 (s, 3H), 4.19 (m, 150H), 3.03 (m, 2H), 2.44 (t, 2H), 2.11 (m, 300H), 1.82 (m, 300H), 1.31 (m, 4H), 1.16 (m, 4H).

SI-2.6.2.3. Preparation of StPGA-HA80kDa via amide coupling

In a round bottom flask with a stirrer, HA80kDa (64.1 mg, Mw=379 g/mol (HA unit) 1 eq) were dissolved in 20 ml of 10 mM HEPES buffer and activated for 60 min. Then added

DMTMM Cl (11.7 mg, Mw=276.7 g/mol, 2.5 eq.) and allowed it to activate for 60 min, finally added StPGA-C6-NH$_2$ (25 mg, Mw=177.4 g/mol, 1eq), and the reaction was left to proceed for 24 h. The crude product was purified with Vivaspin® (MWCO100 kDa) and freeze-dried. The obtained ration StPGA: HA 80kDa was 2:1 calculated from the peak at 1.88 ppm that included 3 protons from the alkyl group of HA and 2 protons from the glutamic unit ((3.49-2.00)/3=0.50)
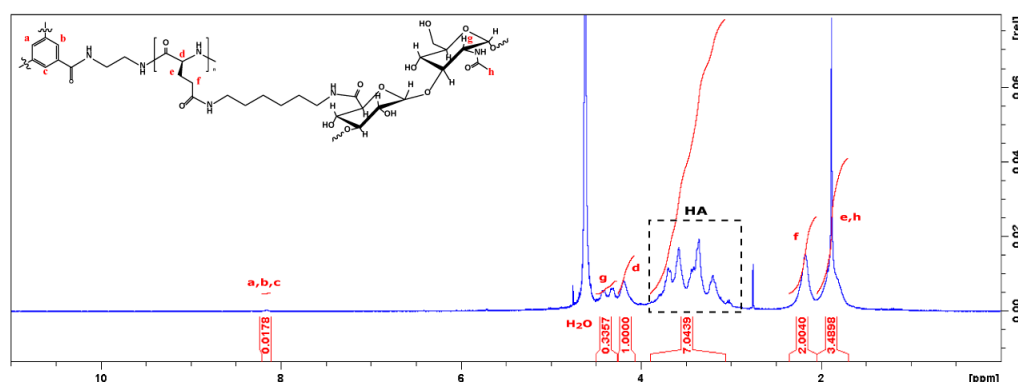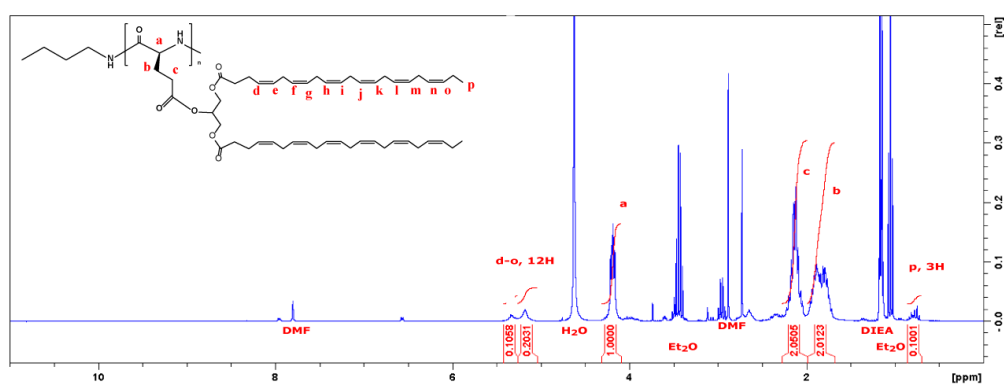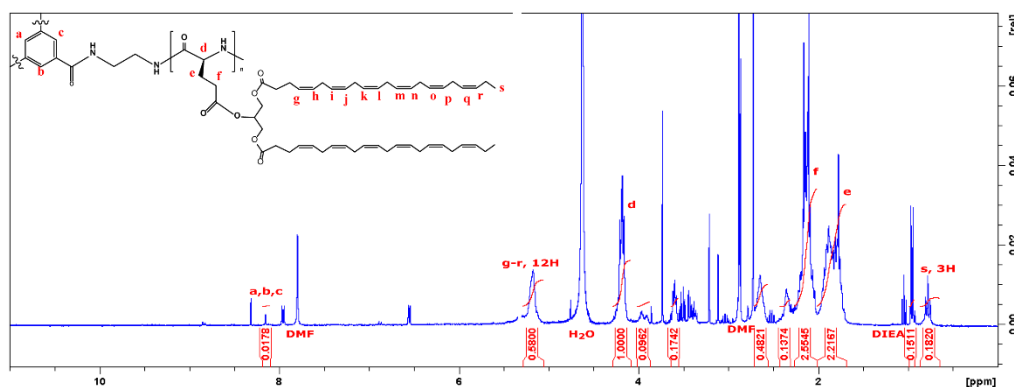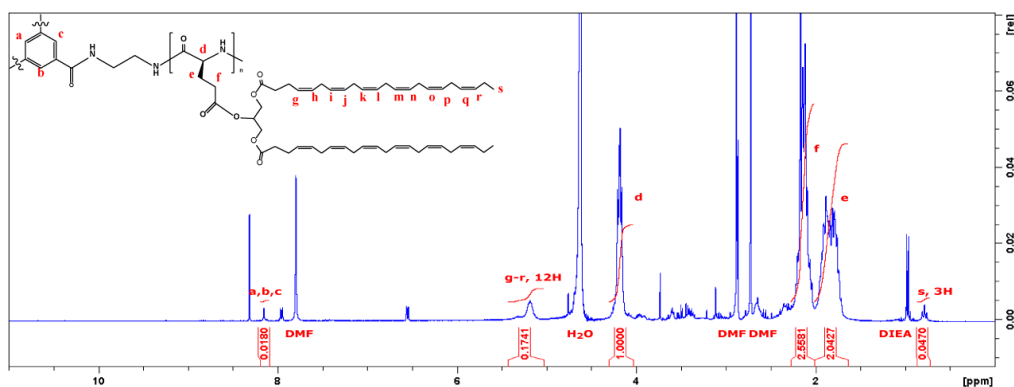

Figure S2.37. StPGA-**HA80kDa (amide coupling):** Product – white powder. Global yield: 74 mg (83 %). *^1H NMR (300 MHz, D$_2$O)*: 8.15 (s, 3H), 4.37 (m, 1H), 4.19 (m, 150H), 3.87-3.07 (m, 13H), 2.18 (m, 300H), 1.88 (m, 300H + s, 3H).

SI-2.7. General Procedure for DHA Conjugation

In a round bottom flask with a stirrer, LinPGA or StPGA H-form (100 mg, Mw=129.1 g/mol (Glu unit), 1eq.) and DMTMM BF$_4$ (57.0/19.0 mg, 0.17/0.058 mmol, Mw=328.1 g/mol) were dissolved in 10 ml of DMF$_{anh}$ under N$_2$, DMAP (2.8/0.94 mg, 0.023/0.008 mmol, Mw=122.17 g/mol) was added in 1 ml of DMF$_{anh}$ and the reaction allowed to activate during 30 min. diDHA (83.0/28.0 mg, 0.12/0.04 mmol, Mw = 713.04 g/mol) dissolved in 1 ml of DMF$_{anh}$ with 0.3 ppm dibutyl hydroxytoluene (BHT, an antioxidant used to prevent free radical-mediated oxidation of DHA) was added to the reaction, pH was adjusted to 8 with DIEA, and the reaction was left to proceed for 48 h protected from light. An equal volume of THF was added to the obtained solution, and the product was precipitated out in cold Et$_2$O and dried under a vacuum to obtain a white solid. The crude product was dissolved in 1 ml of 1M NaHCO$_3$ and dialyzed against water (Cellulose ester membrane, MWCO 3.5-5 kDa, Spectrum®) for 48h, and then the solution was freeze-dried. The conjugate was stored under an inert atmosphere at -20°C, protected from light.

Figure S2.38. StPGA-**DHA (1.5% mol loading):** Product – white powder. Global yield: 74 mg (78 %). *^{1}H NMR (300 MHz, D_2O)*: 8.14 (s, 3H), 5.19 (m, 12H), 4.18 (m, 150H), (m, 300 H), 1.84 (m, 300 H), 0.78 (t, 3H).

Figure S2.39. StPGA-**DHA (6.0% mol loading):** Product – white powder. Global yield: 80 mg (83 %). *^{1}H NMR (300 MHz, D_2O)*: 8.14 (s, 3H), 5.19 (m, 12H), 4.18 (m, 150H), (m, 300 H), 1.84 (m, 300 H), 0.78 (t, 3H).

Figure S2.40. **PGA-DHA (3.3 % mol loading):** Product – white powder. Global yield: 72 mg (75 %). *^{1}H NMR (300 MHz, D_2O)*: 5.19 (m, 12H), 4.18 (m, 150H), (m, 300 H), 1.84 (m, 300 H), 0.78 (t, 3H).

SI-2.8. General Procedure for Preparation of Cu-catalyzed Crosslinked StPGA Systems

Figure S2.20 shows the synthetic route for crosslinked StPGA systems via copper-catalyzed azide-alkyne cycloaddition [9].
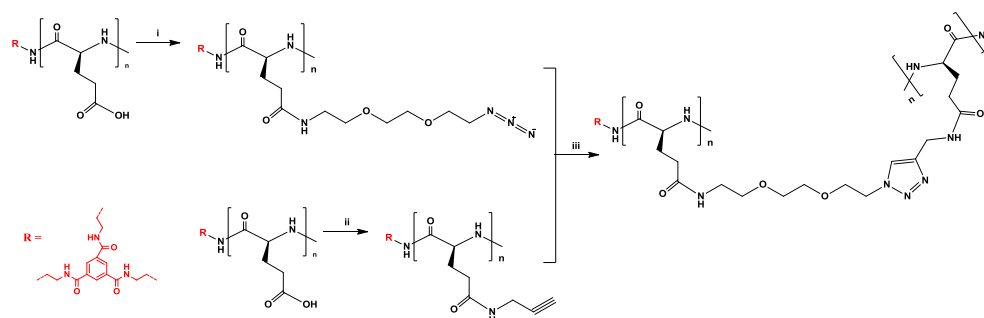

Figure S2.41. Synthesis of crosslinked StPGA systems via copper-catalyzed azide-alkyne cycloaddition: i) Propargylamine, DMTMM BF_4, DIEA, DMF_{anh}, room temperature, N_2 atmosphere; ii) azido-PEG2-amine, DMTMM BF_4, DIEA, DMF_{anh}, room temperature, N_2 atmosphere; iii) ascorbic acid, CuSO4, ddH_2O, three days at 60°C

SI-2.8.1. Preparation of StPGA-propargyl

In a round-bottom flask with a stirrer, StPGA H-form (3.5 g, 27.1 mmol, Mw=129.1 g/mol (Glu unit), 1eq.) and DMTMM BF_4 (1.3 g, 3.96 mmol, Mw=328.1 g/mol, 0.15 eq.) was dissolved in 65 ml of DMF_{anh} under N_2 atmosphere and stirred for 30 min. Then, propargylamine (261 µl, Mw=55 g/mol, ρ=0.86 kg/m^3, 0.15 eq.) in 5 ml of DMF_{anh} was added, pH was adjusted to 8 with DIEA, and the reaction was allowed to proceed for 48 h, at room temperature under N_2 atmosphere. An equal volume of THF was added to the obtained solution, and the product was precipitated out in cold Et_2O and dried under a vacuum to obtain a white solid. The crude product was dissolved in 1 ml of 1M $NaHCO_3$ and dialyzed against water (Cellulose ester membrane, MWCO 0.5-1 kDa, Spectrum®) for 48h, and then the solution was freeze-dried. The targeted modification was 15 %mol, obtained 12.2 % (0.244/2=12.2).
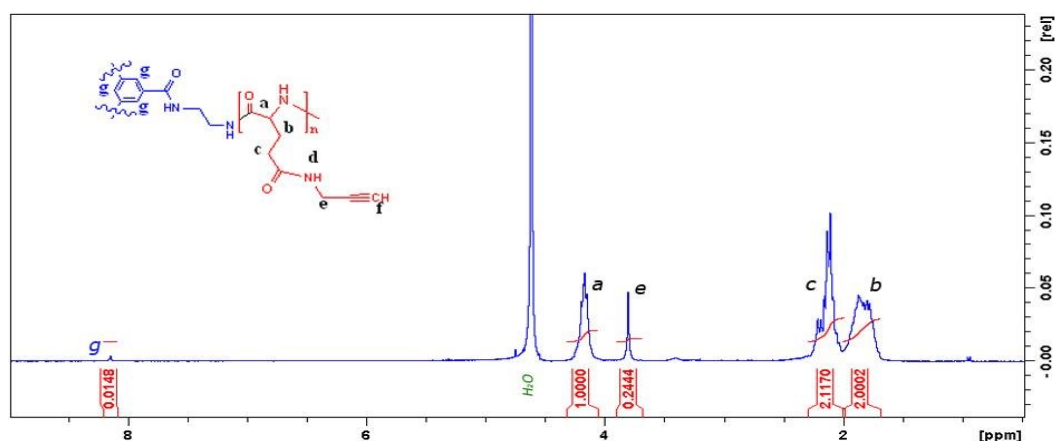
Figure S2.42. St**PGA-propargyl:** Product – white powder. Global yield: 2.5g (69 %). *^{1}H NMR (300 MHz, D$_2$O)*: 8.15 (s, 3H), 4.18 (m, 150H), 3.82 (s, 2H), 2.16 (m, 300 H), 1.84 (m, 300 H).

SI-2.8.2. Preparation of StPGA-azide

In a round-bottom flask with a stirrer, StPGA H-form (3.0 g, 23.1 mmol, Mw=129.1 g/mol (Glu unit), 1eq.) and DMTMMBF$_4$ (0.57 g, 1.74 mmol, Mw=328.1 g/mol, 0.075 eq.) was dissolved in 65 ml DMF$_{anh}$ under N$_2$ atmosphere and stirred for 30 min. Then, azido-PEG2-amine (0.60 g, 1.74 mmol, Mw=346 g/mol, 0.075 eq.) dissolved in 5 ml DMF$_{anh}$, and pH was adjusted to 8 by adding DIEA, and the reaction was allowed to proceed for 48 h, at room temperature under N$_2$ atmosphere. An equal volume of THF was added to the obtained solution, and the product was precipitated out in cold Et$_2$O and dried under a vacuum to obtain a white solid. The crude product was dissolved in 1 ml of 1M NaHCO$_3$ and dialyzed against water (Cellulose ester membrane, MWCO 0.5-1 kDa, Spectrum®) for 48h, and then the solution was freeze-dried. The targeted modification was 7.5 %mol, obtained at 6.76% (0.398+0.134+0.143+0.133)/12=6.73).
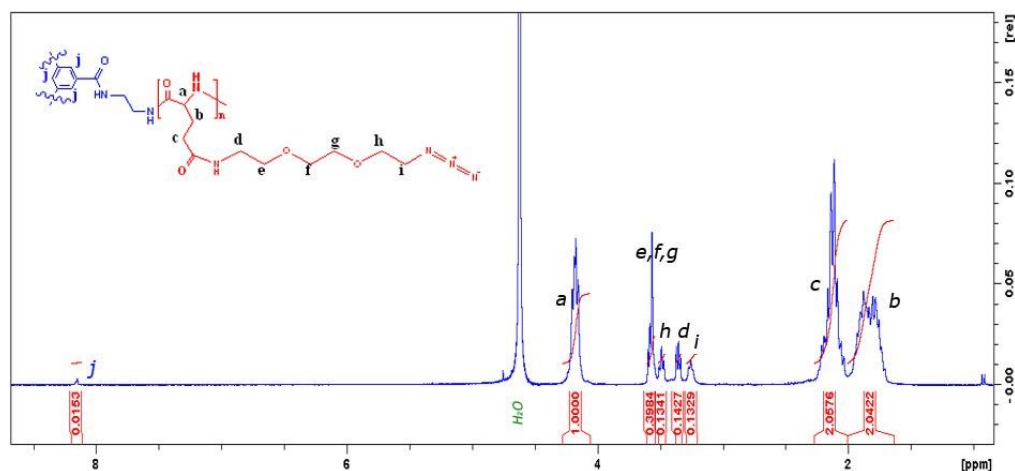
Figure S2.43. St**PGA-azide:** Product – white powder. Global yield: 2.3 g (73 %). *^{1}H NMR (300 MHz, D$_2$O)*: 8.15 (s, 3H), 4.18 (m, 150H), 3.57 (m, 6H), 3.49 (t, 2H), 3.36 (t, 2H), 3.26(t, 2H), 2.12 (m, 300 H), 1.83 (m, 300 H).

SI-2.8.3. Copper-catalyzed azide-alkyne cycloaddition

100 mg of StPGA-propargyl (1eq.) and 100 mg of StPGA-azide (1eq.) were dissolved each in 20 ml ddH2O by sonication 5 min, mixed (final concentration of StPGA-azide and StPGA-propargyl was 2 mg/ml). After two freeze-pump-thaw cycles, ascorbic acid (47.3 mg, Mw=198 g/mol, 5 eq.) in 5 ml ddH2O was added. Again, a freeze-pump-thaw cycle was performed, and CuSO4 (6.0 mg, Mw=160 g/mol, 0.5 eq.) dissolved in 5 ml ddH2O was added. An additional freeze-pump-thaw cycle was performed and allowed to react for three days at 60°C, protected from light. Cu was removed using Quadrasil MTU resins with 20-fold excess resin capacity over 48 h on a shaker. The product was centrifuged, and the supernatant was lyophilized.

The TEM microscopy **(Figure S2.44, A)** confirmed that the particle formation with the size 50-100 nm is in a good correlation with the hydrodynamic size of 87.6 nm obtained with DLS **(Figure S2.44, B)**
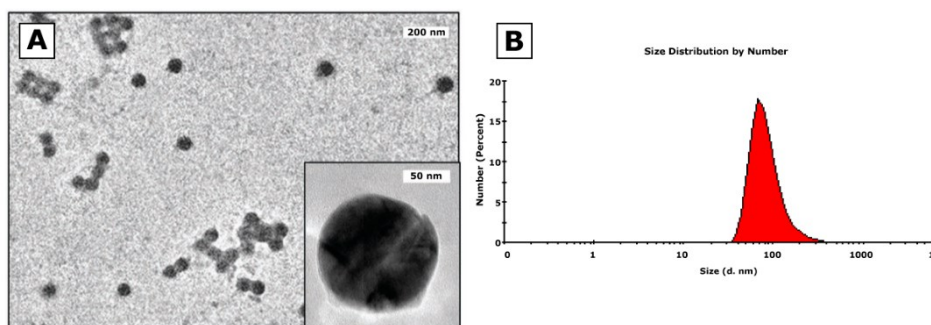
Figure S2.44. StPGA crosslinked particles: **A)** TEM image in water at 1 mg/ml, **B)** DLS data in water at 1 mg/ml.

SI-2.9. General Procedure for Preparation of disulfide crosslinked StPGA Systems

SI-2.9.1. Preparation of StPGA-pyridyl (StPGA-PD)

In a round bottom flask fitted with a stir bar, St-PGA (1 eq.) was dissolved in DMF$_{anh}$ to a concentration of 10 mg/ml under an N_2 atmosphere, DMTMM BF$_4$ (0.075eq) dissolved in DMF$_{anh}$ was added to the reaction mixture, and the reaction was left to proceed under stirring for 30 min. To the obtained solution, pyridyl dithiol cysteamine (0.075eq) dissolved in DMF$_{anh}$ was added to the reaction, pH was adjusted to 8 by adding DIEA, and the reaction was allowed to proceed for 48 h at room temperature under an N_2 atmosphere. The product was precipitated in cold Et$_2$O and dried under a vacuum to obtain a white solid. The crude product was dissolved in water with a minimum of 1M NaHCO3 and purified through Vivaspin® 3KDa with MilliQ water. 1H-NMR determined PD loading by comparing the signals from the PD pyridyl group protons to the PGA α-carbon proton. The targeted modification was 10 %mol.

SI-2.9.2. Nanoprecipitation procedure for obtaining StPGA-SS-CL

In a syringe, a solution of StPGA-PD (20mg, 1.2eq) dissolved in cold MilliQ water (4^{0}C) at 2mg/mL concentration and dithiol (SH-R-SH, 1eq) dissolved in 10mL of cold MilliQ water (4^{0}C) was mixed and poured into cold acetone (400mL) under stirring and left under agitation for 15min. After 4 h at room temperature, b-mercaptoethanol (5eq) was added. The solvent was evaporated under reduced pressure, and the resulting aqueous phase was dialyzed in a Slide-A-Lyzer™ G2 Dialysis Cassette 2K MWC against water for 48h, and then the solution was freeze-dried.

SI-2.10. In vivo Biodistribution Studies

Male BALB/c mice were randomly allocated to the Control group (5 animals) and groups treated with StPGA and StPGA-OL carriers alone and incorporated into HA-CP (with

a minimum of three animals per group). The mice were anesthetized with isoflurane, placed on their back with a slightly elevated head holding in the hand, and the formulations were administered via a micropipette 10 µl into each nostril. After 90 min of post-treatment, the animals were sacrificed, and the main organs (brain, liver, heart, spleen, kidney, lungs, intestine) were harvested and analyzed ex vivo with the in vivo imaging system IVIS® Spectrum System (Perkin Elmer). Two brains were selected for later immunochemistry assays, and Cy5.5 localizations were fixed in 4% PFA and stored at 4°C. First, the two brains were placed into a 50 ml tube in 15 ml of PFA and left overnight under orbital agitation. Then, the brains were washed with 15 ml of dPBS three times, and then 15 ml of 30 % sucrose solution in dPBS was added and left for 48 h at 4°C. Finally, the brains were washed with 15 ml of dPBS three times and left in 0.05% Sodium azide solution in dPBS until fixation. The remaining organs were frozen in liquid Nitrogen for further ex vivo quantification and stored at -80 ^{0}C.

2.5 References

1. Pinheiro, R. G. R., Coutinho, A. J., Pinheiro, M. & Neves, A. R. Nanoparticles for targeted brain drug delivery: What do we know? *Int. J. Mol. Sci.* **22**, (2021).
2. Pardridge, W. M. The blood-brain barrier: bottleneck in brain drug development. *NeuroRx* **2**, 3–14 (2005).
3. Akel, H., Ismail, R. & Csóka, I. Progress and perspectives of brain-targeting lipid-based nanosystems via the nasal route in Alzheimer's disease. *Eur. J. Pharm. Biopharm. Off. J. Arbeitsgemeinschaft fur Pharm. Verfahrenstechnik e.V* **148**, 38–53 (2020).
4. Guo, H. *et al.* Deliver anti-PD-L1 into brain by p-hydroxybenzoic acid to enhance immunotherapeutic effect for glioblastoma. *J. Control. release Off. J. Control. Release Soc.* **320**, 63–72 (2020).
5. Kariolis, M. S. *et al.* Brain delivery of therapeutic proteins using an Fc fragment blood-brain barrier transport vehicle in mice and monkeys. *Sci. Transl. Med.* **12**, (2020).
6. Pardridge, W. M. Blood-Brain Barrier and Delivery of Protein and Gene Therapeutics to Brain. *Front. Aging Neurosci.* **11**, 373 (2019).
7. Terstappen, G. C., Meyer, A. H., Bell, R. D. & Zhang, W. Strategies for delivering therapeutics across the blood–brain barrier. *Nat. Rev. Drug Discov.* **20**, 362–383 (2021).
8. Pardridge, W. M. Why is the global CNS pharmaceutical market so under-penetrated? *Drug discovery today* vol. 7 5–7 (2002).
9. Miao, R., Xia, L.-Y., Chen, H.-H., Huang, H.-H. & Liang, Y. Improved Classification of Blood-Brain-Barrier Drugs Using Deep Learning. *Sci. Rep.* **9**, 8802 (2019).
10. Gribkoff, V. K. & Kaczmarek, L. K. The need for new approaches in CNS drug discovery: Why drugs have failed, and what can be done to improve outcomes. *Neuropharmacology* **120**, 11–19 (2017).
11. Hanif, S. *et al.* Nanomedicine-based immunotherapy for central nervous system disorders. *Acta Pharmacol. Sin.* **41**, 936–953 (2020).
12. Rodriguez-Otormin, F., Duro-Castano, A., Conejos-Sánchez, I. & Vicent, M. J. Envisioning the future of polymer therapeutics for brain disorders. *WIREs Nanomed Nanobiotechnol* **11**,

e1532 (2019).

13. Agrawal, M. *et al.* Nose-to-brain drug delivery: An update on clinical challenges and progress towards approval of anti-Alzheimer drugs. *J. Control. Release* **281**, 139–177 (2018).

14. Gao, X. *et al.* Brain delivery of vasoactive intestinal peptide enhanced with the nanoparticles conjugated with wheat germ agglutinin following intranasal administration. *J. Control. release Off. J. Control. Release Soc.* **121**, 156–167 (2007).

15. Samaridou, E. & Alonso, M. J. Nose-to-brain peptide delivery – The potential of nanotechnology. *Bioorg. Med. Chem.* **26**, 2888–2905 (2018).

16. Binda, A., Murano, C. & Rivolta, I. Innovative Therapies and Nanomedicine Applications for the Treatment of Alzheimer's Disease: A State-of-the-Art (2017-2020). *Int. J. Nanomedicine* **15**, 6113–6135 (2020).

17. Crowe, T. P. & Hsu, W. H. Evaluation of Recent Intranasal Drug Delivery Systems to the Central Nervous System. *Pharmaceutics* **14**, (2022).

18. Singh, R., Brumlik, C., Vaidya, M. & Choudhury, A. A Patent Review on Nanotechnology-Based Nose-to-Brain Drug Delivery. *Recent Pat. Nanotechnol.* **14**, 174–192 (2020).

19. Melnyk, T., Đorđević, S., Conejos-Sánchez, I. & Vicent, M. J. Therapeutic potential of polypeptide-based conjugates: Rational design and analytical tools that can boost clinical translation. *Adv. Drug Deliv. Rev.* **160**, 136–169 (2020).

20. Kenny, A. D. Evaluation of Sodium Poly-α, L-glutamate as a Plasma Expander. *Proc. Soc. Exptl. Biol. Med.* **100**, 778–780 (1959).

21. Mort, J. S. & Buttle, D. J. Molecules in focus Cathepsin B. *Int. J. Biochem. Cell Biol.* **29**, 715–720 (1997).

22. Sun, H. *et al.* Cancer Nanomedicines Based on Synthetic Polypeptides Cancer. *Biomacromolecules* **20**, 4299–4311 (2019).

23. Deming, T. J. Synthesis of Side-Chain Modified Polypeptides. *Chem. Rev.* **116**, 786–808 (2016).

24. Gonz, C. M. & Sarabia-vallejos, M. A. Strategies to Fabricate Polypeptide-Based Structures via Ring-Opening Polymerization of N-Carboxyanhydrides. *Polymers (Basel).* **8**, 551 (2017).

25. Zagorodko, O., Arroyo-Crespo, J. J., Nebot, V. J. & Vicent, M. J. Polypeptide-Based Conjugates as Therapeutics: Opportunities and Challenges. *Macromol. Biosci.* **17**, 1–22 (2017).

26. Rasines Mazo, A. *et al.* Ring opening polymerization of a-amino acids advances in synthesis,, architecture and applications of polypeptides and their hybrids. *Chem. Soc. Rev.* **49**, 4737–4834 (2020).

27. Dimitrov, I. & Schlaad, H. Synthesis of nearly monodisperse polystyrene-polypeptide block copolymers via polymerisation of N-carboxyanhydrides. *Chem. Commun.* **3**, 2944–2945 (2003).

28. Conejos-Sánchez, I., Duro-Castano, A., Birke, A., Barz, M. & Vicent, M. J. A controlled and versatile NCA polymerization method for the synthesis of polypeptides. *Polym. Chem.* **4**, 3182–3186 (2013).

29. Vayaboury, W. & Giani, O. Living Polymerization of a -Amino Acid N -Carboxyanhydrides (NCA) upon Decreasing the Reaction Temperature. *Macromol. Rapid Commun.* **25**, 1221–1224 (2004).

30. Aliferis, T., Iatrou, H. & Hadjichristidis, N. Living Polypeptides. *Biomacromolecules* **5**, 1653–1656 (2004).

31. Deming, T. J. Cobalt and iron initiators for the controlled polymerization of α-amino acid-N-carboxyanhydrides. *Macromolecules* vol. 32 4500–4502 (1999).

32. Deming, T. J. & Curtin, S. A. Chain initiation efficiency in cobalt- and nickel-mediated polypeptide synthesis. *J. Am. Chem. Soc.* **122**, 5710–5717 (2000).

33. Peng, Y. L., Lai, S. L. & Lin, C. C. Preparation of polypeptide via living polymerization of Z-

Lys-NCA initiated by platinum complexes. *Macromolecules* **41**, 3455–3459 (2008).

34. Seidel, S. W. & Deming, T. J. Use of Chiral Ruthenium and Iridium Amido−Sulfonamidate Complexes for Controlled, Enantioselective Polypeptide Synthesis. *Macromolecule* **36**, 969–972 (2003).

35. Using, P. N., Bhaw-luximon, A., Jhurry, D. & Goury, V. Polymerization of γ-Methylglutamate N-Carboxyanhydride Using Al-Schiff's Base Complexes as Initiators. *Macromolecules* **36**, 977–982 (2003).

36. Deming, T. J. Facile synthesis of block copolypeptides of defined architecture. *Nature* **390**, 386–389 (1997).

37. Hadjichristidis, N., Iatrou, H., Pitsikalis, M. & Sakellariou, G. Synthesis of Well-Defined Polypeptide-Based Materials via the Ring-Opening Polymerization of α-Amino Acid. *Chem. Rev.* **109**, 5528–5578 (2009).

38. Walsh, D. J., Hyatt, M. G., Miller, S. A. & Guironnet, D. Recent Trends in Catalytic Polymerizations. *ACS Catal.* **9**, 11153–11188 (2019).

39. Vicent Docón M.j., Duro Castaño, A., Nebot Carda, V. J. WO 2017/025298 A1. 150 (2017).

40. Jiang, J., Zhang, X., Fan, Z. & Du, J. Ring-Opening Polymerization of N‑Carboxyanhydride-Induced Self-Assembly for Fabricating Biodegradable Polymer Vesicles. *ACS Macro Lett.* **8**, 1216–1221 (2019).

41. Nevagi, R. J. *et al.* Polyglutamic acid-trimethyl chitosan-based intranasal peptide nano-vaccine induces potent immune responses against group A streptococcus. *Acta Biomater.* **80**, 278–287 (2018).

42. Noh, Y.-W. *et al.* Polymer Nanomicelles for Efficient Mucus Delivery and Antigen-Specific High Mucosal Immunity. *Angew. Chemie Int. Ed.* **52**, 7684–7689 (2013).

43. Yang, J. *et al.* Poly-γ-glutamic acid/chitosan nanogel greatly enhances the efficacy and heterosubtypic cross-reactivity of H1N1 pandemic influenza vaccine. *Sci. Rep.* **7**, 44839 (2017).

44. Li, J. *et al.* Odorranalectin is a small peptide lectin with potential for drug delivery and targeting. *PLoS One* **3**, 1–10 (2008).

45. Madonna, R. *et al.* Omega-3 fatty acids attenuate constitutive and insulin-induced CD36 expression through a suppression of PPAR α/γ activity in microvascular endothelial cells. *Thromb. Haemost.* **106**, 500–510 (2011).

46. Glatz, J. F. C. & Luiken, J. J. F. P. Dynamic role of the transmembrane glycoprotein CD36 (SR-B2) in cellular fatty acid uptake and utilization. *J. Lipid Res.* **59**, 1084–1093 (2018).

47. Pritchard, K. *et al.* Evaluation of the bioadhesive properties of hyaluronan derivatives: Detachment weight and mucociliary transport rate studies. *Int. J. Pharm.* **129**, 137–145 (1996).

48. Sandri, G. *et al.* Mucoadhesive and penetration enhancement properties of three grades of hyaluronic acid using porcine buccal and vaginal tissue, Caco-2 cell lines, and rat jejunum. *J. Pharm. Pharmacol.* **56**, 1083–1090 (2004).

49. Rydén, L. & Edman, P. Effect of polymers and microspheres on the nasal absorption of insulin in rats. *Int. J. Pharm.* **83**, 1–10 (1992).

50. Morimoto, K. *et al.* Effects of viscous hyaluronate-sodium solutions on the nasal absorption of vasopressin and an analogue. *Pharm. Res.* **8**, 471–474 (1991).

51. Dhuria, S. V, Hanson, L. R. & Frey, W. H. 2nd. Intranasal delivery to the central nervous system: mechanisms and experimental considerations. *J. Pharm. Sci.* **99**, 1654–1673 (2010).

52. Borbás, E. *et al.* In vitro dissolution–permeation evaluation of an electrospun cyclodextrin-based formulation of aripiprazole using μFlux™. *Int. J. Pharm.* **491**, 180–189 (2015).

53. Clarke, L. L. A guide to Ussing chamber studies of mouse intestine. *Am. J. Physiol. Gastrointest. Liver Physiol.* **296**, G1151-66 (2009).

54. Bakand, S., Winder, C. & Hayes, A. Comparative in vitro cytotoxicity assessment of selected gaseous compounds in human alveolar epithelial cells. *Toxicol. Vitr.* **21**, 1341–1347 (2007).

55. Xiang, J., Fang, X. & Li, X. Transbuccal delivery of 2′,3′-dideoxycytidine: in vitro permeation study and histological investigation. *Int. J. Pharm.* **231**, 57–66 (2002).

56. Fallacara, A. *et al.* In vitro characterization of physico-chemical properties, cytotoxicity, bioactivity of urea-crosslinked hyaluronic acid and sodium ascorbyl phosphate nasal powder formulation. *Int. J. Pharm.* **558**, 341–350 (2019).

57. Pund, S., Rasve, G. & Borade, G. Ex vivo permeation characteristics of venlafaxine through sheep nasal mucosa. *Eur. J. Pharm. Sci.* **48**, 195–201 (2013).

58. Bartos, C., Szabó-Révész, P., Horváth, T., Varga, P. & Ambrus, R. Comparison of Modern In Vitro Permeability Methods with the Aim of Investigation Nasal Dosage Forms. *Pharmaceutics* **13**, 846 (2021).

59. Gieszinger, P., Kiss, T., Szabó-Révész, P. & Ambrus, R. The Development of an In Vitro Horizontal Diffusion Cell to Monitor Nasal Powder Penetration Inline. *Pharmaceutics* vol. 13 (2021).

60. Werner, U. & Kissel, T. In-vitro cell culture models of the nasal epithelium: a comparative histochemical investigation of their suitability for drug transport studies. *Pharm. Res.* **13**, 978–988 (1996).

61. Schmidt, M. C., Peter, H., Lang, S. R., Ditzinger, G. & Merkle, H. P. In vitro cell models to study nasal mucosal permeability and metabolism. *Adv. Drug Deliv. Rev.* **29**, 51–79 (1998).

62. Jetten, A. M., Yankaskas, J. R., Stutts, M. J., Willumsen, N. J. & Boucher, R. C. Persistence of abnormal chloride conductance regulation in transformed cystic fibrosis epithelia. *Science* **244**, 1472–1475 (1989).

63. Jefferson, D. M. *et al.* Expression of normal and cystic fibrosis phenotypes by continuous airway epithelial cell lines. *Am. J. Physiol.* **259**, L496-505 (1990).

64. Scholte, B. J. *et al.* Immortalization of nasal polyp epithelial cells from cystic fibrosis patients. *Exp. Cell Res.* **182**, 559–571 (1989).

65. Buchanan, J. A. *et al.* Transformed sweat gland and nasal epithelial cell lines from control and cystic fibrosis individuals. *J. Cell Sci.* **95 (Pt 1)**, 109–123 (1990).

66. Forbes, B. & Ehrhardt, C. Human respiratory epithelial cell culture for drug delivery applications. *Eur. J. Pharm. Biopharm. Off. J. Arbeitsgemeinschaft fur Pharm. Verfahrenstechnik e.V* **60**, 193–205 (2005).

67. Charles, D. D. *et al.* Development of a Novel ex vivo Nasal Epithelial Cell Model Supporting Colonization With Human Nasal Microbiota. *Front. Cell. Infect. Microbiol.* **9**, 165 (2019).

68. Kreft, M. E. *et al.* The Characterization of the Human Nasal Epithelial Cell Line RPMI 2650 Under Different Culture Conditions and Their Optimization for an Appropriate in vitro Nasal Model. *Pharm. Res.* **32**, 665–679 (2015).

69. Borchardt, R. T., Smith, P. L. & Wilson, G. *Models for assessing drug absorption and metabolism. Pharmaceutical biotechnology (USA)* vol. v. 8 (Plenum Press, 1996).

70. Costa, C. P. *et al.* In Vitro Studies on Nasal Formulations of Nanostructured Lipid Carriers (NLC) and Solid Lipid Nanoparticles (SLN). *Pharmaceuticals* **14**, (2021).

71. Pandey, P., Cabot, P. J., Wallwork, B., Panizza, B. J. & Parekh, H. S. Formulation, functional evaluation and ex vivo performance of thermoresponsive soluble gels - A platform for therapeutic delivery to mucosal sinus tissue. *Eur. J. Pharm. Sci.* **96**, 499—507 (2017).

72. Carstens, S., Danielsen, G., Guldhammer, B. & Frederiksen, O. Transport of Insulin Across Rabbit Nasal Mucosa In Vitro Induced by Didecanoyl-L-α-Phosphatidylcholine. *Diabetes* **42**, 1032–1040 (1993).

73. Colombo, G. *et al.* Nasal powders of thalidomide for local treatment of nose bleeding in persons affected by hereditary hemorrhagic telangiectasia. *Int. J. Pharm.* **514**, 229–237 (2016).

74. Naik, A. & Nair, H. Formulation and evaluation of thermosensitive biogels for nose to brain delivery of doxepin. *Biomed Res. Int.* **2014**, 847547 (2014).

75. Majithiya, R. J., Ghosh, P. K., Umrethia, M. L. & Murthy, R. S. R. Thermoreversible-

mucoadhesive Gel for nasal delivery of sumatriptan. *AAPS PharmSciTech* **7**, E80–E86 (2006).

76. Basu, S. & Maity, S. Preparation and characterisation of mucoadhesive nasal gel of venlafaxine hydrochloride for treatment of anxiety disorders. *Indian J. Pharm. Sci.* **74**, 428–433 (2012).

77. Fahmy, U. A. *et al.* Intranasal Niosomal In Situ Gel as a Promising Approach for Enhancing Flibanserin Bioavailability and Brain Delivery: In Vitro Optimization and Ex Vivo/In Vivo Evaluation. *Pharmaceutics* **12**, (2020).

78. Schmidt, M. C., Simmen, D., Hilbe, M. & Boderke, P. Validation of Excised Bovine Nasal Mucosa as In Vitro Model to Study Drug Transport and Metabolic Pathways in Nasal Epithelium. **89**, 396–407 (2000).

79. Antunes Viegas, D. *et al.* Development and application of an ex vivo fosphenytoin nasal bioconversion/permeability evaluation method. *Eur. J. Pharm. Sci. Off. J. Eur. Fed. Pharm. Sci.* **89**, 61–72 (2016).

80. Salade, L., Wauthoz, N., Goole, J. & Amighi, K. How to characterize a nasal product. The state of the art of in vitro and ex vivo specific methods. *Int. J. Pharm.* **561**, 47–65 (2019).

81. Duro-Castano, A. *et al.* Well-Defined Star-Shaped Polyglutamates with Improved Pharmacokinetic Profiles As Excellent Candidates for Biomedical Applications. *Mol. Pharm.* **12**, 3639–3649 (2015).

82. Srinivasan, B. *et al.* TEER measurement techniques for in vitro barrier model systems. *J. Lab. Autom.* **20**, 107–126 (2015).

83. Gerber, W. *et al.* Comparison of RPMI 2650 cell layers and excised sheep nasal epithelial tissues in terms of nasal drug delivery and immunocytochemistry properties. *J. Pharmacol. Toxicol. Methods* **113**, 107131 (2022).

84. Duro-Castano, A. *et al.* Capturing "Extraordinary" Soft-Assembled Charge-Like Polypeptides as a Strategy for Nanocarrier Design. *Adv. Mater.* **29**, 1702888 (2017).

85. Kelly, S. M., Jess, T. J. & Price, N. C. How to study proteins by circular dichroism. *Biochim. Biophys. Acta* **1751**, 119–139 (2005).

86. Moura, L. I. F., Malfanti, A., Peres, C., Matos, A. I. & Florindo, H. F. Functionalized branched polymers : promising immunomodulatory tools for the treatment of cancer and immune disorders. *Mater. Horizons* **6**, 1956–1973 (2019).

87. van der Poll, D. G. *et al.* Design, synthesis, and biological evaluation of a robust, biodegradable dendrimer. *Bioconjug. Chem.* **21**, 764–773 (2010).

88. Peumans, W. J. & Van Damme, E. J. M. Lectins as plant defense proteins. *Plant Physiol.* **109**, 347–352 (1995).

89. Balin, B. J., Broadwell, R. D., Salcman, M. & El-Kalliny, M. Avenues for entry of peripherally administered protein to the central nervous system in mouse, rat, and squirrel monkey. *J. Comp. Neurol.* **251**, 260–280 (1986).

90. Thorne, R. G., Emory, C. R., Ala, T. A. & Frey, W. H. Quantitative analysis of the olfactory pathway for drug delivery to the brain. *Brain Res.* **692**, 278–282 (1995).

91. Lü, S., Liang, S. & Gu, X. Three-dimensional structure of selenocosmia huwena lectin-I (SHL-I) from the venom of the spider selenocosmia huwena by 2D-NMR. *Protein Journal* vol. 18 609–617 (1999).

92. Wang, W., Cole, A. M., Hong, T., Waring, A. J. & Lehrer, R. I. Retrocyclin, an Antiretroviral θ-Defensin, Is a Lectin. *J. Immunol.* **170**, 4708–4716 (2003).

93. Wen, Z. *et al.* Brain targeting and toxicity study of odorranalectin-conjugated nanoparticles following intranasal administration. *Drug Deliv.* **18**, 555–561 (2011).

94. Wen, Z. *et al.* Odorranalectin-conjugated nanoparticles: Preparation, brain delivery and pharmacodynamic study on Parkinson's disease following intranasal administration. *J. Control. Release* **151**, 131–138 (2011).

95. Wu, H. *et al.* A novel small Odorranalectin-bearing cubosomes: Preparation, brain delivery

and pharmacodynamic study on amyloid-β 25-35-treated rats following intranasal administration. *Eur. J. Pharm. Biopharm.* **80**, 368–378 (2012).

96. Yang, X. *et al.* Intranasal Delivery of BACE1 siRNA and Rapamycin by Dual Targets Modified Nanoparticles for Alzheimer's Disease Therapy. *Small* **18**, e2203182 (2022).

97. Chen, J. *et al.* Solanum tuberosum lectin-conjugated PLGA nanoparticles for nose-to-brain delivery: In vivo and in vitro evaluations. *J. Drug Target.* **20**, 174–184 (2012).

98. Piazza, J. *et al.* Haloperidol-loaded intranasally administered lectin functionalized poly(ethylene glycol)-block-poly(D,L)-lactic-co-glycolic acid (PEG-PLGA) nanoparticles for the treatment of schizophrenia. *Eur. J. Pharm. Biopharm.* **87**, 30–39 (2014).

99. Gao, X. *et al.* UEA I-bearing nanoparticles for brain delivery following intranasal administration. *Int. J. Pharm.* **340**, 207–215 (2007).

100. Lundh, B., Brockstedt, U. & Kristensson, K. Lectin-binding pattern of neuroepithelial and respiratory epithelial cells in the mouse nasal cavity. *Histochem. J.* **21**, 33–43 (1989).

101. Kobayashi, D., Naruse, N., Denda, M., Shigenaga, A. & Otaka, A. Deprotection of: S - acetamidomethyl cysteine with copper(ii) and 1,2-aminothiols under aerobic conditions. *Org. Biomol. Chem.* **18**, 8638–8645 (2020).

102. Deepak M. Shendage, Fröhlich, R. & Haufe, G. Highly Efficient Stereoconservative Amidation and Deamidation of α-Amino Acids. *Org. Lett.* **6**, 3675–3678 (2004).

103. Huang, G. & Huang, H. Hyaluronic acid-based biopharmaceutical delivery and tumor-targeted drug delivery system. *J. Control. Release* **278**, 122–126 (2018).

104. Clementino, A. R. *et al.* Structure and Fate of Nanoparticles Designed for the Nasal Delivery of Poorly Soluble Drugs. *Mol. Pharm.* **18**, 3132–3146 (2021).

105. Arpicco, S., De Rosa, G. & Fattal, E. Lipid-Based Nanovectors for Targeting of CD44-Overexpressing Tumor Cells. *J. Drug Deliv.* **2013**, 860780 (2013).

106. Oyarzun-Ampuero, F. A., Rivera-Rodríguez, G. R., Alonso, M. J. & Torres, D. Hyaluronan nanocapsules as a new vehicle for intracellular drug delivery. *Eur. J. Pharm. Sci. Off. J. Eur. Fed. Pharm. Sci.* **49**, 483–490 (2013).

107. Dondeti, P., Zia, H. & Needham, T. E. Bioadhesive and formulation parameters affecting nasal absorption. *Int. J. Pharm.* **127**, 115–133 (1996).

108. Washington, N. *et al.* Determination of baseline human nasal pH and the effect of intranasally administered buffers. *Int. J. Pharm.* **198**, 139–146 (2000).

109. Mallick, R., Basak, S. & Duttaroy, A. K. Docosahexaenoic acid,22:6n-3: Its roles in the structure and function of the brain. *Int. J. Dev. Neurosci. Off. J. Int. Soc. Dev. Neurosci.* **79**, 21–31 (2019).

110. Shinde, R. L., Bharkad, G. P. & Devarajan, P. V. Intranasal microemulsion for targeted nose to brain delivery in neurocysticercosis : Role of docosahexaenoic acid. *Eur. J. Pharm. Biopharm.* **96**, 363–379 (2015).

111. Madane, R. G. & Mahajan, H. S. Curcumin-loaded nanostructured lipid carriers (NLCs) for nasal administration: design, characterization, and in vivo study. *Drug Deliv.* **23**, 1326–1334 (2016).

112. Zussy, C. *et al.* Intranasal Administration of Nanovectorized Docosahexaenoic Acid (DHA) Improves Cognitive Function in Two Complementary Mouse Models of Alzheimer's Disease. *Antioxidants (Basel, Switzerland)* **11**, (2022).

113. Cardoso, C. R. B., Souza, M. A., Ferro, E. A. V., Favoreto, S. J. & Pena, J. D. O. Influence of topical administration of n-3 and n-6 essential and n-9 nonessential fatty acids on the healing of cutaneous wounds. *Wound repair Regen. Off. Publ. Wound Heal. Soc. [and] Eur. Tissue Repair Soc.* **12**, 235–243 (2004).

114. Lu, Y., Tian, H. & Hong, S. Novel 14,21-dihydroxy-docosahexaenoic acids: structures, formation pathways, and enhancement of wound healing. *J. Lipid Res.* **51**, 923–932 (2010).

115. Tejedor, S. *et al.* Polymer Conjugation of Docosahexaenoic Acid Potentiates Cardioprotective

Therapy in Preclinical Models of Myocardial Ischemia/Reperfusion Injury. *Adv. Healthc. Mater.* **10**, e2002121 (2021).

116. Fortuna, A., Alves, G., Serralheiro, A., Sousa, J. & Falcão, A. Intranasal delivery of systemic-acting drugs: Small-molecules and biomacromolecules. *Eur. J. Pharm. Biopharm.* **88**, 8–27 (2014).

117. Ozsoy, Y., Gungor, S. & Cevher, E. Nasal Delivery of High Molecular Weight Drugs. *Molecules* **14**, 3754–3779 (2009).

118. Khunmanee, S., Jeong, Y. & Park, H. Crosslinking method of hyaluronic-based hydrogel for biomedical applications. *J. Tissue Eng.* **8**, 2041731417726464 (2017).

119. Tsuchikama, K. & An, Z. Antibody-drug conjugates: recent advances in conjugation and linker chemistries. *Protein Cell* **9**, 33–46 (2018).

120. van der Vlies, A. J., O'Neil, C. P., Hasegawa, U., Hammond, N. & Hubbell, J. A. Synthesis of Pyridyl Disulfide-Functionalized Nanoparticles for Conjugating Thiol-Containing Small Molecules, Peptides, and Proteins. *Bioconjug. Chem.* **21**, 653–662 (2010).

121. Leitner, V. M., Walker, G. F. & Bernkop-Schnürch, A. Thiolated polymers: evidence for the formation of disulphide bonds with mucus glycoproteins. *Eur. J. Pharm. Biopharm. Off. J. Arbeitsgemeinschaft fur Pharm. Verfahrenstechnik e.V* **56**, 207–214 (2003).

122. Hetényi, G., Griesser, J., Nardin, I. & Bernkop-Schnürch, A. Combination of SEDDS and Preactivated Thiomer Technology: Incorporation of a Preactivated Thiolated Amphiphilic Polymer into Self-Emulsifying Delivery Systems. *Pharm. Res.* **34**, 1171–1179 (2017).

123. Bernkop-Schnürch, A. Thiomers: A new generation of mucoadhesive polymers. *Adv. Drug Deliv. Rev.* **57**, 1569–1582 (2005).

124. Docón, M. J. V., Carda, V. J. N., Bolumar, D. M. & England, R. M. WO/2019/020344 Cross Polymers Composed Of Polysaccharides And Polyamino Acids, And Uses Thereof. (2019).

125. Dolz-Pérez, I. *et al.* Polypeptide-corticosteroid conjugates as a topical treatment approach to psoriasis. *J. Control. Release* **318**, 210–222 (2020).

Chapter 3

Development of Well-defined Poly-L-Glutamate-Palbociclib Conjugates for Pediatric Glioma Treatment

3.1 Introduction

Chapter 1 described the health burden surrounding pediatric brain tumors - disease lethality and the poor performance of existing treatments - as the second most common tumors in children after leukemia [1]. Despite improvements in early diagnosis, the poor survival (12-15 months [2]) of glioblastoma multiform (GBM) patients (the most common malignant brain tumor) highlights the need for new therapeutic strategies for this unmet clinical need.

Adequate drug selection represents a critical feature in the design of successful therapies for pediatric glioma treatment. Disease recurrence and therapeutic resistance to such drugs represent the principal challenges faced during brain tumor treatment. Chemotherapeutic approaches for brain tumors target the epidermal growth factor receptor (EGFR), mutated and/or amplified in 60% of GBM cases [3], with tyrosine kinase inhibitors (TKIs). Unfortunately, the development of therapeutic resistance typically follows rapid positive responses to treatment. Tumor cells coactivate other receptors of tyrosine kinases, such as maintained signaling through the phosphatidylinositol-3-kinase (PI3K) pathway [4]. Resistance can arise by bypassing PI3K through the mammalian target of the rapamycin (mTOR) pathway. CDK4 inhibitors can effectively suppress the mTOR/AKT pathway [5], representing a target in recurrent tumors with persistent cyclin D1 and CDK4 expression (which drives cell proliferation) [6]. Palbociclib (**Figure 3.1A**) functions as a highly selective inhibitor of CDK4 and CDK6 and acts as a downstream inhibitor of most mitogenic signaling pathways; furthermore, this inhibitor suffers from

fewer bypass mechanisms[5]. Therefore, we selected palbociclib as a promising drug for conjugation to our polymeric carriers.

Palbociclib (IBRANCE® [Pfizer], also called PD-0332991) is an orally bioavailable FDA-approved treatment for advanced or metastatic breast cancer when combined with fulvestrant or letrozole. This treatment approach supports an almost two-times longer progression-free survival than fulvestrant or letrozole alone (NCT01942135, NCT01740427) [7]. The previously described inhibition of CDK4 and CDK6 (**Figure 3.1B**) represents the most relevant mechanism of action of palbociclib, which impedes Cyclin D1/CDK4/6 complex formation and the subsequent phosphorylation (p) of the retinoblastoma tumor suppressor protein (Rb). pRb cannot release the E2F transcription factor required for S-phase entry, prompting cell cycle arrest and subsequent apoptosis[8]. Palbociclib also induces a broad spectrum of immunologic events, enhancing the antigen-presenting capability of tumor cells and suppressing the T regulator lymphocytes that activate cytotoxic T cells [9,10]. Resistance to palbociclib can derive from pRb inactivation or the hyperactivity of E2F and cyclin E-CDK2/1 complex, which induce cell-cycle progression independently of CDK4/6 activity. Hyperexpression of p16 (intrinsic resistance) or activation of alternative pathways mTOR and PI3K (acquired resistance) also contribute to the development of resistance [11].
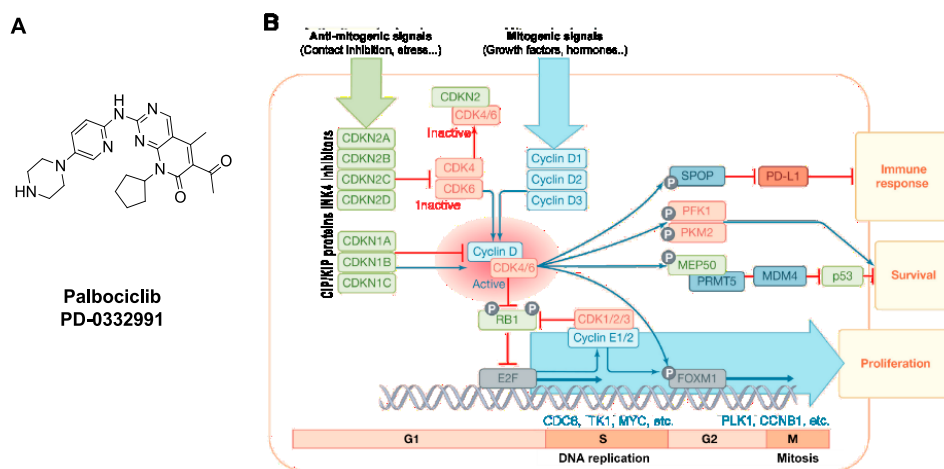

Figure 3.1. (**A**) Chemical structure of palbociclib (**B**) and cell proliferation inhibition mechanism of CDK4/6 inhibitors, adapted from Álvarez-Fernández et al.[8]

The efficacy of palbociclib was demonstrated *in vivo* in GBM and medulloblastoma xenograft mouse models, where it suppressed the growth of intracranial tumors and efficiently crossed the blood-brain and blood-tumor barriers [12,13]. Recently, palbociclib monotherapy was evaluated in clinical trials for breast cancer

patients with central nervous system (CNS) metastasis [14], adult patients with recurrent GBM [15], and pediatric patients with progressive brain tumors [16]. Unfortunately, this approach was ineffective, with a lack of reported efficacy associated with heavily pretreated patients. The findings from ongoing clinical trials and recent preclinical studies [17] of CDK4/6 pathway modulation may deserve further exploration, not only with palbociclib as a single agent but also in combination regimes.

After selecting an adequate drug, the next step is to ensure that this drug reaches the pathological molecular target, bypassing any biological barrier preventing targeted delivery. Nanomedicines are considered the most promising approach for personalized targeted treatment[18]. As stated in Chapter 1, polymer therapeutics are considered one of the first polymer-based nanomedicines with demonstrated clinical benefit [19–21]. In particular, polypeptide-drug conjugates (PDCs) form a critical part of the polymer therapeutics family and are based on synthetic polypeptides as multivalent nanocarriers. Furthermore, they represent an interesting means of delivering small-molecule drugs [20]. PDCs, in particular **poly-L-glutamic acid (PGA)**-based nanoconjugates [20], have gained therapeutic interest as they possess an excellent safety profile, low immunogenicity, high biocompatibility, and biodegradability and proved themselves as effective drug delivery systems [20,22]. Unlimited hierarchical and structural variety of such material can benefit targeted tissue accumulation, and bespoken functionalities can improve/enhance drug delivery via passive targeting in solid tumors due to the enhanced permeability and retention (EPR) effect [23] and the ability to cross biological barriers [24]. PDCs allow for tailored drug loading, the incorporation of drug combinations, and intelligent bio-responsive linkers that release the conjugated drugs under selected exogenous (i.e., light) or endogenous triggers (i.e., pH, enzymes) such as those found at the tumor site [25–27].

The versatility of synthetic chemistry of polypeptide-based material and the possibility of incorporating bioresponsive moieties and biomimetic features enhance the scope of PDCs compared with other nanomedicines of the polymer therapeutics family [19]. Multivalence and straightforward surface modification of synthetic polypeptides are widely used for drug/imaging modality conjugation [20], offering several advantages over free drugs [20], including enhanced solubility, stability, and longer blood circulation times. The recent development of controlled polymerization techniques has allowed the large-scale synthesis of PGA-based nanosystems with different topologies in a controlled and straightforward manner [28]. Previous research has demonstrated that architecture, size, and conformation in a solution of the starting PGA material are critical in cell uptake, half-live, and organ accumulation [29].

The conjugation to the PGA backbone is usually accomplished via esterification or amidation reactions by carbodiimide coupling with high modification efficiencies (up to 90 mol%) [30], highlighting the high loading capacity of these materials. PGA has a demonstrated versatility for conjugating a wide variety of biological agents [31] and a validated capability for combination therapy, allocating drugs of differing chemical characteristics at controlled ratios [32,33]. PGA also allows for multiple stimuli-responsive orthogonal linkers, supporting the specific release of conjugated drug combinations in

response to distinct biological stimuli [27,34]. On top of this, linker/spacer design, drug loading, and carrier topology play crucial roles in the final biological fate of the conjugate by influencing release kinetics and biological activity [24]. Overall, alongside the inherent biodegradability, safety, and versatility of PGA, the advantages of this polymer justify its selection as an ideal drug delivery carrier for pediatric glioma treatment.

After drug and carrier selection, the next step for a rational design of a PDC requires the choice and implementation of **bioresponsive linkers**. The linking chemistry employed is crucial in developing successful nanoconjugates, as drug pharmacokinetics/pharmacodynamics rules the final therapeutic output. The first generation of PDCs employed simple amides, thioethers, or triazole bonds for dug conjugation, which displayed relatively slow degradation, low drug bioavailability, and, thus, low therapeutic activity. Therefore, site-specific cleavable linkers play a crucial role, allowing prolonged stability in the blood circulation and efficient release in the tumor microenvironment if adequately designed by considering endogenous triggers such as acidic pH, increased reductive environment (increased glutathione (GSH) level) or the overexpression of specific proteases (i.e., cathepsin B, matrix metallopeptidase-9, or -12 (MMP-9 or -12)) [35].

Taking these points into consideration, we designed bioresponsive linkers to promote drug release under relevant biological conditions either in the tumor microenvironment and/or the lysosomal cell compartment: a pH-sensitive hydrazone linker and two stimuli-responsive linkers (a GSH-responsive disulfide linker and a Cathepsin B responsive peptidic linker) for the conjugation of palbociclib to PGA.

pH-sensitive linkers represent the most broadly used linking moieties and take advantage of the lower pH of inflammatory sites, the tumor, and the intracellular organelles and vesicles that play essential roles in the uptake of many drug delivery systems [36]. Shen and Ryser first proposed acid-sensitive linkers for polymer-drug conjugates in 1981 to conjugate daunorubicin via cis-aconityl linkage [37]. Their approach supported the lysosomal release of the unmodified drug, with a half-life of less than 3 h at pH 4 and more than 96 h at pH 6 or higher. These types of linkers are well-studied and take advantage of the acidity of the extracellular tumor microenvironment due to the Warburg effect (lower than surrounded healthy tissues) as well as the acidity (pH 4-6) of the intracellular organelles (e.g., endosomes, lysosomes) where the nanoconjugates are encountered after cell internalization by an energy-dependent mechanism such as endocytosis [36]. Based on the differences in pH values between the tumor microenvironment and healthy tissues, acid-cleavable linkers (e.g., orthoester, acetal/ketal, imine, hydrazone, and cis-aconityl moieties) are often used to achieve targeted drug delivery [38,39]. pH-responsive imine and hydrazone linkers are the most used examples due to straightforward reactions between the carbonyl group (aldehyde or ketone) and amine or hydrazide group under mildly acidic conditions. Hydrazone linkers

have been explored in PGA-drug conjugates [32,40,41] and other PDCs and have been assessed in clinical trials [20]

Differential reductive environments provided by the cell-dependent elevated intracellular concentration of glutathione (GSH, a reducing low molecular weight thiol) in the cytosol and lysosomal compartment (1–10 mM), in particular in tumor cells, represents another common endogenous trigger using disulfide linkers as conjugate bioresponsive moieties. Moreover, disulfide linkers enable plasma stability of associated conjugates, where GSH concentration is 1000-fold lower (around 5 μM) compared with the conditions within the tumor microenvironment and/or inside the target cells, which guarantees the stability of the linker in circulation and preferential intracellular cleavage [42].

Finally, protease-specific responsive moieties support site-specific delivery when rationally designing PDCs [20]. As an orthogonal peptidic linker, we selected the Valine-Citrulline motif as a substrate for cathepsin B – a lysosomal protease upregulated in the tumor microenvironment that also plays a crucial role in tumor angiogenesis and invasion [43]. Previous work in the field has demonstrated that the rational design of PGA-drug conjugates can improve therapeutic outcomes as single agents and in combination regime [44]; However, the role of conformation and topology [24] remains underestimated and inadequately studied for polymeric systems. Herein, we investigated the effect on the conformation in a solution of linear (Lin) and star-shaped (St) PGA-palbociclib conjugates bearing bioresponsive linkers in patient-derived GBM and DIPG cells.

While disease monotherapy has been extensively studied, the molecular complexity of diseases like cancer necessitates the simultaneous targeting of multiple molecular pathways, thus requiring combination therapy. Combining multiple drugs targeting different molecular pathways can delay the tumor's ability to adapt. This approach is widely utilized in clinical settings and can enhance therapeutic efficacy by synergistically targeting the same cellular pathways [45,46]. However, the clinical translation of optimized in vitro ratios remains challenging due to variations in individual therapeutic agents' absorption, distribution, and metabolism rates. To overcome this limitation, polymer-based combination conjugates offer an attractive solution by enabling the controlled release of desired drugs at specific ratios upon reaching the target site. The multivalence of polypeptide-based materials allows for the conjugation of multiple drugs and additional targeting moieties on the same polymeric chain, thereby tailoring the properties of the delivery systems to specific organs or tissues.

Within polypeptide-based combination therapies [33,47,48], rational design plays a crucial role in determining the site of action for drug release, the characteristics of the drugs involved, and the availability of drug-conjugatable groups. When conjugation is unfeasible, hybrid methodologies in drug delivery systems can successfully achieve combination approaches. For instance, the utilization of a PEGylated PGA-polylysine (PLL) block copolymer with conjugated deoxycholate (DOCA), loaded with both doxorubicin (DOX) and paclitaxel (PTX), demonstrated significantly enhanced

antitumor efficacy in an A549 lung adenocarcinoma model compared to combinations of free drugs or single drug-loaded nanoparticles [49]. Alternatively, blending methods involving conjugation/complexation and physical loading of hydrophobic drugs can be employed as an alternative approach to reduce the number of synthetic steps and simplify the manufacturing process for combination therapy. This approach maintains the benefits of controlled release for the conjugated/complexed drug while allowing for less controlled release of encapsulated drugs.

This work aimed to synthesize well-defined PGA conjugates of palbociclib to develop an intranasally administered nanotherapy for treating pediatric glioblastoma. This chapter focused on synthesizing linear and star-shaped PGA-palbociclib conjugates via stimuli-responsive linkers. We aimed to define critical features that affect conjugate in vitro activity to better understand their structure-activity relationship. By gaining insights into how different structural features impact the performance of the conjugates, we aim to improve their therapeutic potential. Finally, we identified a combination therapy, synergistic with palbociclib, to further enhance the therapeutic effectiveness of the developed nanotherapy.

Overall, the study focused on synthesizing well-defined conjugates, optimizing linking chemistries, characterizing the physicochemical properties, and proposing a combination therapy approach to improve the efficacy of intranasally administered nanotherapy for pediatric glioblastoma.

3.2. Results and Discussion

To design PGA-palbociclib conjugates that follow a lysosomotropic intracellular drug delivery mechanism (**Section 2.2**), we selected three different bioresponsive linkers to promote drug release under relevant biological conditions either in the tumor microenvironment and/or the lysosomal cell compartment - (1) a pH-sensitive hydrazone linker, (2) a redox-responsive disulfide linker, and (3) a cathepsin B cleavable valine-citrulline peptidic linker. Importantly, to better control the conjugation of palbociclib via a post-polymerization modification of PGA, we first derivatized palbociclib with the selected bioresponsive linker and then covalently conjugated the obtained palbociclib derivative to adequate sidechain-modified PGA.

As a chemical entity, palbociclib bears two functional groups - a secondary amine and a keto-group - that we can use for covalent conjugation to the selected polypeptidic platforms.

3.2.1. Synthesis of pH-responsive PGA-palbociclib Conjugates using a pH-Sensitive Hydrazone Linker

Inspired by the successful use of hydrazone linker for doxorubicin in various polymeric systems, which ensures stability in blood circulation and well-controlled pH-dependent drug release [50,51], we exploited the keto-group of palbociclib to create similar pH-labile conjugates.

We first prepared LinPGA-hyd-palbociclib (hyd = hydrazone linking moiety) by modifying the PGA chain with tert-butyl carbazate, deprotecting the tert-butyloxycarbonyl (BOC)-group with trifluoroacetic acid (TFA), and directly conjugating palbociclib (**Figure 3.3**).
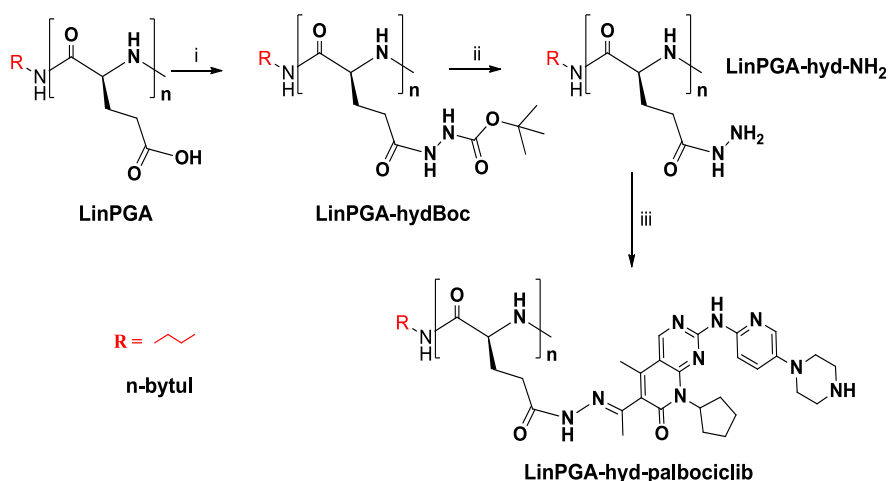
Figure 3.3. Synthesis of LinPGA-hyd-palbociclib conjugates. i) tert-butyl carbazate, DMF, DMTMM BF4; ii) TFA$_{conc}$; iii) palbociclib, DMSO$_{anh}$, HAc$_{cat}$ (SI-3.4.)

Unfortunately, we failed to obtain the expected conjugates in this instance. The ^{1}H-NMR analysis showed no peak shifts in the aromatic region (**Figure 3.4**) compared to the free drug after reaction completion. More importantly, the protons from methyl groups close to the palbociclib keto-group should be affected in the event of the desired reaction; however, we encountered no evident spectral changes in the aliphatic region (**Figure 3.5**). Moreover, after fractionation through an LH-20 size exclusion chromatography (SEC) column in DMF, we only identified the naked polymer and not LinPGA-hyd-palbociclib conjugate by ^{1}H-NMR, thereby confirming the absence of the desired product.
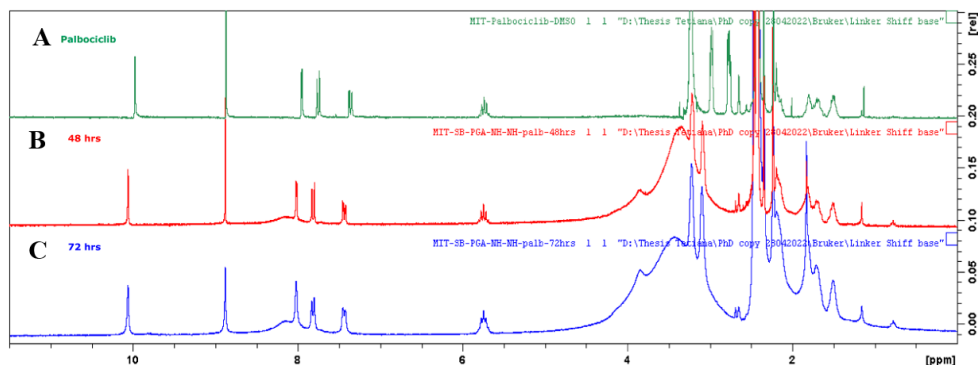
Figure 3.4. Overlaid spectra *¹H NMR (300 MHz, DMSO-d)* of (**A**) palbociclib and the (**B**) reaction after 48 h, and (**C**) 72 h.

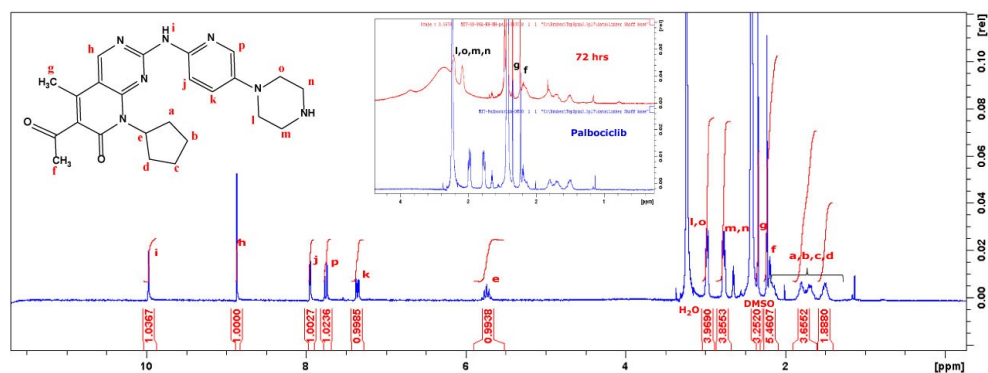**Figure 3.5**. *¹H NMR (300 MHz, DMSO-d)* Magnified aliphatic region of palbociclib and a reaction after 72 h

As the analysis of ¹H-NMR, after the reaction showed the physical mixture of initial compounds instead of the desired product, we hypothesized that the neighboring quinone and pyrimidine rings of palbociclib, form an aromatic structure that affects the reactivity of the keto-group, thereby impeding/limiting palbociclib conjugation through the hydrazone linker.

To confirm the low reactivity of the palbociclib keto-group and exclude a structural hindrance effect caused by PGA chains, we formed a hydrazone bond between palbociclib and 9-fluorenyl methyl carbazate (Fmoc-hydrazine) in anhydrous dichloromethane (DCM$_{anh}$) with molecular sieves (4Å) or Si(EtO)$_4$ as water removal agents and a catalytic amount of acetic acid (AcOH$_{cat}$). **Figure 3.6** describes the proposed synthetic route.
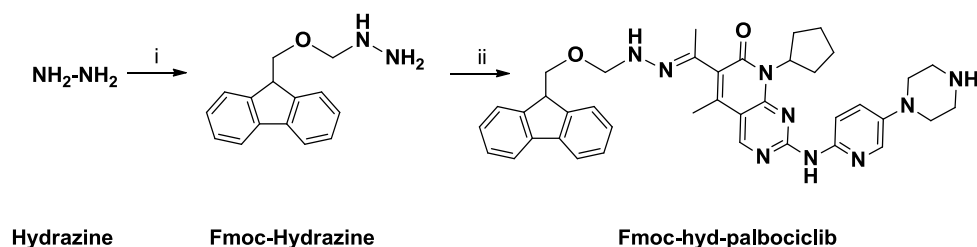
Figure 3.6. Synthesis of Fmoc-hydrazone-palbociclib conjugates. i) 9-fluorenyl methyl chloroformate, ACN ii) palbociclib, DCM$_{anh}$, AcOH$_{cat}$ (SI-3.4.3. – SI-3.4.4.)

Overall, the ^{1}H NMR spectra obtained suggested the presence of a physical mixture of the initial reagents (Fmoc-hydrazine and palbociclib), confirming the inaccessibility and/or lower reactivity of the palbociclib keto-group for hydrazone bond formation (**Figure 3.7**).
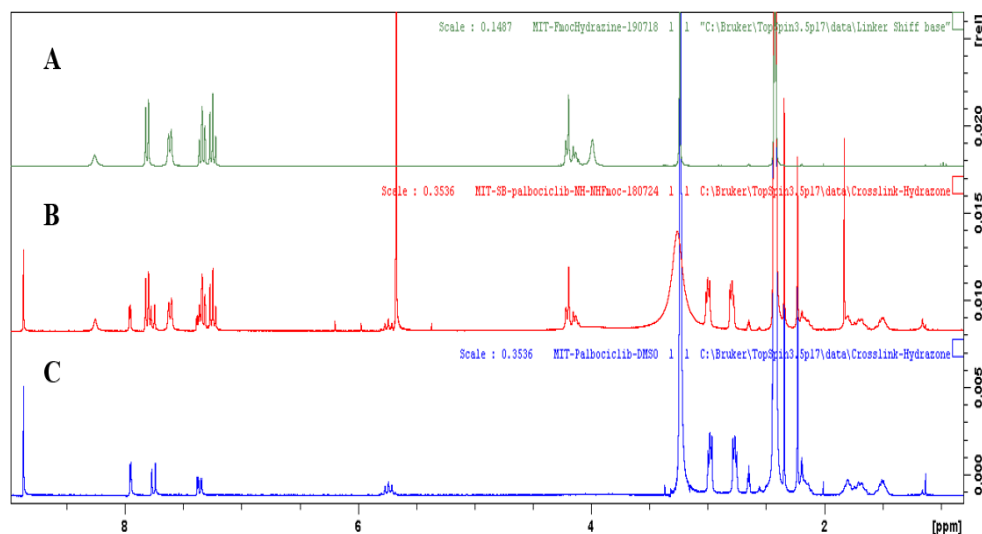

Figure 3.7. Overlaid spectra *^{1}H NMR (300 MHz, DMSO-d)* of (**A**) 9-fluorenyl methyl carbazate, (**B**) the reaction after 24 h, and (**C**) palbociclib.

3.2.2 Design and Development of Redox-responsive PGA-palbociclib Conjugates using a Disulfide Linker

Given the unreactive nature of the keto-group of palbociclib, we explored the possibility of conjugation via its secondary amine (**Fig 3.1A**).

3.2.2.1. Synthesis and Physico-chemical Characterization of PGA-SS-palbociclib Conjugates

Inspired by promising results of disulfide linkers in different drug delivery systems, we selected a rapid self-immolation 1,5-cyclization motif. We prepared a family of linear and star-shaped PGAs (Lin PGA and StPGA) to study the effect of drug loading on their physicochemical properties and therapeutic output. We prepared conjugates in five steps (**Figure 3.8**), beginning with thiol exchange between 2,2-dithiodipyridine and mercaptoethanol, coupling the palbociclib to activated hydroxyl group with *p*-nitrophenyl chloroformate, and a second thiol exchange with cysteamine hydrochloride. The last step comprised conjugation to PGA via amide coupling with the 4-(4,6-dimethoxy-1,3,5-triazin-2-yl) activator (DMTMM).
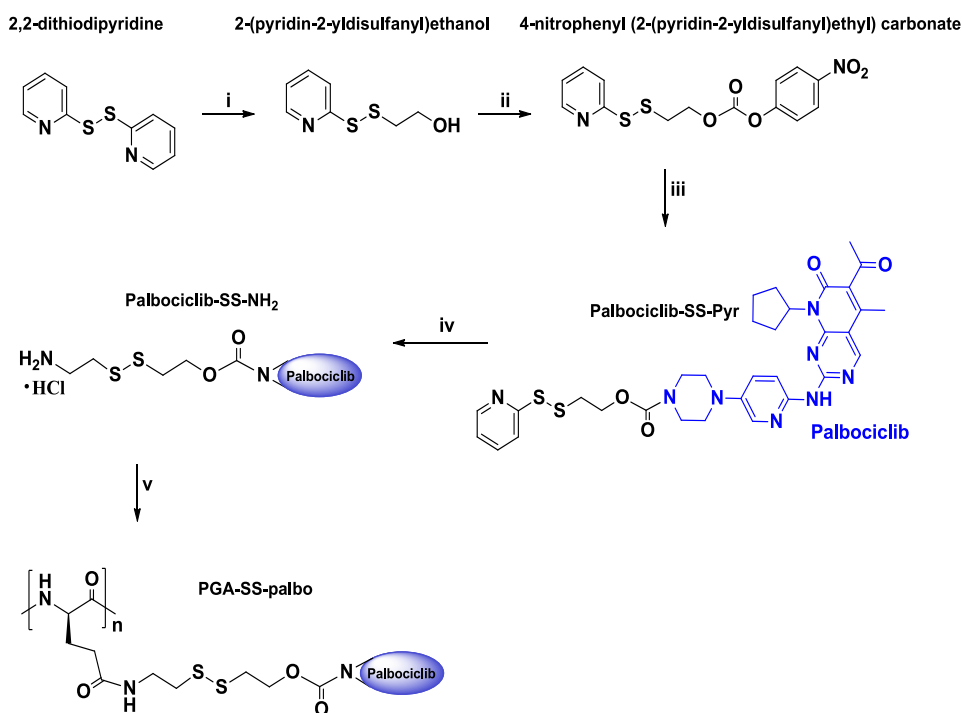

Figure 3.8. Synthesis of PGA-SS-palbociclib conjugates. i) 2,2-dithiodipyridine, MeOH; ii) p-nitrophenyl chloroformate, THF_{anh}, TEA, 0°C; iii) palbociclib, DCM_{anh}, TEA; iv) cysteamine hydrochloride, MeOH:DCM (1:1), TEA; v) PGA, DMF_{anh}, DMTMM·BF$_4$, TEA (**SI-3.4.**) [52]

We successfully synthesized a family of LinPGA and StPGA conjugates using a disulfide self-immolative (-SS-) linker and different drug loadings (**Table 3.1**) and

evaluated the purity of each synthetic step and final conjugate by ^{1}H NMR and size exclusion chromatography (SEC) (**Figure 3.9** and **Figure 3.10**).[20]
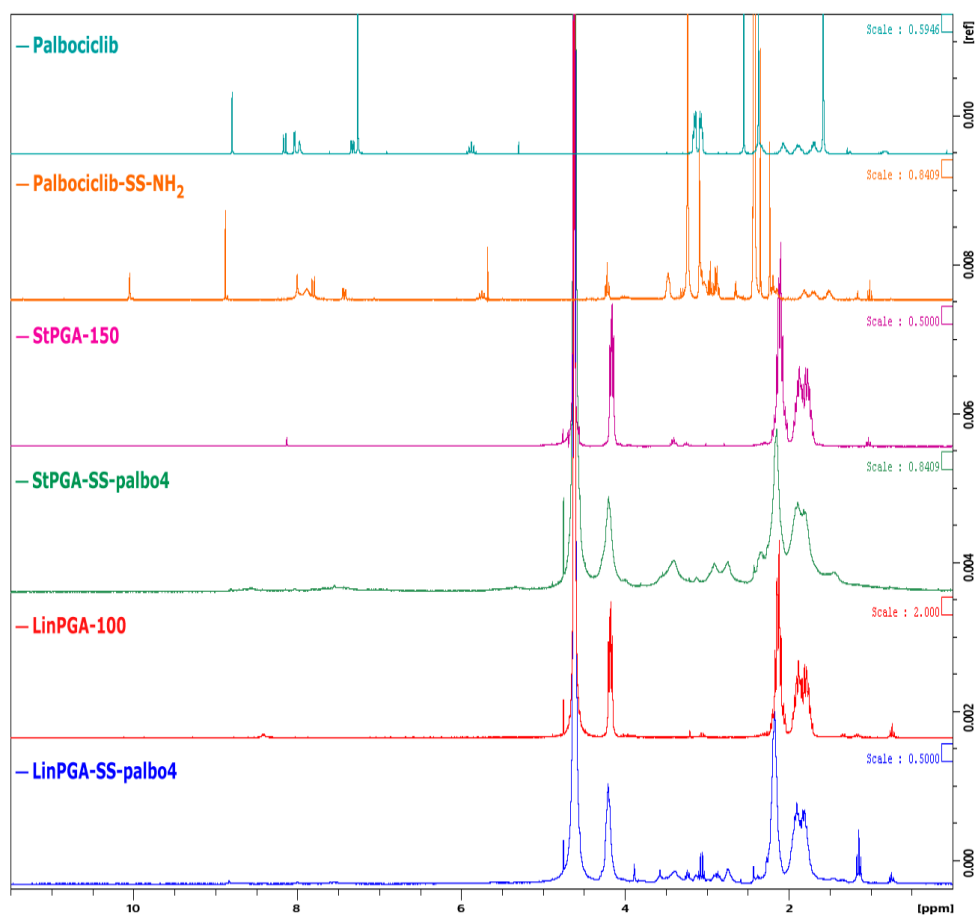

Figure 3.9. Representative ^{1}H NMR spectra of palbociclib, disulfide linker, parent carriers (LinPGA and StPGA), and palbociclib conjugates (linear and star) with the highest drug loading. **Figures S3.8-3.15** show ^{1}H NMR spectra for all synthesized carriers.

We used SEC equipped with RI, UV-Vis, and MALS detectors to demonstrate that all conjugates possessed a homogeneous molecular weight distribution (**Figure 3.10**). Interestingly, the signal from the MALS 90° detector (**Figure 3.10**. **E, F**) varies

depending on the drug loading, suggesting the differential solution conformation of analyzed samples.
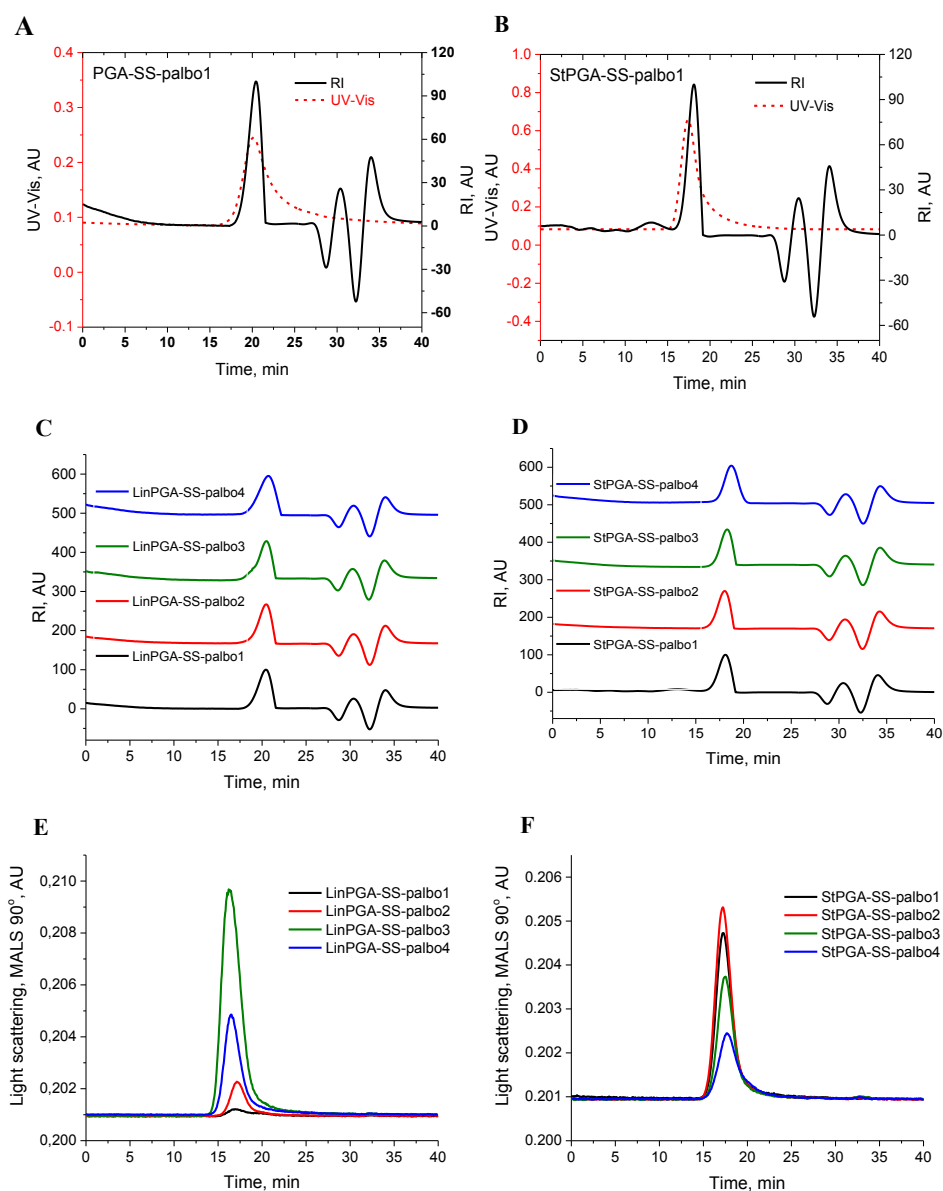

Figure 3.10 Representative SEC chromatograms: overlayed RI detector (solid line) and UV-Vis detector (dashed line, λ=354 nm) for (**A**) LinPGA-SS-palbo and (**B**) StPGA-SS-palbo; RI detector for (**C**) LinPGA-SS-palbo and (**D**) StPGA-SS-palbo with different

drug loading; MALS detector for (**E**) LinPGA-SS-palbo and (**F**) StPGA-SS-palbo with different drug loadings.

We determined total drug loading (TDL, %wt) by UV-Vis analysis (**Figure 3.11** and **Table 3.1**); overall, we observed good agreement with the estimated value obtained from NMR analysis. As parent LinPGA and StPGA do not absorb within the palbociclib region (A_{max} = 353 nm), and PGA-palbociclib conjugates have the same maximum absorbance; there should be no interference with the free drug for quantitative measurements.
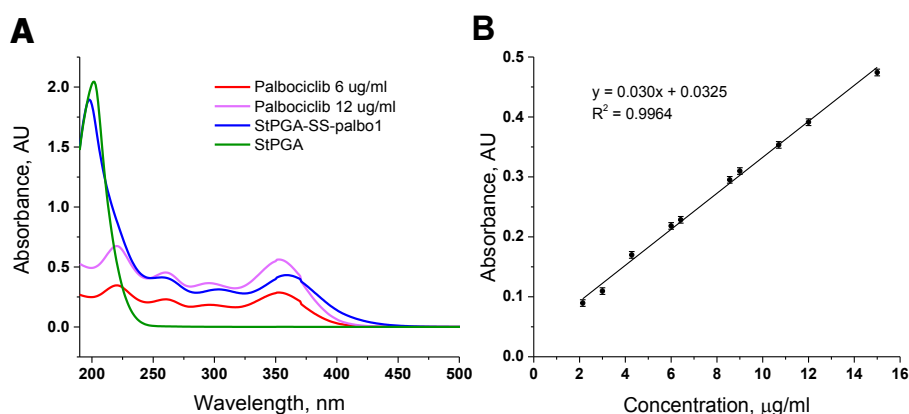

Figure 3.11. (**A**) UV-Vis spectra of palbociclib, control polymer, and PGA-palbociclib conjugate and (**B**) the matrix-matched calibration curve used to quantify the total drug loading.

To verify the absence of signal suppression caused by the matrix effect, we performed a simple experiment (**Figure 3.12**): we spiked an aqueous solution of palbociclib with StPGA (final concentration of 0.1 mg/ml polymer), corresponding to the concentration of conjugates used for TDL measurements. In case of no existing matrix effect, the absorbance value should be identical in both samples; however, we obtained 26% signal suppression in the presence of StPGA. Two viable solutions exist to compensate for this effect: subtract the known value from the assay analysis or perform a matrix-matched calibration. We selected the second option as the most accurate approach, considering the possible batch-to-batch variation of polymer spectral characteristics.
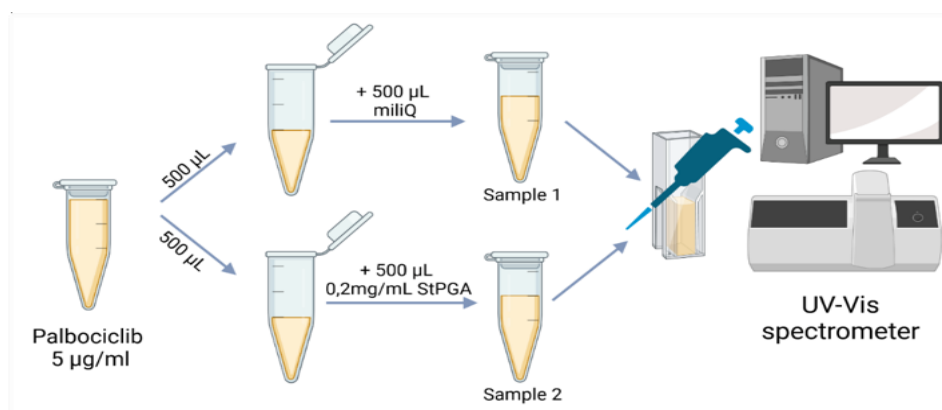
Figure 3.12. Experimental scheme describing how to identify signal suppression by the PGA carrier

We determined free drug content by high-performance liquid chromatography (HPLC) and found this to be below 0.2% wt of the determined TDL. Free drug content of less than 2wt% of total drug loading is mandatory for progression to biological characterization [53]. **Table 3.1** summarizes the most relevant physicochemical characterization of the synthesized PGA-SS-palbociclib conjugates.

Table 3.1 *Physicochemical Characterization of Linear and Star-shaped PGA-palbociclib Conjugates*

Conjugate	TDL[a] (% mol)	TDL[a] (% wt)	Free Drug Content[b] (% wt of TDL)	Z-pot[c] (mV)	R_h[d] (nm)	PDI[e]
StPGA-SS-palbo1	1.0	2.8	<0.2%	-29.6	5.9	0.09
StPGA-SS-palbo2	2.1	5.8	<0.2%	-28.8	4.6	0.13
StPGA-SS-palbo3	4.0	10.2	<0.2%	-28.1	5.4	0.11
StPGA-SS-palbo4	6.2	14.8	<0.2%	-29.1	4.1	0.07
LinPGA-SS-palbo1	1.2	3.4	<0.2%	-29.5	4.2	0.07
LinPGA-SS-palbo2	2.5	5.1	<0.2%	-28.9	4.2	0.11
LinPGA-SS-palbo3	3.5	7.5	<0.2%	-29.3	5.2	0.08
LinPGA-SS-palbo4	5.5	13.4	<0.2%	-29.0	5.5	0.11

[a]TDL - Total drug loading, determined by UV-Vis and supported by NMR, [b]Z-potential, determined by DLS, [d]R_h – hydrodynamic radius, determined by DLS [0.1 mg/ml in PBS], and [e]PDI - Polydispersity index, determined by DLS.

Dynamic Light Scattering (DLS) studies demonstrated a trend of reduced hydrodynamic radius in PBS upon increasing a drug loading; all tested compounds had a negative value of z-potential close to -30 mV **(Table 3.1).**

Circular dichroism (CD) was further used to corroborate better the different scattering intensities obtained for the conjugates with the MALS detector. Upon increase of drug loading, a clear transition from a random coil to α-helix secondary structure was evident for StPGA-SS-palbo conjugates; however, for liner conjugates, a similar transition was not observed, and polymer chains adopted random coil conformation in all the cases (**Figure 3.13A** and **B**). Spectra deconvolution allowed for the estimation of alpha-helix content of around 30% vs 15% for the star and linear conjugates with the highest drug loading, respectively.
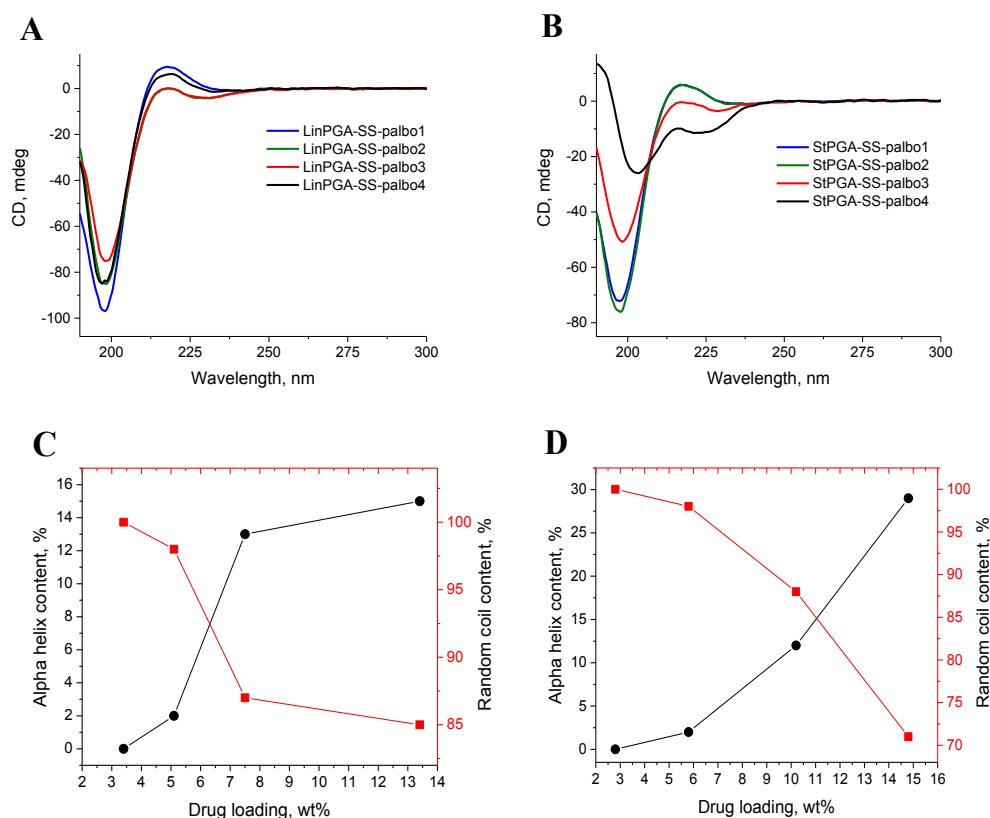

Figure 3.13 CD spectra of (**A**) LinPGA-SS-palbo and (**B**) StPGA-SS-palbo conjugates, 0.12 mg/ml PBS. Content of alpha-helix and random coil conformations as a function of drug loading for (**C**) LinPGA-SS-palbo and (**D**) StPGA-SS-palbo conjugates.

We next performed Small-angle X-ray scattering (SAXS) to study the influence of drug loading on chain conformation and polymer aggregation (**Figure 3.14A**, **Table 3.2**). Analysis of low- and intermediate q-region for LinPGA-palbociclib conjugates revealed a smooth transition from molecularly dissolved molecules (i.e., single, non-aggregated molecules for LinPGA-palbo1) to small, clustered mass fractal aggregates (intermediate loading - LinPGA-palbo2, and LinPGA-palbo3). Further increase of the loading (LinPGA-palbo4) demonstrated a higher level of mass fractal aggregation to the dimensions exceeding the resolution of the instrument (>150 nm in diameter). SAXS profiles of LinPGA-palbo4 in the low-q region had the slope of -1 typically assigned to cylindrical objects rather than fractal aggregates of known types; therefore, we hypothesize that in this regime, polymers adopt a collapsed intermediate chain conformation known as an incomplete crumpled globule. The evolution of the chain conformations was further evaluated by analysis of the high-q Porod region. Slopes of the curves changed from -1.6 (-5/3) (typical swollen coils with self-avoiding walk) in LinPGA-palbo1) to -2 (mass fractal of Gaussian coils) for intermediate and high drug loading. For linear conjugates, point-to-point interactions started manifesting at loadings of around 5 %wt (LinPGA-palbo2), and aggregation started to occur.
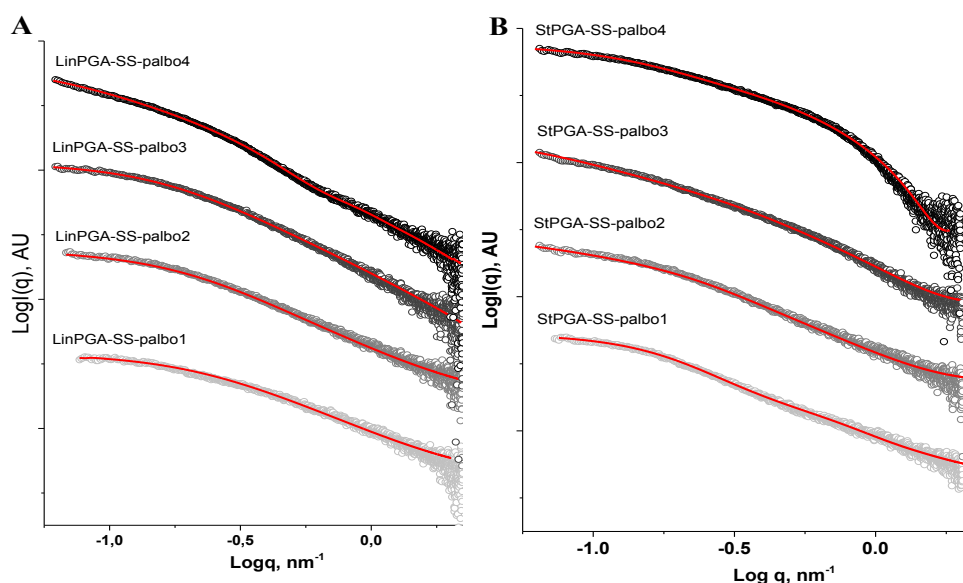

Figure 3.14. SAXS profiles with the fitting of (**A**) LinPGA-SS-palbo and (**B**) StPGA-SS-palbo conjugates with different drug loading, 0.1 mg/ml PBS

***Table 3.2** Characteristic parameters of conjugates derived from SAXS profiles*

Characteristic parameter	Slope low-q Guinier region	Slope intermediate-q Guinier region	Slope Porod region
LinPGA-palbo1	0.0	-1.3	-1.6
LinPGA-palbo2	-0.4	-1.5	-2.0
LinPGA-palbo3	-0.6	-1.6	-2.0
LinPGA-palbo4	-1.0	-1.7	-2.0
StPGA-palbo1	-0.8	-1.6	-2.0
StPGA-palbo2	-0.9	-1.6	-2.0
StPGA-palbo3	-1.2	-1.7	-2.0
StPGA-palbo4	-0.5	-1.0	-4.0

StPGA-palbociclib conjugates with low (StPGA-palbo1) and intermediate loading (StPGA-palbo2 and StPGA-palbo3) demonstrated similar evolution from unimers to fractal aggregates and from Gaussian coils to mass fractal of coils (**Figure 3.14 B**, **Table 3.2**). Interestingly, for the conjugate with the highest loading (StPGA-palbo4), the low- and intermediate-q region slopes decreased to -0.5 and -1, respectively, implying the formation of small objects in solution. Furthermore, a slope of -4 in the high-q region suggested that formed objects developed a highly defined surface contrary to surface fractals observed for the conjugates with lower loadings. The slope of -1 in the intermediate-q range proves the formation of crumpled globules, as illustrated below.

Data was represented as Kratky plots (dependence $q2I(q)=f(q)$) to estimate the compactness of the aggregates. For LinPGA-palbociclib conjugates (**Figure 3.15 A**), a smooth transition from fully disordered individual chains at low loading to partially folded flexible chains upon loading increases. Gradual increase of the peak at 0.278 nm^{-1} and simultaneous decrease of the slope of the curve in high q-range (above 0.6 nm^{-1}) confirmed an increase in compactness of the aggregate upon increase of the loading. A similar trend was also observed for StPGA-palbociclib conjugates (**Figure 3.15 B**), with a defined peak at 0.278 nm^{-1}. Upon further increase in the loading (StPGA-palbo3 and StPGA-palbo4), a second peak at 0.643 nm^{-1} started to develop, and the curve in the high-q range changed to a bell-like shape that was particularly pronounced for StPGA-palbo4. Such transition corresponds to the formation of higher-order structures with restricted chain movements.
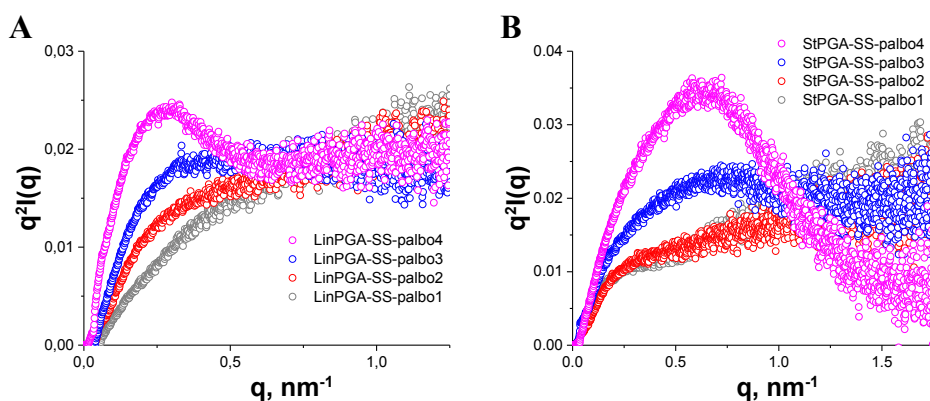
Figure 3.15. Kratky plots of (**A**) PGA-SS-palbo and (**B**) St-SS-palbo conjugates with increasing drug loading: grey (lowest), red, blue, and purple (highest).

FT-IR spectroscopy studies in the Amide I region (1,700–1,600 cm^{-1}) can also be used to characterize the conformation of the polypeptide chains[54]. Changes in polymer compactness for different drug loadings may correlate with changes in the known secondary conformation of polypeptide chains (e.g., random coil, beta-sheet, or alpha helix). Meanwhile, Fourier-transform infrared spectroscopy (FTIR) represents a powerful technique that differentiates between different polypeptide conformations.

The amide I region displayed a shift of the maximum of the main peak upon increased palbociclib loading - from 1654 cm^{-1} to 1658 cm^{-1} for LinPGA-palbociclib conjugates and from 1657 cm^{-1} to 1660 cm^{-1} for StPGA-palbociclib conjugates (**Figure 3.16 A, C**), which generally associates with an increase in alpha-helix content (typical shifts within 1648-1660 cm^{-1}) and a decrease in random coil content (typical shifts within 1642-1657 cm^{-1}). Peaks of the random coil and alpha helix are better separated in proteins; however, in our case (partially substituted polypeptides), the transition between different conformations is blurred due to the random character of side chains substitution. On the second derivative spectra of the amide I region (**Figure 3.16 B, D**), we also observed similar trends for LinPGA-palbociclib and StPGA-palbociclib conjugates – increased area at peaks 1660 cm^{-1} (alpha-helix conformation) and 1694 cm^{-1} (from palbociclib) and decreased area at 1665 cm^{-1} and 1627 cm^{-1}. The origin of the peaks at 1665 cm^{-1} and 1627 cm^{-1} remains unclear but may belong to unconventional secondary structures of PGAs with low substitution. In the amide II region, the maximum of the main peak shifts from 1570 cm-1 to 1575 cm^{-1} for LinPGA-palbociclib conjugates and from 1575 cm^{-1} to 1579 cm^{-1} for StPGA-palbociclib conjugates, a transition that does not associate with secondary structure and instead correlates with the formation of more organized hydrogen bonding networks.
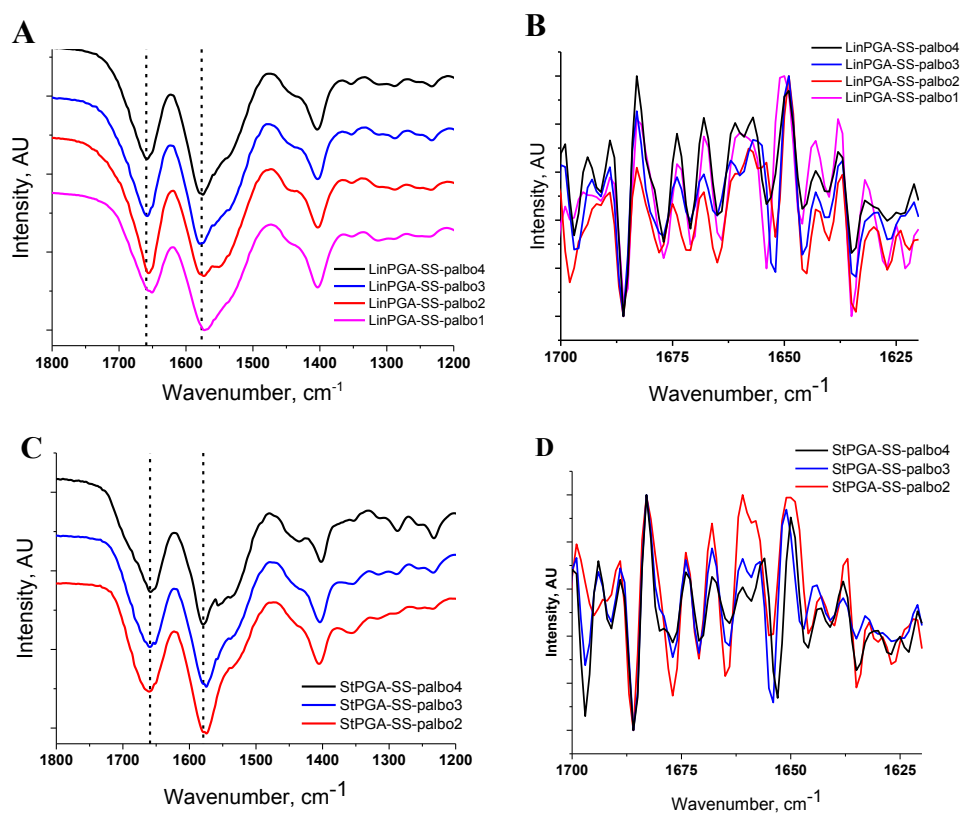
Figure 3.16. Fragment of FT-IR spectra of **(A)** LinPGA-SS-palbociclib and **(C)** StPGA-SS-palbociclib conjugates with increasing drug loading: black (the lowest), red, blue, purple (the highest). Dotted lines at 1659 cm^{-1} and 1575 cm^{-1} demonstrate the shift of the amide I peak upon increasing loading. Second derivative spectra of amide I region of **(B)** LinPGA-SS-palbociclib and **(D)** StPGA-SS-palbociclib

Combining spectroscopic and scattering data allows for developing a general model of conformation evolution in PGA conjugates upon increase of drug loading. At lowest loadings, polymer molecules remain molecularly dissolved, and Coulomb interactions purely control their dynamics. Polymer chains can be considered in a classical Gaussian chain model (LinPGA-palbo1). After reaching a certain critical loading (between 2.5% and 5%, wt), point-to-point interactions start to counterbalance the repulsion between the molecules, leading to big diffuse aggregates with fractal structure (LinPGA-palbo2, LinPGA-palbo3, StPGA-palbo1, StPGA-palbo2 conjugates). Chains also start to cluster and can be described as mass fractals of the Gaussian chains model.

Hydrophobic interactions dominate the aggregation process at higher drug loading, leading to fractal protomicelles containing both point-to-point interactions and hydrophobic collapse zones. Finally, protomicelles form higher-level micellar structures with mixed hydrophobic and hydrophilic regions (LinPGA-palbo4 and StPGA-palbo3). Potentially, strings of protomicelles may form; however, no conclusive evidence was obtained.

Upon further increase of drug loading, micelles compact even more, developing crumpled micelles with defined surfaces and almost complete phase separation (StPGA-palbo4). **Figure 3.17** schematically shows the proposed morphology evolution. While specific differences between the aggregation of linear and star-conjugates are evident, it is reasonable to suggest that they will follow similar evolution upon further increase of drug loading. As the spatial density of hydrophobic drugs is higher for star-conjugates, the morphological transition will occur for them at lower loadings than for linear analogs.
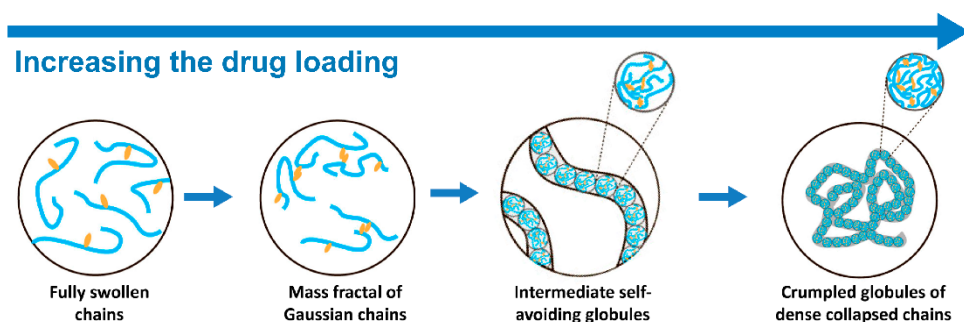

Increasing the drug loading

| Fully swollen chains | Mass fractal of Gaussian chains | Intermediate self-avoiding globules | Crumpled globules of dense collapsed chains |

Figure 3.17. Schematic depiction of the suggested assembly model for PGA-palbociclib conjugates with modulated topology affected by palbociclib loading in an aqueous solution.

We next determined the critical aggregation concentration (CAC) for the disulfide linker conjugates to further evaluate the influence of drug loading into conjugate solution conformation of LinPGA-palbociclib (**Figure 3.18**) and StPGA-palbociclib conjugates (**Figure 3.19**).
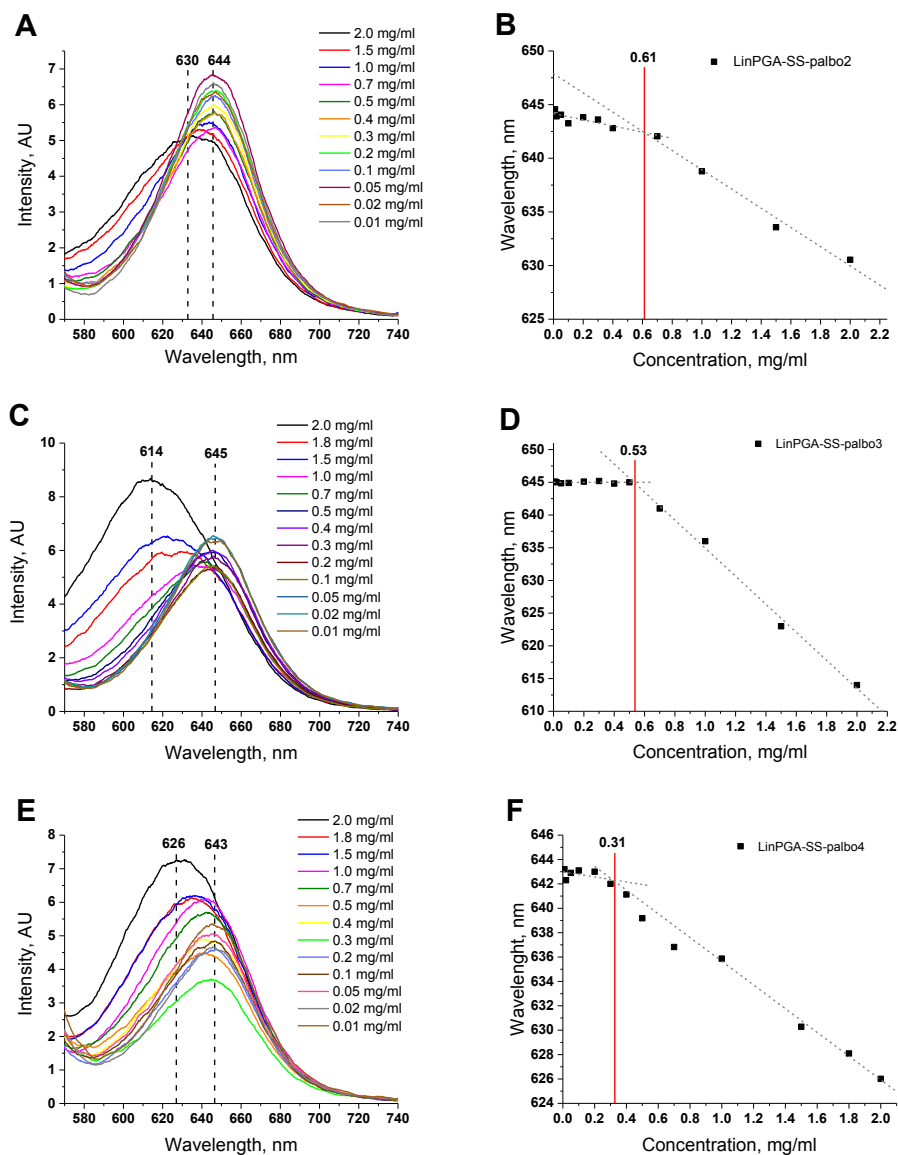
Figure 3.18 (A, C, E) CAC study of LinPGA-SS-palbociclib in PBS using Nile red as a fluorescent probe. **(B, D, F)**The intersection between wavelength shift and the conjugate concentration gives the CAC value (vertical red line)
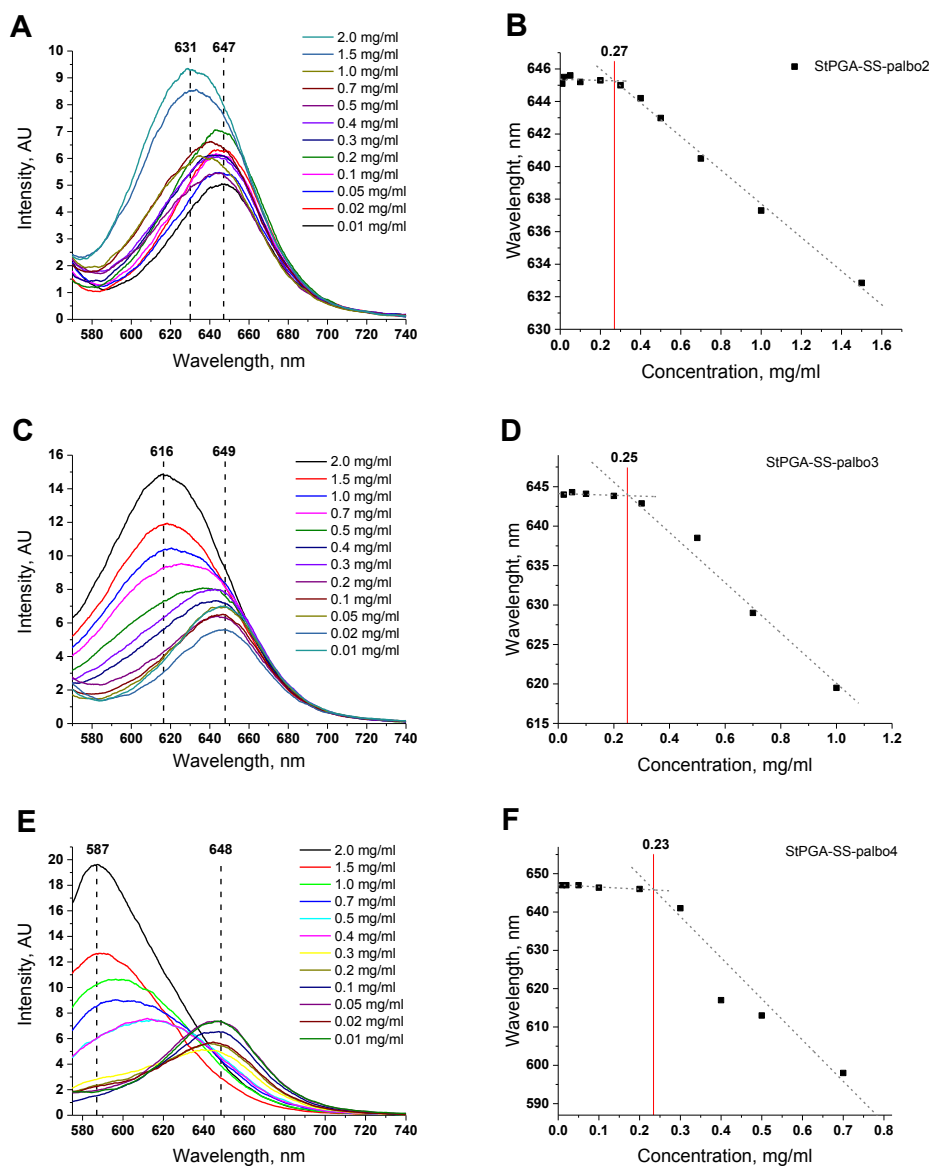
Figure 3.19 (A, C, E) CAC study of StPGA-SS-palbociclib in PBS using Nile red as a probe. **(B, D, F)** The intersection between intensity and the conjugate concentration gives the CAC value (vertical red line).

Conjugates start to form micelles above the CAC value, with nanoassemblies sequestering hydrophobic molecules such as drugs. We employed the Nile red

hydrophobic fluorescence dye [55], which penetrates the hydrophobic pockets of polymeric micelles in case of aggregation and measured its emission spectra**. Figure 3.18** (A, C, E) and **Figure 3.19** (A, C, E) demonstrate the fluorescent spectra of LinPGA and StPGA conjugates. The low Nile red fluorescence intensity (maximum λ=643-650 nm) corresponds to free unincorporated dye and the absence of nanoassemblies at low conjugate concentration. Increasing conjugate concentration towards the CAC prompted an increase in the fluorescence intensity of Nile red (maximum shifts to λ=587 nm), which corresponds to the incorporation of dye within polymeric micelles. The inflection point of this transition can be found by plotting the intensity or wavelength of the peak maximum of Nile Red versus the concentration of the conjugate. **Figure 3.18 (B, D, F)** and **Figure 3.19 (B, D, F)** demonstrate the plotted wavelength of Nile Red at the peak maximum for LinPGA conjugates and StPGA conjugates. **Table 3.**3 reports the calculated CAC values for all PGA-SS-palbo conjugates evaluated.

Table 3.3. CAC values of evaluated PGA-SS-palbociclib conjugates

Conjugate	CAC, mg/ml	Conjugate	CAC, mg/ml
LinPGA-SS-palbo1	0.61	StPGA-SS-palbo1	0.27
LinPGA-SS-palbo2	0.53	StPGA-SS-palbo2	0.25
LinPGA-SS-palbo3	0.31	StPGA-SS-palbo3	0.23

We observed the expected trend for the prepared family of conjugates – the CAC decreased upon increased drug loading. Comparing LinPGA and StPGA conjugate high drug loading analogs, StPGA conjugates possessed lower CAC values than the linear counterparts. This finding may be explained by the restricted flexibility of the star-shaped chain and confirms the more organized and compact structure demonstrated previously with SAXS experiments.

3.2.2.2. Conjugate Solution Conformation Dictates Palbociclib Release Kinetics in a Reducing Environment

To evaluate this conformational phenomenon further, we studied palbociclib release kinetics by exposing LinPGA- and StPGA-palbociclib conjugates to cytosolic (5 mM) and extracellular (10 µM) levels of dithiothreitol (DTT) as a trigger for linker self-immolation. First, we optimized the HPLC method for the pharmacokinetics drug release study (**SI-3.5**). Palbociclib-triggered release from the synthesized conjugates occurs under highly reducing conditions, based on the 1000-fold difference between intra- and extracellular conditions [42]. We observed similar fast palbociclib release for LinPGA-palbociclib conjugates irrespective of drug loading (**Figure 3.20A**). For StPGA-palbociclib conjugates, we observed a delay in palbociclib release for the conjugates with the highest drug loading (**Figure 3.20 B**) - we observed 7% release in 2 h compared to 20% for low drug loading over the same time period (which supports our

previous conformational findings). We also confirmed linker responsiveness by obtaining more than 40% drug release in 8 h with 5 mM DTT but only 3% with 10 μM DTT.
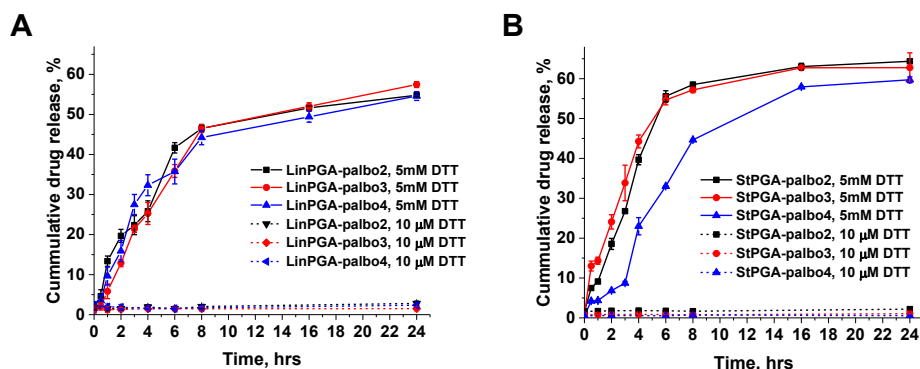

Figure 3.20. Palbociclib drug release from LinPGA-SS-palbociclib (**A**) and StPGA-SS-palbociclib conjugates (**B**) in the presence of 5 mM DTT (mimicking intracellular levels) and 10 μM DTT (mimicking plasma levels). Data presented mean ± SEM (n = 3)

Drug release during self-immolation proceeds in two steps – initial triggered linker cleavage (here, DTT serves as a cell-mimicking reductive trigger) followed by an immolation reaction during which an intact drug (i.e., palbociclib). In this work, we only considered the amount of the intact drug released without evaluating the presence of palbociclib derivatives and incompletely immolated intermediates. Palbociclib is a highly hydrophobic drug that readily precipitates during induced self-immolative cleavage from PGA, so direct HPLC analysis without extraction may lead to diminished release rates (not exceeding 60% after 24 h). In vivo, palbociclib is expected to rapidly convert after self-immolative cleavage to highly water-soluble hydrochloride form under acidic conditions in lysosomes.

No significant differences in palbociclib release were detected for linear and star-conjugates. For both conjugate types, no drug release in the presence of 10 μM DTT was detected (**Figure 3.20**), confirming the stability of self-immolative disulfide linkers in the extracellular environment. In agreement with previously reported examples,[56] plasma stability studies additionally confirmed the stability of the conjugates independently of topology, architecture, and conformation of the conjugates (**Figure S3.19**) (<1% after seven days in all cases). Nevertheless, spectroscopic, scattering, and release studies demonstrated that in the presence of the linker cleavage trigger (i.e., DTT), drug loading, conjugate conformation, and aggregation degree substantially impacted drug release profiles.

3.2.2.3. Biological Evaluation of PGA-SS-palbociclib Conjugates

We next evaluated Palbociclib's biological activity *in vitro* by MTS assay - a colorimetric method for the sensitive quantification of viable cells. The principle of the method is based on the reduction of tetrazolium slightly yellow-colored compound (MTS) and the generation of a colored purple formazan derivative that is quantified by UV-Vis spectroscopy at λ 490-500 nm[57].
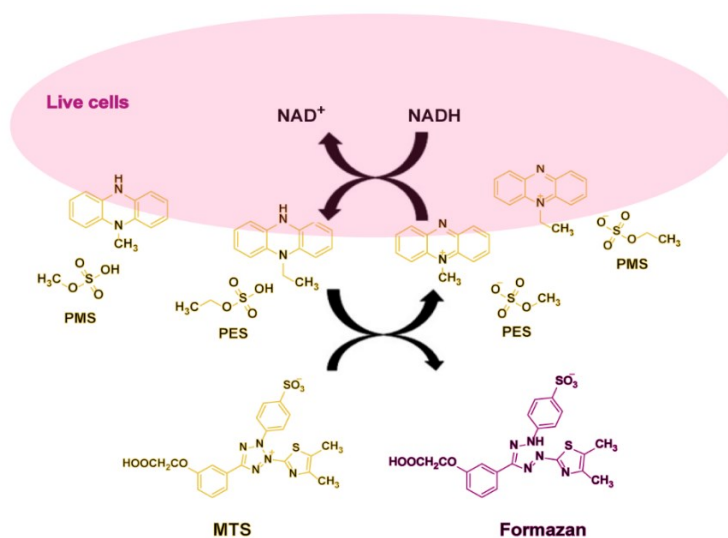

Figure 3.21. Scheme of MTS assay with PES/PMS intermediate electron acceptor for reduction of MTS reagent to colored formazan derivative (Adapted from S. Markossian et al. [58])

Tetrazolium reduction is conducted by NAD(P)H-dependent dehydrogenase enzymes in metabolically active cells. The negative charge of the MTS reagent and its reduced derivative contributes to high solubility in aqueous media; however, this limits cell permeability[59]. Therefore, the MTS reagent is used in combination with an intermediate electron acceptor (PMS) or ethyl sulfate (PES), which permeates viable cells, becomes reduced, exits cells, and reduces the MTS reagent (**Figure 3.21**). A correct read-out of the MTS assay requires metabolically active cells to grow and divide exponentially.

For the *in vitro* evaluation, we used four patient-derived primary cell lines (pediatric glioblastoma - GBM - and pediatric diffuse intrinsic pontine glioma -DIPG) kindly donated by our collaborator Dr. Montero-Carcaboso from Hospital Sant Joan de Déu (Barcelona, Spain). **Figure SI-3.6** describes the cell culture conditions and cell handling protocols.

We first performed a cell growth curve, seeding four P96 plates with DIPG and GBM cells with different cell densities and measuring cell viability after 24, 48, 72, and 96 h via the MTS assay (**Figure 3.22**). We found that 7500 cells/well for both cell lines represented the optimal parameters. Higher cell density (10,000 cells/well) after 4 and 5 h of incubation with MTS/PMS reagent slowed DIPG cell growth and induced a plateaued growth for GBM cells. Lower cell density (5000 cells/well) produces a lower absorbance signal, decreasing the working range of concentration. We discovered that 4 h and 5 h of MTS/PMS reagent incubation were sufficient to obtain an acceptable intensity value.
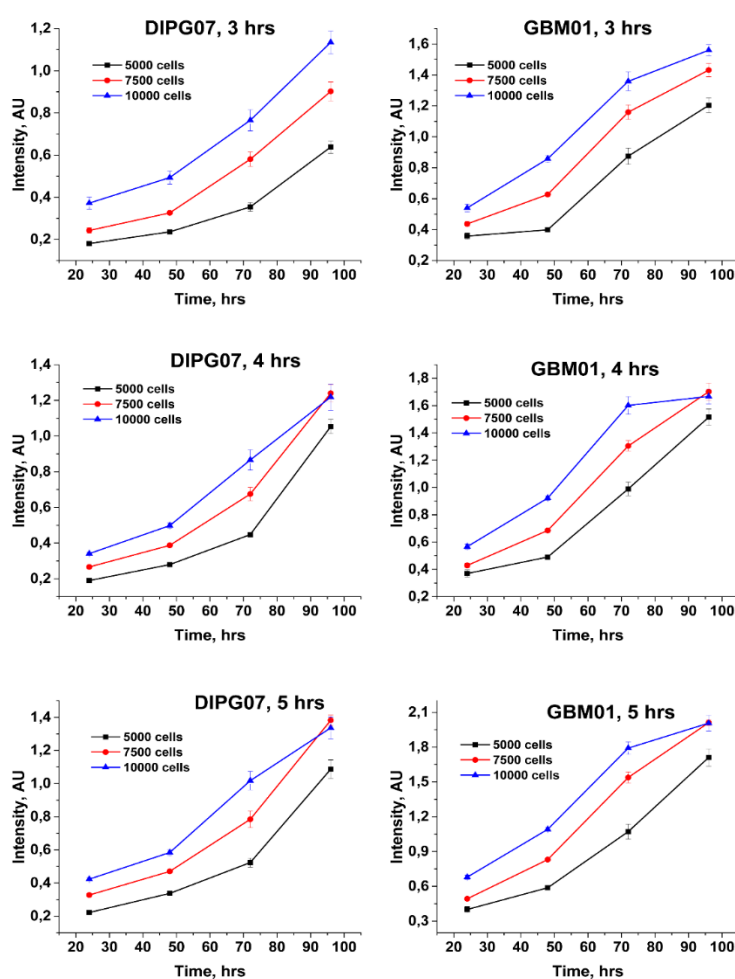

Figure 3.22. Cell growth curve measurements in DIPG and GBM cells with a cell density of 5000, 7500, and 10000 cells/ P96 well and MTS incubation times of 3, 4, and 5 h.

With the optimized MTS parameters, we evaluated the biological activity of palbociclib in four patient-derived cell lines (**Figure 3.23**). The two most sensitive cell lines to palbociclib (DIPG07 and GBM01) were selected for further studies.
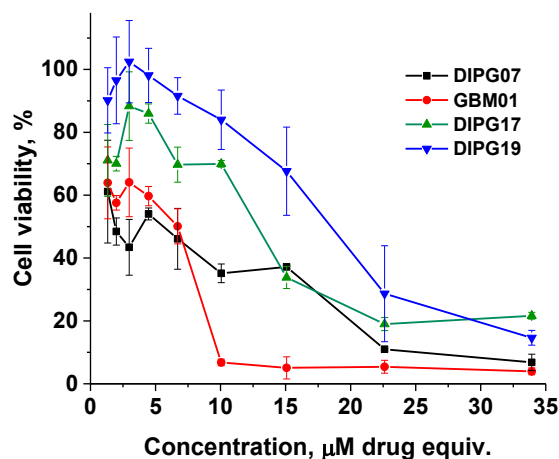

Figure 3.23 Cell viability studies of palbociclib on four different primary cells

Optimized MTS assay parameters confirmed the non-toxic nature of linear and star-PGA carriers, which agrees with previous studies. For free palbociclib, IC50 values in DIPG and GBM cell lines were identical (3.9 μM) (**Figure 3.24**). Further tests demonstrated the biological activity of the conjugates (**Figure 3.24**), which appeared lower than that of the free drug. We hypothesize that the lower activity is a different cell trafficking (i.e., endocytosis for conjugates and free diffusion for palbociclib)[60],[61]. Surprisingly, we observed a reversed correlation between drug loading and cell viability in a way that conjugates with lower loading appeared more active. When the activity of star and linear conjugates was compared, it appeared that StPGA-palbociclib conjugates were more active (76% and 39% cell viability for DIPG and 83% and 54% cell viability for GBM cells for StPGA-palbo4 and StPGA-palbo1, respectively (**Figure 3.24 A and B**).
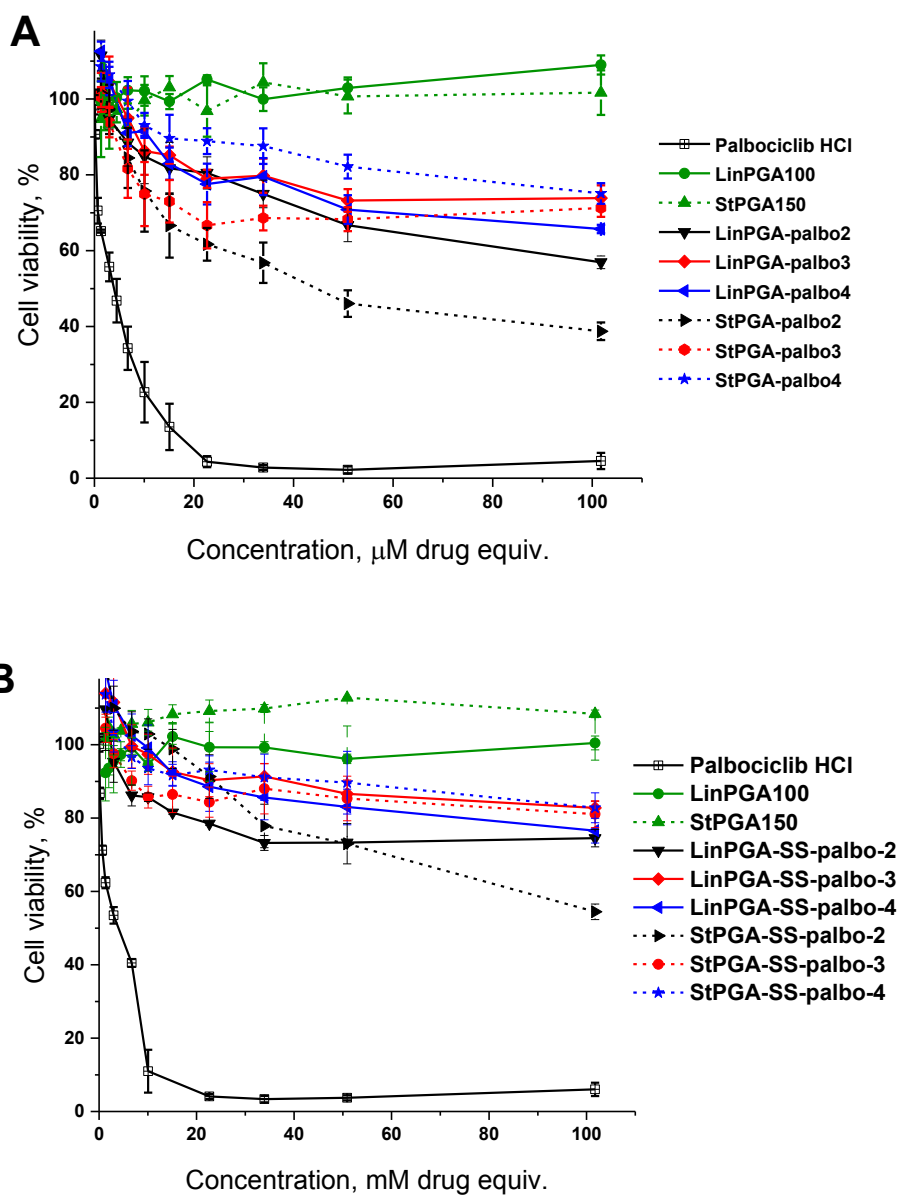
Figure 3.24 Biological evaluation of LinPGA- and StPGA-palbociclib conjugates. Cell viability studies of free Palbociclib, control LinPGA and StPGA polypeptides, and LinPGA- and StPGA-palbociclib conjugates in patient-derived DIPG (A) and GBM (B) 3D cell spheroids. Data presented as mean ± SEM (n = 4)

The toxicity of linear conjugates (**Figure 3.24**) ranged from 74% to 57% for DIPG cells and 84% to 74% for GBM cells; however, conjugates with lower loading also appeared more active. The differences with StPGA-palbociclib conjugates correlate directly with higher chain flexibility of the linear polymeric chains of LinPGA-palbociclib conjugates.

Lower activity of the conjugates with higher loading in the in vitro model correlates well with SAXS and CD results obtained earlier: more densely compacted structures and deeply buried hydrophobic residues result in slower diffusion of the molecules to the cleavage site and, thus, delayed drug release. The latter can, however, be beneficial for in vivo application as it allows for better control of drug release in desired tissue or cell compartments.

As palbociclib is a CDK4/6 inhibitor described to affect cell proliferation via cell cycle arrest [8], we also studied the cell cycle in DIPG (**Figure 3.25A**) and the more proliferative GBM cells (**Figure 3.25B**). Flow cytometry and propidium iodide staining were used to quantify different nuclear DNA content depending on the cell's progression through a division cycle (**SI-3.2**). During proliferation, cells pass through four main stages: G0 – resting non-dividing stage, G1 – growth phase 1 (synthesis of proteins and RNA), S - synthesis phase (starting of DNA replication), G2 – growth phase 2 (DNA synthesis has completed, cells carry two full copies of the genetic material and prepare for mitosis), M – mitosis phase (a nuclear and cytoplasmic division of a cell). Since G2/M phases contain identical DNA, this method cannot distinguish them. The measuring principle is based on stoichiometric DNA labeling, which is proportional to the amount of DNA in the cell. The histogram of DNA content distribution versus fluorescence value is built, and applying the mathematical modeling algorithms, the G0/G1, S, and G2/M phases are derived [62].
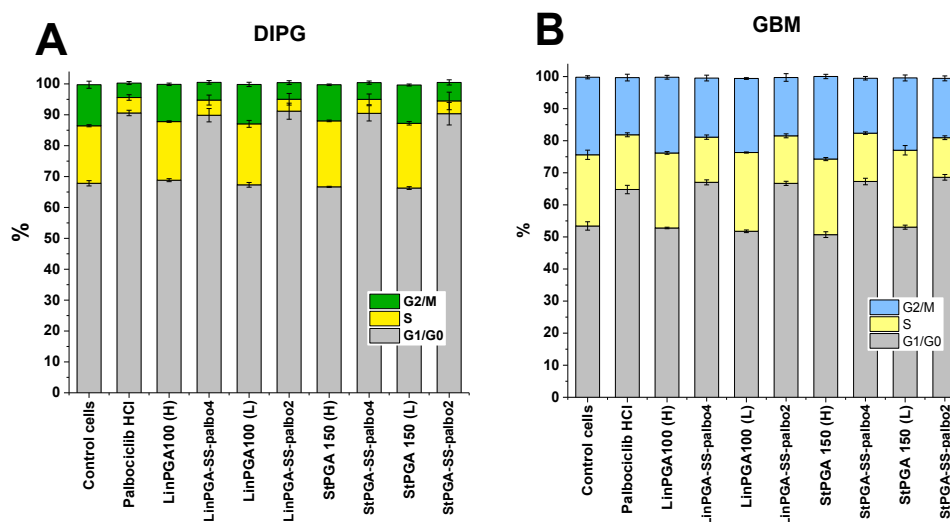
Figure 3.25. Cell cycle studies of palbociclib, LinPGA-palbo2, LinPGA-palbo4, StPGA-palbo2, StPGA-palbo4, and control LinPGA and StPGA polypeptides performed on DIPG (C) and GBM (D) spheroids. Data presented mean ± SEM (n = 3).

Neither linear nor star conjugates had a significant influence on cell cycle arrest in comparison with palbociclib alone (p>0.1), and more than 90% of cells remained in the G1/G0 phase for DIPG and around 67% for GBM cells after treatment. These data prove that conjugation does not affect Palbociclib's mechanism of action– G1/G0 cell cycle arrest. StPGA-palbociclib conjugates demonstrated a more significant antiproliferative effect than LinPGA-palbociclib conjugates analogs in DIPG and GBM cells due to a more compact solution conformation (**Figures 3.13** to **3.16**). Thus, we conclude that conjugation does not affect drug activity, and released palbociclib maintains its activity.

3.2.3 Design and development of Self-immolative Peptidic Linker for PGA-palbociclib Conjugates

In the hope of constructing palbociclib conjugates under a rational design based on the biological scenario and considering the PGA platforms developed for intranasal delivery, we next explored a self-immolative linker based on a protease trigger. As stated previously, specific enzymes become upregulated in the tumor microenvironment [63]. In addition, the selected crosslinked star-shaped polyglutamates via disulfide linkers StPGA-SS-CL as a candidate for intranasal drug delivery is not chemically compatible

with the disulfide self-immolative linker described for palbociclib in **Section 3.2.2.** Thus, as an alternative, we selected a self-immolative peptidic linker capable of being cleaved by Cathepsin B, a cysteine protease with endo- and exo-peptidase activity[64] highly expressed in cancers such as human breast, colon, and prostate tumors, gliomas, and melanomas [65]. Doronina et al. designed the valine-citrulline (ValCit) linker to be sensitive to this protease, allowing stability in the bloodstream but rapid proteolytic cleavage under the conditions found within cancer cells [66]. The successful use of this linker for antibody-drug conjugation (brentuximab vedotin, marketed as Adcetris® [67]) provides evidence of its general utility.

Given this success, polypeptide-drug conjugates have also employed peptidic linkers susceptible to cathepsin B-mediated cleavage. The conjugation of gemcitabine to PEGylated dendrimeric poly-lysine formulation via amide bond generated a polypeptide-drug conjugate with a drug release of approximately 60% in 30 min in the presence of cathepsin B but almost no release in the absence of this protease [68]. Combining a peptide construct with a self-immolative component can improve drug release upon enzyme-triggered cleavage. Leong et al. compared drug release from PEGylated dendrimeric poly-lysine conjugates of doxorubicin using cathepsin B cleavable linkers of differing natures[69]. They reported more rapid drug release for ValCit linkers with a self-immolative diglycolic acid motif (50%) compared to self-immolative GLFG (33%) and non-self-immolating glutaric acid-GLFG linker (26%) over 48 h.

Inspired by the promising results observed for peptidic linkers in polymer-drug conjugates, we selected the ValCit motif to prepare a family of LinPGAs and StPGAs and study, as above, the influence on drug loading aiming to identify the best conjugate for DIPG and/or GBM treatment.

3.2.3.1. Synthesis and Physico-chemical Characterization of PGA-ValCit-palbociclib conjugates

We prepared PGA-ValCit-palbociclib conjugates using a six-step synthetic scheme (**Figure 3.26**), beginning with activating the carboxylic group of 6-maleimidohexanoic acid with N-hydroxysuccinimide (NHS) and followed by ValCit dipeptide amide coupling with the DMTMM activator. We then coupled palbociclib to a hydroxyl group activated with *p*-nitrophenyl chloroformate, followed by the reaction of the maleimide terminal group with cysteamine. The last step comprised conjugation to the PGA carrier via amide coupling with the DMTMM activator.
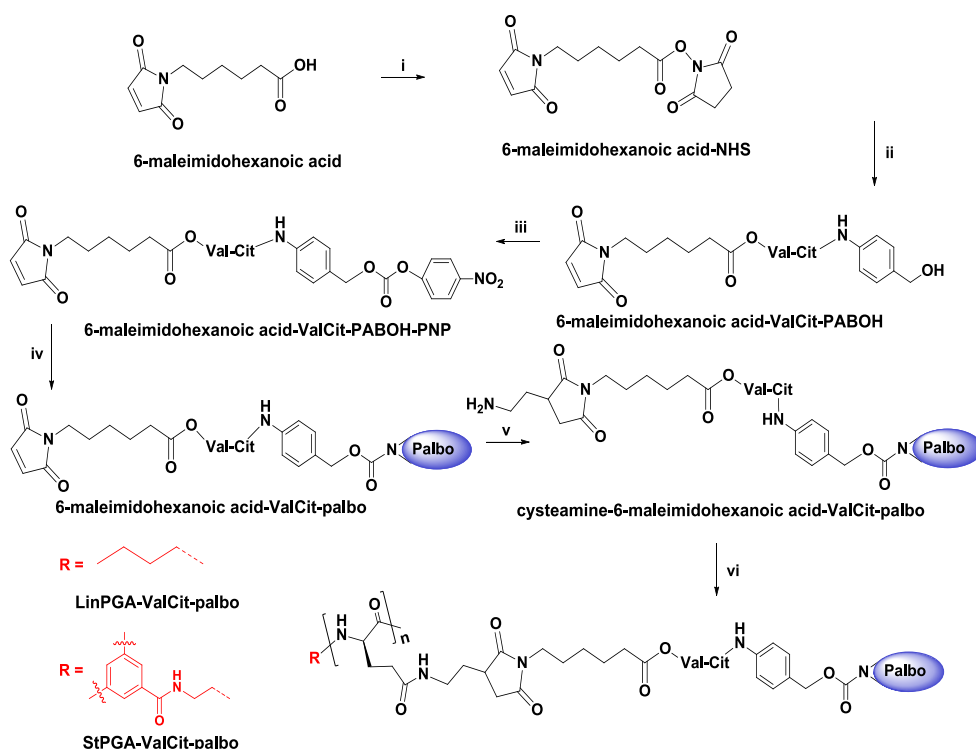
Figure 3.26. Synthesis of PGA-ValCit-palbociclib conjugates. i) NHS, DCC, THF$_{anh}$; ii) ValCit-PABOH, DMF$_{anh}$; iii) p-nitrophenyl chloroformate, DMAA, TEA; iii) palbociclib, DMAA; iv) cysteamine hydrochloride, DMAA; v) PGA, DMF$_{anh}$, DMTMM·BF$_4$, TEA (**SI-3.8.**).

We used a combination of ^{1}H, ^{13}C, Distortionless Enhancement by Polarization Transfer (DEPT 135), and Heteronuclear Multiple Bond Correlation (HMBC) NMR experiments to prove compound identity and purity during each synthetic step (Figure SI 3.33-3.39). We confirmed the completed reaction between the activated ValCit linker and palbociclib with ^{1}H NMR by the appearance of aromatic protons at 9.90, 8.88, 7.81, 7.70, and 7.42 ppm and aliphatic protons at 5.87 ppm (from cyclopentyl ring), 3.48, 3.08 ppm (from piperazine ring), 2.35, and 2.23 ppm (from methyl groups) (**Figure 3.27 A, B** green dotted squares).
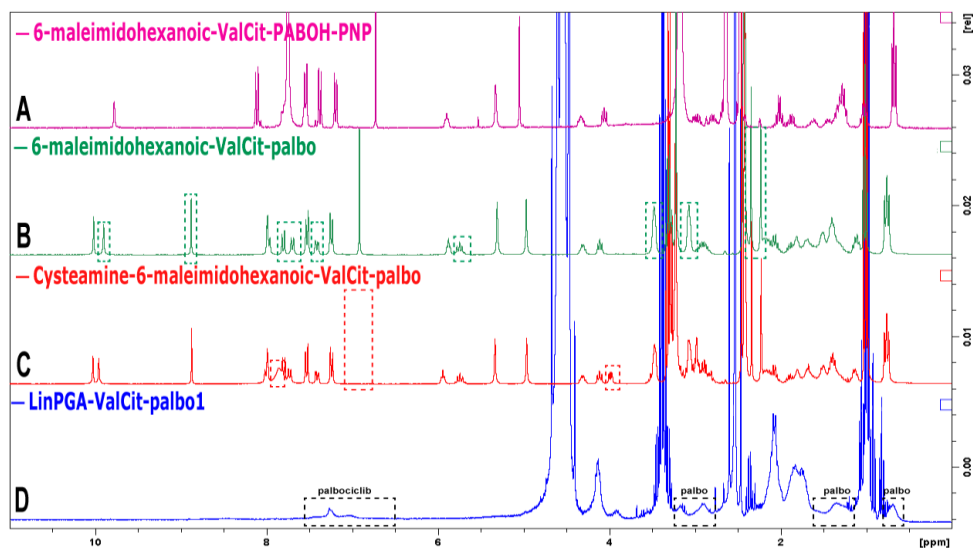
Figure 3.27. Representative ¹H NMR spectra of the activated ValCit linker **(A)**, ValCit-palbociclib linker **(B)**, Cysteamine-ValCit-palbociclib linker **(C)**, linear palbociclib conjugate.

We first attempted to modify PGA with Cys to mimic the widely used antibody modification approach to link the prepared intermediate linker 6-maleimidohexanoic acid-ValCit-palbociclib to PGA[42]; however, purifying the thiolated polymers resulted in significant problems due to crosslinking reactions between the thiol groups. Therefore, we added cysteamine to include a freely accessible primary amine for PGA conjugation. We confirmed the completion of the reaction with cysteamine with ¹H NMR through the disappearance of maleimide protons at 6.91ppm and the appearance of broad singlets from the amino group of cysteamine at 7.86 ppm and enantiotopic proton at 3.99 ppm with a characteristic doublet of doublets splitting due to unequal coupling constants of the axial and equatorial position of maleimide protons (**Figure 3.27 C**, red dotted squares).

We next performed HMBC NMR to prove the identity of the prepared linker (**Figure 3.28**). Proton-carbon correlations between all peaks unambiguously proved compound identity.
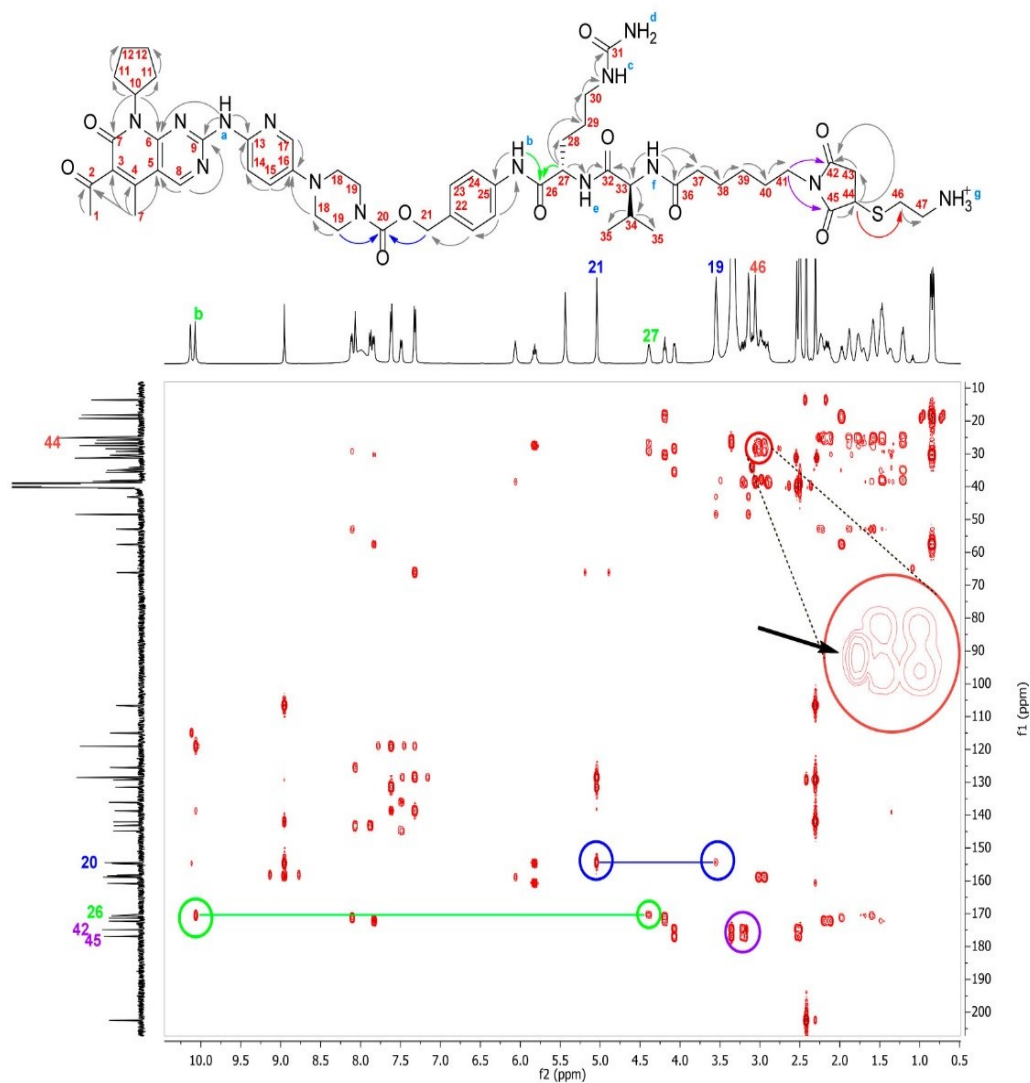
Figure 3.28. HMBC spectrum of cysteamine-6-maleimidohexanoic acid-ValCit-palbociclib linker. All observed correlations are highlighted in the molecule structure (the arrow start corresponds to the hydrogen, and the arrow end corresponds to the correlating carbon atom). Four critical correlations between the main structural blocks are shown in distinct colors as arrows (on the structure) or correlation peaks (on the spectrum). Insertion is an expansion of two overlapped spots; the spot of interest is highlighted with a black arrow. Protons connected to carbons are named as numbers, and protons connected to nitrogens – as letters.

Four key proton-carbon correlations (**Figure 3.28**) showed the connections between four different structural blocks - 1. palbociclib-carbamate, 2. aminobenzoic alcohol residue, 3. 6-maleimidohexanoic acid-ValCit fragment, and 4. cysteamine fragment. H21 and C21 can be easily assigned using the HMQC artifact. H21 shows a cross peak with C20 from the carbamate group. The bond correlation between C20 and H19 proved that a carbamate forms between the morpholine ring of palbociclib and the alcohol of the aminobenzoic alcohol. Assignment of peaks can be successfully continued for C22-C25 and H_b. Cross-peaks between H_b (10.08 ppm) and C26 (170.65 ppm) proved the presence of the amide group formed with the amine of aminobenzoic alcohol and the carboxylic group of citrulline. Following the same strategy, we can reconstruct all connections from C26 to C41. Two cross-peaks, H41-C42 and H41-C45, straightforwardly confirmed the connection of the aminohexanoic acid residue to the maleimide. The successful addition of cysteamine is evident from the cross-peak H46-C44 (see spectrum expansion). Despite the heavy overlap of the spectrum in the region under study, we can identify the desired cross-peak. Following a similar assignment from C19 to C1, we concluded that the structure of palbociclib remains intact. Finally, we identified the terminal amine hydrochloride as a broad peak at 8.00 ppm that integrates three protons.

After PGA conjugation, palbociclib protons were present within the final PGA-ValCit-palbociclib conjugate spectra: aromatic protons at 7.5-6.5 ppm and aliphatic protons at 3.3-2.8, 1.5-1.3, and 0.8 ppm, thereby confirming the drug-linker conjugation. The palbociclib protons presented the characteristic peak broadening (**Figure 3.27 D**).

We successfully synthesized a linear and star-shaped PGA-palbociclib conjugate family using a ValCit linker with different drug loadings. Using matrix-matched calibration, we determined total drug loading (TDL, %wt) by UV-Vis analysis (**Figure 3.29** and **Table 3.4**). Overall, we observed good agreement between estimated values and those obtained from NMR analysis.
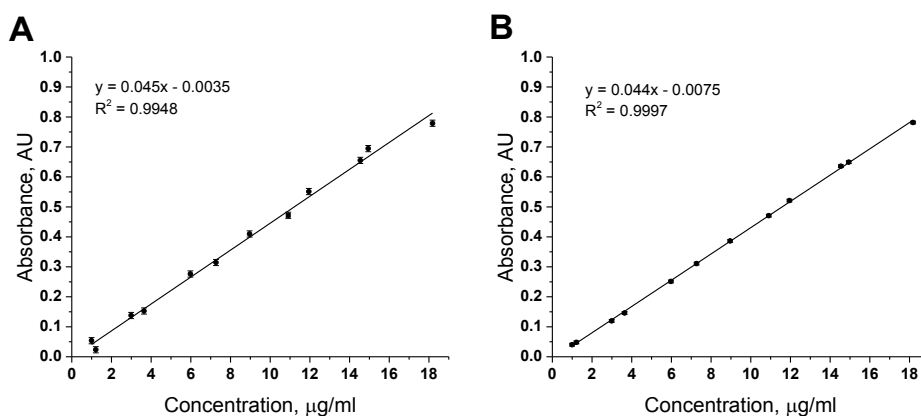
Figure 3.29. A matrix-matched calibration curve was used to quantify the TDL of LinPGA-ValCit-palbo **(A)** and StPGA-ValCit-palbo **(B)** conjugates.

We also determined a free drug content below 0.2% wt of TDL by HPLC, demonstrating the sufficient purification protocol. As stated above, free drug content of less than 2 wt% of total drug loading is mandatory for progression to biological characterization [53]. **Table 3.4** summarizes the physicochemical characterization of the synthesized family of PGA-ValCit-palbociclib conjugates.

Table 3.4 Physicochemical Characterization of PGA-ValCit-palbociclib Conjugates

Conjugate	TDL[a] (% mol)	TDL[a] (% wt)	Free Drug Content[b] (% wt of TDL)	Z-pot[c] (mV)	R_h[d] (nm)	PDI[e]
StPGA-ValCit-palbo1	2.8	6.9	<0.2%	-19.5	12.0	0.10
StPGA-ValCit -palbo2	3.7	8.8	<0.2%	-19.4	11.6	0.07
StPGA-ValCit -palbo3	4.5	10.1	<0.2%	-21.4	12.7	0.04
LinPGA-ValCit -palbo1	3.2	7.7	<0.2%	-24.4	6.8	0.06
LinPGA-ValCit -palbo2	4.0	10.9	<0.2%	-22.2	6.9	0.13
LinPGA-ValCit-palbo3	5.8	12.2	<0.2%	-21.3	6.0	0.07

[a]TDL - Total drug loading, determined by UV-Vis and supported by NMR, [b]Z-potential, determined by DLS, [d]R_h – hydrodynamic radius, determined by DLS [0.1 mg/ml in PBS], and [e]PDI - Polydispersity index, determined by DLS.

Dynamic light scattering (DLS) analysis demonstrated hydrodynamic radius values in PBS around 6 nm for linear conjugates and 12 nm for star-shaped conjugates (**Table 3.4**). All tested conjugates possessed a negative z-potential value close to -20 mV, which is lower if we compare conjugates with disulfide linkers around -30 mV (**Section 3.2.2.1, Table 3.1**). These results can be explained by the contribution of the positively charged citrulline amino acid, which decreases the net charge of conjugates with the ValCit linker.

We next employed CD to study the influence of drug loading on conjugate spatial conformation in solution (**Figure 3.30**).
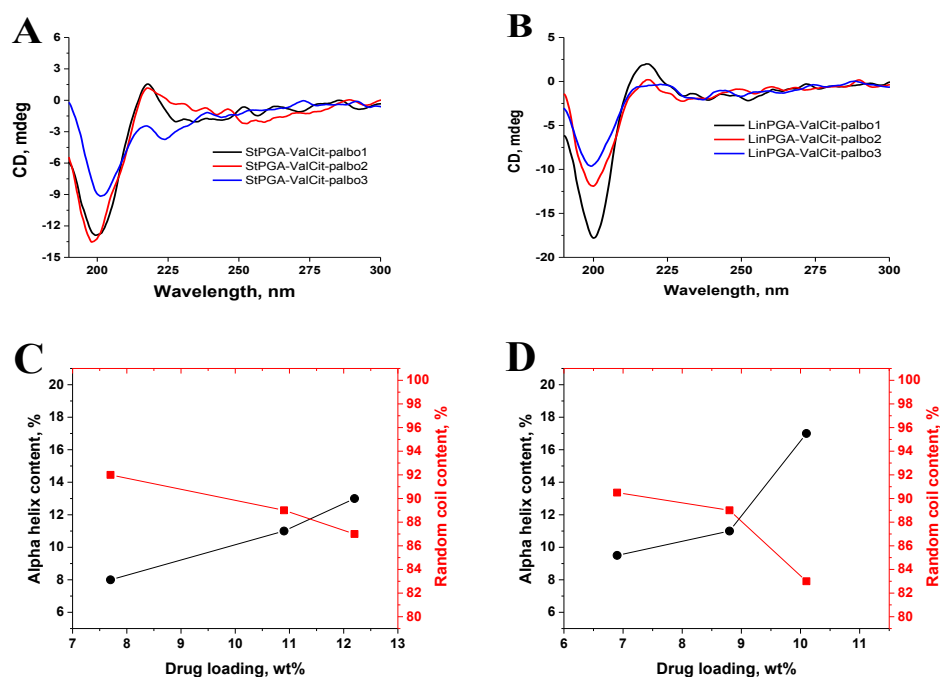
Figure 3.30 CD spectra of (**A**) LinPGA-ValCit-palbo and (**B**) StPGA-ValCit-palbo conjugates at 0.12 mg/ml PBS. Content of alpha-helix and random coil conformations as a function of drug loading for (**C**) LinPGA-ValCit-palbo and (**D**) StPGA-ValCit-palbo conjugates.

We observed a clear transition in the secondary structure from the random coil in StPGAs of low drug loading to α-helix for StPGA conjugates with higher drug loadings and a less evident transition for lower drug loading (**Figure 3.30A**). These results are similar to the StPGA-SS-palbociclib family (**Figure 3.13A and B**), although the α-helix to random coil transition is less pronounced here. This transition may relate to linker length (ValCit > SS) and the more distant hydrophobic component (the drug), which causes structural transitions; however, we did not observe similar transitions for LinPGA conjugates when comparing low and high drug loadings (**Figure 3.30B**).

Deconvolution of CD spectra (**Figure 3.30 C, D**) confirmed a more predominant alpha-helix content (17%) than random coil (7%) in the StPGA-ValCit-palbo conjugates with higher drug loading than for the linear analog (13% and 11%, respectively). These values remain smaller than the 30% alpha-helix content observed for high drug loading in -SS- linker-containing conjugates (**Section 3.2.2.1 Figure 3.13C and D**), indicating that linker length also triggers the conformational transitions.

As in the case of PGA-SS-palbociclib conjugates, we performed in-depth studies using SAXS to better understand the relationship between drug loading and conjugate solution conformation. We did not analyze conjugates with the lowest drug loadings (StPGA-ValCit-palbo1 and PGA-ValCit-palbo1) as point-to-point interactions between palbociclib residues that started to prevail in repulsion between polyelectrolyte chains caused solubility issues. SAXS experiments demonstrated that conjugates with ValCit linkers behaved similarly to those with disulfide linkers in the low-q and intermediate-q Guinier region; however, the conjugates aggregated more robustly (**Figure 3.31**, **Table 3.5**).

We observed a transition between larger to smaller clustered mass fractal aggregates for LinPGA conjugates with ValCit linkers upon increasing loading (**Figure 3.31A**, **Table 3.5**), which corresponds to a transition from intermediate chain collapse (i.e., incomplete crumpled globule) to more organized crumpled globules at the highest loading. Curves corresponding to conjugates with the lower loading have a slope of -3, typical for a surface mass fractal in the Porod region (i.e., particles with diffuse, non-defined surfaces). For conjugates with high loading, the observed slope of -4 corresponds to a mass fractal with a defined surface.
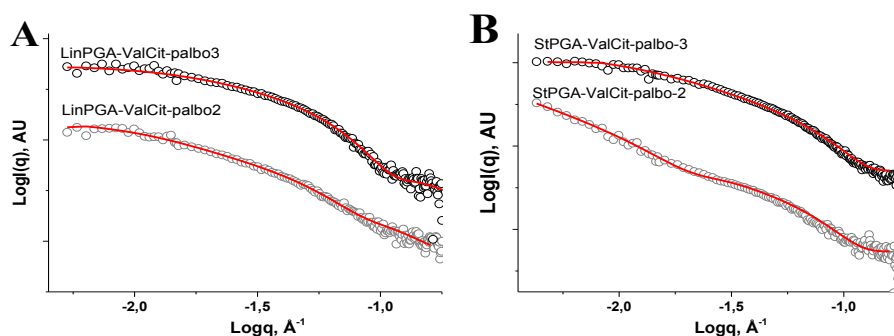
Figure 3.31. SAXS profiles with the fitting of (**A**) LinPGA-ValCit-palbo and (**B**) StPGA-ValCit-palbo conjugates with different drug loading, 0.1 mg/ml PBS.

Table 3.5 Characteristic parameters of PGA-ValCit-palbociclib conjugates derived from SAXS profiles

Characteristic parameter	LinPGA-ValCIt-palbo2	LinPGA-ValCIt-palbo3	StPGA-ValCIt-palbo2	StPGA-ValCIt-palbo3
Slope low-q Guinier region	-0.3	-0.8	-2	-1
Slope intermediate q Guinier region	-1.5	-1.6	-1.8	-1.6
Slope Porod region	-3	-4	-3	-4

StPGA conjugates in the low-q and intermediate-q Guinier region (**Figure 3.31 B**, **Table 3.5**) transitioned from large to compact clustered mass fractal aggregates. Curve slope values remained similar to LinPGA conjugates with equal loading in the Porod region, suggesting similar compactization. This data suggests that another intermediate state between intermediate and defined crumpled micelles exists – crumpled micelles with a diffuse surface (slope of the curve -2 in the low-q region). Fiber-like fractal aggregates start to interact and compact in this structure, forming a secondary fractal structure that remains loose. The secondary fractal structure compacts upon further loading, forming defined crumpled micelles with an adequately defined smooth surface.

We next employed the Kratky plots (dependence $q^2I(q)=f(q)$) to characterize system compactness (**Figure 3.32A and B**), which demonstrated the formation of structures with restricted chain movements and a high degree of order that increases with increased loading. The LinPGA-ValCit-palbo2 conjugate displayed a slightly less ordered structure than the StPGA analog with similar loading (positive slope in the q $\geq$ 0.6 nm-1 range for linear conjugate). All conjugates possessed a defined peak at 0.45 nm^{-1}. The StPGA conjugate with the highest drug loading, StPGA-ValCIt-palbo3, displayed a slight peak shift to 0.49 nm^{-1}; however, this shift remains unclear.

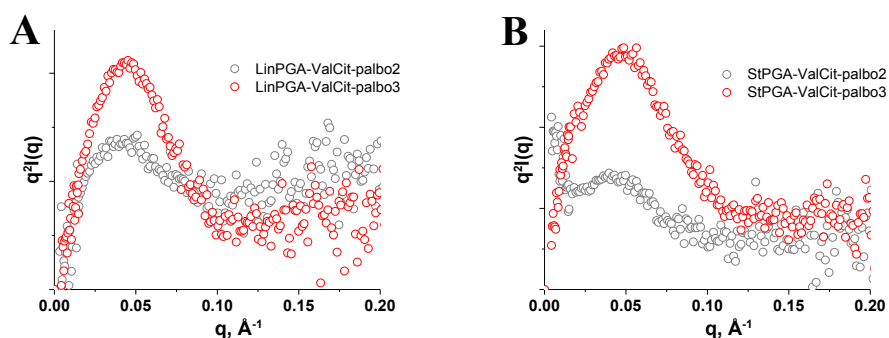**Figure 3.32.** Kratky plots of (**A**) LinPGA-ValCit-palbo and (**B**) StPGA-ValCit-palbo conjugates with increasing drug loading: grey (lowest), red (highest).

Analysis of the amide region of the FTIR spectra (**Figure 3.33 A, B, C, D**) indicated conformational changes in LinPGA and StPGA conjugates depending on the drug loading. The maximum of the main peak shifts from 1651 cm^{-1} to 1656 cm^{-1} for LinPGA conjugates (**Figure 3.33A**) and from 1647 cm^{-1} to 1657 cm^{-1} for StPGA conjugates (**Figure 3.33C**) in the amide I region. We observed similar trends for both LinPGA and StPGA conjugates in the second derivative spectra of the amide I region (**Figure 3.33B and D**) – a red shift of the maximum at 1652 cm^{-1}, the appearance of the peak at 1694 cm^{-1}, and peak changes at 1661 cm^{-1} and 1626 cm^{-1}. The maximum of the main peak in the amide II region shifts from 1576 cm^{-1} to 1579 cm^{-1} for LinPGA conjugates (**Figure 3.33A**) and from 1573 cm^{-1} to 1579 cm^{-1} for StPGA conjugates (**Figure 3.33C**). The

observed trends generally indicate an increase in alpha-helix content similar to the results for the conjugates with disulfide linkers.
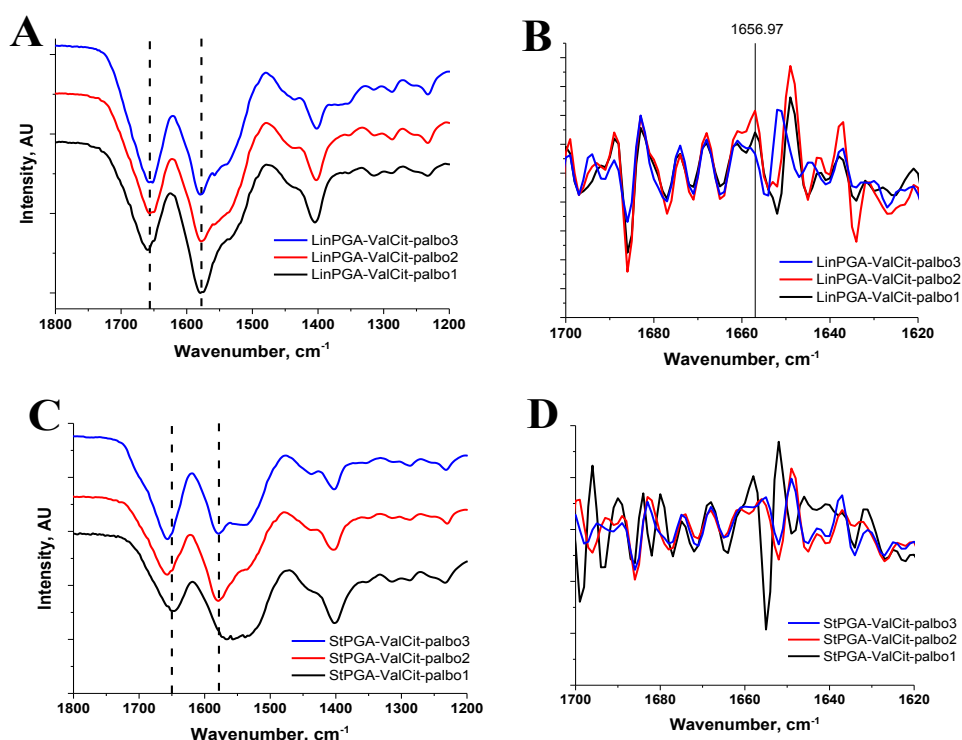
Figure 3.33. Fragment of FT-IR spectra of LinPGA-ValCit-palbo (A) and StPGA-ValCit-palbo (C) conjugates with increasing drug loading: black (lowest), red, blue (highest). Dotted lines at 1659 cm^{-1} and 1575 cm^{-1} demonstrate the appearance of the shoulder and shift of amide I and amide II peaks upon increasing loading. Second derivative spectra of amide I region of LinPGA-ValCit -palbo (B) and StPGA-ValCit -palbo (D).

We next determined the critical aggregation concentration (CAC) for the ValCit linker conjugates to further evaluate the influence of drug loading into conjugate solution conformation (**Figures 3.34** and **3.35**).

Figure 3.34 (A, C, E) CAC study of LinPGA-ValCit-palbo in PBS using Nile red as the fluorescent probe. **(B, D, F)** The intersection between fluorescent intensity and the conjugate concentration gives the CAC value (vertical black dashed line).

Figure 3.35 (A, C, E) CAC study of StPGA-ValCit-palbo in PBS using Nile red as a probe. **(B, D, F)** The intersection between intensity and the conjugate concentration gives the CAC value (vertical black dashed line).
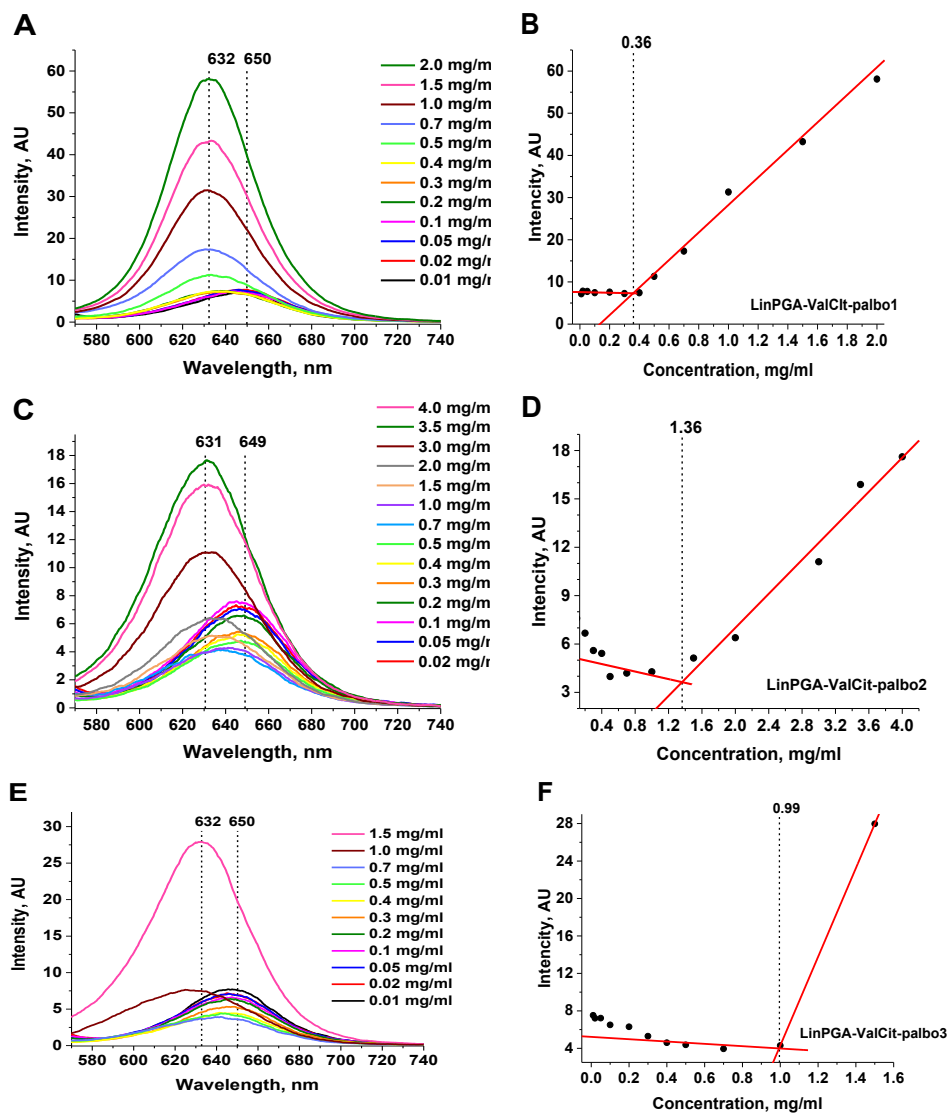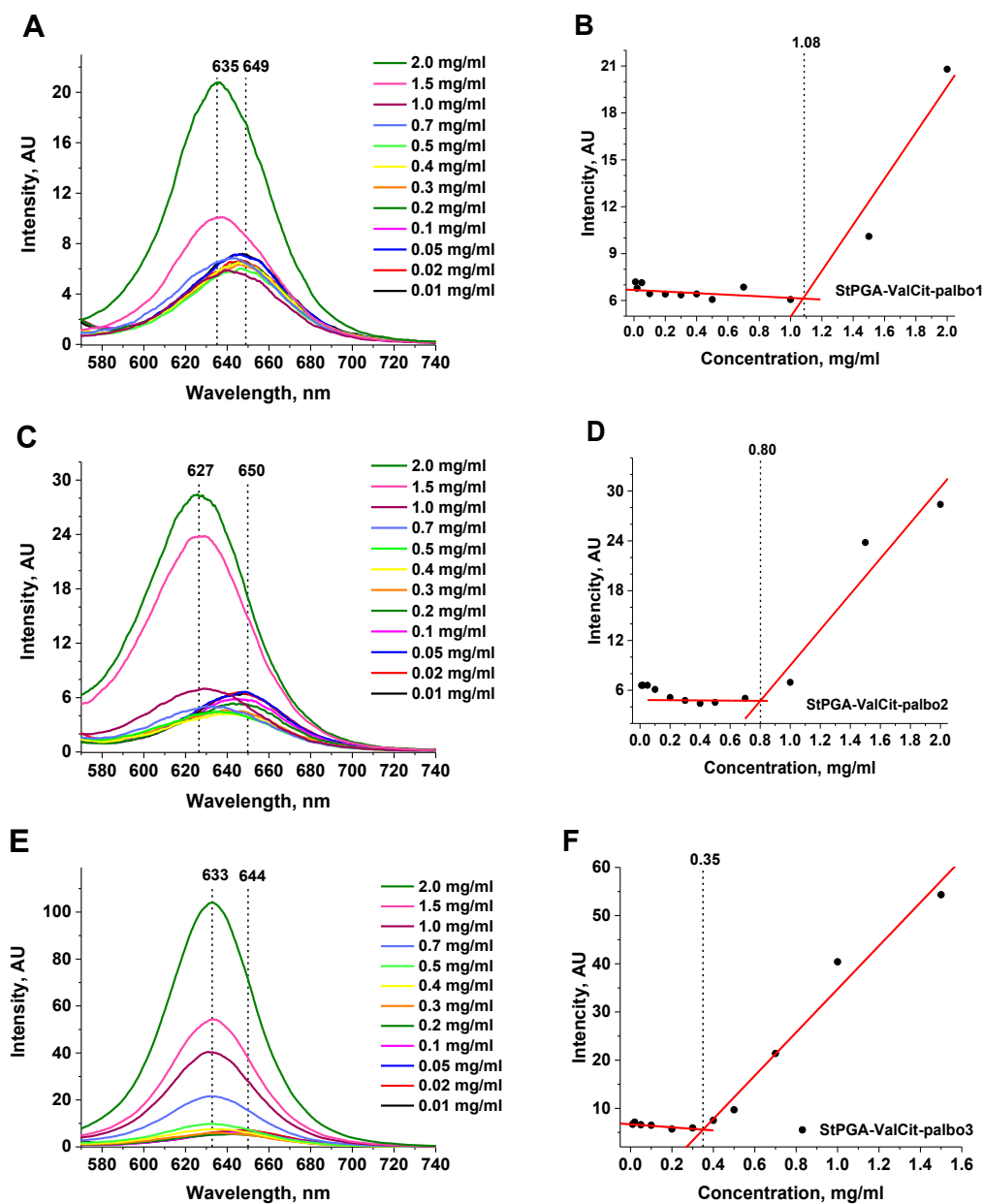
We determined the CAC value of prepared conjugates using the Nile red method [55], where the dye penetrates the hydrophobic pockets of polymeric micelles formed due to the conjugates' aggregation. There are two approaches to determining the CAC by identifying the intersection by plotting the conjugates' concentration versus changing the Nile red's intensity or wavelength at the Nile red's peak maximum. For ValCit conjugated, we observed the smaller peak shift of the dye in comparison with conjugates via disulfide linker, and because of the peak broadening, we used the plotted intensity versus conjugate concentration for CAC determination. **Figure 3.34 (A, C, E)** and **Figure 3.35 (A, C, E)** demonstrate the fluorescent spectra of LinPGA-ValCit-palbociclib and StPGA-ValCit-palbociclib conjugates. The low Nile red fluorescence intensity (maximum λ=650 nm) corresponds to free unincorporated dye and the absence of nanoassemblies at low conjugate concentration. Increasing conjugate concentration towards the CAC prompted an increase in the fluorescence intensity of Nile red (maximum shifts to λ=630 nm), which corresponds to the incorporation of dye within polymeric micelles. The inflection point of this transition can be found by plotting the intensity or wavelength of the peak maximum of Nile Red versus the concentration of the conjugate. **Figure 3.34 (B, D, F)** and Figure **3.35 (B, D, F)** demonstrate the plotted intensity of Nile Red at the peak maximum for LinPGA conjugates and StPGA conjugates. **Table 3.6** reports the calculated CAC values for all PGA-ValCit-palbo conjugates evaluated.

***Table 3.6.** CAC values of evaluated PGA-ValCit-palbociclib conjugates*

Conjugate	CAC, mg/ml	Conjugate	CAC, mg/ml
LinPGA-ValCit-palbo1	0.36	StPGA-ValCit-palbo1	1.08
LinPGA-ValCit-palbo2	1.36	StPGA-ValCit-palbo2	0.80
LinPGA-ValCit-palbo3	0.99	StPGA-ValCit-palbo3	0.35

Unexpectedly, the LinPGA conjugate (**Table 3.6**) with the lowest drug loading (LinPGA-ValCit-palbo1) demonstrated a high aggregation ability, possibly due to point-to-point interactions. This result might explain the solubility issues observed upon increasing the concentration to 2 mg/ml. We observed the expected tendencies for middle and high drug loading for LinPGA and all the conjugates – the CAC decreased upon increased drug loading. Comparing high drug-loading analogs, StPGA conjugates possessed lower CAC values than their linear counterparts. The restricted flexibility of the star-shaped chain may explain this finding.

To further evaluate this conformational phenomenon, we studied palbociclib release kinetics by exposing LinPGA- and StPGA-ValCit-palbociclib conjugates to Cathepsin B as a trigger for peptidic linker cleavage (in 5 mM DTT in sodium acetate buffer to preserve proteolytic activity [34,70]) **(Figure 3.36)**.
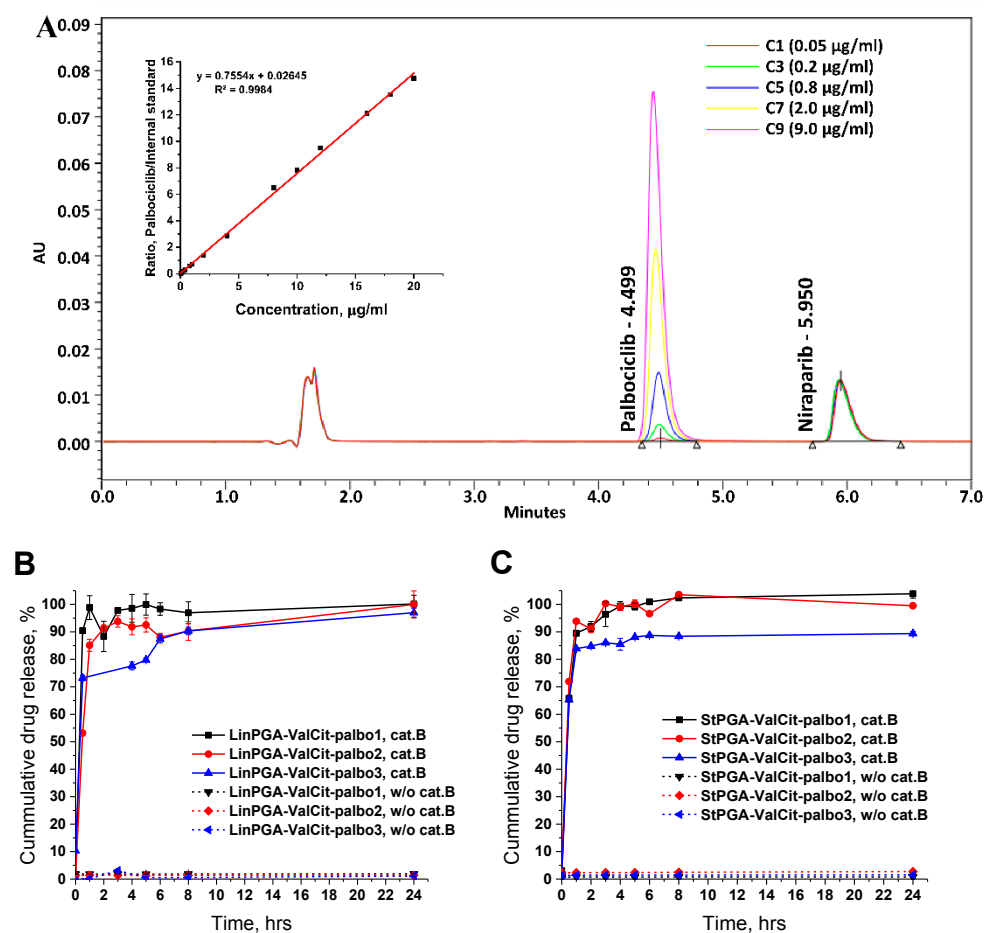
Figure 3.36. (A) Palbociclib calibration curve by HPLC. Palbociclib drug release from LinPGA**(B)** and StPGA **(C)** ValCit-conjugates in the presence/absence of cathepsin B.

We used the HPLC method described for the PGA-SS-palbo conjugates after confirming a lack of interference from the sample matrix and adapted the sample preparation (**SI-3.8**). Cleaved palbociclib does not precipitate due to the slightly acidic pH of the release buffer (5.0); therefore, the complex extraction procedure was avoided. Instead, we employed trichloroacetic acid (TCA) to precipitate any remaining uncleaved conjugate and allow the solubilization of palbociclib and niraparib (used as internal standard) due to the protonation of an amino group from piperazine ring (for palbociclib) or piperidine ring (for niraparib). The final sample preparation step included pH equilibration with NH_4OH, filtration, and injection into the HPLC system.

Figure 3.36 A displays the representative chromatogram and calibration curves for the low and high-concentration regions. We observed rapid drug release (>80% in 1 h) for all conjugates, as reported in the literature for this linker [70,71]. We did not observe differences in drug release rates concerning architectures or drug loadings. Under the same *in vitro* conditions without cathepsin B, conjugates remained stable (<3% of palbociclib in 24 h) (**Fig. 3.39 B and C**).

3.2.3.2. Biological Evaluation of PGA-ValCit-palbociclib Conjugates

As with the previous family of conjugates, we next evaluated the biological activity of conjugates *in vitro* by MTS assay (**Figure 3.37**) in two patient-derived cell lines (DIPG and GBM) following the optimized procedures (**Section 3.2.2.3**). Contrary to the conjugates with disulfide linkers, we did not observe a clear correlation between drug loading and activity and cell dependence for ValCit conjugates; however, conjugates seem to be more cytotoxic in GBM cells at high concentrations, in particular for LinPGA-ValCit-palbo1 conjugate, the only conjugate reaching the IC50 value at 100 μM concentration in GBM cells (**Fig. 3.37A and B**).

In the hope of selecting the most suitable linker based on each cell line's characteristics, we measured cathepsin B levels in both glioma cell lines (method optimization described in **SI-3.15**). GBM cells presented higher intracellular levels of cathepsin B (10.5 mM) than DIPG cells (2.7 mM). This result explains the higher activity of ValCit-palbociclib conjugates in GBM cells, with more significant cell toxicity observed for LinPGA-ValCit-palbo2 in GBM in comparison with DIPG cell (48.9% vs 39.6% cytotoxicity, respectively). The toxicity of conjugates with disulfide linker is significantly lower, from 17.2% to 25.5%, and only for StPGA-ValCit-palbociclib1(star-shape conjugate with the lowest drug loading), the cytotoxicity obtained was 45.6%, comparable to the toxicity of conjugates with Val-Cit linkers.
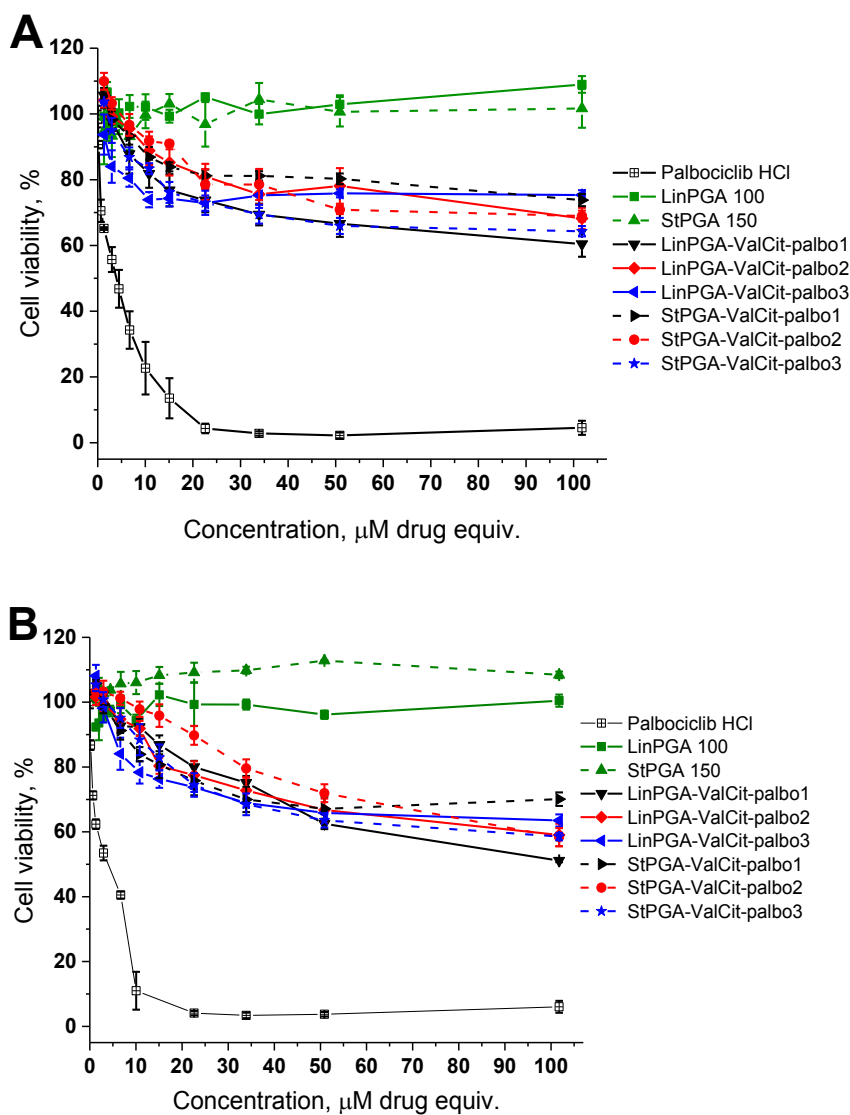
Figure 3.37 Cell viability studies of free Palbociclib, unmodified LinPGA and StPGA polypeptides, and LinPGA-ValCit and StPGA-ValCit-palbociclib conjugates in patient-derived DIPG **(A)** and GBM **(B)** cell lines. Data presented as mean ± SEM (n = 4).

If we compare the activity of conjugates with similar drug loading and different linkers, our findings suggest that the peptidic ValCit linker could offer advantages over the disulfide linker when designing polymer-drug conjugates for glioblastoma treatment (**Figure 3.38 A**), while for DIPG cells the differences are not significant (**Figure 3.38 B**).
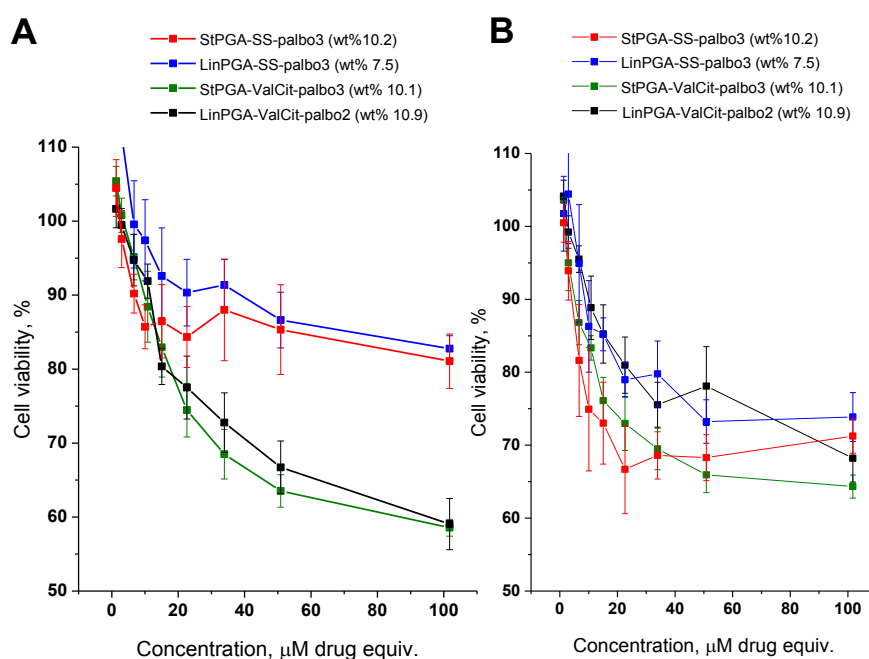
Figure 3.38 Cell viability studies of LinPGA-ValCit, StPGA-ValCit, LinPGA-SS, and StPGA-SS-palbociclib conjugates with similar drug loading around 10 wt% in patient-derived GBM **(A)** and DIPG **(B)** cell lines. Data presented as mean ± SEM (n = 4).

Based on preliminary evidence [72], compact and more globular conformations favor robust diffusion through the glioma spheroids. Therefore, we performed live cell internalization imaging by fluorescence confocal microscopy with a StPGA-ValCit-palbo-Cy5.5 labeled conjugate. For fluorophore labeling, we selected the conjugate with the highest drug loading, StPGA-ValCit-palbo3, due to its better outcome in the in vitro activity and suitability given the next in vivo evaluation step. Since the intranasal administration is limited by the total amount that can be given, higher drug-loading conjugates allow higher drug equivalent doses. Therefore, we labeled a conjugate StPGA-ValCit-palbo3 conjugate with the fluorescent probe - Cy5.5 (**SI-3.9**) and performed an MTS assay to select a suitable concentration that displayed minimal

toxicity but provided a sufficient fluorescent signal to be monitored by confocal imaging. **Figure 3.38** shows the corresponding cell viability for GBM and DIPG cells. We selected a 0.15mg/mL concentration for imaging studies by confocal live imaging (**SI 3.10**), which displayed <20% cell toxicity in both cell lines after 72h of incubation, acceptable for imaging studies in the whole tested concentration range.
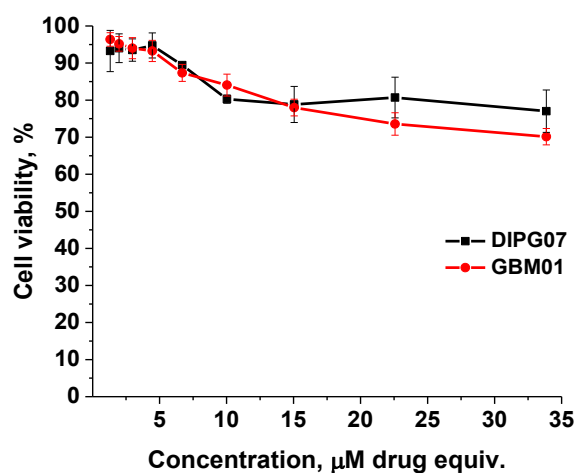
Figure 3.38 Cell viability studies of a StPGA-ValCit-palbo3 conjugate labeled with Cy5.5 in GBM and DIPG cells, MTS 72 h, n=3.

Figure 3.39 shows the internalization of StPGA-ValCit-palbociclib3d-Cy5.5 at 24, 48, and 72 h post-treatment for GBM and DIPG cells. We evaluated the relative level of internalized StPGA-ValCit-palbociclib-Cy5.5 over time with ImageJ software (**Table 3.7**).
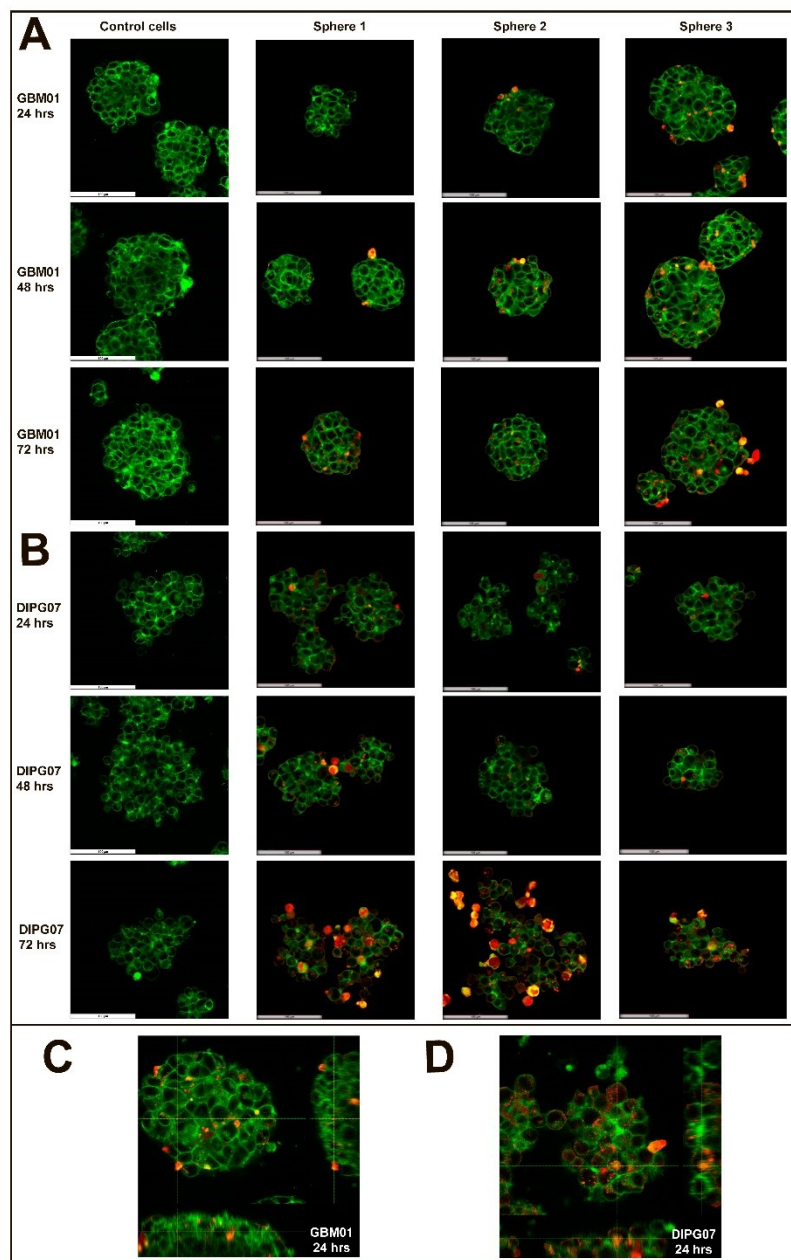
Fig.3.39 Live cell imaging of GBM (A) and DIPG (B) spheroids (control and StPGA-palbociclib-Cy5.5 treated) in standard P96 plates after 24, 48, and 72 h (C) z-stack projection for GBM (D) and DIPG (D) cells after 24 h post-treatment, Images shown as overlayed channels: green – cell mask green (cell membrane marker), red – StPGA-ValCit-palbociclib-Cy5.5

Table 3.7 Internalization of StPGA-palbociclib-Cy5.5 conjugate in GBM and DIPG spheroids

Cell line	Time of post-treatment	Internalization, AU				
		Sphere 1	Sphere 2	Sphere 3	Average	StDev
GBM	24 h	12.5	18.9	27.2	19.5	7.4
GBM	48 h	31.5	36.7	36	34.7	2.8
GBM	72 h	24.7	36.4	36.1	32.4	6.7
DIPG	24 h	20.5	26.2	28.6	25.1	4.2
DIPG	48 h	21.1	29.9	31.8	27.6	5.7
DIPG	72 h	45.1	42.9	50.5	46.2	3.9

We tested several microtiter plates and selected 96 well plates to study uptake and conjugate penetration into spheroids of GBM and DIPG cells. **SI-3.8.11** shows the data on optimizing GBM and DIPG cell growth for confocal microscopy studies. A comparison between P384 and standard P96 plates for GBM cells (**Fig S3.31 A and B**) provides evidence for the significantly lower capacity of P384 plates to form larger spheres; meanwhile, the U-shaped P96 plates (**Fig S3.31C**) supported the growth of single tumorspheres that gradually increased in size over time, however, does not recapitulate the morphological differences between GBM and DIPG cell lines. Thus, we believe that the P96 plate better resembles the unique features of the selected cell lines and, therefore, was selected for the following studies.

As shown in **Table 3.7**, analysis of both GBM (60±14%) and DIPG (54±8%) tumorspheres demonstrated StPGA-ValCit-palbociclib-Cy5 internalization after 24 h, calculated as the relation to the 72 h time point with gradual internalization for DIPG cells till 72 h, and reaching maximum at 48 h for GBM cells.

The GBM tumorspheres did not display any significant changes compared with control cells (untreated) until 72 h post-treatment. The cells have close cell-cell interactions, forming compact tumorspheres of uniform size (**Figure 3.39A**). On the contrary, DIPG tumorspheres (**Figure 3.39B**) became partially disaggregated at 72 h post-treatment. This result may be explained by the influence of released palbociclib from or the conjugate itself on the cell-cell interactions in this cell line at concentration 5 µM drug equiv., which agrees well with the increased cytotoxicity observed in DIPG cells after treatment (**Figure 3.38**). This data suggests that StPGA-palbociclib conjugates, besides cell cycle arrest as a consequence of drug release, not only inhibit cell proliferation but also can interfere with and affect tumorsphere morphology, as noted for DIPG tumorspheres. The data demonstrated that the StPGA-ValCit-palbociclib-Cy5.5 conjugate could penetrate the spheroids in both tested cell lines.

3.2.4. Evaluation of a Combination Therapy to Improve the Efficacy of PGA-palbociclib Conjugates

The drug inavolisib (GDC-0077) was specifically designed to inhibit the α isoform of PI3K (PIK3CA), one of the most frequently mutated oncogenes. Inavolisib demonstrated an excellent safety profile with no cytotoxic effects in primary human hepatocytes while specifically triggering the degradation of the mutant protein without significant change to the wild-type protein [73]. A Phase III study of inavolisib combined with palbociclib and fulvestran for locally advanced or metastatic breast cancer is ongoing (NCT04191499, INAVO120). Mutations of PIK3CA have also been identified within different glioma subgroups [74]. Therefore, we evaluated a combination of palbociclib-inavolisib to enhance the therapeutic effect of our conjugates.

First, we evaluated the synergism between palbociclib and inavolisib in cell viability studies with DIPG cells, which carry the mutation targeted by inavolisib mutation (identified by our collaborator, A. Carcaboso, at Hospital Sant Joan de Déu, Barcelona, Spain). We evaluated different drug ratios by MTS assay and employed the Bliss model as the standard approach to evaluating drug synergism [75], which is based on the calculation of the independent interaction index (τ) expressed by the following equation (Equation 1) [76]:

$$\tau = \frac{d_a}{D_{y,A}} + \frac{d_b}{D_{y,B}} + \frac{d_a d_b}{D_{y,A} D_{y,B}} \begin{cases} < 1 \; Synergistic \; effect \\ = 1 \; Independent \\ > 1 \; Antagonistic \; effect \end{cases} \quad (Equation \; 1)$$

where d_a and d_b are the doses of tested drugs A and B that reach the inhibition rate of y; $D_{y,A}$ and $D_{y,B}$ are the doses of single drugs A and B that reach the same inhibition rate.

This approach requires multiple experiments to set up the same inhibition rate for single drugs and their combinations, which is time and resource-consuming. Therefore, we proposed the use of a derived model to simplify the drug combination evaluation [75], which calculates the Excess over Bliss score (I), which is the difference between the Bliss predicted response ($\hat{y}_{ab}$) at the combination dose (d_a, d_b) of drugs A and B, and the observed response at the same combination dose (Equation 2) [75].

$$I = y_{ab} - \hat{y}_{ab} = y_{ab} - (y_a + y_b - y_a y_b) \begin{cases} > 0 \; Synergistic \; effect \\ = 0 \; Independent \\ < Antagonistic \; effect \end{cases} \quad (Equation \; 2)$$

Antagonistic effect	Synergistic effect		
< 0	0 to 5	5 to 10	>10
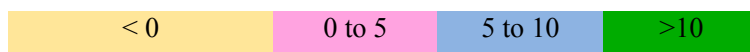
where y_a and y_b are the observed inhibition rates of tested drugs A alone at dose a and B alone at dose b, and $y_{ab\;is}$ the observed inhibition rate of the tested combination with the same dose *a* of drug A and dose *b* of drug B.

Table 3.8 reports the data obtained for palbociclib:inavolisib. We determined a 1:3-5 ratio of palbociclib:inavolisib as synergistic, with an Excess-over-Bliss score of 19.5-21.5.

Table 3.8 Evaluation of the palbociclib: inavolisib combination using the Bliss model

I* (Palbociclib: inavolisib ratio	117:1	78:1	29:1	12:1	7.8:1	5:1	3.3:1	2.9:1	1.3:1
Experiment 1	5.7	16.0	4.5	15.8	16.2	21.8	25.1	4.8	9.4
Experiment 2	9.6	10.1	4.0	13.8	15.0	17.9	18.8	4.8	10.4
Experiment 3	5.8	10.7	7.6	15.0	16.3	18.9	20.6	2.7	5.8
Average	7.0	12.3	5.4	14.9	15.8	19.5	21.5	4.1	8.5
SEM**	1.3	1.9	1.1	0.6	0.4	1.2	1.9	0.7	1.4

* I – Excess over Bliss score** SEM – Standard error of the mean

Inavolisib lacks a functional group accessible for conjugation; therefore, an encapsulation strategy should be implemented. Firstly, inavolisib as the free drug was used to explore if the synergistic effect of the palbociclib-inavolisib combination was maintained with StPGA-SS-palbociclib conjugate (**Table 3.9**). We selected a StPGA-SS-palbociclib2 conjugate due to its higher activity in cells (**Section 3.2.2.2** and **Section 3.2.3.2**) and faster mucosa permeation compared to linear analog (**Chapter 2, Section 2.2.3**). The final formulation will encapsulate inavolisib into polymeric micelles co-administered with the StPGA-palbo conjugates.

The cell viability studies of StPGA-SS-palbo2 and StPGA-SS-palbo3 with free inavolisib confirmed a synergistic effect at a ratio of 5:1 (PGA-palbo:inavolisib) (**Table 3.9**). Furthermore, we evaluated two palbociclib conjugates with different drug loading (StPGA-SS-palbo2 and StPGA-SS-palbo3) in order to check our hypothesis

about the relation between conjugates' drug loading and their biological output. We observed the expected dependency - higher synergism was observed for lower drug-loading conjugates (**Table 3.9**). However, the Excess over Bliss score was lower, 6.0 and 3.8, for the conjugates compared to the free drugs. For a combination with a ratio of 1:3.3, we did not observe synergism, probably due to the kinetics of palbociclib release with less bioavailable free palbociclib and, therefore, less adequate ratio in agreement with the results obtained with both free drugs.

Table 3.9 *Evaluation of the StPGA-SS-palbo/inavolisib combination using Bliss model*

StPGA-SS-palbo: inavolisib ratio	StPGA-SS-palbo2 (5:1)	StPGA-SS-palbo3 (5:1)	StPGA-SS-palbo2 (3.3:1)	StPGA-SS-palbo3 (3.3:1)
Experiment 1	8.3	2.3	-4.0	-9.9
Experiment 2	4.0	4.8	-5.6	-2.9
Experiment 3	5.6	4.4	1.3	-9.8
Average	6.0	3.8	-2.6	-9.0
SEM*	1.3	2.2	0.8	0.8

3.2.5. Encapsulation strategy with Poloxamers as an option for the intranasal administration of the combination therapy PGA-palbociclib conjugate: Inavolisib

Poloxamers (trademark Pluronics®, BASF) are water-soluble triblock copolymers of ethylene oxide (EO) and propylene oxide (PO) arranged in a basic structure: EOx-POy-EOx. Physical properties of poloxamers can be tuned by varying the size of hydrophobic (PO) and hydrophilic (EO) blocks, also denoted as the hydrophilic-lipophilic balance (HLB), which determines the thermodynamic stability of the micelles and affects encapsulation properties and conditions for micelle formation [77]. Until now, pluronic block copolymers have been successfully used as solubilizers for hydrophobic drugs and, similarly to polypeptides, improved solubility, metabolic stability, and drug circulation time of drugs [78]. Moreover, Pluronic materials inhibit drug efflux transporters in the blood-brain barrier, leading to enhanced delivery to the brain [79] and sensitizing cancer cells to increase the toxicity of the applied drugs [80]. Pluronic® polymers are FDA-approved pharmaceutical materials and have been investigated for different therapeutic applications [81].

Pluronics, especially F127, have been widely used as carriers for intranasal delivery due to their thermoresponsiveness. When used in concentrated solutions at around 20 wt%, Pluronics transform from low viscosity transparent solutions at 5^0C to

solid gels upon heating to body temperatures with the transition temperature from 31 to 37⁰C depending on the formulations [77,82–86]. Kabanov's group demonstrated the safety of Pluronics materials (low molecular weight pluronics or a mixture of two different pluronics). A combination of L61 and F127 (SP1049C) for doxorubicin encapsulation reached Phase II clinical trials for advanced adenocarcinoma of the esophagus and gastroesophageal junction [87,88]. Therefore, we chose the F127 poloxamer to encapsulate inavolisib for our combination therapy strategy with PGA-palbociclib conjugates. **Table 3.10** summarizes the physicochemical characteristics and applications of selected Pluronics that could be appropriate for inavolisib encapsulation in combination with PGA-palbo conjugates.

Table 3.10 Physicochemical characteristics of Pluronic "block copolymers"

Copolymer	Mw, Da	Number of EO units	Number of PO units	CMC, M[77]	Administration route	References
L61	2000	4.55	31.03	$1.1 \cdot 10^{-4}$	Intravenous	77,87–89
P85	4600	52.27	39.66	$6.5 \cdot 10^{-5}$	Oral, intranasal, intravenous,	79,89,90
F68	8400	152.73	28.97	$4.8 \cdot 10^{-4}$	Oral, intranasal	79,91
F108	14600	265.45	50.34	$2.2 \cdot 10^{-5}$	Intravenous	89
F127	12600	200.45	65.17	$2.8 \cdot 10^{-6}$	Intranasal, intravenous	77,82–84,86–88,91,92

The formation of poloxamer micelles occurs through a self-assembling equilibrium process that can be predicted from the ratio and size of EO/PO blocks [93]. Aggregation occurs at a concentration of unimers above the CMC, forming spherical, rod-like lamellar micelles [94]. This process includes rapid unimer assembly into metastable aggregates and slow relaxation to thermodynamically stable micelles [95]. The temperature at which the micellization process happens is called "critical micelle temperature" (CMT) and is an essential parameter for micelle formation. Below room temperature, EO and PO blocks within poloxamer are hydrated and water-soluble; upon temperature increases, PO blocks begin dehydrating and becoming insoluble, resulting in micelle formation [78].

There are two commonly used methods to obtain poloxamer micelles. The thin-film hydration method is based on simultaneously dissolving the drug to be encapsulated and poloxamer in a common organic solvent, evaporating the solvent under vacuum rotation at elevated temperature, above critical micelle temperature (CTM), to yield a thin film of drug/polymer, and finally hydrating the film in aqueous solution, and filtering the solution to remove unincorporated drug portion [79]. An alternative method is to prepare the poloxamer aqueous solution at a low temperature (e.g., 40C) and dissolve

the drug following incubation at an increased temperature [89]. Since the selected drug for encapsulation is not water-soluble, we selected the thin-film hydration method and performed several experiments to optimize the critical parameters. For economic reasons, we optimized the method with palbociclib and validated inavolisib for a targeted 10% wt drug loading. **Table 3.11** shows the parameters and results from method development and optimization.

The final method for drug encapsulation (**SI-3.14**) includes solubilizing the drug with pluronic F127 in DCM, mixing by stirring, and vortexing. Subsequently, DCM is eliminated by rotary evaporation at 25^0C, and the resultant thin film is hydrated with preheated Milli-Q water (45^0C or $60^{0,}$ depending on drug stability). The mixture is centrifuged to remove the non-encapsulated drug, and the supernatant is passed through a 0.22 Nylon filter. The final clear micellar solution can be frozen and lyophilized to obtain drug/F127 micelles. **Figure 3.40** shows TEM images of prepared micelles after reconstitution with an average size of 675 nm ± 24 nm, as analyzed with Image J software.
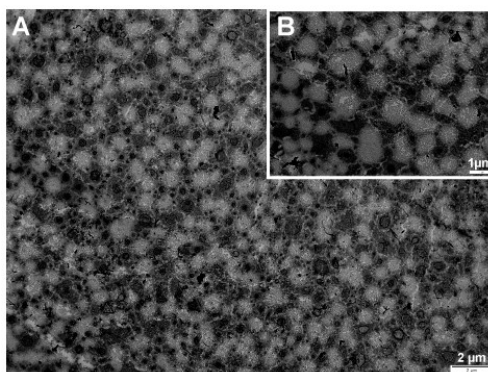

Figure 3.40 TEM photographs of palbociclib micelles, 1 mg/ml, stain - phosphotungstic acid, scale bar (A) 2 μm, (B) 1 μm.

***Table 3.11** Optimization of encapsulation procedure with poloxamer by thin-film hydration method*

E xp	Drug	m, mg	Pluronic	m, mg	Solvent	V, ml	V_{flask}, ml	Stir.[b], min	US[c], min	Vortex, min	$V_{Milli-Q}$, ml	T, °C	Results[d]	EE[e], %
1	Palbo[f]	5	F127	50	DCM	4	10	10	-	5	8	40	+	-
2	Palbo[f]	5	F127	50	MeOH + DCM (1:1)	4+1	10	10	-	5	8	40	-	-
3	Palbo[f]	5	P61	50	DCM	4	10		-	5	8	40	-	-
4	Palbo[f]	2	F127	20	DCM	1	5	10	5	5	3	45	-	-
5	Palbo[f]	2	F127	20	DCM	1	5	10	5	5	3	45	-	-
6	Palbo[f]	2	F127	20	DCM	2	10	10	5	5	3	45	+	90
7	Palbo[f]	3	F127	30	DCM	3	25	10	-	-	2	60	-	-
8	Palbo[f]	3	F127	30	DCM	3	10	20	-	5	3	60	+	-
9	Palbo[f]	3	F127	30	DCM	3	10	20	-	5	2	60	+	-
10	Palbo[f]	3	F127	30	DCM	3	25	20	-	5	3	60	-	-
11	Palbo[f]	5	F127	50	DCM	5	10	20	-	5	5	60	+	95
12	Palbo[f]	5	F127	50	DCM	3	10	20	-	5	3	60	+	92
13	Palbo[f]	5	F127	50	DCM	5	25	20	-	5	5	60	-	-
14	Inav[g]	1	F127	10	DCM	1	10	20	-	5	2	40	+	94

[a]Experiment number, [b]Stirring time at 1000 rpm, [c]Ultra sonication 35 kHz, [d]Determined as positive "+" (if no visible precipitate observed) or negative "-" (if there is precipitation of the drug), [e]Encapsulation efficiency, determined by UV-Vis, [f]Palbociclib, [g]Inavolisib

3.2.6. In vivo Preliminary Data of Conjugate Biodistribution after Intranasal Administration

We carried out preliminary *in vivo* biodistribution studies in healthy mice to evaluate the amount of drug capable of being delivered to the brain via intranasal and validate the purposed combination therapy of PGA-palbociclib conjugates and the pluronic micelles for inavolisib. As described in Chapter 2, we selected the vehicle-hyaluronic acid cross-polymer carrier (HA-CP) for the final intranasal platform, which improves brain accumulation and provides higher residual time in brain tissue. In this system, we incorporated the StPGA-ValCit-palbo3 conjugate with palbociclib micelles (Group A) or without palbociclib micelles (Group B) into HA-CP to modulate the dual delivery of the compounds for further combination therapy. We modified StPGA-ValCit-palbo3 and HA-CP with Cy5.5 (SI-3.10) to allow the *ex vivo* quantification of fluorescence and evaluate the biodistribution of the administered compounds. We performed biodistribution studies in male BALB/c mice after intranasal administration (**SI-3.11**).

Figure 3.41 C shows the quantified Cy5.5 µg/g tissue after organ homogenization and quantification in this preliminary study (**SI-3.12**). As previously demonstrated with IVIS® images, the majority of the compound is present in the intestine at 26.2 ±3.7 % of the injected dose/g tissue(ID/g tissue); the amount in other organs was determined as follows: heart - 0.02 ±0.02 % ID/g tissue, kidney 0.25 ±0.04 % ID/g tissue, spleen 0.25 ±0.07 % ID/g tissue, lungs 0.15 ±0.02 % ID/g tissue, liver 0.28 ±0.01 % ID/g tissue, and brain 0.23 ±0.04 % ID/g tissue. Although the results show high fluorescence in the intestine due to the interconnection between the respiratory and digestive systems and also supported by the capillarity from nose to mouth during the administration procedure, a careful analysis demonstrated fluorescence from StPGA-palbo-Cy5.5 conjugates in the brain (**Figure 3.41 A**). We failed to detect HA-CP-Cy5.5 in the brain (**Figure 3.41B**), possibly due to the low fluorescent labeling of the vehicle with a fluorescent probe. The validation of these promising results that demonstrate the delivery of the designed polyglutamates into the brain is ongoing.
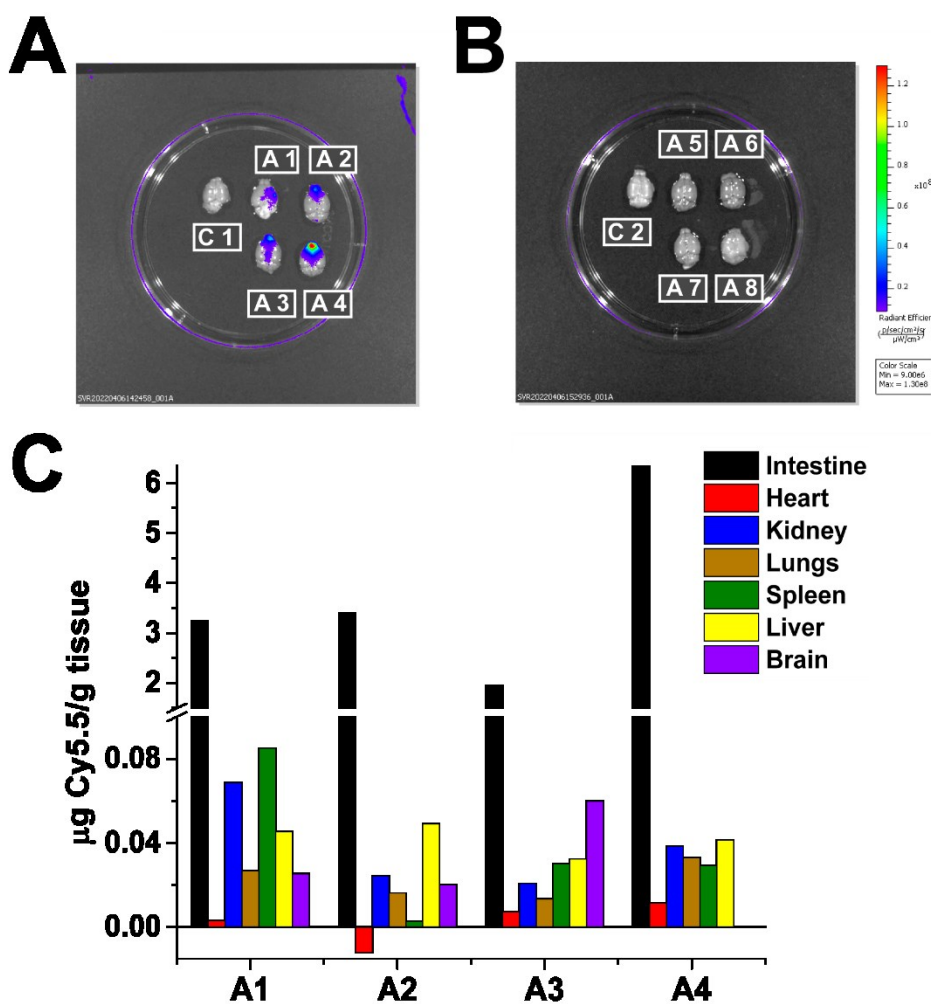
Figure 3.41. *In vivo* biodistribution of **(A)** StPGA-ValCit-palbociclib-Cy5.5 (Animals A1, A2, A3, A4) and **(B)** in combination with palbociclib micelles (Animals A5, A6, A7, A8). Results were obtained 90 min after intranasal administration by ex vivo quantification of Cy5.5 fluorescence by IVIS® technology. C1 and C2 referred to mice in the control group without treatment; **(C)** Ex vivo quantification of fluorescent probe Cy5.5 from homogenized organs by fluorescent spectroscopy with the CLARIOstar Plus plate reader ($\lambda_{excitation}$=640 nm, $\lambda_{emission}$=640 nm).

3.3. Conclusions

Herein, we report the rational design and development of LinPGA and StPGA-palbociclib conjugates as a treatment for pediatric gliomas. We successfully synthesized and characterized two families of polymer conjugates of Palbociclib, a CDK 4/6 inhibitor used in phase I clinical trials but suffering from notable limitations [15,16]. We selected two bioresponsive linkers: a redox-responsive linker triggered by overexpression of GSH and a protease-responsive peptidic ValCit linker triggered by cathepsin B to achieve tumor.-specific release. We explored critical features in conjugate design, including carrier architecture (StPGA vs. LinPGA) and drug loading, to fully understand the relationship between final solution conformation and biological activity in patient-derived DIPG and GBM spheroids and, more importantly, their responsiveness depending on the trigger motif level in the environment of the different models. Analysis of physicochemical properties such as size, ξ potential, and secondary structure by NMR, SEC (RI, MALS), DLS, UV-Vis, and CD suggests the existence of a transition in secondary structure at higher drug loading from random coil to α-helix (more for the disulfide linker and less pronounced for the peptidic analog) for StPGA-based conjugates. The SAXS experiments confirmed the evolution of the conjugate system upon increased drug loading and allowed us to obtain a mathematical model for synthesized conjugates. At very low loadings, conjugates behaved as simple polyelectrolytes upon increased drug loading. Macromolecules aggregate via point-to-point interactions to form large diffuse fractal aggregates and further undergo compactification and form fractal protomicelles that assemble into higher-level self-avoiding globules. The model correlates PGA-palbociclib conjugate solution conformation with different palbociclib loadings for both star-shaped and linear carriers and also includes the influence of the linker length (peptidic ValCit is larger than redox-responsive disulfide linker) to trigger conformational changes.

We demonstrated that the solution conformation of polymer-drug conjugates is a crucial parameter since it affects drug release and biological activity. We observed a delay in the palbociclib release for conjugates with a disulfide linker. We obtained > 50% of drug release at 6 h for conjugates with low and intermediate drug loadings and at 16 h for conjugates with high drug loading in response to 5mM DTT (intracellular conditions). In response to a 10 μM trigger (extracellular conditions), we observed drug release below 3%, proving selective linker responsiveness. The kinetic studies with cathepsin B reported a rapid drug release profile for all conjugates independently of drug loading (more than > 80% of the drug was released at 1 h), corroborating SAXS structural data about surface drug allocation contrary to the drug shielding inside the micelles in the case of the disulfide linker.

We also demonstrated the relation between the solution conformation of PGA-palbociclib conjugates and the biological activity in patient-derived GBM and DIPG models. Depending on the linker, we observed different biological activity: conjugates with the disulfide linker displayed more significant activity in DIPG cells, whereas those with peptidic linker showed higher cytotoxicity in GBM cells. This fact perfectly

correlates with the endogenous redox potential and protease levels encountered in the two patient-derived models.

Finally, we identified a synergistic drug combination of Palbociclib and Inavolisib (GDC0077) for DIPG cells and optimized micellization procedure for hydrophobic drug using F127® poloxamer to design an intranasal polymer-based combination therapeutic approach. The selected systems have already been scaled up, and the preparation for biological evaluation in an in vivo patient-derived model is ongoing.

3.4. Supplementary information

SI-3.1. Materials

SI-3.2. Experimental Methods and Protocols

SI-3.3. General Procedure for the Synthesis of Conjugates via Hydrazone Linker

SI-3.3.1 Preparation of PGA-hydrazine intermediate

SI-3.3.2. Preparation of PGA-hydrazone-palbociclib conjugate

SI-3.3.3. Preparation of Fmoc-hydrazone-palbociclib

SI-3.3.4. Preparation of Fmoc-hydrazine (9-fluorenylmethyl carbazate)

SI-3.3.5. Hydrazone bond formation between palbociclib and Fmoc-hydrazine

SI-3.4. General Procedure for the Synthesis of Conjugates via a Disulfide Linker

SI-3.4.1. Preparation of 2-(pyridin-2-yldisulfanyl)ethanol

SI-3.4.2. Preparation of 4-nitrophenyl (2-(pyridin-2-yldisulfanyl)ethyl) carbonate

SI-3.4.3. Preparation of Palbociclib-SS-Pyr

SI-3.4.4. Preparation of Palbociclib-SS-NH2

SI-3.4. Preparation of PGA-SS-palbociclib conjugates through self-immolative disulfide linker

SI-3.5 HPLC Method Optimization for Release Studies of PGA-SS-palbo Conjugates under reductive conditions

SI-3.5.1. Optimization of HPLC parameter and selection of internal standard

SI-3.5.2. Recovery study

SI-3.5.3. LOD and LOQ determination

SI-3.6 DIPG and GBM cell culture conditions and cell handling protocols

SI-3.6.1. Preparation of TSM Base solution

SI-3.6.2. Preparation of TSM Working solution

SI-3.6.3. Passaging the cells

SI-3.1. Materials

All chemicals were reagent grade, obtained from Sigma or Fisher Scientific. All solvents were of analytical grade from Sharlau Chemicals, Sigma, Fisher Scientific, or freshly distilled in the case of THF anh. Deuterated solvents were obtained from Deutero GmbH. Preparative SEC was performed using Sephadex LH-20 medium from GE. Palbociclib free base was purchased from MedcoChem Co. Ltd (Zhejiang, China). Anhydrous N,N-dimethylformamide (DMF, ≥99.8% anhydrous), methanol (HPLC grade), and tetrahydrofuran anhydrous (99.8%) were purchased from Scharlab SL (Sentmenat, Spain). NCA-Glu(OBz) was provided by PMC Isochem.

SI-3.2. Experimental Methods and Protocols

Nuclear Magnetic Resonance Spectroscopy

NMR measurements were performed on Bruker 300 UltrashieldTM (Bruker, Billerica, United States) with a Bruker B-ACS 60 automation system. 2D experiments were performed with a Bruker 500 Ultrashield plus (Bruker, Billerica, United States) with a Bruker sample case cooled automation system. All the measurements were performed at room temperature. The spectra were processed and analyzed using TopSpin and MestreNova software.

Circular Dichroism Spectroscopy

To measure the absorption of polarized light, the prepared solution was transferred in a quartz cuvette with a light path length of 1cm and measured at room temperature with a J-1500 spectrometer (JASCO corporation, Easton, United States). The resulting spectra were obtained by averaging five consecutive scans. A nitrogen flow of 2.7 L/min was led through the spectrometer. Alpha helix content was calculated by deconvolution of the spectra using an in-house developed program script integrated into MATLAB software.

Gel Permeation Chromatography

The GPC experiment was performed on a VISCOTEK GPCmax coupled to a VISCOTEK TDA302 detector system (Malvern, Malvern, England) - a dual LS detector (7 and 90º), viscometer, and RI detector. Experiment conditions: Column set: PW2500+3000+G (105/103/102 Å porosity), Flow: 0.8 ml/min, Solvent: 0.1% LiBr in DMF, Injection volume: 100μL. Temperature: 60°C. The GPC system was calibrated with 65kDa poly(methyl methacrylate) (PMMA) standard from Polymer Standards Service (PSS, Mainz, Germany).

Size Exclusion Chromatography

The SEC experiment was performed on a Postnova Analytics Modular SEC system (Postnova Analytics GmbH, Landsberg am Lech, Germany) coupled to an RI detector (PN3150 from Postnova Analytics GmbH), a UV-Vis detector (SPD-20A from Shimadzu Scientific Instruments, Kyoto, Japan), a fluorescence detector (RF-20A XS from Shimadzu Scientific Instruments, Kyoto, Japan), and a MALS detector (PN3621 from Postnova Analytics GmbH). Experiment conditions: Column TSKgel G3000PWXL (5 μm, 7.8 mm i.d. x 30 cm, Tosoh Corporation, Tokyo, Japan), Flow: 0.4 ml/min, Solvent: 0.005M PBS, 0.069 M NaCl, Injection volume: 10μL. Samples were prepared in water at a concentration of 2 mg/ml.

Fluorescent Spectroscopy (CAC study)

Fluorescence spectroscopy measurements were performed on an FP-6500 spectrofluorometer (JASCO, Easton, United States) with an excitation wavelength of 550 nm and measured emission spectrum from 575 to 740 nm. Polymer samples were dissolved in PBS and allowed to equilibrate for 2 h. To 800μL of each solution, 1μL of 1 mg/ml Nile Red solution in acetone was added.

Fourier transform infrared spectroscopy

ATR-FTIR measurements were performed on an FT/IR-4700 (JASCO, Easton, United States) using a 400 – 4000 cm^{-1} range. In a typical experiment, one drop of a solution of the compound in water was placed on the diamond crystal and dried.

Dynamic Light Scattering

The DLS size and z-potential measurements were performed on a Malvern Zetasizer nanoseries, nano ZS, ZEN3500 (Malvern Instruments, Malvern, UK). Samples of polymers were prepared in PBS at concentrations of 1 mg/ml and 0.1 mg/ml.

Small-Angle X-Ray Scattering

The SAXS measurements were performed at the BL11 beamline of the Alba synchrotron in Barcelona, Spain. The observed q range was $4.24 \times 10^{-3} Å^{-1} \leq q \leq 3.52 Å^{-1}$, where q is the magnitude of the scattering vector $q = (4\pi/\lambda)\sin(\theta/2)$. If not specified otherwise, measurements were performed in Hilgenberg Mark-tubes made of glass N50 packed with green perforated plastic disk (length 80 mm, outer diameter 1.5mm, wall thickness 0.01 mm). All the solutions in PBS at 0.1 mg/ml were allowed to equilibrate 24 h prior to measurement. Experiments were performed with the use of in-house cells and cell holders. Analysis and fitting were performed with ATSAS and Scatter software packages.

The radius of the gyration R_g can be calculated by plotting intensity Log $I(q)$ as a function of the square of scattering vector q, the so-called Guinier plot. The part of the graph at very low values of q is linear. Equation 3.1 describes the linear dependence from which R_g can be determined.

$$Log\big(I(q)\big) = Log(I(q)_0) - \frac{q^2 R_g{}^2}{3}$$

For the rod-like particles and fibers, a variation of the Guinier plot is used, allowing us to determine the radius of gyration of the rod/fiber cross-section. The cross-section radius can be determined by plotting Log $(qI(q))$ as a function of q. The intermediate part of this graph is linear, where the mathematical description is represented in an equation. From this, the radius of gyration of cross-section R_c can be determined.

$$Log\ (I(q) \times q) = Log\ (I(q)_0 \times q) - \frac{q^2 R_c{}^2}{2}$$

R_g and R_c values correlate with the total length of the fibers L with relation 3.3, from which the length can be calculated.

$$R_g{}^2 = R_c{}^2 + \frac{L^2}{12}$$

Cell Viability Studies

DIPG or GMB cells were seeded in sterile 96-well microliter plates at 7500 cells per well in 50 μl. Plates were incubated for 24 h at 37^{0}C and 5% CO$_2$ before treatment. Then, the compounds were dissolved in cell media, filtered through a 0.22 μm Nylon filter, and 50 μl of serial dilutions were added to the cells. Due to the high variability of formed tumor spheres, six wells were continuously used in replicates for one concentration and at least three different passages of cells for the data reporting. After 72 h of cell incubation with tested compounds, 10 μl of MTS/PMS (20:1) were added to each well, and the cells were incubated for a further 3-4 h. The optical density of each well was measured at 490 nm on the CLARIOstar Plus plate reader (BMG Labtech GmbH, Ortenber, Germany). The absorbance values were represented as the percentage of cell viability, taking as 100 % the value of untreated control cells.

Cell Cycle Studies

DIPG or GMB cells were seeded in a sterile 6-well plate at 222,650 cells/well in 2 ml, corresponding to the cell density optimized for cell viability assay. Plates were incubated for 24 h at 37^{0}C and 5% CO$_2$ before treatment. Then, the compounds were dissolved in cell media, filtered through a 0.22 μm Nylon filter, and 1 ml was added to the cells. The concentrations of free drug and conjugates were selected based on the value IC$_{30}$ toxicity: for DIPG cells - 12.5 μM drug equiv. and used the same concentration for GBM cells, for palbociclib HCl - 0.7uM drug equiv.

After 72 h of cell incubation with tested compounds, cells from a 6-well plate were transferred to a 15 ml conical tube, and the well was washed with 1 ml of dPBS. Then, the cell suspension was centrifuged at 400 G for 5 min, and the supernatant was removed by aspiration. The cell pellet was resuspended in 500 μl of dPBS, centrifuged at 400 G for 5 min, and the supernatant was removed by aspiration. To the cell pellet, 500 μl of cold 70% Ethanol (-20^{0}C) was added by slow vortexing, and the cells were left for at least 1 h at -20^{0}C. Then, the cell suspension was centrifuged at 400 G for 5 min at 4^{0}C, and the supernatant was removed by aspiration. Then, to the cell pellet, 400 μl of cold (4^{0}C) mixture of propidium iodide (PI, a fluorescent dye) and RNase A (an enzyme that specifically degrades RNA) was added (prepared by dissolving 2.5 mg of propidium iodide and 10 mg of RNase A in 100 ml

of PBS). The cell pellet was thoroughly resuspended with a pipette and incubated overnight at 4^0C, protected from light.

For the measurement, 200 µl of the sample was transferred into a 96-well plate and measured using a flow cytometer (CytoFLEX, Beckman Coulter Life Sciences) at a slow flow rate of 10 µl/min. The data accumulation was finished after reaching 10,000 events of single cells. The data analysis was performed with FlowJo 7.6.5 software, using the Dean-Jett-Fox model for data fitting.

SI-3.3. General Procedure for the Synthesis of Conjugates via Hydrazone Linker

Figure S3.1 shows the proposed synthetic route for synthesizing palbociclib conjugates via a hydrazone linker.
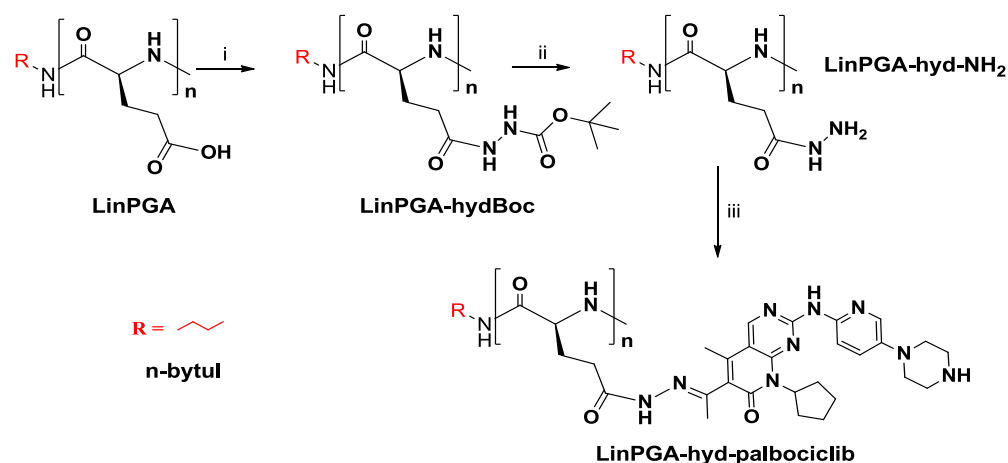

Figure S3.1. Synthesis of LinPGA-hyd-palbociclib conjugates. i) tert-butyl carbazate, DMF, DMTMM BF4; ii) TFA$_{conc}$, room temperature iii) palbociclib, DMSO$_{anh}$, HAc$_{cat}$

SI-3.3.1 Preparation of PGA-hydrazine Intermediate (LinPGA-hyd-NH2)

In a round bottom flask with a stirrer, PGA H-form (500 mg, Mw=129.1 g/mol (Glu unit), 1eq.) and DMTMM BF$_4$ (218 mg, Mw=328.1 g/mol, 0.17 eq.) were dissolved in 15 ml DMF$_{anh}$ under N$_2$, allowed to activate during 30 min, added tert-butyl carbazate (77 mg, Mw=132.2 g/mol, 0.15 eq.) in 5 ml of DMF$_{anh}$, adjusted pH to 8 with TEA, and the reaction was left to proceed for 48 h. An equal volume of THF was added to the obtained solution, and the PGA-hydrazineBoc intermediate was precipitated out in cold Et$_2$O and dried under vacuum to obtain a white solid. The targeted modification was 15 %mol; the obtained modification was 14.2 %mol (calculated from ^{1}*H NMR* 1.274/9=14.2) with a reaction efficiency of 95%.
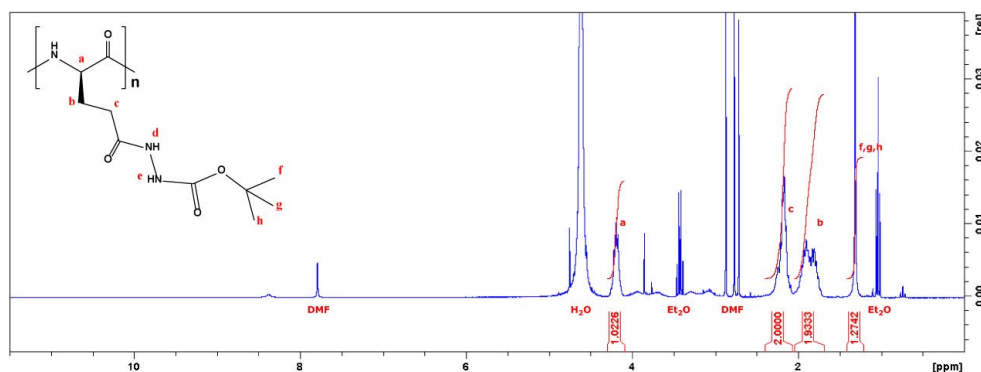
Figure S3.2. **PGA-hydBoc:** Product – white powder. Global yield: 496 mg (86 %). *¹H NMR (300 MHz, D₂O)*: 4.19 (m, 1H), 2.18 (M, 2H), 1.86 (m, 2H), 1.32 (s, 9H)

In a round bottom flask with a stirrer, PGA-hydBoc 496 mg was suspended in 5 ml TFA$_{conc}$ and allowed to react for 60 min; check with ninhydrin 2% aq. solution staining was precipitated in cold Et2O, filtered through a glass filter, and dried under a vacuum to obtain a white solid. The completion of the reaction was confirmed with ¹H NMR by the disappearance of the signal of the BOC group at 1.32 ppm.
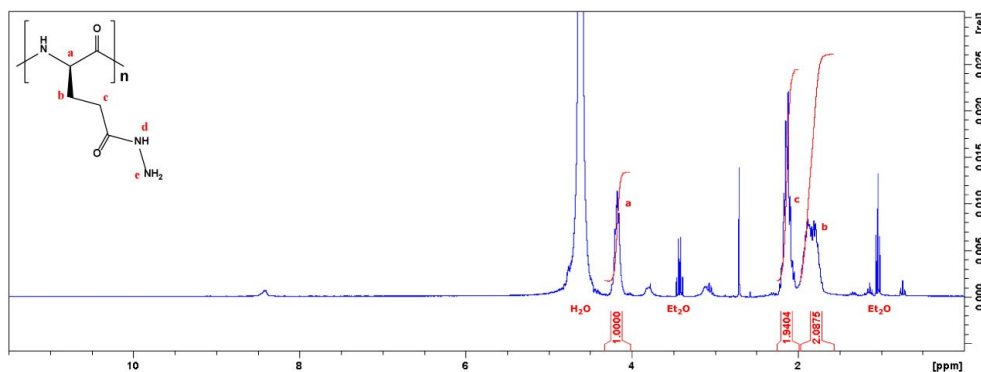
Figure S3.3. **LinPGA-hyd-NH₂:** Product – white powder. Global yield: 435 mg (97 %). *¹H NMR (300 MHz, D₂O)*: 4.19 (m, 1H), 2.18 (M, 2H), 1.86 (m, 2H), 1.32 (s, 9H).

SI-3.3.2 Preparation of PGA-hydrazone-palbociclib Conjugate

In a round bottom flask with a stirrer, PGA-hyd-NH₂ 150 mg (Mw=131 g/mol, average Glu unit, 14.2% mol modification, 1eq.) palbociclib 76.9 mg (Mw=447.5 g/mol, 0.15 eq.) and AcOH$_{glacial}$ 15 µl were dissolved in 20 ml of DMSO$_{anh}$ under N₂ atmosphere and molecular sieves 4Å and allowed to react three days. After 24 h, 48 h, and 72 h, an aliquot of the reaction was taken, and DMSO was evaporated under a vacuum and redissolved in DMSO-d to analyze with NMR.

Figure S3.4 shows the proposed synthetic route for the synthesis of Fmoc-hydrazone-palbociclib conjugates via hydrazone linker to evaluate the reactivity of palbociclib keto-group in a more straightforward setup and exclude the effect of polymer on the reaction.
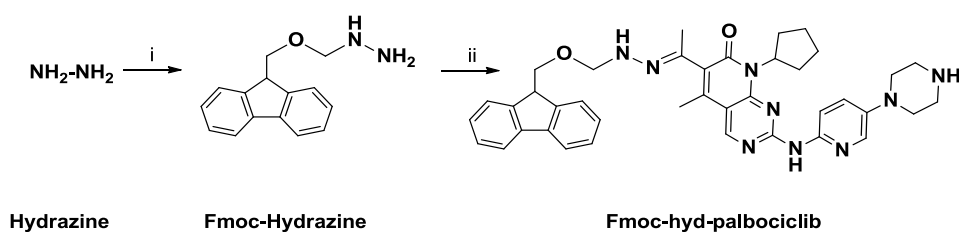
Figure S3.4. Synthesis of Fmoc-hydrazone-palbociclib conjugates. i) 9-fluorenylmethyl chloroformate, ACN ii) palbociclib, DCM$_{anh}$, AcOH$_{cat}$

SI-3.3.3.1. Preparation of Fmoc-hydrazine (9-fluorenylmethyl carbazate)

In a round bottom flask with a stirrer, hydrazine (10 ml, Mw=32.1 g/mol, 80 eq.) was placed under N$_2$, 9-fluorenyl methyl chloroformate (1 g, Mw=258.7 g/mol, 1 eq.) dissolved in 250 ml of ACN was added dropwise and allowed to react 1 h at room temperature. The solvent was evaporated under a vacuum to obtain a white solid, and the pure 9-fluorenyl methyl carbazate was obtained after recrystallization from EtOH$_{abs}$.
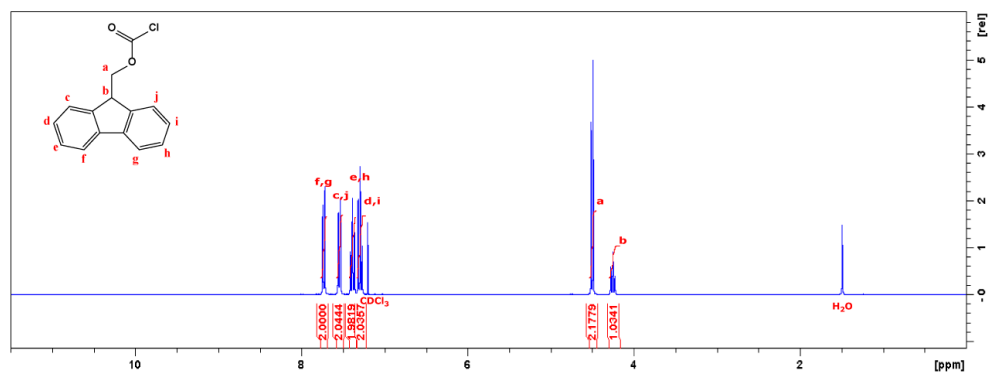
Figure S3.5. **9-fluorenylmethyl chloroformate:** *^{1}H NMR (300 MHz, CDCl$_3$)*: 7.73 (d, 2H), 7.55 (d, 2H), 7.39 (t, 2H), 7.29 (t, 2H), 4.50 (d, 2H), 4.25 (t, 1H)
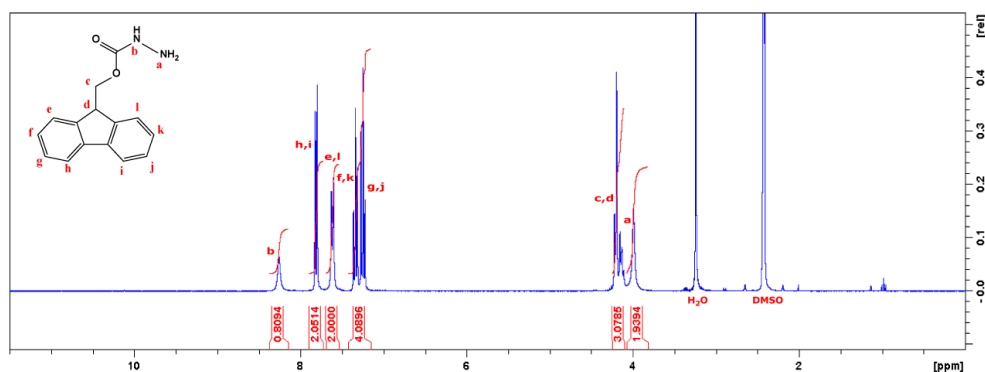
Figure S3.6. **9-fluorenylmethyl carbazate:** *^{1}H NMR (300 MHz, DMSO-d)*: 8.26 (s, 1H), 7.81 (d, 2H), 7.62 (d, 2H), 7.34 (t, 2H), 7.25 (t, 2H), 4.18 (m, 3H), 3.99 (s, 2H)

SI-3.3.3.2.Hydrazone bond formation between palbociclib and Fmoc-hydrazine

In a round bottom flask with a stirrer, palbociclib (65 mg, Mw=447.5 g/mol, 1 eq.) was dissolved in 10 ml of DCM$_{anh}$ with molecular sieves 4Å or Si(EtO)$_4$ as water removal agents under N$_2$ atmosphere. 9-fluorenyl methyl carbazate (37 mg, Mw=254.3 g/mol, 1eq.) in 5 ml of DCM$_{anh}$ and AcOH$_{glacial}$ 15 µl were added, and the reaction was allowed to proceed for 24h at room temperature. The solvent was evaporated under vacuum, and the crude product was analyzed with ^{1}H NMR.

SI-3.4. General Procedure for the Synthesis of Conjugates via a Disulfide Linker

Figure S3.7 shows the proposed synthetic route for synthesizing palbociclib conjugates via a disulfide linker.
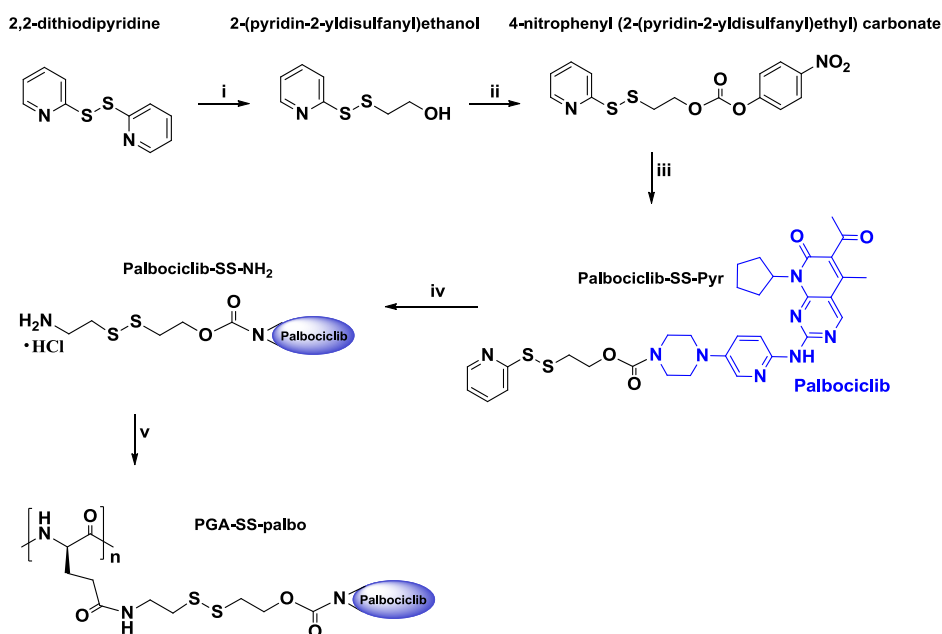
Figure S3.7. Synthesis of PGA-SS-palbociclib conjugates. i) 2,2-dithiodipyridine, MeOH; ii) p-nitrophenyl chloroformate, THF$_{anh}$, TEA, 0ºC; iii) palbociclib, DCM$_{anh}$, TEA; iv) cysteamine hydrochloride, MeOH:DCM (1:1), TEA; v) PGA, DMF$_{anh}$, DMTMM·BF$_4$, TEA

SI-3.4.1. Preparation of 2-(pyridin-2-yldisulfanyl)ethanol

In a round bottom flask with a stirrer, 2,2-dithiopyridine (2g, 9.08 mmol, Mw=220.3 g/mol, 1.5 eq.) was placed in 20 ml of MeOH, purged with N$_2$ for 10 min, added dropwise 2-mercaptoethanol (424 µl, 6.05 mmol, Mw=78.1 g/mol, 1 eq.), the solution turned yellow, and the reaction was left to proceed for 2 h at room temperature. The reaction was monitored by TLC, Rf = 0.5 (MP DCM:EtAc:MeOH = 95:5:1). The reaction mixture was concentrated under reduced pressure, and the residue was subjected to column chromatography on silica gel (MP DCM:EtAc:MeOH = 95:5:1) to give a 2-(pyridin-2-yldisulfanyl)ethanol as a yellow oil.
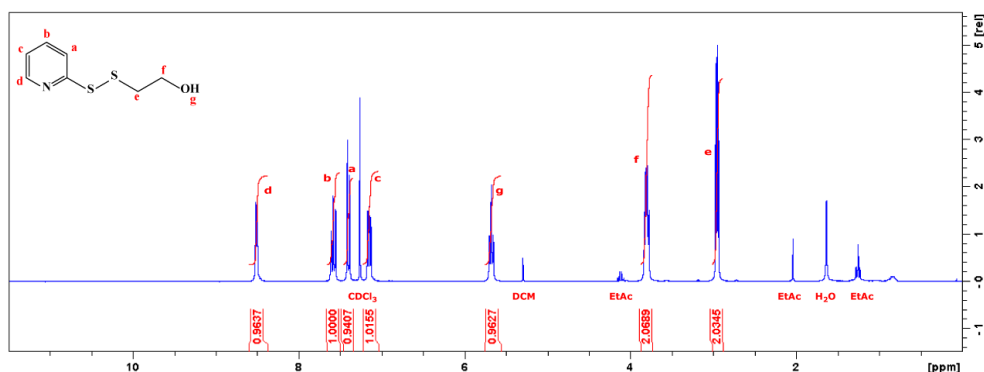
Figure S3.8. **2-(pyridin-2-yldisulfanyl)ethanol:** Product – yellow oil. Global yield: 960 mg (85 %). *¹H NMR (300 MHz, CDCl₃)*: 8.51 (d, 1H), 7.58 (t, 1H), 7.40 (d, 1H), 7.34 (t, 1H), 7.15 (t, 1H), 5.68 (t, 1H), 3.80 (q, 2H), 2.95 (t, 2H)

SI-3.4.2. Preparation of 4-nitrophenyl (2-(pyridin-2-yldisulfanyl)ethyl) carbonate

In a round bottom flask with a stirrer, 2-(pyridin-2-yldisulfanyl)ethanol (450 mg, 2.4 mmol, Mw=187.3 g/mol, 1 eq.) was placed in 50 ml of THF$_{anh}$ under N_2 at 0ºC, added TEA (800 μl, 5.7 mmol, Mw=101.2 g/mol, 2.2 eq.) and 4-nitrophenyl chloroformate (533 mg, 2.6 mmol, Mw=201.6 g/mol, 1.1 eq.), the reaction was left to proceed for 1 h at room temperature, then the solvent was evaporated under reduced pressure. The reaction was quenched with 30 ml of 0.5 M aqueous ammonium chloride solution and extracted three times with 60 ml EtAc. The combined organic layer was dried over anhydrous sodium sulfate and filtered. The filtrate was concentrated under a vacuum, and the residue was subjected to column chromatography on silica gel (MP DCM:EtAc = 95:5) to give a 4-nitrophenyl (2-(pyridin-2-yldisulfanyl)ethyl) carbonate as a transparent oil.
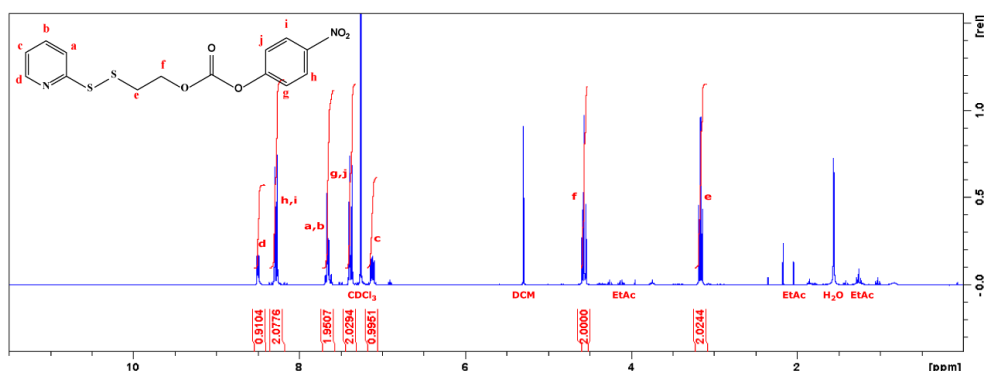
Figure S3.9. **4-nitrophenyl (2-(pyridin-2-yldisulfanyl)ethyl) carbonate:** Product – transparent oil. Global yield: 642 mg (76 %). *¹H NMR (300 MHz, CDCl₃)*: 8.50 (m, 1H), 8.28 (m, 2H), 7.66 (m, 2H), 7.38 (m, 2H), 7.12 (m, 1H), 4.57 (t, 2H), 3.17 (t, 2H)

<u>*SI-3.4.3. Preparation of Palbociclib-SS-Pyr*</u>

In a round bottom flask with a stirrer, palbociclib (400 mg, 0.90 mmol, Mw=447.53 g/mol, 1 eq.) was placed in 100 ml DCM$_{anh}$, added 4-nitrophenyl (2-(pyridin-2-yldisulfanyl)ethyl) carbonate (346 mg, 0.98 mmol, Mw=352.4 g/mol, 1.1 eq.) and TEA (138 μl, 0.98 mmol, Mw=101.2 g/mol, 1.1 eq.), the reaction was left to proceed for 2 h at room temperature. The solvent was evaporated under reduced pressure, and the residue was subjected to column chromatography on silica gel (MP DCM:MeOH = 9:1) to give a Palbociclib-SS-Pyr product as a yellow viscous oil.

**Figure S3.10**. **Palbociclib-SS-Pyr:** Product – yellow viscous oil. Global yield: 546 mg (92 %). *^{1}H NMR (300 MHz, CDCl$_3$)*: 8.80 (s, 1H), 8.48 (m, 1H), 8.19 (d, 1H), 8.04 (d, 1H), 8.00 (s, 1H), 7.66 (m, 2H), 7.34 (dd, 1H), 7.11 (m, 1H), 5.87 (m, 1H), 4.40 (t, 2H), 3.66 (t, 4H), 3.14 (t, 4H), 3.09 (t, 2H), 2.55 (s, 3H), 2.34-2.37 (s+m, 3H+2H), 2.08 (m, 2H), 1.90 (m, 2H), 1.71 (m, 2H)

To prove the identity of the compound, we used HMBC NMR spectra. Three key correlations are highlighted in **Figure S3.11, s**howing the connections between different structural blocks (palbociclib-carbamate-mercaptoethanol fragment-cysteamine fragment). H21 and C21 can be easily assigned using the HSQC artifact. The HMBC of intermediate compound H21 (at 3.62 ppm) shows a cross peak with C20 (at 154.7 ppm) from the carbamate group. The bond correlation between C20 and H19 proves that carbamate forms between the morpholine ring of palbociclib and the alcohol of mercaptoethanol. Following similar assignments from C19 to C1 and from C23 to C27, it is possible to conclude that the structure of palbociclib and thiopyridine ring remains intact, unambiguously proving the compound's identity.

Figure S3.11. HMBC spectrum of **Palbociclib-SS-Pyr**. The molecule's structure highlights all the observed correlations (the arrow start corresponds to the hydrogen, and the end corresponds to the correlating carbon atom). Key correlations between the main structural blocks are shown in distinct colors as arrows (on the structure) or correlation peaks (on the spectrum). Protons connected to carbons are named as numbers, and protons connected to nitrogens as letters.

SI-3.4.4. Preparation of Palbociclib-SS-NH$_2$

In a round bottom flask with a stirrer, Palbociclib-SS-Pyr (540 mg, 0.82 mmol, Mw=660.8 g/mol, 1 eq.) was placed in 16 ml of the mixture MeOH:DCM (1:1), added cysteamine hydrochloride (92.9 mg, 0.82 mmol, Mw=113.6 g/mol, 1 eq.), the mixture allowed to stir for 2 h at room temperature. The reaction was monitored by TLC, Rf = 0.33 (MP DCM: MeOH = 9:1). The solvent was evaporated under reduced pressure, and the residue was precipitated four times in cold diethyl ether from methanol, filtered, and dried under vacuum to give a yellow powder.
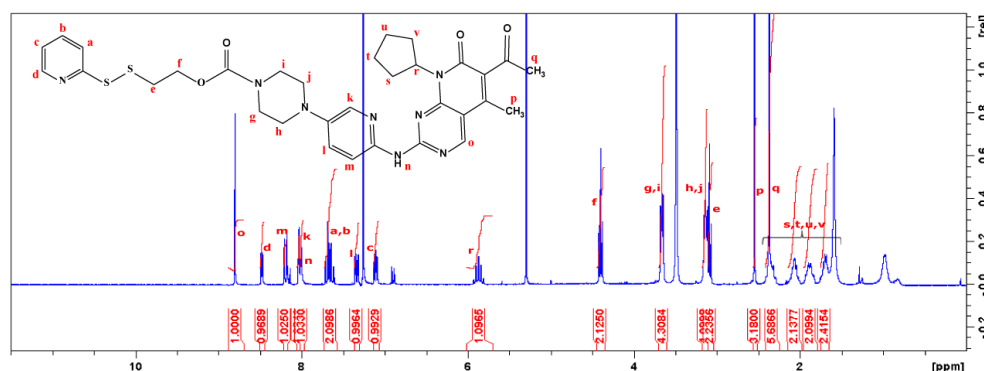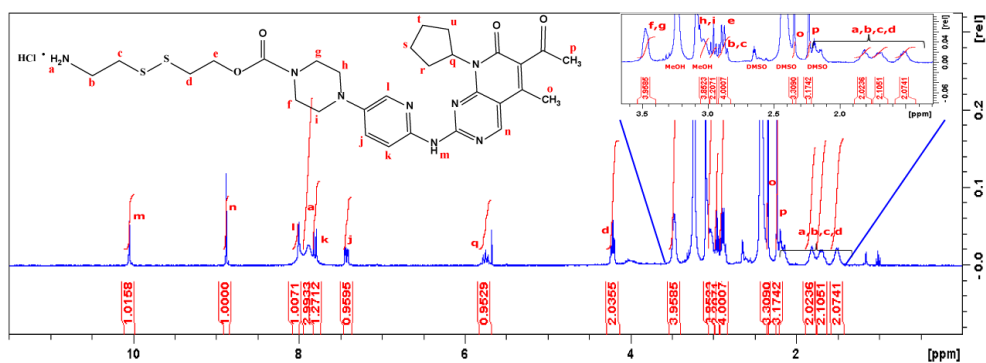
Figure S3.12. **Palbociclib-SS-NH₂:** Product – yellow viscous oil. Global yield: 546 mg (92 %). *¹H NMR (300 MHz, CDCl₃)*: 8.80 (s, 1H), 8.48 (m, 1H), 8.19 (d, 1H), 8.04 (d, 1H), 8.00 (s, 1H), 7.66 (m, 2H), 7.34 (dd, 1H), 7.11 (m, 1H), 5.87 (m, 1H), 4.40 (t, 2H), 3.66 (t, 4H), 3.14 (t, 4H), 3.09 (t, 2H), 2.55 (s, 3H), 2.34-2.37 (s+m, 3H+2H), 2.08 (m, 2H), 1.90 (m, 2H), 1.71 (m, 2H)

To prove the identity of the compound Palbociclib-SS-NH₂, we used HMBC NMR spectra. Similar to the intermediate compound Palbociclib-SS-Pyr, three key correlations are highlighted in **Figure S3.13**, showing the connections between different structural blocks (palbociclib-carbamate-mercaptoethanol fragment-cysteamine fragment).
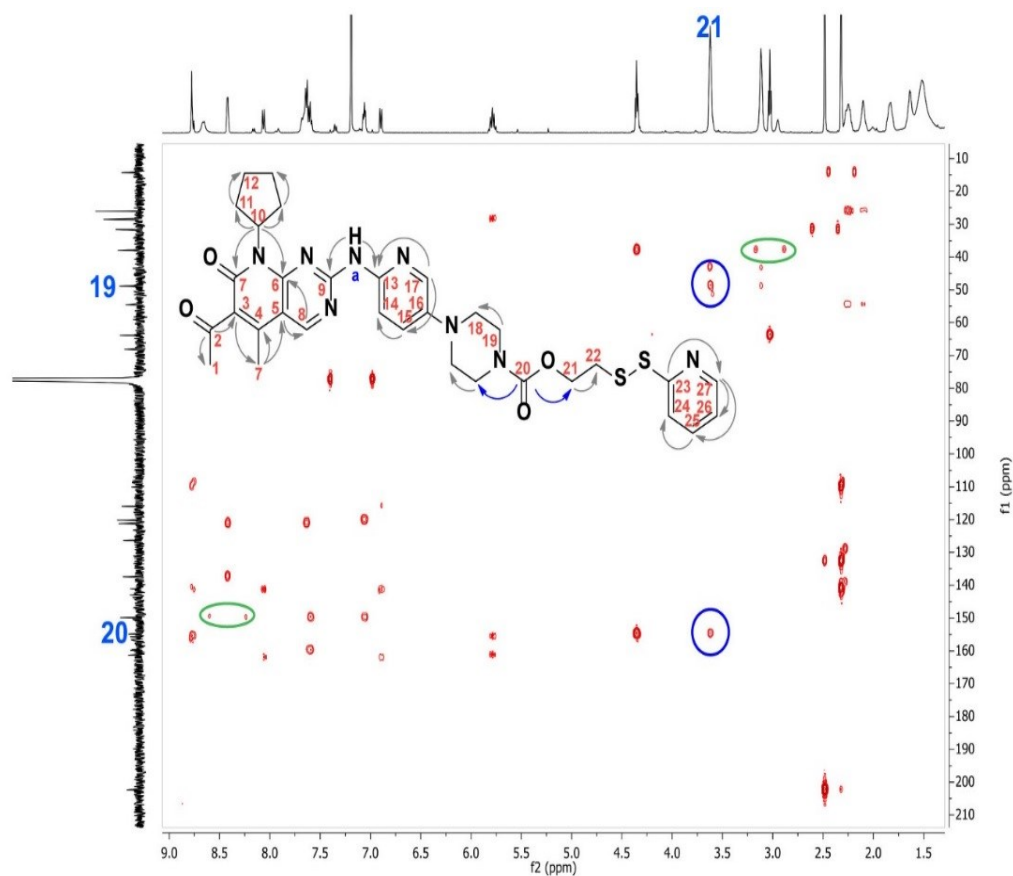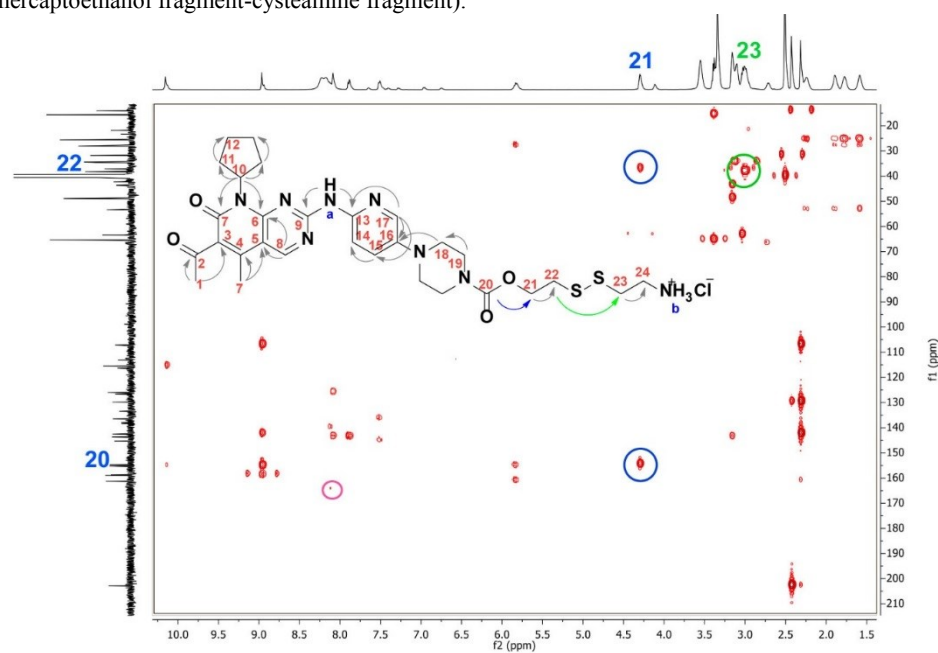

Figure S3.13. HMBC spectrum of **Palbociclib-SS-NH₂**. The molecule's structure highlights all the observed correlations (the arrow start corresponds to the hydrogen, and the end corresponds to the correlating carbon atom). Key correlations between the main structural blocks are shown in distinct colors as arrows (on the structure) or correlation peaks (on the spectrum). Protons connected to carbons are named as numbers, and protons are connected to nitrogens – as letters.

On the HMBC spectrum of the **Palbociclib-SS-NH₂** compound, there is a similar correlation between C20 and H21; however, the correlation between C20 and H19 is too weak. Nevertheless, structural reconstruction from C19 to C1 indirectly proves that the carbamate group is present and that the palbociclib fragment remains unchanged. The second critical correlation is a three-bond correlation between H23 (at 3.01 ppm) and C22 (at 37.53 ppm), demonstrating the formation of expected disulfide and successful exchange reaction.

SI-3.4.5. Preparation of PGA-SS-palbociclib conjugates through self-immolative disulfide linker

In a round bottom flask with a stirrer, LinPGA100 or StPGA150 (100 mg, 0.77 mmol, Mw=129.1 g/mol, 1eq.) was placed in 8 ml of DMF$_{anh}$, added DMTMM BF₄ (28.0/14.0/8.4/4.2mg, 0.086/0.043/0.026/0.013 mmol, Mw=328.1 g/mol, 0.11/0.055/0.033/0.017 eq.) depending on the targeted modification, the mixture allowed to stir 30 min to activate carboxylic groups. Then, Palbociclib-SS-NH₂ (51.4/25.7/15.4/7.7 mg, 0.077/0.039/0.023/0.012 mmol, Mw=663.25 g/mol, 0.10/0.05/0.03/0.015 eq.) depending on the targeted modification, in 2 ml of DMF$_{anh}$ was added, the pH of the solution was adjusted to 8.0 with TEA, and the solution allowed to stir for 48 h at room temperature. The mixture was concentrated (around 50% of the volume) under a reduced vacuum, precipitated in cold diethyl ether, filtered, and dried under a vacuum. The obtained white solid was dissolved in 0.5 M aqueous sodium hydrocarbonate solution and dialyzed against water (Cellulose ester membrane, cut off 500-1000Da, Spectrum®) for 48h, and then the solution was freeze-dried. The conjugates were dissolved in water and purified with Sephadex® G25 column and water as a mobile phase. The combined fractions were lyophilized to give a yellow powder with different intensities depending on the drug loading.

Figure S3.14. Overlaid ¹H NMR spectra (300 MHz, D₂O) of LinPGA-SS-palbociclib with different drug loading. Peak **a** at 0.75 (t, 3H) corresponds to the methyl group of the butylamine initiator, and peaks **b**, **d**, **c** at 4.21 (m, 100H), 2.23 (m, 200H), 1.88 (m, 200H) – to the glutamic units. The obtained ratio of peak integrals **b** and **a** was between 97 and 102, confirming the polymer's integrity during the post-polymerization modification procedures. The protons from palbociclib are present, confirming the completion of the conjugation process: aromatic region (protons **h**, **i**, **g**, **j**, **k**), aliphatic region (protons **e**, **f** at 2.75 (m, 4H) - corresponds to piperazine ring of palbociclib are well separated and could be used for a rough estimation of the degree of modification.
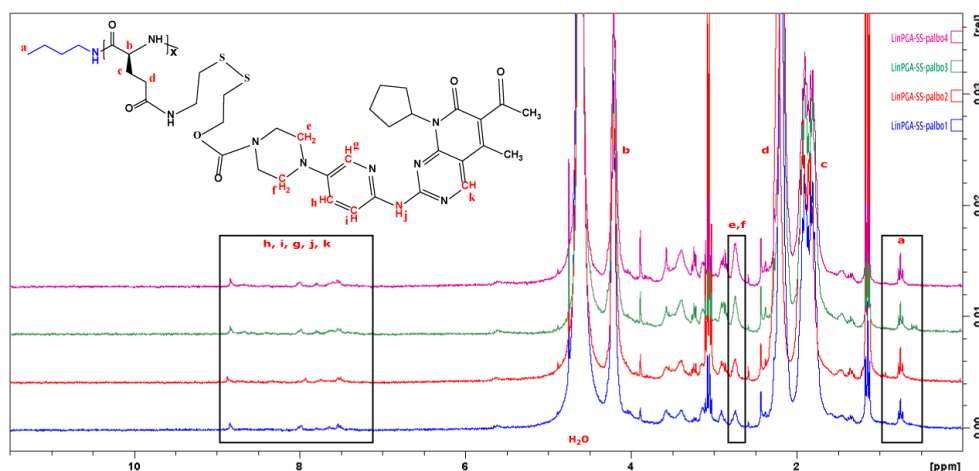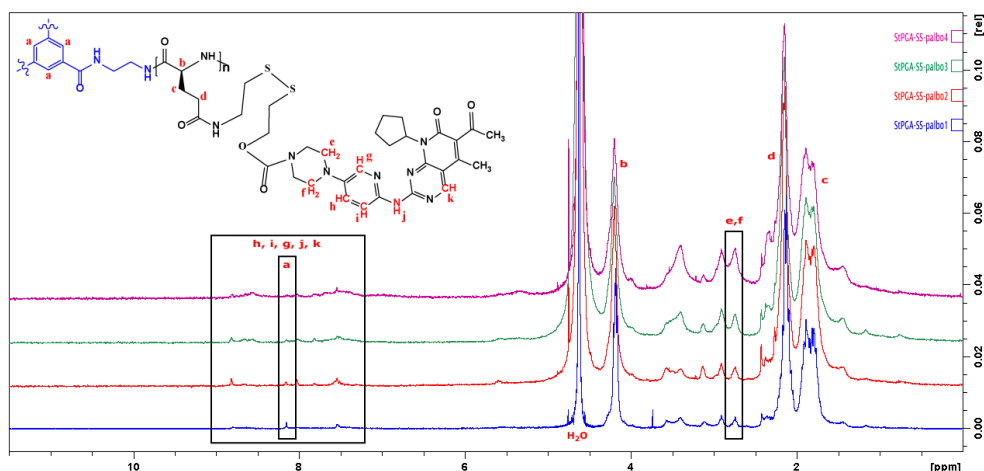
Figure S3.15. Overlaid ^{1}H NMR spectra (300 MHz, D$_2$O) of StPGA-SS-palbociclib with different drug loading. Peak **a** at 8.1 (s, 3H) corresponds to the BTA core of the initiator, and peaks **b**, **d**, **c** at 4.21 (m, 100H), 2.23 (m, 200H), 1.88 (m, 200H) – to the glutamic units. The obtained ratio of peak integrals **b** and **a** was between 141 and 159, confirming the polymer's integrity during the post-polymerization modification procedures. The protons from palbociclib are present, confirming the completion of the conjugation process: aromatic region (protons **h**, **i**, **g**, **j**, **k**), aliphatic region (protons **e**, **f** at 2.75 (m, 4H) - corresponds to piperazine ring of palbociclib are well separated and could be used for a rough estimation of the degree of modification.

SI-3.5. HPLC Method Optimization for Release and Plasma Stability Studies of PGA-SS-palbociclib Conjugates

SI-3.5.1. Optimization of HPLC parameter and selection of internal standard

The release kinetics of palbociclib was studied in 5 mM or 10 μM DTT aqueous solution, mimicking the intra and extracellular reductive environment [42]. Due to the poor solubility of palbociclib in HPLC-compatible solvents (MeOH, ACN), a double extraction procedure was developed. First conjugates were dissolved at 1 mg/ml in water, aliquoted by 100 μl in new 2 ml Eppendorf tubes to which 1 μl of 500 mM or 1 mM DTT aqueous solution was added and incubated at 37^{0}C in the Thermomixer (Eppendorf ® Thermomixer Compact, T1442) with constant shaking at 1000 rpm, covered from light. At selected time points, the 500 μl of DCM and 25 μl of dasatinib in MeOH as internal standard at 100 μg/ml were added, vortexed for 5 min, centrifuged at a maximum speed of 1 min, and transferred 400 μl of DCM fraction into a new 2 ml Eppendorf tube. In this step, we eliminate the palbociclib not cleaved from the PGA polymer, which remained in the aqueous phase. Then, the solvent was evaporated under reduced pressure with SpeedVac; the solid was reconstituted into 1 ml of acidic water pH ~3, vortexed for 5 min, adjusted pH with NH$_4$OH solution to pH ~5, filtered, and injected into HPLC.

The optimized HPLC conditions are as follows:

- Column - size Aeris XB-C18, 150x4.6 mm, particle 3.6 μm (Widepore, Phenomenex)
- Mobile phase - 1mM Ammonium Formate (NH$_4$FA): Acetonitrile: Formic acid (75:25:0.1)

Figure S3.16 shows the representative HPLC chromatogram (A) of the optimized method and corresponding UV-Vis spectra of Palbociclib (B) and Dasatinib (C).
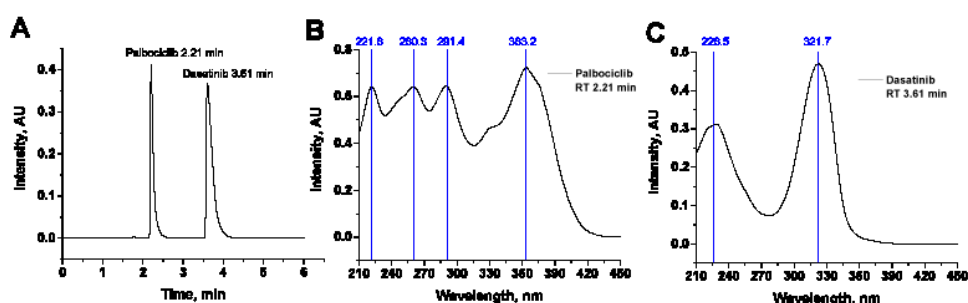
Figure S3.16. Representative HPLC chromatogram of a mixture of palbociclib and dasatinib (A) and corresponding UV-Vis spectra of Palbociclib (B) and Dasatinib (C).

However, after performing the extraction procedure of the palbociclib and dasatinib mixture, we observed partial degradation of dasatinib. On the chromatogram **Figure S3.17 (A),** the peak shape of dasatinib was distorted and split into two peaks at 3.29 min and 3.60 min, with similar UV-Vis spectra, **Figure S3.17 (C)** that corresponds to dasatinib; however, the ration between maximum at 322 nm and 226 nm are different indicating the structural changes, and therefore partial degradation. Palbociclib spectra **Figure S3.17 (B)** is like the one before extraction **Figure S3.17 (B),** indicating the suitability of the extraction procedure for palbociclib.
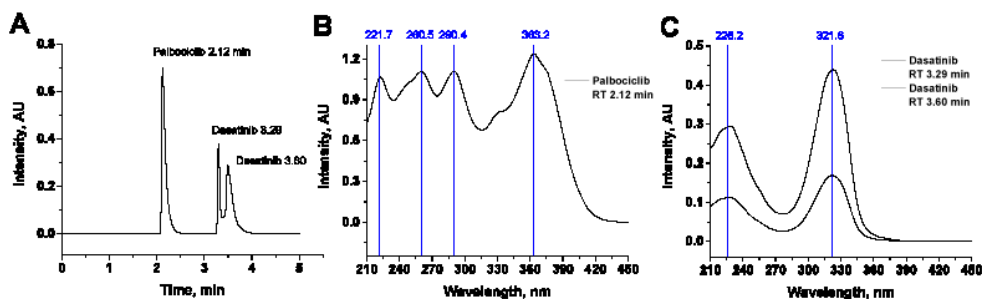
Figure S3.17. Representative HPLC chromatogram of a mixture of palbociclib and dasatinib (A) and corresponding UV-Vis spectra of Palbociclib (B) and Dasatinib (C) after performing the extraction.

As an alternative compound for the internal standard, we have selected niraparib, which, similarly to palbociclib, has a secondary amine group (**Figure S3.18 A**) and, depending on the pH, can be soluble (pH < 5) or insoluble (pH > 8) in aqueous solution. Applying the previously optimized MP, we did not obtain the resolution between palbociclib and niraparib (**Figure S3.18 B**); therefore, we also optimized the ionic buffer strength (**Figure S3.18 C, D, E**) – the optimal was 1mM NH4FA, with higher salt concentration the peaks broadened, with less resolution between peaks; and also we optimized the

amount of FA (**Figure S3.18 F, G, H**) – the optimal was 0.2 %, the general tendency was that with increasing FA content the resolution was increasing; however 0.3% of FA produced pH~3 of MP that is close to the limit of the stationary phase of the column; therefore we selected 0.2% of FA with pH~3.5.
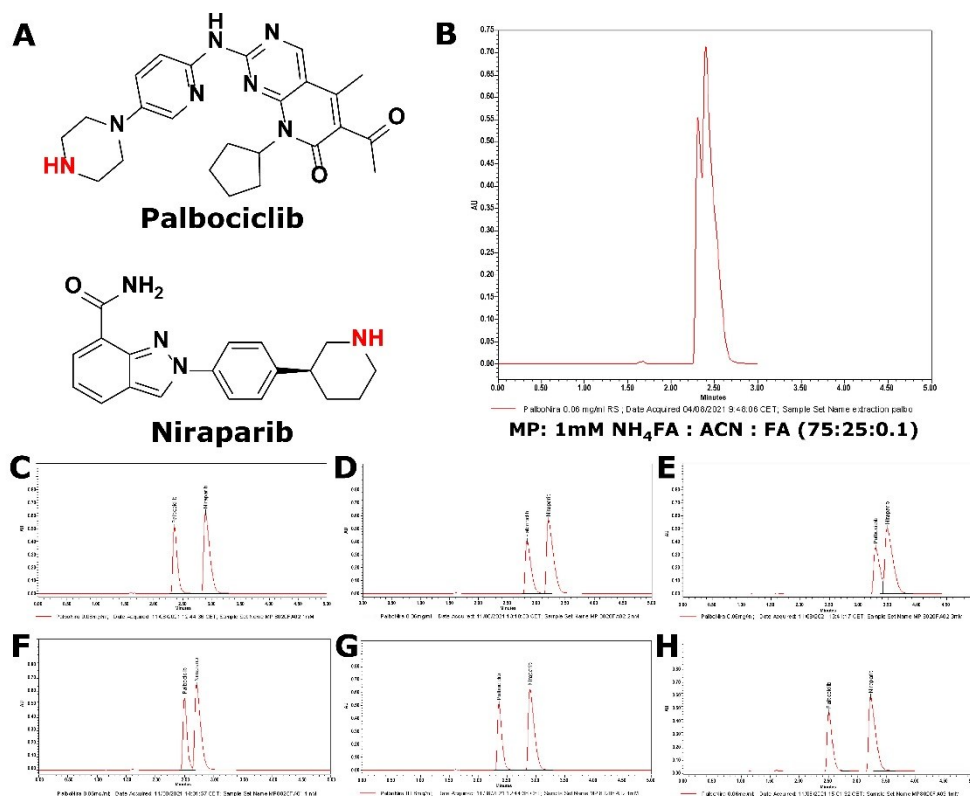
Figure S3.18 Chemical structure of Palbociclib and Niraparib (A); HPLC chromatogram for the initial method with MP 1mM NH_4FA: ACN: FA (75:25:0.1) (B); the effect of buffer ionic strength on the retention time and peak resolution: 1mM NH_4FA, (C), 2mM NH_4FA (D), 3mM NH_4FA (E); the effect of FA content: 0.1% (F), 0.2% (G). 0.3 % (H)

The optimized HPLC method for drug release studies the following: Column-size Aeris XB-C18, 150x4.6 mm, particle 3.6 μm (Widepore, Phenomenex); Mobile phase - 1mM Ammonium Formate (NH_4FA): Acetonitrile: Formic acid (80:20:0.2); Detector wavelength $\lambda = 360$ nm. The stock solution of tested conjugates at 1 mg/ml in water was aliquoted by 100 μl in 2 ml Eppendorf tubes, to which 1 μl of 500 mM or 1 mM DTT aqueous solution was added and incubated at 37^0C in the Thermomixer (Eppendorf ® Thermomixer Compact, T1442) with constant shaking at 1000 rpm, covered from light. At selected time points, the 500 μl of DCM with niraparib as internal standard (20 μg/ml)was added, vortexed for 5 min, centrifuged at maximum speed 1 min, and transferred 400 μl of DCM fraction into

a new 2 ml Eppendorf tube. In this step, we eliminate the palbociclib not cleaved from the PGA polymer, which remained in the aqueous phase. Then, the solvent was evaporated under reduced pressure with SpeedVac; the solid was reconstituted into 1 ml of acidic water pH ~3, vortexed for 5 min, adjusted pH with NH₄OH solution to pH ~5, filtered, and injected into HPLC. The calibration curve was built as a ratio of palbociclib and niraparib peak area versus palbociclib concentration.

SI-3.5.2. Recovery study

The recovery study we performed for both low (10 µg/ml) and high (100 µg/ml) Palbociclib concentrations. We compared the ratio of palbociclib/niraparib peak area between palbociclib/niraparib stock solution and after its spiking with StPGA150 till final polymer concentration of 1 mg/ml, the same as used for drug release studies, followed by the extraction with DCM, and all steps of the sample preparation procedure. The recovery value was 60% (for the low concentration range) and 74% (for the high concentration range), which we used to correct the value we obtained of released palbociclib from the calibration curve. The drug release graph was built as the cumulative value of palbociclib release versus time.

SI-3.5.3. LOD and LOQ determination

The limit of detection (LOD) and limit of quantification (LOQ) for palbociclib was obtained using the following equations

$$LOD = 3.3 \times \frac{SD_y}{m}$$

$$LOQ = 10 \times \frac{SD_y}{m}$$

Where SD_y is the standard deviation associated with the intercept and m is the slope. The SD_y value is obtained from the LINEST function in MS Excel. We obtained LOD 0.11 µg/ml and LOQ 0.33 µg/ml of the developed HPLC method.

SI-3.5.4. HPLC method optimization for plasma stability studies

Conjugates (1 mg/ml) were incubated for 24 h,48 h, and seven days at 37⁰C in freshly extracted rodent plasma. Plasma spiked with free palbociclib was used as a positive control, and plasma was used as a negative control. 300 µl of Milli-Q water and 25 µl of Trichloroacetic acid (TCA) were added to each sample to precipitate plasma proteins and PGA polymer. The solution was incubated for 10 min on ice and centrifuged at maximum speed at 4ºC for 10 min; then, the 400 µl supernatant was collected, the pH adjusted with 30 µl 2.5M NaOH, passed through a 0.22 µm filtered, and analyses by HPLC (**Figure S3.19**)

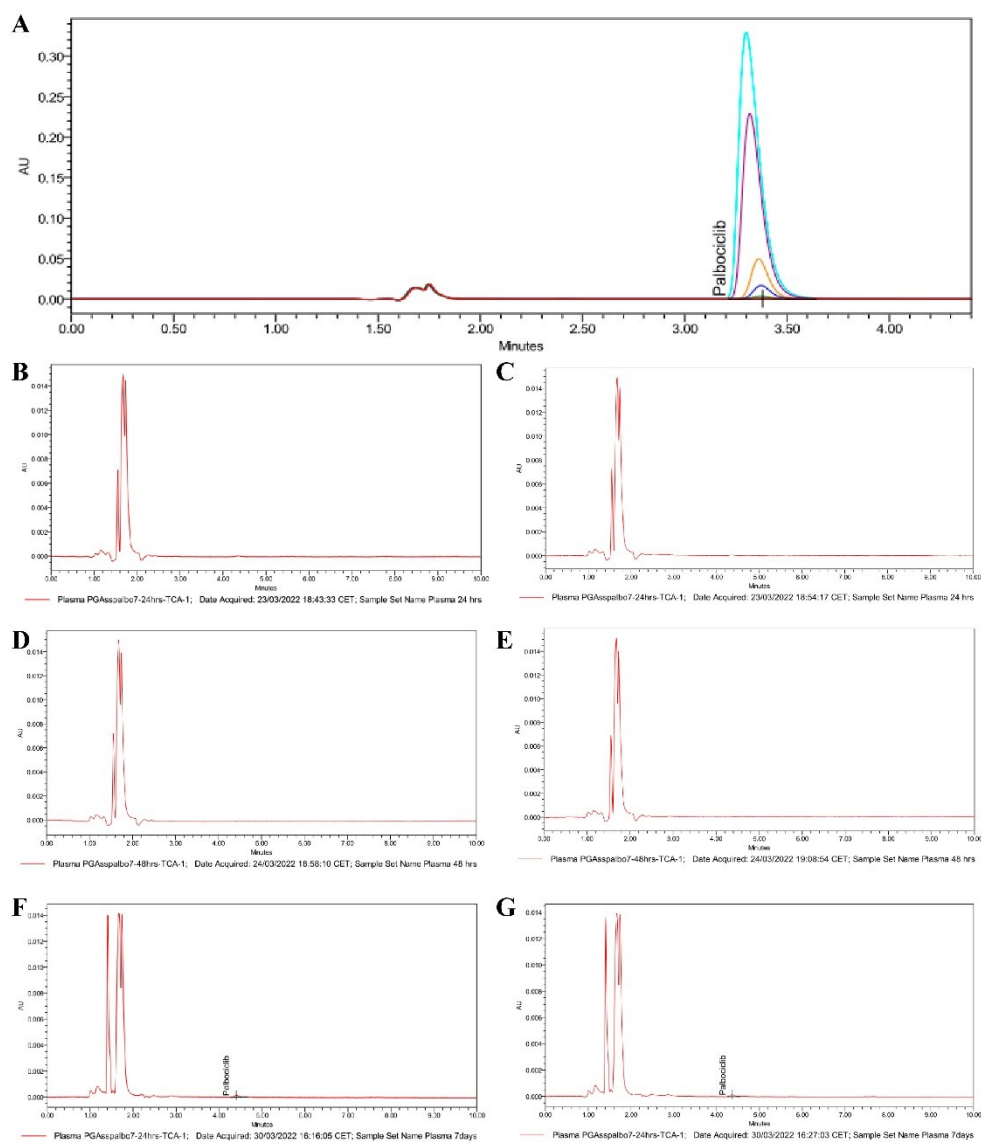**Figure S3.19**. (A) HPLC chromatograms of calibration solutions used for quantification of palbociclib from plasma stability studies; (B, C) HPLC chromatograms of StPGA-SS-palbo2 conjugates after incubation for 24 h in rodent plasma; (D, E) HPLC chromatograms of StPGA-SS-palbo2 conjugate after incubation for 48 h in rodent plasma; (F, G) HPLC chromatograms of StPGA-SS-palbo2 conjugate after incubation for seven days in rodent plasma.

SI-3.6. DIPG and GBM cell culture conditions and cell handling protocols

Patient-derived cells were obtained under an Institutional Review Board-approved protocol and with written informed consent at Hospital Sant Joan de Dèu Barcelona, Spain. Diffuse intrinsic pontine glioma (DIPG) cell line (HSJD-DIPG007) and pediatric Glioblastoma (GBM) cell line (HSJD-GBM-001) were kindly supplied by Dr. Angel Montero-Carcaboso (Hospital Sant Joan de Déu, Barcelona, Spain). As indicated in Table S1, the cells were isolated from patient autopsy (HSJD-DIPG-007) or biopsies at diagnosis (HSJD-GBM-001) [96,97].

The DIPG and GBM cells were maintained in working Tumor Stem Medium (TSM$_{working}$) freshly prepared from Tumor Stem Medium Base (TSM$_{base}$) in T25 or T75 tissue culture flasks with 5-10 ml or 10-15 ml respectively of media. Cells were incubated at 37^{0}C and 5% CO_2. Media was replaced every 3-4 days or once the medium turned yellow.

SI-3.6.1. Preparation of TSM Base solution

In a laminar flow hood, 250 ml of Neurobasal-A Medium (1X), 250 ml of D-MEM-F-12 (1X), 5.0 ml of HEPES buffer solution (1M), 5.0 ml of sodium pyruvate MEM (100mM), 5.0 ml of GlutaMAX-1 Supplement, 5.0 ml of Antibiotic-Antimycotic (100X) were mixed. The prepared TSM$_{base}$ can be stored indefinitely at 4^{0}C.

SI-3.6.2. Preparation of TSM Working solution

In a laminar flow hood, 50 ml of TSM$_{base}$ solution was mixed with 1.0 ml of B27 supplement without vitamin A (50X), 50 μl of Recombinant Human *Epidermal Growth Factor (*EGF, 20 μg/ml), 50 μl of Recombinant Human *Basic* fibroblast growth factor (FGF-basic, 20 μg/ml), 25 μl of platelet-derived growth factor AA (PDGF-AA, 20 μg/ml), 25 μl of platelet-derived growth factor BB (PDGF-BB, 20 μg/ml), 50 μl of Heparin Solution (0.2% prepared in TSM base). TSM Working solution should be prepared immediately before feeding the cells and used within 24 h.

SI-3.6.3. Passaging the cells

In a laminar flow hood, the cells are transferred into 50 ml conical tubes and centrifuged in the tube at 400 G for 3 min. Then, the medium was aspirated, leaving around 100 μl in the tube, followed by the addition of 100 μl pre-warmed TSM working solution, and the cell pellet was resuspended 10-15 times with a p200 pipette by slow pipetting up and down. A pre-warmed TSM working solution was added to the final volume of 10 ml, and the cells were transferred to T25 tissue culture flasks. If a single cell suspension is needed, the cells can be filtered through a 50 μl cell strainer optionally.

SI-3.6.4. Cryopreserving the cells

To cryopreserve the cells, we used Synth-a-Freeze® (Life Technologies). First, the cell culture freezing medium was thawed entirely and kept on ice during the use. The cell suspensions or small tumorspheres were transferred in a laminar flow hood into a 50 ml conical tube and centrifuged at 400 G for 3 min. Then, the medium was aspirated, and the cell pellet was resuspended in Synth-a-Freeze (1 ml for T25 or 3 ml for T75 tissue culture flasks) and aliquoted into appropriate cryogenic storage vials.

The vials should be placed in Styrofoam and stored at -80^0C for at least 24 h until two weeks after the cells can be transferred for long-term storage in liquid nitrogen ($-196\,^0C$).

SI-3.6.5. Thawing Cryopreserved cells

The cells should be thawed quickly in a 37^0C water bath without vortexing. Then, in a laminar flow hood with a pipette, the cells are transferred to a sterile 50 ml conical tube and added to 9 ml of pre-warmed, freshly prepared $TSM_{working}$ solution. The cell suspension is gently mixed by slow pipetting up and down 2-3 times and centrifuged at 400 G for 3 min. The supernatant is decanted as much as possible; the cell pellet is resuspended in 10 ml of pre-warmed $TSM_{working}$ solution, and the cell mixture is placed into a T25 tissue culture flask.

SI-3.7. General Procedure for the Synthesis of Conjugates via a ValCit Linker

Figure S3.20 shows the proposed synthetic route for synthesizing palbociclib conjugates via a disulfide linker.
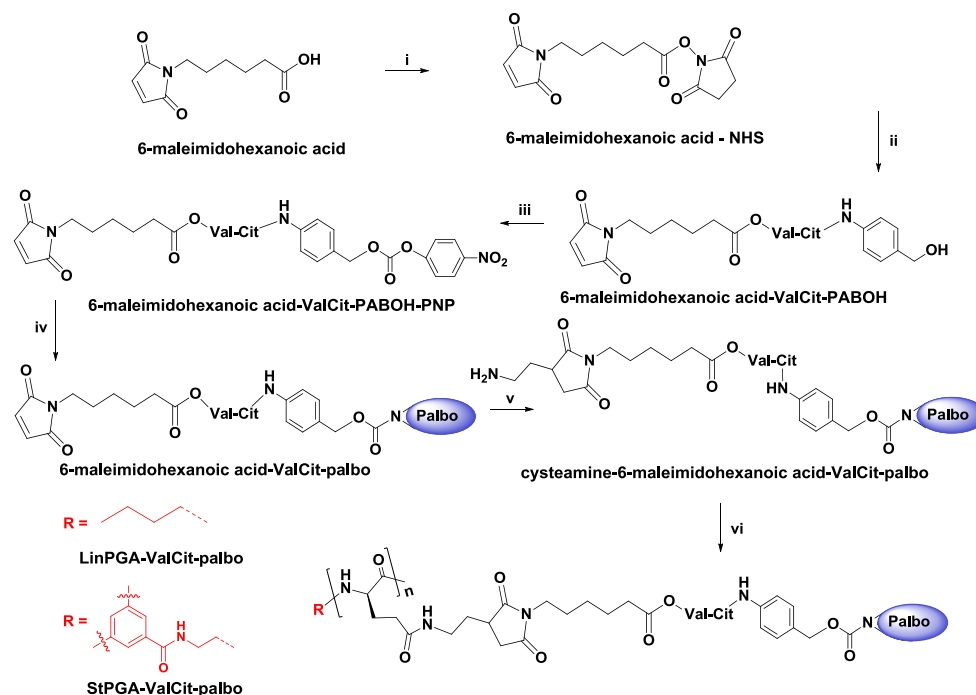
Figure S3.20. Synthesis of PGA-ValCit-palbociclib conjugates. i) NHS, DCC, THF$_{anh}$; ii) ValCit-PABOH, DMF$_{anh}$; iii) p-nitrophenyl chloroformate, DMAA, TEA; iii) palbociclib, DMAA; iv) cysteamine hydrochloride, DMAA; v) PGA, DMF$_{anh}$, DMTMM·BF$_4$, TEA

SI-3.7.1. Preparation of 6-maleimidohexanoic acid NHS

In a round bottom flask with a stirrer, 6-maleimidohexanoic acid (1.7 g, 7.7 mmol, Mw=211.2 g/mol, 1 eq.) and N-hydroxysuccinimide (NHS, 1.1 g, 9.5 mmol, Mw=115.1 g/mol, 1.2 eq) were placed in 35 ml of THF$_{anh}$, added DCC (1.9 g, 9.2 mmol, Mw=206.3 g/mol, 1.2 eq.) dropwise in 15 ml of THF$_{anh}$, and the reaction was left to proceed on ice overnight. The precipitate was removed by centrifugation. The supernatant was concentrated under reduced pressure, and the product was extracted once with THF (20 mL) and two times with DCM (20 mL). The white precipitate, dicyclohexylurea (determined with 1H NMR), was filtered out, and the supernatant was concentrated under reduced pressure to yield a product.
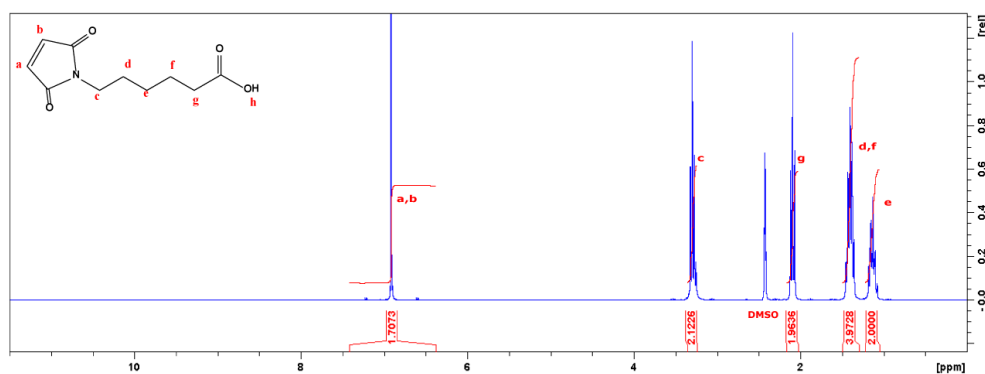
Figure S3.21. 1 6-maleimidohexanoic acid: *^{1}H NMR (300 MHz, DMSO-d)*: 6.91 (s, 2H), 3.30 (t, 2H), 2.09 (t, 2H), 1.40 (m, 4H), 1.13 (m, 2H)
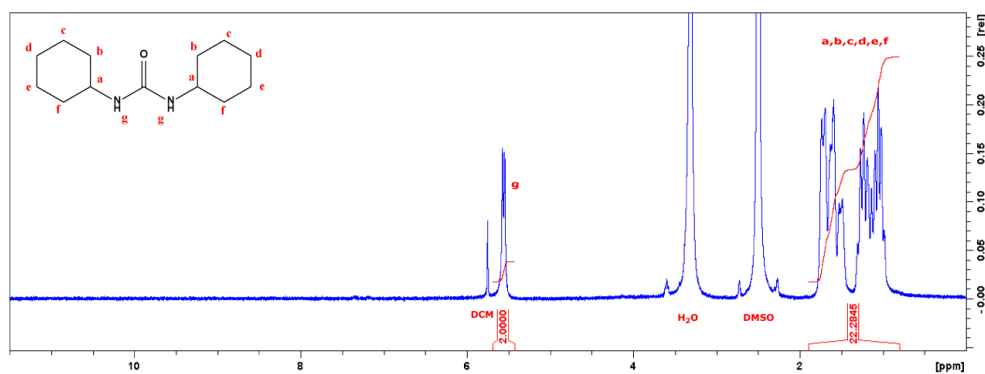
Figure S3.22. 2 dicyclohexylurea (precipitate after DCM extraction): *^{1}H NMR (300 MHz, DMSO-d)*: 5.56 (d, 2H), 1.81-0.91 (m, 12H)

227
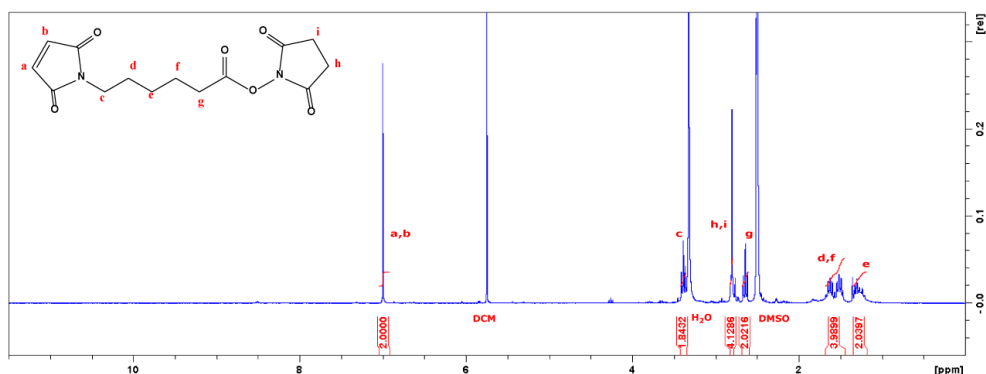
Figure S3.23. 6-maleimidohexanoic acid - NHS: Product – yellowish oil. Global yield: 2.38 g (96 %). *^{1}H NMR (300 MHz, DMSO-d)*: 7.00 (s, 2H), 3.39 (t, 2H), 2.80 (s, 4H), 2.64 (t, 2H), 1.67-1.46 (m, 4H), 1.30 (m, 2H)

SI-3.7.2. Preparation of 6-maleimidohexanoic-ValCit-PABOH

In a round bottom flask with a stirrer, 6-maleimidohexanoic acid-NHS (183 mg, 0.59 mmol, Mw=308.29 g/mol, 1.5 eq.) was dissolved in 5ml of DMF$_{anh}$ under N$_2$, added ValCit-PABOH (150 mg, 0.39 mmol, Mw=379.45 g/mol, 1 eq.) in 1 ml of DMF$_{anh}$, and was left to proceed for 2 h. The reaction was monitored by TLC, Rf = 0.6 (MP DCM:MeOH = 85:15). The reaction mixture was concentrated under reduced pressure, washed two times with 10 mL Et$_2$O, then three times with 10 mL EtAc, and dried under vacuum.

Figure S3.24. 6-maleimidohexanoic acid-ValCit-PABOH: Product – yellowish powder. Global yield: 220 mg (94 %). *^{1}H NMR (300 MHz, DMSO-d)*: 9.80 (s, 1H), 7.96 (d, 1H), 7.71 (d, 1H), 7.46 (d, 2H), 7.15 (d, 2H), 6.93 (s, 2H), 5.88 (t, 1H), 5.31 (s, 2H), 4.99 (t, 1H), 4.35-4.30 (d+m, 3H), 4.11 (t, 1H), 3.29 (t, 2H), 2.89 (m, 2H), 2.07 (m, 2H), 1.89 (m, 2H), 1.64-1.25 (m, 9H), 1.12 (m, 2H), 0.76 (dd, 6H).

SI-3.7.3. Preparation of 6-maleimidohexanoic-ValCit-PABOH-PNP

In a round bottom flask with a stirrer, 6-maleimidohexanoic acid-PABOH (220 mg, 0.37 mmol, Mw=588.65 g/mol, 1 eq.) was dissolved in 2ml of DMAA$_{anh}$ under N$_2$, added 4-nitrophenyl chloroformate (150 mg, 0.74 mmol, Mw=201.57 g/mol, 2 eq.) in 0.5 ml of DMAA$_{anh}$, TEA (180 μL, 1.29 mmol, Mw=101.19 g/mol, ρ=0.726 g/cm^3, 3.5 eq.), the reaction mixture turned yellow, was left to proceed overnight at room temperature. The reaction was monitored by TLC, Rf = 0.85 (MP DCM:MeOH = 85:15). The reaction mixture was concentrated under reduced pressure, and the residue was subjected to column chromatography on silica gel (MP DCM:MeOH = 85:15) to give a solid white product.
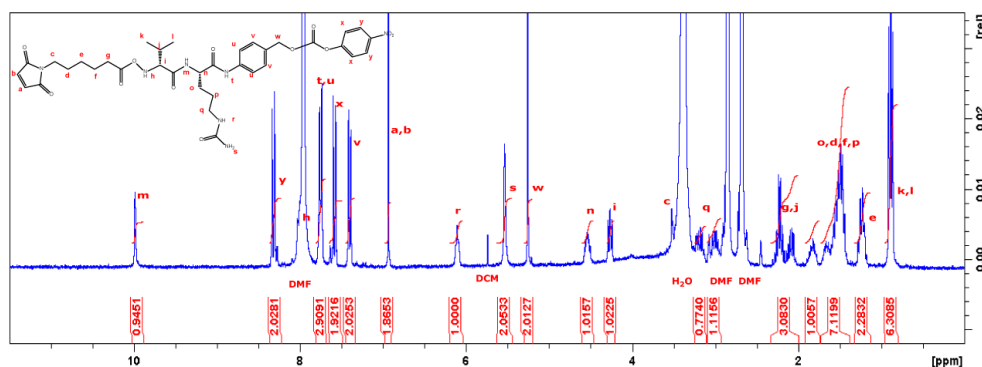
Figure S3.25. 6-maleimidohexanoic acid-ValCit-PABOH-PNP: Product – white powder. Global yield: 150 mg (53 %). *^{1}H NMR (300 MHz, DMSO-d)*: 9.99 (s, 1H), 8.32 (d, 2H), 7.75 (d, 3H), 7.58 (d, 2H), 7.40 (d, 2H), 6.94 (s, 2H), 6.11 (t, 1H), 5.54 (s, 2H), 5.26 (s, 2H), 4.54 (m, 1H), 4.27 (dd, 1H), 3.18-3.00 (m, 2H), 2.26-2.06 (m, 3H), 1.88-1.44 (m, 8H), 1.23 (m, 2H), 0.89 (t, 6H).

SI-3.7.4. Preparation of 6-maleimidohexanoic-ValCit-palbo

In a round bottom flask with a stirrer, palbociclib free base (55 mg, 0.12 mmol, Mw=447.53 g/mol, 1.2 eq.) was dissolved under heating in 40 ml DMAA$_{anh}$, added TEA (19 μL, 1.29 mmol, Mw=101.19 g/mol, ρ=0.726 g/cm^3, 1.3 eq.), purged with N$_2$, added 6-maleimidohexanoic-ValCit-PABOH-PNP in 5 ml of DMAA$_{anh}$ (76 mg, 0.10 mmol, Mw=753.76 g/mol, 1 eq.), and the reaction mixture was left to proceed for 1 h at room temperature. The reaction was monitored by TLC, Rf = 0.3 (MP DCM:MeOH = 9:1). The reaction mixture was concentrated under reduced pressure at room temperature. The elevated temperature should be avoided since it leads to Diels-Alder cyclization between maleimide moiety and the aromatic ring of palbociclib. The crude product was subjected to column chromatography on silica gel (MP DCM:MeOH = 9:1) to give a yellow solid.
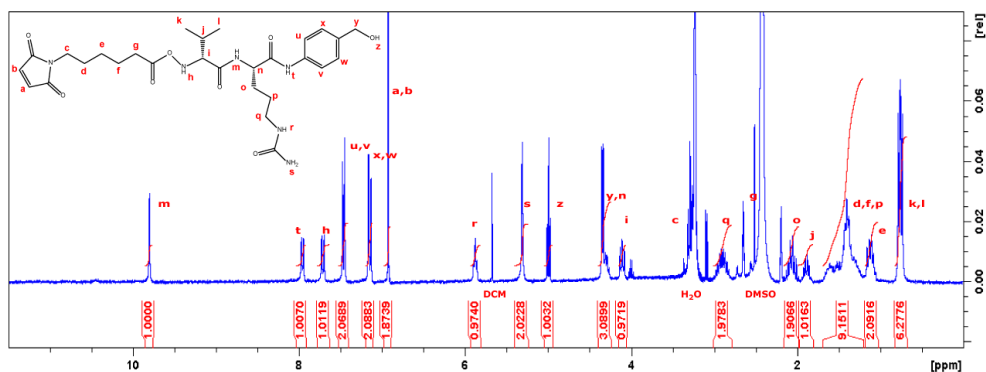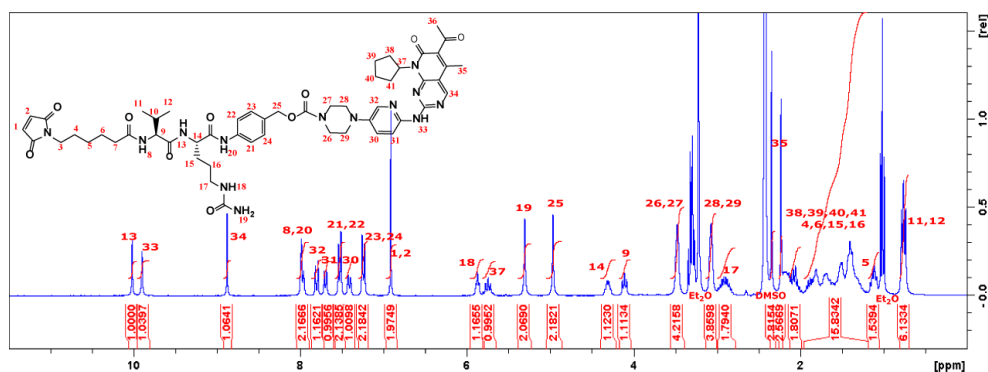
Figure S3.26. 6-maleimidohexanoic acid-ValCit-palbo: Product – yellow powder. Global yield: 82 mg (78 %). *¹H NMR (300 MHz, DMSO-d)*: 10.02 (s, 1H), 9.90 (s, 1H), 8.88 (s, 1H), 7.99 (d+d, 2H), 7.81 (d, 1H), 7.70 (d, 1H), 7.53 (d, 2H), 7.42 (dd, 1H), 7.24 (d, 2H), 6.91 (s, 2H), 5.87 (t, 1H), 5.75 (m, 1H), 5.31 (s, 2H), 4.97 (s, 2H), 4.31 (m, 1H), 4.10 (t, 1H), 3.48 (m, 4H), 3.08 (m, 4H), 2.91 (m, 2H), 2.35 (s, 3H), 2.23 (s, 3H), 2.06-1.25 (m, 18H), 1.12 (m, 2H), 0.76 (dd, 6H).

SI-3.7.5. Preparation of cysteamine-6-maleimidohexanoic-ValCit-palbo

In a round bottom flask with a stirrer, 6-maleimidohexanoic acid-ValCit-palbo (46 mg, 0.044 mmol, Mw=1046.2 g/mol, 1 eq.) and cysteamine HCl (6 mg, 0.05 mmol, Mw=113.6 g/mol, 1.2 eq.) was dissolved in 5 ml DMF$_{anh}$, added TEA (8 µL, 0.057 mmol, Mw=101.19 g/mol, ρ=0.726 g/cm³, 1.3 eq.), the reaction was left to proceed for 2 h at room temperature. The intermediate was precipitated in cold Et$_2$O and dried under a vacuum to obtain a white solid.
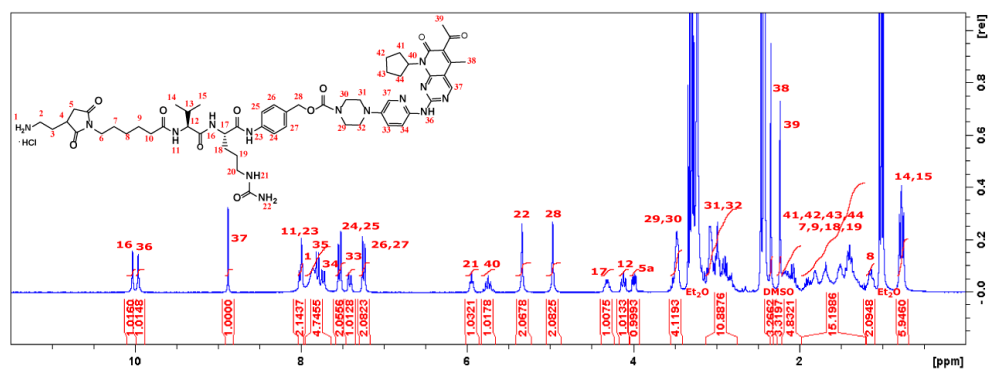
Figure S3.27. cysteamine-6-maleimidohexanoic acid-ValCit-palbo: Product – yellow powder. Global yield: 80 mg (90 %). *¹H NMR (300 MHz, DMSO-d)*: 10.02 (s, 1H), 9.96 (s, 1H), 8.88 (s, 1H), 7.99 (d+d, 2H), 7.90-7.72 (s+d+d, 5H), 7.53 (d, 2H), 7.41 (dd, 1H), 7.24 (d, 2H), 5.95 (t, 1H), 5.75 (m, 1H), 5.34 (s, 2H), 4.97 (s, 2H), 4.31 (m, 1H), 4.12 (t, 1H), 3.99 (dd, 1H), 3.48 (m, 4H), 3.11-2.80 (m, 11H), 2.34 (s, 3H), 2.23 (s, 3H), 2.20-2.03 (m, 5H), 1.94-1.25 (m, 15H),1.14 (m, 2H), 1.01 (t, 6H).

<u>*SI-3.7.6. Preparation of PGA-ValCit-palbociclib conjugates through a self-immolative peptidic linker*</u>

In a round bottom flask with a stirrer, LinPGA100 or StPGA150 (15 mg, 0.12 mmol, Mw=129.1 g/mol, 1eq.) was placed in 3 ml of DMSO$_{anh}$, added DMTMM BF$_4$ (2.1/2.9/4.2mg, 0.006/0.009/0.013 mmol, Mw=328.1 g/mol, 0.055/0.077/0.11 eq.) depending on the targeted modification, the mixture allowed to stir 30 min to activate carboxylic groups. Then, cysteamine-6-maleimidohexanoic-ValCit-palbo (6.6/9.2/13.1 mg, 0.0059/0.0081/0.012 mmol, Mw=1127.7 g/mol, 0.05/0.07/0.10 eq.) depending on the targeted modification, in 2 ml of DMSO$_{anh}$ was added, the pH of the solution was adjusted to 8.0 with TEA, and the solution allowed to stir for 48 h at room temperature. The product was precipitated in cold diethyl ether, filtered, and dried under a vacuum. The obtained white solid was dissolved in 0.5 M aqueous sodium hydrocarbonate solution and dialyzed against water (Cellulose ester membrane, cut off 500-1000Da, Spectrum®) for 48h, and then the solution was freeze-dried. The conjugates were dissolved in water and purified with Sephadex® G25 column and water as a mobile phase. The combined fractions were lyophilized to give a yellow powder with different intensities depending on the drug loading.

SI-3.8. HPLC Method Optimization for Release Studies of PGA-ValCit-palbo Conjugates

The media for release kinetics of PGA-ValCit-palbo conjugates was selected based on the available literature [34,70] using 5IU of Cathepsin B enzyme as a trigger for linker cleavage and sodium acetate buffer pH 5.0 with 5mM DTT – optimal conditions for the cysteine-rich enzyme. The HPLC method was adapted from the previously described method for PGA-SS-palbo conjugates. Mobile phase - 1mM Ammonium Formate (NH$_4$FA): Acetonitrile: Formic acid (80:20:0.1). Column: Aeris XB-C18, 150x4.6 mm, particle size 3.6 μm (Widepore, Phenomenex).

All buffers were freshly prepared before the drug release study and equilibrated at 37°C.

Working buffer pH 5.0: 102.5 mg of sodium acetate (NaAc, Mw=82.0 g/mol) and 18.6 mg of Ethylenedinitrilotetraacetic acid disodium salt (EDTA, Mw=372.24 g/mol) was dissolved in Milli-Q water, adjusted pH to 5.0 with sodium hydroxide (NaOH) or acetic acid (HAc) if needed and fill the volume to 50 ml.

<u>*Cathepsin B stock solution*</u> (940 nM, 50 IU/ml): the whole bottle of Cathepsin B from bovine spleen standard (Sigma-Aldrich, C6286-25UN) was dissolved in 500 μl of Milli-Q water and aliquoted by 60 μl into 1.5 ml Eppendorf tubes and stored at -80°C no longer than 20 days.

Activation buffer: 9.3 mg of dithiothreitol (DTT, Mw=154.25 g/mol) and 11.2 mg of EDTA (Mw=372.24 g/mol) was dissolved in 1 ml of Milli-Q water.

<u>*25 mM NaAc:*</u> 2.1 mg of NaAc (Mw=82.0 g/mol) was dissolved in 1 ml of Milli-Q water.

The prepared PGA-ValCit-palbociclib conjugates at 2 mg/ml were aliquoted by 500 μl into two 1.5 ml Eppendorf tubes for study with and without cathepsin B and equilibrated at 37 °C. The Cathepsin B stock solution was quickly thawed at a 37°C water bath, then 60 μl of activation buffer and 60 μl of 25 mM NaAc solution were added, and the mixture was incubated at 37°C in the Thermomixer (Eppendorf ® Thermomixer Compact, T1442) with constant shaking at 1000 rpm, covered from light during 15 min. Then, the activated cathepsin B solution was diluted with 384 μl of working buffer pH 5.0 and vortexed for 1 min. 500 μl of this cathepsin B solution was added to prepare 500 μl of conjugate samples, incubated at 37°C in the Thermomixer with constant shaking at 1000 rpm, covered from light (final conjugate concentration 1 mg/ml, final cathepsin B concentration 100 nM).

The preparation steps for the study without cathepsin B were the same, except that stock solutions were used with equal volumes of Milli-Q water instead of Cathepsin B.

At selected time points, 10 μl of the solution was taken, added 90 μl of the MP with Internal standard (final concentration 10 μg/ml), acidified the solution with 2 μl of 13.5 M TCA solution, adjusted pH with NH4OH solution to pH ~5, filtered, and injected into HPLC.

Figure S3.28 shows the representative HPLC chromatograms of the developed method with sufficient separation between the palbociclib peak and internal standard (**Figure S3.28 A**) and their corresponding UV-Vis spectra (**Figure S3.28 B, C**).

To confirm no interferences with palbociclib and internal standards from the selected release media, we injected DTT and cathepsin B solutions into the HPLC system (**Figure S3.28 D, E**). At the selected detection wavelength λ=364 nm, there were no peaks detected. The representative chromatogram of the StPGA-ValCit-palbo2 conjugates at 2 h of kinetic studies with cathepsin B (**Figure S3.28 F**) demonstrated a similar pattern to the standard solution (**Figure S3.28 A**), with similar retention time and identical UV-Vis spectra (**Figure S3.28 G, H**) proving the identity of the analytes.

Additionally, on the chromatogram of StPGA-ValCit-palbo2 conjugate (**Figure S3.28 F**), the peak at 7.78 min appeared similar but not identical to palbociclib UV-Vis spectra B (**Figure S3.28 K**). This peak can be assigned to not fully degraded palbociclib linker with para aminobenzyl alcohol moiety attached. As expected, this intermediate product has a higher retention time than palbociclib due to the stronger interaction between the stationary column phase and the amino group. The amount of this intermediate side product is exceptionally low (less than 2%) and decreases with time, demonstrating the efficiency of the linker self-immolation step after enzyme cleavage.

DTT is another compound in the sample that we did not detect when evaluating the freshly prepared solution for the suitability of the HPLC system. However, in the conjugates samples with a time, the oxidized form of DTT [98] is present; even so, it is not absorbing at λ=364 nm used for analyte quantification; the chromatogram at λ=280 nm (**Figure S3.28 I**) with corresponding UV-Vis spectra B (**Figure S3.28 J**) demonstrated good separation of the oxidized DTT with palbociclib.

A

Niraparib 5.30 min

Palbociclib 4.28 min

Intensity, AU / Time, min

B

221,1 259,5 290,1 364,3

Palbociclib RT 4.28 min

Intensity, AU / Wavelength, nm

C

238.6 307.6

Niraparib RT 4.28 min

Intensity, AU / Wavelength, nm

D

Cathepsin B (10X); Vial: 12

AU / Minutes

E

DTT, EDTA (activation buffer); Vial: 13

AU / Minutes

F

Detection wavelengh λ=364 nm

Palbociclib 4.09 min

Niraparib 5.32 min

Palbociclib deriv. 7.78 min

Intensity, AU / Time, min

G

221.0 259.3 289.9 363.9

Palbociclib RT 4,09 min

Intensity, AU / Wavelength, nm

H

238.3 308.7

Niraparib RT 5,32 min

Intensity, AU / Wavelength, nm

Figure S3.28. Representative HPLC chromatograms of palbociclib with niraparib internal standard (A) and corresponding UV-Vis spectra of Palbociclib (B) and Niraparib (C). Chromatograms of cathepsin B (D) and DTT (E) solutions were used to assess the possible interferences from the released media. Chromatogram of StPGA-ValCit-palbo2 conjugates at 2 h of kinetic studies with cathepsin B at the λ=364 nm (F) and λ=280 nm (I), with the corresponding UV-Vis spectra of palbociclib (G), Niraparib (H), Oxidized DTT (J) and not fully self-immolated palbociclib linker (K).

SI-3.9. General Procedure for Fluorophore Labeling with Cy5.5

In a round bottom flask with a stirrer, PGA Na-form (100 mg, Mw=129.1 g/mol (Glu unit), 1 eq.) was placed in 10 ml of Milli-Q water, added DMTMM Cl (4.3 mg, 0.015 mmol, Mw=276.6 g/mol, 0.02 eq.), the mixture allowed to stir 30 min to activate carboxylic groups. Then, Cy5.5 (i.e., 0.02 eq. for 2 % modification) was added in ddH2O. The pH was adjusted to 8 by adding sodium bicarbonate 1 M. Reaction was left to proceed for 24 h, protected from light. The products were submitted to Sephadex G25 and dialysis using Vivaspin® MWCO 5000 for purification. Cy5.5 content was estimated by fluorescence (λem: 595 nm, λex: 680 nm) after building an appropriate calibration curve of Cy5.5 dye in PBS buffer. Yields: 60-70 %. Conjugation efficiency 70-90 %.

SI-3.10. Internalization study with Confocal life cell imaging

The GBM or DIPG cells were seeded at 23438 cells/cm^2 in sterile 384-well microliter black plate (P384) - 2344 cells/well in 25 µl of cell media or 96-well microliter standard plate (P96) - 7500 cell/well in 50 µl of cell media. Plates were incubated for 24 h at 37^{0}C and 5% CO$_2$ before treatment. The StPGA-ValCit-palbociclib-Cy5.5 conjugate labeled with Cy5.5 dissolved in cell media and filtered through a 0.22 µm Nylon filter was added to evaluated cells in 25 µl (P384) or 50 µl of freshly prepared cell media. 2 h before the selected time points, 1.2 µL cell mask green (Stock solution 25X), 0.6 µL Hoechst (100 µg/ml stock solution) was added to stain cell membrane and nuclei, respectively. The separate wells with cells and only conjugate-Cy5.5, Cell mask green, or Hoechst were prepared to

optimize microscope parameters. After optimizing the laser parameters, the selected settings were used for all experiments. The data treatment was performed with Image J software.

<u>Microtiter Plate Selection for Internalization Study with GBM and DIPG Cells</u>

Due to economic reasons, confocal microscopy studies are usually performed in 384-well microtiter plates to reduce the number of markers used. Initially, GBM were seeded in a sterile 384-well microtiter black plate at the same cell density used for MTS studies. After 24 h, cell membrane and nuclei markers were added to the cells 2 h before starting the measurement. After optimizing the laser parameters and initiating the timelapse study, we added the StPGA-ValCit-palbo3-Cy5.5 conjugate and fresh cell media to the tested cells.

We observed apparent cell uptake and robust distribution throughout spheroids at 60 min (**Figure S3.29**).
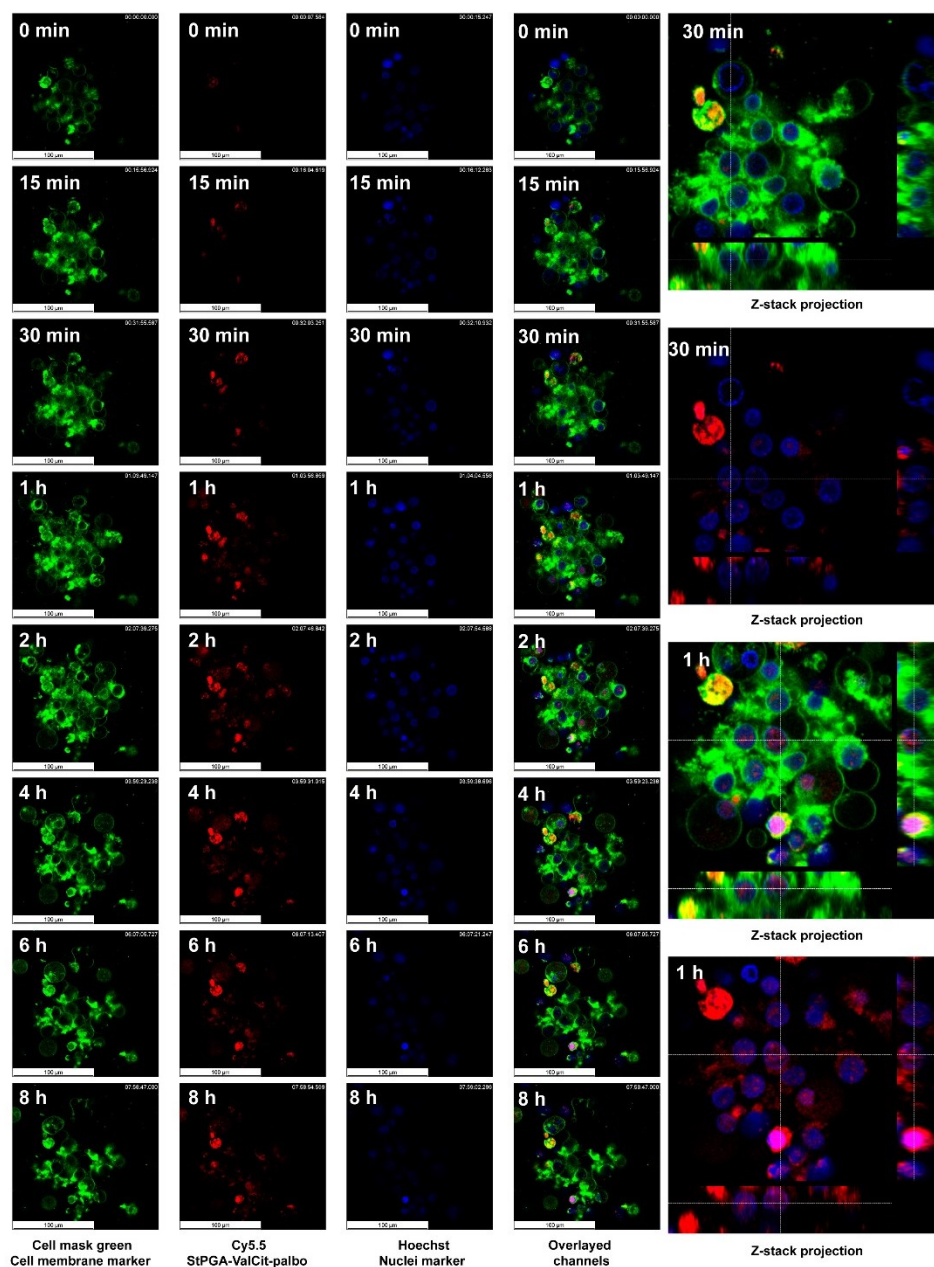
Figure S3.29. Confocal live images of GBM tumorspheres at different time points with separated channels: green–cell mask green (cell membrane marker), red – StPGA-ValCit-palbociclib labeled with Cy5.5, blue – Hoechst (nuclei marker), and zoomed region from the z-stack projection for time points 30 and 60 min with overlayed color channels.

After 4 h, we observed tumor sphere disintegration, which may relate to irradiation toxicity from lasers. Therefore, we removed Hoechst nuclear staining without the time-lapse study and repeated the experiment. Figure 3.43 shows two images of both tumorspheres post-treatment with StPGA-ValCit-palbo-Cy5.5 conjugate without prior time-lapse measurements. The StPGA-ValCit-palbo-Cy5.5 conjugate internalized well within the small GBM tumorspheres (**Figure S3.30 A, B**); however, DIPG formed irregular tumorspheres, and StPGA-ValCit-palbo internalized at a low level (**Figure S3.30 C, D**).
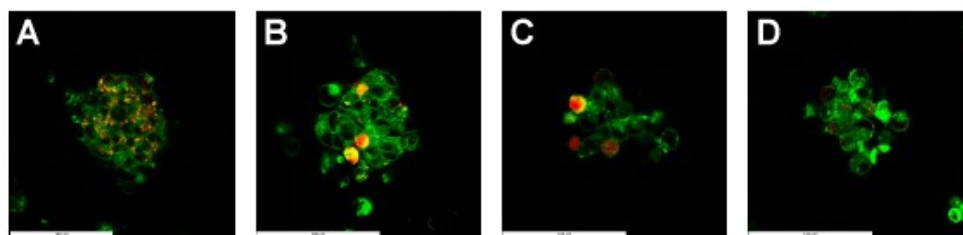
Figures 3.30 Live confocal images of GBM (A, B) and DIPG tumorspheres in duplicates (C, D) at 24 h post-treatment with StPGA-ValCit-palbo-Cy5.5 conjugate. The green channel corresponds to cell mask green (cell membrane marker), red – to StPGA-ValCit-palbociclib labeled with Cy5.5.

To understand the poor ability of GBM and especially DIPG cells to form tumorspheres, we monitored cell growth using Leica DMi8 Inverted Microscope and compared tumorsphere formation in P384 black plates used for confocal studies, standard P96 plates used for MTS assay, and U-shaped P96 plates, given a recent study that reported better reproducibility for in vitro three-dimensional tumor cell cultures [99] (**Figure S3.31**).
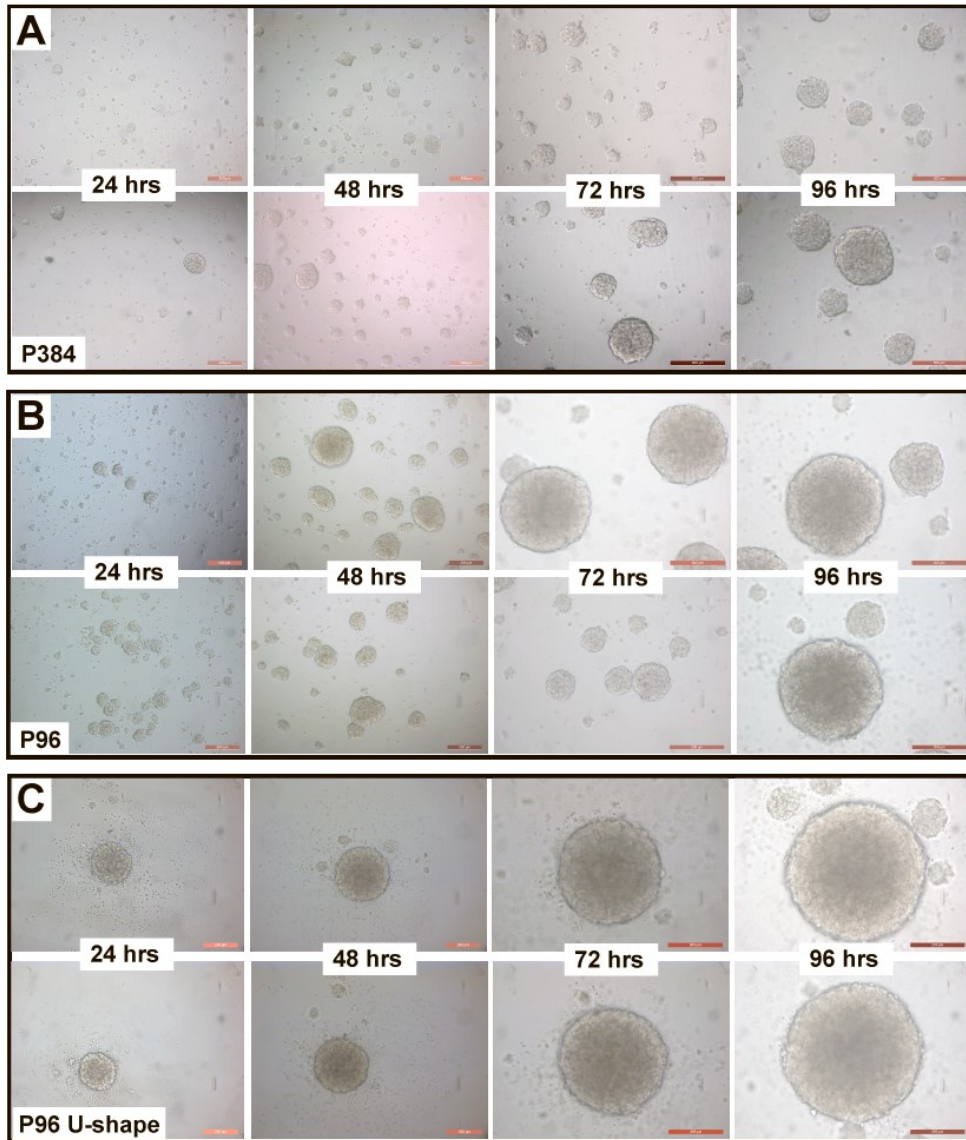
Figure S3.31. Live cell imaging of GBM cells seeded in (A) P384, (B) standard P96, and (C) U-shaped P96 plates at 24, 48, 72, and 96 h. The images were taken with a Leica DMi8 Inverted Microscope in duplicates from different wells for each time point.

Tables S3.1, S3.2, and **S3.3** report the statistical evaluation of images performed with ImageJ software and calculated values of the minimum, maximum, average area, and diameter for GBM tumorspheres seeded in P384 plates, standard P96 plates, and U-shaped P96 plates, respectively.

Table S3.1. Statistical evaluation of images from Leica DMi8 Inverted Microscope with Image J software of GBM cells seeded in a P384 plate.

Well position-time	N**	Max. Area, nm^2	Min. Area, nm^2	Average Area, nm^2	StDev, nm^2	Max. d, nm	Min. d, nm	Average d, nm	StDev, nm
1-24 h	10	10801.8	366.8	1834.7	3195.1	108.6	25.1	39.2	25.8
2-24 h	10	2021.3	317.7	934.3	615.7	47.9	20.5	33.7	9.7
24 h*	20	10801.8	317.7	1384.5	2286.6	108.6	20.5	36.5	19.2
1-48 h	10	6288.6	1547.9	3335.2	1530.4	89.7	39.0	62.3	17.2
2-48 h	10	14625.9	2655.6	4963.5	3523.2	139.8	53.9	76.1	24.0
48 h*	20	14625.9	1547.9	4149.4	2772.5	139.8	39.0	69.2	21.5
1-72 h	10	5758.1	1708.9	3230.4	1247.1	87.2	44.9	60.0	14.5
2-72 h	7	19576.2	2860.2	7294.7	5706.1	156.5	59.6	91.6	33.0
72 h*	17	19576.2	1708.9	5262.6	4163.6	156.5	44.9	75.8	28.0
1-96 h	7	11997.9	2809.1	6902.8	3448.8	125.4	64.2	94.5	21.8
2-96 h	5	33439.0	3128.8	14227.5	11541.4	206.1	49.9	121.7	57.0
96 h*	12	33439.0	2809.1	10565.2	8315.7	206.1	49.9	108.1	40.5

* Average result from duplicates** Number of analyzed tumorspheres

As shown in **Table S3.1**, the average diameter of the tumor spheres for GBM cells seeded in the P384 plate increased from 37 at 24 h to 108 nm at 96 h; however, tumorspheres seeded in a standard P96 plate (**Table S3.2**) displayed a size twice as large, increasing from 68 nm at 24 h to 236 nm at 96 h. We can also estimate the number of cells that form tumorspheres from these data by dividing sphere volume by a single cell volume. In P384 plates, GBM cells in 24 h form smaller spheres from a minimum of 6.5 cells (average 36), compared to a minimum of 58 cells (average 237) for a standard P96 plate. Additionally, these differences increase over time – we observed a minimum number of cells of 94 (average 949) for the P384 plate at 96 h but a minimum of 624 (average 9819) for the standard P96 plate.

We believe this discrepancy can be explained by plate material – the P384 black plate with a transparent glass bottom seems unsuitable for the growth of GBM cells as tumorspheres. Therefore, we employed a standard polystyrene P96 plate for confocal studies.

Table S3.2. Statistical evaluation of images from Leica DMi8 Inverted Microscope with Image J software of GBM cells seeded in a standard P96 plate.

Well position-time	N**	Max. Area, nm^2	Min. Area, nm^2	Average Area, nm^2	StDev, nm^2	Max. d, nm	Min. d, nm	Average d, nm	StDev, nm
1-24 h	10	7323.4	2836.7	5160.6	1596.2	105.6	58.6	79.0	14.7
2-24 h	10	5799.8	1708.3	3251.3	1695.4	77.6	42.7	57.0	13.1
24 h*	20	7323.4	1708.3	4205.9	1878.2	105.6	42.7	68.0	17.6
1-48 h	10	26537.5	5053.8	10617.5	6406.1	169.3	80.7	111.0	28.3
2-48 h	10	48000.3	5614.5	15396.9	13414.5	251.3	79.0	127.0	52.7
48 h*	20	48000.3	5053.8	13007.2	10520.9	251.3	79.0	119.0	42.0
1-72 h	7	15053.1	3414.8	7565.1	4026.7	140.0	62.2	94.5	27.2
2-72 h	4	81743.6	9751.6	43223.0	37353.3	336.1	122.4	234.0	97.2
72 h*	11	81743.6	3414.8	25394.1	27421.9	336.1	62.2	164.3	90.7
1-96 h	3	102970.6	4752.9	46093.1	50918.9	361.6	94.0	217.8	134.9
2-96 h	2	107090.4	15244.8	61167.6	64944.6	361.2	145.3	253.3	152.7
96 h*	5	107090.4	4752.9	53630.3	49183.2	361.6	94.0	235.6	123.7

* Average result from duplicates** Number of analyzed tumorspheres

Table S3.3. Statistical evaluation of the Leica DMi8 Inverted Microscope images with Image J software of GBM cells seeded in a U-shaped P96 plate.

Well position-time	N**	Max. Area, nm²	Min. Area, nm²	Average Area, nm²	StDev, nm²	Max. d, nm	Min. d, nm	Average d, nm	StDev, nm
24 h	3	42248	37763	40005	3171	228	213	220	11.1
48 h	3	77068	72641	74855	3130	326	308	317	12.5
72 h	3	120774	114984	117879	4095	382	378	380	2.5
96 h	3	195075	191417	193246	2587	504	499	501	3.5

* Average result from duplicates** Number of analyzed tumorspheres

When analyzing data from U-shape P96 plates (**Table S3.3**), we found that the average diameter of GBM tumorspheres increased from 220 nm at 24 h to 501 nm at 96 h, corresponding to 8040 cells per tumorsphere at 24 h and 94,654 at 96 h. The larger tumorsphere size, when compared to a standard P96 plate, derives from the shape of the well, which restricts cell movements and forces the formation of a single tumorsphere.

Moreover, the size and shape of the sphere in this plate type are similar to the cells seeded in a standard P96 plate. Despite exceptional reproducibility regarding sphere growth over time with uniform size, the discussion about mimicking the tumor microenvironment, in this case, is questionable, and we believe that the standard P96 plate, where heterogeneous spheres are formed without any physical restrictions resemble, better the actual tumor development.

Table S3.4, S3.5. and **S3.6**. describe the statistical evaluation of the images performed with ImageJ software and calculated values of the minimum, maximum, average area, and diameter for DIPG tumorspheres seeded in P384, standard P96 plates, and U-shaped P96 plates, respectively.

Table S3.4. Statistical evaluation of images from Leica DMi8 Inverted Microscope with Image J software of DIPG cells seeded in a P384 plate.

Well position-time	N**	Max. Area, nm²	Min. Area, nm²	Average Area, nm²	StDev, nm²	Max. d, nm	Min. d, nm	Average d, nm	StDev, nm
1-24 h	10	3270.9	1215.2	2071.7	779.2	56.3	38.2	46.8	5.9
2-24 h	10	3137.1	888.5	1741.7	724.0	60.1	29.6	46.4	9.2
24 h*	20	3270.9	888.5	1906.7	751.4	60.1	29.6	46.6	7.5
1-48 h	10	4507.5	1935.5	2896.3	888.1	67.9	48.7	53.7	6.6
2-48 h	10	3191.1	1595.6	2517.2	546.2	63.9	41.8	53.9	7.2
48 h*	20	4507.5	1595.6	2706.8	743.5	67.9	41.8	53.8	6.7
1-72 h	10	5490.7	1948.1	3681.0	1278.2	83.3	51.9	66.9	10.8
2-72 h	10	11383.3	3523.9	5732.2	2299.6	94.8	51.0	74.5	16.0
72 h*	20	11383.3	1948.1	4706.6	1268.7	94.8	51.0	70.7	12.9
1-96 h	10	6455.1	2701.0	4862.6	1319.0	91.4	58.3	74.7	14.1
2-96 h	10	7624.6	2498.2	5068.8	1582.0	88.0	48.6	69.5	14.5
96 h*	20	7624.6	2498.2	4965.7	2677.6	91.4	48.6	72.1	62.6

* Average result from duplicates** Number of analyzed tumorspheres

As shown in **Table S3.4**, the average diameter of the tumor spheres for DIPG cells seeded in the P384 plate increased from 47 nm at 24 h to 72 nm at 96 h; however, we observed damaged cells and an aggregate-like composition with a lack of the proper cell-cell connections when compared with the tightly formed tumorspheres containing live cells formed in standard P96 plates (**Figure S3.32**). We also observed larger tumorsphere sizes in standard P96 plates, increasing from 61 nm at 24 h to 434 nm at 96 h (**Table S3.5**). We discovered the minimum number of DIPG cells required to form a single tumorsphere of 20 (average 76) in P384 plates and 49 cells (average 174) in standard P96 plates. Furthermore, these differences increased over time –at least 86 cells (average 281) at 96 h for P384 plates and 8886 cells (average 61313) for standard P96 plates. These stark differences suggest that DIPG cells continue to grow exponentially and form large spheroids in standard P96 plates, demonstrating a clear advantage over P384 plates, where cells possess a slower proliferative rate and tumorspheres start to disintegrate after 48 h. Therefore, as for GBM cells, we employed standard polystyrene P96 plates for confocal studies when using DIPG cells.

Table 3.5. Statistical evaluation of images from Leica DMi8 Inverted Microscope with Image J software of DIPG cells seeded in a standard P96 plate.

Well position-time	N**	Max. Area, nm²	Min. Area, nm²	Average Area, nm²	StDev, nm²	Max. d, nm	Min. d, nm	Average d, nm	StDev, nm
1-24 h	7	4196.1	2869.0	3563.7	509.4	75.6	52.8	63.9	7.4
2-24 h	8	4776.3	1849.5	2859.4	972.4	84.1	40.3	59.1	13.6
24 h*	15	4776.3	1849.5	3211.6	846.4	84.1	40.3	61.5	11.1
1-48 h	10	88180.3	12783.6	35300.5	22701.6	327.7	135.4	188.7	60.4
2-48 h	10	72817.8	18693.4	41230.5	18071.4	304.6	136.8	213.6	59.8
48 h*	20	88180.3	12783.6	38265.5	20200.6	327.7	135.4	201.1	59.9
1-72 h	5	256346.9	36779.5	164779.2	90131.2	593.2	213.2	405.7	135.6
2-72 h	4	196634.4	42128.9	120953.9	65136.4	416.0	235.5	357.3	84.3
72 h*	9	256346.9	36779.5	142866.5	81526.9	593.2	213.2	381.5	111.9
1-96 h	5	294626.2	43165.7	197290.0	94254.4	555.3	227.8	467.7	135.5
2-96 h	4	180277.3	93287.0	144477.5	41518.3	446.5	328.4	399.9	52.2
96 h*	9	294626.2	43165.7	170883.7	122623.3	555.3	227.8	433.8	168.3

* Average result from duplicates** Number of analyzed tumor spheres
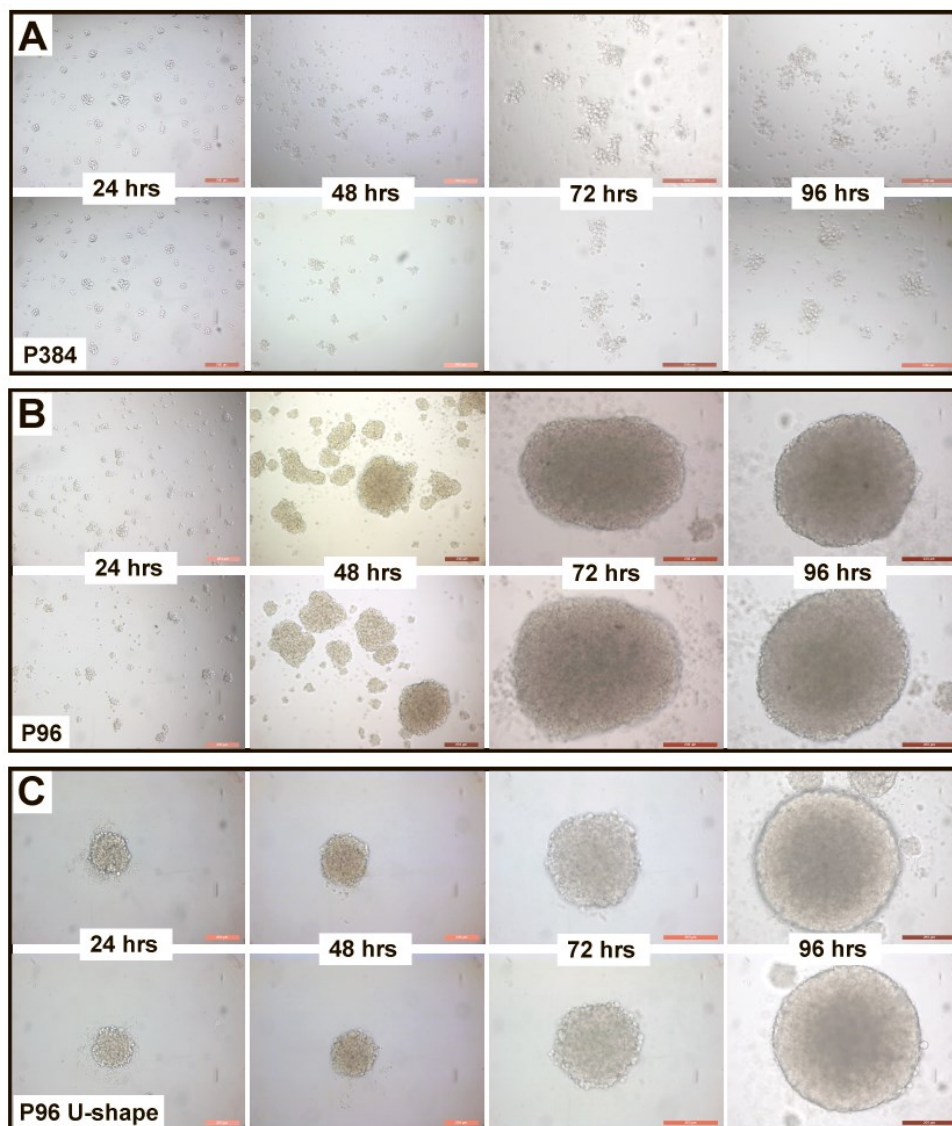
Figure S3.32. Live cell imaging of DIPG cells seeded in (A) P384, (B) standard P96, and (C) U-shaped P96 well plates at 24, 48, 72, and 96 h. The images were taken with Leica DMi8 Inverted Microscope; two wells are shown for each time point.

Table S3.6. Statistical evaluation of images from Leica DMi8 Inverted Microscope with Image J software of DIPG cells seeded in a U-shaped P96 plate.

Well position-time	N^{**}	Max. Area, nm^2	Min. Area, nm^2	Average Area, nm^2	StDev, nm^2	Max. d, nm	Min. d, nm	Average d, nm	StDev, nm
24 h	8	52176	37822	43792	5281	250	203	235	16.8
48 h	8	76133	57391	67186	7153	309	265	290	14.9
72 h	8	99151	66748	85830	9967	353	282	329	25.3
96 h	8	229319	121894	169837	40858	547	404	469	57.4

* Average result from duplicates ** Number of analyzed tumorspheres

Studies of the U-shape P96 plate (**Table S3.6**) revealed that the average DIPG tumorsphere diameter increased from 235 nm at 24 h to 469 nm at 96 h, corresponding to 9687 cells per sphere at 24 h and 77,260 at 96 h. While tumorsphere size displays similarities to those seeded in standard P96 plates, tumorsphere shape differs considerably. Standard P96 plates support the formation of several elongated tumorspheres from DIPG cells, whereas U-shaped plates support the formation of a single round tumorsphere. Moreover, tumorsphere size, shape, and growth rate for DIPG and GBM cells cultured in U-shape P96 plates display broad similarities, obliterating all the differences between these cell lines with essentially different morphology, metabolic profile, and cell-cell interactions. Thus, we believe that the P96 plate better resembles the unique features of the selected cell lines and, therefore, was selected for the following studies.

These comparisons supported the choice of standard P96 plates for confocal studies.

SI-3.11. Preliminary in vivo biodistribution studies

Male BALB/c mice (age two weeks, m=20.9 ±0.3 g) were randomly allocated to Group A (four animals), Group B (four animals), or the Control group (two animals). The StPGA-ValCit-palbo-Cy5.5 and palbociclib micelles incorporated into the HA-CP-Cy5.5 vehicle were administered to Group A, and palbociclib micelles incorporated into HA-CP-Cy5.5 were administered to Group B, Control group did not receive any treatment. The mice were anesthetized with isoflurane, placed on their back with a slightly elevated head holding in the hand, and the formulations were administered via a micropipette 10 µl into each nostril. After 90 min of post-treatment, the animals were sacrificed, and the main organs (brain, liver, heart, spleen, kidney, lungs, intestine) were harvested and analyzed ex vivo with the in vivo imaging system IVIS® Spectrum System (Perkin Elmer). Two brains were selected for later immunochemistry assays, and Cy5.5 localizations were fixed in 4% PFA and stored at 4°C. First, the two brains were placed into a 50 ml tube in 15 ml of PFA and left overnight under orbital agitation. Then, the brains were washed with 15 ml of dPBS three times, and then 15 ml of 30 % sucrose solution in dPBS was added and left for 48 h at 4°C. Finally, the brains were washed with 15 ml of dPBS three times and left in 0.05% Sodium azide solution in dPBS until fixation. The remaining organs were frozen in liquid Nitrogen for further ex vivo quantification and stored at -80 ^{0}C.

SI-3.12. Ex vivo quantification of Cy5.5 in the harvested organs

The harvested and stored organs at -80 0C were quickly thawed at room temperature and placed on ice. Organs were homogenized in dPBS pH=7.4 with an Ultraturrax device using optimized volume, time, and speed depending on the organ. Table SI-3.2 shows the homogenization parameters for each organ.

Table S3.7 Parameters for organ homogenization with Ultraturrax device

Organ	Volume (dPBS), ml	Time, sec	Speed (rpm)
Heart	1	60	10.000
Lungs	1	30	10.000
Spleen	1	30	10.000
Liver	2	60	10.000
Kidneys	1.5	60	10.000
Brain	2	60	7500
Intestine	3	60	10.000

The Ultraturrax device was washed with Milli-Q water and dried after each organ homogenization cycle. The homogenized organ suspension was centrifuged at 4000 rpm for 1 h at 4^0C, and 100 µl of supernatant was transferred in triplicates to a black P96 plate for fluorescence measurement with a CLARIOstar Plus plate reader. The corresponding calibration curve with Cy5.5 in dPBS was prepared in the 0.125-70 ng/ml range. The instrumental parameters: $\lambda_{excitation}$ = 640 nm, $\lambda_{emission}$ = 700 nm, Gain 3927, Focal height 6.0). To assess conjugate total extraction, pellets were washed with Milli-Q water, and the fluorescence was measured, but no significant signal was observed.

SI-3.13. Encapsulation method of hydrophobic drugs into F127 poloxamer micelles

For targeted 10 % with drug loading, the 5 mg of the drug to be encapsulated dissolved in 5 ml of DCM added to 50 mg of pluronic F127 and left stirring for 20 min, followed by vortex 5 min. The solvent is eliminated by rotary evaporation at 25^0C to obtain a thin film, which is hydrated with preheated Milli-Q water to 45^0C or 60^0, depending on the drug stability, for 30 min in a water bath. The mixture was centrifuged at 4000 rpm for 5 min to remove the non-encapsulated drug, and the supernatant was filtered through a 0.22 Nylon filter. Finally, the clear micelle solution was frozen and lyophilized to obtain drug/F127 micelles. The obtained encapsulation efficiency for the prepared formulation was 90-95 %

SI-3.14. General procedure to measure the GSH activity level in not adherent cells

Following the manufacturer's instructions, the GSH level in cells was determined using the detection assay kit (ab205811, Abcam).

Briefly, 250 000 cells were transferred into 1,5 ml Eppendorf tubes, washed two times with cold dPBS, and centrifuged for 7 min at 0.4 rcf. The cell pellet was resuspended in 100 µl of Mammalian Lysis Buffer provided in the kit, homogenized by pipetting, and followed again by centrifugation for

15 min at 4^0C at the max speed. 90 µl of supernatant was transferred to another Eppendorf tube for deproteinization by adding 18 µl of TCA solution and 2,27 ml ddH$_2$O to 5 g of TCA powder. The solution was vortexed thoroughly and incubated on ice for 5-10 min, followed by centrifugation for 5 min at 12000G at 4^0C. The supernatant was transferred to another Eppendorf tube and neutralized with sodium bicarbonate (NaHCO$_3$) to have pH 4-6, vortexed, and centrifuged for 15 min at 13000 G at 4^0C. The 50 µl of supernatant in triplicates were transferred into 96 microtiter well plates. The GSH calibration curve was prepared from reagents provided in the kit, in 500 µl Eppendorf tubes, by adding 247.5 µl of Assay Buffer to 2.5 µl of stock GSH standard (1mM) followed by two-fold dilutions. The diluted GSH standards are unstable and were used within 4 h. 50 µl of prepared solution in duplicates were transferred into 96 microtiters well plate. Also, 50 µl of the Assay Buffer was transferred into a 96 microtiter well plate and used as a blank. The Thiol Green Indicator provided in the kit was diluted 100 times in Assay buffer, and 50 µl of the prepared solution was added to GSH standards, blank, and cells. The fluorescence of each well was measured at $\lambda_{exitation}$= 460 nm and $\lambda_{emmision}$ = 520 nm on the CLARIOstar Plus plate reader (BMG Labtech GmbH, Ortenber, Germany). The test samples' GSH concentrations (µM) were calculated from the calibration curve.

SI-3.15. General procedure to measure the cathepsin B activity level in not adherent cells

The schematic representation of the enzymatic reaction for measurement of cathepsin B activity is shown in Figure 23. The quantification of cathepsin B is based on the indirect measurement of fluorescent compound released upon enzymatic cleavage proportional to the available enzyme in the tested cells. To liberate lysosomal cathepsin B, the triton X-100 (Triton) - a nonionic surfactant- disrupts the cell membrane. An inhibitor of cathepsin B activity – Leupeptin (established, reversible inhibitor of lysosomal cysteine proteinase) [100] was used as a negative control. Another possibility we also tested is to use another cathepsin B inhibitor - CA074, a suicide inhibitor that binds irreversibly to the free thiol group of [29]Cys in the enzyme's active site and forms a covalent thioether bond [64].
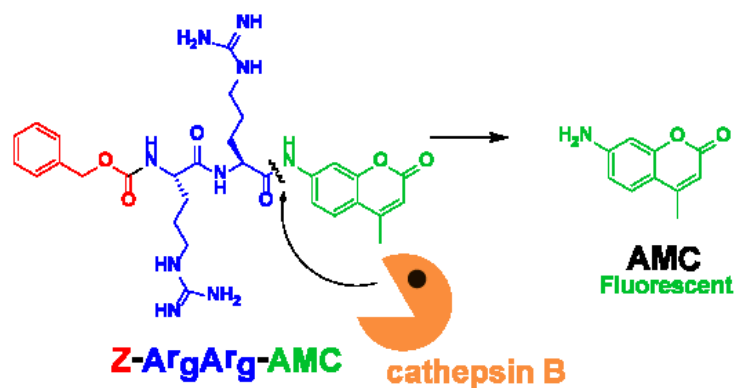

Figure S3.33 Schematic representation of the cathepsin B enzymatic cleavage of Z-ArgArg-AMC substrate

The cells to be analyzed are counted with trypan blue by mixing an equal volume of cell suspension and 0.4% trypan blue solution, allowed to incubate for 2 min at room temperature, and counted within 3-5 min (more prolonged incubation leads to cell death) using below equation 3.

$$Number\ of\ Cells\ \left(\frac{cells}{ml}\right) = \frac{N_1 + N_2}{2} \times \frac{1}{2} \times 10000\ (Equation\ 3)$$

Where N_1 and N_2 – number of viable cells counted in quadrants 1 and 2 respectively, 1/2 – dilution factor, 10000 – Hemocytometer factor.

All buffers were freshly prepared before the experiment and equilibrated at 37°C. The buffer preparation procedure below is suitable for analyzing two cell lines, including the cathepsin B calibration curve.

HBSS (2X): 600 µl of Hanks' Balanced Salt Solution (HBSS, 10X) was added to 2400 Milli-Q water and mixed well.

DTT (20X): 617 mg of DTT (Mw=154.25 g/mol) dissolved in 4000 µl of Milli-Q water (1M solution, in cells, should be used at 50 mM)

HBSS*DTT (2X): 8 ml of Hanks' Balanced Salt Solution (HBSS, 10X), 4 ml of DTT (20X), and 28 ml of Milli-Q water were added; pH was adjusted to 6.6 if needed with sodium hydroxide.

HBSS*DTT (1X): 1.5 ml of Hanks' Balanced Salt Solution (HBSS, 10X), 0.75 ml of DTT (20X), and 5.25 ml of Milli-Q water were added, and pH was adjusted to 6.6 if needed with sodium hydroxide.

Triton (4X)): 100 µl of Triton (100X) was added to 1250 µl of HBSS 2X solution and 1150 µl of Milli-Q water.

Substrate Z-ArgArg-AMC (4X): 100 µl of stock Z-ArgArg-AMC (10mM solution in DMSO) was added to 1250 µl of HBSS (2X) solution, and 1150 µl of Milli-Q water (final concentration to be used in cells 100 µM).

The prepared 1.5 ml Eppendorf tubes, the cell suspension volumes corresponding to 150000, 300000, and 60000 cells for each cell line were placed. The cells were washed with 1.0 ml dPBS two times by centrifugation at 7 min and 0.4 rct and aspiration of the media with a Pasteur pipette. Then, 1000 µl of HBSS*DTT (1X) was added to all samples and incubated for 30 min at 37 °C, and 100 µl was aliquoted to a black P96 plate, and corresponding solutions were added as noted in Table SI-3.3. The kinetics were measured with a Victor2 spectrophotometer, using $\lambda_{excitation}$ = 355nm and $\lambda_{emission}$ = 460nm, with the controlled temperature at 37°C and the cycle of 1 measure every 180 s over 45 min.

Figure S3.34 shows the results obtained for DIPG and GBM cells at different cell densities per well. As expected, the intensity of the negative control of cells with only Triton added, responsible for cell membrane disruption and enzyme cathepsin B liberation, was low since the substrate was not added to the cells. Also, the intensity of the cells incubated with Leupeptin was low due to the inhibition of cathepsin B and the inability to degrade the fluorescent substrate. These negative controls demonstrate the suitability of the developed method and the absence of media interference or nonspecific degradation of the measured fluorescent substrate. However, the cells with the added substrate, without adding Triton, also demonstrated increasing fluorescence intensity over time, which can be explained by partial degradation of the cells during the manipulations and not optimal media to maintain cell viability. Another reason can be the surface cathepsin B enzyme activity that often changes during neoplastic progression and is characteristic for tumor cells in addition to the intracellular lysosomal cathepsin B localization [63].

Table S3.8 Plate layout used for cathepsin B activity measurements

	1	2	3	4	5	6	7	8	9	10	11	12
		GBM				Cathepsin B			DIPG			
A	dPBS	Blank	Blank	Blank	Blank	Blank	Blank	Blank	Blank	Blank	Blank	dPBS
B	dPBS	15000	15000	15000	15000	C1-1	C2-1	15000	15000	15000	15000	dPBS
C	dPBS	15000	15000	15000	15000	C1-2	C2-2	15000	15000	15000	15000	dPBS
D	dPBS	30000	30000	30000	30000	C1-3	C2-3	30000	30000	30000	30000	dPBS
E	dPBS	30000	30000	30000	30000	C1-4	C2-4	30000	30000	30000	30000	dPBS
F	dPBS	60000	60000	60000	60000	C1-5	C2-5	60000	60000	60000	60000	dPBS
G	dPBS	60000	60000	60000	60000	C1-6	C2-6	60000	60000	60000	60000	dPBS
H	dPBS	Blank	Blank	Blank	Blank	Blank	Blank	Blank	Blank	Blank	Blank	dPBS
		T	T, S	T, S, I	S	T,S	T,S	T	T, S	T, S, I	S	

dPBS - Dulbecco's phosphate-buffered saline solution, 200 µl in each well; Blank – corresponds to the wells without cells, where 100 µl of HBSS*DTT (1X) was pipetted instead to use as control for fluorescence measurements; C1 and C2 corresponds to the wells for calibration curve prepared from cathepsin B dissolved in HBSS*DTT (1X) at the concentration range 0.015 – 47 µM, and placed 200 µl in each well. For all cells in the columns 2-12 the corresponding solutions specified below was added, to have the final volume 200 µl in each well.

T - 50 µl HBSS*DTT (2X), 25 µl Milli-Q water, 25 µl Triton (4X)
T,S - 50 µl HBSS*DTT (2X), 25 µl Triton (4X), 25 µl substrate (4X)
T,S,I - 50 µl HBSS*DTT (2X), 25 µl Triton (4X), 25 µl substrate (4X), 1µl Leupeptin inhibitor (10mM)
S – 50 µl HBSS*DTT (2X), 25 µl Milli-Q water, 25 µl Milli-Q substrate (4X)
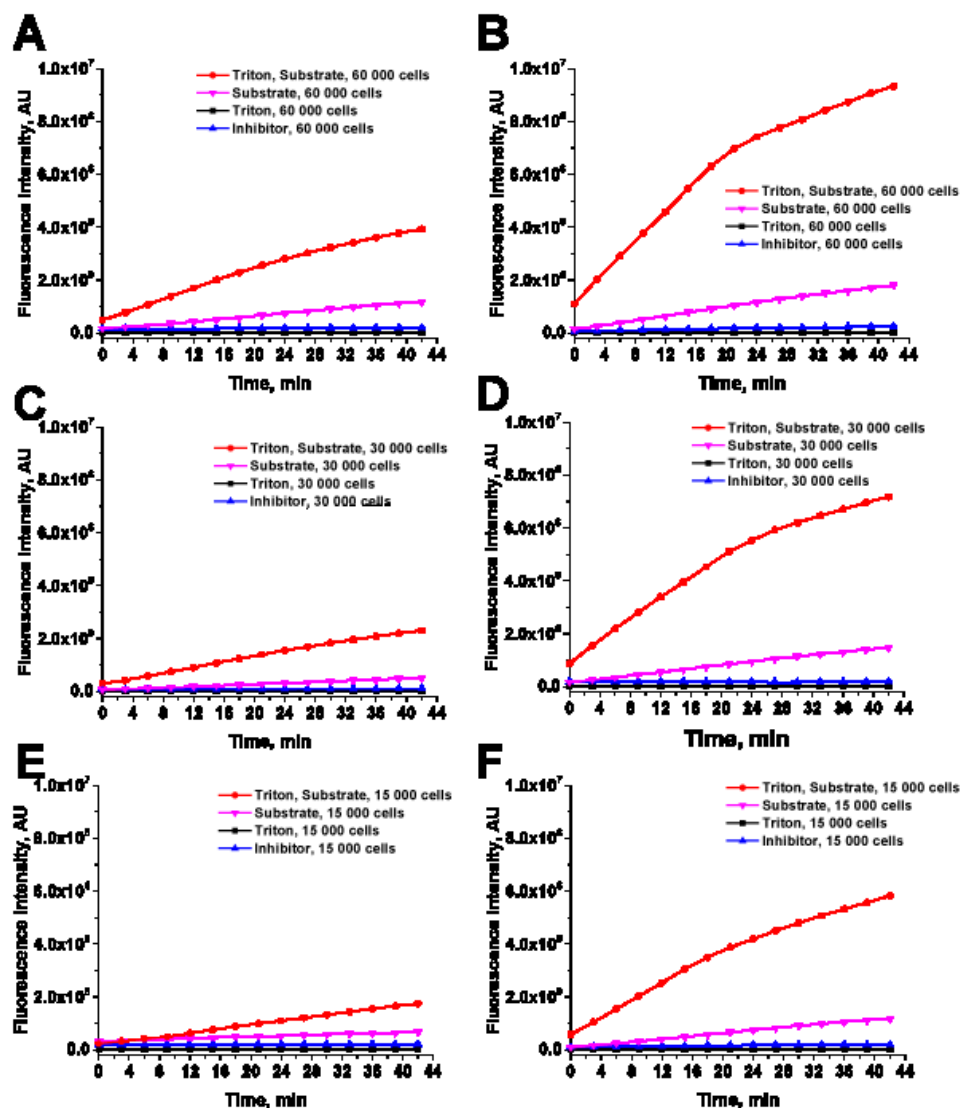
Figure S3.34 Kinetics curve for measurement cathepsin B activity, with negative control (Substrate, Triton, Inhibitor) for DIPG and GBM cells seeded at different densities 60000 cells/well (A, B), 30000 cells per well (C, D), and 15000 cells/well (E, F)

The cathepsin B activity has a linear response up to 15 min of the analysis; however, after 20 min, the intensity response decreases for no apparent reason, which can be a depletion of the substrate amount. Therefore, we used the15 min time point for cathepsin B quantification. **Figure S3.35** shows the calibration curve and linear concentration range for quantitative analysis.
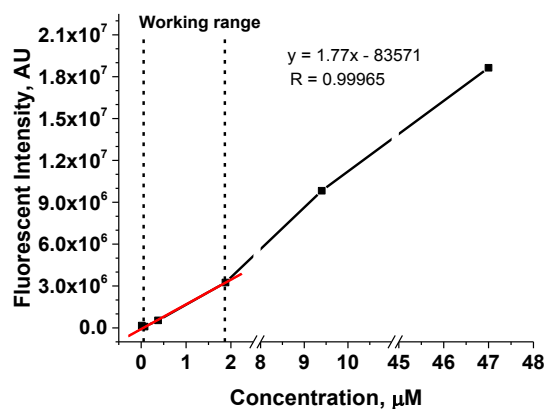
Figure S3.35 Calibration curve of cathepsin B, used for quantitative analysis

3.5. References

1. Http://www.who.int/gho/mortality_burden_disease/causes_death/top_10/en. who.pdf.
2. Zanca, C. *et al.* Glioblastoma cellular cross-talk converges on NF-κB to attenuate EGFR inhibitor sensitivity. *Genes Dev.* **31**, 1212–1227 (2017).
3. Brennan, C. W. *et al.* The somatic genomic landscape of glioblastoma. *Cell* **155**, 462–477 (2013).
4. Cloughesy, T. F., Cavenee, W. K. & Mischel, P. S. Glioblastoma: From Molecular Pathology to Targeted Treatment. *Annu. Rev. Pathol. Mech. Dis.* **9**, 1–25 (2014).
5. Knudsen, E. S. & Witkiewicz, A. K. The Strange Case of CDK4/6 Inhibitors: Mechanisms, Resistance, and Combination Strategies. *Trends in Cancer* **3**, 39–55 (2017).
6. Goel, S. *et al.* Overcoming Therapeutic Resistance in HER2-Positive Breast Cancers with CDK4/6 Inhibitors. *Cancer Cell* **29**, 255–269 (2016).
7. https://clinicaltrials.gov. clinicaltrials.
8. Álvarez-Fernández, M. & Malumbres, M. Mechanisms of Sensitivity and Resistance to CDK4/6 Inhibition. *Cancer Cell* **37**, 514–529 (2020).
9. Klein, M. E., Kovatcheva, M., Davis, L. E., Tap, W. D. & Koff, A. CDK4/6 Inhibitors: The Mechanism of Action May Not Be as Simple as Once Thought. *Cancer Cell* **34**, 9–20 (2018).
10. Schettini, F. *et al.* CDK 4/6 inhibitors as single agent in advanced solid tumors. *Front. Oncol.* **8**, 1–12 (2018).
11. Serra, F. *et al.* Palbociclib in metastatic breast cancer: Current evidence and real-life data. *Drugs Context* **8**, 1–16 (2019).
12. Michaud, K. *et al.* Pharmacologic inhibition of cyclin-dependent kinases 4 and 6 arrests the growth of glioblastoma multiforme intracranial xenografts. *Cancer Res.* **70**, 3228–3238 (2010).

13. Cook Sangar, M. L. *et al.* Inhibition of CDK4/6 by palbociclib significantly extends survival in medulloblastoma patient-derived xenograft mouse models. *Clin. Cancer Res.* **23**, 5802–5813 (2017).

14. Nguyen, L. V., Searle, K. & Jerzak, K. J. Central nervous system-specific efficacy of CDK4/6 inhibitors in randomized controlled trials for metastatic breast cancer. *Oncotarget* **10**, 6317–6322 (2019).

15. Taylor, J. W. *et al.* Phase-2 trial of palbociclib in adult patients with recurrent RB1-positive glioblastoma. *J. Neurooncol.* **140**, 477–483 (2018).

16. Van Mater, D. *et al.* A phase I trial of the CDK 4/6 inhibitor palbociclibin pediatric patients with progressive brain tumors: A Pediatric Brain Tumor Consortium study (PBTC-042). *Pediatr. Blood Cancer* **68**, 1–10 (2021).

17. Estepa-Fernández, A. *et al.* Combination of palbociclib with navitoclax based-therapies enhances in vivo antitumoral activity in triple-negative breast cancer. *Pharmacol. Res.* **187**, 106628 (2023).

18. Shi, J., Kantoff, P. W., Wooster, R. & Farokhzad, O. C. Cancer nanomedicine : progress, challenges and opportunities. *Nat Rev Cancer* **17**, 20–37 (2017).

19. Duncan, R., Edward, K. & Avenue, V. I. I. The dawning era of polymer therapeutics. **2**, 347–360 (2003).

20. Melnyk, T., Đorđević, S., Conejos-Sánchez, I. & Vicent, M. J. Therapeutic potential of polypeptide-based conjugates: Rational design and analytical tools that can boost clinical translation. *Adv. Drug Deliv. Rev.* **160**, 136–169 (2020).

21. Parveen, S., Arjmand, F. & Tabassum, S. Clinical developments of antitumor polymer therapeutics. *RSC Adv.* **9**, 24699–24721 (2019).

22. Sun, H. *et al.* Cancer Nanomedicines Based on Synthetic Polypeptides Cancer. *Biomacromolecules* **20**, 4299–4311 (2019).

23. Fang, J., Islam, W. & Maeda, H. Exploiting the dynamics of the EPR effect and strategies to improve the therapeutic effects of nanomedicines by using EPR effect enhancers. *Adv. Drug Deliv. Rev.* **in press**, (2020).

24. Zagorodko, O., Arroyo-crespo, J. J., Nebot, V. J. & Vicent, M. J. Polypeptide-Based Conjugates as Therapeutics: Opportunities and Challenges. *Macromol. Biosci.* **17**, 1–22 (2017).

25. Duncan, R. Polymer therapeutics as nanomedicines : new perspectives. *Curr. Opin. Biotechnol.* **22**, 492–501 (2011).

26. Canal, F., Sanchis, J. & Vicent, M. J. Polymer–drug conjugates as nano-sized medicines. *Curr. Opin. Biotechnol.* **22**, 894–900 (2011).

27. El-sawy, H. S., Al-abd, A., Ahmed, T., El-say, K. M. & Torchilin, V. P. Stimuli-Responsive Nano-Architectures Drug Delivery Systems to Solid Tumor Micromilieu : Past, Present and Future Perspectives Stimuli-Responsive Nano-Architectures Drug Delivery Systems to Solid Tumor Department of Pharmaceutics and Pharmaceutical Techn. *ACS Nano* **12**, 10636–10664 (2018).

28. Conejos-Sánchez, I., Duro-Castano, A., Birke, A., Barz, M. & Vicent, M. J. A controlled and versatile NCA polymerization method for the synthesis of polypeptides. *Polym. Chem.* **4**, 3182–3186 (2013).

29. Duro-Castano, A. *et al.* Well-Defined Star-Shaped Polyglutamates with Improved Pharmacokinetic Profiles As Excellent Candidates for Biomedical Applications. *Mol. Pharm.* **12**, 3639–3649 (2015).

30. Deming, T. J. Synthesis of Side-Chain Modified Polypeptides. *Chem. Rev.* **116**, 786–808 (2016).

31. Barz, M., Duro-Castano, A. & Vicent, M. J. A versatile post-polymerization modification method for polyglutamic acid: synthesis of orthogonal reactive polyglutamates and their use

in "click chemistry". *Polym. Chem.* **4**, 2989–2994 (2013).

32. Arroyo-Crespo, J. J. *et al.* Tumor microenvironment-targeted poly-L-glutamic acid-based combination conjugate for enhanced triple negative breast cancer treatment. *Biomaterials* **186**, 8–21 (2018).

33. Arroyo-crespo, J. J. *et al.* Anticancer Activity Driven by Drug Linker Modification in a Polyglutamic Acid-Based Combination-Drug Conjugate. *Adv. Funct. Mater.* **1800931**, 1–13 (2018).

34. Cai, H. *et al.* A Nanostrategy for Efficient Imaging-Guided Antitumor Therapy through a Stimuli-Responsive Branched Polymeric Prodrug. *Adv. Sci. (Weinheim, Baden-Wurttemberg, Ger.* **7**, 1903243 (2020).

35. Kavand, A., Anton, N., Vandamme, T., Serra, A. & Chan-seng, D. Synthesis and functionalization of hyperbranched polymers for targeted drug delivery. *J. Control. Release* **321**, 285–311 (2020).

36. Chen, B. *et al.* Current Multistage Drug Delivery Systems Based on the Tumor Microenvironment. *Theranostics* **7**, 538–558 (2017).

37. Shen, W.-C. & Ryser, H. J.-P. Cis-aconityl spacer between daunomycin and macromolecular carriers: A model of pH-sensitive linkage releasing drug from a lysosomotropic conjugate. *Biochem. Biophys. Res. Commun.* **102**, 1048–1054 (1981).

38. Praveen, K. *et al.* pH-Responsive "Supra-Amphiphilic" Nanoparticles Based on Homoarginine Polypeptides. *ACS Appl. Bio Mater.* **2**, 4162–4172 (2019).

39. Deirram, N., Zhang, C., Kermaniyan, S. S., Johnston, A. P. R. & Such, G. K. pH-Responsive Polymer Nanoparticles for Drug Delivery. *Macromol. Rapid Commun.* **40**, 1800917 (2019).

40. Xu, R. *et al.* An injectable nanoparticle generator enhances delivery of cancer therapeutics. *Nat. Biotechnol.* **34**, 414–418 (2016).

41. Markovsky, E., Baabur-Cohen, H. & Satchi-Fainaro, R. Anticancer polymeric nanomedicine bearing synergistic drug combination is superior to a mixture of individually-conjugated drugs. *J. Control. Release* **187**, 145–157 (2014).

42. Tsuchikama, K. & An, Z. Antibody-drug conjugates: recent advances in conjugation and linker chemistries. *Protein Cell* **9**, 33–46 (2018).

43. Mort, J. S. & Buttle, D. J. Molecules in focus Cathepsin B. *Int. J. Biochem. Cell Biol.* **29**, 715–720 (1997).

44. Giraldo, E. *et al.* A rationally designed self-immolative linker enhances the synergism between a polymer-rock inhibitor conjugate and neural progenitor cells in the treatment of spinal cord injury. *Biomaterials* **276**, 121052 (2021).

45. Ianevski, A. *et al.* Prediction of drug combination effects with a minimal set of experiments. *Nat. Mach. Intell.* **1**, 568–577 (2019).

46. Pemovska, T., Bigenzahn, J. W. & Superti-Furga, G. Recent advances in combinatorial drug screening and synergy scoring. *Curr. Opin. Pharmacol.* **42**, 102–110 (2018).

47. Pisarevsky, E. *et al.* Rational Design of Polyglutamic Acid Delivering an Optimized Combination of Drugs Targeting Mutated BRAF and MEK in Melanoma. *Adv. Ther.* **2000028**, 1–17 (2020).

48. Tomaszewski, W., Sanchez-Perez, L., Gajewski, T. F. & Sampson, J. H. Brain tumor microenvironment and host state: Implications for immunotherapy. *Clin. Cancer Res.* **25**, 4202–4210 (2019).

49. Lv, S. *et al.* Biomaterials Co-delivery of doxorubicin and paclitaxel by PEG-polypeptide nanovehicle for the treatment of non-small cell lung cancer. *Biomaterials* **35**, 6118–6129 (2014).

50. Li, B. *et al.* A dual pH- and reduction-responsive anticancer drug delivery system based on PEG–SS–poly(amino acid) block copolymer. *RSC Adv.* **7**, 30242–30249 (2017).

51. Kaminskas, L. M. *et al.* Pulmonary administration of a doxorubicin-conjugated dendrimer

enhances drug exposure to lung metastases and improves cancer therapy. *J. Control. Release* **183**, 18–26 (2014).

52. Melnyk, T., Masiá, E., Zagorodko, O., Conejos-Sánchez, I. & Vicent, M. J. Rational design of poly-L-glutamic acid-palbociclib conjugates for pediatric glioma treatment. *J. Control. Release* **355**, 385–394 (2023).

53. Vicent, M. J. *et al.* Polymer therapeutics designed for a combination therapy of hormone-dependent cancer. *Angew. Chemie - Int. Ed.* **44**, 4061–4066 (2005).

54. Yang, H., Yang, S., Kong, J., Dong, A. & Yu, S. Obtaining information about protein secondary structures in aqueous solution using Fourier transform IR spectroscopy. *Nat. Protoc.* **10**, 382–396 (2015).

55. Mondal, S. *et al.* Programmed supramolecular nanoassemblies: Enhanced serum stability and cell specific triggered release of anti-cancer drugs. *Nanoscale Adv.* **1**, 1571–1580 (2019).

56. Chipman, S. D., Oldham, F. B., Pezzoni, G. & Singer, J. W. Biological and clinical characterization of paclitaxel poliglumex (PPX, CT-2103), a macromolecular polymer-drug conjugate. *Int. J. Nanomedicine* **1**, 375–383 (2006).

57. Kuete, V., Karaosmanoğlu, O. & Sivas, H. Anticancer Activities of African Medicinal Spices and Vegetables. in *Medicinal Spices and Vegetables from Africa: Therapeutic Potential Against Metabolic, Inflammatory, Infectious and Systemic Diseases* 271–297 (2017). doi:10.1016/B978-0-12-809286-6.00010-8.

58. Markossian, S. *et al. Assay Guidance Manual.* (2004).

59. D, S. S. *et al.* Evaluation of a soluble tetrazolium/formazan assay for cell growth and drug sensitivity in culture using human and other tumor cell lines. *Cancer Res.* **48**, 4827–4833 (1988).

60. Manzanares, D. & Ceña, V. Endocytosis: The Nanoparticle and Submicron Nanocompounds Gateway into the Cell. *Pharmaceutics* **12**, (2020).

61. Seymour, L. W. *et al.* Tumour tropism and anti-cancer efficacy of polymer-based doxorubicin prodrugs in the treatment of subcutaneous murine B16F10 melanoma. *Br. J. Cancer* **70**, 636–641 (1994).

62. Nunez, R. DNA measurement and cell cycle analysis by flow cytometry. *Curr. Issues Mol. Biol.* **3**, 67–70 (2001).

63. Mohamed, M. M. & Sloane, B. F. Cysteine cathepsins: Multifunctional enzymes in cancer. *Nat. Rev. Cancer* **6**, 764–775 (2006).

64. Schmitz, J. *et al.* Cathepsin B: Active site mapping with peptidic substrates and inhibitors. *Bioorg. Med. Chem.* **27**, 1–15 (2019).

65. Aggarwal, N. & Sloane, B. F. Cathepsin B: Multiple roles in cancer. *Proteomics - Clin. Appl.* **8**, 427–437 (2014).

66. Doronina, S. O. *et al.* Development of potent monoclonal antibody auristatin conjugates for cancer therapy. *Nat. Biotechnol.* **21**, 778–784 (2003).

67. Sochaj, A. M., Świderska, K. W. & Otlewski, J. Current methods for the synthesis of homogeneous antibody–drug conjugates. *Biotechnol. Adv.* **33**, 775–784 (2015).

68. Zhang, C. *et al.* Enzyme-responsive peptide dendrimer-gemcitabine conjugate as a controlled-release drug delivery vehicle with enhanced antitumor efficacy. *Acta Biomater.* **55**, 153–162 (2017).

69. Leong, N. J. *et al.* Doxorubicin Conjugation and Drug Linker Chemistry Alter the Intravenous and Pulmonary Pharmacokinetics of a PEGylated Generation 4 Polylysine Dendrimer in Rats. *J. Pharm. Sci.* **107**, 2509–2513 (2018).

70. Dubowchik, G. M. *et al.* Cathepsin B-labile dipeptide linkers for lysosomal release of doxorubicin from internalizing immunoconjugates: model studies of enzymatic drug release and antigen-specific in vitro anticancer activity. *Bioconjug. Chem.* **13**, 855–869 (2002).

71. Dubowchik, G. M. & Firestone, R. A. Cathepsin B-sensitive dipeptide prodrugs. 1. A model

study of structural requirements for efficient release of doxorubicin. *Bioorg. Med. Chem. Lett.* **8**, 3341–3346 (1998).

72. Kim, Y., Pourgholami, M. H., Morris, D. L. & Stenzel, M. H. Effect of Cross-Linking on the Performance of Micelles As Drug Delivery Carriers: A Cell Uptake Study. *Biomacromolecules* **13**, 814–825 (2012).

73. Song, K. W. *et al.* RTK-Dependent Inducible Degradation of Mutant PI3Kα Drives GDC-0077 (Inavolisib) Efficacy. *Cancer Discov.* **12**, 204–219 (2022).

74. Brito, C. *et al.* PIK3CA Mutations in Diffuse Gliomas: An Update on Molecular Stratification, Prognosis, Recurrence, and Aggressiveness. *Clin. Med. Insights. Oncol.* **16**, 11795549211068804 (2022).

75. Liu, Q., Yin, X., Languino, L. R. & Altieri, D. C. Evaluation of Drug Combination Effect Using a Bliss Independence Dose–Response Surface Model. *Stat. Biopharm. Res.* **10**, 112–122 (2018).

76. Chou, T. C. & Talalay, P. Quantitative analysis of dose-effect relationships: the combined effects of multiple drugs or enzyme inhibitors. *Adv. Enzyme Regul.* **22**, 27–55 (1984).

77. Kozlov, M. Y., Melik-Nubarov, N. S., Batrakova, E. V. & Kabanov, A. V. Relationship between pluronic block copolymer structure, critical micellization concentration and partitioning coefficients of low molecular mass solutes. *Macromolecules* **33**, 3305–3313 (2000).

78. Kabanov, A. V., Batrakova, E. V. & Alakhov, V. Y. Pluronic block copolymers as novel polymer therapeutics for drug and gene delivery. *J. Control. Release* **82**, 189–212 (2002).

79. Chen, T. *et al.* Pluronic P85/F68 Micelles of Baicalein Could Interfere with Mitochondria to Overcome MRP2-Mediated Efflux and Offer Improved Anti-Parkinsonian Activity. *Mol. Pharm.* **14**, 3331–3342 (2017).

80. Batrakova, E. V. *et al.* Alteration of genomic responses to doxorubicin and prevention of MDR in breast cancer cells by a polymer excipient: Pluronic P85. *Mol. Pharm.* **3**, 113–123 (2006).

81. Yu, J., Qiu, H., Yin, S., Wang, H. & Li, Y. Polymeric Drug Delivery System Based on Pluronics for Cancer Treatment. *Molecules* **26**, (2021).

82. Shelke, S., Shahi, S., Jalalpure, S. & Dhamecha, D. Poloxamer 407-based intranasal thermoreversible gel of zolmitriptan-loaded nanoethosomes: formulation, optimization, evaluation and permeation studies. *J. Liposome Res.* **26**, 313–323 (2016).

83. Adnet, T. *et al.* Pharmacotechnical Development of a Nasal Drug Delivery Composite Nanosystem Intended for Alzheimer's Disease Treatment. *Pharmaceutics* **12**, (2020).

84. Lakshmi, P. V. & Harini, K. Design and Optimization of Thermo-reversible Nasal in situ Gel of Atomoxetine Hydrochloride Using Taguchi Orthogonal Array Design. *Dhaka Univ. J. Pharm. Sci.* (2019).

85. Ricci, E. J., Bentley, M. V. L.., Farah, M., Bretas, R. E. S. & Marchetti, J. M. Rheological characterization of Poloxamer 407 lidocaine hydrochloride gels. *Eur. J. Pharm. Sci.* **17**, 161–167 (2002).

86. Jagdale, S., Shewale, N. & Kuchekar, B. S. Optimization of Thermoreversible In Situ Nasal Gel of Timolol Maleate. *Scientifica (Cairo).* **2016**, 6401267 (2016).

87. Batrakova, E. *et al.* Fundamental Relationships Between the Composition of Pluronic Block Copolymers and Their Hypersensitization Effect in MDR Cancer Cells. *Pharm. Res.* **16**, 1373–1379 (1999).

88. Alakhova, D. Y., Zhao, Y., Li, S. & Kabanov, A. V. Effect of Doxorubicin/Pluronic SP1049C on Tumorigenicity, Aggressiveness, DNA Methylation and Stem Cell Markers in Murine Leukemia. *PLoS One* **8**, 1–14 (2013).

89. Batrakova, E. V. *et al.* Anthracycline antibiotics non-covalently incorporated into the block copolymer micelles: In vivo evaluation of anti-cancer activity. *Br. J. Cancer* **74**, 1545–1552 (1996).

90. Yuan, D. *et al.* Intranasal delivery of N-terminal modified leptin-pluronic conjugate for treatment of obesity. *J. Control. Release* **263**, 172–184 (2017).

91. Qian, S., Wong, Y. C. & Zuo, Z. Development, characterization and application of in situ gel systems for intranasal delivery of tacrine. *Int. J. Pharm.* **468**, 272–282 (2014).

92. Pisal, S. S., Paradkar, A. R., Mahadik, K. R. & Kadam, S. S. Pluronic gels for nasal delivery of Vitamin B12. Part I: Preformulation study. *Int. J. Pharm.* **270**, 37–45 (2004).

93. Linse, P. & Malmsten, M. Temperature-dependent micellization in aqueous block copolymer solutions. *Macromolecules* **25**, 5434–5439 (1992).

94. Nagarajan, R. Solubilization of hydrocarbons and resulting aggregate shape transitions in aqueous solutions of Pluronic® (PEO–PPO–PEO) block copolymers. *Colloids Surfaces B Biointerfaces* **16**, 55–72 (1999).

95. Bodratti, A. M. & Alexandridis, P. Formulation of poloxamers for drug delivery. *J. Funct. Biomater.* **9**, (2018).

96. Vinci, M. *et al.* Functional diversity and cooperativity between subclonal populations of pediatric glioblastoma and diffuse intrinsic pontine glioma cells. *Nat. Med.* **24**, 1204–1215 (2018).

97. Jansen, M. H. A. *et al.* Bevacizumab Targeting Diffuse Intrinsic Pontine Glioma: Results of 89Zr-Bevacizumab PET Imaging in Brain Tumor Models. *Mol. Cancer Ther.* **15**, 2166–2174 (2016).

98. Seo, A., Jackson, J. L., Schuster, J. V & Vardar-Ulu, D. Using UV-absorbance of intrinsic dithiothreitol (DTT) during RP-HPLC as a measure of experimental redox potential in vitro. *Anal. Bioanal. Chem.* **405**, 6379–6384 (2013).

99. Vinci, M. *et al.* Advances in establishment and analysis of three-dimensional tumor spheroid-based functional assays for target validation and drug evaluation. *BMC Biol.* **10**, 29 (2012).

100. Montenez, J. P., Delaissé, J. M., Tulkens, P. M. & Kishore, B. K. Increased activities of cathepsin B and other lysosomal hydrolases in fibroblasts and bone tissue cultured in the presence of cysteine proteinases inhibitors. *Life Sci.* **55**, 1199–1208 (1994).

Chapter 4

General Discussion

Pediatric brain tumors are an understudied condition with a poor prognosis. The incidence rate of pediatric cancer remains high, making it a significant burden on public health systems[1,2], with approximately 400,000 children diagnosed with a brain tumor each year[3]. Moreover, malignant brain and central nervous system (CNS) tumors account for 21% of all tumors in children and represent the second leading cause of pediatric cancer deaths after leukemia[2].

Unfortunately, the causes of pediatric cancer remain incompletely understood. Genetic disorders can explain only 4% of pediatric brain tumors[4], with conclusive evidence indicating environmental factors as a direct cause. Patients with allergies and asthma display a reduced risk of glioma, which may be attributed to the activation of immune surveillance and the elimination of defective cells [5]. Insufficient funding, a lack of comprehensive statistical data, ethical and practical obstacles in establishing collaborations, fewer dedicated studies on brain tumors in children compared to adults, and a limited number of research groups working specifically on pediatric tumors with established in vivo models represent the main factors contributing to the inadequate amount of research on this malignancy.

Glioma is a prevalent CNS tumor type in children classified into low-grade gliomas (LGGs) and high-grade gliomas (HGGs) [6]. Pediatric LGGs are less likely to become malignant and can often be cured by complete surgical removal; standard chemotherapy yields an overall five-year survival rate of approximately 95%[7]. Pediatric HGGs continue to be incurable malignancies with the highest mortality rate with a five-year survival of 4.7%; diffuse intrinsic pontine glioma (DIPG) patients display a survival time of less than a year [8]. Pediatric and adult HGG differ significantly, and attempts to repurpose

standard therapeutic regimens used in adults (such as temozolomide, lomustine, and bevacizumab) have proven ineffective[9]. The lack of effective treatments for this patient population makes early diagnosis ineffective, highlighting the urgent need for novel therapeutic approaches and increased scientific research focusing on pediatric CNS tumors.

4.1. A Strategy to Improve the Effectiveness of Pediatric Brain Tumor Treatment

The main factor contributing to the suboptimal performance of current brain tumor therapy is the presence of the blood-brain barrier (BBB) [10], which restricts the penetration of most intravenously administered drugs. The work undertaken in this thesis focused on the development of *polymer-drug conjugates* that deliver drugs to the brain via *intranasal administration* as a novel platform for pediatric brain tumor treatment focusing on the HGG subtypes glioblastoma multiform (GBM) and diffuse intrinsic pontine glioma (DIPG). To note, the primary cancer cell lines were kindly donated by Prof. Angel Montero-Carcaboso at Hospital Sant Joan de Déu (Barcelona, Spain)

In the rational design of our conjugates, we considered that drug(s) permeation through the nasal mucosa depends on intrinsic nanocarrier physicochemical properties, including size, nature, architecture, or surface decoration, which we investigated in **Chapter 2**. Once in the brain, the next challenge is to selectively target the release of the selected drug(s) in the target cells; therefore, we comprehensively characterized the selected preclinical models (pediatric patient-derived GBM and DIPG) regarding their intracellular properties in the search for triggers that could activate our conjugate at the site of action and securing adequate intracellular drug release. We selected elevated redox and lysosomal serine protease cathepsin B levels as drug release triggers. Consequently, we developed responsive self-immolative linkers to conjugate the CDk4/6 inhibitor palbociclib [11] to linear and branched polyglutamates. After in vitro assessment in GBM and DIPG models, we evaluated selected palbociclib conjugates in combination with Inavolisib (GDC0077), a PIK3α-specific inhibitor that therapeutically synergizes with palbociclib in metastatic breast cancer [12] as described in **Chapter 3**.

4.1.1 Development of an Intranasal Drug Delivery Platform

The intranasal administration route emerged as an alternative to directly targeting therapeutics to the CNS, avoiding the BBB altogether [13]. Besides its non-invasive nature, intranasal administration offers easy self-administration, rapid drug absorption, improved drug bioavailability, avoidance of the gastrointestinal tract and first-pass metabolism, and a rapid onset of action with lower side effects. Intranasal administration permits elevated brain targeting (~10-fold increase) compared to intravenous administration, requiring lower drug doses to achieve clinical outcomes [14]. Polymeric

formulations facilitate nose-to-brain transport by improving mucosal solubility, stability, and permeation; however, the application of polymer therapeutics, in particular polymer-drug conjugates, by intranasal administration for CNS delivery remains relatively unstudied; hyaluronate as a polymeric carrier has shown promise in a preclinical model of hypoxic-ischemic encephalopathy [15].

Herein, we selected polyglutamic acid (PGA) as a carrier due to its excellent safety profile, ability to be synthesized with different topologies, and straightforward post-polymerization modifications via available carboxylic side groups[16,17]. Using a well-established method in the group, we successfully synthesized linear and star PGA-based carriers utilizing α-amino acid N-carboxy anhydride ring-opening polymerization (NCA-ROP) [17–19] (as described in **Chapter 2.2.1**) and studied how carrier shape, size, and surface decoration affect mucosal passage.

Multiple factors affect different stages of intranasal delivery, so we performed a series of comparative experiments to estimate the effect of composition on mucosal penetration. To screen the designed constructs, we established an ex vivo model based on the excised ovine nasal mucosa and a vertical Franz diffusion cell as it resembles human tissue better than nasal tissues from other animals [20,21] (explained in **Chapter 2.2.2**.). We labeled our polymeric carriers with Oregon Green (OG) and spectrophotometrically analyzed samples taken from the receptor chamber after the permeation study to compare the nanocarrier kinetic profile constructed to mucosal passage. Interestingly, we observed that star-shaped PGAs (StPGAs) possessed a better permeation ability than linear analogs (**Chapter 2.2.3**), demonstrating the importance of carrier conformation.

In the first step, we identified several already reported moieties with mucoadhesive/mucodiffusive properties that could facilitate mucosa permeation after conjugation to linear PGAs and StPGA: carbohydrate-binding peptides such as lectin-like peptides[22–27], glycosaminoglycans such as hyaluronic acid (HA)[28–31], and polyunsaturated fatty acids such as docosahexaenoic acid (DHA)[32,33]. Among lectin-like peptides, we selected odorranalectin (OL) as it specifically binds to the L-fucose glycan moiety[34] broadly present on the olfactory epithelium of nasal mucosa[35]. Additional OL advantages include a relatively smaller size than other lectins and only one disulfide bridge in its structure that allows site-specific conjugation, avoiding massive manipulation that could trigger peptide degradation during the carrier derivatization process.

To conjugate OL to PGA, we developed two synthetic routes using the peptide's C- and N-terminal ends using direct coupling and conventional functional group protection/deprotection, respectively (**Chapter 2.2.4**). While the type of connection does not strongly affect the physicochemical properties of the conjugates, the permeation profile appeared drastically different. The C-terminal modification did not affect permeation compared to non-modified PGA (both showed first-order kinetics profile), suggesting the blockage of any OL-mediated improvements. N-terminal modification

revealed zero-order permeation kinetics typical for facilitated transport (i.e., active OL-assisted permeation enhancement). We also conjugated HA via an ester bond using NHS/EDC as coupling agents (**Chapter 2.2.5**) and DHA via an ester bond using DMTMM as an activator [36] (**Chapter 2.2.6**). HA modification only slightly improved permeation when covalently linked compared to the parental PGA. Importantly, DHA modification highlighted the relevancy of mucodiffusive ligand exposure: a lower degree of modification promotes point-to-point aggregation and a size increase and thus decreases passage compared to a higher degree of modification. The size increase at a lower modification degree is commonly observed in polyelectrolytes conjugated to hydrophobic drugs [37]; direct approaches to overcome this issue remain unreported.

We obtained optimal permeation results for surface modification with OL compared to the derivatized PGA conjugates. The observed superiority of OL as a mucodiffusive/mucoadhesive moiety compared with HA and DHA derives from its lower level of hydrophobicity, which diminishes the promotion of point-to-point aggregation at low loading levels observed when using DHA.

Next, given the superior nature of StPGA compared to linear PGA, we compared the effect of size by crosslinking our StPGA and the role of crosslinker nature. We evaluated two types of covalent crosslinking strategies to stabilize stPGA constructs, obtaining ~90 nm particles (StPGA-CL) prepared via copper-catalyzed click chemistry from azide- and alkyne-modified StPGA[38] and ~200 nm particles (StPGA-SS-CL) prepared via nanoprecipitation with a dithiol agent from StPGAs modified with 2-aminoethyl 2-pyridyl disulfide (**Chapter 2.2.7**). StPGAs self-assemble into larger nanostructures ranging from 30 to 100 nm, quickly breaking down in biological fluids [38]. The permeation of StPGA-CL remained lower than non-crosslinked StPGA unimers (~ 10 nm) (20.3% versus 69.0% in 9 h), probably due to size-limited permeation activity and higher charge density than unimers; however, additional studies are necessary to determine the correlation between particle compactness, size, charge density with mucosa penetration. Meanwhile, crosslinked StPGAs with disulfide bonds (StPGA-SS-CL) demonstrated significantly better mucosal passage (94.8% in 9 h), confirming the reported ability of thiolated polymers to promote mucosal passage based on thiol/disulfide exchange within cysteine-rich subdomains of mucus glycoproteins [39,40].

In addition to the above-described nanocarriers, we employed a next-generation HA-based mucoadhesive agent as a permeation enhancer (HA-CP® (from Polypeptide Therapeutic Solutions S.L. [Valencia, Spain][41]) as a vehicle. HA-CP® was specifically designed to enhance skin permeation of soluble active principles, including nanomedicines [41,42]. HA-CP® represents a reticulated hydrogel composed of HA crosslinked with linear PGA via L-lysine residues. HA-CP® can also incorporate nanocarriers and any water-soluble free drug to act as a depot for continuous drug release alone and in combination with the synthesized nanoconjugates.

The use of HA-CP® as a vehicle in our mucosa permeation studies significantly improved the cumulative permeation of a unimeric StPGA carrier evaluated compared

to PBS. When embedded in HA-CP®, StPGA significantly enhanced mucosa permeation and changed its permeation profile from common first-order kinetics to sigmoidal kinetics. HA-CP®-embedded stPGA demonstrated delayed permeation, with a slower kinetic rate and lower accumulation at 10 h (63% versus 73%) and significantly higher at 24 h (100% versus 79%) than stPGA unimers in PBS.

These experiments demonstrated the critical importance of mucodiffusive components in the nanocarrier (i.e., S-S moieties) and vehicle (HA-CP®), which could be employed together to achieve a synergistic effect and efficiently overcome nose-to-brain transport limitations.

4.1.2 In Vivo Preliminary Validation of the Intranasal Platform

Based on the permeation studies with an established ex vivo model, we selected StPGA, StPGA-OL, and StPGA-CL-SS as nanocarriers and fluorescently labeled them with a Cy5.5 NIR probe for further in vivo biodistribution studies on healthy mice. We intranasally administered nanocarriers in PBS or HA-CP® as vehicles (**Chapter 2.2.8**). In addition to brain accumulation, we evaluated organ biodistribution after excision at different time points by optical imaging (IVIS® Spectrum). We obtained quantitative data after organ homogenization and quantification of the Cy5.5 signal on the CLARIOstar Plus plate reader, implementing the corresponding calibration curve of the fluorescent probe. In agreement with the ex vivo data, using HA-CP® as a vehicle supported a significantly higher percentage of administered doses reaching the brain in all cases. This optimal outcome derives from the ability of HA-CP® to act as a mucoadhesive depot that facilitates and enhances residence time in the olfactory mucosa, triggering a greater diffusion to the brain - 2.2% of the administered dose (ID) for StPGA-OL compared to 0.6% without incorporation into hydrogel after 30 min post-intranasal administration. The rapid delivery can explain the lower percentage and, thus, more rapid elimination that correlates with the signal decrease for all evaluated formulations, suggesting either elimination of the carrier or polymer degradation followed by dye excretion. We observed maximum delivery for StPGA-CL-SS incorporated into HA-CP® at 90 min (2.2 % of ID) while remaining relatively low at 30 min (0.4% of ID).

In collaboration with Prof. J.M. García-Verdugo and Dr. V. Herranz-Pérez, the histological analysis of brain slices confirmed the brain delivery of our carriers, with the localization of peptide-modified nanocarrier (StPGA-OL) in the cytoplasm of various cells of the olfactory bulb or even in a greater extent in the hippocampus in the case of StPGA-CL-SS, demonstrating the brain diffusion ability for all carriers and even the possibility of a different distribution in brain areas depending on nanocarrier use.

In summary, the in vivo results demonstrated the feasibility of our intranasal platform for brain delivery when based on StPGAs and, in particular, when administered with HA-CP® as a vehicle, being able to successfully 1) reach the brain more efficiently

than intravenously administered analogs [43,44] with no sign of toxicity, and 2) localize in different brain areas in a time-dependent and specific manner depending on intrinsic architectural features.

Final demonstrations and quantifications of differential brain area accumulation represent ongoing tasks with further in vivo experiments employing readout fluorescence and MRI after labeling the nanocarriers with DOTA-Gd.

4.1.3 Rational Design and Synthesis of Polyglutamate-based Palbociclib Conjugates

After demonstrating that our StPGA nanocarriers reach and diffuse within the brain, we sought to demonstrate their capacity for intracellular drug transportation to achieve the desired anticancer therapeutic behavior for treating pediatric brain tumors. To pass cellular barriers and release cargoes in selected cells/organelles, drugs should be conjugated to the selected nanocarrier via responsive linkers susceptible to degradation under exogenous (i.e., radiation or light) or endogenous conditions as used herein (i.e., pH, redox, or protease levels). The presence of side-chain carboxylic acid groups in PGA-based nanocarriers enables the direct conjugation of drugs, targeted moieties, and fluorescent probes with adequate functionalities through, for example, esterification or amidation reactions [45]. Importantly, PGAs represent hydrophilic nanocarriers, and the conjugation of hydrophobic drugs may alter the solution conformation adopted depending on drug loading, and the nature of the polymer-drug liker used.
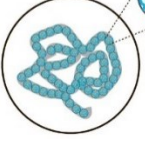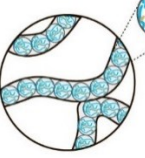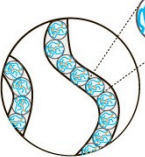
We selected palbociclib- a selective CDK 4/6 inhibitor.- based on the high efficacy reported in different GBM and medulloblastoma xenograft models[46,47]. Palbociclib was also recently evaluated in clinical trials for recurrent GBM in adults and children[48,49]. To study how nanoconjugate conformation affected the overall physicochemical and biological properties of the designed nanoconjugates, we developed a family of linear and star-shaped PGA conjugates of palbociclib and correlated nanoconjugate solution conformation, with palbociclib release kinetics, cell uptake and anticancer activity in each of the primary pediatric cell models used.

Palbociclib possesses a secondary amine and a keto group that can be used for conjugation. First, we attempted to establish the pH-responsive hydrazone linker between the carbonyl group of palbociclib and modified PGAs with hydrazide groups **(Chapter 3.2.1)**. However, we did not obtain the desired product, which can be attributed to the low reactivity of the keto-group, thereby impeding/limiting palbociclib conjugation. The functionalization of the secondary amine group of palbociclib via carbamate linkage was successful - we developed two synthetic procedures for self-immolative linkers via 1,5-cyclization for redox-responsive disulfide linkage **(Chapter 3.2.2)** and 1.6-quinone methide elimination for cathepsin B cleavable valine-citrulline linker **(Chapter 3.2.3)** and synthesized a family of conjugates. As a result of a five-step synthesis for the redox-responsive linker, we obtained StPGA-SS- palbociclib,

and LinPGA-SS-palbociclib conjugates with total drug loadings ranging from 3 to 15 wt% (Table 3.1). In parallel, via a six-step synthesis, we prepared analog conjugates utilizing a cathepsin B valine-citrulline (Val-Cit) linker and yielded StPGA-ValCit-palbociclib and LinPGA-ValCit-palbociclib conjugates with total drug loadings ranging from 7 to 12 wt% (Table 3.4). We evaluated the purity of each synthesis step and the final conjugates by ^{1}H NMR and 2D NMR. Dynamic light scattering (DLS) analysis confirmed similar hydrodynamic radius values in PBS (around 5 nm) for all conjugates, consistent with unimeric polymer-drug conjugates. All evaluated compounds displayed a net negative z-potential close to -30 mV. We also demonstrated that all conjugates possessed a homogeneous molecular weight distribution using SEC.

When evaluating conjugate conformation by circular dichroism (CD), we observed a clear transition from a random coil secondary structure to an α-helix upon increasing drug loading for the StPGA-based conjugates compared to linear analogs. Deconvolution of CD spectra confirmed the higher organization order of StPGA conjugates, with around 30% alpha-helix content for the highest drug loading conjugates with disulfide linker versus only 15% for linear analogs and conjugates with Val-Cit linker **(Chapter 3.2.2.1. and 3.2.3.1)**

To understand the above-noted findings, we performed small-angle X-ray scattering (SAXS) experiments at the ALBA synchrotron (Barcelona, Spain) **(Chapters 3.2.2.1. and 3.2.3.1)**. The results demonstrated that increased palbociclib loading conjugated through a Val-Cit linker non-significantly alters polymer structure, and we hypothesized the linker length as the critical parameter to trigger conformational changes. Contrary to the conjugates with disulfide linkers, we observed a well-defined isosbestic point on the SAXS profile, indicating the conformational changes only for StPGA conjugates. For the highest drug loading, we assume the formation of a highly organized structure, most probably core-shell micelles; on the contrary, we observed no significant differences in drug loading changes for StPGA conjugates with Val-Cit linker and for all linear PGA conjugates. The Kratky plot confirmed the SAXS profile analysis, where the influence of the hydrophobic drug on the molecule flexibility was evident for linear conjugates, and the signal proportionally increased with drug loading. The StPGA conjugates with disulfide linker instead displayed a dominant peak in the middle-q region of the graph, which indicates changes in molecule conformation and the presence of a more organized structure upon increasing conjugate drug loading. For Val-Cit conjugates with StPGA, we observed a similar but less pronounced trend. Overall, SAXS experiments allowed us to formulate an assembly model for linear, and StPGA-palbociclib conjugates with the corresponding description and model used for data fitting, as shown in the summary figure below.

Model	Crumpled globules of dense collapsed chains	Mass fractal of self-avoiding globules	Intermediate self-avoiding globules	Mass fractal of Gaussian chains	Fully swollen chains
Description	Secondary mass fractal structures further collapse, forming small dense micelles with a defined surface.	Higher level self-avoid-ding fractal aggregates start to form point-to-point interaction, creating secondary mass fractal structures.	Macromolecules form fractal protomicelles via mixed mechanisms. Protomicelles assemble into higher level self-avoid-ding fractal aggregates.	Macromolecules aggregate via point-to-point interactions, forming large diffuse fractal aggregates with partially screened electrostatic	Solution behaves as a simple polyelectrolyte with partially screened electrostatic interactions
Conjugates	StPGA-SS-palbo4, LinPGA-ValCit-palbo2*, LinPGA-ValCit-palbo3, StPGA-ValCit-palbo3	StPGA-ValCit-palbo2	LinPGA-SS-palbo4, StPGA-SS-palbo3, LinPGA-ValCit-palbo2*	LinPGA-SS-palbo2, LinPGA-SS-palbo3, StPGA-SS-palbo1, StPGA-SS-palbo2	LinPGA-SS-palbo1
Fitting model	$I(q) = \frac{s_1}{V} \cdot \int_0^{\frac{\pi}{2}} \left\lvert 2 \left\langle \frac{2J_1(qR\sin\alpha)}{qR\sin\alpha} \cdot \frac{\sin\left(\frac{qL\cos\alpha}{2}\right)}{\frac{qL\cos\alpha}{2}} \right\rangle \right\rvert^2 \cdot$ $\sin\alpha \, d\alpha + s_2 \cdot$ $\frac{3[\sin(qR)^2-(qR)^2\cos(qR)^2]}{(qR)^6} \cdot$ $\frac{\Gamma(D_m-1)\zeta^{D_m-1}}{[1+(q\zeta)^2]^{(D_m-1)/2}} \cdot$ $\sin[(D_m-1)\tan^{-1}(q\zeta)]$	$I(q) = s_1 \cdot$ $\frac{3[\sin(qR)^2-(qR)^2\cos(qR)^2]}{(qR)^6} \cdot$ $\frac{\Gamma_1(D_{m1}-1)\zeta_1^{D_{m1}-1}}{[1+(q\zeta_1)^2]^{(D_{m1}-1)/2}} \cdot$ $\sin[(D_{m1}-1)\tan^{-1}(q\zeta_1)] +$ $S_2 \cdot$ $\frac{3[\sin(qR)^2-(qR)^2\cos(qR)^2]}{(qR)^6} \cdot$ $\frac{\Gamma_2(D_{m2}-1)\zeta_2^{D_{m2}-1}}{[1+(q\zeta_2)^2]^{(D_{m2}-1)/2}} \cdot$ $\sin[(D_{m2}-1)\tan^{-1}(q\zeta_2)]$	$I(q) = s_1 \cdot$ $\frac{3[\sin(qR)^2-(qR)^2\cos(qR)^2]}{(qR)^6} \cdot$ $\frac{\Gamma_1(D_{m1}-1)\zeta_1^{D_{m1}-1}}{[1+(q\zeta_1)^2]^{(D_{m1}-1)/2}} \cdot$ $\sin[(D_{m1}-1)\tan^{-1}(q\zeta_1)] +$ $S_2 \cdot$ $\frac{3[\sin(qR)^2-(qR)^2\cos(qR)^2]}{(qR)^6} \cdot$ $\frac{\Gamma_2(D_{m2}-1)\zeta_2^{D_{m2}-1}}{[1+(q\zeta_2)^2]^{(D_{m2}-1)/2}} \cdot$ $\sin[(D_{m2}-1)\tan^{-1}(q\zeta_2)]$	$I(q) = I_1(q) + s \cdot$ $\frac{3[\sin(qR)^2-(qR)^2\cos(qR)^2]}{(qR)^6} \cdot$ $\frac{\Gamma(D_m-1)\zeta^{D_m-1}}{[1+(q\zeta)^2]^{(D_m-1)/2}} \cdot$ $\sin[(D_m-1)\tan^{-1}(q\zeta)]$	(a)** $I_1(q) = scale \cdot I(0) \cdot$ $2\left[\frac{1}{(1+(D-1)\frac{(qR_g)^2}{2D-1}} \right]^{\frac{1}{D-1}} + \frac{(qR_g)^2-}{2D-1}$ $\frac{(qR_g)^4}{D\frac{(2D-1)^2}{}}$ (b)** $I_1(q)$ $= \frac{98}{27 < R_g^2 > q^2} \left[\frac{3}{7} < R_g^2 \right.$ $> q^2 - e^{-\frac{3}{7} < R_g^2 > q^2}$ $\left. + e^{-\frac{6}{7} < R_g^2 > q^2} \right]$

Parameters used in the models: q is the magnitude of the scattering vector $q = (4\pi/\lambda) \sin(\theta/2)$, Đ is polydispersity, R_g is the radius of gyration, $< R_g^2 >$ is ensemble average R_g, R is the radius of the building block, Dm is the **mass** fractal dimension, ζ is the cut-off length, α is the angle between the axis of the cylinder and $\vec{q}$, L is the contour length of the cylinder, R is the radius of the cylinder, and J_1 is the first-order Bessel function.
* LinPGA-ValCit-palbo2 exists as a mixture of intermediate self-avoiding globules and crumpled micelles. ** $I_1(q)$ are shown separately for linear (Eq. (a)) and star-polymers (Eq. (b)).

Overall, SAXS and CD data demonstrate the evolution of the conjugate system upon increased drug loading. At very low loadings, conjugates behaved as simple polyelectrolytes and can be described with a model of fully swollen Gaussian chains (as electrostatic repulsions are partially screened in PBS solution, they are not considered in the model). Upon increased drug loading, macromolecules aggregate via point-to-point interactions to form large diffuse fractal aggregates. Upon further increases in loading, macromolecules start to compact and form fractal protomicelles via mixed mechanisms (point-to-point interactions and hydrophobic collapse). Protomicelles assemble into higher-level self-avoiding globules; however, it remains unclear whether they possess a structure of flexible cylinders or diffuse fractals. At even higher loading, conjugates collapsed into compact crumpled micelles (with a diameter below 50 nm).

To confirm linker responsiveness, we studied drug release kinetics of conjugates in simulated in vitro biological conditions with the presence/absence of the corresponding trigger for linker cleavage: dithiothreitol (DTT) at 5 mM (mimicking intracellular levels) and 10 μM (mimicking extracellular levels) for the redox-responsive linker; and cathepsin B – for the Val-Cit linker. Interestingly, we observed a delay in palbociclib release for the StPGAs with redox-responsive linkers with the highest drug loading compared to linear analogs. We observed 7% palbociclib release in 2 h compared to 20% from conjugates with low drug loading, which correlates with our previous conformational findings. We suggest that the dense structure of conjugates with high drug loading traps the drug within the polymeric nanoconstructs for longer; even so, the covalent bond between the drug and carrier is already broken. For conjugates with a peptidic linker, we observed a similar, less obvious trend for higher drug loading correlated with SAXS data, indicating a less compact structure than disulfide linker due to the longer linkage between palbociclib and PGA chains. For both types of linkers, we confirmed linker responsiveness. For the disulfide linker, we obtained more than 50% release after 8 h with 5 mM DTT but only 2% palbociclib release with 10 μM DTT. For the Val-Cit linker, we observed rapid drug release of more than 80% in 1 h with cathepsin B and good stability of the linker with less than 2% palbociclib release in the absence of cathepsin B.

4.1.4. Effect of Physico-chemical Characteristics of Polyglutamates-based Palbociclib Conjugates on their Biological Activity

As the next step after the in-depth characterization of PGA-based palbociclib conjugates, we aimed to correlate their physicochemical properties with their biological activity. Previous studies in our laboratory demonstrated the differential behavior of PGAs depending on the size and topology regarding cell uptake, blood circulation time, and organ biodistribution after intravenous administration [39]. In this regard, we investigated the toxicity of our family of conjugates in patient-derived GBM and DIPG tumor spheroids **(Chapters 3.2.2.2. and 3.2.3.2)**. We first analyzed naked polypeptidic carriers (StPGA150 and LinPGA100) and palbociclib with optimized MTS parameters.

The results demonstrated the non-toxic nature of naked PGA up to the concentrations evaluated; meanwhile, we observed an IC_{50} of palbociclib of 3.9 μM for both DIPG and GBM cells. As expected, subsequent evaluations of conjugates provided evidence of activity; however, this remained lower than the activity of the free palbociclib due to different cell trafficking – synthesized nanoconjugates follow endocytosis while palbociclib rapidly diffuses.

Importantly, disulfide linker conjugates demonstrated a robust inverse correlation between cell viability and drug loading: the higher the drug loading, the lower activity, with less evident differences in toxicity for linear conjugates with a similar tendency. These results demonstrated the importance of conformation and structural compactness of conjugates for in vitro cell viability; however, it remains unclear if the activity of conjugates with higher drug loading decreases or if this is the effect of drug release delay, as previously shown from the kinetic studies. Considering the exponential cellular growth in viability studies, a few hours of delay can significantly underestimate toxicity.

We observed higher activity of conjugates with disulfide linkers in DIPG cells, a finding related to higher intracellular glutathione levels (0.94 mM) compared to GBM cells (0.52 mM), which could prompt more significant linker cleavage, drug release, and therapeutic output. Therefore, GSH levels represent a biomarker to stratify patients that will maximally respond to this treatment strategy. Contrary to conjugates with Val-Cit linker, the differences between linear and StPGAs and discrepancies in toxicity for different drug loading remained less evident. These results agree with previous conformational studies, which demonstrated that palbociclib attached via a longer Val-Cit linker does not significantly affect the conjugate solution conformation; however, conjugates with peptidic linker displayed more significant activity in GBM cells compared to the disulfide linker. These results may be explained by the higher intracellular level of cathepsin B – 10.5 mM for GBM cells versus 2.7 mM for DIPG cells; therefore, optimal glioblastoma treatment should involve the ValCit linker.

In StPGA-palbociclib conjugates (in which the discrepancy in cell viability remained higher for different drug loadings), we performed cell cycle studies to confirm that drug conjugation does not affect the mechanism of action of palbociclib, which affects cell proliferation via cell cycle arrest [40]. The data revealed differences between GBM and DIPG cell lines, with 53% and 68% of GBM and DIPG cells in the G1/G0 phase, suggesting the higher proliferative status of GBM cells. For cells treated with conjugates, we discovered more than 90% of cells in the G1/G0 phase for DIPG and around 67% for GBM, demonstrating that conjugates can arrest cell proliferation; however, we did not observe a significant difference between conjugates with low and high drug loading, probably due to the already elevated activity of the conjugates, sample variability, and methodological limitations.

We then performed live-cell imaging with the Leica fluorescence confocal microscope to demonstrate that our polymer-drug conjugates penetrated tumor

spheroids. We labeled StPGA-palbociclib conjugates with Cy5.5 and the cell membrane with CellMask Green (Invitrogen Molecular Probes™). We also attempted to stain nuclei with DAPI; however, we observed the disintegration of the tumor spheroids due to the light toxicity caused by the laser. Thus, we removed the nucleus stain for further experiments and took images only after 24, 48, and 72 h post-incubation with the different treatments, mimicking the MTS assay protocol. Upon conjugate incubation, we observed apparent cell uptake and internalization processes after 24 h in both tumor spheroids, with increasing values up to 72 h. Of note, GBM spheroids did not significantly change in size and compactness up to 72 h post-treatment; however, we observed the partial disaggregation of DIPG spheroids at 72 h, in agreement with the more significant cytotoxicity observed in the DIPG cells upon treatment with palbociclib conjugates. This data allowed us to conclude that StPGA-palbociclib conjugates, besides the cell cycle arrest, also disrupt the morphology of DIPG tumor spheroids.

4.1.5. Evaluation of the Combination Therapy to Increase the Efficacy of Palbociclib

Due to the molecular heterogeneity and complexity of tumor cells, combining drugs that target different pathways represents a widely used strategy to increase the efficacy of anticancer therapy. In combination with palbociclib, we identified inavolisib (GDC-0077), an inhibitor of the α isoform of PI3K that displays much higher affinity to the mutant protein in tumor cells than to wild-type, demonstrating an excellent safety profile with no toxicity in primary human hepatocytes [41,42].

We evaluated the palbociclib: GDC0077 combination in cell viability studies in DIPG cells, as GDC0077 is highly active for the mutant type (**Chapter 3.3.1**). Using the Bliss model, we determined a ratio 1:3-5 palbociclib:GDC0077 as synergistic and moved toward the final combination nanosystem. As an initial approach, we use the free drug for combination studies with our synthesized palbociclib-conjugates, confirming the synergism in the same ratio (1:5). As GDC0077 does not have any functional group for polymer conjugation, we developed a suitable encapsulation protocol based on poloxamers F127 using thin film hydration, with 97% efficiency for 10% wt of drug encapsulation (**Chapter 3.3.2**). We envisioned the final formulation of identified combination as the hybrid methods of palbociclib conjugated to the StPGAs via a self-immolative linker (redox-responsive for DIPG and peptidic Val-Cit linker for GBM) and inavolisib encapsulated into poloxamers F127 micelles, and using the crosslinked HA-PGA hydrogel system as a vehicle for intranasal delivery.

4.2. References

1. Siegel, R. L., Miller, K. D., Fuchs, H. E. & Jemal, A. Cancer statistics, 2022. *CA. Cancer J. Clin.* **72**, 7–33 (2022).
2. Ward, E., DeSantis, C., Robbins, A., Kohler, B. & Jemal, A. Childhood and adolescent cancer statistics. *CA. Cancer J. Clin.* **64**, 83–103 (2014).
3. Steliarova-Foucher, E. *et al.* International incidence of childhood cancer, 2001-10: a population-based registry study. *Lancet. Oncol.* **18**, 719–731 (2017).
4. Johnson, K. J. *et al.* Childhood brain tumor epidemiology: a brain tumor epidemiology consortium review. *Cancer Epidemiol. biomarkers Prev. a Publ. Am. Assoc. Cancer Res. cosponsored by Am. Soc. Prev. Oncol.* **23**, 2716–2736 (2014).
5. Amirian, E. S. *et al.* Approaching a Scientific Consensus on the Association between Allergies and Glioma Risk: A Report from the Glioma International Case-Control Study. *Cancer Epidemiol. biomarkers Prev. a Publ. Am. Assoc. Cancer Res. cosponsored by Am. Soc. Prev. Oncol.* **25**, 282–290 (2016).
6. Louis, D. N. *et al.* The 2016 World Health Organization Classification of Tumors of the Central Nervous System: a summary. *Acta Neuropathol.* **131**, 803–820 (2016).
7. Sturm, D., Pfister, S. M. & Jones, D. T. W. Pediatric Gliomas: Current Concepts on Diagnosis, Biology, and Clinical Management. *J. Clin. Oncol.* **35**, 2370–2377 (2017).
8. Warren, K. E. Diffuse intrinsic pontine glioma: poised for progress. *Front. Oncol.* **2**, 205 (2012).
9. Hauser, P. Classification and Treatment of Pediatric Gliomas in the Molecular Era. *Child. (Basel, Switzerland)* **8**, (2021).
10. Agrawal, M. *et al.* Nose-to-brain drug delivery: An update on clinical challenges and progress towards approval of anti-Alzheimer drugs. *J. Control. Release* **281**, 139–177 (2018).
11. Duro-Castano, A., Movellan, J. & Vicent, M. J. Smart branched polymer drug conjugates as nano-sized drug delivery systems. *Biomater. Sci.* **3**, 1321–1334 (2015).
12. Conejos-Sánchez, I., Duro-Castano, A., Birke, A., Barz, M. & Vicent, M. J. A controlled and versatile NCA polymerization method for the synthesis of polypeptides. *Polym. Chem.* **4**, 3182–3186 (2013).
13. Vicent Docón, M.j., Duro Castaño, A., Nebot Carda, V. J. WO 2017/025298 A1. 150 (2017).
14. Wen, Z. *et al.* Brain targeting and toxicity study of odorranalectin-conjugated nanoparticles following intranasal administration. *Drug Deliv.* **18**, 555–561 (2011).
15. Wen, Z. *et al.* Odorranalectin-conjugated nanoparticles: Preparation, brain delivery and pharmacodynamic study on Parkinson's disease following intranasal administration. *J. Control. Release* **151**, 131–138 (2011).
16. Yang, X. *et al.* Intranasal Delivery of BACE1 siRNA and Rapamycin by Dual Targets Modified Nanoparticles for Alzheimer's Disease Therapy. *Small* **18**, e2203182 (2022).
17. Chen, J. *et al.* Solanum tuberosum lectin-conjugated PLGA nanoparticles for nose-to-brain delivery: In vivo and in vitro evaluations. *J. Drug Target.* **20**, 174–184 (2012).
18. Gao, X. *et al.* UEA I-bearing nanoparticles for brain delivery following intranasal administration. *Int. J. Pharm.* **340**, 207–215 (2007).
19. Wu, H. *et al.* A novel small Odorranalectin-bearing cubosomes: Preparation, brain delivery and pharmacodynamic study on amyloid-β 25-35-treated rats following intranasal administration. *Eur. J. Pharm. Biopharm.* **80**, 368–378 (2012).
20. Sandri, G. *et al.* Mucoadhesive and penetration enhancement properties of three grades of hyaluronic acid using porcine buccal and vaginal tissue, Caco-2 cell lines, and rat jejunum. *J. Pharm. Pharmacol.* **56**, 1083–1090 (2004).
21. Rydén, L. & Edman, P. Effect of polymers and microspheres on the nasal absorption of insulin in rats. *Int. J. Pharm.* **83**, 1–10 (1992).

22. Morimoto, K. *et al.* Effects of viscous hyaluronate-sodium solutions on the nasal absorption of vasopressin and an analogue. *Pharm. Res.* **8**, 471–474 (1991).

23. Pritchard, K. *et al.* Evaluation of the bioadhesive properties of hyaluronan derivatives: Detachment weight and mucociliary transport rate studies. *Int. J. Pharm.* **129**, 137–145 (1996).

24. Shinde, R. L., Bharkad, G. P. & Devarajan, P. V. Intranasal microemulsion for targeted nose to brain delivery in neurocysticercosis : Role of docosahexaenoic acid. *Eur. J. Pharm. Biopharm.* **96**, 363–379 (2015).

25. Madane, R. G. & Mahajan, H. S. Curcumin-loaded nanostructured lipid carriers (NLCs) for nasal administration: design, characterization, and in vivo study. *Drug Deliv.* **23**, 1326–1334 (2016).

26. Li, J. *et al.* Odorranalectin is a small peptide lectin with potential for drug delivery and targeting. *PLoS One* **3**, 1–10 (2008).

27. Lundh, B., Brockstedt, U. & Kristensson, K. Lectin-binding pattern of neuroepithelial and respiratory epithelial cells in the mouse nasal cavity. *Histochem. J.* **21**, 33–43 (1989).

28. Docón, M. J. V., Carda, V. J. N., Bolumar, D. M. & England, R. M. WO/2019/020344 Cross Polymers Composed Of Polysaccharides And Polyamino Acids, And Uses Thereof. (2019).

29. Duro-Castano, A. *et al.* Capturing "Extraordinary" Soft-Assembled Charge-Like Polypeptides as a Strategy for Nanocarrier Design. *Adv. Mater.* **29**, 1702888 (2017).

30. Leitner, V. M., Walker, G. F. & Bernkop-Schnürch, A. Thiolated polymers: evidence for the formation of disulphide bonds with mucus glycoproteins. *Eur. J. Pharm. Biopharm. Off. J. Arbeitsgemeinschaft fur Pharm. Verfahrenstechnik e.V* **56**, 207–214 (2003).

31. Bernkop-Schnürch, A. Thiomers: A new generation of mucoadhesive polymers. *Adv. Drug Deliv. Rev.* **57**, 1569–1582 (2005).

32. Dolz-Pérez, I. *et al.* Polypeptide-corticosteroid conjugates as a topical treatment approach to psoriasis. *J. Control. Release* **318**, 210–222 (2020).

33. Pardridge, W. M. Blood-Brain Barrier and Delivery of Protein and Gene Therapeutics to Brain. *Front. Aging Neurosci.* **11**, 373 (2019).

34. Li, C. Poly(l-glutamic acid)–anticancer drug conjugates. *Adv. Drug Deliv. Rev.* **54**, 695–713 (2002).

35. Michaud, K. *et al.* Pharmacologic inhibition of cyclin-dependent kinases 4 and 6 arrests the growth of glioblastoma multiforme intracranial xenografts. *Cancer Res.* **70**, 3228–3238 (2010).

36. Cook Sangar, M. L. *et al.* Inhibition of CDK4/6 by palbociclib significantly extends survival in medulloblastoma patient-derived xenograft mouse models. *Clin. Cancer Res.* **23**, 5802–5813 (2017).

37. Taylor, J. W. *et al.* Phase-2 trial of palbociclib in adult patients with recurrent RB1-positive glioblastoma. *J. Neurooncol.* **140**, 477–483 (2018).

38. Van Mater, D. *et al.* A phase I trial of the CDK 4/6 inhibitor palbociclibin pediatric patients with progressive brain tumors: A Pediatric Brain Tumor Consortium study (PBTC-042). *Pediatr. Blood Cancer* **68**, 1–10 (2021).

39. Duro-Castano, A. *et al.* Well-Defined Star-Shaped Polyglutamates with Improved Pharmacokinetic Profiles As Excellent Candidates for Biomedical Applications. *Mol. Pharm.* **12**, 3639–3649 (2015).

40. Álvarez-Fernández, M. & Malumbres, M. Mechanisms of Sensitivity and Resistance to CDK4/6 Inhibition. *Cancer Cell* **37**, 514–529 (2020).

41. Song, K. W. *et al.* RTK-Dependent Inducible Degradation of Mutant PI3Kα Drives GDC-0077 (Inavolisib) Efficacy. *Cancer Discov.* **12**, 204–219 (2022).

42. Brito, C. *et al.* PIK3CA Mutations in Diffuse Gliomas: An Update on Molecular Stratification, Prognosis, Recurrence, and Aggressiveness. *Clin. Med. Insights. Oncol.* **16**, 11795549211068804 (2022).

Chapter 5

Final Conclusions

The work carried out during the development of this thesis provides evidence for the successful generation of an intranasal polypeptide-based platform for pediatric brain tumor treatment. Herein, we highlight the primary outcomes of this work:

Chapter 2

1. We successfully synthesized linear and star-shaped poly-L-glutamic acid carriers using NCA-ROP with PDI below 1.10.

2. We selected hyaluronic acid (HA), docosahexaenoic acid (DHA), and odorranalectin peptide (OL) as promising candidates to enhance brain delivery efficacy after intranasal administration. We successfully developed synthetic protocols for post-polymerization modification of polyglutamates with the aforementioned compounds. To study how the size of the carrier affects mucosal permeation, we prepared crosslinked PGA nanoconstructs with non-cleaveable (via azide-alkyne cycloaddition click chemistry strategy) and redox labile disulfide bonds with the size of ~90 nm and ~200 nm. We also tested a hydrogel system (HA-CP) prepared from HA and polyglutamic acid crosslinked with L-lysine provided by Polypeptide Therapeutic Solutions S.L. (Valencia, Spain) and the physical mixture of HA and StPGA to compare with the covalently bound HA system.

3. To screen our polymeric carrier systems, we successfully established an ex-vivo model based on vertical Franz diffusion cells with sheep mucosa to mimic human tissue. From the kinetic profiles observed in the permeation study, we identified the relevance of (i) *mucodiffusive ligand exposure* – lower exposure promoted aggregation of DHA and thus inhibits permeation; (ii) *carrier topology* – star-shaped PGAs displayed more rapid permeation than linear analogs; (iii) *size* – large particles displayed poor diffusion; however, crosslinked carriers via disulfide bonds demonstrated enhanced permeation and highlighted the importance of the mucodiffusive component; (iv) *HA modification* – slightly improved the permeation compare to unmodified StPGA; (v) *hydrogel HA-CP and physical mixture StPGA and HA* - demonstrated initially slow kinetics but comparable to StPGA or higher accumulation level (in case of HA-CP) at 24 h, which may find use in sustainable drug release; and (vi) *odorranalectin modification* - demonstrated the most rapid permeation among all evaluated compounds.

4. The in vivo biodistribution studies validated our PGA-based intranasal platform as reaching and diffusing through the brain. The StPGA carriers modified with OL peptides and StPGA crosslinked via disulfide bonds incorporated into hydrogel HA-CP vehicle demonstrated 2.4 and 2.2 %AD brain accumulation.

Chapter 3

1. We designed two self-immolative linkers (a redox-responsive disulfide and a cathepsin B-responsive ValCit linker) and successfully conjugated the selected model drug palbociclib to both LinPGA and StPGA carriers with different drug loading.

2. The structure characterization with CD and small-angle X-ray scattering (SAXS) experiments demonstrated the evolution of the polymer-drug system upon increasing the drug loading. Based on SAXS data, we suggested the fitting models for prepared conjugates from unorganized simple polyelectrolyte solution described by the Fully swollen chains model (conjugates with low drug loading) to the crumpled globules with collapsed chains model (conjugates with the highest drug loading). The length of the linker is inversely correlated with the magnitude of drug influence on the carrier structure: the shorter the linker, the higher the drug influence.

3. The type of the linker and drug loading significantly influence the release profile. For the peptidic linker, the kinetic studies with cathepsin B demonstrated a rapid drug release for all conjugates independently on drug

loading: more than > 80% of the drug was released at 1h. Contrary to the shorter redox responsive linker upon 5mM DTT trigger (intracellular conditions), we observed a delay in the palbociclib release for conjugates with the highest drug loading – we observed more than 50% drug release at 6 h for conjugates with % w/w 5.1, 7.5 and at 16 h for conjugate with % w/w 13.4. For both linkers, the drug release without cathepsin B or upon 10 μM trigger (extracellular conditions) remained below 3%, demonstrating the stability of the linker and trigger responsiveness. The kinetics data corroborated our model derived from the SAXS data and suggested the surface drug allocation for conjugates with a long peptidic linker, contrary to the drug shielding inside the micelles in the case of a disulfide linker.

4. LinPGA- and StPGA-palbociclib conjugates displayed robust cytotoxic activities in patient-derived glioblastoma (GBM) and diffuse intrinsic pontine glioma (DIPG) cell lines determined by MTS assay in vitro. Conjugates with peptidic linkers displayed more significant activity in GBM cells, which correlated with almost four times higher levels of cathepsin B than DIPG cells. Conjugates with disulfide linker displayed higher cytotoxicity in DIPG cells, which aligned with two times higher GSH levels in this cell line. Importantly, we observed a strong correlation between cell viability and drug loading for the conjugates - the higher the drug loading, the lower activity – which can be attributed to the differential conjugate solution conformation and agrees with structural data obtained from SAXS experiments. Of note, the lower toxicity of conjugates with high drug loading resulted from delayed drug release due to the more compact structure, and the exponential cell growth in MTS assay results in a significant impact. However, in an in vivo scenario, the compact structure of a drug delivery system may be more beneficial and allow greater stability and, thus, improved safety.

5. As an enhancement of palbociclib therapy, we identified a synergistic drug combination of palbociclib and inavolisib (GDC0077) for DIPG cells. Due to the lack of an available functional group of Inavolisib, we optimized the micellization procedure using F127® poloxamer. The selected systems have already been scaled up, and the preparation for biological evaluation in an in vivo patient-derived model is ongoing.